Simulation of water-vapor two-phase flows with non-condensable gas.

Lucie Quibel

Thèse

INSTITUT DE RECHERCHE MATHÉMATIQUE AVANCÉE

UMR 7501

Strasbourg

présentée pour obtenir le grade de docteur de l'Université de Strasbourg
Spécialité MATHÉMATIQUES APPLIQUÉES

Lucie Quibel

Simulation d'écoulements diphasiques eau-vapeur en présence d'incondensables

Soutenue le 18 Septembre 2020
devant la commission d'examen

Philippe Helluy, directeur de thèse
Héloïse Beaugendre, rapporteur
Christophe Chalons, rapporteur
Gloria Faccanoni, examinateur
Yannick Hoarau, examinateur
Olivier Hurisse, examinateur

irma.math.unistra.fr

IRMA
Institut de Recherche Mathématique Avancée

cnrs

Université de Strasbourg

Université de Strasbourg

UNIVERSITÉ DE STRASBOURG

ÉCOLE DOCTORALE nº 269
Mathématiques, Sciences de l'Information et de l'Ingénieur (MSII)

UMR Nº 7501
UMR Institut de Recherche en Mathématique Avancée (IRMA)

THÈSE présentée par :

Lucie QUIBEL

soutenue le : **18 septembre 2020**

pour obtenir le grade de : **Docteur de l'Université de Strasbourg**

Discipline/Spécialité : Mathématiques

Simulation d'écoulements diphasiques eau-vapeur en présence d'incondensables

THÈSE DIRIGÉE PAR :
M. Philippe HELLUY, Professeur, Université de Strasbourg

RAPPORTEURS :
Mme Héloïse BEAUGENDRE, Maître de Conférences, Université de Bordeaux
M. Christophe CHALONS, Professeur, Université de Versailles Saint-Quentin-en-Yvelines

AUTRES MEMBRES DU JURY :
M. Yannick HOARAU, Professeur, Université de Strasbourg
Mme Gloria FACCANONI, Maître de Conférences, Université de Toulon
M. Olivier HURISSE, Ingénieur-Chercheur, EDF R&D, Encadrant industriel

Contents

Remerciements

J'ai essayé de faire tenir mes remerciements en une belle page aérée, je le promets... mais c'est un échec patent. Tant pis, ce sont trois pages fleuves qui s'annoncent.

Ce travail a été réalisé au sein du département Mécanique des Fluides Energie et Environnement d'EDF R&D à Chatou. Je tiens à remercier Isabelle Flour, chef du département MFEE ainsi que Thomas Papaconstantinou, ancien chef adjoint du département. Merci à mes deux chefs de groupe successifs : à Bruno Audebert de m'avoir laissé une seconde chance après mon premier entretien raté, et à Christelle Raynaud de m'avoir témoigné toute sa confiance aux moments importants. Plus généralement, je tiens à remercier tous les membres du groupe Incendies et Accidents Graves, qui m'ont intégrée à l'équipe dès mon arrivée en stage et qui ont tous contribué à créer un cadre agréable pour cette thèse.

Merci à Héloïse Beaugendre et à Christophe Chalons d'avoir rapporté très attentivement et avec une grande précision sur ce manuscrit, ainsi qu'à Gloria Faccanoni et Yannick Hoarau d'avoir accepté d'être membres de mon jury de thèse. Merci à tous pour votre gentillesse et votre bonne volonté, qui auront permis d'organiser la soutenance au mieux, malgré un contexte sanitaire et ferroviaire compliqué. Merci également à Samuel Kokh de m'avoir soufflé la bonne idée pour retransmettre la visio et à Guillaume Jomée d'avoir passé un temps non négligeable à m'aider à la mettre en place.

Merci à Philippe Helluy mon directeur de thèse, pour son implication dans ce travail malgré la distance et ses idées toujours novatrices.

Merci à Olivier Hurisse, mon encadrant de thèse à EDF. Merci pour ton soutien au quotidien, ton enthousiasme pour la technique et la confiance dont tu m'as toujours témoigné. Ta force tranquille et tes passions ont été très inspirantes pour moi.

Impossible de ne pas avoir un mot particulier pour Jean-Marc Hérard. Un immense merci Jean-Marc. Merci d'avoir toujours suivi mon travail, depuis ma soutenance de stage jusqu'à ma soutenance de thèse (où heureusement que tu t'es démené pour arriver l'avant-veille, nous n'avons pas chômé !). Merci pour tes conseils avisés qui se sont toujours révélés déterminants pour envoyer la balle. Merci de m'avoir incité et aidé à donner des cours en L1 à Jussieu : ce fut extrêmement formateur et cela a débloqué beaucoup de choses en me donnant beaucoup plus d'assurance. Merci de m'avoir proposé de travailler avec toi sur la modélisation de cet écoulement triphasique à quatre champs : alors que certains volets de ma thèse ont requis beaucoup d'opiniâtreté, ce fut une vraie partie de plaisir que tu m'as offert là (oui, malgré les 30 feuilles A3 de calculs pour prouver le caractère LD de cette sacrée onde de couplage). Merci enfin pour tout le reste : les cafés du matin, nos discussions cartes IGN, cinéma et j'en passe. Merci de m'avoir fait confiance et d'avoir partagé tant de choses avec moi, d'un point de vue professionnel comme d'un point de vue personnel.

Merci également à Fatiha Nmira d'avoir toujours gardé un oeil discret mais attentif sur mon travail. Merci de m'avoir toujours prise au sérieux et de m'avoir aidé à appeler au secours aux moments clefs.

Un grand merci à tous les trois encore. Nos discussions méridiennes, à rêver de montagne, à spleener sur le devenir du monde ou à débriefer les plénières, me manqueront, c'est certain.

Un petit mot pour les autres doctorants que j'ai côtoyés à EDF et très brièvement à Strasbourg. Je salue ici mes collègues de promo, Li, Riccardo et Vladimir, ainsi que mes aînés Charles, David, Clément, Gaëtan, Meissam,

Cécile, Thibaut, Sarah, Hamza et William et j'envoie tous mes encouragements aux suivants, notamment Manon et Ali. A nouveau, un petit mot particulier pour toi Guillaume : je te souhaite le meilleur pour la suite et j'espère que tu t'amuseras autant que moi avec tes écoulements triphasiques ! Et merci à Marie et Philippe, mes collègues strasbourgeois de la SEME : ce fut une semaine très sympathique que celle passée à vos côtés et j'ai beaucoup apprécié de vous recroiser à Strasbourg ensuite.

Durant ces trois années, j'ai eu la chance de rencontrer beaucoup de gens différents, à EDF comme dans le milieu universitaire. J'ai une petite pensée particulière pour Florence D., Sofiane H., Kresna A., Erik d.M., Sébastien T., Franchine N., ou encore Aline W., avec qui j'ai eu plaisir à discuter et à échanger sur leurs parcours.

Une thèse, ce n'est pas un long fleuve tranquille et je n'aurais pas été au bout de ce travail sans le soutien sans faille de mes proches que je souhaite remercier ici du fond du coeur.

Je commence par toi Antoine. Car tout ceci a commencé avec toi, qui m'a conseillé pour trouver mon stage de fin d'études et qui m'a ramassé à la petite cuillère pour rebondir et réussir mon second entretien. Merci pour ton soutien indéfectible au quotidien pendant ces quatre ans. C'est tellement dur de te remercier en quelques lignes, c'est pourquoi je reviendrai à toi un peu plus tard.

Merci au Centre groupe d'être là depuis tant d'années et de m'avoir aidé à faire la part des choses quand j'en avais besoin. Merci d'avoir été à fond derrière moi pendant la retransmission de la soutenance en visio, on eût dit que vous assistiez à un match de foot !!! Merci beaucoup de former cette belle famille hétéroclite avec des membres de tous horizons (car oui, qu'on se le dise, ma famille habite dans le Loir-et-Cher). Plus précisément, merci à :

Marie Bo., Elodie (accompagnée de Richard) et Cassandre qui sont là depuis plus de 14 (!) ans;

les néo-parisiens Amandine & Ahmed, Cécile, Edwige & Gaël, Lydie et Gaylord : une spéciale dédicace à nos karaokés endiablés !;

les Tourangeaux Gaëlle & Thomas, ainsi que Léna, témoin d'une fiabilité sans faille, & Rémi, certainement un des seuls à avoir lu mon premier article;

Charlotte & Thomas exilés dans le Perche;

et les irréductibles Vendômois Céline & Dom et Marie G. & Thomas.

Je termine par ma sister Marie, qui m'inspire énormément et à qui je souhaite plein de belles aventures à la découverte des trésors de cette planète aux côtés d'Andries.

Merci à Marine et Claudine, à la bonne humeur inébranlable, sans qui je n'aurais jamais survécu à la prépa. Claudine, ça m'inspire grave que tu te frottes les mains quand tu vois un problème survenir. Marine, mon distributeur de sourires et de conseils attitré, ma témoin toujours présente, merci pour ton soutien sans faille. Toi aussi tu es une vraie pro pour me ramasser à la petite cuillère. Décidemment, vivent les cuillères : c'est tellement festif une cuillère, et c'est surtout hyper pratique pour manger 1,5 kg de beurre (salé), la chose la plus réconfortante au monde.

J'en arrive à la Team "Tous à Bord" ! Marie, littéralement ma première témoin, avant même le départ en Russie, à la sincérité désarmante; Mathilde, avec qui j'ai partagé tous mes états d'âme je crois, car toi seule comprends comment on peut être aussi stressée ;) Deux angoissées de la vie, ça va loin, même jusqu'en Chine et en Russie, surtout quand on a des épinards dans le frigo...; Barbara, pour ton dévouement à la Science et ton acharnement à la pédagogie qui ont été de vrais moteurs dans mon travail; Julie évidemment, toujours partante, et pour qui rien n'est impossible ! Et une énorme pensée pour Lidia, qui me manque beaucoup, mais que j'ai hâte de revoir, à Madrid, dans le Sud, ou n'importe où ailleurs.

Merci aux Camarades de la guilde Vendômoise, Guillaume, Julie et Cécile (et oui encore !) ! Toujours partants pour un resto à refaire le monde et à débattre de qui est devenu le plus bobo d'entre nous. Votre sincérité et nos éclats de rire auront été de précieux atouts dans les moments difficiles. Un petit mot particulier pour toi, cher camarade Guigui, liés à jamais par l'ordre alphabétique : merci de t'être toujours intéressé à mes recherches et je te souhaite le meilleur pour la fin des tiennes.

Dans la même veine, merci à Alexis, notre voisin en or, pour tous les (trop) nombreux verres à la Butte aux Cailles, qui nous auront même menés dans les Yvelines et dans le Loir-et-Cher, qui l'eût cru. Quand tu veux pour un petit périple à coup de Racat'mobile !

Merci à Larissa, ma tandem, pour nos "Jours Fixes" hebdomadaires. Grâce à toi, j'ai toujours eu l'impression de progresser au moins une fois par semaine ! Vielen Dank und Prost ! J'en profite pour adresser un petit mot aux doctorants chimistes du MMC, qui m'ont souvent accueillie bien volontiers dans leurs soirées : j'ai eu un grand plaisir à découvrir la vie étudiante du quartier Latin avec vous.

Avec la fin de la thèse, c'est aussi la vie parisienne qui s'achève. Ce fut une chouette période, où j'ai adoré rencontrer beaucoup de gens très différents. Je salue en particulier Eva, Leslie, Mathilde, Etienne, J-D, Lucile et Miléna, et tous les autres que j'oublie forcément.

Un petit mot pour Tiphaine : merci pour tous ces messages (pardon : romans) où je t'ai raconté les hauts, les bas, les joies et les peines de cette thèse, mais aussi avant cela, de mes études à l'ENSTA.

Merci à Anne-Christine D., qui m'a transmis le goût des études et la joie dans l'effort grâce à ses cours de latins. Face aux obstacles les plus inexpugnables, je garde cette maxime en exergue dans mon coeur : Macte animo generose puer sic itur ad astra.

Merci à mes parents, qui m'ont toujours soutenue dans mes études et au-delà. Merci d'avoir toujours cru en moi, de m'avoir inculqué des valeurs fortes, le sens du travail et la joie des choses simples. Merci de m'avoir toujours écoutée sans me raccrocher au nez, même quand je radotais des heures durant sur mes équations d'état qui faisaient n'importe quoi ou sur mon code qui bugguait sans raison. Merci pour vos conseils et votre bienveillance. Merci de nous avoir recueillis en mars 2020 : grâce à vous, cette période particulière fut très douce à vivre. La qualité finale de mon manuscrit vous doit beaucoup, j'ai eu des conditions de rêve pour terminer cette thèse à vos côtés. Merci à Jeanne et Pierre-Louis de supporter votre grande soeur relou. Heureusement que vous êtes là pour me faire rire quand ça ne va pas. Merci ma petite soeurette de m'avoir accueillie chez toi régulièrement, en particulier quand je donnais mes cours à Jussieu, avec du chocolat et les reines du shopping pour les jours difficiles et d'avoir géré Twitch à l'heure fatidique. Merci Loulou d'avoir traversé la France entière pour être là le jour J, et pour le taux d'humidité à 55% : tu as contribué directement à la mise en données du chapitre 3 ! Je vous souhaite beaucoup de succès à tous les deux et j'ai hâte de venir vous embêter bientôt en chair et en os.

Je vous aime tous les quatre très fort. Un énorme merci d'être tous venus à la soutenance, malgré les kilomètres et les incertitudes, et d'avoir fait de ce moment un chouette moment, alors que ça n'était pas gagné.

Et je finis par toi Antoine. Car ce travail, je l'ai mené à termes grâce à toi : à toi qui m'as écouté râler chaque soir, qui as supporté mes crises de nerfs après les retours difficiles en RER, qui as dû me rassurer contre le coronavirus, les inondations, le monde du travail et les retards de train. A toi qui m'as aidé à voir tout ce que j'avais déjà accompli plutôt de me focaliser sur ce qui ne marchait pas. A toi qui m'as fait relativiser quand j'en avais besoin. A toi qui m'as inspiré grâce à ton propre travail de thèse et qui m'as donné envie de faire aussi bien que toi. A toi qui m'as soutenue à bout de bras dans les deux dernières semaines pré-soutenance et qui s'es battu comme un beau diable pour en faire un truc sympa, alors que tout partait en vrille. Ta confiance rayonne, me protège et me rend plus forte. J'admire tellement ta pugnacité et ton enthousiasme, je suis fière que tu m'aies choisie, je n'en reviens toujours pas. J'ai eu une chance incroyable de te rencontrer et de vivre avec toi et je remercie la vie pour ça. Tout continue avec toi à présent, j'ai hâte de voir ce que la suite nous réserve. Je t'aime et je te dédie ce manuscrit.

Introduction

Cette thèse a pu être menée suite au contrat EDF-CIFRE 2017/0476. Elle s'est déroulée au sein du département Mécanique des Fluides, Énergie et Environnement (MFEE) sur le site EDF Lab à Chatou, en collaboration avec l'Institut de Recherche Mathématique Avancée (IRMA, UMR 7501) à Strasbourg.

1 Contexte industriel

1.1 Sûreté des réacteurs à eau pressurisée (REP)

La France compte à l'heure actuelle 57 réacteurs nucléaires. EDF, en tant qu'exploitant, est responsable de la sûreté de ces installations. En pratique, la stratégie de défense en profondeur est appliquée : plusieurs niveaux de protection sont mis en place, s'échelonnant graduellement de procédures en fonctionnement nominal, à la prévention des incidents plus ou moins graves jusqu'à la gestion de crise en cas d'accident. La philosophie de cette doctrine consiste à questionner la vulnérabilité de chaque dispositif de sûreté, et de le doubler par un autre dispositif indépendant. L'objectif global est ainsi de maintenir le confinement de la radioactivité quoi qu'il arrive. Dans ce cadre, la R&D d'EDF développe des outils numériques visant à simuler des scénarios accidentels. Leur étude permet d'améliorer en permanence la sûreté des installations, que ce soit pour la conception des nouveaux réacteurs comme les EPR (European Pressurized Reactor), lors des réexamens périodiques de sûreté des centrales, ou encore pour évaluer l'extension de la durée d'exploitation des réacteurs actuels au-delà de 40 ans.

Les réacteurs français sont tous des réacteurs à eau pressurisée (REP). Leur principe général est le suivant : la réaction nucléaire de fission a lieu dans le coeur du réacteur, situé dans la cuve. Ce coeur est composé par des assemblages combustibles (entre 150 et 200), regroupant chacun 264 crayons. Un crayon est en fait un tube entouré d'une gaine en alliage de zirconium, où sont empilées 272 pastilles de combustible. La gaine constitue donc la première barrière d'étanchéité empêchant la dispersion de radioactivité des produits de la réaction de fission. Le fluide caloporteur est l'eau, qui va extraire la chaleur produite lors de la réaction nucléaire. Les échanges de chaleur ont lieu grâce à trois circuits indépendants (figure 1) :

- le circuit primaire, dans lequel de l'eau pressurisée à 155 bars extrait la chaleur issue de la réaction de fission en circulant à travers le coeur au contact des crayons des assemblages combustible. La température de cette eau est d'environ 300 °C. Le circuit primaire constitue la deuxième barrière de confinement de la radioactivité, la dernière barrière étant l'enceinte du bâtiment réacteur.

- l'eau du circuit secondaire, à plus basse pression (entre 60 et 80 bars), est chauffée par l'eau du circuit primaire dans le générateur de vapeur (GV) jusqu'à 280 °C. La vapeur ainsi créée va alimenter les turbines, qui elles mêmes vont actionner l'alternateur pour

générer de l'électricité. La vapeur passe enfin dans le condenseur et revient à l'état liquide. Ainsi, contrairement au circuit primaire où l'eau reste toujours à l'état liquide en fonctionnement nominal, le changement de phase est inhérent au fonctionnement du circuit secondaire.

- le circuit tertiaire, qui permet de refroidir la vapeur du circuit secondaire afin de la recondenser.

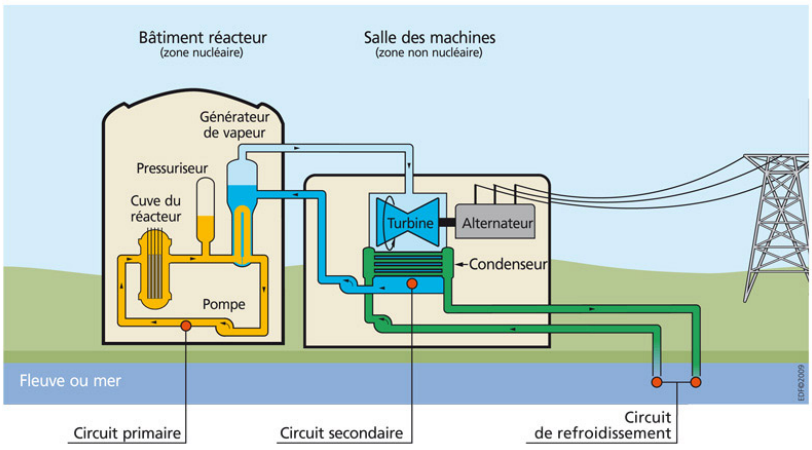

FIGURE 1 – *Schéma décrivant le fonctionnement d'un réacteur à eau pressurisée (REP) ; source : IRSN*

Cette thèse s'intéresse à des scénarios accidentels pouvant hypothétiquement affecter le circuit primaire du réacteur, au cours desquels des écoulements multiphasiques peuvent apparaître. Le champ d'application des modèles sur lesquels nous avons travaillé concerne plus généralement tout type d'écoulements multiphasiques comprenant de l'eau pouvant subir un changement de phase.

1.2 Scénarios accidentels étudiés

Cette thèse vise à simuler les scénarios accidentels suivants :

- l'Accident de Perte de Réfrigérant Primaire (APRP), dans lequel on envisage une brèche dans le circuit primaire, entraînant une dépressurisation brutale conduisant à la vaporisation soudaine de l'eau liquide pressurisée en vapeur ;

- l'explosion vapeur, qui pourrait se produire suite à un accident grave menant à la fonte du coeur : en effet, le mélange de combustible et de gaine fondus, appelé corium, extrêmement chaud, pourrait percer la cuve et entrer en contact avec de l'eau plus froide qui pourrait être retenue dans le puits de cuve. L'écart de température serait tel que l'eau subirait une vaporisation très brutale, qui conduirait à la formation d'ondes de choc très violentes.

Les phénomènes précédents impliquent des situations de transitoires rapides, dans lesquelles l'eau liquide va brutalement se vaporiser, causant des ondes de choc pouvant potentiellement endommager les structures. Etant donné la dangerosité des phénomènes étudiés, les manipulations et installations expérimentales sont très complexes à mettre en oeuvre et relativement peu de données sont disponibles. Les essais principaux ayant permis de développer le logiciel thermohydraulique de référence CATHARE [8], listés dans [22], ont eu lieu dans les années 80 et 90 sur le site du CEA à Grenoble et constituent une base de données

encore largement utilisée. A l'heure actuelle, les outils de modélisation, notamment les outils CFD, permettent de suppléer partiellement aux essais expérimentaux à grande échelle (de toutes façons quasiment impossibles à réaliser), car ils permettent notamment de mieux évaluer les incertitudes d'une mesure expérimentale, et de cibler précisément les manipulations complémentaires à mettre en place.

Compte-tenu de cette importance des outils numériques, les logiciels de simulation doivent répondre à un cahier des charges très strict pour être certifiés par l'Autorité de Sûreté Nucléaire (ASN). En particulier, le guide 28 de l'ASN [40] précise ainsi qu'un code de calcul se doit d'être **vérifié** puis **validé** :

- la **vérification** consiste à s'assurer que les équations du modèle proposé sont correctement résolues d'un point de vue mathématique et informatique ; dans cette thèse, nous nous sommes attachés à utiliser des modèles pour lesquels des solutions analytiques pouvaient être exhibées, et à réaliser des études de convergence en maillage permettant de vérifier la consistance des méthodes numériques utilisées (voir chapitres 1, 3, 5) ;

- la **validation** consiste à éprouver la pertinence physique de notre modèle en se comparant à des données expérimentales. Dans cette thèse, nous nous sommes essentiellement appuyés sur des cas tests de type SUPERCANON [74], visant à simuler un APRP (voir chapitre 3).

2 Contexte scientifique

Les écoulements mis en jeu dans les situations accidentelles d'intérêt sont donc des écoulements multiphasiques subissant des situations de transitoires rapides, où les composants suivants peuvent être présents :

- l'eau, présente sous forme liquide comme sous forme vapeur ;

- les gaz, qualifiés d'incondensables, dont l'air ambiant, présent dans le bâtiment réacteur, et les éventuels produits de dégradation de la gaine (hydrogène...) ;

- éventuellement, dans le cas de l'explosion vapeur, le corium fondu.

Nous précisons le vocabulaire utilisé dans la suite de ce manuscrit :

- "composant" désigne une substance chimique donnée (l'eau, qui peut être présente sous forme liquide ou sous forme vapeur).

- "phase" désigne un état de la matière (liquide, gazeux ou solide). Un écoulement avec du liquide et une phase gazeuse constituée d'un mélange de vapeur et d'air est donc un écoulement diphasique. Par extension, on considère que deux liquides immiscibles consituent deux phases : un écoulement avec deux phases liquides immiscibles et une phase gazeuse sera appelé un écoulement triphasique.

- "champ" désigne un composant dans une phase donnée ; ainsi, un écoulement triphasique avec de l'eau liquide, de l'eau vapeur, de l'air et du corium fondu sera appelé un écoulement à quatre champs.

2.1 Ecoulements diphasiques eau-vapeur

La représentation des écoulements diphasiques eau-vapeur est un enjeu de modélisation depuis plus de 50 ans. Elle part le plus souvent de l'idée intuitive suivante, proposée notamment dans [57] : décrire un écoulement multiphasique comme une juxtaposition d'écoulements monophasiques, séparés par des interfaces mobiles. Dans cette thèse, des approches eulériennes sont considérées, par opposition aux approches lagrangiennes dans lesquelles on cherche à suivre exactement les interfaces au cours du temps. Les approches eulériennes reposent sur des méthodes de moyennisation qui peuvent être spatiales, temporelles ou statistiques. On parle dans ce cas d'interfaces diffuses.

Parmi les approches eulériennes, on distingue deux grandes familles de modèles :

- les modèles homogènes, dans lesquels on suppose un équilibre cinématique entre l'eau liquide et l'eau vapeur. Une seule vitesse commune est donc considérée pour décrire l'écoulement, si bien que le mélange est considéré comme un seul et même fluide.
- les modèles bifluides, dans lesquels chaque phase possède son propre champ de vitesse.

Dans cette thèse, des modèles homogènes sont étudiés dans les chapitres 1 et 3 tandis qu'un modèle de type bifluide est proposé au chapitre 4.

2.1.1 Modèles homogènes

Dans les modèles homogènes, une seule vitesse est donc considérée pour décrire l'écoulement, si bien que le mélange est traité comme étant un seul et même fluide. On peut noter que le déséquilibre de vitesses peut aussi être réintroduit à l'aide d'une corrélation, comme dans les modèles de dérive (Drift-flux-model en anglais) [3].

La difficulté des modèles homogènes réside dans la construction d'une équation d'état pour le mélange, cohérente avec les premier et second principes de la thermodynamique. La plupart des modèles homogènes construisent cette équation à l'aide d'une ou plusieurs hypothèses d'équilibre supplémentaire(s) entre les phases. Un modèle homogène complètement équilibré (HEM : Homogeneous Equilibrium Model en anglais, voir par exemple [17]) suppose ainsi, en plus de l'équilibre en vitesse, l'équilibre en pression, en température et en potentiel chimique entre les phases. Un modèle est dit homogène relaxé (HRM : Homogeneous Relaxed Model en anglais) quand au moins une hypothèse d'équilibre est relaxée. Des modèles HRM peuvent ainsi supposer l'égalité des pressions liquide et vapeur [2, 62, 41] ou l'égalité des températures [2, 28], ou encore l'égalité des pressions et la saturation de la vapeur d'eau [25, 10, 30].

Dans cette thèse, nous avons travaillé sur le modèle homogène proposé dans [7, 59] et étudié ensuite notamment dans [27, 69, 61, 46]. Dans ce modèle, la seule hypothèse d'équilibre est l'équilibre cinématique : chaque phase possède en effet sa propre pression, sa propre température et son propre potentiel chimique. L'équation d'état de mélange est construite afin de satisfaire le second principe de la thermodynamique par maximisation de l'entropie de mélange. Gérer des écoulements complètement hors équilibre thermodynamique peut en effet être nécessaire pour simuler certains transitoires rapides, comme cela a été mis en évidence dans [54] pour l'expérience SUPERCANON [74]. En effet, on observe dans l'expérience SUPERCANON des "undershoots" de pression sous la pression de saturation, suggérant que l'eau persiste à l'état liquide en deça de la pression de saturation théorique. Il semble ainsi que les simulations à l'équilibre thermodynamique, sans prise en compte de

l'état transitoire dans lequel l'écoulement persiste quelques instants hors de l'équilibre thermodynamique, surestiment parfois les niveaux de pression attendus d'environ une dizaine de bars [54].

De plus, il a été mis en évidence que certaines hypothèses d'équilibre partiel pouvaient mener à la perte du caractère strict de la concavité de l'entropie de mélange [7, 35, 29], ce qui peut avoir des conséquences sur les propriétés du modèle (voir section 2.3).

L'avantage des modèles homogènes est leur structure convective simple, de type Euler. De plus, ils dégénèrent naturellement vers les cas monophasiques. En revanche, ils sont parfois insuffisants, notamment pour les écoulements fortement stratifiés ou pour certaines applications où connaître les vitesses phasiques est essentiel. C'est le cas de l'explosion vapeur : estimer les écarts de vitesse permet d'évaluer l'aire interfaciale et donc les effets de dislocations des gouttes de corium, responsables d'un transfert de chaleur massif vers le liquide susceptible de déclencher une explosion [9, 70].

2.1.2 Modèles bifluides

Dans les modèles bifluides, par exemple [6, 62, 38, 60, 20, 34], chaque phase possède son propre champ de vitesse, mais aussi sa propre équation d'état. Ainsi, il n'y a pas à construire d'équation d'état de mélange, puisque la thermodynamique est gérée phase par phase. De plus, les modèles bifluides permettent de traiter les écoulements hors-équilibre, étant donné qu'ils définissent naturellement une pression, une température et un potentiel chimique pour chaque phase.

Les modèles bifluides ont une structure convective plus complexe que les modèles homogènes, avec des valeurs propres plus nombreuses. Les coûts de calcul associés à leur simulation sont souvent plus importants comparés aux modèles homogènes, notamment si les valeurs propres du modèle sont trop proches les unes des autres, obligeant à utiliser des maillages avec des cellules suffisamment petites pour les distinguer.

Dans cette thèse, un modèle multiphasique à quatre champs et trois phases (une phase liquide contenant de l'eau pure ; une autre phase liquide, non miscible avec la précédente, consitituée de corium fondu ; une dernière phase gazeuse formée d'un mélange miscible de gaz incondensable et de vapeur d'eau) a été proposé, reposant sur la même démarche de modélisation que celle utilisée pour construire les modèles multiphasiques [20, 33, 48, 49, 47, 51, 52].

2.2 Aspects thermodynamiques

Le présent travail s'intéresse en particulier aux aspects thermodynamiques de la modélisation, notamment dans les chapitres 1, 2, 3.

2.2.1 Equations d'état réalistes

Avec la construction thermodynamique proposée pour les modèles homogènes étudiés dans [7, 27, 69], la loi d'état de mélange est obtenue par maximisation de l'entropie de mélange, qui s'écrit comme la somme des entropies phasiques pondérées par les fractions de masse. Ainsi, la thermodynamique de mélange est déterminée à partir des lois d'état phasiques. Dans le cas des modèles bifluides, la thermodynamique étant découplée phase par phase, il faut également se doter de lois d'état phasiques réalistes.

Les lois d'état phasiques admissibles doivent respecter des critères de convexité afin d'assurer l'hyperbolicité des modèles utilisés (voir section 2.3). Pour prendre en compte les états hors-équilibres (voir section 2.1.1), il faut également pouvoir étendre les équations d'état phasiques au-delà de leur domaine de définition usuel (dans le domaine liquide pour une loi d'état vapeur et respectivement). Elles doivent de plus être des lois d'état complètes. Cela signifie que toutes les grandeurs thermodynamiques phasiques doivent pouvoir être définies sans ambiguité à partir de l'équation d'état. Par exemple, si on choisit le triplet (s, τ, e) où s est l'entropie massique, τ le volume spécifique et e l'énergie interne spécifique, les changements de plans thermodynamiques sont calculés grâce à la relation de Gibbs :

$$Tds - Pd\tau = de,$$

où T est la température, et P la pression. D'autres choix de plans thermodynamiques sont possibles, en considérant d'autres triplets que (s, τ, e) : ils sont recensés par exemple dans [29]. En revanche, les lois d'état cubiques, très souvent utilisées pour décrire les hydrocarbures dans l'industrie [73], ne sont pas directement admissibles pour nos modèles. Les exprimer sous forme complète demande un travail attentif [37] et impose certaines contraintes, notamment en termes de convexité [29].

Classiquement, les lois d'état analytiques les plus utilisées dans le cadre nucléaire sont des lois d'état analytiques de gaz raides (stiffened gas : SG en anglais), une extension du gaz parfait modifiée pour reproduire la raideur de l'eau, dont les coefficients sont en général ajustés empiriquement à l'aide d'un point expérimental comme proposé dans [23]. On peut également citer la loi Noble-Able Stiffened Gas (NASG) [65], une extension du gaz raide qui donne des résultats intéressants en ajoutant un coefficient translatant le volume spécifique. Malheureusement, la précision de ces lois reste limitée autour du point de fonctionnement choisi, ce qui peut s'avérer restrictif pour des simulations de type APRP ou explosion vapeur dans lesquelles une vaste gamme de pressions et de températures sont observées, si bien que des lois d'état plus réalistes sont parfois nécessaires pour améliorer la qualité des simulations.

Des lois de référence sont disponibles pour l'eau : il s'agit de la formulation IAPWS-97 [77]. Malheureusement, elle ne peut pas être utilisée en pratique dans les codes industriels de CFD en raison de son coût CPU prohibitif. Il est donc nécessaire de proposer une tabulation de cette loi d'état, compatible avec nos exigences de vérification des codes de calcul fixées dans [40]. En effet, la vérification impose de ne pas tabuler les grandeurs thermodynamiques indépendamment, sans quoi la relation de Gibbs, permettant de changer de plan thermodynamique de façon consistante, ne serait plus satisfaite. Dans le chapitre 1, une tabulation respectant ces principes a été utilisée. En plus de sa construction délicate, une loi tabulée impose l'utilisation de méthodes numériques très robutes. C'est pourquoi une étude de lois d'état analytiques a été proposée au chapitre 2, afin d'identifier un compromis entre la simplicité du gaz raide et les difficultés numériques d'une loi tabulée.

2.2.2 Situations hors-équilibre thermodynamique

Dans cette thèse, nous nous intéressons à la simulation d'écoulements persistant plus longtemps en déséquilibre thermodynamique que dans les situations usuelles (où l'hypothèse de l'équilibre thermodynamique instantané est suffisante). En revanche, nos modèles ne nous permettent pas de simuler des états métastables. La distinction entre états hors équilibre et états métastables est rappelée dans [4] : un état métastable est un état d'équilibre thermodynamique local, dont on peut s'écarter à condition d'appliquer une perturbation suffisamment importante tandis qu'un écoulement hors-équilibre est dans un état thermodynamique

instable qui revient "lentement" (c'est-à-dire de façon non instantanée) vers l'équilibre thermodynamique. Une façon originale de prendre en compte les états métastables a été proposée dans [58, 35, 36], en considérant une même équation d'état (l'équation de Van der Waals) pour les deux phases liquide et vapeur.

Les modèles homogènes issus du modèle [7] permettent donc de représenter des écoulements hors équilibre thermodynamique. Partant d'un écoulement caractérisé par les fractions phasiques $Y = (\alpha, y, z)$, où α est la fraction volumique de vapeur, y la fraction de masse de vapeur et z la fraction d'énergie de vapeur, le retour à l'équilibre a lieu grâce à des termes sources qui s'écrivent :

$$\frac{Y^{equilibre} - Y}{\lambda},$$

où $Y^{equilibre}$ représentent les fractions de volume, de masse et d'énergie de vapeur à l'équilibre thermodynamique. On peut noter que les modèles bifluides comprennent eux aussi des termes sources traduisant le retour à l'équilibre, ce qui demande de définir encore davantage d'échelles de temps de relaxation [66]. Dans [55], d'autres formes de termes sources ont été proposées, en s'inspirant des termes sources utilisés dans les modèles homogènes issus de [7] : ces nouvelles fermetures permettent de réduire un peu le nombre d'échelles de temps à définir.

Malheureusement, peu de références bibliographiques sont disponibles concernant cette échelle de temps de relaxation, si bien qu'il est difficile de proposer une loi d'évolution pour λ en se fondant sur des considérations physiques. On peut citer le chapitre 1 de la thèse d'Ancellin [4] qui recense quelques travaux concernant les aspects de thermodynamique hors-équilibre, ou encore la proposition de Bilicki et Kestin dans [10], qui a été réétudiée récemment dans la thèse de Lochon [67].

2.2.3 Importance des incondensables

Dans les situations accidentelles considérées, d'autres gaz en plus de la vapeur d'eau peuvent être présents : l'air ambiant, qui peut se dissoudre dans l'eau via une éventuelle brèche, ou encore les produits de dégradation de la gaine du combustible tels que l'hydrogène. Ces gaz sont désignés dans ce manuscrit par le terme "incondensables" car, dans nos applications d'intérêt, ils ne sont présents que sous forme gazeuse et ne sont pas susceptibles de changer d'état. Des études expérimentales [53] ont mis en évidence que la condensation était fortement influencée par la proportion de gaz incondensables relativement à la vapeur dans la phase gazeuse. Ce paramètre est également déterminant dans la probabilité d'observer ou non une explosion vapeur [1]. Des études numériques ont reproduit cette influence, comme dans [5].

Ainsi, les propriétés thermodynamiques de changement de phase, telle que la température de saturation, sont modifiées par la présence des incondensables et il semble essentiel de proposer des modèles capables de les prendre en compte, comme c'est d'ailleurs le cas dans les codes industriels de référence utilisés pour simuler une explosion vapeur [70, 8]. C'est pourquoi les chapitres 3 et 4 de cette thèse s'intéressent à des modèles dans lesquels on introduit les incondensables en plus de l'eau liquide et de la vapeur d'eau.

2.3 Structure mathématique des modèles étudiés

Afin d'être en mesure de proposer des solutions analytiques permettant de vérifier nos modèles selon les règles fixées par [40], il est primordial de s'assurer que les modèles multiphasiques considérés possèdent certaines propriétés mathématiques essentielles :

- **Hyperbolicité** : elle garantit la stabilité des solutions en temps ; si cette condition n'est pas respectée, on s'expose à des explosions de la solution numérique en temps fini, comme montré par exemple dans [50]. Pour les modèles considérés dans cette thèse, on montrera que la (stricte) concavité des entropies phasiques implique la (stricte) hyperbolicité des modèles.

- **Existence d'une inégalité d'entropie pour le système global** : c'est cette inégalité qui permet de sélectionner la solution physique pertinente en assurant le second principe y-compris dans les chocs.

- **Unicité des relations de saut** : cette propriété, évidente pour les modèles homogènes construits sur le système d'Euler, est aussi vérifiée par les modèles bifluides de type [20] grâce au caractère linéairement dégénéré de l'onde de couplage.

Ces propriétés seront systématiquement étudiées pour tous les modèles utilisés dans cette thèse. Si elles ont souvent été examinées dans le cas diphasique eau liquide - eau vapeur, les travaux concernant les modèles multiphasiques à au moins trois champs sont moins nombreux : on peut citer les références [5, 43] qui s'intéressent à des modèles homogènes à trois champs et les travaux [47, 48, 71, 13, 76, 52, 44] qui concernent des modèles bifluides.

3 Objectifs des travaux

Cette thèse vise ainsi à améliorer la simulation de certains scénarios accidentels de type APRP ou explosion vapeur, en s'intéressant notamment aux changements de phase dans des écoulements qui persistent en dehors de l'équilibre thermodynamique lors de transitoires rapides très brutaux. Cela passe en particulier par le choix de lois d'état phasiques les plus réalistes possibles, ainsi que par la prise en compte des gaz incondensables pouvant être présents.

Dans le chapitre 1, le modèle diphasique homogène eau-vapeur [7] est muni d'une loi d'état tabulée à partir de la formulation IAPWS-97 [77]. Le code est notamment vérifié à l'aide d'études de convergence sur des problèmes de Riemann, pour lesquels on a construit une solution analytique. Des premiers résultats de validation ont pu être obtenus, en utilisant pour le temps de relaxation λ une loi que nous avons proposée en nous appuyant sur la théorie de la nucléation. Cependant, le couplage requiert des schémas numériques à la fois précis et robustes, tels que le schéma de relaxation proposé dans [16], et induit certaines difficultés numériques qui pourraient s'avérer limitantes sur d'autres configurations. C'est pourquoi nous avons passé en revue différentes lois d'état classiques pour l'eau liquide et vapeur dans le chapitre 2 : le but était d'identifier des lois d'état admissibles (c'est-à-dire, complètes et avec les bonnes propriétés de convexité), si possible analytiques, afin de trouver un compromis entre la simplicité des lois d'état de type stiffened gas et la lourdeur d'une tabulation comme celle utilisée au chapitre 1. Cette étude a mis en évidence que la loi NASG modifiée comme dans [11], en prenant une capacité thermique massique à pression constante C_p fonction de la température (appelée NASG-CK dans ce chapitre) était relativement proche de IAPWS-97, notamment pour l'eau liquide. Le chapitre 3 étudie une extension du modèle homogène [7] prenant en compte des gaz incondensables. Le modèle obtenu, déjà étudié théoriquement dans [43], a été vérifié et utilisé pour simuler un cas test SUPERCANON [74], en utilisant la loi NASG-CK identifiée au chapitre 2 pour représenter l'eau liquide. Le chapitre 4 propose un autre modèle permettant de prendre en compte les incondensables, ainsi que le corium fondu pour permettre de simuler une explosion vapeur. Ce chapitre est un chapitre de pure modélisation, qui présente la construction du modèle.

Enfin, le chapitre 5 propose un travail transversal à l'ensemble de la thèse, concernant des aspects numériques liés à la sortie de structure d'ondes en dehors du domaine de calcul. En effet, les cas de transitoires rapides étudiés peuvent faire apparaître des ondes de choc ou des ondes de détente, susceptibles de quitter le domaine d'étude avant la fin de la simulation. Le chapitre 5 poursuit un travail initié dans la thèse de Colas [18], qui met en évidence une inconsistance des conditions limites classiquement utilisées dans certains codes industriels.

4 Synthèse des travaux

Chapitre 1 : Simulations d'écoulements eau-vapeur hors-équilibre thermodynamique à l'aide d'un modèle homogène muni d'une loi d'état tabulée

Dans ce premier chapitre, on s'intéresse à la simulation d'écoulements ne comportant que de l'eau liquide et de l'eau vapeur (sans gaz incondensables), dans des configurations où le retour à l'équilibre thermodynamique n'est pas instantané. Le modèle considéré est le modèle diphasique homogène proposé dans les références [7, 59, 45] et déjà largement étudié dans la littérature (cf par exemple [27, 69, 61, 46]). Il permet de gérer des écoulements hors-équilibre thermodynamique, puisque la seule hypothèse d'équilibre entre les deux phases est l'hypothèse initiale d'équilibre de vitesse : chaque phase possède sa propre pression P, sa propre température T et son propre potentiel chimique μ. Le système d'équations aux dérivées partielles du modèle final repose sur le système d'Euler, complété par trois équations portant sur les fractions $Y = (\alpha, y, z)$ phasiques de vapeur où α est la fraction de volume, y la fraction de masse et z la fraction d'énergie z :

$$\begin{cases} \dfrac{\partial}{\partial t}(\rho Y) + \dfrac{\partial}{\partial x}(\rho U Y) = \dfrac{\rho(Y^{equilibre} - Y)}{\lambda}, \\ \dfrac{\partial}{\partial t}(\rho) + \dfrac{\partial}{\partial x}(\rho U) = 0, \\ \dfrac{\partial}{\partial t}(\rho U) + \dfrac{\partial}{\partial x}\left(\rho U^2 + P\right) = 0, \\ \dfrac{\partial}{\partial t}(\rho E) + \dfrac{\partial}{\partial x}(U(\rho E + P)) = 0. \end{cases}$$

L'originalité de ce travail est de munir ce modèle homogène de lois d'état phasiques réalistes. Il s'agit de lois tabulées, obtenues à partir de la formulation IAPWS-97 [77], une des lois d'état industrielles de référence pour l'eau, qui s'avère malheureusement trop coûteuse en temps de calcul pour être utilisée telle quelle dans des codes CFD. La construction de la loi tabulée est une tâche délicate. En effet, afin de pouvoir effectuer des changements de variables thermodynamiques cohérents (en particulier, obtenir la pression P et la température T à partir du volume spécifique τ et de l'énergie interne massique e et réciproquement), les grandeurs thermodynamiques ne doivent pas être tabulées indépendamment les unes des autres. La méthode utilisée consiste à choisir un potentiel thermodynamique (ici le potentiel chimique $\mu(P,T)$ dans le plan pression température) et à construire la tabulation de façon à vérifier l'équivalent de la relation de Gibbs dans ce plan thermodynamique :

$$d\mu = \tau dP - s dT.$$

Evidemment, la relation de Gibbs n'est pas vérifiée analytiquement par la loi tabulée : les inversions thermodynamiques sont calculées via des algorithmes de Broyden dont il est important de s'assurer d'un niveau de précision suffisant à convergence. La donnée d'un bon point de départ est essentielle à la robustesse d'un tel algorithme et peut poser problème

dans certaines configurations trop brutales.

La méthode numérique employée est classique. Elle est fondée sur la méthode des pas fractionnaires [78] et utilise un splitting de Lie-Trotter d'ordre 1. A chaque itération, le système convectif est d'abord résolu à l'aide de schémas volume finis explicites d'ordre 1 :

$$\begin{cases} \dfrac{\partial}{\partial t}(\rho Y) + \dfrac{\partial}{\partial x}(\rho U Y) = 0, \\ \dfrac{\partial}{\partial t}(\rho) + \dfrac{\partial}{\partial x}(\rho U) = 0, \\ \dfrac{\partial}{\partial t}(\rho U) + \dfrac{\partial}{\partial x}\left(\rho U^2 + P\right) = 0, \\ \dfrac{\partial}{\partial t}(\rho E) + \dfrac{\partial}{\partial x}(U(\rho E + P)) = 0, \end{cases}$$

et dans un second temps, l'équilibre thermodynamique est calculé à l'aide d'un algorithme proposé initialement dans [28], puis les termes sources sont appliqués en résolvant implicitement le système suivant :

$$\begin{cases} \dfrac{\partial}{\partial t}(\rho Y) = \dfrac{\rho(Y^{equilibre} - Y)}{\lambda}, \\ \dfrac{\partial}{\partial t}(\rho) = 0, \\ \dfrac{\partial}{\partial t}(\rho U) = 0, \\ \dfrac{\partial}{\partial t}(\rho E) = 0. \end{cases}$$

Pour s'assurer de la consistance de notre loi d'état, des cas tests de vérification ont été mis en place : il s'agit de problèmes de Riemann, construits étape par étape de manière à être capable d'en exhiber une solution analytique. De très nombreuses configurations ont été testées, en faisant varier :

- la nature des ondes qui sont générées au cours du temps, que l'on peut contrôler en imposant que certaines ondes soient transparentes : les cas tests de cette étude contiennent soit des ondes pures (une seule onde de choc ou une seule onde de contact), ou soit une onde de choc et une onde de contact ;
- l'échelle de temps de relaxation λ utilisée : des cas tests de convection pure ($\lambda \to \infty$) et des cas tests avec convection puis relaxation instantanée vers l'équilibre thermodynamique ($\lambda = 0$) ont été étudiés ;
- les lois d'états phasiques utilisées pour fermer le modèle : en plus de notre loi tabulée, nous avons vérifié notre code à l'aide de lois de gaz raides ;
- la nature des états gauche et droite initiaux, qui peuvent être diphasiques ou monophasiques.

Cette étude a mis en évidence que la loi tabulée imposait l'utilisation de schémas numériques particulièrement robustes : le schéma de VFRoe-ncv [14] a ainsi été mis en défaut, tandis que le schéma de relaxation proposé par Chalons et Coulombel [16] s'est rélévé presque aussi robuste que le schéma de Rusanov [75] tout en étant plus efficace et bien plus précis. En terme de résultat, la loi d'état tabulée permet bien de retrouver les mêmes ordres de convergence que les lois de gaz raides classiques. On a tout de même relevé que dans certains cas, pour des maillages très fins, la convergence est limitée par le seuil de précision

choisi dans les algorithmes de Broyden utilisés pour les inversions thermodynamiques, ce qui n'est pas restrictif à condition de le choisir suffisamment petit.

La dernière partie de ce chapitre propose un modèle original pour l'échelle de temps de relaxation $\lambda > 0$ caractérisant le retour à l'équilibre thermodynamique. Peu de références sont disponibles dans la littérature pour caractériser cette échelle de temps. Des "modèles-jouets" ont été utilisés dans [54] et ont mis en évidence l'importance de ce paramètre pour améliorer le réalisme des simulations dans des configurations de type SUPERCANON [74]. Le modèle proposé s'appuie sur la théorie classique de la nucléation (cf par exemple [24]) et utilise des hypothèses simplificatrices utilisées notamment dans [15] ou [68]. Le modèle est le suivant :

$$t_{nuc} = \left(\frac{a_0}{\Delta P}\right)^3 \exp\left(\frac{\varphi E_a}{k_B T}\right),$$

où E_a est une énergie d'activation qui s'écrit : $E_a = \dfrac{16\pi\gamma^3}{3(\Delta P)^2}$, avec γ obtenu à l'aide d'une corrélation de IAPWS 94 [72]. L'intérêt du modèle est d'introduire des comportements plus physiques que dans les modèles-jouets proposés dans [54] avec un nombre réduit de paramètres à fixer par l'utilisateur (a_0 et φ).

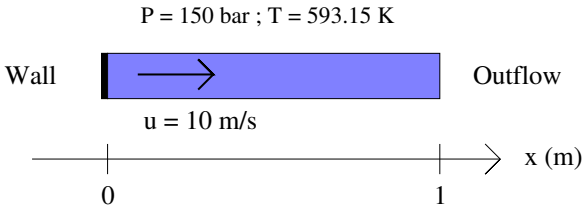

FIGURE 2 – *Détente en paroi dans du liquide en aval d'une vanne fermée brutalement : quelques bulles de vapeur vont apparaître près de la paroi.*

Ce premier modèle a été testé sur une configuration très simple schématisée sur la figure 2 : une détente près d'une paroi dans du liquide mis en mouvement (par exemple, lors de la fermeture soudaine d'une vanne). Les résultats obtenus sont avant tout qualitatifs. Des comportements complexes, avec des effets de seuil suggérant une persistance observable de l'écoulement hors de l'équilibre thermodynamique avant un retour assez brutal à l'équilibre, ont pu être mis en évidence, notamment en prenant φ proche de 0. Le paramètre $\varphi \in [0,1]$ caractérise la nature de la nucléation (homogène quand $\varphi = 1$ ou hétérogène sinon). La présence des impuretés facilite la formation de bulles, ce qui est traduit dans le modèle par une diminution de l'énergie d'activation en prenant $\varphi < 1$. Les premiers résultats numériques obtenus suggèrent que la nucléation hétérogène est plus appropriée que la nucléation homogène pour expliquer les effets hors-équilibre. Le rôle des impuretés nous apparaît donc comme essentiel pour comprendre les effets thermodynamiques hors-équilibre car ce sont elles qui vont aider à initier la vaporisation (qui est rendue très difficile dans de l'eau pure, quand la nucléation est homogène) et qui pourraient expliquer une certaine variabilité des "runs" dans l'expérience SUPERCANON [74]. Or, les micro-bulles de gaz incondensables dissoutes dans l'eau constituent des impuretés presque incontournables dans nos écoulements d'intérêt, ce qui nous conforte dans notre conviction que la prise en compte des incondensables est essentielle pour augmenter la qualité de nos simulations, comme nous l'envisagerons dans les chapitres 3 et 4.

Chapitre 2 : Etude de quelques équations d'état classiques pour l'eau liquide et l'eau vapeur dans le plan pression-température

Une loi d'état tabulée comme celle du chapitre 1 reste assez lourde à programmer de façon consistante avec la relation de Gibbs et nécessite des méthodes numériques très robustes. L'idéal serait de disposer de lois d'état phasiques analytiques plus simples à utiliser et qui garantiraient tout de même un bon niveau de précision. Ce chapitre passe en revue quelques lois d'état classiques pour représenter l'eau liquide puis l'eau vapeur, et ambitionne de les hiérarchiser en termes de précision relativement à la loi de référence IAPWS-97 [77].

Dans ce chapitre, nous rappelons d'abord que les lois d'état admissibles pour nos modèles multiphasiques doivent satisfaire un certain nombre de critères : il doit s'agir de lois d'état complètes, permettant des inversions de plans thermodynamiques aisées et vérifiant certains critères de positivité et de convexité.

Les lois d'état passées en revue sont les suivantes :

- la loi d'état de gaz raide (stiffened gas en anglais) ;
- la loi d'état Noble-Able stiffened gas (NASG) [65] et son extension proposée dans [11] (désignée par le sigle NASG-CK), qui considère une capacité thermique à pression constante C_p fonction de la température, en s'appuyant sur les coefficients de la loi Chemkin [64], qui est également testée ;
- les lois cubiques, et plus particulièrement la loi Soave-Redlich-Kwong (SRK) (cf par exemple [73, 39]) ; ces dernières lois sont classiquement données sous forme incomplète, et un travail attentif a été mené, en s'appuyant sur [37], afin de la réexprimer sous une forme complète.

Nous avons choisi pour cette étude certains critères de comparaison nous permettant de hiérarchiser ces lois d'état en termes de précision. Notre premier parti pris est de travailler uniquement dans le plan pression-température. Ainsi, toutes les lois d'état ont été exprimées en termes de potentiel chimique μ fonction de la pression P et de la température T. Cette formulation permet de déduire facilement les grandeurs suivantes, à l'aide des dérivées premières et secondes de μ en fonction de P et T : l'entropie massique s, le volume spécifique τ, la capacité thermique spécifique à pression constante C_p ainsi que α_p le coefficient de dilatation thermique à pression constante et χ_T le coefficient de compressibilité à température constante. Nos comparaisons reposent sur le calcul des erreurs relatives err_ϕ pour chacune des équations d'état testées (notée EOS), avec ϕ l'une des six grandeurs précédentes (μ, s, τ, C_p, α_p, ou χ_T) :

$$err_\phi = \left| \frac{\phi^{EOS} - \phi^{IAPWS}}{\phi^{IAPWS}} \right|.$$

Les lois d'état ont été étudiées avec les paramètres classiquement utilisés dans la littérature, ainsi qu'avec des paramètres obtenus en minimisant les erreurs relatives sur certaines grandeurs (μ, τ et C_p). Les comparaisons ont été effectuées sur de grands domaines liquide et vapeur. L'optimisation des coefficients des lois d'état s'est avérée assez ardue : la difficulté majeure est d'optimiser les coefficients pour minimiser l'erreur à la fois sur le potentiel chimique et sur l'ensemble de ses dérivées successives. Les domaines de validité d'une loi d'état en termes de pression et de température sont souvent disjoints pour les différentes variables considérées, en particulier pour la vapeur.

Les principaux résultats obtenus sont les suivants :

- Nous avons pu illustrer quantitativement la dégradation du niveau de précision d'une loi d'état de gaz raide lorsqu'elle est calée comme dans [23], en "linéarisant" la loi d'état autour d'un point de référence. Les résultats sont relativement satisfaisants pour le potentiel chimique et l'entropie ; en revanche, le gaz raide est moins précis pour estimer le volume spécifique τ et la capacité thermique C_p, à hautes températures pour le liquide, et sur presque tout le domaine pour la vapeur (à l'exception d'un domaine d'une quizaine de bars centré sur le point de référence).

- La loi SRK donne pour la vapeur des résultats comparables au gaz raide, tout en améliorant significativement la précision sur τ. Les résultats de cette étude sont plus mitigés pour le liquide, sauf à très hautes températures.

- La loi NASG étend significativement le domaine de précision du gaz raide, notamment pour le volume spécifique τ. Prendre une capacité thermique C_p dépendante de la température n'a pas d'effet majeur sur la précision pour la vapeur. En revanche, l'extension NASG-CK nous est apparue comme le meilleur compromis parmi l'ensemble des lois testées dans cette étude pour le liquide.

La loi NASG-CK a donc été choisie pour représenter le liquide dans le chapitre 3. De façon générale, il semble intéressant d'employer la loi NASG, aussi bien pour l'eau liquide que pour l'eau vapeur, car cette loi possède une forme analytique presque aussi simple que le gaz raide tout en améliorant significativement l'estimation du volume spécifique.

Chapitre 3 : Un modèle homogène avec prise en compte des gaz incondensables, muni d'une loi d'état liquide réaliste semi-analytique (la loi "Noble-Able-Chemkin stiffened gas")

Ce chapitre considère une extension du modèle du chapitre 1 capable de prendre en compte les gaz incondensables. Ce modèle a déjà été étudié dans [43], où la construction d'une loi de mélange thermodynamique satisfaisant le second principe a été présentée. Il a également été utilisé dans sa forme équilibrée muni de lois phasiques de gaz raides dans [5]. Dans ce chapitre, nous commençons par rappeler les grandes étapes de modélisation aboutissant au modèle [43], selon les principes déjà utilisés dans l'annexe du chapitre 1. Nous détaillons particulièrement les conséquences des hypothèses hybrides de miscibilité. En effet, contrairement au cas diphasique eau-vapeur sans incondensables, la dégénérescence du modèle vers les cas monophasiques ou les cas à deux champs doit être examinée avec attention.

La grande originalité de ce travail consiste à munir ce modèle d'une loi d'état NASG-CK [11] pour l'eau liquide, comme identifié au chapitre 2. La présence des incondensables complique le calcul de l'équilibre thermodynamique par rapport à l'algorithme initial proposé dans [28] : il se ramène à la résolution d'un système non-linéaire de deux équations à deux inconnues, ce qui impose d'utiliser un algorithme de Broyden ou une double-dichotomie parfois un peu délicats à mettre en oeuvre. La vapeur et les incondensables sont décrits à l'aide de lois d'état de gaz raides. En effet, une loi NASG avait au départ été envisagée pour la vapeur, mais nous avons constaté que son emploi complexifierait encore le calcul de l'équilibre thermodynamique, puisqu'il faudrait alors résoudre un système couplé de trois équations à trois inconnues dans ce cas. Ainsi, alors que le modèle muni de trois lois de gaz raides comme dans [5] est très simple à simuler, la complexité augmente très rapidement dès que l'on utilise simultanément deux lois analytiques un peu plus réalistes.

Le modèle a été implémenté et vérifié, en construisant des problèmes de Riemann suivant les mêmes principes qu'au chapitre 1. Un cas de validation SUPERCANON [74] a été mis en place.

Chapitre 4 : Un modèle triphasique à quatre champs pour des écoulements comprenant des phases miscibles et immiscibles

Le chapitre 4 est un chapitre de modélisation pure qui présente un modèle multifluide original visant à simuler des écoulements comprenant de l'eau liquide l, de l'eau vapeur v, des incondensables g et du corium fondu s. Le modèle est construit pas à pas, suivant une démarche similaire à celle mise en oeuvre dans les références [20, 33, 48, 47, 52]. La spécificité de ce travail est que les écoulements d'intérêt comportent à la fois une phase miscible (la phase gazeuse, composée de vapeur d'eau et d'incondensables) et des phases non-miscibles (les deux phases d'eau liquide et de corium fondu ainsi que la phase gazeuse). En effet, dans le cadre barotrope, lorsque tous les champs du modèle forment des phases non-miscibles, des résultats ont pu être démontrés dans [76] lorsque la vitesse d'interface est la vitesse d'une des phases : il s'agit notamment de la convexité de l'entropie de mélange ou de la symétrisation des systèmes multiphasiques constitués d'un nombre arbitraire $N \geq 2$ de composants non-miscibles. En revanche, dans des modèles multifluides avec au moins une phase constituée d'un mélange miscible, comme dans [52], la généralisation mathématique en dimension supérieure n'est pas triviale et doit être étudiée au cas par cas, comme dans ce chapitre.

Le point de départ de la modélisation est un système de lois de conservation de masse, de moment et d'énergie pour chaque champ, incluant des termes non-conservatifs traduisant les échanges entre les constituants :

$$\left\{\begin{array}{rcl} \partial_t \alpha_k + \mathbf{v}_I.\nabla \alpha_k & = & \Phi_k \\ \partial_t m_k + \nabla.(m_k \mathbf{u}_k) & = & \Gamma_k \\ \partial_t (m_k \mathbf{u}_k) + \nabla.(m_k \mathbf{u}_k \otimes \mathbf{u}_k) + \nabla(\alpha_k P_k) + \sum\limits_{k' \neq k} \pi_{kk'} \nabla \alpha_{k'} & = & \mathbf{S}_{\mathbf{Q}k} \\ \partial_t (\alpha_k E_k) + \nabla.(\alpha_k \mathbf{u}_k (E_k + P_k)) - \sum\limits_{k' \neq k} \pi_{kk'} \partial_t \alpha_{k'} & = & S_{Ek} \end{array}\right.$$

Afin d'être en mesure de gérer correctement les termes non-conservatifs $\sum\limits_{k' \neq k} \pi_{kk'} \nabla \alpha_{k'}$, nous nous restreignons à des modèles admettant une inégalité d'entropie et des relations de sauts définies de façon unique. Nous commençons par nous doter d'une entropie naturelle pour le système (la somme des entropies phasiques), qui vérifie une inégalité d'entropie admissible. Ce choix de modélisation conduit à des fermetures imposées pour les termes $\pi_{kk'}$ par la définition de la vitesse d'interface v_I, ainsi qu'à des contraintes permettant de construire des termes sources satisfaisant l'inégalité d'entropie. D'autre part, certains choix particuliers de v_I [21, 42] conduisent à une onde de couplage linéairement dégénérée et permettent ainsi d'obtenir l'unicité des relations de saut champ par champ : il s'agit des cas avec une vitesse v_I "décentrée" (i.e. égale à l'une des vitesses phasiques, par exemple celle du corium u_s) ou alors du cas où v_I vaut la vitesse moyenne de l'écoulement $v_I = u_m = \frac{1}{\sum\limits_k m_k} \sum\limits_k m_k u_k$.

Le modèle ainsi obtenu est d'abord appréhendé sans spécifier de fermeture pour v_I : en particulier, la matrice de convection est explicitée de façon générale. L'hyperbolicité du modèle est démontrée (en dehors des cas de résonance). La nature des ondes du système est ensuite examinée. Les relations de saut définissant les chocs de façon unique sont données. Enfin, nous démontrons que le système est symétrisable pour tout v_I, ce qui garantit grâce au théorème de Kato [63] l'existence d'une unique solution locale en temps régulière au problème de Cauchy loin de la résonance.

D'autres propriétés sont ensuite étudiées en fixant $v_I = u_s$. Le domaine thermodynamique admissible de positivité des énergies internes est ainsi préservé par le modèle au

cours du temps, de même que les équilibres de pression, cohérents avec la loi de Dalton : $P_l = P_v + P_g = P_s$. Enfin, les effets de relaxation de pression ont été examinés : il s'agit de s'assurer que le système isolé (sans transferts de masse, de moment ou d'énergie), sans convection, relaxe bien vers l'équilibre de pression prescrit par la loi de Dalton. La relaxation vers l'équilibre de pression est bien vérifiée par le système, à condition que les écarts de pression $\Delta_l P = P_l - (P_v + P_g)$ et $\Delta_s P = P_s - (P_v + P_g)$ soient suffisamment petits. Ce seuil de pression a été estimé et n'est pas restrictif pour des applications de type nucléaire. Nous avons également mis en évidence que le retour à l'équilibre peut s'accompagner d'oscillations stables. Des comportements similaires ont déjà été observés dans la littérature et ce chapitre se termine par un inventaire des effets constatés pour plusieurs modèles bifluides lors de l'examen du processus de relaxation de pression : l'effet de seuil apparaît dès que le modèle comporte une équation d'énergie [12, 52] tandis que les oscillations sont susceptibles de se produire dès que le modèle comprend au moins trois phases non-miscibles [13, 12] (elles sont absentes dans les modèles diphasiques, y-compris dans le modèle avec une phase miscible [52]).

Chapitre 5 : Analyse d'erreur numérique portant sur des conditions limites discrètes pour le système d'Euler

Dans nos cas d'application de scénarios accidentels, il est possible que des structures d'ondes rapides telles que des ondes de choc ou des ondes de détente quittent le domaine de calcul Ω avant la fin de la simulation (figure 3). Dans ce cas, les conditions limites discrètes imposées sur le bord du domaine $\partial\Omega$ pourraient avoir une influence sur les résultats. Nous insistons bien sur le fait que la frontière $\partial\Omega$ est purement artificielle : il s'agit d'une frontière numérique, que l'utilisateur peut déplacer à sa guise en agrandissant le domaine de calcul Ω.

Ce chapitre prolonge l'étude du chapitre 3 de la thèse de Colas [18]. Il s'intéresse à l'erreur numérique due aux conditions limites artificielles imposées sur les frontières du domaine de calcul dans des cas mono-dimensionnels. Plus précisément, en considérant le système d'Euler monophasique, nous avons réalisé des études de convergence en maillage à l'aide de problèmes de Riemann, en faisant en sorte qu'une onde de choc ou une onde détente quitte entièrement le domaine Ω avant la fin de la simulation (les autres ondes étant toujours à cet instant à l'intérieur de Ω, afin d'isoler les effets de chaque type d'onde). Nous précisons que les conditions limites envisagées ne nécessitent aucune information sur l'extérieur du domaine Ω.

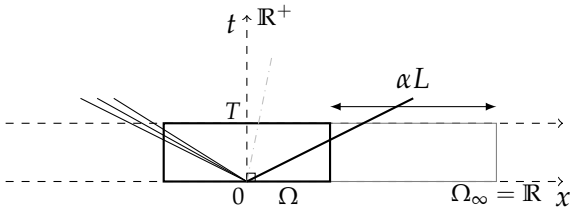

FIGURE 3 – *Domaine de calcul borné $\Omega \subsetneq \Omega_\infty$, avec Ω_∞ un domaine infini en espace.*

Les conditions limites étudiées sont prescrites en définissant un état extérieur $\mathbf{W}^n_{ext}$ artificiel dans une cellule virtuelle, symétrique à la cellule $\mathbf{W}^n_i$ du bord du domaine par rapport à la frontière $\partial\Omega$: les flux numériques de bord sont ainsi calculés de la façon suivante :

$$\mathbf{g}^n_{1/2} = \mathbf{g}(\mathbf{W}^n_{ext,1}, \mathbf{W}^n_1) \quad \text{and} \quad \mathbf{g}^n_{N+1/2} = \mathbf{g}(\mathbf{W}^n_N, \mathbf{W}^n_{ext,N}).$$

Plusieurs types de conditions limites ont été comparées :

- une formulation BC_0 dans laquelle l'état de bord $\mathbf{W}_i^n$ est dupliqué dans la cellule extérieure : $\mathbf{W}_1^n = \mathbf{W}_{ext,1}^n$ ou $\mathbf{W}_N^n = \mathbf{W}_{ext,N}^n$ (il s'agit d'une formulation classique, souvent utilisée dans les codes industriels) ;
- une formulation BC_r, construite en supposant que l'onde qui sort du domaine est une onde de détente : l'état $\mathbf{W}_{ext}^n$ est alors construit à partir des invariants de Riemann conservés dans la détente, et en intuitant la vitesse extérieure via la relation $u_{ext}^n = 2u_N^n - u_{N-1}^n$.
- une formulation BC_s, dite de champ lointain, dans laquelle on considère que la cellule de bord est reliée via une cellule virtuelle de taille infiniment grande à droite du domaine à l'état initial droit $\mathbf{W}_R^0$ (voir figure 3).

Ces conditions limites ont été testées pour différent schémas numériques : le schéma VFRoe-ncv [31, 32], le schéma VFRoe-ncv avec relaxation d'énergie [32], basé sur le schéma original de Coquel et Perthame dans [19], un schéma de relaxation proposé par Chalons et Coulombel [16] et un schéma de Rusanov.

Avec le schéma VFRoe-ncv, la sortie de l'onde de détente ne pose pas de problème lorsque la formulation BC_0 classique est employée. La formulation BC_r, pourtant construite spécifiquement pour être plus cohérente avec le passage d'une onde détente, n'apporte pas d'amélioration significative de la précision. En revanche, dans les cas tests avec sortie d'une onde de choc, la solution numérique obtenue n'est pas consistante avec la solution analytique attendue lorsque la formulation BC_0 est utilisée. La formulation BC_s proposée génère quant à elle une solution consistante. Malheureusement, nous ne sommes pas parvenus à expliquer théoriquement ce résultat.

Un comportement très étrange a été observé lorsque les schémas de relaxation ont été testés. En effet, ces schémas supposent l'introduction d'un paramètre qui doit satisfaire une condition sous-caractéristique afin d'assurer la stabilité numérique, qui s'écrit sous la forme :

$$a > \max\left(\frac{c_l(\tau_l, e_l)}{\tau_l}, \frac{c_r(\tau_r, e_r)}{\tau_r}\right).$$

Dans le cas où une onde de détente quitte le domaine Ω, la condition BC_0 permet d'obtenir une solution numérique consistante seulement si le paramètre de relaxation est exactement égal à la borne inférieure imposée par la condition sous-caractéristique, c'est-à-dire si :

$$a = \max\left(\frac{c_l(\tau_l, e_l)}{\tau_l}, \frac{c_r(\tau_r, e_r)}{\tau_r}\right).$$

A nouveau, nous n'avons pas d'argument théorique permettant d'expliquer cette observation.

Enfin, quand une onde de choc quitte le domaine, la formulation BC_s ne permet plus d'obtenir une formulation consistante avec le schéma de relaxation [16] ou le schéma de Rusanov. Nous ne sommes donc pas encore parvenus à exhiber une formulation de conditions limites discrètes permettant d'obtenir une solution numérique consistante lorsqu'une onde de choc sort du domaine de calcul **compatible avec tous les schémas numériques**.

Les deux annexes suivantes présentent des travaux réalisés en marge de cette thèse sur des thématiques complémentaires.

Annexe A : Un modèle homogène triphasique compressible avec trois phases immiscibles

Cet article présente un modèle original, construit à partir du modèle diphasique utilisé au chapitre 1, permettant de représenter des écoulements triphasiques avec trois phases non-miscibles. Des simulations visant à reproduire un accident de réactivité (RIA en anglais, voir [56]) sont réalisées.

Annexe B : Simulation d'un modèle diphasique compressible à l'aide d'une méthode de Lattice-Boltzmann

Le modèle du chapitre 3 est simulé à l'aide d'une méthode de Lattice-Boltzmann. Une approche cinétique, similaire à ce qui a été fait dans [26], est présentée. Des cas tests d'explosion vapeur sont réalisés.

5 Valorisation des travaux

Les travaux présentés dans ce manuscrit ont fait l'objet des éléments de valorisation suivants :

- Les travaux du chapitre 1 ont été publiés dans la revue *Computers & Fluids* sous la référence :

  P. Helluy, O. Hurisse and L. Quibel, Assessment of numerical schemes for complex two-phase flows with real equations of state, *Computer & Fluids*, 196 (104347), 2019.

  Ils ont été présentés au congrès international ICIAM 9 (Valence, juillet 2019).

- Les travaux du chapitre 2 ont été entrepris à la suite de la Semaine d'Études Maths-Entreprise (SEME) ayant eu lieu à Strasbourg en novembre 2018, où un sujet de recherche a été proposé et étudié. Le travail de la SEME a été retranscrit dans un rapport disponible sur HAL sous la référence :

  L. Quibel, P. Helluy, M. Chion, P. Ricka. Mélanger des gaz raides pour créer de nouvelles lois d'état. *Rapport de recherche*, IRMA, Université de Strasbourg ; EDF R&D, 2019. (hal-02114552)

- Les travaux du chapitre 3 font l'objet d'un preprint en cours de rédaction.

  Ils devaient être exposés lors d'une présentation orale au "Workshop on Compressible Multiphase Flows" (Strasbourg, mai 2020), annulé en raison de la pandémie de Covid-19. Un exposé sur des sujets similaires est de plus prévu à la conférence ATH'2020, qui a été reportée à l'automne 2020.

- Les travaux du chapitre 4 ont été acceptés pour publication dans *ESAIM :Mathematical Modelling and Numerical Analysis*, sous la référence :

  J.-M.. Hérard , O. Hurisse and L. Quibel, A four-field three-phase flow model with both miscible and immiscible components, *ESAIM :Mathematical Modelling and Numerical Analysis*, 2020.

- Les travaux du chapitre 5 ont été présentés lors du congrès FVCA IX (Bergen, juin 2020) et apparaissent dans les proceedings associés sous la référence :

  C. Colas, M. Ferrand, J.-M. Hérard, O. Hurisse, E. Le Coupanec, and L. Quibel, A Numerical Convergence Study of some Open Boundary Conditions for Euler Equations, 2020, Springer Proceedings in Mathematics & Statistics, ISBN 978-3-030-43650-6, Vol 323.

- L'annexe A contient un travail lié à cette thèse, présenté au "Workshop on Compressible Multiphase Flows" (Strasbourg, mai 2018) et apparaissant dans les proceedings associés sous la référence :

  O. Hurisse and L. Quibel, A homogeneous model for compressible three-phase flows involving heat and mass transfer. *ESAIM : Proceedings and Surveys*, 66 (2019) 84-108.

- L'annexe B contient un travail lié à cette thèse, présenté lors du congrès international FVCA IX (Bergen, juin 2020) et apparaissant dans les proceedings associés sous la référence :

  P. Helluy, O. Hurisse and L. Quibel, Simulation of a liquid-vapour compressible flow by a Lattice Boltzmann Method, 2020, Springer Proceedings in Mathematics & Statistics, ISBN 978-3-030-43650-6, Vol 323.

Références

[1] R. AKIYOSHI, S. NISHIO et I. TANASAWA. "A study on the effect of non-condensible gas in the vapor film on vapor explosion". In : *International journal of heat and mass transfer* 33.4 (1990), p. 603-609. DOI : https://doi.org/10.1016/0017-9310(90)90159-R (cf. p. xv).

[2] G. ALLAIRE, S. CLERC et S. KOKH. "A five-equation model for the numerical simulation of interfaces in two-phase flows". In : *Comptes Rendus de l'Académie des Sciences - Series I - Mathematics* 331.12 (2000), p. 1017-1022. URL : http://www.sciencedirect.com/science/article/pii/S0764444200017535 (cf. p. xii).

[3] A. AMBROSO, C. CHALONS, F. COQUEL, T. GALIÉ, E. GODLEWSKI, P.-A. RAVIART, N. SEGUIN et al. "The drift-flux asymptotic limit of barotropic two-phase two-pressure models". In : *Communications in Mathematical Sciences* 6.2 (2008), p. 521-529. DOI : https://dx.doi.org/10.4310/CMS.2008.v6.n2.a13 (cf. p. xii).

[4] M. ANCELLIN. "Physical and numerical modeling of interfacial phase change during wave impacts". Theses. Université Paris-Saclay, mar. 2017. URL : https://tel.archives-ouvertes.fr/tel-01512951 (cf. p. xiv, xv).

[5] M. BACHMANN, S. MÜLLER, P. HELLUY et H. MATHIS. "A Simple Model for Cavitation with Non-condensable Gases". In : *Hyperbolic Problems: Theory, Numerics and Applications*. T. 18. World Scientific, 2012, p. 289-296. DOI : 10.1142/9789814417099_0024. URL : https://hal.archives-ouvertes.fr/hal-01420483 (cf. p. xv, xvi, xxi).

[6] M. BAER et J. NUNZIATO. "A two-phase mixture theory for the deflagration-to-detonation transition (DDT) in reactive granular materials". In : *Journal of Multiphase Flows* 12 (1986), p. 861-889. DOI : https://doi.org/10.1016/0301-9322(86)90033-9 (cf. p. xiii).

[7] T. BARBERON et P. HELLUY. "Finite volume simulation of cavitating flows". In : *Computers and Fluids* 34.7 (2005), p. 832-858. URL : https://hal.archives-ouvertes.fr/hal-00139597 (cf. p. xii, xiii, xv-xvii).

[8] F. BARRE et M. BERNARD. "The CATHARE code strategy and assessment". In : *Nuclear engineering and design* 124.3 (1990), p. 257-284. DOI : https://doi.org/10.1016/0029-5493(90)90296-A (cf. p. x, xv).

[9] G. BERTHOUD. "Vapor explosions". In : *Annual Review of Fluid Mechanics* 32.1 (2000), p. 573-611. DOI : https://doi.org/10.1146/annurev.fluid.32.1.573 (cf. p. xiii).

[10] Z. BILICKI et J. KESTIN. "Physical aspects of the relaxation model in two-phase flow". In : *Proceedings of the Royal Society of London A: Mathematical, Physical and Engineering Sciences*. T. 428. 1875. The Royal Society. 1990, p. 379-397. DOI : https://doi.org/10.1098/rspa.1990.0040 (cf. p. xii, xv).

[11] P. BOIVIN, M. CANNAC et O. LE METAYER. "A thermodynamic closure for the simulation of multiphase reactive flows". In : *International Journal of Thermal Sciences* 137 (mar. 2019), p. 640-649. URL : https://hal.archives-ouvertes.fr/hal-01981954 (cf. p. xvi, xx, xxi).

[12] H. BOUKILI et J.-M. HÉRARD. "Simulation and preliminary validation of a three-phase flow model with energy". working paper or preprint. Jan. 2020. URL : https://hal.archives-ouvertes.fr/hal-02426425 (cf. p. xxiii).

[13] H. BOUKILI et J.-M. HÉRARD. "Relaxation and simulation of a barotropic three-phase flow model". In : *ESAIM: Mathematical Modelling and Numerical Analysis* 53 (2019), p. 1031-1059. DOI : 10.1051/m2an/2019001. URL : https://hal.archives-ouvertes.fr/hal-01745161 (cf. p. xvi, xxiii).

[14] T. BUFFARD, T. GALLOUËT et J.-M. HÉRARD. "A sequel to a rough Godunov scheme: application to real gases". In : *Computers and Fluids* 29.7 (2000), p. 813-847. URL : https://hal.archives-ouvertes.fr/hal-01579990 (cf. p. xviii).

[15] F. CAUPIN et E. HERBERT. "Cavitation in water: a review". In : *Comptes Rendus Physique* 7.9-10 (2006), p. 1000-1017. DOI : https://doi.org/10.1016/j.crhy.2006.10.015 (cf. p. xix).

[16] C. CHALONS et J.-F. COULOMBEL. "Relaxation approximation of the Euler equations". In : *Journal of Mathematical Analysis and Applications* 348.2 (2008), p. 872-893. ISSN : 0022-247X. URL : https://hal.archives-ouvertes.fr/hal-01838843 (cf. p. xvi, xviii, xxiv).

[17] S. CLERC. "Numerical Simulation of the Homogeneous Equilibrium Model for Two-Phase Flows". In : *Journal of Computational Physics* 161.1 (2000), p. 354-375. ISSN : 0021-9991. DOI : https://doi.org/10.1006/jcph.2000.6515. URL : http://www.sciencedirect.com/science/article/pii/S002199910096515X (cf. p. xii).

[18] C. COLAS. "Time-implicit integral formulation for fluid flow modelling in congested media". PhD Thesis. Aix-Marseille Université, nov. 2019. URL : https://tel.archives-ouvertes.fr/tel-02382958 (cf. p. xvii, xxiii).

[19] F. COQUEL et B. PERTHAME. "Relaxation of energy and approximate Riemann solvers for general pressure laws in fluid dynamics". In : *SIAM Journal on Numerical Analysis* 35.6 (1998), p. 2223-2249. DOI : https://doi.org/10.1137/S0036142997318528 (cf. p. xxiv).

[20] F. COQUEL, T. GALLOUËT, J.-M. HÉRARD et N. SEGUIN. "Closure laws for a two-fluid two-pressure model". In : *Comptes Rendus Mathématique* 334.10 (2002), p. 927-932. URL : https://hal.archives-ouvertes.fr/hal-01484345 (cf. p. xiii, xvi, xxii).

[21] F. COQUEL, J.-M. HÉRARD, K. SALEH et N. SEGUIN. "A class of two-fluid two-phase flow models". In : *42nd AIAA Fluid Dynamics Conference and Exhibit*. New Orleans, United States : AIAA, juin 2012. DOI : 10.2514/6.2012-3356. URL : https://hal.archives-ouvertes.fr/hal-01582645 (cf. p. xxii).

[22] J. COUTURIER et M. SCHWARZ. *Etat des recherches dans le domaine de la sûreté des réacteurs à eau sous pression*. EDP sciences Les Ulis, 2017. URL : %7Bhttps://www.irsn.fr/FR/Larecherche/publications-documentation/collection-ouvrages-IRSN/Documents/RDreacteurs_francais_WEB.pdf%7D (cf. p. x).

[23] F. DAUDE, P. GALON, Z. GAO et E. BLAUD. "Numerical experiments using a HLLC-type scheme with ALE formulation for compressible two-phase flows five-equation models with phase transition". In : *Computers & Fluids* 94 (mai 2014), p. 112-138. DOI : https://doi.org/10.1016/j.compfluid.2014.02.008 (cf. p. xiv, xxi).

[24] P. G. DEBENEDETTI. *Metastable liquids: concepts and principles*. Princeton University Press, 1996 (cf. p. xix).

[25] P. DOWNAR-ZAPOLSKI, Z. BILICKI, L. BOLLE et J. FRANCO. "The non-equilibrium relaxation model for one-dimensional flashing liquid flow". In : *International Journal of Multiphase Flow* 22.3 (1996), p. 473-483. DOI : https://doi.org/10.1016/0301-9322(95)00078-X (cf. p. xii).

[26] F. DRUI, E. FRANCK, P. HELLUY et L. NAVORET. "An analysis of over-relaxation in a kinetic approximation of systems of conservation laws". In : *Comptes Rendus Mécanique* 347.3 (jan. 2019), p. 259-269. DOI : 10.1016/j.crme.2018.12.001. URL : https://hal.archives-ouvertes.fr/hal-01839092 (cf. p. xxv).

[27] G. FACCANONI. "Study of a Fine Model of Liquid-Vapor Phase Change. Contribution to the Boiling Crisis Study." Thèse de doct. Ecole Polytechnique X, nov. 2008. URL : https://pastel.archives-ouvertes.fr/tel-00363460 (cf. p. xii, xiii, xvii).

[28] G. FACCANONI, S. KOKH et G. ALLAIRE. "Modelling and Simulation of Liquid-Vapor Phase Transition in Compressible Flows Based on Thermodynamical Equilibrium." In : *Mathematical Modelling and Numerical Analysis* 46.05 (sept. 2012), p. 1029-1054. URL : https://hal.archives-ouvertes.fr/hal-00976983 (cf. p. xii, xviii, xxi).

[29] G. FACCANONI et H. MATHIS. "Admissible Equations of State for Immiscible and Miscible Mixtures". In : *ESAIM: Proceedings and Surveys* (2019). URL : https://hal.archives-ouvertes.fr/tel-00363460 (cf. p. xiii, xiv).

[30] E. FAUCHER, J.-M. HÉRARD, M. BARRET et C. TOULEMONDE. "Computation of flashing flows in variable cross-section ducts". In : *International Journal of Computational Fluid Dynamics* 13.3 (2000), p. 365-391. URL : https://hal.archives-ouvertes.fr/hal-01580046 (cf. p. xii).

[31] T. GALLOUËT, J.-M. HÉRARD et N. SEGUIN. "On the use of symmetrizing variables for vacuum". In : *Calcolo* 40.3 (2003), p. 163-194. URL : https://hal.archives-ouvertes.fr/hal-00003439 (cf. p. xxiv).

[32] T. GALLOUËT, J.-M. HÉRARD et N. SEGUIN. "Some recent Finite Volume schemes to compute Euler equations using real gas EOS". In : *International Journal for Numerical Methods in Fluids* 39 (2002), p. 1073-1138. URL : https://hal.archives-ouvertes.fr/hal-01290885 (cf. p. xxiv).

[33] T. GALLOUËT, J.-M. HÉRARD et N. SEGUIN. "Numerical modeling of two-phase flows using the two-fluid two-pressure approach". In : *Mathematical Models and Methods in Applied Sciences* volume 14, numéro 5 (2004), p. 663-700. URL : https://hal.archives-ouvertes.fr/hal-00003327 (cf. p. xiii, xxii).

[34] S. GAVRILYUK et R. SAUREL. "Mathematical and Numerical Modeling of Two-phase Compressible Flows with Micro-inertia". In : *J. Comput. Phys.* 175.1 (jan. 2002), p. 326-360. ISSN : 0021-9991. DOI : http://dx.doi.org/10.1006/jcph.2001.6951 (cf. p. xiii).

[35] H. GHAZI. "Modelling compressible flows with phase transition and metastable states". Theses. Université de Nantes, nov. 2018. URL : https://tel.archives-ouvertes.fr/tel-01976189 (cf. p. xiii, xv).

[36] H. GHAZI, F. JAMES et H. MATHIS. "A nonisothermal thermodynamical model of liquid-vapor interaction with metastability". working paper or preprint. Oct. 2019. URL : https://hal.archives-ouvertes.fr/hal-02336478 (cf. p. xv).

[37] V. GIOVANGIGLI et L. MATUSZEWSKI. "Supercritical fluid thermodynamics from equations of state". In : *Physica D: Nonlinear Phenomena* 241.6 (2012), p. 649-670. DOI : https://doi.org/10.1016/j.physd.2011.12.002 (cf. p. xiv, xx).

[38] J. GLIMM, D. SALTZ et D. SHARP. "Two-pressure two-phase flow". In : *Advances In Nonlinear Partial Differential Equations And Related Areas: A Volume in Honor of Professor Xiaqi Ding*. World Scientific, 1998, p. 124-148. DOI : https://doi.org/10.1142/9789812815811_0008 (cf. p. xiii).

[39] A. R. GOODWIN, J. SENGERS et C. J. PETERS. *Applied Thermodynamics of Fluids*. The Royal Society of Chemistry, 2011, P001-509. DOI : http://dx.doi.org/10.1039/9781849730983 (cf. p. xx).

[40] *Guide de l'ASN numéro 28 : Qualification des outils de calcul scientifique utilisés dans la démonstration de sûreté nucléaire - première barrière*. juillet 2017. URL : https://www.asn.fr/Professionnels/Installations-nucleaires/Centrales-nucleaires/Guides-de-l-ASN-dans-le-domaine-des-installations-nucleaires/Guide-de-l-ASN-n-28-Qualification-des-outils-de-calcul-scientifique-utilises-dans-la-demonstration-de-surete-nucleaire (cf. p. xi, xiv, xv).

[41] H. GUILLARD et A. MURRONE. *A five equation reduced Model for compressible two phase flow problems*. Rapp. tech. RR-4778. INRIA, mar. 2003. URL : https://hal.inria.fr/inria-00071808 (cf. p. xii).

[42] V. GUILLEMAUD. "Modelling and numerical simulation of two-phase flows using the two-fluid two-pressure approach". Thèse de doct. (in French), Université de Provence - Aix-Marseille I, mar. 2007. URL : https://tel.archives-ouvertes.fr/tel-00169178 (cf. p. xxii).

[43] H. MATHIS. "A thermodynamically consistent model of a liquid-vapor fluid with a gas". In : *ESAIM: Mathematical Modelling and Numerical Analysis* 53.1 (2019), p. 63-84. DOI : https://doi.org/10.1051/m2an/2018044 (cf. p. xvi, xxi).

[44] M. HANTKE et S. MÜLLER. "Closure conditions for a one temperature non-equilibrium multi-component model of baer-nunziato type". In : *ESAIM: Proceedings and Surveys* 66 (2019), p. 42-60. DOI : https://doi.org/10.1051/proc/201966003 (cf. p. xvi).

[45] P. HELLUY. "Simulation numérique des écoulements multiphasiques: de la théorie aux applications". Habilitation à diriger des recherches. Université du Sud Toulon Var, 2005. URL : https://tel.archives-ouvertes.fr/tel-00657839 (cf. p. xvii).

[46] P. HELLUY et N. SEGUIN. "Relaxation models of phase transition flows". In : *ESAIM: Mathematical Modelling and Numerical Analysis* 40.2 (2006), p. 331-352. URL : https://hal.archives-ouvertes.fr/hal-00139607 (cf. p. xii, xvii).

[47] J.-M. HÉRARD. "A class of compressible multiphase flow models". In : *Comptes Rendus Mathématique* 354.9 (2016), p. 954-959. URL : https://hal.archives-ouvertes.fr/hal-01348880 (cf. p. xiii, xvi, xxii).

[48] J.-M. HÉRARD. "A three-phase flow model". In : *Mathematical and Computer Modelling* 45 (2007), p. 732-755. DOI : 10.1016/j.mcm.2006.07.018. URL : https://hal.archives-ouvertes.fr/hal-01265367 (cf. p. xiii, xvi, xxii).

[49] J.-M. HÉRARD. "An hyperbolic two-fluid model in a porous medium". In : *Comptes Rendus Mécanique* 336 (2008), p. 650-655. DOI : 10.1016/j.crme.2008.06.005. URL : https://hal.archives-ouvertes.fr/hal-01265406 (cf. p. xiii).

[50] J.-M. HÉRARD et O. HURISSE. "A simple method to compute standard two-fluid models". In : *International Journal of Computational Fluid Dynamics* 19.7 (2005), p. 475-482. DOI : 10.1080/10618560600566885. URL : https://hal.archives-ouvertes.fr/hal-01293567 (cf. p. xvi).

[51] J.-M. HÉRARD et H. LOCHON. "A simple turbulent two-fluid model". In : *Comptes Rendus Mécanique* 344.11-12 (2016), p. 776-783. DOI : 10.1016/j.crme.2016.10.010. URL : https://hal.archives-ouvertes.fr/hal-01339435 (cf. p. xiii).

[52] J.-M. HÉRARD et H. MATHIS. "A three-phase flow model with two miscible phases". In : *ESAIM: Mathematical Modelling and Numerical Analysis* 53, 1373-1389 (avr. 2019). URL : https://hal.archives-ouvertes.fr/hal-01976938 (cf. p. xiii, xvi, xxii, xxiii).

[53] J. HUANG, J. ZHANG et L. WANG. "Review of vapor condensation heat and mass transfer in the presence of non-condensable gas". In : *Applied thermal engineering* 89 (2015), p. 469-484. DOI : https://doi.org/10.1016/j.applthermaleng.2015.06.040 (cf. p. xv).

[54] O. HURISSE. "Numerical simulations of steady and unsteady two-phase flows using a homogeneous model". In : *Computers and Fluids* 152 (juil. 2017), p. 88-103. URL : https://hal.archives-ouvertes.fr/hal-01489039 (cf. p. xii, xiii, xix).

[55] O. HURISSE. "Various choices of source terms for a class of two-fluid two-velocity models". working paper or preprint. Déc. 2019. URL : https://hal.archives-ouvertes.fr/hal-02462215 (cf. p. xv).

[56] *Institut de Radioprotection et de Sûreté Nucléaire (IRSN), Reactivity-Initiated Accident (RIA)*. 2019. URL : https://www.irsn.fr/FR/connaissances/Installations_nucleaires/Les-centrales-nucleaires/criteres_surete_ria_aprp/Pages/1-accident-reactivite-RIA.aspx (cf. p. xxv).

[57] M. ISHII. *Thermo-Fluid Dynamics theory of two-phase flow*. Eyrolles, 1975 (cf. p. xii).

[58] F. JAMES et H. MATHIS. "A Relaxation model for liquid-vapor phase change with metastability". In : *Communications in Mathematical Sciences* 74.8 (2016), p. 2179-2214. DOI : 10.4310/CMS.2016.v14.n8.a4. URL : https://hal.archives-ouvertes.fr/hal-01178947 (cf. p. xv).

[59] S. JAOUEN. "Etude mathématique et numérique de stabilité pour des modeles hydrodynamiques avec transition de phase". Thèse de doct. Paris 6, 2001 (cf. p. xii, xvii).

[60] H. JIN, J. GLIMM et D. SHARP. "Compressible two-pressure two-phase flow models". In : *Physics letters A* 353.6 (2006), p. 469-474. DOI : https://doi.org/10.1016/j.physleta.2005.11.087 (cf. p. xiii).

[61] J. JUNG. "Numerical simulations of two-fluid flow on multicores accelerator". Thèse de doct. Université de Strasbourg, oct. 2013. URL : https://tel.archives-ouvertes.fr/tel-00876159 (cf. p. xii, xvii).

[62] A. K. KAPILA, R. MENIKOFF, J. B. BDZIL, S. F. SON et D. S. STEWART. "Two-phase modeling of deflagration-to-detonation transition in granular materials: Reduced equations". In : *Physics of Fluids* 13.10 (2001), p. 3002-3024. DOI : https://doi.org/10.1063/1.1398042 (cf. p. xii, xiii).

[63] T. KATO. "The Cauchy problem for quasi-linear symmetric hyperbolic systems". In : *Archive for Rational Mechanics and Analysis* 58.3 (1975), p. 181-205. DOI : https://doi.org/10.1007/BF00280740 (cf. p. xxii).

[64] R. J. KEE, F. M. RUPLEY, E. MEEKS et J. A. MILLER. *CHEMKIN-III: A FORTRAN chemical kinetics package for the analysis of gas-phase chemical and plasma kinetics*. Rapp. tech. Sandia National Labs., Livermore, CA (United States), 1996. URL : https://www.osti.gov/biblio/481621 (cf. p. xx).

[65] O. LE MÉTAYER et R. SAUREL. "The Noble-Abel Stiffened-Gas equation of state". In : *Physics of Fluids* 28 (2016), p. 046102. DOI : 10.1063/1.4945981. URL : https://hal.archives-ouvertes.fr/hal-01305974 (cf. p. xiv, xx).

[66] H. LOCHON. "Modélisation et simulation d'écoulements transitoires eau-vapeur en approche bifluide". Thèse de doct. Aix Marseille Université, 2016. URL : https://tel.archives-ouvertes.fr/tel-01379453/document (cf. p. xv).

[67] H. LOCHON, F. DAUDE, P. GALON et J.-M. HÉRARD. "Computation of fast depressurization of water using a two-fluid model: revisiting Bilicki modelling of mass transfer". In : *Computers and Fluids* 156 (oct. 2017), p. 162-174. DOI : 10.1016/j.compfluid.2017.07.008. URL : https://hal.archives-ouvertes.fr/hal-01401816 (cf. p. xv).

[68] H. J. MARIS. "Introduction to the physics of nucleation". In : *Comptes Rendus Physique* 7.9-10 (2006), p. 946-958. DOI : https://doi.org/10.1016/j.crhy.2006.10.019 (cf. p. xix).

[69] H. MATHIS. "Theoretical and numerical study of phase transition flows". Thèse de doct. Université de Strasbourg, sept. 2010. URL : https://tel.archives-ouvertes.fr/tel-00516683 (cf. p. xii, xiii, xvii).

[70] R. MEIGNEN, B. RAVERDY, S. PICCHI et J. LAMOME. "The challenge of modeling fuel–coolant interaction: Part II–Steam explosion". In : *Nuclear Engineering and Design* 280 (2014), p. 528-541. DOI : http://dx.doi.org/10.1016/j.nucengdes.2014.08.028 (cf. p. xiii, xv).

[71] S. MÜLLER, M. HANTKE et P. RICHTER. "Closure conditions for non-equilibrium multicomponent models". In : *Continuum Mechanics and Thermodynamics* 28.4 (2016), p. 1157-1189. DOI : https://doi.org/10.1007/s00161-015-0468-8 (cf. p. xvi).

[72] T. PETROVA et R. DOOLEY. "Revised release on surface tension of ordinary water substance". In : *Proceedings of the International Association for the Properties of Water and Steam, Moscow, Russia* (2014), p. 23-27. URL : http://www.iapws.org/relguide/Surf-H2O-2014.pdf (cf. p. xix).

[73] R. PRIVAT. "Développement du modèle PPR78 pour décrire, comprendre et prédire les diagrammes de phases hautes et basses pressions des systèmes binaires et des fluides pétroliers". Thèse de doct. Institut National Polytechnique de Lorraine, 2008. URL : https://hal.univ-lorraine.fr/tel-01753008 (cf. p. xiv, xx).

[74] B. RIEGEL. "Contribution à l'étude de la décompression d'une capacité en régime diphasique". Thèse de doct. 1978 (cf. p. xi, xii, xvi, xix, xxi).

[75] V. V. RUSANOV. "The calculation of the interaction of non-stationary shock waves with barriers". In : *Zhurnal Vychislitel'noi Matematiki i Matematicheskoi Fiziki* 1.2 (1961), p. 267-279. DOI : https://doi.org/10.1016/0041-5553(62)90062-9 (cf. p. xviii).

[76] K. SALEH et N. SEGUIN. "Some mathematical properties of a barotropic multiphase flow model". working paper or preprint. Déc. 2019. URL : https://hal.archives-ouvertes.fr/hal-01921027 (cf. p. xvi, xxii).

[77] W. WAGNER et H.-J. KRETZSCHMAR. *International Steam Tables: Properties of Water and Steam Based on the Industrial Formulation IAPWS-IF97*. Springer-Verlag Berlin Heidelberg, 2008. ISBN : 9783540742340. DOI : http://dx.doi.org/10.1007/978-3-540-74234-0 (cf. p. xiv, xvi, xvii, xx).

[78] N. YANENKO. *Méthode à pas fractionnaires: résolutions de problèmes polydimensionnels de physique mathématique*. Collection Intersciences. A. Colin, 1968. URL : https://books.google.fr/books?id=JBIyvgAACAAJ (cf. p. xviii).

Chapter 1

Simulations of out-of-equilibrium two-phase flows with a homogeneous model equipped with a look-up table as equation of state

The main content of this chapter has been published under the reference:

P. Helluy , O. Hurisse and L. Quibel, Assessment of numerical schemes for complex two-phase flows with real equations of state, *Computer & Fluids*, 196 (104347), 2019.

After a brief introduction, this article is reproduced. Some additionnal test cases and results are last presented in two additional appendixes (see appendix 1.E about verification work and appendix 1.F about relaxation time).

Synthesis of the chapter

We study in this chapter a homogeneous model, able to describe a mixture out of the thermodynamical equilibrium. Indeed, the only equilibrium assumption in the model is a kinematic equilibrium.

First, the homogeneous model is built step by step from extensive quantities. The key point of the modelling is the definition of the mixture entropy from Gibbs phasic relations: indeed, it enables to build a complete EOS for the mixture. The resulting model can be written as the Euler equations for the mixture quantities in addition to three equations on volume, mass and energy vapor fractions. These phasic fractions are convected and submitted to source terms, defined in accordance with the second principle of thermodynamics. Two closures must be defined by the user :

- an equation of state for both phases;
- a time scale, appearing in the source terms for fractions, characterizing the return towards the thermodynamical equilibrium.

This chapter has two main goals :

- verifying the coupling of the homogeneous model with a complex equation of state, a look-up table (LuT) for both phases;
- proposing a simplified model for the relaxation time scale, based on the nucleation theory.

The realistic equation of state used in this chapter is a look-up table, based on the IAPWS-IF97 formulation [52]. Such complex equations of state require very robust numerical schemes. Three numerical schemes have been compared through convergence studies on several Riemann problems : the Rusanov scheme, a VF-Roe scheme and a relaxation scheme, proposed by Chalons and Coulombel [10]. Only the Rusanov scheme and the relaxation scheme are robust enough to achieve the coupling with the look-up table. The verification study highlights that the relaxation scheme is more accurate as well as more efficient than the Rusanov scheme, which is very interesting for industrial test cases.

Many Riemann problems have been considered. First, only the convective part of the model (without source terms) has been taken into account with two so-called out-of-equilibrium Riemann problems studied in the article. Two additionnal Riemann problems with isolated waves (only a shock wave or only a contact wave) are presented in appendix 1.E of this chapter. The results illustrate how the relaxation scheme improves accuracy compared with the Rusanov scheme : the accuracy gain is significant for the contact wave, as soon as the mesh size is fine enough.

At-equilibrium Riemann problems have then been considered : after the convection step, the mixture fractions instantaneously tend towards the fractions satisfying the thermodynamical equilibrium. This supplementary step does not create particular problems (see article and appendix 1.E). We insist on the fact that the possibility to recover analytical solutions with complex equations of state like look-up tables is on its own a result. Nevertheless, a nuance has to be mentioned : the last Riemann problem presented in appendix 1.E highlights the accuracy limitation due to thermodynamical inversions occuring in the look-up table.

Unfortunately, such verification work cannot be achieved for a rarefaction wave because exact solutions cannot be built with enough accuracy. At best, a reference solution can be obtained, as presented in appendix 1.B, which is not enough to get a convergence curve.

In the homogeneous model, the return to the equilibrium is ensured by a relaxation process in accordance with the second law of thermodynamics. This relaxation process involves a characteristic time λ, which needs to be defined by the user. Very few references are available in the litterature about such out-of-equilibrium time scales and building a closure based on physical considerations is a difficult task. In the last part of the article, we focus on a simple test case : vaporisation occuring near a wall due to a rarefaction wave. The aim is to evaluate the strong influence of λ on the numerical results. First, constant values λ have been studied; then, we propose a very simplified model for λ based on the nucleation theory. Even if this latter simplified model is not completely physical, it enables to get complex and interesting behaviors. In appendix 1.F, some additionnal simulations with several time scales obtained with the nucleation closure are presented.

Abstract

Some accidental scenarii studied in the framework of the nuclear safety analysis involve liquids undergoing strong pressure drops at high temperature. In order to perform realistic simulations of such situations, a code based on a model that can handle both the thermodynamical disequilibrium between liquid and vapor and complex equations of state is required. We propose herein to test a homogeneous model built on the basis of the Euler system of equations and complemented by a mixture pressure law. The latter is defined in accordance with the Gibbs relation on the basis of the phasic pressures which are defined through a look-up table based on the IAPWS-97 formulation. A wide range of verification problems (Riemann problems) is then studied to assess the behavior of the numerical schemes for this complex equation of state. The tested relaxation scheme is the best compromise between accuracy and stability. At last, a simple test case of vaporisation near a wall is investigated in order to test some return to thermodynamical-equilibrium time-scale based on the nucleation theory.

Introduction

A nuclear pressurized water reactor (PWR) is composed of several heat exchangers in which the water is used as a heat-transfer medium and can undergo phase change (vaporisation and condensation). A PWR contains two main loops in which water flows in liquid or vapour state: the primary and the secondary circuits, exchanging heat through the steam generator. The primary circuit contains liquid water which collects the heating power of the nuclear core and brings it into the steam-generator. In this circuit, the temperature can reach $320°C$ and, to avoid vaporisation, the pressure is maintained at 155 bars, that means, above the saturation pressure. In the steam generator, the primary coolant flows into pipes that are surrounded by the water of the secondary circuit. The secondary fluid enters the steam generator as liquid. It then receives heat of the primary coolant on contact with the primary pipes and vaporizes. The steam-generator's outlet of the secondary circuit is then mainly composed of steam. The latter is used to generate electric power through turbines and it is afterwards condensed (through the use of an other heat-exchanger and a third circuit) to re-enter the steam generator as liquid. In this secondary circuit, the pressure level is much lower than in the primary circuit (in the range $50 - 70$ bars, depending on the steam generator).

When the reactor is at nominal operating point, the mass transfer and the heat exchanges imply small thermodynamical variations. Nevertheless, when accidental scenarii are considered, brutal thermodynamical variations are assumed. For instance, if one focuses on the breaches in the shell of the primary circuit, two major scenarii are studied.

- The Loss Of Coolant Accident (or LOCA) corresponds to a breach for which the primary liquid coolant enters into contact with the air of the reactor building at 1 bar. The violent pressure drop from 155 bars to 1 bar implies a rapid blowdown and the propagation of a depressurization wave into the primary circuit. This depressurization is associated with the vaporisation of the primary coolant.
- When a breach in a pipe that contains the primary coolant in the steam generator occurs, the pressurized liquid water enters into contact with a steam-liquid mixture at a lower pressure. As in the LOCA situation, a depressurization wave propagates into the primary circuit leading to the steam creation in the primary loop.

These two scenarii are associated with high pressure drops and high temperatures. In such situations, the fast transients can thus lead to non-equilibrium thermodynamics [4]. Hence,

the simulation of such rapid transients requires a model in which the thermodynamical disequilibria between the two phases are taken into account.

A first class of models that can be used for such scenarii is the so-called two-fluid model as those proposed in [2, 42, 28, 39, 14, 26]. In this class of models, the full thermodynamical disequilibrium is accounted for, in terms of the pressure, the temperature and the chemical potential (or Gibbs free enthalpy). Moreover, each phase is described by its own velocity. This two-velocity assumption has a drawback when dealing with the numerical simulation. Indeed, these models can possess eigenvalues that are very close to each other, for instance in situations involving a strong drag force. In order to distinguish the different waves associated with these close eigenvalues on the numerical approximations, one can thus have to deal with meshes that contain small enough cells, leading to an unaffordable computational cost for industrial applications in 3D. In the sequel, we choose to present a model that possesses a simpler eigenstructure. The latter makes the assumption that the two phases have the same velocity and is based on a model relying on the Euler set of equations. Therefore, the model inherits the Euler eigenstructure and enters the so-called class of the homogeneous models.

Most of two-phase flow homogeneous models proposed since around 40 years are based on one or more thermodynamical equilibrium assumptions (for instance: [42, 1, 21, 22, 29, 16, 24]). The homogeneous model used in this work does not make any equilibrium assumption for the thermodynamics: the phasic temperatures, pressures and chemical potentials may be different within each phase. On the one hand, this choice has been made to account for the full thermodynamical disequilibrium: the pressure disequilibrium may allow to enrich the model by introducing a bubble dynamics model as proposed in [26, 17, 18]. On the other hand, this allows to tackle some specificity of the mixture Equations Of States (EOS) obtained with equilibrium assumptions. It has indeed been reported that equilibrium assumptions may lead to a loss of strict concavity of the mixture entropy [3, 27, 23] and then to non-uniqueness of solutions of the Riemann problems.

This homogeneous model proposed in [3, 38, 31], and studied for instance in [21, 44, 41, 33], is based on the Euler system of equations complemented by a complex pressure law and by three unknowns: a **volume** fraction, a **mass** fraction and an **energy** fraction. These fractions allow to quantify the gap to the equilibrium state, reached when the system is isolated from the surroundings. In the model, the return to this equilibrium state is ensured by three source terms on the fractions involving a **unique** relaxation time-scale law. The whole model is built in order to be consistent with the second law of thermodynamics and is hyperbolic if each phasic entropy is concave with respect to the phasic specific volume and the phasic specific internal energy, and if the mixture temperature is positive [23, 35, 36]. The model and its properties are presented in section 1.1.

The model has been tested either on Riemann problems [35, 32] and on simulations reproducing elementary experimental facilities [36]. In both cases, the phasic EOS were defined through Stiffened Gas EOS [45] which is an extension of the perfect gas EOS. Even if the results presented in [36] are satisfactory, the Stiffened Gas EOS is too rough to describe **accurately** all the thermodynamical properties of the water on situations with **large variations** of the thermodynamical states, such as those depicted above. A look-up table has then been developed, based on the idea of [34] and using the IAPWS-97 [52] formulation as input data. The main recipes of this look-up table are presented in section 1.2.

The whole numerical scheme is described in section 1.3. In [35, 36, 32], the numerical

schemes used to compute the numerical approximations of the solutions of the model were all robust enough to deal with Stiffened Gas EOS. Unfortunately, few of these numerical schemes are able to handle complex EOS as the one proposed in section 1.2. Indeed, three numerical schemes for the convective part have been tested : the Rusanov scheme [48], a VFRoe-ncv scheme [6] and a relaxation scheme [10], based on the ideas of [49, 13, 5, 12]. In practise, problems of robustness have been encountered with VFRoe-ncv scheme used with the look-up table; therefore, only Rusanov scheme and the relaxation scheme have been compared when using it. In section 1.4, their behavior is then studied on a wide range of Riemann problems for the EOS defined through the look-up table of section 1.2. This verification procedure is mandatory to grasp the behavior of the numerical schemes in canonical situations. Furthermore it is required in the framework of the safety studies, where proofs of confidence on the simulation tools are to be given. The relaxation scheme is the best compromise between accuracy and robustness when using the look-up table.

In [36], the impact of the relaxation time-scale law has been shown by the mean of toy laws. These laws have no physical background, and they are based on the observations reported in [16]. In section 1.5, we propose a model for the relaxation time-scale on the basis of the classical nucleation theory [15], with some simple assumptions used in [8] or [43]. Since the nucleation theory only holds for the birth of steam bubbles in liquid, we have chosen a situation where the domain is entirely filled with liquid and where steam production remains reasonable: a depressurization occuring near a wall. This case can be schematic of what happens downstream a valve suddendly closed in a pipe in which high pressurized water flows. On can note that a very similar phenomenon occurs in the early stage of the SUPERCANON experiment reported in [47] and which was reproduced in [36].

1.1 A homogeneous model for two-phase flows

In this section, the considered model is only briefly presented in intensive variables. The whole building approach is available in appendix 1.A, starting from an extensive description of the system by a volume $\mathcal{V}$ (in m^3) of the mixture, corresponding to a mass $\mathcal{M}$ (in kg) and an internal energy $\mathcal{E}$ (in J).

Thermodynamically, each phase $k = l, v$ (liquid or vapor) is described by its own complete equation of state, expressed as a specific entropy $s_k(\tau_k, e_k)$ ($JK^{-1}kg^{-1}$) as a function of τ_k the specific volume (m^3kg^{-1}) and e_k the specific energy (Jkg^{-1}) and satisfying the Gibbs relation:

$$T_k ds_k = de_k + P_k d\tau_k, \tag{1.1}$$

where

$$\frac{1}{T_k} = \left.\frac{\partial s_k}{\partial e_k}\right|_{\tau_k} \quad ; \quad \frac{P_k}{T_k} = \left.\frac{\partial s_k}{\partial \tau_k}\right|_{e_k}. \tag{1.2}$$

Let us introduce the volume fraction α_k, the mass fraction y_k and the energy fraction z_k of phase k:

$$Y_k = (\alpha_k, y_k, z_k). \tag{1.3}$$

These fractions satisfy conservation relations:

$$1 = \alpha_l + \alpha_v \quad ; \quad 1 = y_l + y_v \quad ; \quad 1 = z_l + z_v, \tag{1.4}$$

and vary in accordance with the second principle of thermodynamics (cf appendix 1.A). Thanks to them, phasic quantities can be expressed from the mixture quantities:

$$\tau_k = \frac{\alpha_k}{y_k}\tau \quad ; \quad e_k = \frac{z_k}{y_k}e. \tag{1.5}$$

The mixture entropy s is defined as:

$$s(Y, \tau, e) = y_l s_l(\tau_l, e_l) + y_v s_v(\tau_v, e_v). \tag{1.6}$$

Using phasic Gibbs relations (1.1), thermodynamical mixture quantities can be deduced from phasic ones; they read:

$$P(Y, \tau, e) = \frac{\alpha_l \frac{P_l}{T_l} + \alpha_v \frac{P_v}{T_v}}{\frac{z_l}{T_l} + \frac{z_v}{T_v}} \quad ; \quad \frac{1}{T}(Y, \tau, e) = \frac{z_l}{T_l} + \frac{z_v}{T_v}. \tag{1.7}$$

The set of partial differential equations in conservative form is:

$$\begin{cases} \dfrac{\partial}{\partial t}(\rho Y) + \dfrac{\partial}{\partial x}(\rho U Y) = \rho\Gamma, \\ \dfrac{\partial}{\partial t}(\rho) + \dfrac{\partial}{\partial x}(\rho U) = 0, \\ \dfrac{\partial}{\partial t}(\rho U) + \dfrac{\partial}{\partial x}\left(\rho U^2 + P\right) = 0, \\ \dfrac{\partial}{\partial t}(\rho E) + \dfrac{\partial}{\partial x}(U(\rho E + P)) = 0. \end{cases} \tag{1.8}$$

with the following source terms:

$$\Gamma = \left(\frac{\bar{\alpha}_l - \alpha_l}{\lambda}, \frac{\bar{y}_l - y_l}{\lambda}, \frac{\bar{z}_l - z_l}{\lambda}\right),$$

where $(\bar{\alpha}_l, \bar{y}_l, \bar{z}_l)$ are the equilibrium fractions which maximize the mixture entropy for a given (τ, e). The user must specify one EOS (see section 1.2) for each phase and the time-scale $\lambda > 0$ describing the return to the thermodynamical equilibrium (see section 1.5 and appendix 1.C).

It can been shown that this model has interesting mathematical properties. These properties are summarized here and the reader can refer to [3, 23, 38, 31, 44, 41, 36, 37] for more details.

- The eigenstructure of the model is composed of 2 genuinely non-linear waves associated to the eigenvalues $U \pm c$, where c is the mixture sound speed, and one linearly degenerate wave associated to the eigenvalue U.
- The model is hyperbolic provided that the phasic entropies s_k are concave (see (H_7) in appendix 1.A) and that the mixture temperature is non-negative. The condition on the mixture temperature is of importance. Indeed, the concavity of the entropies together with the positivity of the mass fractions guarantees that c^2/T is non-negative. However some simple EOS (as the Van der Waals EOS) admit non-positive energy. This may lead to non-positive energy fractions and a possible drawback is to get a negative mixture temperature even when assumption (H_9) (see appendix 1.A) holds. Such situations can then correspond to a loss of hyperbolicity.
- Shocks are defined in a unique manner through the Rankine-Hugoniot relations.
- Assuming classical assumptions on the initial and boundary conditions for the fractions, and provided that the equilibrium fractions remain in $[0,1]^3$, the fractions remain in $[0,1]^3$.

1.2 Complex equations of state

In order to close the model presented in section 1.1, we need to specify: one EOS for each phase in terms of the specific entropy $(\tau_k, e_k) \mapsto s_k(\tau_k, e_k)$, and a law for the time-scale λ which describes the return to the thermodynamical equilibrium defined by $\bar{W}$. We focus here on the phasic EOS.

A classical way to deal with steam-liquid simulation is to use Stiffened Gas EOS [45]. These EOS are extensions of the perfect gas EOS. They are associated with quite simple formula involving five parameters. The specific phasic entropy then reads:

$$s_k(\tau_k, e_k) = C_{v,k} \ln \left((e_k - \Pi_k \tau_k) \tau_k^{\gamma_k - 1} \right) + s_k^0, \tag{1.9}$$

where $C_{v,k}$ is the heat capacity, $-\Pi_k$ is the minimal pressure[1], γ_k is the adiabatic coefficient ($\gamma_k > 1$) and s_k^0 is a reference specific-entropy.

In the situations that we intend to address, the domain of evolution of the thermodynamical quantities is important and these Stiffened Gas EOS may be not accurate enough, at least not for all the quantities. A more complex EOS with a better description of the properties of the fluids on wide domains is thus needed. Such EOS have been proposed, as Cubic EOS or Viriel formulations, but they are unfortunately not in complete form [23], which means that some thermodynamical quantities may not be defined. The IAPWS-97 formulation [52] is defined in a complete form since the the EOS is given as the Gibbs free enthalpy with respect to the pressure and the temperature. Nevertheless, this function is very complex and an important drawback is the high computational cost which is a crucial point for the simulation of fluid dynamics. In order to decrease this computational cost, **a Look-up Table** (LuT) has been implemented on the basis of the IAPWS-97 formulation[2].

We describe here how this LuT is built. Since the model deals with non-equilibrium thermodynamics and since each phase has to possess its own EOS, a LuT is built for each phase.

The (P, T)-plane is chosen as an entry of the LuT and the Gibbs free enthalpy $\mu_k(P, T)$ is given for each phase. In order to remain consistent with the Gibbs relation for each phase (1.1), all the other quantities have to be computed from the derivatives of

$$\mu_k(P, T) = e_k(P, T) + P\tau_k(P, T) - Ts_k(P, T).$$

Indeed, by differentiating μ_k and by using the phasic Gibbs relation (1.1) we get:

$$d\mu_k = \tau_k dP - s_k dT,$$

so that the specific volume and the specific entropy are respectively defined as:

$$\tau_k(P, T) = \partial \mu_k / \partial P_{|T} \quad \text{and} \quad s_k(P, T) = -\partial \mu_k / \partial T_{|P}.$$

The specific energy then follows $e_k(P, T) = \mu_k(P, T) - P\tau_k(P, T) + Ts_k(P, T)$.

Remark 1.1 — In order to fulfill the phasic Gibbs relation (1.1), the quantities τ_k, s_k and e_k should not be tabulated independently. □

[1] The phasic entropy and the phasic sound speeds are defined for $P_k > -\Pi_k$; and the phasic temperature is positive for $P_k > -\Pi_k$

[2] The methodology proposed here to build a LuT is obviously not restricted to the IAPWS formulation.

As in [34], the thermodynamical plane (P, T) is discretized using a Quadtree approach which is balanced to get a regular discretization of the plane, enabling a quick research through the look-up table in practical simulations. Some domains of the (P, T)-plane are refined. This is actually the case: in the neighborhood of the saturation curve, at low pressures, at low temperatures and at high pressures on the saturation curve. The LuT used in the next sections has been built for pressures from 0.1 bar to 219 bars, so that we avoid vicinity of the critical point. The temperature range is $[283.0\ K; 1070.0\ K]$.

Figure 1.1 shows some visualizations of the quadtree mesh for different ranges of pressures and temperatures. On each cell of the (P, T)-plane, the IAPWS-97 Gibbs enthalpy μ_k is interpolated using a polynomial spline in P and T. The most important point is to preserve the Gibbs relations (1.1). It is required that μ_k belongs to $\mathcal{C}^1$ on the whole domain. Therefore, splines of order 3 are used and a specific treatment is applied to each cell connected to wider cells. For these cells, at each node that is common with a wider cell, the values of μ_k and its derivatives are not obtained from IAPWS-97. These values are replaced by the values of μ_k and its derivatives computed from the interpolated spline of the wider cell. Hence we ensure the continuity of the interpolated value μ_k and of its derivatives with respect to P and T at the junction between the cells of different sizes. For this purpose, the computation of the spline coefficients is then done by decreasing order of the size of the cells. The final level of refinement of the quadtree is chosen so as to get a relative error between the IAPWS values of μ_k and the interpolated values less than a threshold. In the LuT used in the next sections, this threshold has been chosen equal to 10^{-5}, and the final mesh contains more than 163000 cells.

The use of meshes based on quadtree techniques is a great advantage because it allows the local refinement of the description together with a reasonable computational cost for the search of the cell in which the properties have to be estimated. In fact, for a given (P^0, T^0), the cost of the search of the quadtree's cell containing (P^0, T^0) is proportional to the depth of this cell in the quadtree structure (i.e. the smaller the target cell is, the more expensive its search is).

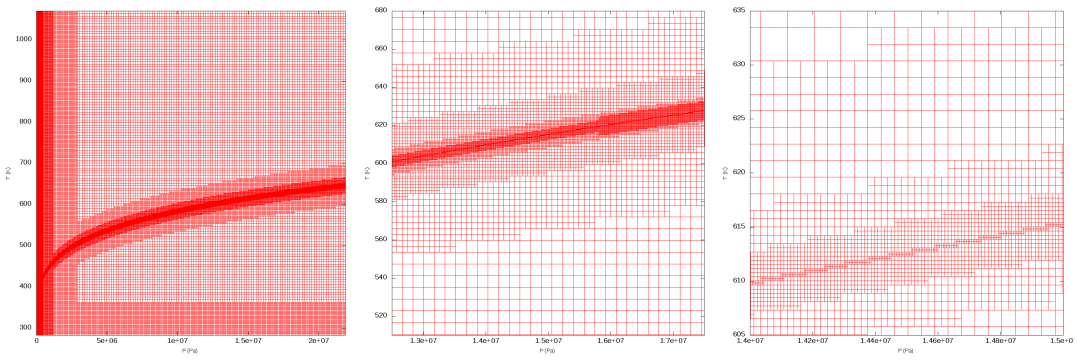

Figure 1.1 – *Mesh of the (P, T)-plane. The left figure shows the whole mesh, and the log-like domain corresponds to the mesh refinement around the saturation curve. The two figures on the right show zooms on the saturation curve zone.*

We are dealing with compressible phenomena so that the model of section 1.1 has to be discretized in conservative form (numerical schemes are described in section 1.3). Hence the "natural" variables for the conservative part of the model are (τ, e). Since the LuT EOS is defined in the (P, T)-plane, and in order to maintain the consistency of the thermodynamical description through a complete LuT, we need to compute the change of variables $(\tau_k, e_k) \mapsto (P_k, T_k)$. More precisely, for any value of the specific volume τ_k^0 and specific energy e_k^0, we

have to find the pressure P_k and the temperature T_k that fulfill:

$$\begin{cases} e_k(P_k, T_k) = e_k^0, \\ \tau_k(P_k, T_k) = \tau_k^0, \end{cases} \tag{1.10}$$

where the functions $(P_k, T_k) \mapsto e_k(P_k, T_k)$ and $(P_k, T_k) \mapsto \tau_k(P_k, T_k)$ are obtained from the LuT. From a numerical point of view, the computation of an approximate solution of (1.10) through a Newton-type algorithm can be tricky and it requires an accurate initial guess of the solution. For this purpose, a second LuT has been built for each phase. This second LuT is based on a non-balanced quadtree for the (τ, e)-plane. At each vertice (τ_k^i, e_k^i) of the mesh corresponds a couple (P_k^i, T_k^i) such that $e_k(P_k^i, T_k^i) = e_k^i$ and $\tau_k(P_k^i, T_k^i) = \tau_k^i$. This second LuT is not used directly, but using bilinear interpolation, it represents a database to provide initial guesses to solve the general problem (1.10). With the help of this second LuT, solving (1.10) requires less iterations and it is more robust. For the sections below, this second LuT contains 166000 cells.

Remark 1.2 — In practice, considering the Stiffened Gas EOS as a reference, the order of magnitude of the computation costs is 700 times higher for the direct IAPWS formulation and it is 8 times higher with the LuT EOS as depicted above. Obviously, the gain in CPU time strongly depends on the test case and on the LuT used (the local refinement and the depth of the quadtree are strongly involved). □

1.3 Numerical method

The overall numerical method is based on a fractional step method [53] using a Lie-Trotter splitting. The initial condition problem associated with system of equations (1.8) can be written:

$$\frac{\partial}{\partial t}(W) = -\frac{\partial}{\partial x}(\mathcal{F}(W)) + \mathcal{G}(W), \quad W(t=0) = W^0, \tag{1.11}$$

where $\mathcal{F}$ correspond to the convective flux and $\mathcal{G}$ to the source terms. A straightforward Lie-Trotter splitting has been chosen here. It consists in solving at time $t = t^n$ the following two sub-systems during a time step Δt^n:

$$(i) \quad \frac{\partial}{\partial t}(W_a) = -\frac{\partial}{\partial x}(\mathcal{F}(W_a)), \quad W_a(t^n) = W^n, \tag{1.12}$$

which gives $W_a(t^n + \Delta t^n)$;

$$(ii) \quad \frac{\partial}{\partial t}(W_b) = \mathcal{G}(W_b), \quad W_b(t = t^n) = W_a(t^n + \Delta t^n). \tag{1.13}$$

Since this splitting is first order with respect to time, each sub-system is solved using first order schemes.

The first sub-system takes into account the convective part. For that purpose, first-order explicit and conservative finite volumes schemes are used. Their general form for a one-dimensional framework with cells Ω_i is:

$$|\Omega_i|(W_i^{n+1} - W_i^n) = -\Delta t^n((F(W_i^n, W_{i+1}^n) - F(W_{i-1}^n, W_i^n)), \tag{1.14}$$

where W_i^n denotes the space-average value of W on the cell Ω_i at time t^n. The time step Δt^n is computed from the variable W_i^n and from the mesh size $|\Omega_i|$ in order to fulfill stability constraint. The two-point numerical flux F depends on the used scheme. In the following, we have tested three different schemes: Rusanov scheme [48], a VFRoe-ncv scheme using variables (Y, τ, U, P) [6] and the relaxation scheme proposed in [10]. These schemes are described in section 1.3.1.

The second sub-system (1.13) corresponds to a system of ordinary derivative equations. In this sub-system, the return to equilibrium is accounted for. Since the time-step is computed to fulfill a stability constraint of the numerical scheme used for the first sub-system, this second step is achieved using an implicit scheme. The latter is detailed in section 1.3.2.

Remark 1.3 — For the sake of simplicity, each sub-system is solved using a unique time-step and the time-step for solving the source-terms step is the time-step computed for the convective part.

1.3.1 Numerical schemes for the convective sub-system

This section is devoted to the numerical schemes used to compute the two-point numerical fluxes F considering two neighboring cells. The quantities in the cell on the left (resp. right) of the interface between the two cells are denoted by a subscript l (resp. r).

Rusanov scheme (see [48]) and VFRoe-ncv scheme using variables (u, P, τ) (see [6]) are very classical and the details about these schemes can be found in the previous references.

The studied relaxation scheme was initially proposed in [10] and it is based on the work of [49, 13, 5, 40]. The main idea is to compute the numerical flux on the basis of an enlarged hyperbolic system associated with a strong relaxation term. This enlarged system is chosen so that all its characteristic fields are linearly degenerate. Hence, the solution of the associated Riemann problem at each interface between two cells is easy to compute. The relaxation term, accounted for in the enlarged system by a source term, then allows to recover formally the initial system of equations.

We follow here the proposition detailed in [10]. One additional scalar unknown $\mathcal{T}$ is introduced with the initial condition:

$$\forall x,\ \mathcal{T}(0,x) = \tau(0,x).$$

A new pressure Π is also defined, which can be seen as a linearization of the pressure P with respect to the variable τ around $\mathcal{T}$:

$$\Pi = P(Y,\mathcal{T},e) + a^2(\mathcal{T}-\tau), \tag{1.15}$$

where a is a positive parameter. At last, a relaxation specific total energy Σ is introduced in order to be consistent with the pressure Π:

$$\Sigma = \frac{u^2}{2} + e + \frac{\Pi^2 - P^2(Y,\mathcal{T},e)}{2a^2}, \tag{1.16}$$

We set Z the enlarged variable: $Z = (Y,\tau,U,\Sigma,\mathcal{T})$. The enlarged system to solve is then the following:

$$\begin{cases} \partial_t(\rho Y) + \partial_x(\rho Y U) = 0, \\ \partial_t\rho + \partial_x(\rho U) = 0, \\ \partial_t(\rho U) + \partial_x(\rho U^2 + \Pi) = 0, \\ \partial_t(\rho\Sigma) + \partial_x(\rho U\Sigma + U\Pi) = 0, \\ \partial_t(\rho\mathcal{T}) + \partial_x(\rho\mathcal{T}U) = \dfrac{1}{\epsilon}\rho(\tau-\mathcal{T}), \end{cases} \tag{1.17}$$

where the relaxation source terms for $\mathcal{T}$ are characterized by the parameter $\epsilon \geq 0$. A crucial point is that all the characteristic fields of the convective part of system (1.17) are linearly degenerate and associated with the speed waves:

$$\lambda_1 = U_l - a\tau_l, \quad \lambda_2 = U^*, \quad \lambda_3 = U_r + a\tau_r, \tag{1.18}$$

with:

$$U^* = \frac{1}{2}(U_l + U_r) + \frac{1}{2a}(\Pi_l - \Pi_r). \tag{1.19}$$

The parameter a, that appears in the definitions of Π and σ (resp. (1.15) and (1.16)), should satisfy a stability condition [5] which is related to the sub-characteristic condition for the enlarged system (1.17):

$$a > \max\left(\frac{c_l(Y_l,\tau_l,e_l)}{\tau_l}, \frac{c_r(Y_r,\tau_r,e_r)}{\tau_r}\right), \tag{1.20}$$

where $c(Y,\tau,e)$ denotes the sound speed associated with the pressure law P:

$$c(Y,\tau,e) = -\tau^2 \frac{\partial}{\partial\tau}(P)\bigg|_{Y,s}.$$

Moreover, a is chosen so that the eigenvalues fulfill the relation:

$$\lambda_1 < \lambda_2 < \lambda_3, \tag{1.21}$$

where λ_k is detailed in (1.18); this last condition is equivalent to:

$$\tau_l^* > 0 \quad \text{and} \quad \tau_r^* > 0. \tag{1.22}$$

Thanks to relations (1.21), the self-similar solution $\mathcal{Z}\left(x/t, Z_l, Z_r\right)$ of the Riemann problem at the interface separating two cells (l and r) for the convective part of system (1.17) can be written:

$$\mathcal{Z}\left(\frac{x}{t}, Z_l, Z_r\right) = \begin{cases} Z_l, & \text{if } x/t < \lambda_1 \\ Z_l^*, & \text{if } \lambda_1 < x/t < \lambda_2 \\ Z_r^*, & \text{if } \lambda_2 < x/t < \lambda_3 \\ Z_r, & \text{if } \lambda_3 < x/t \end{cases} \tag{1.23}$$

with

$$\tau_l^* = \tau_l + \frac{1}{a}(U^* - U_l) \quad ; \quad \tau_r^* = \tau_r - \frac{1}{a}(U^* - U_r)\,; \tag{1.24}$$

$$\Sigma_l^* = \Sigma_l + \frac{1}{a}(\Pi_l U_l - \Pi^* U^*); \Sigma_r^* = \Sigma_r - \frac{1}{a}(\Pi_r U_r - \Pi^* U^*)\,; \tag{1.25}$$

$$\mathcal{T}_l^* = \mathcal{T}_l \quad ; \quad \mathcal{T}_r^* = \mathcal{T}_r \quad ; \quad \Upsilon_l^* = \Upsilon_l; \quad \Upsilon_r^* = \Upsilon_r\,; \tag{1.26}$$

$$U_l^* = U_r^* = U^* \quad ; \quad \Pi_l^* = \Pi_r^* = \Pi^* \tag{1.27}$$

where we have set:

$$\Pi^* = \frac{1}{2}(\Pi_l + \Pi_r) + \frac{a}{2}(U_l - U_r)$$

and where U^* is given in (1.19). From a numerical point of view, we have chosen an instantaneous relaxation: $\epsilon \to 0$. As a consequence, we have $\mathcal{T} \to \tau$, $\Pi \to P$ and $\Sigma \to E$, so that the two-point numerical flux corresponding to the relaxation scheme [10] is solely based on the value $\mathcal{Z}\left(x/t = 0, Z_l, Z_r\right)$ of the solution $\mathcal{Z}$ at the interface between the two-cells l and r. It reads:

$$F(W_l, W_r) = \left(\frac{\Upsilon U}{\tau}, \frac{U}{\tau}, \frac{U^2}{\tau} + \Pi, \frac{U\Sigma}{\tau} + U\Pi\right),$$

where Υ, τ, U, and Σ are the components of $\mathcal{Z}\left(x/t = 0, Z_l, Z_r\right)$ and where Π also arises from the solution $\mathcal{Z}\left(x/t = 0, Z_l, Z_r\right)$.

Remark 1.4 — For all the simulations that we have performed, the choice of a in agreement with the constraint (1.20) has always been sufficient to ensure that the constraint (1.21) was fulfilled. □

We briefly recall some important properties of the relaxation scheme, proved in [9] for a more general context of Euler system with several pressures. In the following, index j refers to one mesh cell:

- $\mathcal{L}_1$ stability: $\rho_j^{n+1} > 0$ and $e_j^{n+1} > 0\ \forall j$;
- discrete entropy inequality:

$$\rho S_j^{n+1} \leq \rho S_j^n - \frac{\Delta t}{\Delta x}\{(\rho S u)(0; {Z_j}^n; {Z_{j+1}}^n) - (\rho S u)(0; {Z_{j-1}}^n; {Z_j}^n)\};$$

- maximum principle:

$$\min(S_{j-1}^n, S_j^n, S_{j+1}^n) \leq S_j^{n+1} \leq \max(S_{j-1}^n, S_j^n, S_{j+1}^n).$$

1.3.2 Numerical scheme for the source-term sub-system

The second sub-system (1.13) corresponds to a system of ordinary differential equations:

$$\begin{cases} \dfrac{\partial}{\partial t}(Y) = \dfrac{\overline{Y}(\tau, e) - Y}{\lambda}, \\ \dfrac{\partial}{\partial t}(\rho) = 0, \\ \dfrac{\partial}{\partial t}(\rho U) = 0, \\ \dfrac{\partial}{\partial t}(\rho E) = 0. \end{cases} \tag{1.28}$$

We first remark that the specific volume and the specific energy are constant, as a consequence it can be written in an equivalent manner:

$$\begin{cases} \dfrac{\partial}{\partial t}(Y(t)) = \dfrac{\overline{Y}(\tau(0), e(0)) - Y(t)}{\lambda(t)}, \\ \dfrac{\partial}{\partial t}(\rho(t)) = 0, \\ \dfrac{\partial}{\partial t}(U(t)) = 0, \\ \dfrac{\partial}{\partial t}(e(t)) = 0. \end{cases} \tag{1.29}$$

Obviously, when the parameter λ is constant, system (1.29) can be integrated exactly. Thus, in system (1.29), $\lambda(t)$ is replaced by its initial value $\lambda(0)$, and the approximate solutions for the fraction are then computed as the exact solutions of the approximated sub-system:

$$\frac{\partial}{\partial t}(Y(t)) = \frac{\overline{Y}(\tau(0), e(0)) - Y(t)}{\lambda(0)}. \tag{1.30}$$

For an initial condition given by the value at time t^n, the final approximation at time $t^{n+1} = t^n + \Delta t^n$ then reads:

$$\begin{cases} Y(t^{n+1}) = Y(t^n)\, e^{\dfrac{-\Delta t^n}{\lambda(t^n)}} + \overline{Y}(t^n)\,(1 - e^{\dfrac{-\Delta t^n}{\lambda(t^n)}}), \\ \rho(t^{n+1}) = \rho(t^n), \\ U(t^{n+1}) = U(t^n), \\ e(t^{n+1}) = e(t^n). \end{cases} \tag{1.31}$$

Remark 1.5 — It can easily be checked than when dealing with instantaneous thermodynamical relaxation, $\lambda(0) \to 0$, the scheme gives $Y(t^{n+1}) \to \overline{Y}(t^n)$. The associated thermodynamical states then correspond to the states that maximize the mixture entropy at $(\tau, e)(t^n)$. When $\overline{Y}(t^n) \in]0, 1[$, the pressure, temperature and chemical potential equilibria are ensured. □

Remark 1.6 — The update formula (1.31) for the fraction $Y(t^{n+1})$ is a barycenter between $Y(t^n)$ and $\overline{Y}(t^n)$. Hence, provided that $Y(t^n)$ and $\overline{Y}(t^n)$ lie in $[0, 1]^3$, $Y(t^{n+1})$ also lies in $[0, 1]^3$. □

1.4 Approximate solutions of Riemann problems

In this section, the numerical schemes of section 1.3 are assessed by the mean of Riemann Problems. For that purpose, Stiffened Gas EOS and the LuT of section 1.2 have been used. Considering the consistency of the schemes or the asymptotic rate of convergence, it could be sufficient to focus on Stiffened Gas EOS. Nevertheless, verification procedure can be seen as an unbiased tool to compare numerical schemes with respect to a known reference-solution. Different aspects can thus be compared as: the accuracy with respect to the mesh-size, the accuracy with respect to the CPU-time -which is very important for industrial applications-, the behavior for canonical solutions as isolated waves.

In the following, several Riemann problems are considered for the model of section 1.1. They are only composed of contact waves and shock waves. As depicted on figure (1.2), we consider: a ghost wave for the field $U - c$, a contact wave U and a shock wave $U + c$. Depending on the test case, the contact wave U and the shock $U + c$ may be ghost waves in order to study the accuracy of the schemes for isolated waves. The analytical rarefaction waves are far more complex to evaluate with accuracy when using the LuT, as depicted in appendix 1.B. We do not consider these regular waves in the sequel.

Considering that the model of section 1.1 possesses a convective part and source terms that bring the system back to the thermodynamical equilibrium, "out-of-equilibrium" Riemann problems -with $\lambda \to \infty$- and "at-equilibrium" Riemann problem -with $\lambda \to 0$- are proposed. For out-of-equilibrium Riemann problems, only the convective part of the numerical procedure is considered. For the latter, the analytical solutions of the Riemann problem are computed using the mixture EOS for $Y = \overline{Y}$. In the simulation, we apply the whole scheme of section 1.3 based on a Lie-splitting: we first account for the convective terms with an out-of-equilibrium mixture EOS, and the thermodynamical equilibrium is then enforced through the source terms. The aim of these tests is to check the convergence of the relaxation approach for the simulation of cases where the mixture EOS is not regular (in particular the sound speed of the mixture EOS at-equilibrium).

The general setting of the Riemann problems is the following, see figure (1.2). We consider the one-dimensional domain $x \in [0\ m, 1\ m]$ and the initial discontinuity is located at $x_d = 1/2\ m$. This domain is discretized using uniform meshes. The exact solution consists in the left and right initial states, respectively denoted by 1 and 3 on figure (1.2), separated by a uniform intermediate state, denoted by 2 on figure (1.2). When two ghost waves are imposed, the state 2 obviously coincides with the state 1 or 3. For each EoS, Stiffened Gas or LuT, we can compute the analytical solution of the Riemann problem. In the case of the LuT EoS, the initialization of each state must be done carefully because the LuT is defined on the $(P, T)-$plane and the use of an other plane may lead to a loss of accuracy. This is obviously not the case for Stiffened Gas EoS. The method used to compute the analytical solutions of the Riemann problem is classical. Several different test cases have been considered. The table 1.1 sums up their main characteristics and the initial data for each test case are reported in appendix 1.D.

The analytical solutions are then used to compute the relative L^1-error of the numerical approximations obtained with the different schemes. For an approximated solution Ψ^{approx} and an exact solution Ψ^{exact}, since the mesh size is uniform, the relative L^1-error is computed at time t^n on the whole mesh as:

$$\frac{\sum_i |\Psi_i^{approx,n} - \Psi^{exact}(x_i, t^n)|}{\sum_i |\Psi^{exact}(x_i, t^n)|},$$

where x_i is the barycenter of the cell i. Obviously, when $\sum_i |\Psi^{exact}(x_i, t^n)| = 0$ this relative error is meaningless and we then consider the mere L^1-error:

$$\sum_i |\Psi_i^{approx,n} - \Psi^{exact}(x_i, t^n)|.$$

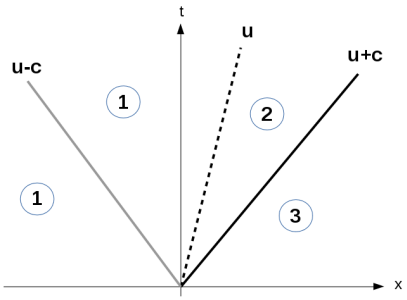

Figure 1.2 – *Riemann problem with one intermediate state; U-C: ghost wave; U: contact wave; U+C: shock wave*

§	Waves	Eq. ?	EOS	Initial states Left/Right	Data
1.4.1	C + S	No	SG	liq. + vap. / liq. + vap.	1.D.1
1.4.1	C + S	No	LuT	liq. + vap. / liq. + vap.	1.D.1
1.4.2	C + S	Yes	LuT	liq. + vap. / liq. + vap.	1.D.2
1.4.3.1	S	Yes	LuT	liq. / liq. + vap.	1.D.3
1.4.3.2	C	Yes	LuT	liq. / liq. + vap.	1.D.4

Table 1.1 – *List of the presented test cases. In the second colmun, "C" stands for contact and "S" for shock. The third column "Eq. ?" specifies if the EOS is at equilibrium ("Yes"), with $\lambda \to 0$, or out-of-equilibrium ("No"), with $\lambda \to +\infty$. The fourth column recalls the nature of the initial states (liquid, vapor or mixture). The last column refers to the appendix where initial data are given.*

1.4.1 Out of equilibrium test cases for the Stiffened Gas EOS and the LuT

In this section, we investigate the behavior of the three schemes of section 1.3.1 for Riemann problems involving the out-of-equilibrium EOS. For both test cases we focus on the convective part and the source terms are not accounted for, i.e. $\lambda \to \infty$. The first Riemann problem is based on the Stiffened Gas EOS, whereas the second one involved the mixture EOS using the LuT. Since these two Riemann problems only involve a contact wave and a shock wave, it is possible to choose the same left states and the same intermediate states. The right states have then been chosen so that the right densities are equal. Obviously, since the Stiffened Gas EOS and the LuT are different for the right pressures, the right velocities and the shock speeds are different.

We first want to point out that VFRoe-ncv scheme fails during the very first iterations on the test case with the LuT. lie outside the domain of definition of the LuT. Rusanov scheme and the relaxation scheme are not subject to these drawbacks and are thus more robust while using the LuT. As a consequence, only Rusanov scheme and the relaxation scheme have been used with the LuT in the following. For the Stiffened Gas EOS, the three numerical schemes have been tested.

1.4.1.1 Asymptotic rate of convergence

The convergence curves at time $t_{end} = 2.5\ 10^{-4}\ s$ are plotted on figure (1.3a) for the Stiffened Gas EOS and on figure (1.3b) for the LuT. Since we are dealing with Riemann problems that involve linearly degenerate waves and genuinely non-linear waves, the asymptotic rate of convergence should be $1/2$. Indeed, this order $1/2$ is reached for the volume fraction α (the behavior is the same for the three fractions) on the finest mesh for all schemes in both cases: all the other quantities will reach the same order with finer meshes.

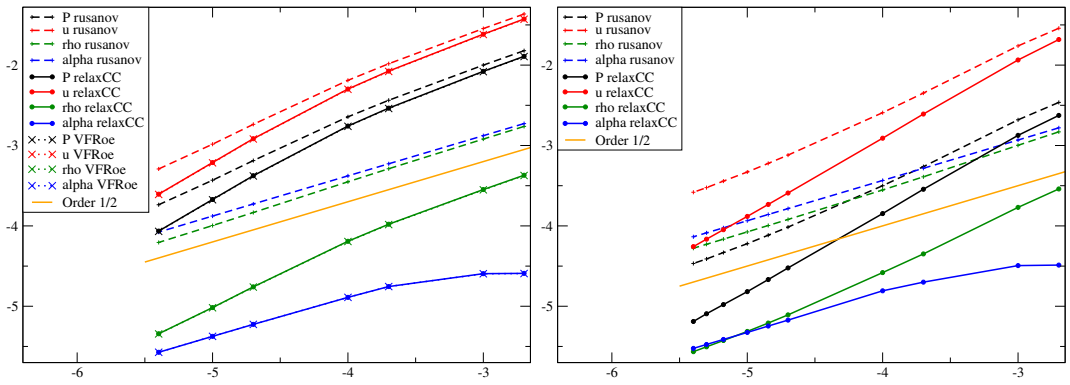

(a) *Stiffened Gas test case.* (b) *LuT test case.*

Figure 1.3 – *Convergence curves for the Riemann problems out of equilibrium: logarithm of the relative L^1-error versus the logarithm of the mesh size with uniform meshes containing from 500 to 250 000 cells.. The error is plotted for the approximate solutions obtained with the different schemes and for P, U, ρ, α.*

When focusing on the Stiffened Gas test case (see figure (1.3a)), the relaxation scheme and VFRoe-ncv scheme have very similar behaviors and they are less diffusive than Rusanov scheme. This can be observed with the results for the fraction α. Considering the analytical solution, the fraction does not depend on the genuinely linear waves and it travels with the velocity of the contact wave which is equal to $1\ m/s$ in our case (see appendix 1.D.1). Hence at time $t_{end} = 2.5\ 10^{-4}\ s$, the initial discontinuity on α has covered a distance of $L = 1 \times t_{end} = 2.5\ 10^{-4}\ m$. As long as the size of a cell of the mesh is greater than L, the approximated contact will remain in the same cell during the simulation $t \in [0, t_{end}]$. So that the relative error with respect to the exact solution will not vary a lot. Since the logarithm (base 10) of L is equal to -3.6, this explains the constant relative error for α on the coarse meshes on figure (1.3a) (i.e. for abscissa greater than -3.6). The same behavior occurs for the LuT test case with the relaxation scheme on figure (1.3b). This behavior is not observed here for Rusanov scheme because of its high level of numerical diffusion on the contact waves.

1.4.1.2 Accuracy and efficiency

Due to our choice for the analytical solutions, the profiles for P, U and α along the domain are uniform on each side of a traveling discontinuity:

- P and U only jump across the shock wave;
- α only jumps across the contact wave.

On the contrary, the density ρ has two jumps, one across the shock wave and one across the contact wave. Preservation of pressure or velocity through the contact wave is a well

known problem; see for instance [50]. Moreover, it has been shown in [25] that preservation of constant values through a contact wave requires some constraints on the EOS depending on the numerical diffusivity of the numerical method. Here, due to the form of the mixture EOS of the studied model, it is not possible to get the same behavior on the approximated solutions for the contact wave, at least on coarse meshes. Indeed, U and P present spurious waves at the location of the contact wave. Even if these spurious waves tend to vanish when the mesh is refined (approximate solutions converge towards the analytical solution with $[U] = [P] = 0$ in the contact wave), the accuracy is influenced by these spurious waves. These waves can be observed on figure (1.8).

For the two test cases, see figures (1.3a) and (1.3b), VFRoe-ncv scheme and the relaxation scheme provide a better accuracy than Rusanov scheme, at least for the density and the fractions, which strongly depend on the contact wave. The accuracy on the pressure and on the velocity is only slightly improved for coarse meshes. Nevertheless, this improvement increases when the mesh is refined. This is due to the low velocity of the contact wave ($1\ m/s$) and is related to the remark of the previous section. Indeed, as soon as the mesh is fine enough to provide an accurate approximation of the contact wave, the accuracy on pressure and the velocity increases because the spurious waves described above tend to vanish rapidly.

For the LuT test case, see figure (1.3b), we observe similar behavior: the relaxation scheme is far better than Rusanov scheme for the fractions and the density and the error is comparable for on U and P on coarse meshes. Moreover, the accuracy improvement with the relaxation scheme becomes more and more important when the mesh is refined.

On the figures (1.4a) and (1.4b), the error is plotted as a function of CPU-time in order to compare the schemes in term of efficiency. For a given CPU-time, the relaxation scheme gives the best accuracy for both EOS. When focusing on the Stiffened Gas test case, the relaxation scheme and VFRoe-scheme have a very similar efficiency (see figure 1.4a), with a slight advantage for the relaxation scheme. Indeed, the computation of VFRoe-ncv flux requires an additional thermodynamical computation. In the LuT test case, the efficiency gain with the relaxation scheme compared with Rusanov scheme is even more significant than in the Stiffened Gas test case. With the LuT, the number of thermodynamical computations is the same than with the stiffened gas EOS but each one is more CPU-time consuming. Rusanov scheme and the relaxation scheme require exactly the same calls to the LuT, but the gain in accuracy with the relaxation scheme allows to use coarser meshes. As a consequence, a given accuracy is then achieved with far less calls to the LuT with the relaxation scheme and CPU-time is thus saved.

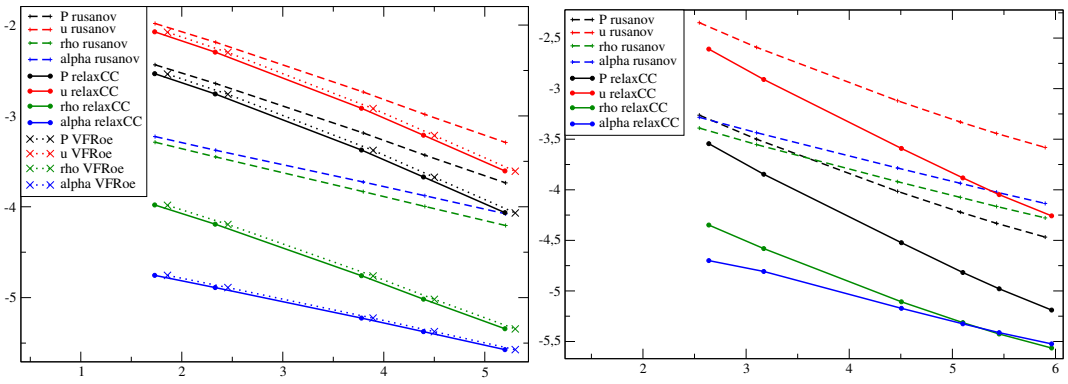

(a) *Stiffened Gas test case.* (b) *LuT test case.*

Figure 1.4 – *Comparison of the CPU-time for Riemann problems out of equilibrium with uniform meshes containing from 500 to 250 000 cells: logarithm of the relative L^1-error versus the logarithm of the CPU-time. The error and CPU-time are plotted for the approximate solutions obtained with the different schemes and for P, U, ρ, α.*

1.4.2 At equilibrium test case: convection and relaxation effects

In this paragraph, a Riemann problem assuming thermodynamical equilibrium is considered (see appendix 1.D.2). This means that the source terms are now taken into account: for each time-iteration, after the convection step, the fractions relax towards the equilibrium. We want to assess here the convergence rate of the Lie splitting described in section 1.3 with a source-term step that ensures the instantaneous relaxation towards the thermodynamical equilibrium. The Riemann problem cosidered here is composed of a contact wave and a $U + c$ shock wave. The convergence curves are presented on figure (1.5).

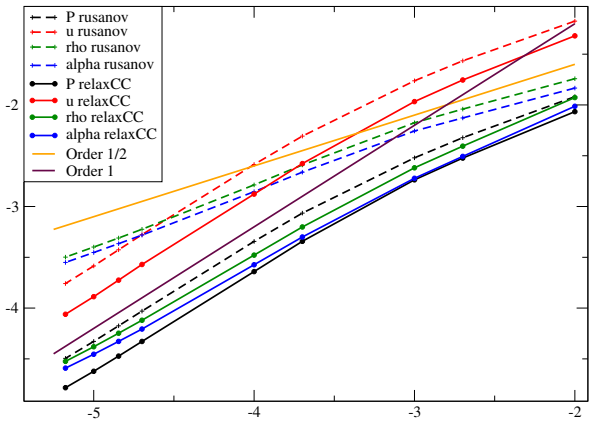

Figure 1.5 – *Convergence curve for the Riemann problems at equilibrium computed with the LuT: logarithm of the error versus logarithm of the mesh size. Four quantites are plotted: P, U, ρ, α for two different numerical schemes (Rusanov and relaxation). The meshes contain from 100 to 200 000 regular cells.*

Since the numerical schemes used for the convection step have an asymptotic rate of convergence of $1/2$, since the source terms are discretized using a first order scheme in time and since the Lie splitting is a first order splitting, the asymptotic rate of convergence of the whole fractional step algorithm should be $1/2$. This order can be observed for Rusanov scheme when considering the fractions and the density. Nevertheless, the pressure and

the velocity have not yet reached this asymptotic rate of convergence. When turning to the numerical approximations obtained with the relaxation scheme, none of the variables has reached $1/2$, even if the slopes of the curves for the density and the fractions tend to decrease on fine meshes.

1.4.3 At equilibrium test cases with a pure liquid initial state

Industrial applications provide a lot of situations in which vaporisation occurs in a pure liquid domain. One is thus faced with the problem of computations that involve a pure liquid domain and a domain in which liquid and vapour coexist. We thus propose here Riemann problems at thermodynamical equilibrium, with a transition from pure liquid towards a mixture of liquid and vapour. Two Riemann problems are considered with a liquid left state and a right state composed of a mixture of liquid and vapour. Each of these two Riemann problems involves only one wave (see appendixes 1.D.3 and 1.D.4):

1. for the first one we only consider a $U + c$ shock-wave;

2. for the second one we only consider a contact-wave.

The two other waves are then ghost waves. These cases are difficult to handle for the numerical schemes because the liquid thermodynamical behavior is very different from the mixture one. The transition through the single wave is thus associated with strong variations of the physical quantities, in particular considering the sound speed.

1.4.3.1 Shock-wave with a liquid left initial state

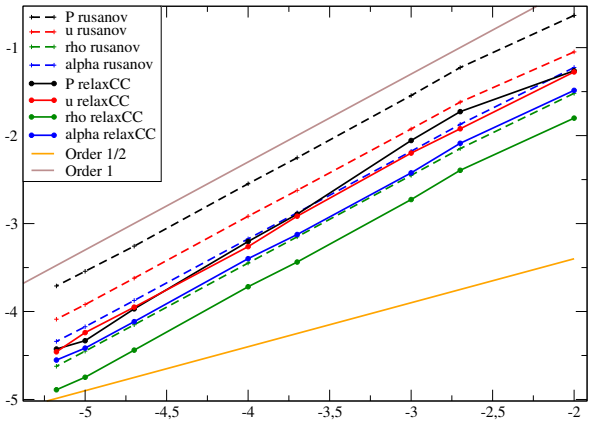

Figure 1.6 – *Convergence curve for a shock-wave: logarithm of the error versus logarithm of the mesh size. The left initial state is a pure liquid state and the right initial state is a mixture of liquid and vapour, both are at thermodynamical equilibrium. Four quantities are plotted: P, U, ρ, α. The meshes contain from 100 to 150 000 regular cells.*

For this test case, the relaxation scheme was not robust enough and the computation stops in the very first iterations. In fact, in order to compute the fluxes between two cells, denoted by the subscripts r and l, the relaxation scheme uses an intermediate state with a modified pressure Π^* computed as:

$$\Pi^* = \frac{a}{2}(U_l - U_r) + \frac{1}{2}(\Pi_l + \Pi_r)$$

with the parameter

$$a^2 > \max(\frac{c_l}{\tau_l}, \frac{c_r}{\tau_r}).$$

In the present case, l is a liquid state and r a liquid-vapour mixture state (see appendix 1.D.3). Hence $c_l/\tau_l >> c_r/\tau_r$, and c_l/τ_l is very large, which leads to large parameter a. This has two drawbacks. First, the time-step is based on the value of a through the spectral radius and large values of a imply very small time-step. Moreover, since the difference between left and right initial velocities is not equal to zero, the pressure Π^* reaches too large values. Then the balance of the resulting numerical fluxes leads after few iterations to thermodynamical states that do not belong to the domain of definition of the LuT and the computation stops.

To overcome these difficulties, we have introduced a “Rusanov switch" into our code when computing the numerical fluxes with the relaxation scheme. Indeed, if the maximal eigenvalue computed with the parameter a is much greater than the maximal eigenvalue computed with Rusanov scheme, the relaxation numerical fluxes are replaced by the numerical fluxes obtained using Rusanov scheme. This modified version of the relaxation scheme is denoted in the following by the relaxation scheme with Rusanov switch. For the present test case, this switch only occurs on few cell-interfaces around the contact wave. For instance, for a mesh with 1000 cells, Rusanov switch only occurs for the interface at the middle of the domain during the first 12 time iterations.

The relaxation scheme with Rusanov switch is robust enough for the present test case (see figure 1.6). Since the switch only occurs on few cell-interfaces the accuracy of the relaxation scheme with Rusanov switch remains more accurate than Rusanov scheme. On the next test case, a comparison of Rusanov scheme, the relaxation scheme and the relaxation scheme with Rusanov switch is proposed.

1.4.3.2 Contact-wave with a liquid left state

For this test case (see 1.D.4), the "relative" velocity at the shock location remains small and the relaxation scheme -without Rusanov switch- is robust enough. We are thus able to compare the results obtained with: Rusanov scheme, the relaxation scheme and the relaxation scheme with Rusanov switch. On figure (1.7), the error between the numerical approximations and the analytical solution is plotted with respect to the mesh size. The asymptotic convergence rate of $\frac{1}{2}$ is recovered for the finer meshes, even if Rusanov scheme needs very fine meshes to provide good approximations of the velocity. Moreover, the relaxation scheme enables a great improvement of the accuracy compared with Rusanov scheme: a little more than one order of magnitude on each quantity (see figure (1.7)). Indeed, Rusanov scheme creates large spurious waves around the contact wave as illustrated on figure (1.8). Some pressure oscillations are also created with the relaxation scheme and relaxation scheme with Rusanov switch, but their amplitude is a hundred times smaller. This behaviour is classical and it has been reported in [25].

When focusing on the comparison of the relaxation scheme and the relaxation scheme with Rusanov switch, one can evaluate the loss of accuracy due to the switch with figure (1.7). It can be noted that the introduction of the switch reduces the accuracy of the relaxation scheme on coarse meshes but that this loss tends to vanish when the mesh is refined. Indeed, Rusanov switch only occurs on a few cell-interfaces and the loss of accuracy concerns an almost constant number of cell-interfaces **whatever the mesh size is**. Hence, the more cells there are in the whole mesh, the less significant is the loss of accuracy due to Rusanov switch.

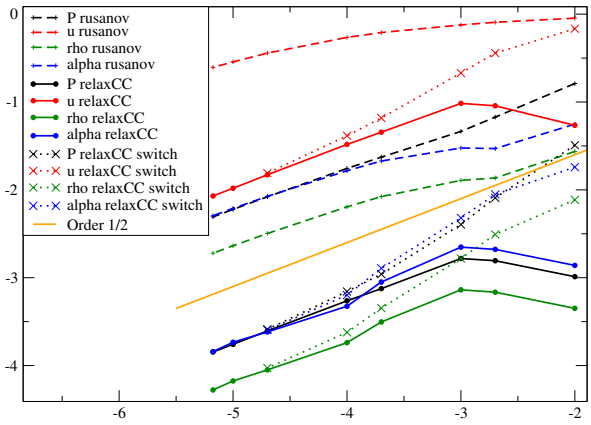

Figure 1.7 – *Convergence curve for a contact-wave: logarithm of the error versus logarithm of the mesh size. The left initial state is a pure liquid state and the right initial state is a mixture of liquid and vapour, both are at thermodynamical equilibrium. Four quantities are plotted: P, U, ρ, α. The meshes contain from 100 to 150 000 regular cells.*

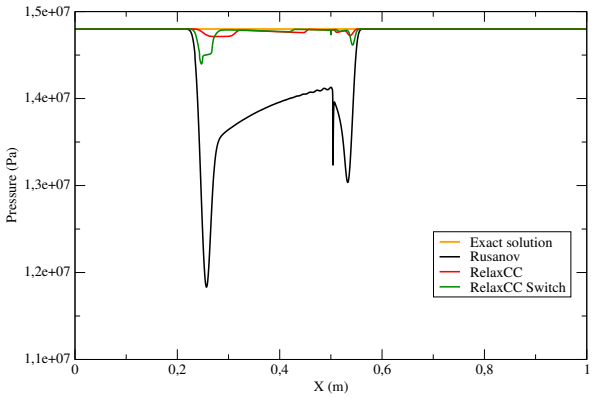

Figure 1.8 – *Pressure as a function of x at $t_{end} = 2.5\ 10^{-4}$ s for a mesh with 5000 cells. The contact wave remains close to $x = 0.5$ and spurious numerical waves are created on both sides of the contact wave.*

1.4.3.3 Conclusions for the at equilibrium test case with a liquid left state

In all cases, we have not encountered a loss of the asymptotic rate of convergence despite the sudden transition from liquid to two-phase flow. Nevertheless, the relaxation scheme is not always robust enough. This is the case for the shock-wave case proposed above. In order to tackle this loss of robustness the relaxation scheme with Rusanov switch as been tested when the parameter a arising from the Whitham condition becomes too high. This modification is applied only on a few cell-interfaces, the loss of accuracy is thus limited to coarse meshes, as it has been illustrated with the contact-wave case. However, it should be noted that even on very coarse meshes, the relaxation scheme with Rusanov switch provides a better accuracy than Rusanov scheme.

1.4.4 Conclusions

- When considering Stiffened Gas equation-of-state, the relaxation scheme is as accurate and efficient as VFRoe-ncv scheme. Unfortunately, VFRoe-ncv scheme is not robust enough when using the LuT. For the LuT, using an accurate scheme as the relaxation

scheme enables to consider coarser meshes than with Rusanov scheme. This leads to fewer computations of the thermodynamical quantities for a given accuracy, and thus to far less expensive computations of the approximated solutions.

- Nevertheless, for the most severe cases, the relaxation scheme may fail. The relaxation scheme with Rusanov switch is robust enough for such cases and enables to keep a correct accuracy level.
- Verification test-cases are possible even with a complex equation of state and it allows to assess the behaviour of different schemes for canonical situations. The test-cases proposed above involve sudden phase transition from liquid to a two-phase flow, and the source terms have been accounted for considering equilibrium situations. Indeed, analytical solutions of the system with non-instantaneous thermodynamical relaxation are far more complex to exhibit.

1.5 Validation case: study of vaporisation near a wall due to a rarefaction wave

Our model aims to simulate some accidental scenarii, like a LOCA scenario. The SUPERCANON experiment [47] is an experimental device representative of this scenario: a tube contains pressurized liquid water at $T = 573.15K$ and $P = 150$ bar. The surronding room contains air at atmospheric pressure $P = 1$ bar. The cap is opened at the beginning of the experiment. The pressure then drops until a value close to the saturation pressure at $T = 573.15K$. This first pressure wave is a rarefaction wave that travels with a high speed in the liquid. When the rarefaction wave reaches the closed-end of the tube, vaporisation begins and is strongly influenced by out of equilibrium effects. In the model of the section 1.1, these effects are ruled by the relaxation time λ chosen by the user. A study has been realized in [36], using toy laws for the relaxation time: it appears that the arrival of the first rarefaction wave on the wall and the first vaporisation of the liquid due to the pressure drop are very sensitive to the choice of the closure law for λ. Experiments [47] also present various behaviors for a same experimental set up, which might be explained by the quantity of impurities in the liquid.

In this last section, we study a more simple case: vaporisation near a wall due to a sudden pressure drop in the liquid. The aim is to focus on two types of relaxation time laws: constant values for this characteristic time scale as well as closure laws based on the nucleation theory have been tested. For the latter, we study a simplified model with only two parameters.

1.5.1 Presentation of the test case

We consider a tube filled with liquid water at P=150 bar and T=593.15K, closed on the left and open on the right (see figure 1.9). The initial fluid velocity is imposed at +10 m/s: it induces a depressurization wave at the wall, which propagates towards the right outlet. When pressure decreases at the wall, vapor appears : the same phenomenon can be observed in the SUPERCANON experiment. This case can also be schematic of what happens downstream a valve closed abruptly in a pipe in which flows high pressurized water

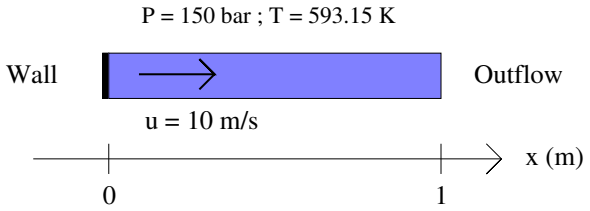

Figure 1.9 – *Sketch of the validation test case: depressurization wave in out-going liquid*

1.5.2 Simple model for relaxation time based on Nucleation Theory

Nucleation refers to the apparition of the first new phase nuclei during a first order phase transition. A classical assumption (see for instance [15]) is that the bubble nucleation rate J (the number of bubbles created per unit time in unit volume) follows an Arrhenius law:

$$J = J_0 \exp\left(-\frac{E_a}{k_B T}\right), \tag{1.32}$$

where k_B is the Boltzmann constant, T is the liquid temperature, J_0 is a prefactor and E_a is an activation energy. From this nucleation rate J, we propose a simplified model for a time scale t_{nuc} characterizing the nucleation. From assumptions made for instance in [8] or [43], we define:

$$\boxed{t_{nuc} = \left(\frac{a_0}{\Delta P}\right)^3 \exp\left(\frac{\varphi E_a}{k_B T}\right)}, \tag{1.33}$$

where E_a is defined by (1.85): $E_a = \dfrac{16\pi\gamma^3}{3(\Delta P)^2}$, and γ is estimated with the IAPWS 94 correlation [46]. $\varphi \in [0,1]$ depends on the nucleation type : homogeneous nucleation occurs when $\varphi = 1$; whereas heterogeneous nucleation occurs when φ is in $]0,1[$. The whole approach to get this simplified model as well as the chosen correlation for γ, are described in appendix 1.C.

In the simplified model (1.33), we have only two parameters to define: a_0 in (Pa.s), homogeneous to a dynamical viscosity, and $\varphi \in [0,1]$. Even if it is not a complete realistic model, it describes two important physical effects :

- Thanks to the Arrhenius law, heteregeneous nucleation only begins if a minimal energy barrier is reached;
- Dependance on $\dfrac{1}{\Delta P^3}$ reflects a physical behaviour which seems relevant: when $\Delta P \to \infty$, the return towards thermodynamical equilibrium becomes instantaneous; whereas when $\Delta P \simeq 1$, the return towards equilibrium may require a finite time, which enables the persistence of out-of-equilibrium states for small ΔP.

1.5.3 Numerical results

In the following simulations, the domain is $[0,1]$, the mesh contains 5000 cells and the final time is 10^{-3}s. Empirically, we observe that, according to the CFL condition and the mesh size, the time step is almost constant, around $5\ 10^{-8}$s.

1.5.3.1 Constant relaxation times

Constant relaxation times have first been considered. Although they are probably not physically relevant, they enable to illustrate how out of equilibrium effects can change or not the solution.

The difference between pressure (P) and saturation pressure (P_{sat}) near the wall is plotted on figure 1.10. Because of water moving to the right of the tube, a rarefaction wave appears at the wall, travelling to the right: pressure then decreases, until it reaches the saturation pressure. After that, vaporisation may occur.

When relaxation time tends to zero (case '$\lambda = 10^{-30}$ s'), thermodynamical equilibrium is instantaneously reached: it means that $P = P_{sat}$ during the whole simulation. In fact, as soon as the relaxation time is small enough, pressure almost directly decreases to reach the saturation pressure and remains constant at this value during the whole simulation.

However, when the relaxation time is high, a pressure undershoot appears at the very beginning of the simulation: the pressure decreases below the saturation pressure, which

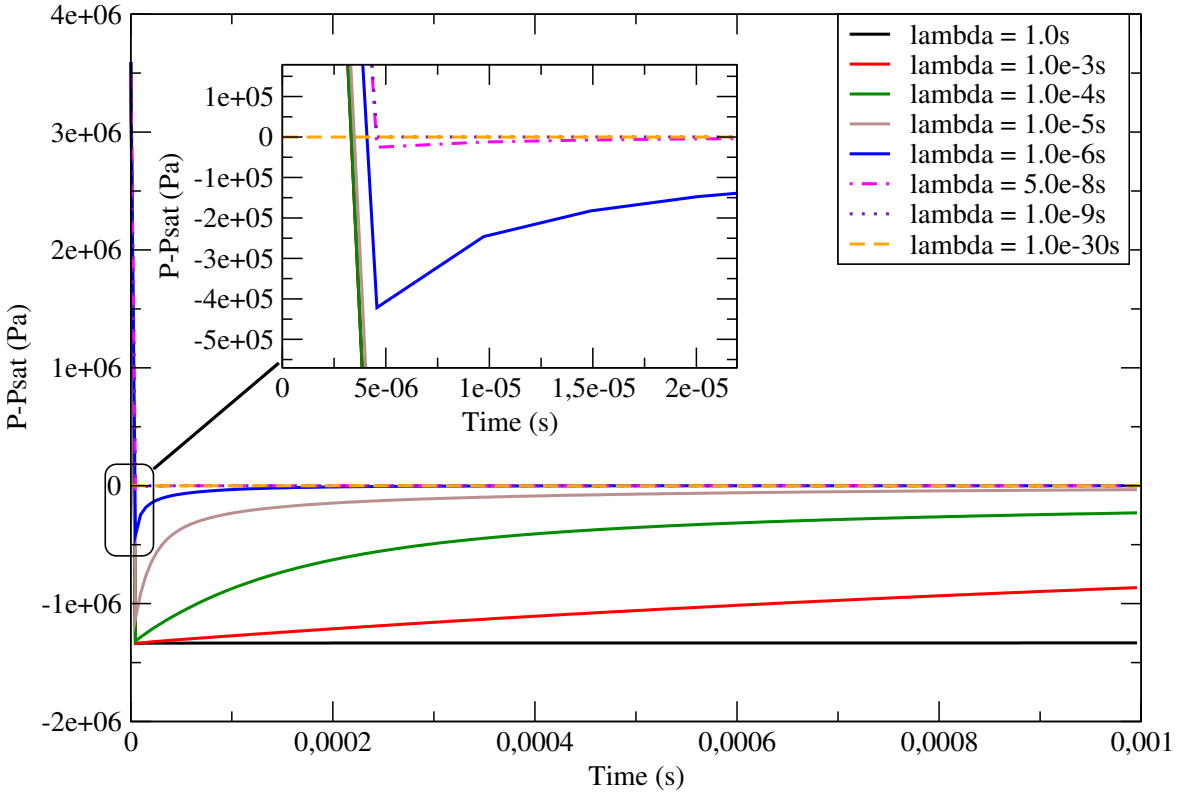

Figure 1.10 – *Difference between the pressure and the saturation pressure near the wall as a function of time (s) for several constant relaxation times. The second window inside the first graph shows a zoom on the beginning of the simulation for the smaller relaxation times.*

postpones the beginning of the vaporisation. The higher λ is, the more the pressure decreases. Indeed, high relaxation times prevent from reaching the thermodynamical equilibrium: the vaporisation can not occur and the flow remains liquid. Without phase change, the only possibility to release energy of the rarefaction wave for the system is to reduce the pressure. After the first brutal drop, pressure increases rather slowly towards the saturation pressure, depending on the time scale λ.

On figure 1.11, pressure and volume fraction are plotted with respect to x at the end of the simulation ($t = 10^{-3}$ s). For small relaxation times, vapor creation is located at the left side of the tube, whereas vapor is more spread throughout the tube when the relaxation time is high. The pressure undershoot is more important when λ is high.

1.5.3.2 Relaxation times based on nucleation theory

In this part, we take $\lambda = t_{nuc}$ as expressed by (1.33). Two parameters have to be chosen: a_0 and φ.

- For this first study, we fix $a_0 = 1.7\ 10^5$ Pa.s. This choice is not based on physical argument. Remembering the order of magnitude of ΔP in the simulation from the previous subsection, this value of a_0 empirically gives λ with the same order of magnitude than the time step. The idea here is to study the behaviour of the exponential term in t_{nuc}.
- Several φ have thus been tested: $\varphi \in \{1;\ 6.5\ 10^{-3};\ 5\ 10^{-3};\ 3.3\ 10^{-3};\ 5\ 10^{-4};\ 1\ 10^{-4}\}$. We recall that homogeneous nucleation occurs when $\varphi = 1$; when heterogeneous

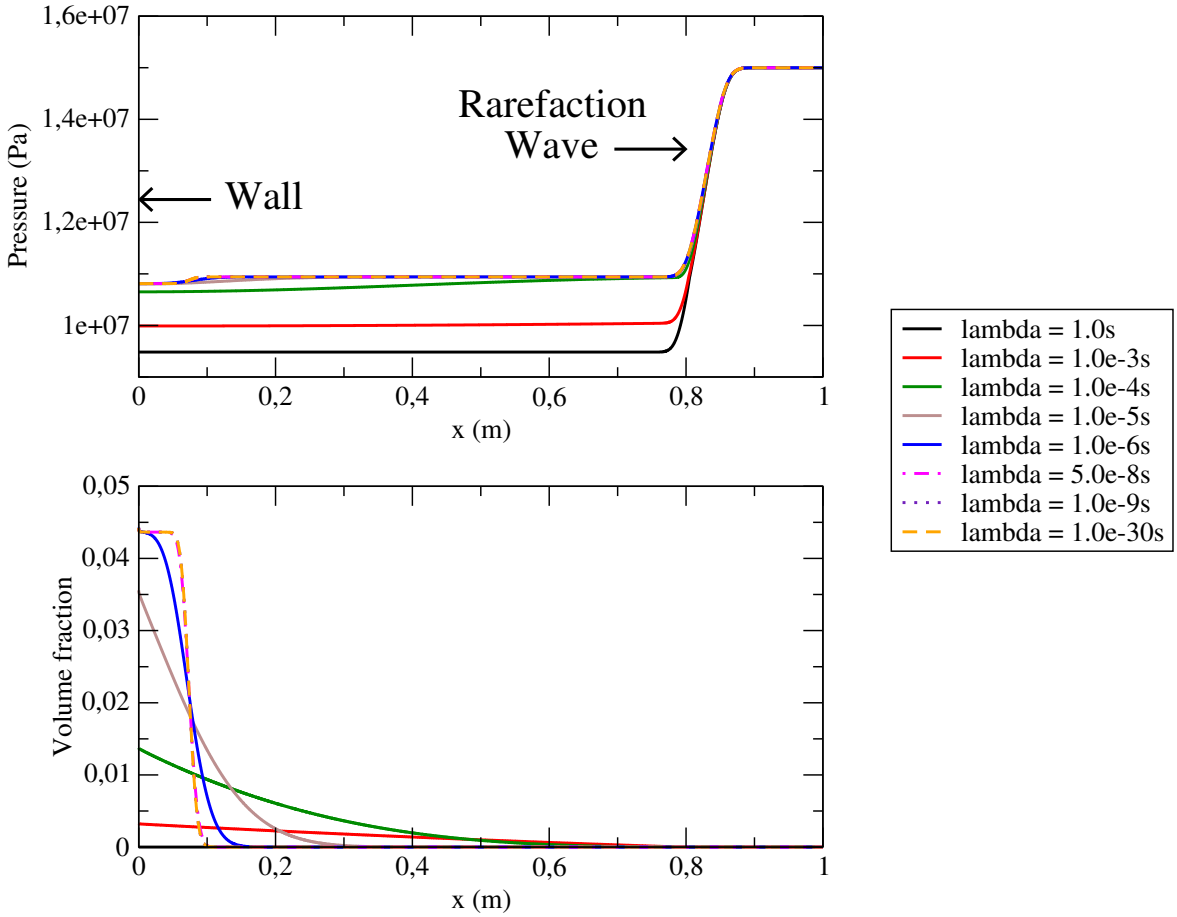

Figure 1.11 – *Pressure (Pa) and volume fraction as a function of x (m) for several constant relaxation times at the end of the simulation (t=10^{-3} s).*

nucleation occurs, φ is in $]0, 1[$.

On figure 1.12, the difference $P - P_{sat}$ (Pa) is plotted as a function of the time t (s) near the wall. A violent pressure undershoot below the saturation pressure occurs at the very beginning of the simulation. When nucleation is completely homogenenous ($\varphi = 1$), the pressure stays almost constant and far below saturation pressure: this case is very similar to the case with constant and very high relaxation time ('$\lambda = 1$ s', see figure 1.10). With a homogeneous nucleation, E_a is thus high and does not allow to create bubbles. The parameter φ that tends to decrease this energy then plays an important role. The magnitude of the undershoot slightly vary with φ: the more heterogeneous nucleation is ($\varphi \to 0$), the lower the pressure undershoot is. In fact, the parameter φ has a greater influence on the duration of the pressure undershoot than on its magnitude.

On figure 1.13, pressure and volume fraction are plotted at the end of the simulation with respect to x: by comparison with the simulations with constant λ, the stiffness of the Arrhenius term in t_{nuc} (1.33) leads to complex behaviors for the pressure drop. Some oscillations occur for $x \simeq 0.05$ m, around the frontier between the pure liquid domain and the two-phase domain. These oscillations are numerically stable and tend to vanish when the mesh is refined. Last, it can be observed that the relaxation time law based on nucleation theory modifies the vapor creation: contrary to constant relaxation times (see figure 1.11), a greater amount of vapor appears in a more localized area close to the wall (see figure 1.13).

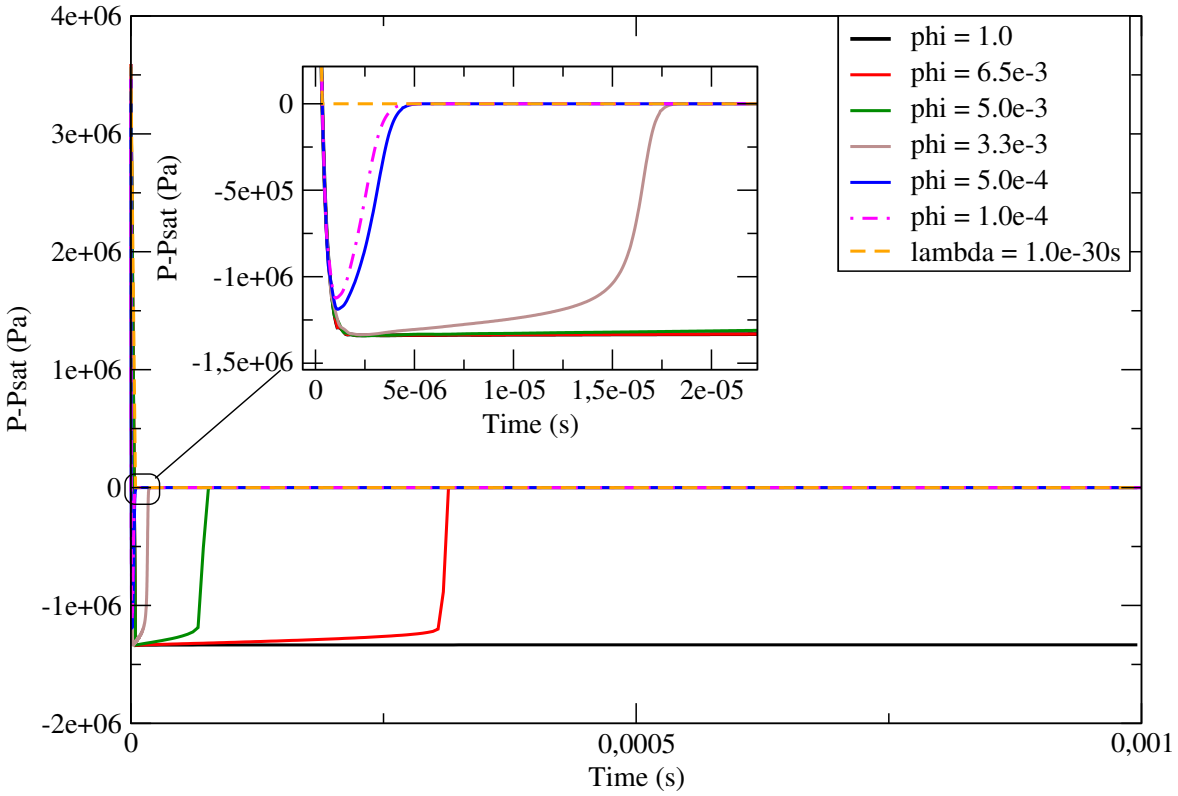

Figure 1.12 – *Difference between the pressure and the saturation pressure near the wall as a function of time (s) for several nucleation relaxation times, with fixed a_0 and variable φ. The more φ is closed to 0, the more nucleation is facilated. The second window inside the first graph shows a zoom on the beginning of the simulation for relaxation times with $\varphi \to 0$.*

Finally, changing the relaxation time laws leads to a change of the thermodynamical path towards thermodynamical equilibrium. Several behaviors of the mixture are observed depending on the chosen relaxation time law. They are summed up on figure 1.14:

- an initial strong pressure undershoot without return towards equilibrium before the simulation ends ('$\lambda = 1$ s' or 'Nucleation, $\varphi = 1.0$');
- a mixture staying almost at thermodynamical equilibrium during the whole simulation ('$\lambda = 5.0\ 10^{-8}$ s');
- an initial strong pressure undershoot with smooth return towards thermodynamical equilibrium ('$\lambda = 1.0\ 10^{-5}$ s');
- an initial strong pressure undershoot with jumps throughout T-P plane ('Nucleation with $\varphi = 5.0\ 10^{-3}$' or 'Nucleation with $\varphi = 1.0\ 10^{-4}$').

Even if our simplified nucleation model is not completely physical in its current form, this study shows how strongly relaxation time laws can modify mixture behavior throughout the simulation.

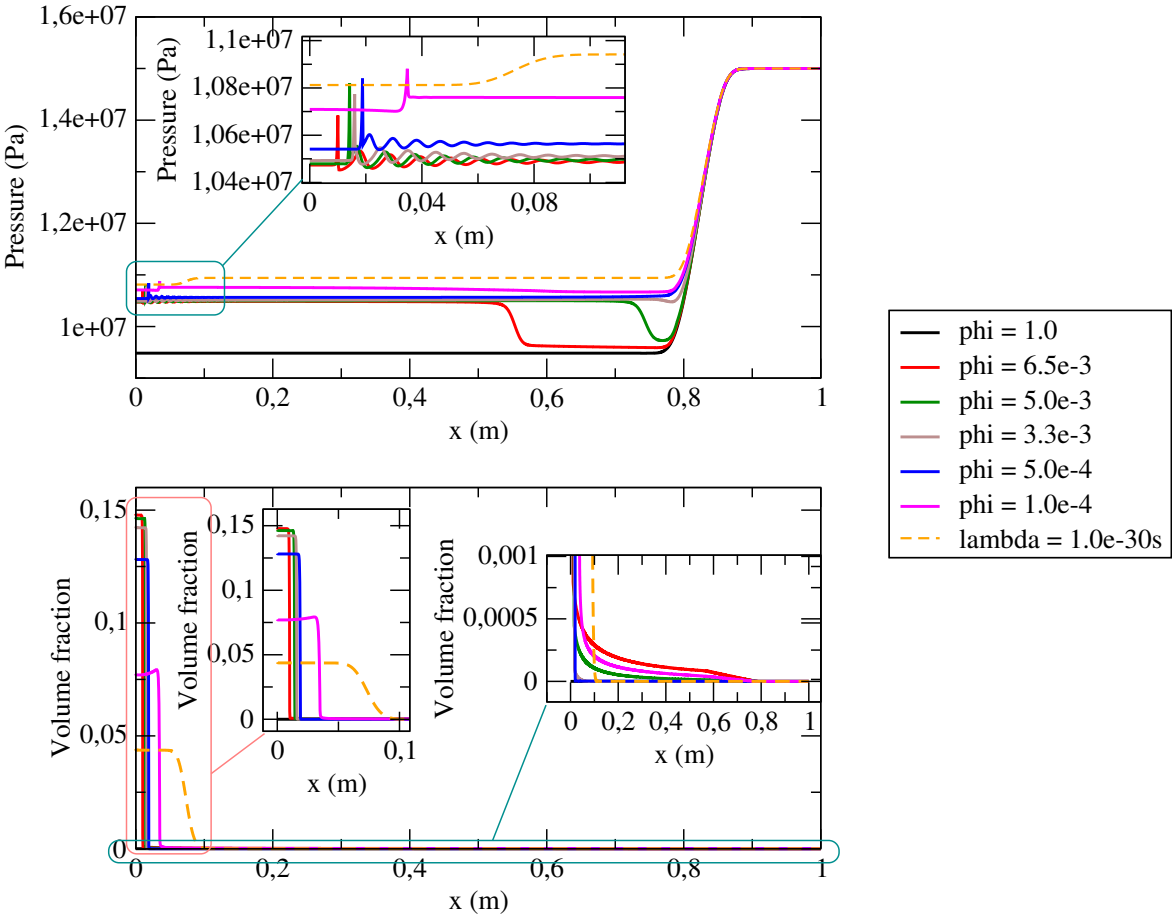

Figure 1.13 – *Pressure (Pa) and volume fraction as a function of x (m) for several relaxation times based on nucleation theory at the end of the simulation (t=10^{-3} s). The two smaller windows inside the main graph are two zooms: one on the smaller x, the other on the smaller volume fractions.*

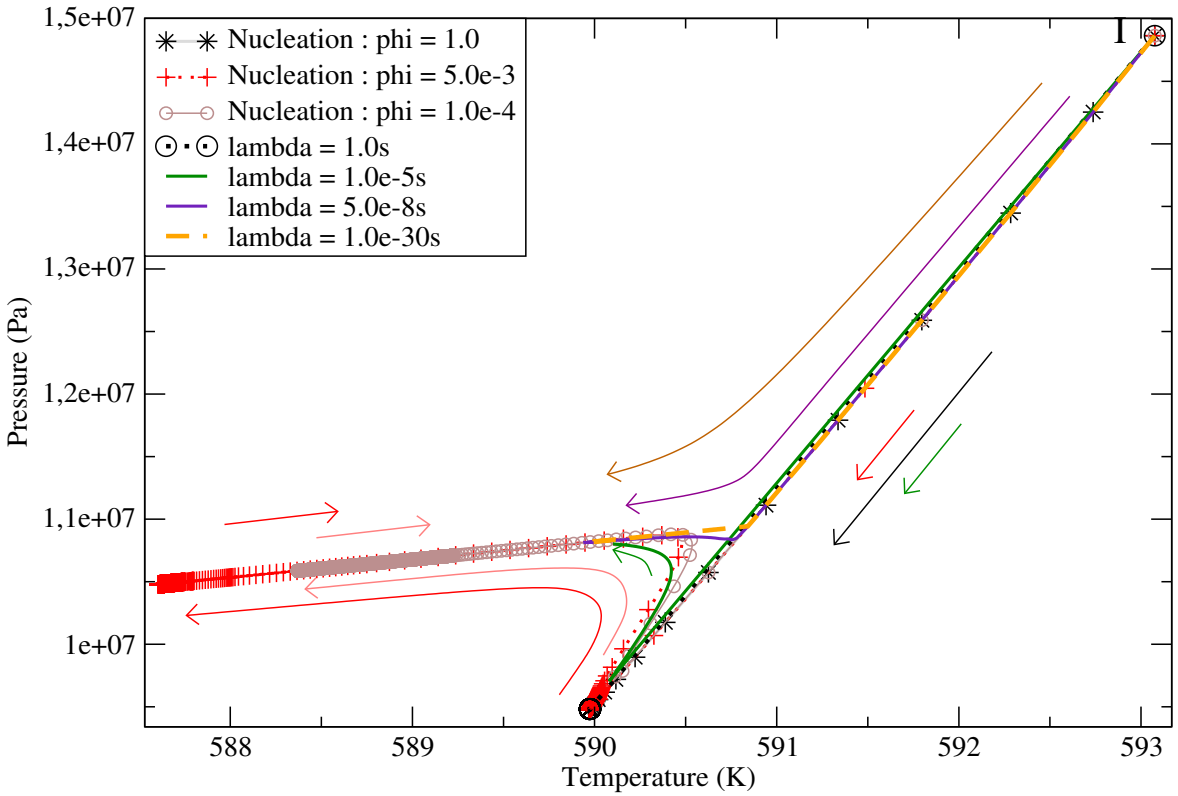

Figure 1.14 – *Thermodynamical path within the time near the wall is plotted in the Temperature (K) - Pressure (Pa) plane. The initial point for all curves is on the hand-right corner (denoted by the circle I). The thermodynamical equilibrium (denoted by the circle F) is the point that all simulations should reach for large enough time, provided that* $\lambda > 0$*. If* $\lambda = 0$*, the final point is the point* $P = 9.4810^6$ *Pa* $T = 589$ *K at the bottom of the figure. Here some simulations are still out of thermodynamical equilibrium at the final simulation time* $t = 10^{-3}$ *s. The paths towards thermodynamical equilibrium depends on the characteristic time-scale* λ*. Arrows show the travel directions in the T-P plane along the simulation time.*

Conclusion

The homogeneous model of section 1.1 has been used with a complex equation of state based on the look-up table (LuT) of section 1.2. This LuT allows to save computation time with respect to the direct use of the IAPWS-97 formulation (computations with the LuT are 90 times faster) and provides more realistic values than a classical analytical EOS as the Stiffened Gas on a wide range of pressure and temperature. In a numerical point of view, the relaxation scheme proposed in [10] has been implemented and its behaviour has been assessed on different Riemann problems involving both a Stiffened Gas EOS and the look-up table described in section 1.2. This relaxation scheme provides a great accuracy and a very satisfactory robustness, which are both mandatory when using industrial look-up tables. In section 1.5, the influence of the time-scale λ that rules the return to the thermodynamical equilibrium has been investigated: various values of λ have been compared to a very simple - yet non-linear - model based on the nucleation theory. The results are very interesting and this work should be pursued by performing some comparisons on the basis of relevant out-of-equilibrium experiments. Moreover, the nucleation theory includes surface tension effects and a further improvement of the present work could be to include in the model both the interfacial area and the surface tension effects.

Acknowledgements

The last author receives financial support by ANRT through an EDF/CIFRE grant number 2017/0476. Computational facilities were provided by EDF. The authors thank the reviewers for their helpful remarks, improving the paper structure.

References

[1] G. ALLAIRE, S. CLERC, and S. KOKH. "A five-equation model for the numerical simulation of interfaces in two-phase flows". In: *Comptes Rendus de l'Académie des Sciences - Series I - Mathematics* 331.12 (2000), pp. 1017–1022. URL: http://www.sciencedirect.com/science/article/pii/S0764444200017535 (cit. on p. 4).

[2] M. BAER and J. NUNZIATO. "A two-phase mixture theory for the deflagration-to-detonation transition (DDT) in reactive granular materials". In: *Journal of Multiphase Flows* 12 (1986), pp. 861–889. DOI: https://doi.org/10.1016/0301-9322(86)90033-9 (cit. on p. 4).

[3] T. BARBERON and P. HELLUY. "Finite volume simulation of cavitating flows". In: *Computers and Fluids* 34.7 (2005), pp. 832–858. URL: https://hal.archives-ouvertes.fr/hal-00139597 (cit. on pp. 4, 7, 36, 39).

[4] J. BARTAK. "A study of the rapid depressurization of hot water and the dynamics of vapour bubble generation in superheated water". In: *International Journal of Multiphase Flow* 16.5 (1990), pp. 789–798. DOI: https://doi.org/10.1016/0301-9322(90)90004-3 (cit. on pp. 3, 49).

[5] F. BOUCHUT. *Nonlinear stability of finite Volume Methods for hyperbolic conservation laws And Well-Balanced schemes for sources*. Springer Science & Business Media, 2004 (cit. on pp. 5, 12).

[6] T. BUFFARD, T. GALLOUËT, and J.-M. HÉRARD. "A sequel to a rough Godunov scheme: application to real gases". In: *Computers and Fluids* 29.7 (2000), pp. 813–847. URL: https://hal.archives-ouvertes.fr/hal-01579990 (cit. on pp. 5, 11).

[7] H. B. CALLEN. *Thermodynamics and an Introduction to Thermostatistics*. John Wiley & sons, 1985 (cit. on p. 36).

[8] F. CAUPIN and E. HERBERT. "Cavitation in water: a review". In: *Comptes Rendus Physique* 7.9-10 (2006), pp. 1000–1017. DOI: https://doi.org/10.1016/j.crhy.2006.10.015 (cit. on pp. 5, 25, 49, 50).

[9] C. CHALONS and F. COQUEL. "Navier-Stokes equations with several independent pressure laws and explicit predictor-corrector schemes". In: *Numerische Mathematik* 101.3 (2005), pp. 451–478. DOI: https://doi.org/10.1007/s00211-005-0612-7 (cit. on p. 13).

[10] C. CHALONS and J.-F. COULOMBEL. "Relaxation approximation of the Euler equations". In: *Journal of Mathematical Analysis and Applications* 348.2 (2008), pp. 872–893. ISSN: 0022-247X. URL: https://hal.archives-ouvertes.fr/hal-01838843 (cit. on pp. 2, 5, 11–13, 31).

[11] E. CLOUET. *Modeling of nucleation processes*. 2010. URL: https://hal.archives-ouvertes.fr/hal-00449858v2 (cit. on p. 50).

[12] F. COQUEL, E. GODLEWSKI, and N. SEGUIN. "Relaxation of fluid systems". In: *Mathematical Models and Methods in Applied Sciences* 22.08 (2012), p. 1250014. URL: https://hal.archives-ouvertes.fr/hal-00776822 (cit. on p. 5).

[13] F. COQUEL and B. PERTHAME. "Relaxation of energy and approximate Riemann solvers for general pressure laws in fluid dynamics". In: *SIAM Journal on Numerical Analysis* 35.6 (1998), pp. 2223–2249. DOI: https://doi.org/10.1137/S0036142997318528 (cit. on pp. 5, 12).

[14] F. COQUEL, T. GALLOUËT, J.-M. HÉRARD, and N. SEGUIN. "Closure laws for a two-fluid two-pressure model". In: *Comptes Rendus Mathématique* 334.10 (2002), pp. 927–932. URL: https://hal.archives-ouvertes.fr/hal-01484345 (cit. on p. 4).

[15] P. G. DEBENEDETTI. *Metastable liquids: concepts and principles*. Princeton University Press, 1996 (cit. on pp. 5, 24, 49).

[16] P. DOWNAR-ZAPOLSKI, Z. BILICKI, L. BOLLE, and J. FRANCO. "The non-equilibrium relaxation model for one-dimensional flashing liquid flow". In: *International Journal of Multiphase Flow* 22.3 (1996), pp. 473–483. DOI: https://doi.org/10.1016/0301-9322(95)00078-X (cit. on pp. 4, 5).

[17] F. DRUI. "Eulerian modeling and simulations of separated and disperse two-phase flows : development of a unified modeling approach and associated numerical methods for highly parallel computations". PhD thesis. Université Paris-Saclay, July 2017. URL: https://tel.archives-ouvertes.fr/tel-01618320 (cit. on p. 4).

[18] F. DRUI, A. LARAT, S. KOKH, and M. MASSOT. "Small-scale kinematics of two-phase flows: identifying relaxation processes in separated- and disperse-phase flow models". In: *Journal of Fluid Mechanics* 876 (Oct. 2019), pp. 326–355. DOI: 10.1017/jfm.2019.538. URL: https://hal.archives-ouvertes.fr/hal-01349441 (cit. on p. 4).

[19] M. EL MEKKI, C. RAMBOZ, L. PERDEREAU, K. SHMULOVICH, and L. MERCURY. "Lifetime of superheated water in a micrometric synthetic fluid inclusion". In: *Metastable Systems Under Pressure : Platform new technologies and environnemental applications*. NATO Science for Peace and Security Series A: Chemistry and Biology. Odessa, Ukraine: Springer Verlag, Oct. 2008, pp. 279–292. DOI: 10.1007/978-90-481-3408-3. URL: https://hal-insu.archives-ouvertes.fr/insu-00349576 (cit. on p. 49).

[20] G. ERMAKOV and E. LIPNYAGOV. "Criterion of homogeneous boiling-up of superheated liquids". In: *Thermophysics and Aeromechanics* 15.4 (2008), pp. 623–630. DOI: https://doi.org/10.1007/s11510-008-0011-5 (cit. on p. 50).

[21] G. FACCANONI. "Study of a Fine Model of Liquid-Vapor Phase Change. Contribution to the Boiling Crisis Study." PhD thesis. Ecole Polytechnique X, Nov. 2008. URL: https://pastel.archives-ouvertes.fr/tel-00363460 (cit. on p. 4).

[22] G. FACCANONI, S. KOKH, and G. ALLAIRE. "Modelling and Simulation of Liquid-Vapor Phase Transition in Compressible Flows Based on Thermodynamical Equilibrium." In: *Mathematical Modelling and Numerical Analysis* 46.05 (Sept. 2012), pp. 1029–1054. URL: https://hal.archives-ouvertes.fr/hal-00976983 (cit. on p. 4).

[23] G. FACCANONI and H. MATHIS. "Admissible Equations of State for Immiscible and Miscible Mixtures". In: *ESAIM: Proceedings and Surveys* (2019). URL: https://hal.archives-ouvertes.fr/tel-00363460 (cit. on pp. 4, 7, 8, 36, 38).

[24] E. FAUCHER, J.-M. HÉRARD, M. BARRET, and C. TOULEMONDE. "Computation of flashing flows in variable cross-section ducts". In: *International Journal of Computational Fluid Dynamics* 13.3 (2000), pp. 365–391. URL: https://hal.archives-ouvertes.fr/hal-01580046 (cit. on p. 4).

[25] T. GALLOUËT, J.-M. HÉRARD, and N. SEGUIN. "Some recent Finite Volume schemes to compute Euler equations using real gas EOS". In: *International Journal for Numerical Methods in Fluids* 39 (2002), pp. 1073–1138. URL: https://hal.archives-ouvertes.fr/hal-01290885 (cit. on pp. 18, 21).

[26] S. GAVRILYUK and R. SAUREL. "Mathematical and Numerical Modeling of Two-phase Compressible Flows with Micro-inertia". In: *J. Comput. Phys.* 175.1 (Jan. 2002), pp. 326–360. ISSN: 0021-9991. DOI: http://dx.doi.org/10.1006/jcph.2001.6951 (cit. on pp. 4, 38).

[27] H. GHAZI. "Modelling compressible flows with phase transition and metastable states". Theses. Université de Nantes, Nov. 2018. URL: https://tel.archives-ouvertes.fr/tel-01976189 (cit. on pp. 4, 36).

[28] J. GLIMM, D. SALTZ, and D. SHARP. "Two-pressure two-phase flow". In: *Advances In Nonlinear Partial Differential Equations And Related Areas: A Volume in Honor of Professor Xiaqi Ding*. World Scientific, 1998, pp. 124–148. DOI: https://doi.org/10.1142/9789812815811_0008 (cit. on p. 4).

[29] H. GUILLARD and A. MURRONE. *A five equation reduced Model for compressible two phase flow problems*. Tech. rep. RR-4778. INRIA, Mar. 2003. URL: https://hal.inria.fr/inria-00071808 (cit. on p. 4).

[30] H. MATHIS. "A thermodynamically consistent model of a liquid-vapor fluid with a gas". In: *ESAIM: Mathematical Modelling and Numerical Analysis* 53.1 (2019), pp. 63–84. DOI: https://doi.org/10.1051/m2an/2018044 (cit. on p. 36).

[31] P. HELLUY. "Simulation numérique des écoulements multiphasiques: de la théorie aux applications". Habilitation à diriger des recherches. Université du Sud Toulon Var, 2005. URL: https://tel.archives-ouvertes.fr/tel-00657839 (cit. on pp. 4, 7, 36).

[32] P. HELLUY, O. HURISSE, and E. LE COUPANEC. "Verification of a two-phase flow code based on an homogeneous model". In: *International Journal on Finite Volumes* 13 (Nov. 2016). URL: https://hal.archives-ouvertes.fr/hal-01396200 (cit. on p. 4).

[33] P. HELLUY and N. SEGUIN. "Relaxation models of phase transition flows". In: *ESAIM: Mathematical Modelling and Numerical Analysis* 40.2 (2006), pp. 331–352. URL: https://hal.archives-ouvertes.fr/hal-00139607 (cit. on p. 4).

[34] M. HOFFMANN. "An Explicit Discontinuous Galerkin Method for Parallel Compressible Two-Phase Flow". PhD thesis. University of Stuttgart, 2017. DOI: http://dx.doi.org/10.18419/opus-9476 (cit. on pp. 4, 9).

[35] O. HURISSE. "Application of an homogeneous model to simulate the heating of two-phase flows". In: *International Journal on Finite Volumes* 11 (May 2014), http://www.latp.univ–mrs.fr/IJFV/spip.php?article52. URL: https://hal.archives-ouvertes.fr/hal-01114808 (cit. on p. 4).

[36] O. HURISSE. "Numerical simulations of steady and unsteady two-phase flows using a homogeneous model". In: *Computers and Fluids* 152 (July 2017), pp. 88–103. URL: https://hal.archives-ouvertes.fr/hal-01489039 (cit. on pp. 4, 5, 7, 24, 63).

[37] O. HURISSE and L. QUIBEL. "A homogeneous model for compressible three-phase flows involving heat and mass transfer." In: *ESAIM: Proceedings and Surveys* 66 (2019), pp. 84–108. URL: https://hal.archives-ouvertes.fr/hal-01976903 (cit. on p. 7).

[38] S. JAOUEN. "Etude mathématique et numérique de stabilité pour des modeles hydrodynamiques avec transition de phase". PhD thesis. Paris 6, 2001 (cit. on pp. 4, 7, 36).

[39] H. JIN, J. GLIMM, and D. SHARP. "Compressible two-pressure two-phase flow models". In: *Physics letters A* 353.6 (2006), pp. 469–474. DOI: https://doi.org/10.1016/j.physleta.2005.11.087 (cit. on p. 4).

[40] S. JIN and Z. XIN. "The relaxation schemes for systems of conservation laws in arbitrary space dimensions". In: *Communications on pure and applied mathematics* 48.3 (1995), pp. 235–276. DOI: https://doi.org/10.1002/cpa.3160480303 (cit. on p. 12).

[41] J. JUNG. "Numerical simulations of two-fluid flow on multicores accelerator". PhD thesis. Université de Strasbourg, Oct. 2013. URL: https://tel.archives-ouvertes.fr/tel-00876159 (cit. on pp. 4, 7, 36, 38).

[42] A. K. KAPILA, R. MENIKOFF, J. B. BDZIL, S. F. SON, and D. S. STEWART. "Two-phase modeling of deflagration-to-detonation transition in granular materials: Reduced equations". In: *Physics of Fluids* 13.10 (2001), pp. 3002–3024. DOI: https://doi.org/10.1063/1.1398042 (cit. on p. 4).

[43] H. J. MARIS. "Introduction to the physics of nucleation". In: *Comptes Rendus Physique* 7.9-10 (2006), pp. 946–958. DOI: https://doi.org/10.1016/j.crhy.2006.10.019 (cit. on pp. 5, 25, 49, 50).

[44] H. MATHIS. "Theoretical and numerical study of phase transition flows". PhD thesis. Université de Strasbourg, Sept. 2010. URL: https://tel.archives-ouvertes.fr/tel-00516683 (cit. on pp. 4, 7, 36, 38).

[45] O. MÉTAYER, J. MASSONI, and R. SAUREL. "Élaboration des lois d'état d'un liquide et de sa vapeur pour les modèles d'écoulements diphasiques". In: 43 (Mar. 2004), pp. 265–276. DOI: https://doi.org/10.1016/j.ijthermalsci.2003.09.002 (cit. on pp. 4, 8).

[46] T. PETROVA and R. DOOLEY. "Revised release on surface tension of ordinary water substance". In: *Proceedings of the International Association for the Properties of Water and Steam, Moscow, Russia* (2014), pp. 23–27. URL: http://www.iapws.org/relguide/Surf-H2O-2014.pdf (cit. on pp. 25, 50).

[47] B. RIEGEL. "Contribution à l'étude de la décompression d'une capacité en régime diphasique". PhD thesis. 1978 (cit. on pp. 5, 24, 63).

[48] V. V. RUSANOV. "The calculation of the interaction of non-stationary shock waves with barriers". In: *Zhurnal Vychislitel'noi Matematiki i Matematicheskoi Fiziki* 1.2 (1961), pp. 267–279. DOI: https://doi.org/10.1016/0041-5553(62)90062-9 (cit. on pp. 5, 11).

[49] I. SULICIU. "On the thermodynamics of fluids with relaxation and phase transitions. Fluids with relaxation". In: *Internat. J. Engrg. Sci* 36 (1998), pp. 921–947 (cit. on pp. 5, 12).

[50] E. TORO. *Riemann Solvers and Numerical Methods for Fluid Dynamics: A Practical Introduction*. Springer Berlin Heidelberg, 2009. ISBN: 9783540498346. URL: https://books.google.fr/books?id=SqEjX0um8o0C (cit. on p. 18).

[51] D. TURNBULL and J. C. FISHER. "Rate of nucleation in condensed systems". In: *The Journal of chemical physics* 17.1 (1949), pp. 71–73. DOI: https://doi.org/10.1063/1.1747055 (cit. on p. 50).

[52] W. WAGNER and H.-J. KRETZSCHMAR. *International Steam Tables: Properties of Water and Steam Based on the Industrial Formulation IAPWS-IF97*. Springer-Verlag Berlin Heidelberg, 2008. ISBN: 9783540742340. DOI: http://dx.doi.org/10.1007/978-3-540-74234-0 (cit. on pp. 2, 4, 8).

[53] N. YANENKO. *Méthode à pas fractionnaires: résolutions de problèmes polydimensionnels de physique mathématique*. Collection Intersciences. A. Colin, 1968. URL: https://books.google.fr/books?id=JBIyvgAACAAJ (cit. on p. 11).

Appendices

1.A Building of the homogeneous model

In this section, we build step by step a homogeneous model to describe a mixture of liquid and vapour, by considering at first the extensive variables [7], as made in [3, 38, 31, 44, 41]. The only equilibrium assumption in the model is a kinematic equilibrium. In particular, the model enables to describe the mixture out of the thermodynamical equilibrium. The return to equilibrium is ensured by a relaxation process in agreement with the second law of thermodynamics.

1.A.1 Extensive description of the system

Three extensive quantities are needed to describe a two-phase mixture [7]. Let us consider a volume $\mathcal{V}$ (in m^3) of the mixture, corresponding to a mass $\mathcal{M}$ (in kg) and an internal energy $\mathcal{E}$ (in J). Within this mixture, each phase $k = l, v$ is described with the same quantities: a volume $\mathcal{V}_k$ (in m^3), a mass $\mathcal{M}_k$ (in kg) and an energy $\mathcal{E}_k$ (in J).

Some assumptions are made:

(H_1) The geometric repartition of the phases inside the volume V is not taken into account.

(H_2) The surface tension is neglected.

(H_3) The whole volume $\mathcal{V}$ is occupied by some fluid (vacuum occurrence is not considered here).

(H_4) The phases are **not miscible**.

With these assumptions, we can easily express the conservation of volume, mass and energy as:

$$\mathcal{V} = \mathcal{V}_l + \mathcal{V}_v \quad ; \quad \mathcal{M} = \mathcal{M}_l + \mathcal{M}_v \quad ; \quad \mathcal{E} = \mathcal{E}_l + \mathcal{E}_v. \tag{1.34}$$

The hypothesis (H_3) and (H_4) are mandatory to write the first equation of (1.34) on the volumes. When dealing with the miscible case (i.e. when (H_4) is not fulfilled), one can for instance make the assumption that the two phases occupy the whole volume. In such a case, the first equation of (1.34) is replaced by two equations describing the equality of the volumes, $\mathcal{V} = \mathcal{V}_l = \mathcal{V}_v$, which leads to another system of equations. This case does not enter the scope of the present work and it has been investigated in details in [27, 23, 30].

The aim is now to describe the evolution of this system in accordance with the first and second laws of thermodynamics and Newton's laws of dynamics. We proceed in two steps by adopting a lagrangian point of view. In section 1.A.2 and 1.A.3 we first consider the thermodynamical behavior of a fixed quantity of mixture. For this purpose we follow a classical approach [44, 41] based on the evolution of a closed and isolated mass of mixture in agreement with the second law of thermodynamics. Then, in section 1.A.4, we account for the evolution of this mass of mixture within the whole flow by applying the first law of thermodynamics and Newton's law.

1.A.2 Thermodynamical quantities

1.A.2.1 Kinematic equilibrium

The kinematic equilibrium between the phases is assumed, i.e.:

(H_5) both phases are convected with the same velocity U.

Thanks to this assumption of equal velocity ($U_l = U_v = U$), the dynamical behavior of the system can be described by modelling the behavior of an element $(\mathcal{V}, \mathcal{M}, \mathcal{E})$ of the mixture along a streamline. In particular, since $U_k = U$, the derivative along a streamline of phase k of a quantity Φ,

$$d_k\Phi = (\partial_t\Phi + U_k\partial_x\Phi)\, dt,$$

corresponds to the same operator for both phases. So that the derivative along a streamline does not depend on the indice k:

$$d_k\Phi = (\partial_t\Phi + U\partial_x\Phi)\, dt = d\Phi. \tag{1.35}$$

This last equation (1.35) is a key relation which will enable us to simply derive the model.

1.A.2.2 Phasic thermodynamical quantities

In order to close the system, we need to define a complete EOS for each phase. For this purpose, we assume that each phase is described by an extensive entropy $(W_k) \mapsto S_k(W_k)$ (in J/K), where we have set $W_k = (\mathcal{V}_k, \mathcal{M}_k, \mathcal{E}_k)$. Some hypotheses are needed on S_k to guarantee useful properties for the final model:

(H_6) $(W_k) \mapsto S_k(W_k)$ is $\mathcal{C}^2$.

(H_7) $(W_k) \mapsto S_k(W_k)$ is concave.

(H_8) $\forall a \in \mathbb{R}^+, \forall W_k,\ S_k(aW_k) = aS_k(W_k)$.

(H_9) $\forall W_k,\ \dfrac{\partial S_k}{\partial \mathcal{E}_k} > 0$

In agreement with the Classical Irreversible Thermodynamics (CIT) theory, the classical Gibbs relation holds for each phase:

$$T_k d_k\mathcal{S}_k = d_k\mathcal{E}_k + P_k d_k\mathcal{V}_k - \mu_k d_k\mathcal{M}_k. \tag{1.36}$$

Thanks to (1.35), it can be rewritten as:

$$T_k d\mathcal{S}_k = d\mathcal{E}_k + P_k d\mathcal{V}_k - \mu_k d\mathcal{M}_k. \tag{1.37}$$

The extensive entropy S_k using the variables $(\mathcal{V}_k, \mathcal{M}_k, \mathcal{E}_k)$ is a complete EOS for phase k when associated with the Gibbs relation (1.37). This means that all the thermodynamical quantitites can be computed thanks to the derivatives of S_k:

$$\frac{P_k}{T_k} = \left.\frac{\partial S_k}{\partial \mathcal{V}_k}\right|_{\mathcal{M}_k,\mathcal{E}_k} \tag{1.38}$$

$$\frac{1}{T_k} = \left.\frac{\partial S_k}{\partial \mathcal{E}_k}\right|_{\mathcal{V}_k,\mathcal{M}_k} \tag{1.39}$$

$$\frac{\mu_k}{T_k} = -\left.\frac{\partial S_k}{\partial \mathcal{M}_k}\right|_{\mathcal{V}_k,\mathcal{E}_k} \tag{1.40}$$

where P_k is the pressure of phase k (in Pa), T_k (in K) is the temperature of phase k, and μ_k (in J/kg) is the Gibbs free enthalpy of phase k.

1.A.2.3 Thermodynamical quantities of the mixture

We note $W = (\mathcal{V}_l, \mathcal{M}_l, \mathcal{E}_l, \mathcal{V}_v, \mathcal{M}_v, \mathcal{E}_v) = (W_l, W_v)$. Thanks to (H_2), we assume that the entropy of the mixture S is:

$$(W) \mapsto S(W) = S_l(W_l) + S_v(W_v) \tag{1.41}$$

This mixture entropy should be defined using another relation if surface tension (or other effects, see [26]) had to be accounted for.

We define $\mathcal{H}(\mathcal{M})$, a subset of $(\mathbb{R}_+^*)^6$ so that all the states $W \in \mathcal{H}(\mathcal{M})$ have the same total mass $\mathcal{M}$:

$$\mathcal{H}(\mathcal{M}) = \left\{ W \in (\mathbb{R}_+^*)^6; \mathcal{M}_l + \mathcal{M}_v = \mathcal{M} \right\}.$$

If the entropy S is concave thanks to the definition (1.41) and properties (H_5) and (H_7), it can be proved that S is strictly concave on $\mathcal{H}(\mathcal{M})$ (see [23, 44, 41]).

Using the Gibbs relation for each phase (1.37), the definition of the mixture entropy (1.41) and relation (1.35), a Gibbs relation for the mixture can be easily exhibited:

$$\begin{aligned} d\mathcal{S} &= d\mathcal{S}_l + d\mathcal{S}_v = \frac{1}{T_l} d\mathcal{E}_l + \frac{1}{T_v} d\mathcal{E}_v \\ &+ \frac{P_l}{T_l} d\mathcal{V}_l + \frac{P_v}{T_v} d\mathcal{V}_v - \frac{\mu_l}{T_l} d\mathcal{M}_l - \frac{\mu_v}{T_v} d\mathcal{M}_v \end{aligned} \tag{1.42}$$

Thanks to the relation $d\Phi_k = \Phi d\left(\frac{\Phi_k}{\Phi}\right) + \frac{\Phi_k}{\Phi} d\Phi$, Gibbs relation (1.42) for the mixture can be written in the form:

$$\begin{aligned} dS &= \left(\frac{\mathcal{E}_l}{\mathcal{E}} \frac{1}{T_l} + \frac{\mathcal{E}_v}{\mathcal{E}} \frac{1}{T_v}\right) d\mathcal{E} + \left(\frac{\mathcal{V}_l}{\mathcal{V}} \frac{P_l}{T_l} + \frac{\mathcal{V}_v}{\mathcal{V}} \frac{P_v}{T_v}\right) d\mathcal{V} \\ &- \left(\frac{\mathcal{M}_l}{\mathcal{M}} \frac{\mu_l}{T_l} + \frac{\mathcal{M}_v}{\mathcal{M}} \frac{\mu_v}{T_v}\right) d\mathcal{M} \\ &+ \mathcal{E} \frac{1}{T_l} d\left(\frac{\mathcal{E}_l}{\mathcal{E}}\right) + \mathcal{E} \frac{1}{T_v} d\left(\frac{\mathcal{E}_v}{\mathcal{E}}\right) \\ &+ \mathcal{V} \frac{P_l}{T_l} d\left(\frac{\mathcal{V}_l}{\mathcal{V}}\right) + \mathcal{V} \frac{P_v}{T_v} d\left(\frac{\mathcal{V}_v}{\mathcal{V}}\right) \\ &- \mathcal{M} \frac{\mu_l}{T_l} d\left(\frac{\mathcal{M}_l}{\mathcal{M}}\right) - \mathcal{M} \frac{\mu_v}{T_v} d\left(\frac{\mathcal{M}_v}{\mathcal{M}}\right) \end{aligned} \tag{1.43}$$

Then, using relation (1.43), we can identify a mixture pressure P, a mixture temperature T and a mixture Gibbs free enthalpy μ:

$$\frac{P}{T} = \frac{\mathcal{V}_l}{\mathcal{V}} \frac{P_l}{T_l} + \frac{\mathcal{V}_v}{\mathcal{V}} \frac{P_v}{T_v} \tag{1.44}$$

$$\frac{1}{T} = \frac{\mathcal{E}_l}{\mathcal{E}} \frac{1}{T_l} + \frac{\mathcal{E}_v}{\mathcal{E}} \frac{1}{T_v} \tag{1.45}$$

$$\frac{\mu}{T} = \frac{\mathcal{M}_l}{\mathcal{M}} \frac{\mu_l}{T_l} + \frac{\mathcal{M}_v}{\mathcal{M}} \frac{\mu_v}{T_v}. \tag{1.46}$$

and we thus get the Gibbs relation:

$$\begin{aligned} & dS - \tfrac{1}{T}\left(d\mathcal{E} + Pd\mathcal{V} - \mu d\mathcal{M}\right) \\ = \; & \mathcal{E} \frac{1}{T_l} d\left(\frac{\mathcal{E}_l}{\mathcal{E}}\right) + \mathcal{V} \frac{P_l}{T_l} d\left(\frac{\mathcal{V}_l}{\mathcal{V}}\right) \quad - \mathcal{M} \frac{\mu_l}{T_l} d\left(\frac{\mathcal{M}_l}{\mathcal{M}}\right) \\ + \; & \mathcal{E} \frac{1}{T_v} d\left(\frac{\mathcal{E}_v}{\mathcal{E}}\right) + \mathcal{V} \frac{P_v}{T_v} d\left(\frac{\mathcal{V}_v}{\mathcal{V}}\right) \quad - \mathcal{M} \frac{\mu_v}{T_v} d\left(\frac{\mathcal{M}_v}{\mathcal{M}}\right) \end{aligned} \tag{1.47}$$

The terms on the left-hand side of this relation define the evolution of the mixture quantities and are related to the interaction with the surronding fluid, whereas the terms on the right-hand side are exchange terms between the phases. In order to give a complete time-evolution model of our system, we need to express the derivative terms of (1.47) in terms of W.

1.A.3 Modelling exchange terms between the phases

Let us first focus on the exchange terms in (1.47). We thus consider an isolated amount of mixture so that: $d\mathcal{E} = d\mathcal{V} = d\mathcal{M} = 0$. In other words, we consider a subset $\mathcal{D}(\mathcal{V}, \mathcal{M}, \mathcal{E})$ of $\mathcal{H}(\mathcal{M})$ so that all the states $W \in \mathcal{D}(\mathcal{V}, \mathcal{M}, \mathcal{E})$ have the same total volume $\mathcal{V}$, the same total mass $\mathcal{M}$ and the same total energy $\mathcal{E}$:

$$\mathcal{D}(\mathcal{V}, \mathcal{M}, \mathcal{E}) = \{W \in \mathcal{H}(\mathcal{M}) \, ; \, \mathcal{V}_l + \mathcal{V}_v = \mathcal{V} \, ; \, \mathcal{E}_l + \mathcal{E}_v = \mathcal{E}\} \, .$$

In order to respect the second law of thermodynamics, the mixture entropy S of such an isolated system must increase. As a consequence, the models for $d\left(\mathcal{V}_k/\mathcal{V}\right)$, $d\left(\mathcal{M}_k/\mathcal{M}\right)$ and $d\left(\mathcal{E}_k/\mathcal{E}\right)$ must be chosen so that $dS \geq 0$.

The Gibbs relation (1.47) becomes for such an isolated system:

$$\begin{array}{rcl} dS & = & \mathcal{E}\dfrac{1}{T_l}d\left(\dfrac{\mathcal{E}_l}{\mathcal{E}}\right) + \mathcal{V}\dfrac{P_l}{T_l}d\left(\dfrac{\mathcal{V}_l}{\mathcal{V}}\right) - \mathcal{M}\dfrac{\mu_l}{T_l}d\left(\dfrac{\mathcal{M}_l}{\mathcal{M}}\right) \\ & + & \mathcal{E}\dfrac{1}{T_v}d\left(\dfrac{\mathcal{E}_v}{\mathcal{E}}\right) + \mathcal{V}\dfrac{P_v}{T_v}d\left(\dfrac{\mathcal{V}_v}{\mathcal{V}}\right) - \mathcal{M}\dfrac{\mu_v}{T_v}d\left(\dfrac{\mathcal{M}_v}{\mathcal{M}}\right) \end{array} \tag{1.48}$$

As in [3], we assume that the time-evolution of these quantities are of the form:

$$(H_8) \quad \left\{ \begin{array}{l} d\left(\dfrac{\mathcal{V}_k}{\mathcal{V}}\right) = \dfrac{\bar{\mathcal{V}}_k - \mathcal{V}_k}{\lambda \mathcal{V}} dt, \\ d\left(\dfrac{\mathcal{M}_k}{\mathcal{M}}\right) = \dfrac{\bar{\mathcal{M}}_k - \mathcal{M}_k}{\lambda \mathcal{M}} dt, \\ d\left(\dfrac{\mathcal{E}_k}{\mathcal{E}}\right) = \dfrac{\bar{\mathcal{E}}_k - \mathcal{E}_k}{\lambda \mathcal{E}} dt, \end{array} \right. \tag{1.49}$$

with $\lambda > 0$. The state $\bar{W} = (\bar{\mathcal{V}}_l, \bar{\mathcal{M}}_l, \bar{\mathcal{E}}_l, \bar{\mathcal{V}}_v, \bar{\mathcal{M}}_v, \bar{\mathcal{E}}_v)$ then corresponds to the state that the system will asymptotically reach. Let us define $\bar{W}$ so that models (1.49) comply with the second law of thermodynamics.

By differentiating the mixture entropy S with respect to the variable W, we get:

$$dS = \nabla_W(S)(W).dW. \tag{1.50}$$

Since we have an isolated system, $d\mathcal{V} = d\mathcal{M} = d\mathcal{E} = 0$, which implies:

$$\begin{array}{rcl} dW & = & \left(\mathcal{V}d\left(\dfrac{\mathcal{V}_l}{\mathcal{V}}\right), \mathcal{M}d\left(\dfrac{\mathcal{M}_l}{\mathcal{M}}\right), \mathcal{E}d\left(\dfrac{\mathcal{E}_l}{\mathcal{E}}\right), \right. \\ & & \left. \mathcal{V}d\left(\dfrac{\mathcal{V}_v}{\mathcal{V}}\right), \mathcal{M}d\left(\dfrac{\mathcal{M}_v}{\mathcal{M}}\right), \mathcal{E}d\left(\dfrac{\mathcal{E}_v}{\mathcal{E}}\right)\right) \end{array} \tag{1.51}$$

From (1.49), (1.50) and (1.51) it follows that:

$$dS = \nabla_W(S).\left(\frac{\bar{W} - W}{\lambda}\right) dt. \tag{1.52}$$

Since S is strictly concave on $\mathcal{H}(\mathcal{M})$, it is also strictly concave on $\mathcal{D}(\mathcal{V},\mathcal{M},\mathcal{E})$. This property implies that the tangent plane to S at any point W of $\mathcal{H}(\mathcal{M})$ is above S:

$$\forall W_0 \in \mathcal{H}(\mathcal{M}), S(W_0) \leq S(W) + \nabla_W(S)(W).(W_0 - W). \tag{1.53}$$

In particular, we can write the concavity condition (1.53) for $W_0 = \bar{W}$, which leads to:

$$\nabla_W(S)(W).(\bar{W} - W) \geq S(\bar{W}) - S(W)$$

so that from (1.52) we get:

$$dS \geq \frac{(S(\bar{W}) - S(W))}{\lambda} dt. \tag{1.54}$$

As a consequence, **one possible choice** to guarantee the growth of the entropy with the models (1.49) is to define the state $\bar{W}$ as the point which maximizes the mixture entropy for a fixed $(\mathcal{V},\mathcal{M},\mathcal{E})$:

$$S(\bar{W}) = \max_{\mathcal{D}(\mathcal{V},\mathcal{M},\mathcal{E})} (S(W)) \tag{1.55}$$

Thanks to the strict concavity of S on $\mathcal{D}(\mathcal{V},\mathcal{M},\mathcal{E})$, this point exists and is unique. Hence, with the definition (1.55) for the state $\bar{W}$, the growth of the mixture entropy of an isolated system is ensured by the models (1.49).

Moreover, Gibbs relation (1.48) on $\mathcal{D}(\mathcal{V},\mathcal{M},\mathcal{E})$ can be simplified by using relations (1.34). Indeed, when focusing on the volume relation in (1.34), we have:

$$\begin{array}{rcl} \sum_k d\left(\frac{\mathcal{V}_k}{\mathcal{V}}\right) & = & \sum_k \left(\left(\frac{d\mathcal{V}_k}{\mathcal{V}}\right) - \mathcal{V}_k \left(\frac{d\mathcal{V}}{\mathcal{V}^2}\right)\right) \\ & = & \frac{d(\sum_k \mathcal{V}_k)}{\mathcal{V}} - (\sum_k \mathcal{V}_k)\left(\frac{d\mathcal{V}}{\mathcal{V}^2}\right) = 0 \end{array}$$

Obviously, the same results can be obtained for masses and energies, so that we have the following relations:

$$\begin{array}{c} d\left(\frac{\mathcal{V}_l}{\mathcal{V}}\right) = -d\left(\frac{\mathcal{V}_v}{\mathcal{V}}\right); \\ d\left(\frac{\mathcal{M}_l}{\mathcal{M}}\right) = -d\left(\frac{\mathcal{M}_v}{\mathcal{M}}\right) \quad ; \quad d\left(\frac{\mathcal{E}_l}{\mathcal{E}}\right) = -d\left(\frac{\mathcal{E}_v}{\mathcal{E}}\right). \end{array} \tag{1.56}$$

Eventually, by introducing relations (1.56) in Gibbs relation (1.48), we obtain the following relation on $\mathcal{D}(\mathcal{V},\mathcal{M},\mathcal{E})$:

$$\begin{array}{rcl} dS & = & \mathcal{E}\left(\frac{1}{T_l} - \frac{1}{T_v}\right) d\left(\frac{\mathcal{E}_l}{\mathcal{E}}\right) + \mathcal{V}\left(\frac{P_l}{T_l} - \frac{P_v}{T_v}\right) d\left(\frac{\mathcal{V}_l}{\mathcal{V}}\right) \\ & - & \mathcal{M}\left(\frac{\mu_l}{T_l} - \frac{\mu_v}{T_v}\right) d\left(\frac{\mathcal{M}_l}{\mathcal{M}}\right) \end{array} \tag{1.57}$$

Since the mixture entropy is strictly concave on $\mathcal{D}(\mathcal{V},\mathcal{M},\mathcal{E})$, it possesses a unique maximum $\bar{W}$ on $\mathcal{D}(\mathcal{V},\mathcal{M},\mathcal{E})$. If this maximum is not reached on the boundary of $\mathcal{D}(\mathcal{V},\mathcal{M},\mathcal{E})$, the derivative of S with respect to $\mathcal{V}_l/\mathcal{V}$, $\mathcal{M}_l/\mathcal{M}$ and $\mathcal{E}_l/\mathcal{E}$ must vanish at $\bar{W}$. The latter is thus defined by the following relations:

$$\left\{ \begin{array}{l} P_l(\bar{\mathcal{V}}_l, \bar{\mathcal{M}}_l, \bar{\mathcal{E}}_l) = P_v(\bar{\mathcal{V}}_v, \bar{\mathcal{M}}_v, \bar{\mathcal{E}_v}) \\ T_l(\bar{\mathcal{V}}_l, \bar{\mathcal{M}}_l, \bar{\mathcal{E}}_l) = T_v(\bar{\mathcal{V}}_v, \bar{\mathcal{M}}_v, \bar{\mathcal{E}}_v) \\ \mu_l(\bar{\mathcal{V}}_l, \bar{\mathcal{M}}_l, \bar{\mathcal{E}}_l) = \mu_v(\bar{\mathcal{V}}_v, \bar{\mathcal{M}}_v, \bar{\mathcal{E}}_v) \end{array} \right. \tag{1.58}$$

When the maximum is reached on the boundary of $\mathcal{D}(\mathcal{V},\mathcal{M},\mathcal{E})$, system (1.58) does not make sense since the derivatives of the mixture entropy do not vanish inside $\mathcal{D}(\mathcal{V},\mathcal{M},\mathcal{E})$. Such

situations correspond to single-phase cases for which W_1 or W_2 is equal to $(0, 0, 0)$.

The modelling of the evolution of the phasic volumes, phasic masses and phasic energies (1.49) enforces the system to return to the equilibrium state $\bar{W}$, which corresponds to the classical thermodynamical equilibrium state. The latter is defined as the state ensuring the pressure, temperature and Gibbs enthalpy equilibria (1.58). It has been shown in this section that these source terms (1.49) comply with the second law of the thermodynamics provided that the relaxation time-scale λ is chosen non-negative.

1.A.4 Dynamical evolution of the mixture quantities

The previous subsection describes a model for the evolution of each phase of an element $(\mathcal{V}, \mathcal{M}, \mathcal{E})$ isolated from the rest of the fluid. The interaction between the surrounding fluid and the the mixture described by the variables $(\mathcal{V}, \mathcal{M}, \mathcal{E}, U)$ is now considered by using the following classical assumptions:

(H_{10}) the mass $\mathcal{M}$ is conserved along the streamlines:

$$d\mathcal{M} = 0; \tag{1.59}$$

(H_{11}) the variation of the volume $\mathcal{V}$ is due to the divergence of the velocity field U:

$$d\mathcal{V} = \mathcal{V}\nabla_x.(U)dt; \tag{1.60}$$

(H_{12}) the variation of the velocity U follows the Newton's law, considering here that only the forces due to the pressure are accounted for:

$$d(\mathcal{M}\mathcal{U}) = -\mathcal{V}\nabla_x(P)dt, \tag{1.61}$$

where P corresponds to the mixture pressure defined by (1.44);

(H_{13}) the first law of thermodynamics applies to the energy $\mathcal{E}$:

$$d\mathcal{E} = -Pd\mathcal{V} + Qdt; \tag{1.62}$$

it means that the variation of $\mathcal{E}$ is due to the work of the external forces (only the pressure forces here) and to the heat exchange Q of the system with its surrondings.

Remark 1.7 — Thanks to assumptions (H_{10}) and (H_{13}), with $Q = 0$, we have $d\mathcal{E} + Pd\mathcal{V} - \mu d\mathcal{M} = 0$. Hence the general Gibbs relation (1.47) reduces to the Gibbs relation for a isolated system (1.57).

1.A.5 The set of Partial Derivative Equations (PDE) in intensive form

From now the system has been described using extensive variables. Indeed, extensive variables provide a more comprehensive description of the model. But, since our aim is to build a set of partial derivative equations, it is convenient to use an intensive description of the system. In this section, we derive the extensive descritption of the two-phase flow of the previous sections into an intensive description.

1.A.5.1 Fractions and phasic specific quantities

The mass conservation assumption (H_{10}) enables to define specific quantities (per unit of mass). The specific volume of the mixture is thus defined as $\tau = \mathcal{V}/\mathcal{M}$ (in m^3/kg), and the specific energy of the mixture is $e = \mathcal{E}/\mathcal{M}$ (in J/kg). We recall the notations for the volume fraction α_k, the mass fraction y_k and the energy fraction z_k of phase k:

$$Y_k = (\alpha_k, y_k, z_k) = \left(\frac{\mathcal{V}_k}{\mathcal{V}}, \frac{\mathcal{M}_k}{\mathcal{M}}, \frac{\mathcal{E}_k}{\mathcal{E}}\right) \tag{1.63}$$

The phasic specific volume and the phasic specific energy of phase k are then:

$$\begin{array}{rcccccl} \tau_k & = & \dfrac{\mathcal{V}_k}{\mathcal{M}_k} & = & \dfrac{\mathcal{V}_k}{\mathcal{V}}\dfrac{\mathcal{M}}{\mathcal{M}_k}\dfrac{\mathcal{V}}{\mathcal{M}} & = & \dfrac{\alpha_k}{y_k}\tau; \\ e_k & = & \dfrac{\mathcal{E}_k}{\mathcal{M}_k} & = & \dfrac{\mathcal{E}_k}{\mathcal{E}}\dfrac{\mathcal{M}}{\mathcal{M}_i}\dfrac{\mathcal{E}}{\mathcal{M}} & = & \dfrac{z_k}{y_k}e. \end{array} \tag{1.64}$$

The conservation equations (1.34) become:

$$1 = \alpha_l + \alpha_v \quad ; \quad 1 = y_l + y_v \quad ; \quad 1 = z_l + z_v. \tag{1.65}$$

The thermodynamical evolution equation (1.49) can be written:

$$d\alpha_k = \frac{\bar{\alpha_k} - \alpha}{\lambda}dt; \quad dy_k = \frac{\bar{y}_k - y_k}{\lambda}dt; \quad dz_k = \frac{\bar{z}_k - z_k}{\lambda}dt \tag{1.66}$$

where $\bar{Y_k} = (\bar{\alpha}_k, \bar{y}_k, \bar{z}_k) = \left(\dfrac{\bar{V}_k}{V}, \dfrac{\bar{M}_k}{M}, \dfrac{\bar{E}_k}{E}\right)$ denotes the equilibrium fractions.

1.A.5.2 Specific mixture entropy and Gibbs relation

Let us define the mass $\mathcal{M}_k$ as $\mathcal{M}_k = \mathcal{M}'_k \mathbb{I}_{kg}$, where $\mathbb{I}_{kg}$ is equal to 1 kg and $\mathcal{M}'_k \in \mathbb{R}^+ - \{0\}$ is dimensionless. By denoting s_k the specific entropy of phase k, $s_k = S_k/\mathcal{M}_k$, and by using the property (H_8), we have:

$$s_k\left(\frac{X_k}{\mathcal{M}_k}\right) = \frac{S_k(X_k, \mathcal{M}_k)}{\mathcal{M}_k} = \frac{1}{\mathbb{I}_{kg}} S_k\left(\frac{X_k}{\mathcal{M}'_k}, \frac{\mathcal{M}_k}{\mathcal{M}'_k}\right) = \frac{1}{\mathbb{I}_{kg}} S_k\left(\frac{X_k}{\mathcal{M}'_k}, \mathbb{I}_{kg}\right).$$

where X_k stands here for $(\mathcal{V}_k, \mathcal{E}_k)$. We thus get the link between extensive and intensive quantities:

$$s_k\left(\frac{X_k}{\mathcal{M}_k}\right) = \frac{1}{\mathbb{I}_{kg}} S_k\left(\frac{X_k}{\mathcal{M}'_k}, \mathbb{I}_{kg}\right) = \frac{S_k(X_k, \mathcal{M}_k)}{\mathcal{M}_k} \tag{1.67}$$

The specific mixture entropy can be defined as:

$$\forall W \in \mathcal{H}(\mathcal{M}),\ \mathcal{M} > 0,\ s\left(\frac{W}{\mathcal{M}}\right) = \frac{S(W)}{\mathcal{M}}. \tag{1.68}$$

By using the relation (1.67) for the phasic entropies we get the expression of the specific mixture entropy:

$$\begin{array}{rcl} s\left(\dfrac{W}{\mathcal{M}}\right) = \dfrac{S_l(W_l)}{\mathcal{M}} + \dfrac{S_v(W_v)}{\mathcal{M}} & = & \dfrac{\mathcal{M}_l}{\mathcal{M}}\dfrac{S_l(W_l)}{\mathcal{M}_l} + \dfrac{\mathcal{M}_v}{\mathcal{M}}\dfrac{S_v(W_v)}{\mathcal{M}_v} \\ & = & \dfrac{\mathcal{M}_1}{\mathcal{M}} s_l\left(\dfrac{X_l}{\mathcal{M}_l}\right) + \dfrac{\mathcal{M}_v}{\mathcal{M}} s_v\left(\dfrac{X_v}{\mathcal{M}_v}\right). \end{array}$$

The mixture entropy s can finally be re-written using the fractions of phase l:

$$s(\alpha_l, y_l, z_l, \tau, e) = y_l s_l \left(\frac{\alpha_l}{y_l}\tau, \frac{z_l}{y_l}e \right) + (1-y_l) s_v \left(\frac{(1-\alpha_l)}{(1-y_l)}\tau, \frac{(1-z_l)}{(1-y_l)}e \right)$$

In the same way, the Gibbs relation for the mixture can be written using the intensive quantites:

$$\begin{aligned} ds &= \frac{1}{T}de + \frac{P}{T}d\tau + \tau\left(\frac{P_l}{T_l} - \frac{P_v}{T_v}\right)d\alpha_l \\ &- \left(\frac{\mu_l}{T_l} - \frac{\mu_v}{T_v}\right)dy_l + e\left(\frac{1}{T_l} - \frac{1}{T_v}\right)dz_l \end{aligned} \tag{1.69}$$

where the mixture temperature and the mixture pressure are:

$$\begin{aligned} \frac{1}{T} &= z_l \frac{1}{T_l(\tau_l, e_l)} + z_v \frac{1}{T_v(\tau_v, e_v)}; \\ \frac{P}{T} &= \alpha_l \frac{P_l(\tau_l, e_l)}{T_l(\tau_l, e_l)} + \alpha_v \frac{P_v(\tau_v, e_v)}{T_v(\tau_v, e_v)}. \end{aligned} \tag{1.70}$$

1.A.5.3 Intensive PDE in a one dimensional framework

The equations (1.59), (1.61), (1.62) can be written with intensive quantities:

$$\begin{cases} d\tau = \tau \nabla_x.(U)dt \\ dU = -\tau \nabla_x(P)dt \\ de = -Pd\tau + qdt \end{cases} \tag{1.71}$$

where $q = Q/M$, the specific heat-power is set to zero in the following:

$$q = 0. \tag{1.72}$$

Let us note the mixture density:

$$\rho = 1/\tau, \tag{1.73}$$

the specific total energy of the mixture:

$$E = e + |U|^2/2, \tag{1.74}$$

and the vector gathering the fractions:

$$Y = (\alpha_l, y_l, z_l)^t. \tag{1.75}$$

By using the relation (1.35), which states that:

$$d\Phi = \left(\partial_t \Phi + U\partial_x \Phi\right) dt, \tag{1.76}$$

it can be shown that the set of derivative equations (1.71) and (1.66) lead to the set of partial differential equations in conservative form:

$$\begin{cases} \dfrac{\partial}{\partial t}(\rho Y) + \dfrac{\partial}{\partial x}(\rho U Y) = \rho \Gamma, \\ \dfrac{\partial}{\partial t}(\rho) + \dfrac{\partial}{\partial x}(\rho U) = 0, \\ \dfrac{\partial}{\partial t}(\rho U) + \dfrac{\partial}{\partial x}\left(\rho U^2 + P\right) = 0, \\ \dfrac{\partial}{\partial t}(\rho E) + \dfrac{\partial}{\partial x}\left(U(\rho E + P)\right) = 0. \end{cases} \tag{1.77}$$

The system (1.77) is closed with the relations (1.64), (1.65), (1.70), and the source terms are:

$$\Gamma = \left(\frac{\bar{\alpha}_l - \alpha_l}{\lambda}, \frac{\bar{y}_l - y_l}{\lambda}, \frac{\bar{z}_l - z_l}{\lambda} \right).$$

The time-scale $\lambda > 0$ describing the return to the thermodynamical equilibrium has to be chosen by the user.

Remark 1.8 — Following remark 1.7, Gibbs relation for intensive quantities (1.69) becomes

$$ds = \tau \left(\frac{P_l}{T_l} - \frac{P_v}{T_v} \right) d\alpha_l - \left(\frac{\mu_l}{T_l} - \frac{\mu_v}{T_v} \right) dy_l + e \left(\frac{1}{T_l} - \frac{1}{T_v} \right) dz_l. \tag{1.78}$$

The mixture entropy s is then convected with the velocity U, and subjected to the source terms Γ:

$$\frac{\partial}{\partial t} (\rho s) + \frac{\partial}{\partial x} (\rho U s) = \rho \Gamma \nabla_Y (s)_{|\tau,e}. \tag{1.79}$$

□

1.B Reference solution for a rarefaction wave with the LuT

Let us consider a single phase flow with a complex EOS, for instance in the form of the LuT proposed in the article. In the following we deal with a $u-c$ rarefaction wave, but the conclusions would obviously be the same for a $u+c$ rarefaction wave. For any point $.^*$ in a $u-c$ rarefaction wave separating a left state L and a right state R, the Riemann invariants are constant, which means in our case that:

$$s^* = s^L, \quad \text{and} \quad u^* + \int_{P_L}^{P^*} \frac{dP}{\rho c(s_0, P)} = u^L. \tag{1.80}$$

When using simple analytical EOS, as Stiffened Gas EOS for instance, the integral in the second condition of (1.80) can be explicitly computed. It is also easy to compute an isentropic path, which corresponds to the first condition of (1.80). Finally for such simple EOS, the definition of a point in the rarefaction wave relies on a local implicit computation (through a Newton algorithm or a dichotomy for instance) for system (1.80). The latter can be done up to the round-off error of the computer.

With our complex EOS based on the (P,T) plane, the isentropic path can only be approximated from the left state to the right state using Newton-like algorithm. Moreover, the integral arising in the second condition of (1.80) can not be explicitly written. It must also be approximated using classical integration algorithm along the isentropic path. We have thus two sources of numerical approximation in the definition of the thermodynamical path of the rarefaction wave.

On the other hand, our particular choice for the polynomials (cubic splines) of the LuT leads to an even more important drawback. Indeed, as depicted above, we can approximate the rarefaction wave in the thermodynamical plane (P,T) using numerical algorithms, but we are not able to project this thermodynamical path onto the (t,x) plane. A point $.^*$ of the $u-c$ rarefaction wave is connected to the point (t,x^*) thanks to the relation:

$$\frac{x^*-x_0}{t} = u^* - c^*.$$

Since the rarefaction wave is a regular wave between two time-space points (t,x^L) and (t,x^R), u^*-c^* has to be continuous and monotonic to allow a regular projection. It should then be noted that the sound speed c can be written with respect to the second order derivatives of μ:

$$c^2 = \left(\frac{\chi_T}{\tau} - \frac{T\alpha_P^2}{C_p}\right)^{-1}, \tag{1.81}$$

where

$$C_p = -T\left.\frac{\partial^2\mu}{\partial T^2}\right|_P \; ; \; \alpha_p = \frac{1}{\tau}\left.\frac{\partial^2\mu}{\partial p\partial T}\right|_{T,p} \; ; \; \chi_T = \frac{1}{\tau}\left.\frac{\partial^2\mu}{\partial p^2}\right|_T. \tag{1.82}$$

Since our LuT is based on cubic splines, it only ensures a $\mathcal{C}^1$ μ, but we can not ensure the continuity of c between to neighboring cells of the LuT. We are thus not able to perform the projection of the rarefaction wave from the thermodynamical plane (P,T) to the (t,x) plane.

Finally, due to our complex EOS, we could only perform a weak comparison between the approximated solution given by our code and an approximated rarefaction wave in the thermodynamical $(P,T)-$plane. This comparison is weak in the sense that we would get a "reference" rarefaction wave obtained through a numerical integration and not an analytical one. In order to perform this weak comparison in the (t,x) plane, we should use a higher

polynomial basis instead of the splines, so that the sound speed would be continuous and monotonic on the whole domain.

We propose here to build a "reference" solution for a $u - c$ rarefaction wave as depicted above. We consider initial data such that the left state is a pressurized liquid state and the right state is pure vapor at saturation (see table 1.B.1). The quantities e, ρ and $\phi_2 = \int_{P_L}^{P^*} \frac{dP}{\rho c(s_0, P)}$ are continuous and they have been plotted on figures 1.B.1, 1.B.2 and 1.B.3 with respect to the pressure. The quantity $\xi^* = \frac{x^* - x_0}{t} = u^* - c^*$ is plotted on figure 1.B.4, the non-monotonic behavior associated to c can be clearly seen.

Data for LuT	Left state	Right state
α	0	1
y	0	1
z	0	1
ρ kg/m^3	725.86	43.90
u (m/s)	0	9.90
P (Pa)	1.50 10^7	8.23 10^6

Table 1.B.1 – *Initial data for an isolated rarefaction wave at equilibrium with liquid left state and vapor right state.*

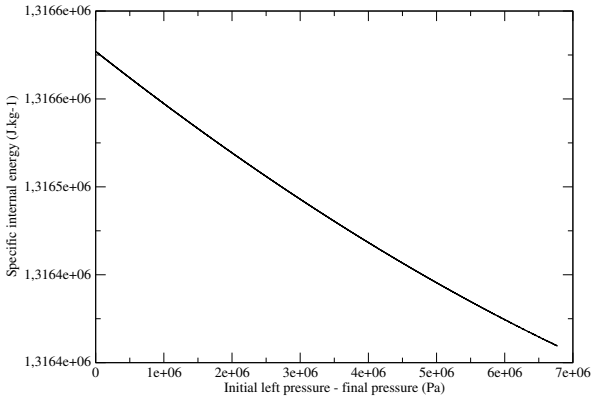

Figure 1.B.1 – *Specific internal energy e (in $J.kg^{-1}$) along the discrete isentropic path $\mathcal{S}_{s_0}$ (abscissas are the opposite of the pressure gap between the final pressure and the initial left pressure equal to* 150 10^5 *Pa).*

As an illustration, a "reference" solution can be built by introducing $\tilde{\xi}$ which corresponds to a linear regression of ξ (cf figure 1.B.4). This new quantity $\tilde{\xi}$ is continuous and monotonic; moreover, at each $\tilde{\xi}$, we can associate unique values for the quantities P, ρ, e, ϕ_2, c. In this way, the thermodynamical path of the rarefaction wave can be projected on the (t, x) plane. Figure 1.B.5 show thermodynamical paths in the (P, T)-plane for three different meshes at the final step compared with the reference solution. Mesh refinement qualitatively improves the solution, in particular for states at low pressure. Final pressure profiles seem correct (see figure 1.B.6). Obviously, this rarefaction wave can not be used for verification purposes, the way of projecting the rarefaction wave through $\tilde{\xi}$ is not accurate enough and just allows to illustrate the encountered difficulties.

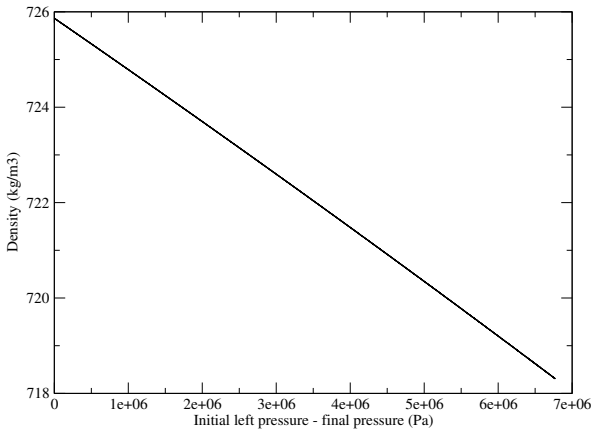

Figure 1.B.2 – *Density ρ (in $kg.m^{-3}$) along the discrete isentropic path (abscissas are the opposite of the pressure gap between the final pressure and the initial left pressure equal to* 150 10^5 *Pa).*

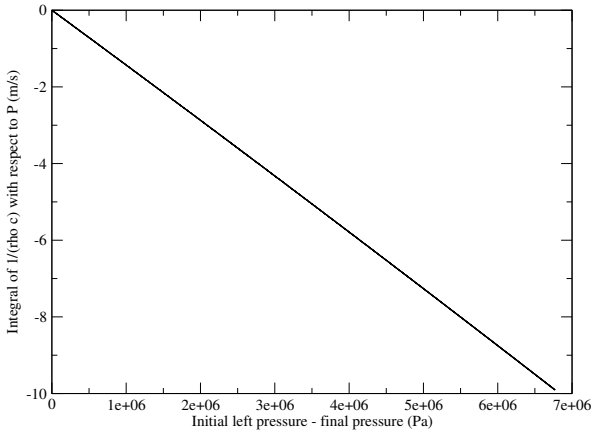

Figure 1.B.3 – $\Phi_2 = \int_{P_L}^{P^*} \frac{dP}{\rho c(s_0, P)}$ *(in $m.s^{-1}$) along the isentropic path (abscissas are the opposite of the pressure gap between the final pressure and the initial left pressure equal to* 150 10^5 *Pa).*

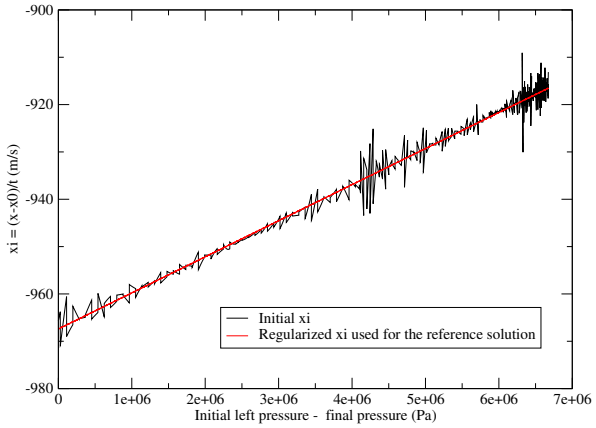

Figure 1.B.4 – $\xi^* = \frac{x^* - x_0}{t} = u^* - c^*$ *along the discrete isentropic path and regularized $\tilde{\xi}$ used in the reference solution (abscissas are the opposite of the pressure gap between the final pressure and the initial left pressure equal to* 150 10^5 *Pa).*

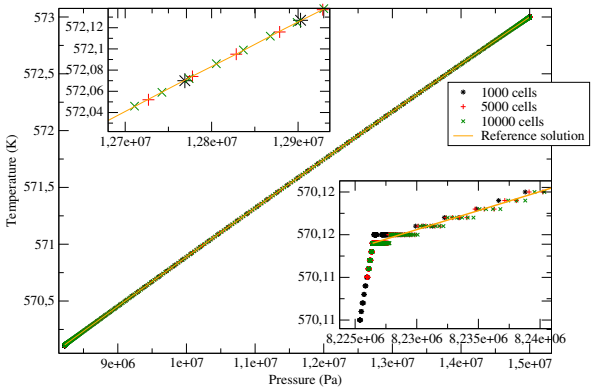

Figure 1.B.5 – *Thermodynamical states at the final time in the PT-plane for several meshes compared with the reference solution.*

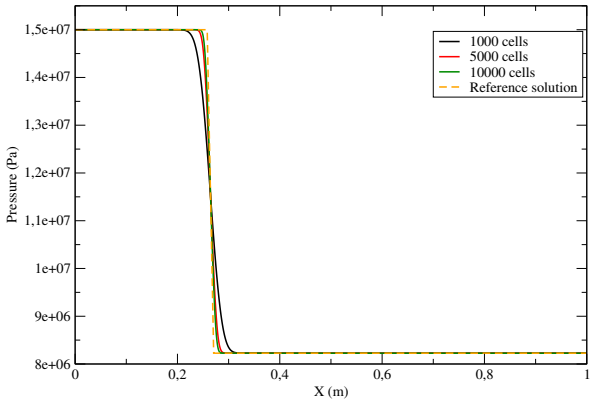

Figure 1.B.6 – *Pressure (Pa) as a function of X (m) at the final time compared with the reference solution.*

1.C Simple model for relaxation time based on Nucleation Theory

The Classical Nucleation Theory has been developed for many years [15]. This theory assumes that the bubble nucleation rate J (the number of bubbles created per unit time in unit volume) follows an Arrhenius law:

$$J = J_0 \exp\left(-\frac{E_a}{k_B T}\right), \tag{1.83}$$

where $k_B = 1.38064852\ 10^{-23} JK^{-1}$ is the Boltzmann constant, T is the liquid temperature, J_0 is a prefactor and E_a is an activation energy. J_0 and E_a are defined in the following.

Indeed, when a bubble is created, it enables to dissipate extra energy of superheated liquid: this energy amount decreases as R^3, with R the radius of the created bubble. At the same time, an energy amount, increasing as R^2, is required to maintain the liquid-vapor interface. Both effects balance each other for a critical radius R_c:

$$R_c = \frac{2\gamma}{\Delta P}, \tag{1.84}$$

where $\Delta P = P_l - P_{sat}$ and γ is the liquid-vapor surface tension.

For spherical bubbles with a radius R_c, the required work for nucleation is minimal. This minimal nucleation work is defined as the activation energy E_a which appears in (1.83). It reads:

$$E_a = \frac{16\pi\gamma^3}{3(\Delta P)^2}. \tag{1.85}$$

It means that bubbles with a radius $R < R_c$ tend to disappear whereas bubbles with a radius $R > R_c$ are able to grow. Following an Arrhenius law (1.83), nucleation occurs when the barrier energy E_a has the same order of magnitude that thermal fluctuations $k_B T$. However, this energy barrier E_a can be very high because it applies to pure liquid without impurities (*homogeneous nucleation*), which are not the conditions that we may find in industrial applications. Indeed, if impurities are present in water (which is the case for nuclear circuits), bubbles creation is easier (*heterogeneous nucleation*). To take this assumption into account, the activation energy is decreased as in [4] by multiplying E_a with $\varphi \in]0,1[$:

$$J = J_0 \exp\left(-\frac{\varphi E_a}{k_B T}\right). \tag{1.86}$$

Then, the probability $\mathcal{P}(t)$ that no bubble appears within a time t is:

$$\mathcal{P}(t) = \exp(-JVt)$$

where V is the volume of liquid. A common assumption [8, 43, 19] provides that nucleation indeed occurs after the time t so that: $\mathcal{P}(t) = \frac{1}{2}$. Then, a characteristic time-scale for the delay before nucleation appearance t_{nuc} can be defined with $\mathcal{P}(t_{nuc}) = \frac{1}{2}$, i.e.:

$$t_{nuc} = t^0_{nuc} \exp\left(\frac{\varphi E_a}{k_B T}\right), \tag{1.87}$$

with

$$t^0_{nuc} = \frac{\ln(2)}{J_0 V}. \tag{1.88}$$

There is no consensus in the litterature about the prefactor J_0. In [20], J_0 is taken almost constant with temperature and pressure. On the contrary, complex models have been proposed, for instance in [51] or [11]. In our study, we chose a simple model, proposed in [8] or [43]. J_0 is taken as the product of thermal frequency $\frac{k_B T}{h}$ and $\frac{1}{V_c}$, where $h = 6.62607015\ 10^{-34} Js$ is the Planck constant and $V_c = \frac{4\pi R_c^3}{3}$ is the volume of a critical nucleus:

$$J_0 = \frac{k_B T}{h} \frac{3}{4\pi} \frac{1}{R_c^3}. \tag{1.89}$$

Finally we get, with (1.84) and (1.89):

$$t_{nuc}^0 = \frac{\ln(2)}{V} \frac{1}{J_0} = \frac{\ln(2)}{V} \frac{h}{k_B T} \frac{4\pi}{3} R_c^3 = \frac{\ln(2)}{V} \frac{h}{k_B T} \frac{4\pi}{3} \left(\frac{2\gamma}{\Delta P} \right)^3.$$

We chose to simplify this prefactor: indeed, a lot of terms are almost constant during our simulations. It allows to reduce the number of paramaters for our numerical studies. We keep only the dependance with $\frac{1}{\Delta P^3}$ in our final simplified model:

$$\boxed{t_{nuc} = \left(\frac{a_0}{\Delta P} \right)^3 \exp\left(\frac{\varphi E_a}{k_B T} \right)}, \tag{1.90}$$

where E_a is defined by (1.85): $E_a = \frac{16\pi\gamma^3}{3(\Delta P)^2}$, and γ is estimated with the IAPWS 94 correlation [46]:

$$\gamma = B_0(1 + b(1 - \frac{T}{T_c})) \left(\frac{T}{T_c} \right)^{\nu}, \tag{1.91}$$

where: $B_0 = 235.8\ 10^{-3}\ mN/m$; $b = -0.625$; $\nu = 1.256$ and $T_c = 647.096K$ (water critical temperature).

In the simplified model (1.90), only two parameters have thus to be defined: a_0 in (Pa.s), homogeneous to a dynamical viscosity, and $\varphi \in [0, 1]$.

1.D Initial data for Riemann problems test cases

1.D.1 Out of equilibrium test cases (1.4.1)

Here are the parameters used for the Stiffened Gas (SG) for the test case of section 1.4.1. The parameters for the vapour are:

$$\left[\begin{array}{c} C_{V,v} = 4.477815802223535\ 10^3\ JK^{-1}kg^{-1}, \\ \gamma_v = 1.084875362318841, \\ \Pi_v = 4.1904297086743001\ 10^6\ Pa, \\ s_v^0 = -1.137650328291112\ 10^4\ JK^{-1}kg^{-1}, \end{array}\right.$$

and for the liquid we have:

$$\left[\begin{array}{c} C_{V,l} = 1.395286166711847\ 10^3\ JK^{-1}kg^{-1}, \\ \gamma_l = 1.665128030303030, \\ \Pi_l = 3.725876146842836\ 10^8\ Pa, \\ s_l^0 = 1.0\ 10^4\ JK^{-1}kg^{-1}. \end{array}\right.$$

Data for SG	Left state	Intermediate state
α	$4.16003754536212\ 10^{-1}$	$4.68486052082106\ 10^{-1}$
y	$1.0\ 10^{-1}$	$1.2\ 10^{-1}$
z	$1.47660058572024\ 10^{-1}$	$1.75144882351565\ 10^{-1}$
ρ (kg/m^3)	393.940361842377	363.89814762278274
u (m/s)	1.0	1.0
P (Pa)	$1.48\ 10^7$	$1.48\ 10^7$

Data for SG	Right state
α	$4.68486052082106\ 10^{-1}$
y	$1.2\ 10^{-1}$
z	$1.75144882351565\ 10^{-1}$
ρ (kg/m^3)	351.12092230108595
u (m/s)	-33.6320500771937
P (Pa)	$2.80621107450730\ 10^6$

σ =952.696245321188e m/s (shock speed)

Data for LuT	Left state	Intermediate state	Right state
α	$4.16\ 10^{-1}$	$4.68\ 10^{-1}$	$4.68\ 10^{-1}$
y	$1.0\ 10^{-1}$	$1.2\ 10^{-1}$	$1.2\ 10^{-1}$
z	$1.48\ 10^{-1}$	$1.75\ 10^{-1}$	$1.75\ 10^{-1}$
ρ (kg/m^3)	393.94	363.90	351.12
u (m/s)	1.0	1.0	-19.15
P (Pa)	$1.48\ 10^7$	$1.48\ 10^7$	$1.07\ 10^7$

σ =554.61 m/s (shock speed)

1.D.2 Equilibrium test case with mixtures for both initial states (1.4.2)

Data for LuT	Left state	Intermediate state	Right state
α	$4.16\ 10^{-1}$	$6.16\ 10^{-1}$	$8.31\ 10^{-1}$
y	$1.0\ 10^{-1}$	$2.0\ 10^{-1}$	$2.84\ 10^{-1}$
z	$1.48\ 10^{-1}$	$2.80\ 10^{-1}$	$4.20\ 10^{-1}$
ρ (kg/m^3)	393.94	291.57	162.27
u (m/s)	1.0	1.0	-113.53
P (Pa)	$1.48\ 10^7$	$1.48\ 10^7$	$1.00\ 10^7$

σ =554.607603536485 m/s (shock speed)

1.D.3 Equilibrium test case with only a shock, with a liquid left initial state (1.4.3.1)

Data for LuT	Left state	Right state
α	0	6.8910^{-1}
y	0	$6.73\ 10^{-2}$
z	0	$1.40\ 10^{-1}$
ρ (kg/m^3)	742.97	259.49
u (m/s)	1.0	-155.77
P (Pa)	$1.48\ 10^7$	$5.0\ 10^6$

σ =85.14 m/s (shock speed)

1.D.4 Equilibrium test case with only a contact, with a liquid left initial state (1.4.3.2)

Data for LuT	Left state	Right state
α	0	$6.16\ 10^{-1}$
y	0	$2.0\ 10^{-1}$
z	0	2.8010^{-1}
ρ (kg/m^3)	742.97	291.57
u (m/s)	1.0	1.0
P (Pa)	$1.48\ 10^7$	$1.48\ 10^7$

1.E Additional verification test cases and accuracy limitation of the LuT

All the studied verification test cases are listed in the table 1.E.1, the test cases presented in the article as well as the test cases presented in the present appendix.

Subsection	Waves	Equilibrium	EOS	Initial states Left/Right
1.E.1	C	No	LuT	liq. + vap. / liq. + vap.
1.E.1	S	No	LuT	liq. + vap. / liq. + vap.
Article	C + S	No	SG	liq. + vap. / liq. + vap.
Article	C + S	No	LuT	liq. + vap. / liq. + vap.
1.E.2	S	Yes	LuT	liq. + vap. / liq. + vap.
1.E.2	C	Yes	LuT	liq. + vap. / liq. + vap.
Article	C + S	Yes	LuT	liq. + vap. / liq. + vap.
Article	C	Yes	LuT	liq. / liq. + vap.
Article	S	Yes	LuT	liq. / liq. + vap.
1.B	R	Yes	LuT	liq. / vap.

Table 1.E.1 – *List of the presented test cases. In the second colmun, "C" stands for contact, "S" for shock and "R" for rarefaction wave. The second column gives specify if the EOS is at equilibrium ("Yes"), with $\lambda \to 0$, or out-of-equilibrium ("No"), with $\lambda \to \infty$.*

The four additionnal verification test cases with isolated waves presented here are the following:

- two out-of-equilibrium Riemann problem with two-phase flow initial states are studied (appendix 1.E.1) :
  - one with an isolated contact wave;
  - a second with an isolated shock wave.

- secondly, two at-equilibrium Riemann problem with mixtures as initial states are studied (appendix 1.E.2):
  - one with an isolated contact wave;
  - a second with an isolated shock wave.

1.E.1 Out-of-equilibrium test cases for two isolated waves

In this subsection, two out-of-equilibrium Riemann problems are studied (source terms are not considered). Initial data are presented in the table, for the contact wave (table 1.E.2) and for the shock wave (table 1.E.3).
Convergence curves for a Riemann problem with an isolated contact are plotted on figure 1.E.1 whereas convergence curves for a Riemann problem with an isolated shock are plotted on figure 1.E.2. Correct asymptotic convergence orders are recovered in both cases : (1/2 for the contact wave and 1 for the shock wave).
Moreover, the relaxation scheme enables an accuracy gain in both cases, compared with the Rusanov scheme. Nevertheless, this gain is far more important for an isolated contact wave than for a shock wave.

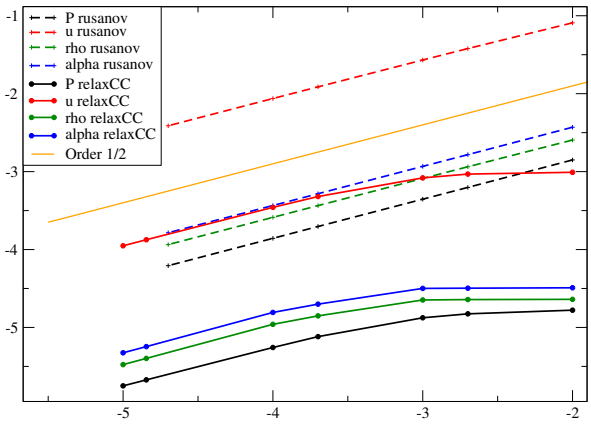

Figure 1.E.1 – *Convergence curve for an out of equilibrium Riemann problem with an isolated contact wave computed with the LuT: logarithm of the error versus logarithm of the mesh size. Four quantites are plotted: P, U, ρ, α for two different numerical schemes (Rusanov and relaxation). The meshes contain from 100 to 200 000 regular cells.*

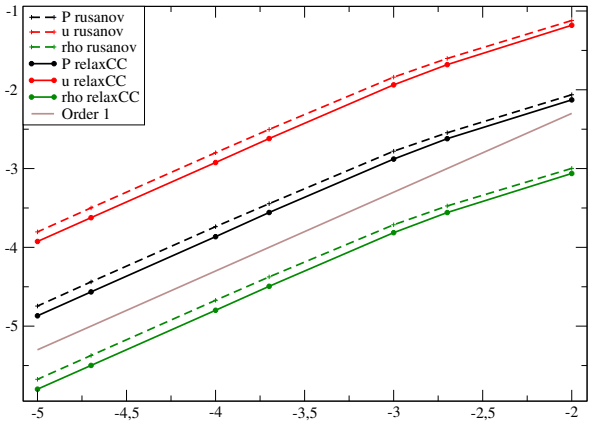

Figure 1.E.2 – *Convergence curve for an out of equilibrium Riemann problem with an isolated shock wave computed with the LuT: logarithm of the error versus logarithm of the mesh size. Four quantites are plotted: P, U, ρ, α for two different numerical schemes (Rusanov and relaxation). The meshes contain from 100 to 200 000 regular cells.*

Data for LuT	Left state	Right state
α	$4.16\ 10^{-1}$	$4.68\ 10^{-1}$
y	$1.0\ 10^{-1}$	$1.2\ 10^{-1}$
z	$1.48\ 10^{-1}$	$1.75\ 10^{-1}$
ρ (kg/m^3)	393.94	363.90
u (m/s)	1.0	1.0
P (Pa)	$1.48\ 10^{7}$	$1.48\ 10^{7}$

Table 1.E.2 – *Initial data for isolated contact wave, out-of-equilibrium test case.*

1.E.2 At equilibrium test cases : inconsistency due to the look-up tables

In this subsection, two at-equilibrium Riemann problems are studied with two-phase flow initial states : one with an isolated shock wave (initial data on table 1.E.4), the other with an isolated contact wave (initial data on table 1.E.5).

On figure 1.E.3, convergence curves for the shock waves are plotted for both numerical

Data for LuT	Left state	Right state
α	$4.16\ 10^{-1}$	$4.68\ 10^{-1}$
y	$1.0\ 10^{-1}$	$1.2\ 10^{-1}$
z	$1.48\ 10^{-1}$	$1.75\ 10^{-1}$
ρ (kg/m^3)	363.90	351.12
u (m/s)	1.0	-19.15
P (Pa)	$1.48\ 10^{7}$	$1.07\ 10^{7}$

Table 1.E.3 – *Initial data for isolated shock wave, out-of-equilibrium test case; σ =554.61 m/s (shock speed).*

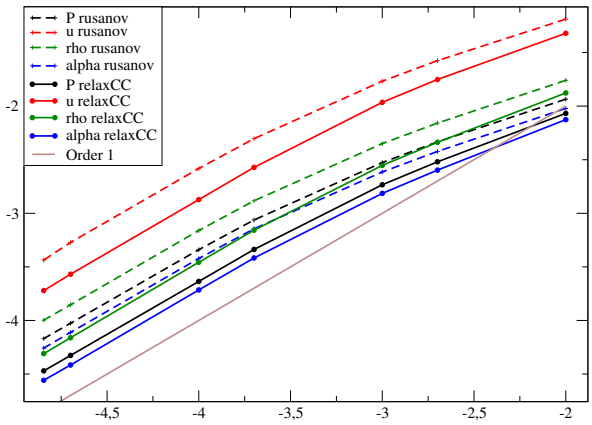

Figure 1.E.3 – *Convergence curve for the Riemann problems at equilibrium computed with the LuT with only a shock wave : logarithm of the error versus logarithm of the mesh size. Four quantites are plotted: P, U, ρ, α for two different numerical schemes (Rusanov and relaxation). The meshes contain from 100 to 200 000 regular cells.*

Data for LuT	Left state	Right state
α	$6.16\ 10^{-1}$	$8.31\ 10^{-1}$
y	$2.00\ 10^{-1}$	$2.84\ 10^{-1}$
z	$2.80\ 10^{-1}$	$4.20\ 10^{-1}$
ρ kg/m^3	291.57	162.27
u (m/s)	1.0	-135.31
P (Pa)	$1.48\ 10^{7}$	$1.00\ 10^{7}$

Table 1.E.4 – *Initial data for an isolated contact wave at equilibrium with mixtures for left and right states.*

schemes. One more time, right convergence order is recovered.

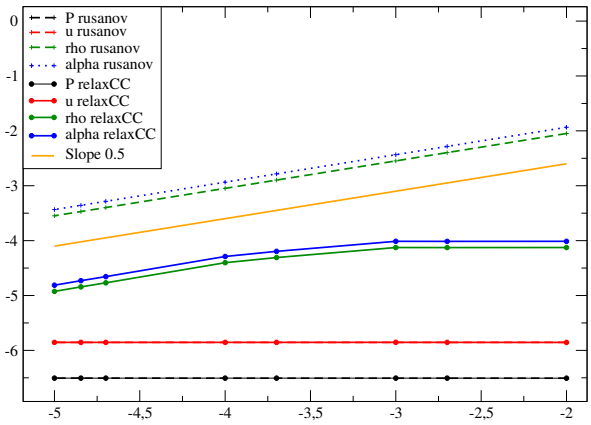

Figure 1.E.4 – *Convergence curve for the Riemann problems at equilibrium computed with the LuT with only a contact wave : logarithm of the error versus logarithm of the mesh size. Four quantites are plotted: P, U, ρ, α for two different numerical schemes (Rusanov and relaxation). The meshes contain from 100 to 200 000 regular cells.*

Data for LuT	Left state	Right state
α	$4.16\ 10^{-1}$	$6.16\ 10^{-1}$
y	$1.0\ 10^{-1}$	$2.0\ 10^{-1}$
z	$1.48\ 10^{-1}$	$2.80\ 10^{-1}$
ρ kg/m^3	393.94	291.57
u (m/s)	1.0	1.0
P (Pa)	$1.48\ 10^7$	$1.48\ 10^7$

Table 1.E.5 – *Initial data for an isolated contact wave at equilibrium with mixtures for left and right states.*

This test case with only a contact wave is not severe so that both the Rusanov scheme and the relaxation scheme are accurate. The spurious numerical waves around the contact have a very small amplitude. On figure 1.E.4, it can be seen that the L^1-error for the approximate variables U and P is constant and small. This illustrates the limited accuracy of the LuT for the variable changes between the (P,T)-plane and the (ρ,e)-plane.
As depicted in the section 1.2 of the article, this change of variables is based on the computation on an approximated solution of system :

$$\left\{ \begin{array}{l} e_k(P_k,T_k) = e_k^0, \\ \tau_k(P_k,T_k) = \tau_k^0, \end{array} \right. \tag{1.92}$$

Starting with the same pressure for the left and right states, $P_L = P_R = 1.48\ 10^7\ Pa$, and the same temperatures $T_L = T_R = 614.236889173817\ K$, the choice of the different values of the fractions (α_L, y_L, z_L) (resp. (α_R, y_R, z_R)) gives different values for the mixture specific volume and energy (τ_L, e_L) (resp. (τ_R, e_R)). Then using relations :

$$\tau_i = \frac{\mathcal{V}_i}{\mathcal{M}_i} = \frac{\mathcal{V}_i}{\mathcal{V}}\frac{\mathcal{M}}{\mathcal{M}_i}\frac{\mathcal{V}}{\mathcal{M}} = \frac{\alpha_i}{y_i}\tau \text{ and } e_i = \frac{\mathcal{E}_i}{\mathcal{M}_i} = \frac{\mathcal{E}_i}{\mathcal{E}}\frac{\mathcal{M}}{\mathcal{M}_i}\frac{\mathcal{E}}{\mathcal{M}} = \frac{z_i}{y_i}e, \tag{1.93}$$

and (1.92), one can compute from $(\alpha_L, y_L, z_L, \tau_L, e_L)$ (resp. $(\alpha_R, y_R, z_R, \tau_R, e_R)$) a mixture pressure $\tilde{P}_L$ (resp. $\tilde{P}_L$) and a mixture temperature $\tilde{T}_L$ (resp. $\tilde{T}_L$). We get then:

$$\begin{array}{l} \text{err}^{P_L} = |P_L - \tilde{P_L}|/P_L \simeq 3.7\ 10^{-7}, \\ \text{err}^{T_L} = |T_L - \tilde{T_L}|/T_L \simeq 1.0\ 10^{-8}, \\ \text{err}^{P_R} = |P_R - \tilde{P_R}|/P_R \simeq 2.7\ 10^{-14}, \\ \text{err}^{T_R} = |T_R - \tilde{T_R}|/T_R \simeq 1.5\ 10^{-15}. \end{array}$$

Hence the change of variables from the plane (P, T) to the plane (ρ, e), and back to the plane (P, T), has a limited accuracy. Here the accuracy on the pressure can not be less than the error err^{P_L}. Since $\log(\mathrm{err}^{P_L}) \simeq -6.4$, this explains the flat profile of the error-curve for the pressure on figure 1.E.4. As a consequence, for this test case, for very fine meshes the asymptotic rate of convergence can not be reached for the pressure. Since all the variables are coupled through the mixture equation of state, their convergence curves will reach a flat profile on very fine meshes.

1.F Additional test cases for the relaxation time

Our simplified model based on the nucleation theory is the following :

$$\boxed{t_{nuc} = \frac{a_0}{\Delta P^3} \exp\left(\frac{\varphi E_a}{k_B T}\right)}. \tag{1.94}$$

Two parameters have to be defined a_0 and φ. In the following, a_0 is fixed and several φ are tested.

1.F.1 Additional test cases for nucleation relaxation time

Here are shown additional test cases for more φ than in the article. Two figures are presented : one for φ between 3.25 10^{-3} and 1; the other for φ between 1.0 10^{-4} and 5 10^{-3}. The aim of this study was to catch all the different behaviors which can be observed by changing φ.

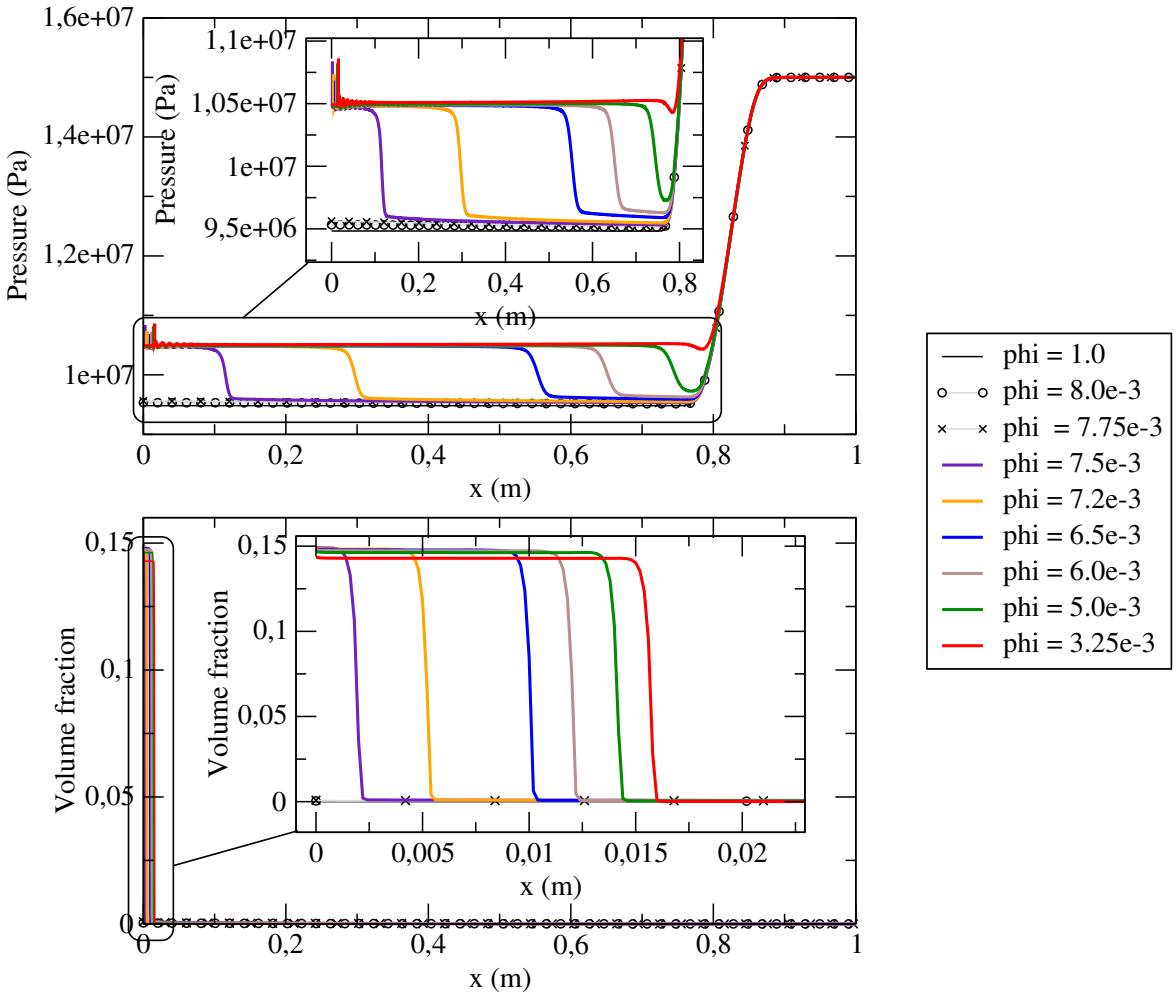

Figure 1.F.1 – *Pressure (Pa) and volume fraction as a function of x (m) for several relaxation times based on nucleation theory at the end of the simulation (t=*10^{-3} *s). The two smaller windows inside the main graph are two zooms : one on the smaller x, the other on the smaller volume fractions.* φ *is between* 3.25 10^{-3} *and* 1.

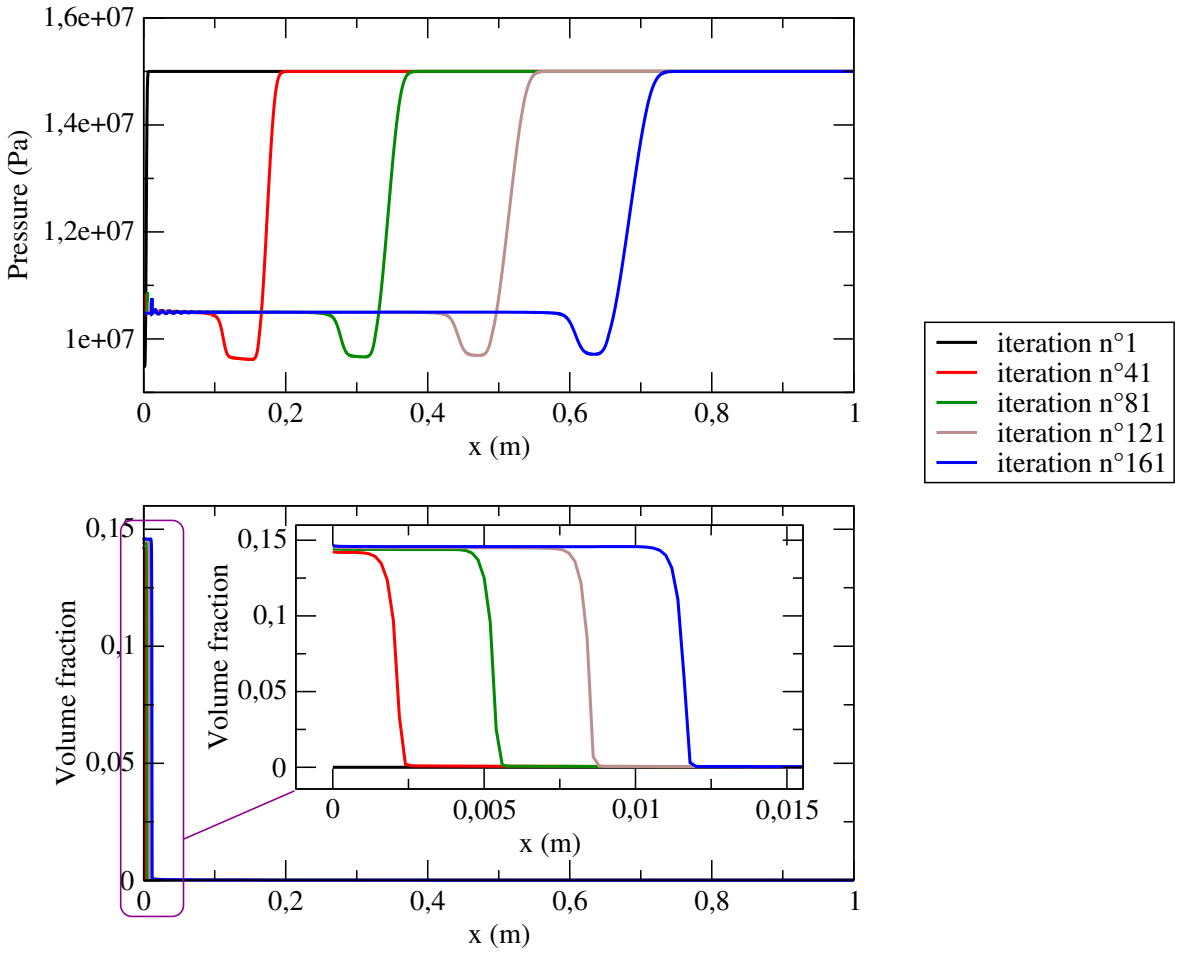

Figure 1.F.2 – *Pressure (Pa) as a function of x (m) for several iteration for a nucleation time scale with* $\varphi = 5\ 10^{-3}$.

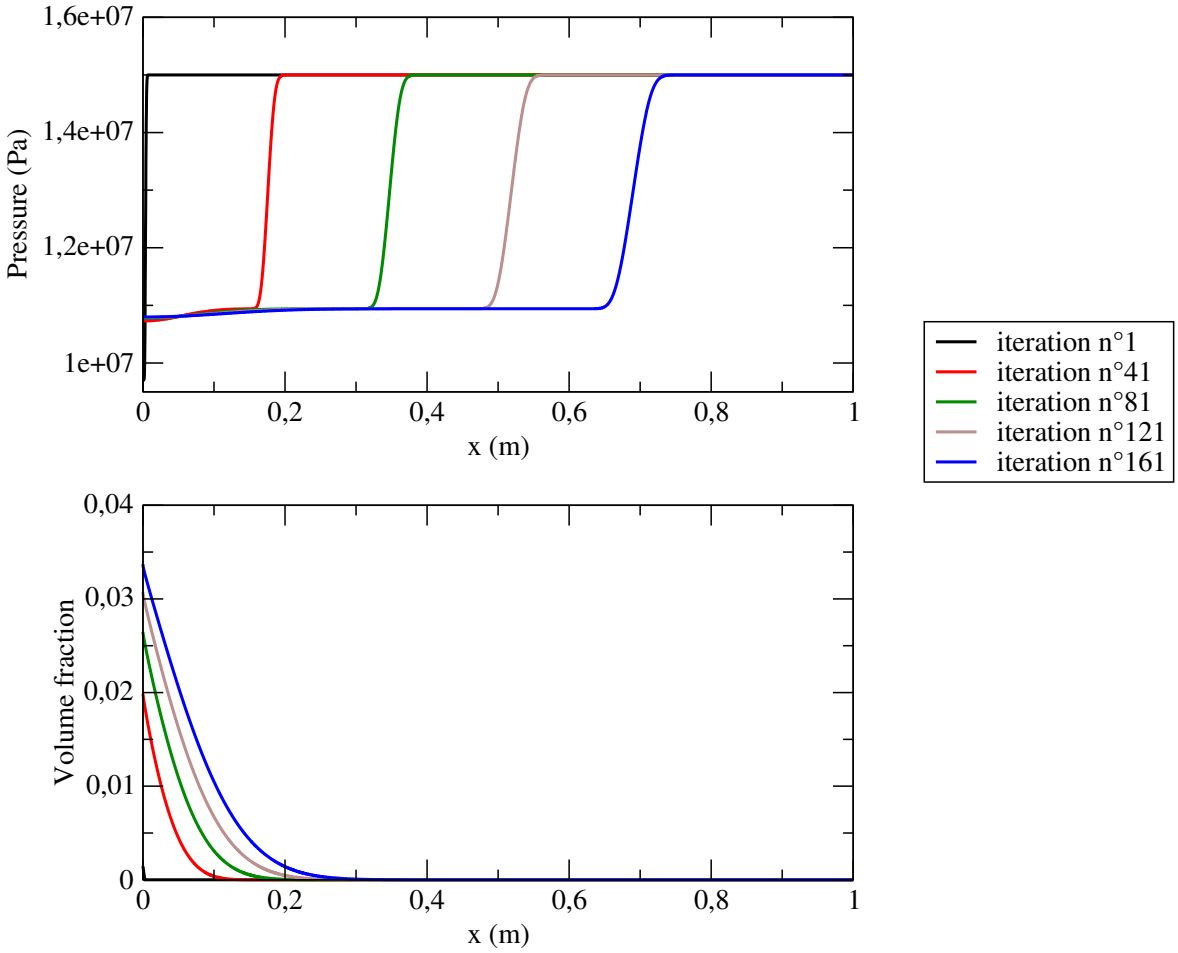

Figure 1.F.3 – *Pressure (Pa) as a function of x (m) for several iteration for a constant relaxation time scale with* $\lambda = 10^{-5}$.

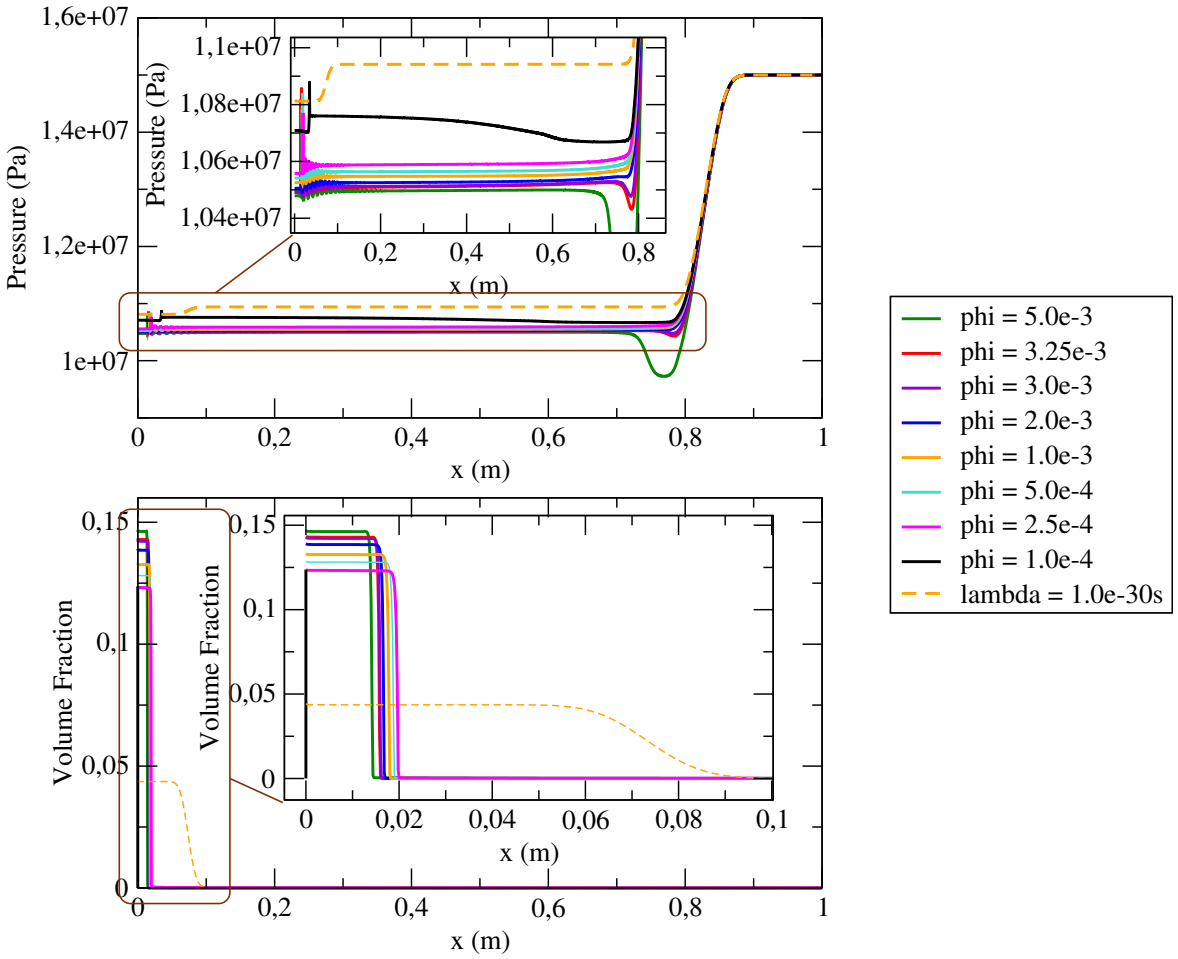

Figure 1.F.4 – *Pressure (Pa) and volume fraction as a function of x (m) for several relaxation times based on nucleation theory at the end of the simulation (t=*10^{-3} *s). The two smaller windows inside the main graph are two zooms : one on the smaller x, the other on the smaller volume fractions.* φ *is between* 1.0 10^{-4} *and* 5 10^{-3}

For φ close to 1 (figure 1.F.1), a pressure undershoot appears. The smaller φ is, the smaller this undershoot becomes and the more vapor is produced. The pressure undershoot appears since the vapor apparition at the very beginning of the simulation (figure 1.F.2). As a comparison, the time evolution of pressure profile as a function of x for a constant relaxation time is presented on figure 1.F.3.

For φ smaller than 2 10^{-3} (figure 1.F.4), no pressure undershoot appears. The case $\varphi = 10^{-4}$ is intermediate between the equilibrium case ($\lambda = 10^{-30}$ s) and the other cases.

Nevertheless, at the moment, no other intermediate case could have been computed because of the lack of robustness of the look-up table.

1.F.2 Nucleation relaxation time with mesh refinement

Some pressure oscillations are observed near the wall for the nucleation relaxation times (figures 1.F.1 and 1.F.4), behind a pressure peak appearing at the same abscisse as the vapor front. The oscillations beat because of the peak. When the mesh is refined (cf figure 1.F.5), the oscillations amplitude decreases. Nevertheless, the pressure peak seems more important. No oscillation occur with the Rusanov scheme, but the scheme is very diffusive and not enough accurate to catch the same pressure level as the relaxation scheme.

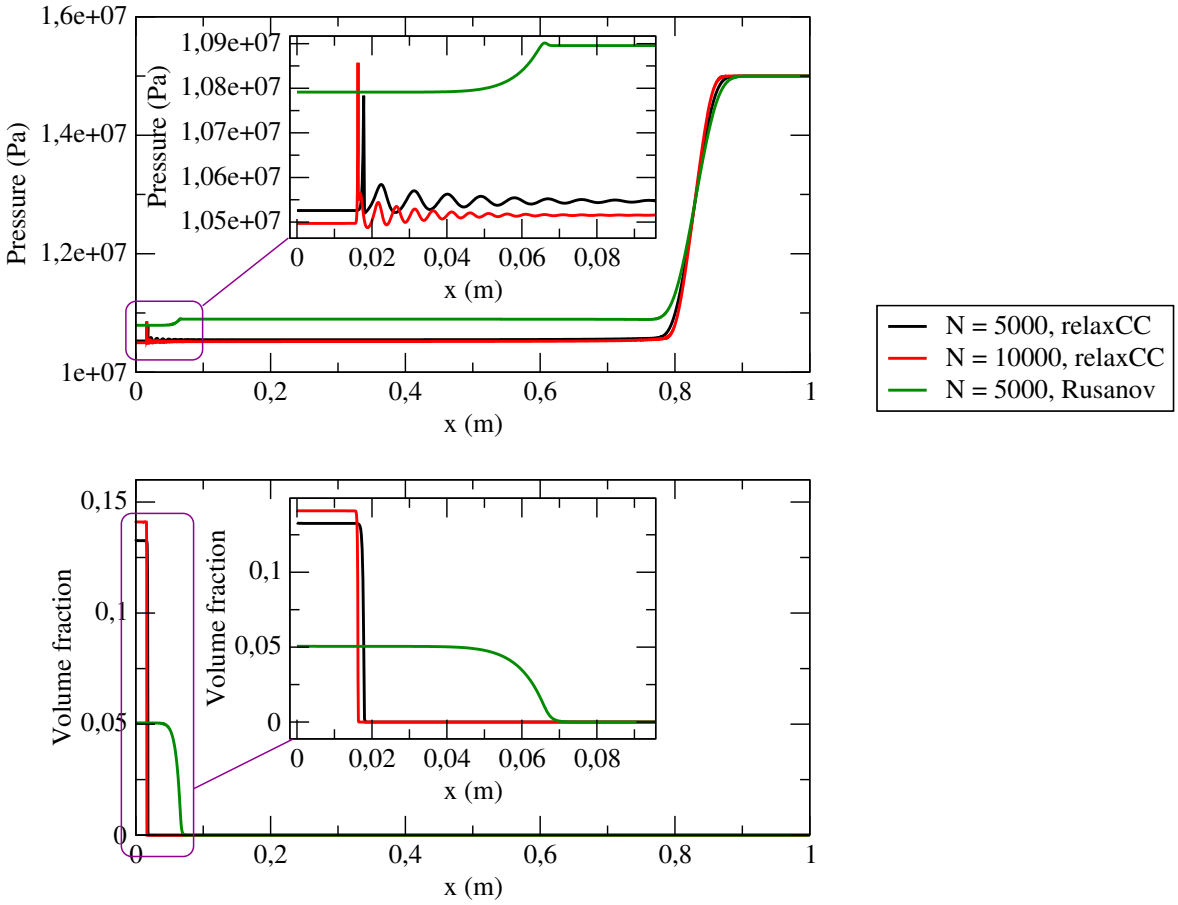

Figure 1.F.5 – *Pressure (Pa) and volume fraction as a function of x (m) for several relaxation times based on nucleation theory at the end of the simulation (t=10^{-3} s). The two smaller windows inside the main graph are two zooms : one on the smaller x, the other on the smaller volume fractions. Curves for the relaxation schemes with two different meshes (5000 cells or 10000 cells) and curves for the Rusanov scheme are shown.*

1.F.3 Comparison with the relaxation time toylaws from [36]

Some toylaws for relaxation time have been proposed in [36] to reproduce experimental date from SUPERCANON test case [47]. They are compared here with constant relaxation times and nucleation relaxation times (cf figures 1.F.6, 1.F.7 and 1.F.8). The toylaws behavior is closed to a constant relaxation time in this case, whereas it enables to catch a very more complex behavior in the SUPERCANON test case [36]. This suggests that the relaxation time law depends a lot on the considered test case.

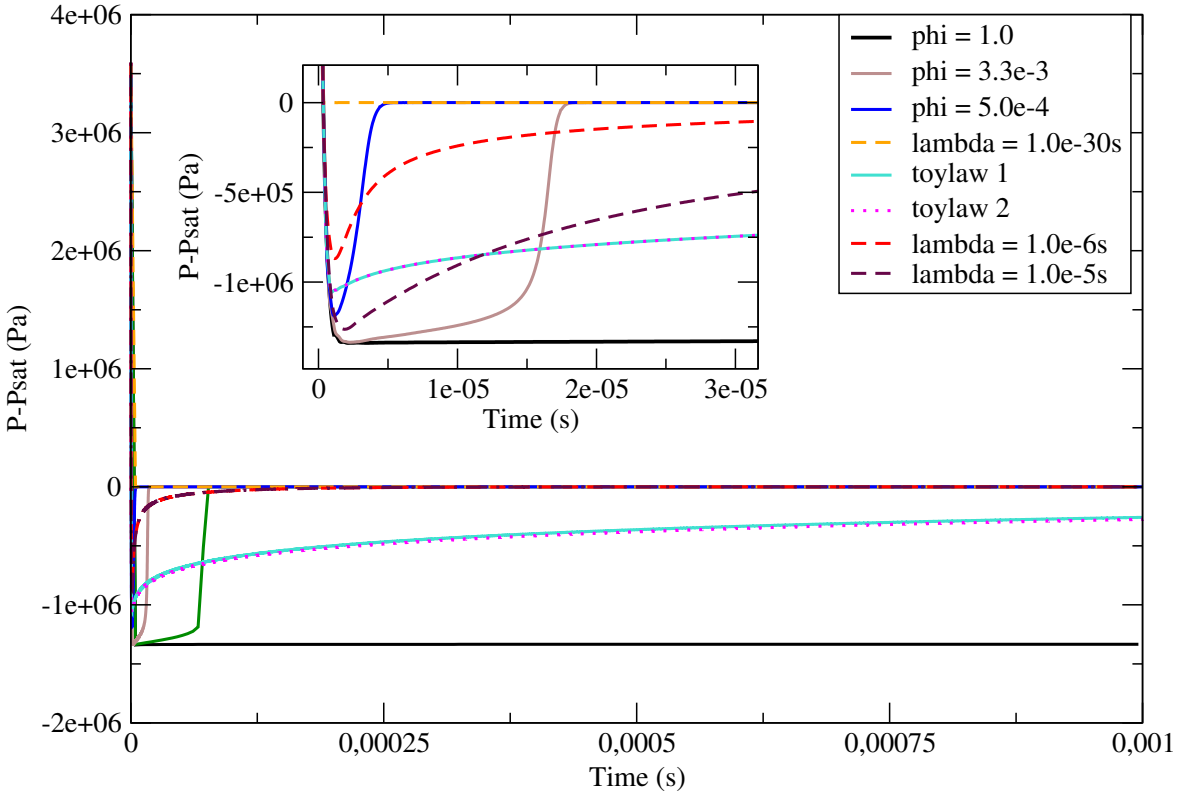

Figure 1.F.6 – *Difference between the pressure and the saturation pressure near the wall as a function of time (s) for several nucleation relaxation times, with fixed a_0 and variable φ. The more φ is closed to 0, the more nucleation is facilated. The second window inside the first graph shows a zoom on the beginning of the simulation for relaxation times with $\varphi \to 0$.*

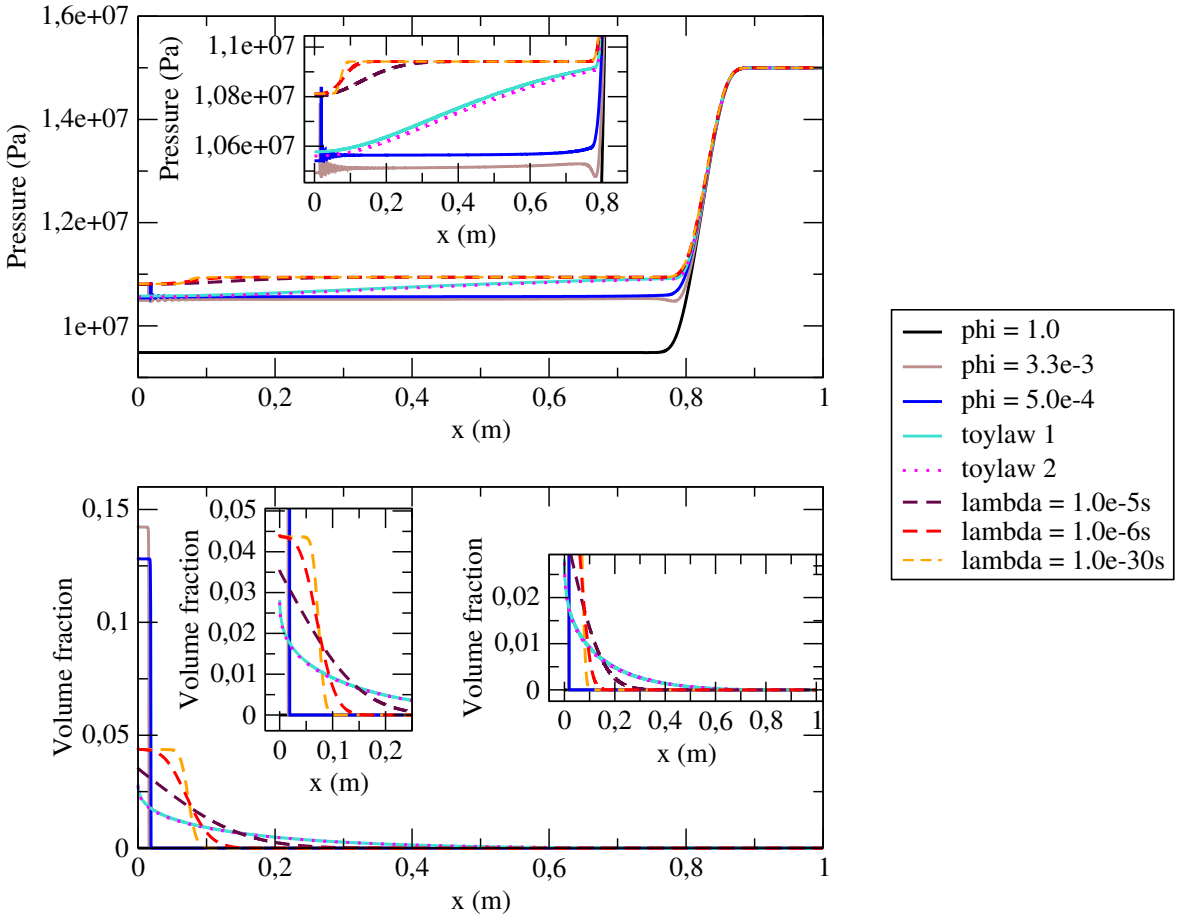

Figure 1.F.7 – *Pressure (Pa) and volume fraction as a function of x (m) for several relaxation times based on nucleation theory at the end of the simulation (t=10^{-3} s). The two smaller windows inside the main graph are two zooms : one on the smaller x, the other on the smaller volume fractions.*

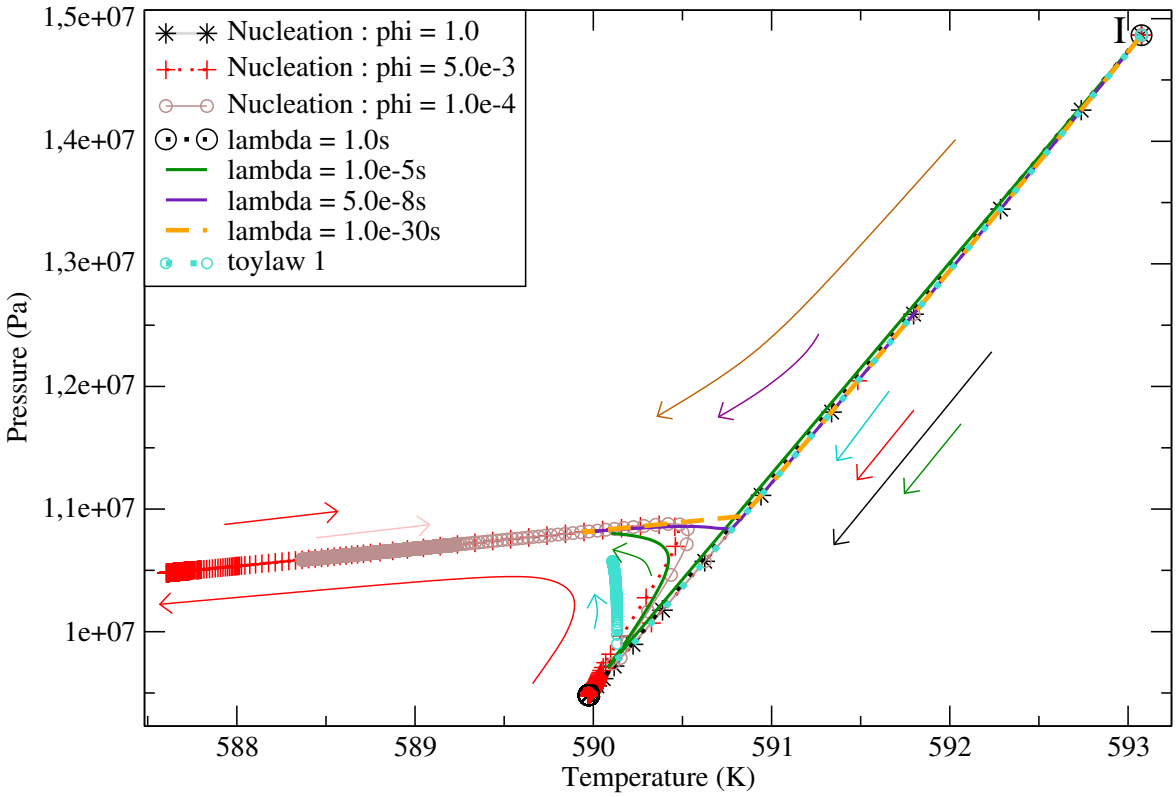

Figure 1.F.8 – *Thermodynamical path within the time near the wall is plotted in the Temperature (K) - Pressure (Pa) plane. The initial point for all curves is on the hand-right corner (denoted by the circle I). The thermodynamical equilibrium (denoted by the circle F) is the point that all simulations should reach for large enough time, provided that* $\lambda > 0$*. If* $\lambda = 0$*, the final point is the point* $P = 9.4810^6$ *Pa* $T = 589$ *K at the bottom of the figure. Here some simulations are still out of thermodynamical equilibrium at the final simulation time* $t = 10^{-3}$ *s. The paths towards thermodynamical equilibrium depends on the characteristic time-scale* λ*. Arrows show the travel directions in the T-P plane along the simulation time.*

Chapter 2

Study of some classical equations of state for water in the pressure-temperature plane.

Introduction

In order to close the homogeneous model depicted in Chapter 1, equations of state (EOS) are required. Two phasic EOS have to be provided: one for the liquid water and one for the steam water. Indeed, the mixture EOS is naturally built by the model from the phasic EOS by the relaxation (instantaneous or not) towards the thermodynamical equilibrium (ensuring entropy maximization), thanks to the source terms on the phasic fractions. Another choice would be to consider a unique EOS for the whole mixture; this choice is made in some cavitation models (like in [3]); then, this unique EOS can be a look-up table [40] or an analytical EOS [29]. Note that in Chapter 1, two different phasic EOS have been used (one for liquid and one for vapor). One can also build a mixture equation of state with a similar approach, but by considering the same phasic EOS for both phases, as studied in [19, 11, 12] with the Van der Waals EOS: this procedure enables to convexify the Van der Waals EOS, in order to get an admissible EOS for the considered model.

Three types of classical phasic EOS are considered in this chapter:

- analytical EOS derived from the perfect gas EOS; for instance, the stiffened gas EOS [6] and its extensions like the Noble-Able stiffened gas EOS [27] or the Chemkin EOS [22]. These EOS have to be fitted around a reference point. They are sometimes not accurate enough for liquid water.
- cubic EOS, i.e. analytical EOS derived from the Van der Waals EOS [34], like the Soave-Redlich-Kwong EOS [39, 13], classically given as incomplete EOS. They are widely used to predict vapor-liquid-equilibria for hydrocarbons mixture in the oil industry, notably Redlich-Kwong EOS, Peng-Robinson EOS and their extensions [14].
- the IAPWS-97 formulation [41], one industrial reference EOS dedicated to water. Its main drawback is its high computational cost, very restrictive for CFD simulations. In order to overcome this difficulty, look-up tables based on the IAPWS-97 formulation can be used as EOS, like in Chapter 1; still, its building is tricky and it induces some numerical difficulties.

Ideally, it seems appealing to dispose of intermediate EOS: simpler and cheaper than a IAPWS look-up table, with a sufficient accuracy even when considering liquid water. This

chapter aims to identify such intermediate EOS; or, at least, to assess some classical EOS (among others): which EOS would represent a good compromise for our model between accuracy and simplicity ? Indeed, to our knowledge, few studies have been led to precisely estimate the accuracy of EOS for water on wide liquid and vapor domains. In [30], an extension of Van der Waals EOS (the Jeffery-Austin EOS, see [21]), defined as a function of the pressure and the specific volume, has been compared with IAPWS-95 [42] on a large thermodynamical domain. The present work aims to complete this study by comparing several classical EOS, defined this time as functions of the pressure and the temperature.

First, the requirements of an admissible EOS for the homogeneous model of Chapter 1 are presented: an admissible EOS should be a complete EOS, for which thermodynamical plane inversions are easy and satisfying some convexity constraints. Then, some classical EOS from the litterature are investigated, in terms of admissibility as well as accuracy with respect to IAPWS-97 (taken as a reference).

Let us introduce some notations, useful in the whole chapter:

- $R = \dfrac{r}{M}$ the perfect gas constant, with $r = 8.31446261815324\ J.kg^{-1}.mol^{-1}$ and $M = 18.01528\ g.mol^{-1}$;
- P the pressure (Pa);
- T the temperature (K);
- τ the specific volume $(m^3.kg^{-1})$ and $\rho = \dfrac{1}{\tau}$ the density $(kg.m^{-3})$;
- e the specific internal energy $(J.kg^{-1})$ and E the total energy, $E = e + k$ with k the kinetic energy;
- s the specific entropy $(J.kg^{-1}.K^{-1})$;
- μ the Gibbs potential $(J.kg^{-1})$ defined as $\mu = e - Ts + P\tau$;
- f the Helmholtz free energy $(J.kg^{-1})$ defined as $\mu = e - Ts$;
- C_p the heat capacity at constant pressure $(J.kg^{-1}.K^{-1})$;
- C_v the heat capacity at constant volume $(J.kg^{-1}.K^{-1})$;
- α_p the thermal expansion coefficient at constant pressure (K^{-1});
- χ_T the compressibility coefficient at constant temperature (Pa^{-1});
- c the sound speed $m.s^{-1}$.

A subject has been proposed during the maths-companies study group in Strasbourg from 12 to 18 November 2018 linked to this PhD chapter: "Mixtures of gases to build complex equations of state". The idea was to build complex EOS by considering the miscible mixture of two stiffened gases: we aimed to optimize the parameters of the two mixed stiffened gas to improve the accuracy of the mixture EOS relatively to IAPWS-97. The main advantage of such approach is that the mixture EOS is an admissible EOS for the model of Chapter 1. However, the optimization problem is difficult to manage, so that the final mixture EOS of two optimized stiffened gases only slightly improve the accuracy of a unique stiffened gas EOS. A report in French is available on HAL [35] and reproduced in appendix 2.B.

2.1 Admissible equations of state (EOS)

In order to characterize the thermodynamical behavior of a component in a given physical domain, an equation of state (EOS) is necessary. It consists in a function describing a potential Ψ (internal energy, entropy, Gibbs potential...) in a thermodynamical plane, which is made up of two intensive physical quantities ϕ_1 and ϕ_2, varying in a domain $\mathrm{dom}(\phi_1, \phi_2)$: then, (ϕ_1, ϕ_2)-plane enables to reproduce the physical domain of interest, when stating $(\phi_1, \phi_2) \in \mathrm{dom}(\phi_1, \phi_2)$.

In the following, an admissible EOS is defined as **an admissible EOS for the model presented in Chapter 1**. Such an admissible EOS should:

1. be a complete EOS;
2. enable easy thermodynamical plane inversions;
3. fulfill some mathematical constraints (convexity, positivity);
4. accurately treat the area around the critical point.

The following paragraphs enlighten each requirement.

2.1.1 Complete EOS

A complete EOS $\Psi(\Phi_1, \Phi_2)$ is so that all the thermodynamical quantities can be defined from the successive derivatives of Ψ with respect to Φ_1 with Φ_2 constant and conversely.

To each thermodynamical plane can be associated a natural thermodynamical potential defining a complete EOS. The Legendre transform enables to easily obtain another thermodynamical potential in another thermodynamical plane from a given EOS [28] (more details are given section 2.1.2 just below). A very comprehensive list of possible thermodynamical potentials can be found in appendix A of [10] and Chapter 2 of [8]. In the following, three thermodynamical potentials will be mainly used :

- the Gibbs potential $\mu = e - Ts + P\tau$ in (P, T)-plane;
- the specific entropy s in (τ, e)-plane;
- the Helmholtz free energy $f = e - Ts$ in (τ, T)-plane.

Their natural thermodynamical plane as well as their first derivatives are recalled in table 2.1. It should be pointed out that, in the homogeneous model of Chapter 1, the following hypothesis is made:

$$\left.\frac{\partial e}{\partial s}\right|_{\tau} = T > 0.$$

Thanks to this assumption, there is a bijective change of variables to switch from $s(\tau, e)$ towards $e(\tau, s)$ [5, 28].

Classical cubic EOS are defined in terms of $P(\tau, T)$, which is not a complete EOS, since s is then not fully defined. In fact, when using (τ, T)-plane, the potential defining a complete EOS is $f(\tau, T)$, defining both P and s. Note that incomplete EOS can be useful, for instance to describe pressure constant regime like in [7].

Potential	Entry plane	"Gibbs relation"	Conjugate variables
μ	(P,T)	$d\mu = -sdT + \tau dP$	$\tau = \left.\frac{\partial \mu}{\partial P}\right\|_T ; s = -\left.\frac{\partial \mu}{\partial T}\right\|_P$
s	(τ,e)	$ds = \frac{P}{T}d\tau + \frac{1}{T}de$	$\frac{P}{T} = \left.\frac{\partial s}{\partial \tau}\right\|_e ; \frac{1}{T} = \left.\frac{\partial s}{\partial e}\right\|_\tau$
e	(τ,s)	$de = Tds - Pd\tau$	$P = -\left.\frac{\partial e}{\partial \tau}\right\|_s ; T = \left.\frac{\partial e}{\partial s}\right\|_\tau$
f	(τ,T)	$df = -sdT - Pd\tau$	$P = -\left.\frac{\partial f}{\partial \tau}\right\|_T ; s = -\left.\frac{\partial f}{\partial T}\right\|_\tau$

Table 2.1 – *Potentials defining a complete EOS in a given thermodynamical plane.*

From second derivatives of μ, three coefficients can be defined:

- the heat capacity at constant pressure C_p $(JK^{-1}kg^{-1})$;
- the thermal expansion coefficient at constant pressure α_p (K^{-1});
- the compressibility coefficient at constant temperature χ_T (Pa^{-1}):

$$C_p = -T\left.\frac{\partial^2 \mu}{\partial T^2}\right|_P \quad ; \quad \alpha_p = \frac{1}{\tau}\left.\frac{\partial^2 \mu}{\partial P \partial T}\right|_{T,P} \quad ; \quad \chi_T = -\frac{1}{\tau}\left.\frac{\partial^2 \mu}{\partial P^2}\right|_T .$$

These coefficients are useful to characterize a fluid: for instance, they can be measured to study the supercritical behavior of a fluid (see for instance [1]).

Note that the sound celerity c $(m.s^{-1})$, defined as:

$$c^2 = -\tau^2 \left.\left(\frac{\partial p}{\partial \tau}\right)\right|_s = -\frac{\tau^2}{\left.\left(\frac{\partial \tau}{\partial p}\right)\right|_s},$$

can be deduced from the first and second derivatives of μ in (P,T)-plane; since:

$$c^2 = -\tau^2 / \left(\left.\left(\frac{\partial \tau}{\partial p}\right)\right|_T - \left.\left(\frac{\partial \tau}{\partial T}\right)\right|_p \frac{\left.\left(\frac{\partial s}{\partial p}\right)\right|_T}{\left.\left(\frac{\partial s}{\partial T}\right)\right|_P} \right),$$

where τ and s are given in first line of table 2.1. It reads:

$$c^2 = \left(\frac{\chi_T}{\tau} - \frac{T\alpha_P^2}{C_p}\right)^{-1}. \tag{2.1}$$

2.1.2 Change of thermodynamical planes

As density ρ $(kg.m^{-3})$ and total energy ρE $(J.m^{-3})$ are conservative variables in the homogeneous two-phase flow model of Chapter 1, the natural thermodynamical plane is (τ,e)-plane.

However, in the model of Chapter 1, the thermodynamical equilibrium is computed at each time step in the (P,T)-plane thanks to the algorithm proposed in [9]. Moreover, a lot of classical numerical methods require at each time step t^n to get the pressure P^n from τ^n and e^n, so that the numerical fluxes can be computed to obtain τ^{n+1} and e^{n+1} at the end of the time step.[1] Then, at least two thermodynamical planes have to be considered to simulate the model, which means that an admissible EOS should be easily written in several thermodynamical planes.

Remark 2.1 — In practice, because of the chosen algorithms (notably the method from [9] used to compute the thermodynamical equilibrium), the (P,T)-plane is more often used in the code than the (τ,e)-plane. □

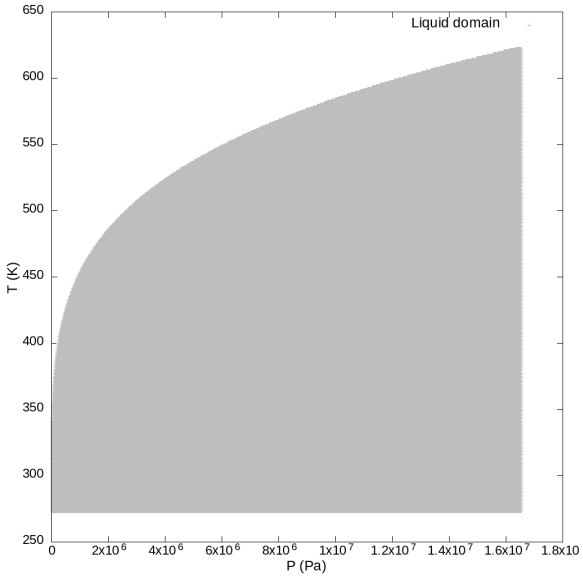

Figure 2.1 – *Physical domain of liquid water: in the* (P,T)*-plane.*

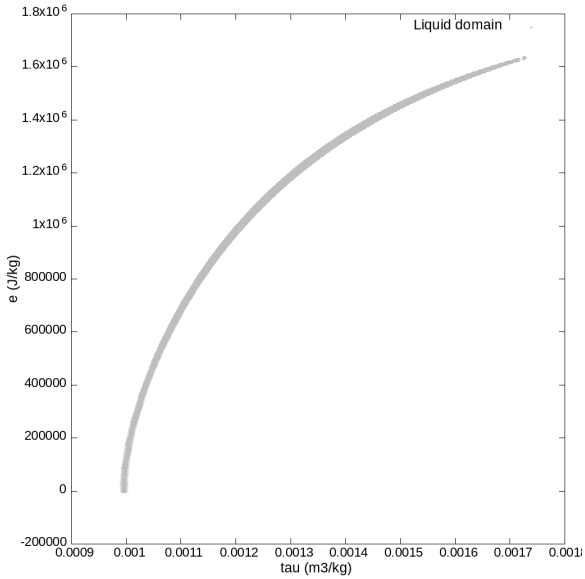

Figure 2.2 – *Physical domain of liquid water: in the* (τ,e)*-plane (data from IAPWS-97).*

Liquid water domain and vapor water domain obtained with the IAPWS-97 formulation are represented in (P,T)-plane on figures 2.1 and 2.3 and in (τ,e)-plane on figures 2.2 and 2.4. Because of the stiffeness of the liquid, visualisations in (τ,e)-plane are much more difficult than in (P,T)-plane. Moreover, (P,T)-plane is a more intuitive thermodynamical plane, in particular to describe the phase changes, which occurs at constant P, T and μ (see Chapter 1).

That is why we preferably work in the following with EOS written in terms of Gibbs potential μ as function of (P,T), by having in mind that the EOS $\mu(P,T)$ should be easily inverted towards (τ,e)-plane.

Remark 2.2 — As far as the IAPWS-97 look-up table from Chapter 1 is concerned, the EOS is given in (P,T)-plane as $\mu(P,T)$ and inverted towards (τ,e)-plane thanks to a Broyden algorithm. Most robustness issues encountered in simulations come from this inversion. □

[1] Note that this is not the case for Rusanov scheme: Rusanov fluxes do not need to compute the pressure, and only conservative variables ρ and ρe are involved.

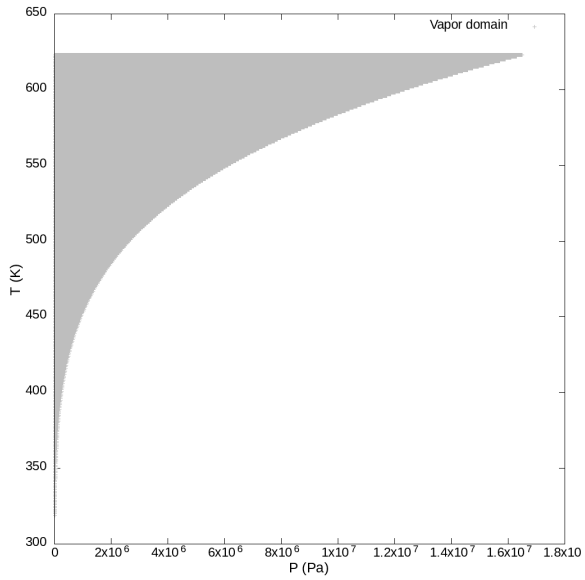

Figure 2.3 – *Physical domain of steam water: in the* (P,T)*-plane.*

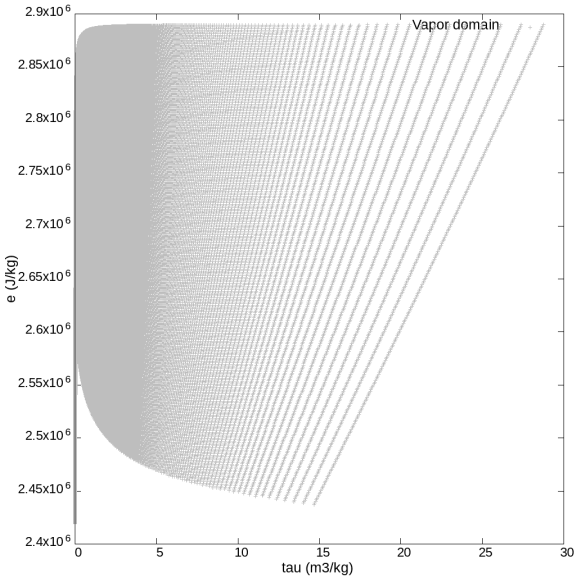

Figure 2.4 – *Physical domain of steam water: in the* (τ,e)*-plane (data from IAPWS-97).*

2.1.3 Convexity constraints due to hyperbolicity

In order to ensure hyperbolicity for the homogeneous model of Chapter 1, specific entropy $s(\tau,e)$ has to be strictly concave with respect to (τ,e) (see [10, 16, 17]). This convexity constraint can be explained in several thermodynamical planes thanks to Legendre transformations [28]. Legendre transform definition is recalled (definition 2.1), as well as main Legendre transformations of thermodynamical potentials (property 2.1).

Definition 2.1 (Legendre Transform)
Consider $f : \mathcal{R}^n \to \mathcal{R}$. Its Legendre transform $f^* : \mathcal{R}^n \to \mathcal{R}$ is defined as:

$$f^* : s \mapsto \sup_{\mathrm{dom}(f)} \{s.x - f(x)\}, \quad \text{with } \mathrm{dom}(f) = \{x \in \mathcal{R} / \ f(x) \text{ is finite}\}.$$

Moreover, for a function $g : (x_1,x_2) \in \mathcal{R}^2 \to \mathcal{R}$, g^{*,x_1} defined as:

$$g^{*,x_1} : s \mapsto \sup_{\mathrm{dom}(g)} \{s.x_1 - f(x_1,x_2)\}$$

is the partial Legendre transforms of g with respect to x_1.

Property 2.1 (Legendre Transform of thermodynamical potentials)

$$e^*(\tau^*,s^*) = e^*(-P,T) = -\mu(P,T),$$

$$f^{*,\tau}(\tau^*,T) = e^*(-P,T) = -\mu(P,T).$$

Proof :

- $\left.\frac{\partial e}{\partial s}\right|_{\tau} = T$ and $\left.\frac{\partial e}{\partial \tau}\right|_{s} = -P$ so that
  $e^*(\tau^*, s^*) = e^*(-P, T) = sT - P\tau - e(\tau, s) = -\mu(P, T)$.
- $\left.\frac{\partial f}{\partial \tau}\right|_{T} = -P$ so that
  $f^*(\tau^*, T) = f^*(-P, T) = -\tau P - f(\tau, T) = -\tau P - (e - Ts) = -\mu(P, T)$.

Thanks to property 2.2 and results of property 2.1, equivalent convexity constraints can be written in other thermodynamical planes, as depicted in table 2.2.

Property 2.2 (Legendre Transform and convexity)
If $f : (x, .) \to f(x, .)$ is convex (respectively concave) with respect to x, then $f^* : s \to f^*(s, .)$ is convex (respectively concave) with respect to s.

Potential	Entry plane	Convexity constraint
s	(τ, e)	strictly concave with respect to (τ, e)
μ	(P, T)	strictly concave with respect to (P, T)
f	(τ, T)	stricly concave with respect to $(-\tau, T)$

Table 2.2 – *Equivalent concavity constraints in several thermodynamical planes.*

Remark 2.3 — For the model of Chapter 1, the conditions:

$$(i) \quad s_k \text{ strictly concave with respect to } (\tau_k, e_k),$$
$$(ii) \quad T_k > 0,$$

are in fact sufficient conditions to ensure hyperbolicity (see [17]). Hyperbolicity holds if and only if the sound speed c is real. □

2.1.4 Treatment of the critical area

The critical point (P_c, T_c) is defined as a thermodynamical state beyond which (i.e. for $P > P_c$ or $T > T_c$) liquid and vapor are no more distinguishable. Nevertheless, for around two decades, some experimental works have highlighted that some thermodynamical quantities (like the heat capacity C_p) have an extremum along a line called Widom line [1], which would imply a kind of "phase transition" even in the supercritical domain (called by the authors "supercritical pseudo-boiling"). However, this concept is still debatted at the moment and the critical area stays widely misunderstood.

The mixture model proposed in [19, 11, 12] to account for metastable state could represent a solution to treat the critical point. In these works, both phases are represented by the same Van der Waals cubic EOS. Since this EOS allows to deal with the critical point, the resulting mixture model inherits from this property. It would be then very interesting to extend the approach proposed in [19, 11, 12] to more realistic phasic EOS, in order to provide a more accurate mixture EOS with a relevant treatement of the critical point.

However, even if the critical point is correctly treated by an EOS, its accuracy is often decreased in the critical area compared with the rest of the domain: it appears that the critical pressure and temperature obtained with classical EOS, such as cubic EOS, are somehow overestimated and lead to inconsistency with experimental data when fitting vapor-liquid-equilibria [20]. Indeed, in the vicinity of the critical point, experimental measurements lead to the following estimations (see [37]):

$$\begin{aligned} C_v &\propto k_{\alpha_0} + k_{\alpha_1}(\frac{T}{T_c} - 1)^{-\alpha} + ..., \\ \rho_L - \rho_V &\propto k_{\beta_1}(\frac{T}{T_c} - 1)^{\beta} + ..., \\ \chi_T &\propto k_{\gamma_1}(\frac{T}{T_c} - 1)^{-\tilde{\gamma}} + ..., \\ P - P_c &\propto k_{\delta_1}(\frac{T}{T_c} - 1)^{\delta} + ..., \end{aligned} \tag{2.2}$$

where α, β, $\tilde{\gamma}$ and δ are universal exponents for all fluids. Unfortunately, these critical exponents are inconsistent with those obtained with classical EOS (see table 2.3). In the literature, one of the most studied method to improve the realism of an EOS in the vicinity of the critical point is a crossover procedure, proposed by Kiselev [24]. The principle is to correct the critical exponents α, β, $\tilde{\gamma}$ and δ; it can be applied to any classical EOS: for instance, to generalized cubic EOS (see [23]), to CPA EOS (see [20]), or to SRK EOS (see [18]).

Universal critical exponents	α	β	$\tilde{\gamma}$	δ
Obtained from experiments ([37])	0.110	0.326	1.23	4.79
Obtained with a classical EOS such cubic EOS ([20])	0	0.5	1	3

Table 2.3 – *Inconsistency of universal critical exponents for classical EOS*

Still, for now, we restrict our work to a thermodynamical domain excluding the critical area.

2.2 Description of the EOS considered in the sequel

2.2.1 IAPWS-97 formulation

The IAPWS-97 formulation [41] is one industrial reference EOS for water. Optimized for industrial needs, it is based on the IAPWS-95 formulation, an analytical EOS built from a very large database (about 20 000 experimental data), which has been widely assessed in terms of uncertainties [42].

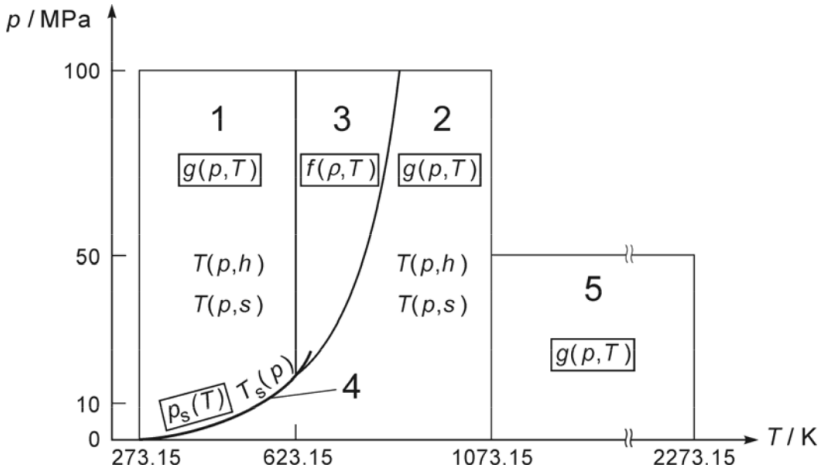

Figure 2.5 – *Regions and equations of IAPWS-IF97, extracted from [41].*

In practice, the (P,T)-plane is divided in several areas, as depicted in figure 2.5 ($P \leq 100MPa$ and $T \in [273.15K, 1073.15K]$; $P \leq 50MPa$ and $T \in [1073.15K, 2273.15K]$): on each area, IAPWS-97 EOS is an analytical formula, built by interpolating the experimental data. The IAPWS-97 formulation gives the Gibbs free enthalpy with respect to the pressure and the temperature (or Helmholtz free energy with respect to the density and the temperature in region 3), so that IAPWS EOS is a complete EOS, at least inside each area.[2]

The main drawback of this EOS is its high computational cost: for instance, the EOS in region 1 is a sum of 34 terms defined as $\alpha_i(P-P_0)^{p_i}(T-T_0)^{q_i}$, with $p_i \in [|0,31|]$, $q_i \in [|-41,17|]$ and α_i a real coefficient with 10 significant digits. It is a strong limitation for a CFD simulation since an EOS is used in each mesh cell at each time step. In order to reduce the CPU-time, a look-up table based on IAPWS-97 formulation has been built in Chapter 1: such techniques are tricky because Gibbs relation $Tds - pd\tau = de$ should be ensured by the look-up table, which means that thermodynamical quantities can not be independently tabulated. Moreover, the resulting EOS leads to somehow complex thermodynamical inversions from $(P,T)-$plane towards $(\tau,e)-$plane. An estimation of the CPU-time improvement due to the look-up table has been given in Chapter 1: considering the Stiffened Gas EOS as a reference, the computational cost is 700 times higher with the IAPWS-97 formulation and it is only 8 times higher with the look-up table.

In the following, the IAPWS-97 formulation is taken as a reference: the other EOS will be assessed by comparing them with the IAPWS EOS. The physical domain is restricted to $P \in [0.1bar, P_{23min} = 165.29164252605bar]$ and $T \in [273.15K, T_{23min} = 623.15K]$, to be far enough from the critical area.

[2] The derivative quantities may be tricky to define on the borders of each area.

2.2.2 Stiffened gas EOS (SG)

The stiffened gas EOS [6] is an extension of the perfect gas EOS, with additionnal parameters enabling to better describe the liquid behavior. Classically, this EOS is written in the (τ, e)-plane:

$$s^{SG}(\tau, e) = C_v \ln\left((e - Q - \pi\tau)\tau^{\gamma-1}\right) + s_0, \tag{2.3}$$

which can be rewritten in (P, T)-plane, since $\mu = e - Ts + P\tau$:

$$\mu^{SG}(P, T) = \gamma C_v T + Q - T(\gamma C_v \ln(T) - (\gamma - 1)C_v \ln(P + \Pi) + k), \tag{2.4}$$

where k is a constant ($JK^{-1}kg^{-1}$) depending on the parameters γ, C_v, Q, Π and s_0. The stiffened gas parameters are the following:

- C_v ($JK^{-1}kg^{-1}$) is the calorific capacity at constant volume,
- γ is the adiabatic index, a non-dimensional coefficient greater than 1,
- $-\Pi$ (Pa) is the minimal admissible pressure (which can be negative),
- Q (Jkg^{-1}) is a reference enthalpy,
- s_0 ($JK^{-1}kg^{-1}$) is a reference entropy.

Note that the perfect gas EOS is recovered when $Q = \Pi = 0$. Due to the simplicity of its form, SG EOS (2.4) leads to explicit change of thermodynamical planes. Moreover, the first and second derivatives of μ^{SG} are simple to compute:

$$\tau^{SG}(P, T) = \frac{C_v(\gamma - 1)T}{P + \Pi} \quad ; \quad s^{SG}(P, T) = \gamma C_v \ln(T) - (\gamma - 1)C_v \ln(P + \Pi) + k; \tag{2.5}$$

so that the constant k can be explicitely written:

$$k = C_v \ln(C_v) + C_v(\gamma - 1)\ln(C_v(\gamma - 1)) + s_0, \tag{2.6}$$

and

$$C_p^{SG} = \gamma C_v \quad ; \quad \alpha_P^{SG}(T) = \frac{1}{T} \quad ; \quad \chi_T^{SG}(P) = \frac{1}{P + \Pi}. \tag{2.7}$$

It should be noticed that C_p is constant, χ_T depend only on P and Π and α_P depends only on T and is independent from all the SG coefficients.

From (2.1) and (2.7), the sound speed c can be deduced, as well as the following property 2.3:

Property 2.3
The stiffened gas EOS (2.4) is an admissible EOS for the model from Chapter 1 since it is a complete EOS with explicit change of thermodynamical planes, ensuring the hyperbolicity of the model since the sound speed $c = c^{SG}(P, T)$ fulfills:

$$c^2 = \gamma(\gamma - 1)C_v T > 0 \quad \forall (P, T > 0).$$

SG parameters are fitted to experimental data around a reference point, as proposed in [6]. The method is recalled in appendix 2.A. As a consequence, stiffened gas EOS behaves like a "linearization" around a physical point, which means that the accuracy will decrease far from the reference point. Nevertheless, to our knowledge, this loss of accuracy has not been studied in details; such a study will be presented in section 2.3.3.1 for liquid and 2.3.4.1 for vapor.

2.2.3 Noble-Able stiffened gas EOS (NASG)

The Noble-Able stiffened gas EOS is an extension of the classical stiffened gas EOS proposed in [27] and recently improved in [2] by enabling heat capacity depending on temperature. The covolume b ($m^3.kg^{-1}$) is introduced, so that:

$$\mu^{NASG}(P,T) = bP + \gamma C_v T + Q - T(\gamma C_v \ln(T) - (\gamma-1)C_v \ln(P+\Pi) + k). \tag{2.8}$$

k is fitted thanks to a reference point, like in the SG EOS:

$$k = (bP^{ref} + \gamma C_v T^{ref} + Q - \mu^{ref})/T^{ref} - \gamma C_v \ln(T^{ref}) + (\gamma-1)C_v \ln(P^{ref}+\Pi). \tag{2.9}$$

NASG formula are very close to those obtained for the stiffened gas EOS, written in section 2.2.2, except for τ^{NASG}, α_P^{NASG}, χ_T^{NASG}:

$$\tau^{NASG}(P,T) = \tau^{SG}(P,T) + b \quad ; \quad s^{NASG}(P,T) = s^{SG}(P,T) \quad ; \quad C_p^{NASG} = C_p^{SG}; \tag{2.10}$$

$$\alpha_P^{NASG}(P,T) = \left[T + \frac{b(P+\Pi)}{C_v(\gamma-1)}\right]^{-1} = \frac{C_v(\gamma-1)}{C_v(\gamma-1)T + b(P+\Pi)}; \tag{2.11}$$

$$\chi_T^{NASG}(P,T) = \left(\frac{T}{P+\Pi}\right)\alpha_P^{NASG}(P,T) = \frac{C_v(\gamma-1)T}{(P+\Pi)(C_v(\gamma-1)T + b(P+\Pi))}; \tag{2.12}$$

and similarly to property 2.3, property 2.4 holds.

Property 2.4
The Noble-Able stiffened gas EOS (2.8) is an admissible EOS ensuring the hyperbolicity of the model from Chapter 1 since since the sound speed $c = c^{NASG}(P,T)$ fulfills:

$$c^2 = \frac{1}{\alpha_P^2 T}\gamma(\gamma-1)C_v > 0 \quad \forall (P, T > 0).$$

Remark 2.4 — Like for the stiffened gas EOS, inverting the NASG EOS from the (P,T)-plane towards the (τ,e)-plane is explicit. Indeed, since:

$$T = \frac{1}{C_v}(e - Q - \Pi(\tau - b)) = T(\tau,e) \quad ; \quad P = \frac{(\gamma-1)(e-Q)}{\tau - b} - \gamma\Pi = P(\tau,e),$$

$s^{NASG}(P,T)$ can be explicitely rewritten as a complete EOS in this plane $s^{NASG}(\tau,e)$. □

2.2.4 Chemkin EOS (CK)

Classically, Chemkin EOS [22] is written as follows:

$$\mu^{CK}(P,T) = \mu_0(T) + \mathcal{C}(T)\ln\left(\frac{P}{P_{ref}}\right), \tag{2.13}$$

with

$$\mu_0(T) = H_0(T) - TS_0(T), \tag{2.14}$$

where:

$$H_0(T) = RT\left(A + \frac{B}{2}T + \frac{C}{3}T^2 + \frac{D}{4}T^3 + \frac{E}{5}T^4 + \frac{F}{T}\right), \tag{2.15}$$

and

$$S_0(T) = R\left(A\ln(T) + BT + \frac{C}{2}T^2 + \frac{D}{3}T^3 + \frac{E}{4}T^4 + G\right) \tag{2.16}$$

i.e.

$$\mu_0(T) = RT\left(A(1-\ln(T)) - \frac{B}{2}T - \frac{C}{6}T^2 - \frac{D}{12}T^3 - \frac{E}{20}T^4 + \frac{F}{T} - G\right), \tag{2.17}$$

and

$$\mathcal{C}(T) = C_v(\gamma - 1)T. \tag{2.18}$$

Classical coefficients are given for information in table 2.4: they are relevant for vapor around a reference point $P_{ref} = 1bar$ and $T_{ref} = 375.15K$ and for temperature $300K < T < 1000K$.

Coefficients	Classical Chemkin coefficients
A (dimensionless)	$0.03386842e2$
B (K^{-1})	$0.03474982e-1$
C (K^{-2})	$-0.06354696e-4$
D (K^{-3})	$0.06968581e-7$
E (K^{-4})	$-0.02506588e-10$
F (K)	-0.03020811e+6
G (dimensionless)	0.02590232e+2
γ (dimensionless)	1.31660136
C_v $(JK^{-1}kg^{-1})$	1436.761418

Table 2.4 – *Coefficients for classical Chemkin EOS, describing steam water for* $300K < T < 1000K$*; A, B, C, D, E, F and G are given in the reference [22] whereas* γ*,* C_v *are those obtained from IRC Fluid Property Calculator [4] at* $P_{ref} = 1bar$ *and* $T_{ref} = 375.15K$*.*

In this work, a slightly different form from (2.13) is preferred, more similar to the SG EOS, by keeping definitions (2.14) and (2.18) for $\mu_0(T)$ and $\mathcal{C}(T)$, and introducing an additional coefficient Π (in Pa):

$$\boxed{\mu^{CK}(P,T) = \mu_0(T) + \mathcal{C}(T)\ln(P+\Pi)}. \tag{2.19}$$

Some quantities are the same as with a stiffened gas EOS:

$$\tau^{CK}(P,T) = \tau^{SG}(P,T) \quad ; \quad \alpha_p^{CK}(T) = \alpha_p^{SG}(T) \quad ; \quad \chi_T^{CK}(P) = \chi_T^{SG}(P). \tag{2.20}$$

whereas the entropy is the following:

$$s^{CK}(P,T) = R\left(A\ln(T) + BT + \frac{C}{2}T^2 + \frac{D}{3}T^3 + \frac{E}{4}T^4 + G\right) - C_v(\gamma-1)\ln(P+\Pi) \tag{2.21}$$

and the heat capacity depends on temperature:

$$C_p^{CK}(T) = R(A + BT + CT^2 + DT^3 + ET^4). \tag{2.22}$$

Whereas SG EOS and NASG EOS are always admissible for the model of Chapter 1 (propertys 2.3 and 2.4), the Chemkin EOS is admissible under a condition on sound speed c (2.23), as summarized in property 2.5:

Property 2.5
The modified Chemkin EOS (2.19) is an admissible EOS ensuring the hyperbolicity of the model from Chapter 1 **if the following condition on the sound speed** $c = c^{CK}(P,T)$ **holds**:

$$c^2 = T\left(\frac{1}{(\gamma-1)C_v} - \frac{1}{C_p(T)}\right)^{-1} = T\frac{C_p(T)(\gamma-1)C_v}{(C_p(T)-(\gamma-1)C_v)} > 0 \quad \forall (P,T>0). \tag{2.23}$$

□

Condition (2.23) leads to conditions on γ, C_v, B, C, D and E. We do not write them in a general way for a sake of readability. However, we checked with Maple that (2.23) is fulfilled for the set of parameters given in sections 2.3.3.3 and 2.3.4.3.

Remark 2.5 — With the Chemkin EOS (modified with $\Pi \neq 0$ or not), inverting the EOS from the (P,T)-plane towards the (τ,e)-plane is no more explicit. Supposed that τ and e are known, the procedure to get $s(\tau,e)$ is the following: P can be written as a function of τ and T:

$$P = \frac{C_v(\gamma-1)T}{\tau} - \Pi = P(\tau,T),$$

so that e can be rewritten as a function of τ and T only:

$$e = RT(A + \frac{B}{2}T + \frac{C}{3}T^2 + \frac{D}{4}T^3 + \frac{E}{5}T^4 + \frac{F}{T}) - C_v(\gamma-1)T + \Pi\tau = e(\tau,T).$$

Eventually, T can be deduced from τ and e by implicitely solving the previous equation (for instance with a Newton algorithm). Then, up to an implicit resolution of $e = (\tau,T)$ to find T, the complete EOS in (τ,e)-plane $s^{CK}(\tau(P,T),e(\tau,T))$ can be obtained from $\mu^{CK}(P,T)$.

2.2.5 Noble-Able Chemkin stiffened gas EOS (NASG-CK)

In [2], the authors proved that NASG EOS can be extended to cope with a variable C_p depending on the temperature T: in particular, they recommend to define C_p with the NASA polynomials, used in the Chemkin EOS.

Thus, we propose the following EOS, by gathering the main features of NASG EOS and Chemkin EOS i.e. the introduction of a specific volume b ($m^3.kg^{-1}$) and a variable C_p defined as a polynomial of T:

$$\begin{aligned} &\mu^{NASG-CK}(P,T) = \mu^{CK}(P,T) + bP = \mu_0(T) + bP + \mathcal{C}(T)\ln(P+\Pi), \\ \text{with}: \quad &\mu_0(T) = RT\left(A(1-\ln(T)) - \frac{B}{2}T - \frac{C}{6}T^2 - \frac{D}{12}T^3 - \frac{E}{20}T^4 + \frac{F}{T} - G\right), \\ &\mathcal{C}(T) = C_v(\gamma-1)T. \end{aligned} \tag{2.24}$$

We get:

$$\begin{aligned}
\tau^{NASG-CK}(P,T) &= b + \frac{C_v(\gamma-1)T}{P+\Pi};\\
s^{NASG-CK}(P,T) &= R\left(A\ln(T) + BT + \frac{C}{2}T^2 + \frac{D}{3}T^3 + \frac{E}{4}T^4 + G\right) - C_v(\gamma-1)\ln(P+\Pi);\\
C_p^{NASG-CK}(T) &= R(A + BT + CT^2 + DT^3 + ET^4);\\
\alpha_P^{NASG-CK}(P,T) &= \frac{C_v(\gamma-1)}{C_v(\gamma-1)T + b(P+\Pi)};\\
\chi_T^{NASG-CK}(P,T) &= \frac{C_v(\gamma-1)T}{(P+\Pi)(C_v(\gamma-1)T + b(P+\Pi))}.
\end{aligned} \tag{2.25}$$

The admissibility condition is very similar to the one obtained with Chemkin EOS (property 2.5):

Property 2.6
The Noble-Able Chemkin EOS (2.24) is an admissible EOS ensuring the hyperbolicity of the model from Chapter 1 **if the following condition on the sound speed** $c = c(P,T)^{NASG-CK}$ **holds**:

$$c^2 = \frac{1}{T\alpha_P^2}\frac{C_p(T)(\gamma-1)C_v}{(C_p(T) - (\gamma-1)C_v)} > 0 \quad \forall (P, T > 0). \tag{2.26}$$

□

We checked that coefficients used in sections 2.3.3.4 and 2.3.4.4 lead to an admissible EOS.

Remark 2.6 — Inverting the NASG-CK EOS from the (P,T)-plane towards the (τ, e)-plane requires an implicit resolution, exactly like the Chemkin EOS (see remark 2.5). □

2.2.6 Soave-Redlich-Kwong EOS (SRK)

SRK EOS belongs to the so-called cubic class of EOS [34, 14]. Cubic EOS have been derived from the Van der Waals EOS, defined as:

$$P(\tau,T) = \frac{RT}{\tau - b} - \frac{a}{\tau^2}. \tag{2.27}$$

The general classical form for a cubic EOS is:

$$P(\tau,T) = \frac{RT}{\tau - b} + \frac{a(T)}{(\tau - br_1)(\tau - br_2)}. \tag{2.28}$$

Remark 2.7 — Other extensions of Van der Waals exist; for instance, the Jeffery-Austin EOS [21], used in [30], aims to take into account hydrogen bond effects with a parameter $b(T)$ which depends on temperature:

$$P(\tau,T) = \frac{\tilde{\alpha}RT}{\tau(\tau - \lambda b(T))} - \frac{\tilde{a}}{\tau^2} + \frac{RT}{\tau}. \tag{2.29}$$

□

EOS	r_1	r_2	$a(T)$	References
Van der Waals	0	0	a	[19, 11, 12]
Redlich-Kwong (RK)	0	-1	$a_c\sqrt{T_c/T}$	[36]
Peng-Robinson (PR)	$-1-\sqrt{2}$	$-1+\sqrt{2}$	$a_c\left[1+m\left(1-\sqrt{T/T_c}\right)\right]^2$	[33]
Soave-Redlich-Kwong (SRK)	0	-1	$a_c\left[1+m\left(1-\sqrt{T/T_c}\right)\right]^2$	[39, 13]

Table 2.5 – *Some examples of classical cubic EOS.*

As explained in section 2.1.1, a cubic EOS is not a complete EOS; then, in general, no explicit formula can be found for $\mu(P,T)$ (see section 2.2.6.2).

There are plenty of cubic EOS studied in the litterature, defined with various r_1, r_2 and $T \to a(T)$: table 2.5 give some popular examples. Classically, a unique cubic EOS is used to describe a fluid in the whole thermodynamical domain (without distinguishing liquid and vapor). Even the area near the critical area is naturally managed with a cubic EOS [12].

The model of Chapter 1 can handle cubic EOS with different sets of parameters for liquid and for vapor: then, in the following, since the critical area is not considered, liquid and vapor will be described with two different cubic EOS.

2.2.6.1 SRK EOS in (τ, T)-plane

In this study, we focus only on a particular cubic EOS, like in [13]: the Soave-Redlich-Kwong equation (SRK) [39]. It consists in (2.30) with $r_1 = 0$, $r_2 = -1$ and a particular function for $a(T)$ (see (2.31) below). SRK EOS reads:

$$P(\tau,T) = \frac{RT}{\tau - b} + \frac{a(T)}{\tau(\tau+b)} \tag{2.30}$$

with

$$a(T) = a_c\alpha(T); \quad a_c = \Omega_a\frac{R^2T_c^2}{P_c}; \quad \alpha(T) = \left[1+m\left(1-\sqrt{\frac{T}{T_c}}\right)\right]^2, \tag{2.31}$$

$$b = \Omega_b\frac{RT_c}{P_c}, \tag{2.32}$$

and

$$m = m_0 + m_1\omega + m_2\omega^2, \tag{2.33}$$

where ω is the acentric factor (defined for each component); $\omega = 0.3442920843$ for water. Classically (see [34]), the values of table 2.6 are considered.

Ω_a	Ω_b	m_0	m_1	m_2	ω
0.457235529	0.0777960739	0.37464	1.54226	-0.26992	0.3442920843

Table 2.6 – *Classical dimensionless coefficients for SRK EOS*

2.2.6.2 Expressing the SRK EOS in (P,T)-plane

SRK EOS (2.30) is not a complete EOS. However, for each T, a unique τ^{SRK} can be deduced from P by implicitely solving a cubic equation thanks to Cardan method or a Newton algorithm:

$$\tau^3 + \tau^2\left(\frac{RT}{P}\right) + \tau\left(-b^2 - \frac{RTb}{P} + \frac{a(T)}{P}\right) - \frac{a(T)b}{P} = 0. \tag{2.34}$$

The method is precisely described in [34] (in the appendix of Chapter 3). It only requires to know the state (liquid or vapor) of the water at the considered (P,T), which is not restrictive since only phasic EOS are needed here. The unicity of $\tau^{SRK}(P,T)$ is due to stability considerations.

A quantity Φ is then written as in [13]:

$$\Phi^{SRK}(P,T) = \Phi^{PG}(P,T,P_{ref},T_{ref}) + \Phi^{corr}(\tau^{SRK}(P,T),T,P_{ref},T_{ref}), \tag{2.35}$$

with Φ^{PG} the quantity obtained with a perfect gas EOS (see section 2.2.2) and Φ^{corr} obtained with $\tau^{SRK}(P,T)$. The reference point (P_{ref},T_{ref}) is needed to fix the perfect gas parameters γ, C_v and s_0 (used in Φ^{PG}), as well as some constants in the correction Φ^{corr}. We note:

$$\mu_{ref} = \mu^{IAPWS}(P_{ref},T_{ref})\ ;\ s_{ref} = s^{IAPWS}(P_{ref},T_{ref}).$$

$\tau^{SRK}(P,T)$ will be sometimes denoted by τ in this section for a sake of readability. Despite this notation, we highlight that τ is still a function of P and T. We recall from section 2.2.2 that:

$$\mu^{PG}(P,T,P_{ref},T_{ref}) = C_v\gamma T - TC_v\ln\left((C_vT)^\gamma P^{1-\gamma}\right) - Ts_0(,P_{ref},T_{ref}), \tag{2.36}$$

with

$$s_0(P_{ref},T_{ref}) = C_v\ T_{ref}\left(\gamma - \ln[(C_vT_{ref})^\gamma P_{ref}^{1-\gamma}]\right) - s_{ref}. \tag{2.37}$$

Then, SRK EOS depends in fact on 8 parameters: Ω_a, Ω_b, m_0, m_1, m_2, ω, as well as on perfect gas parameters γ and C_v.

In order to get a complete EOS, $P(\tau,T)$ is integrated with respect to $-\tau$, to get the corresponding potential $f(\tau,T)$ (see section 2.1.1), by noting ϵ_{ref} the integration constant depending on the reference point:

$$\begin{aligned} f^{corr}(\tau,T,P_{ref},T_{ref}) &= RT\ln\left|\frac{\tau}{\tau-b}\right| + \left|\frac{a(T)}{b}\right|\ln\left|\frac{\tau}{\tau+b}\right| + \epsilon_{ref}(P_{ref},T_{ref}) \\ &= \tilde{f}^{corr}(\tau,T) + \epsilon_{ref}(P_{ref},T_{ref}). \end{aligned} \tag{2.38}$$

Correction s^{corr} is obtained by deriving $-f^{corr}(\tau,T)$ with respect to T:

$$s^{corr}(\tau,T) = R\ln\left|\frac{\tau-b}{\tau}\right| - \left|\frac{a'(T)}{b}\right|\ln\left|\frac{\tau}{\tau+b}\right|,\ \text{with } a'(T) = \frac{da}{dT}. \tag{2.39}$$

It reads then:

$$\begin{aligned} \mu^{corr}(\tau,T,P_{ref},T_{ref}) &= \tilde{f}^{corr}(\tau,T) + P\tau + \epsilon_{ref}, \\ &= \tilde{\mu}^{corr}(\tau,T) + \epsilon_{ref}(P_{ref},T_{ref}). \end{aligned} \tag{2.40}$$

By using the reference point:

$$\mu_{ref} = \underbrace{\mu^{PG}(P_{ref},T_{ref},P_{ref},T_{ref})}_{\mu^{PG}_{ref}} + \underbrace{\tilde{\mu}^{corr}(\tau^{SRK}(P_{ref},T_{ref}),T_{ref})}_{\tilde{\mu}^{corr}_{ref}} + \epsilon_{ref}(P_{ref},T_{ref}), \tag{2.41}$$

i.e.:

$$\epsilon_{ref}(P_{ref}, T_{ref}) = \mu_{ref} - \mu_{ref}^{PG} - \tilde{\mu}_{ref}^{corr}. \tag{2.42}$$

We finally get:

$$\begin{aligned}
& \mu^{SRK}(P,T) = \mu^{PG}(P,T,P_{ref},T_{ref}) + \mu^{corr}(\tau^{SRK}(P,T)=\tau,T,P_{ref},T_{ref}),\\
\text{with}: \quad & \mu^{PG}(P,T,P_{ref},T_{ref}) = C_v\gamma T - TC_v \ln\left((C_vT)^{\gamma}P^{1-\gamma}\right) - Ts_0(P_{ref},T_{ref});\\
& s_0(P_{ref},T_{ref}) = C_v\ T_{ref}\left(\gamma - \ln[(C_vT_{ref})^{\gamma}P_{ref}^{1-\gamma}]\right) - s_{ref};\\
& \mu^{corr}(\tau,T,P_{ref},T_{ref}) = \tilde{\mu}^{corr}(\tau,T) + \epsilon_{ref}(P_{ref},T_{ref});\\
& \tilde{\mu}^{corr}(\tau,T) = RT\ln\left|\frac{\tau}{\tau-b}\right| + \left|\frac{a(T)}{b}\right|\ln\left|\frac{\tau}{\tau+b}\right| + P\tau;\\
& \epsilon_{ref}(P_{ref},T_{ref}) = \mu_{ref} - \mu_{ref}^{PG} - \tilde{\mu}_{ref}^{corr}.
\end{aligned} \tag{2.43}$$

Note that $s^{SRK}(P,T)$ is also known thanks to (2.35) and (2.39). One can also deduce $C_p^{SRK}(P,T)$, $\alpha_P^{SRK}(P,T)$ and $\chi_T^{SRK}(P,T)$, thanks to $\left.\frac{\partial P}{\partial \tau}\right|_T$, $\left.\frac{\partial \tau}{\partial T}\right|_P$ and $\left.\frac{\partial P}{\partial T}\right|_\tau$:

$$\left.\frac{\partial P}{\partial \tau}\right|_T = -\left(\frac{RT}{(\tau-b)^2} + \frac{a(T)(2\tau+b)}{\tau^2(\tau+b)^2}\right) \quad ; \quad \left.\frac{\partial P}{\partial T}\right|_\tau = \frac{R}{\tau-b} + \frac{a'(T)}{\tau(\tau+b)};$$

$$\left.\frac{\partial \tau}{\partial T}\right|_P = \frac{(b-\tau)(a'(T)+R\tau)}{P(3\tau^2-b^2)+RT(2\tau-b)+a(T)};$$

$$C_v^{corr}(\tau^{SRK}(P,T),T) = \frac{Ta''(T)}{b}\ln\left|\frac{\tau}{\tau+b}\right|; \tag{2.44}$$

$$C_p^{corr}(\tau^{SRK}(P,T),T) = C_v^{corr}(\tau^{SRK}(P,T),T) - R - T\left.\frac{\partial P}{\partial T}\right|_\tau^2 \left.\frac{\partial P}{\partial \tau}\right|_T^{-1}; \tag{2.45}$$

$$\alpha_P^{corr}(\tau^{SRK}(P,T),T) = \frac{1}{\tau}\times\left.\frac{\partial \tau}{\partial T}\right|_P; \tag{2.46}$$

$$\chi_T^{corr}(\tau^{SRK}(P,T),T) = \frac{1}{\tau}\times\left.\frac{\partial \tau}{\partial P}\right|_T = \left(\tau\left.\frac{\partial P}{\partial \tau}\right|_T\right)^{-1}. \tag{2.47}$$

Contrary to stiffened gas or Chemkin EOS, α_P^{SRK} and χ_T^{SRK} depend on several SRK parameters.

Remark 2.8 — We point out that, contrary to the previous EOS derived from the stiffened gas EOS 2.2.2, the final SRK EOS in the $(P,T)-$plane given by $\mu^{SRK}(P,T)$ (2.43) is an implicit EOS, because it requires to solve implicit equation (2.34). □

2.2.6.3 Admissibility of SRK EOS

Since cubic EOS are often studied as pressure laws in (τ, T)-plane, the required convexity constraints for the model from Chapter 1 are not classically studied. However, some admissibility conditions have been exhibited in [26], involving some convexity constraints which are mandatory to get a relevant physical behavior (for instance, a correct variation of C_p with respect to T in the supercritical domain). The authors prove that Soave α-function (2.31) used to build the SRK EOS is admissible for all components (in the usual temperature range). Moreover, in [13], it has been shown that, under some technical conditions, μ is concave with respect to P.

Nevertheless, we did not study the concavity constraints for SRK EOS in a general way. Indeed, the sign of c^2 is hard to determine analytically from the formula obtained with (2.1). Similarly, the concavity of μ^{SRK} with respect to (P, T) is not obvious, since the expressions for:

$$\left.\frac{\partial \tau^{SRK}}{\partial T}\right|_P \text{ and } \left.\frac{\partial \tau^{SRK}}{\partial P}\right|_T$$

are not simple. For the particular parameters used in section 2.3.3.5 and 2.3.4.5 (optimized or not), c^2 has been computed with (2.1): c^2 is always positive, in the liquid as well as in the vapor case.

2.2.6.4 Remarks on more complex cubic EOS

Note that cubic EOS are mainly used in the industry for oils and unpolar components. For polar fluids, like water, more complex cubic EOS exist, like translated Soave-Redlich-Kwong equation [32], Cubic-Plus-Association (CPA) EOS [25] or the Perturbed-Chain Statistical Associating Fluid Theory (PC-SAFT) EOS [15]. A recent comparison of previous EOS for pure water can be found in [38]: some limitations of CPA EOS and PC-SAFT EOS appear near the critical regions and translated Peng-Robinson EOS is particularly recommanded by the author.

Unfortunately, the previous EOS are incomplete EOS, given as $P(\tau, T)$: solving a more complex equation than (2.34) is required to invert it towards the (P, T)-plane. Moreover, studying the concavity of such as EOS is tricky, like for the SRK EOS (section 2.2.6.3). They are thus not been investigated in the sequel.

2.3 Accuracy of classical EOS compared with IAPWS-97

2.3.1 General approach

In this part, the following classical EOS are studied on large (P,T)-domains ($P \in [0.1\ bar, P_{23min} = 165.29164252605\ bar]$ and $T \in [273.15\ K, T_{23min} = 623.15\ K]$):

- the stiffened gas EOS (section 2.2.2), denoted by SG EOS in the following;
- the Noble-Able stiffened gas EOS (section 2.2.3), denoted by NASG EOS;
- the Chemkin EOS (section 2.2.4), denoted by CK EOS;
- the Soave-Redlich-Kwong EOS (section 2.2.6.2), denoted by SRK EOS.

A liquid domain is studied in subsection 2.3.3 whereas a vapor domain is studied in subsection 2.3.4. On each (P,T)-domain, for a tested EOS, the following quantities are computed and compared with corresponding data obtained with IAPWS-97 taken as a reference:

- μ^{EOS};
- its first derivatives (with respect to P and T): τ^{EOS} and s^{EOS};
- its second derivatives (with respect to P and T): C_p^{EOS}, α_P^{EOS} and χ_T^{EOS}.

Each EOS has been tested:

- with the classical parameters that are mainly used in the litterature;
- with parameters obtained after an optimization procedure, explained in section 2.3.2.

Assessing the accuracy of an EOS is not an easy task since various criteria are possible, depending on the targeted applications. Recalling the definition of the relative error err_ϕ for a quantity ϕ:

$$err_\phi = \left| \frac{\phi^{EOS} - \phi^{IAPWS}}{\phi^{IAPWS}} \right|,$$

we chose the following (subjective) indicators:

- the mean, minimal and maximal relative error for each quantity;
- the percentage of the physical domain where the relative error is smaller than 5% for each quantity;
- the percentage of the physical domain where the relative error is smaller than 5% for the three quantities μ, τ, C_p at the same time;
- error maps for each quantity, showing the relative error at each point (P,T), with an error limited by a ceiling of 10%: as soon as a point has its color corresponding to the maximal value of 10%, it means that the relative error at this point is at least equal to 10% (but it can be much more in fact).

2.3.2 Optimization of an EOS

The following objective function $\mathcal{C}^{EOS}$ has been chosen to optimize the parameters of each EOS:

$$\mathcal{C}^{EOS} = \frac{\|\mu^{IAPWS} - \mu^{EOS}\|_2}{\|\mu^{IAPWS}\|_2} + \frac{\|\tau^{IAPWS} - \tau^{EOS}\|_2}{\|\tau^{IAPWS}\|_2} + \frac{\|C_p^{IAPWS} - C_p^{EOS}\|_2}{\|C_p^{IAPWS}\|_2}, \quad (2.48)$$

where $\forall x \in \mathcal{R}^n, \|x\|_2 = \sum_{i=1}^{n} \sqrt{|x_i|^2}$ with n the number of data in the domain.

Some preliminary tests showed that it was very difficult to improve the accuracy of all the quantities at the same time (see [35]): then, we focus ourselves on μ (the potential from which all the other quantities will be deduced), τ (a key property to correctly reproduce water physical behavior) and C_p (which is often used to experimentally characterize a fluid, see [1]). This is obviouly a subjective choice and another choice could lead to different results.

The optimization problem is ill-conditioned. It naturally depends on the initial point (classical parameters from litterature have been chosen) and convergence is very hard to obtain. Nelder-Mead algorithm from Optimlib library [31] has been used to solve the optimization problem (2.48) (gradient algorithms have also been tested, but they were not stable enough).

2.3.3 Liquid domain

2.3.3.1 Liquid Stiffened Gas EOS (SG)

SG EOS is studied:

- with coefficients obtained by the empirical method described in appendix 2.A (called initial SG in the following);
- with coefficients obtained thanks to the optimization procedure of section 2.3.2 (called optimized SG in the following).

Both coefficients sets are given in table 2.7.

Coefficients	Initial liquid SG	Optimized liquid SG
γ (dimensionless)	2.20450088490914	1.39864082368510
C_v $(JK^{-1}kg^{-1})$	1.94652267829233e+03	3.19641035947920e+03
Q (Jkg^{-1})	-1.24518858183585e+06	-1.24606074764184e+06
Π (Pa)	9.08244451055483e+08	4.79690712132593e+08
k $(JK^{-1}kg^{-1})$	2.42646239964186e+04	3.07594603384284e+02

Table 2.7 – *Coefficients for the initial and the optimized SG EOS for liquid. Initial SG is fitted by the empirical method proposed in [6] (recalled in appendix 2.A), with the following reference point:* $P_{liq}^{ref} = 80bar$, $T_{liq}^{ref} = 425K$.

As far as the initial SG is concerned, fitted by the method proposed in [6], accuracy is high around the reference point for μ, τ, s and C_p. In details, the relative error is less than 2%:

- in a very large domain for μ and s; this is the case for any pressure since $T >\simeq 300K$ (figures 2.6 and 2.10).
- around two temperatures $T \simeq 425K$ and $T \simeq 600K$ for τ (figure 3.3).
- around $T \simeq 425K$ for C_p, with an acceptable error at low temperatures and a high error since $T >\simeq 500K$ (figure 2.12).

At the end of the day, the domain of high accuracy for all the main quantities of our study μ, τ and C_p is restricted to a limited area $P \times (T \in [425K \pm 25K])$.

Moreover, it should be noticed that the empirical method is very satisfying, since the optimization does not improve significantly the accuracy: indeed, results for optimized SG are very similar to those obtained for the intial SG (figures 2.7, 2.9, 2.11 and 2.13). In details, the optimization decreases the maximal relative errors on μ, by slightly deteriorating the other indicators (see table 2.8). General accuracy seems decreased on C_p (figure 2.13), but improved on τ (figure 2.9).

Note that α_P is independent from SG coefficients while χ_T only depends on Π (2.7): α_P and χ_T are both badly estimated on the whole domain (table 2.8 and figures 2.14, 2.15).

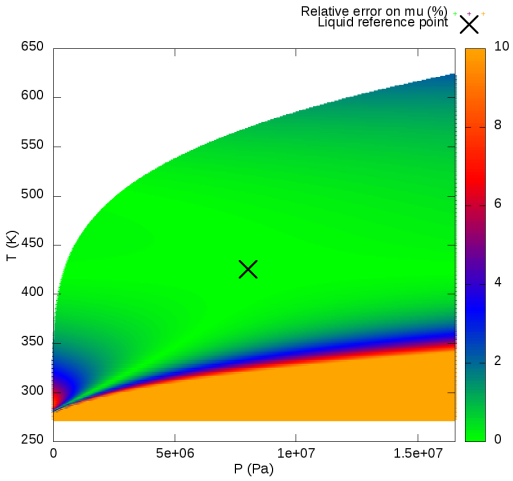

Figure 2.6 – *Relative error on μ compared with IAPWS-97, initial liquid SG, with error saturation at* 10%.

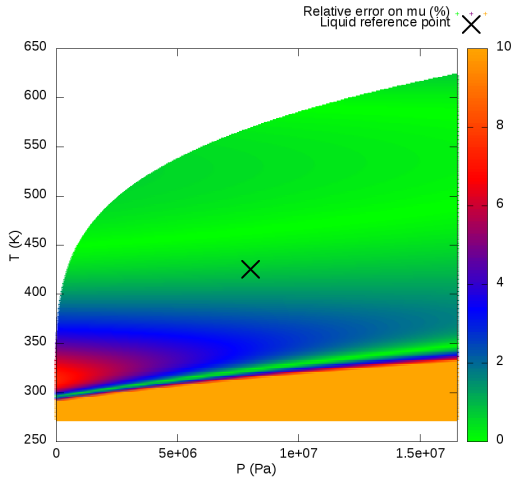

Figure 2.7 – *Relative error on μ compared with IAPWS-97, optimized liquid SG, with error saturation at* 10%.

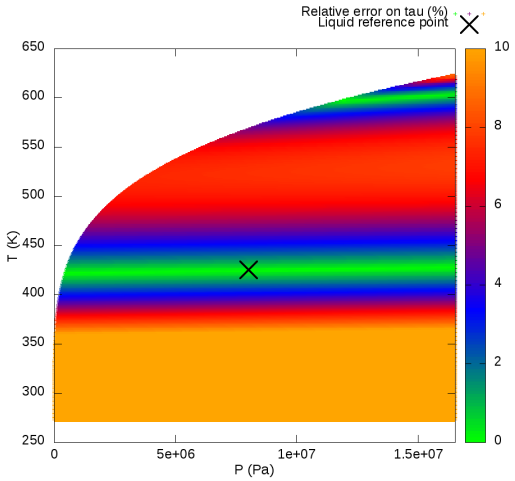

Figure 2.8 – *Relative error on τ compared with IAPWS-97, initial liquid SG, with error saturation at* 10%.

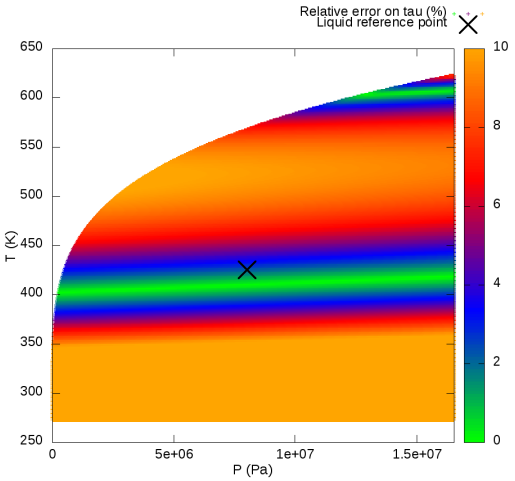

Figure 2.9 – *Relative error on τ compared with IAPWS-97, optimized liquid SG, with error saturation at* 10%.

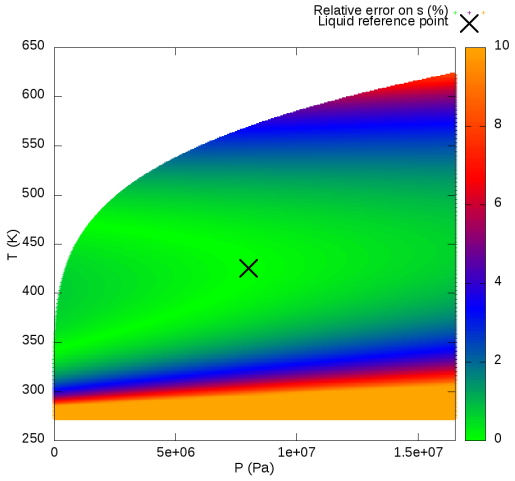

Figure 2.10 – *Relative error on s compared with IAPWS-97, initial liquid SG, with error saturation at* 10%.

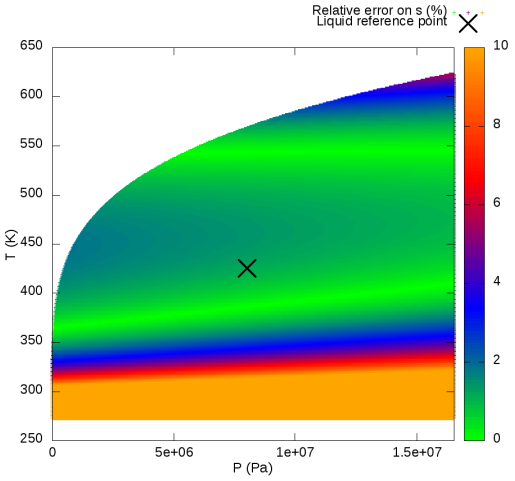

Figure 2.11 – *Relative error on s compared with IAPWS-97, optimized liquid SG, with error saturation at* 10%.

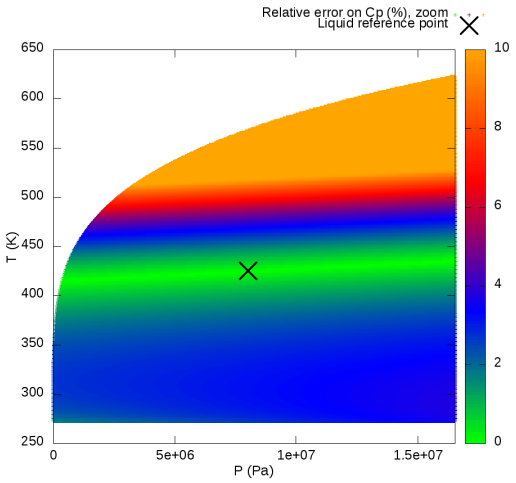

Figure 2.12 – *Relative error on C_p compared with IAPWS-97, initial liquid SG, with error saturation at* 10%.

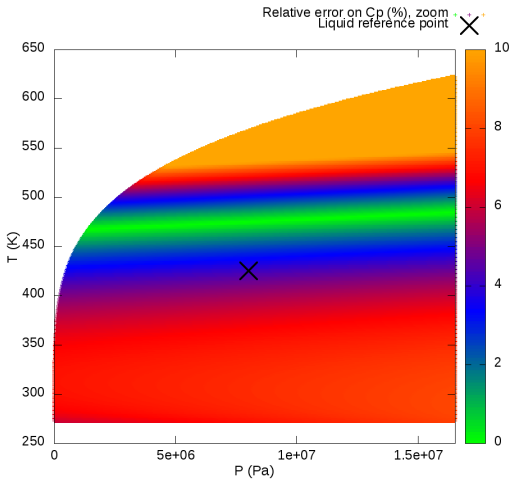

Figure 2.13 – *Relative error on C_p compared with IAPWS-97, optimized liquid SG, with error saturation at* 10%.

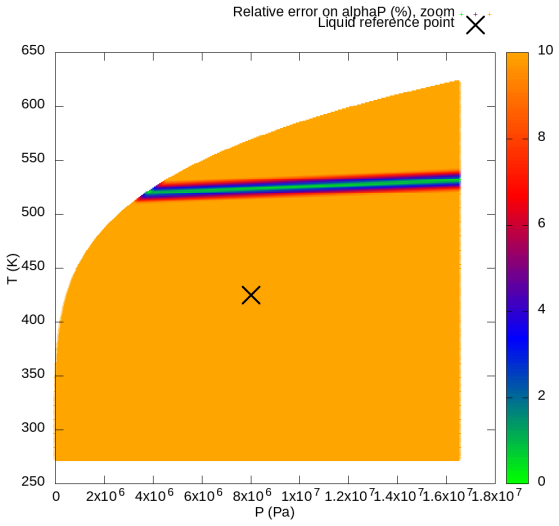

Figure 2.14 – *Relative error on α_P compared with IAPWS-97, initial and optimized liquid SG, with error saturation at* 10%.

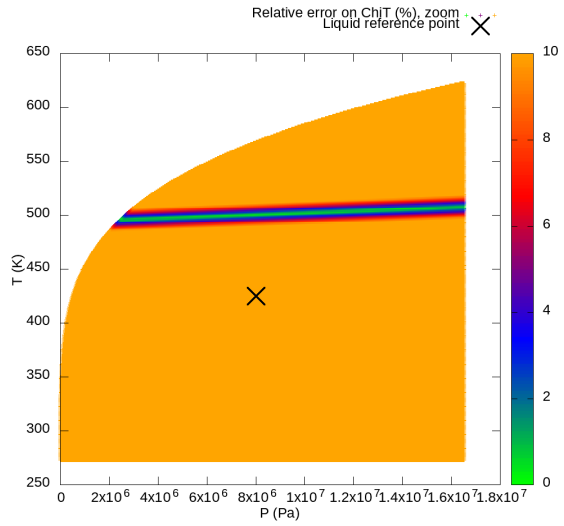

Figure 2.15 – *Relative error on χ_T compared with IAPWS-97, initial and optimized liquid SG, with error saturation at* 10%.

Indicators (%)		Initial liquid SG	Optimized liquid SG
Mean relative errors	on μ	40	38
	on τ	9.6	9.7
	on s	$\simeq 260$	$\simeq 730$
	on C_p	5.6	7.0
	on α_P	$\simeq 10^3$	$\simeq 10^3$
	on χ_T	89	230
Min relative errors	on μ	$\simeq 10^{-8}$	$\simeq 10^{-7}$
	on τ	$\simeq 10^{-6}$	$\simeq 10^{-7}$
	on s	$\simeq 10^{-7}$	$\simeq 10^{-7}$
	on C_p	$\simeq 10^{-6}$	$\simeq 10^{-6}$
	on α_P	$\simeq 10^{-4}$	$\simeq 10^{-4}$
	on χ_T	$\simeq 10^{-6}$	$\simeq 10^{-5}$
Max relative errors	on μ	$\simeq 10^8$	$\simeq 10^7$
	on τ	30	29
	on s	$\simeq 10^8$	$\simeq 10^8$
	on C_p	56	55
	on α_P	$\simeq 10^9$	$\simeq 10^9$
	on χ_T	160	377
% of domain with err $< 5\%$	on μ	81	82
	on τ	31	26
	on s	84	78
	on C_p	73	33
	on α_P	2.7	2.7
	on χ_T	3	1.4
	on μ, τ and C_p	26	13

Table 2.8 – *Accuracy indicators for the liquid SG EOS, with both initial and optimized parameters.*

2.3.3.2 Liquid Noble-Able Stiffened Gas EOS (NASG)

NASG EOS is studied:

- with coefficients γ, C_v, Q and Π given in [2] and k deduced from the reference point data ($P_{liq}^{ref} = 80bar$, $T_{liq}^{ref} = 425K$) with (2.9) (called initial NASG in the following);
- with coefficients obtained thanks to the optimization procedure of section 2.3.2 (called optimized NASG in the following).

Both coefficients sets are given in table 2.9.

Coefficients	Initial liquid NASG	Optimized liquid NASG
γ (dimensionless)	1.012	1.80452283793987
C_v $(JK^{-1}kg^{-1})$	4.13537549407115e+03	2.47901143763817e+03
Q (Jkg^{-1})	-1.143e+06	-1.25154193237972e+06
Π (Pa)	1.835e+08	1.50951138020921e+09
k $(JK^{-1}kg^{-1})$	-2.25336776626839e+04	1.69603596995375e+04
b (m^3kg^{-1})	9.203e-04	5.66354041434956e-04

Table 2.9 – *Coefficients for the initial and the optimized NASG EOS, for vapor. Initial NASG coefficients are those given in [2] with a k deduced from the reference point data ($P_{liq}^{ref} = 80bar$, $T_{liq}^{ref} = 425K$) thanks to (2.9).*

Results are very similar to SG EOS (see 2.3.3.1). Compared with SG EOS, a great improvement is obtained on τ, particularly for the optimized parameter (figures 2.18 and 2.19). The initial NASG EOS has a remarkable accuracy on μ and s (figures 2.16 and 2.20), deteriorated by the optimization (figures 2.17 and 2.21): a correct μ does not ensure that derivative quantities are correctly estimated (see table 2.10). Initial NASG C_p is correct only at low temperatures (figure 2.22) but optimized C_p is very closed to the SG case (figure 2.23).

Accuracy on α_P is similar as in the SG case and accuracy on χ_T is quite improved for the initial NASG (figure 2.25) but very low for the optimized NASG (figure 2.24; see also tables 2.8 and 2.10).

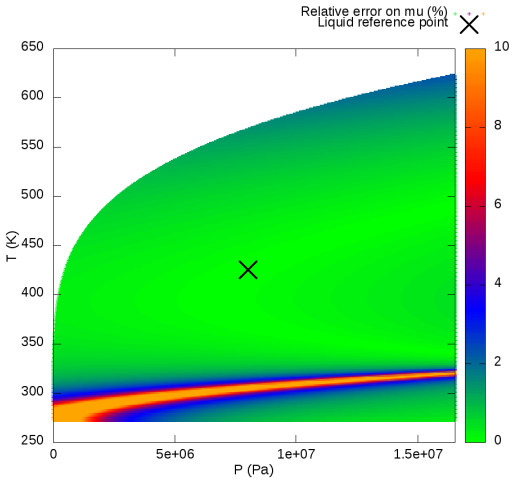

Figure 2.16 – *Relative error on μ compared with IAPWS-97, initial liquid NASG, with error saturation at* 10%.

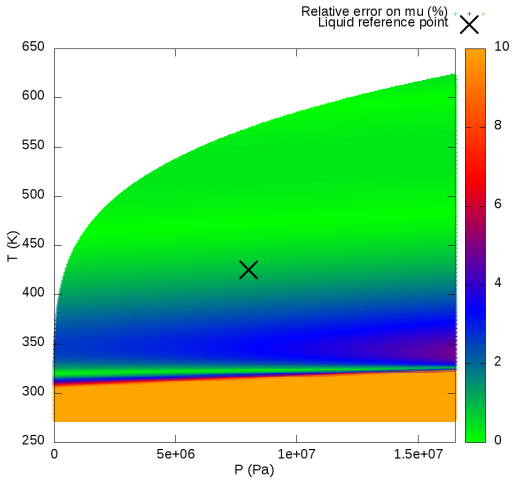

Figure 2.17 – *Relative error on μ compared with IAPWS-97, optimized liquid NASG, with error saturation at* 10%.

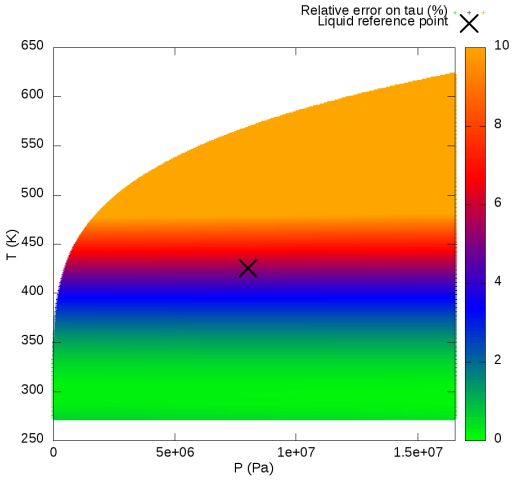

Figure 2.18 – *Relative error on τ compared with IAPWS-97, initial liquid NASG, with error saturation at* 10%.

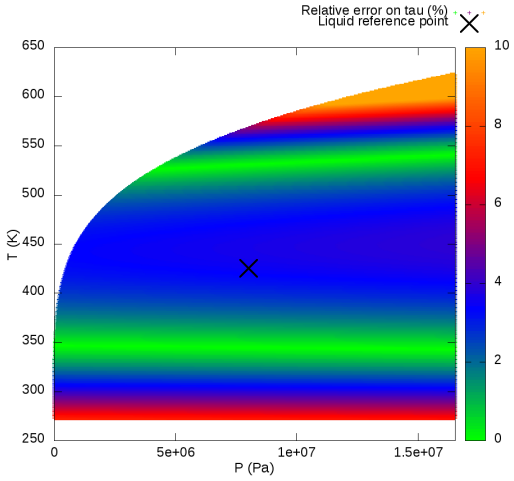

Figure 2.19 – *Relative error on τ compared with IAPWS-97, optimized liquid NASG, with error saturation at* 10%.

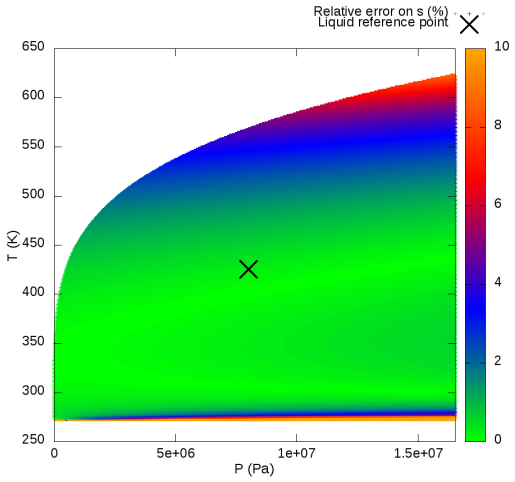

Figure 2.20 – *Relative error on s compared with IAPWS-97, initial liquid NASG, with error saturation at* 10%.

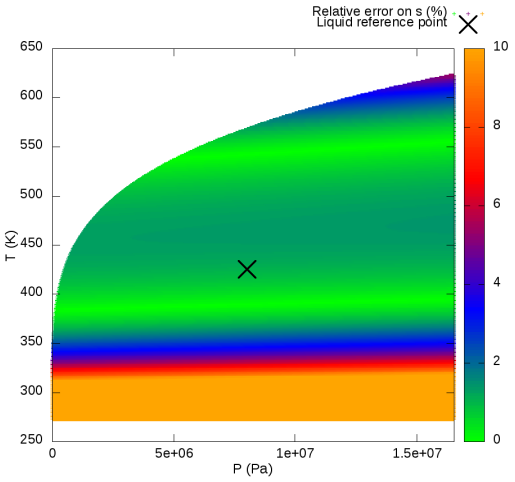

Figure 2.21 – *Relative error on s compared with IAPWS-97, optimized liquid NASG, with error saturation at* 10%.

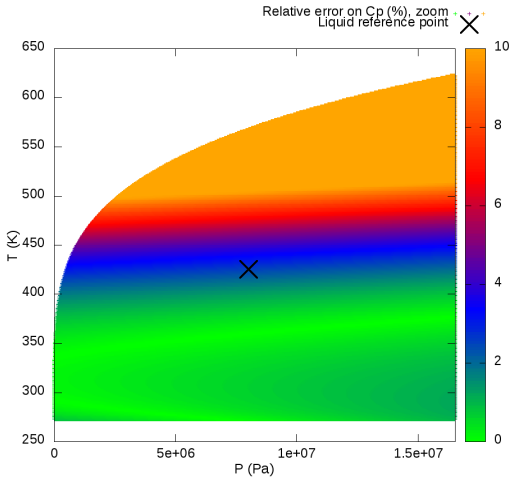

Figure 2.22 – *Relative error on C_p compared with IAPWS-97, initial liquid NASG, with error saturation at* 10%.

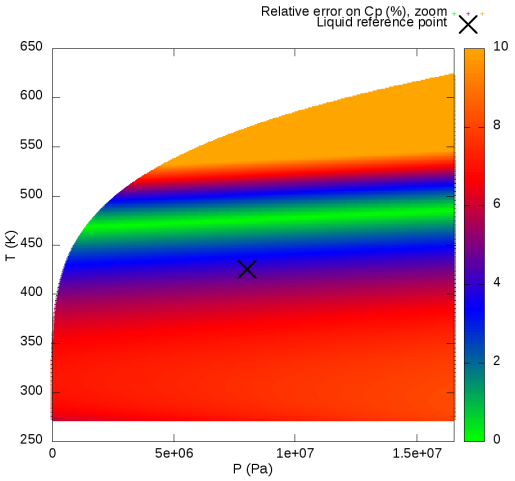

Figure 2.23 – *Relative error on C_p compared with IAPWS-97, optimized liquid NASG fitted by the empirical method, with error saturation at* 10%.

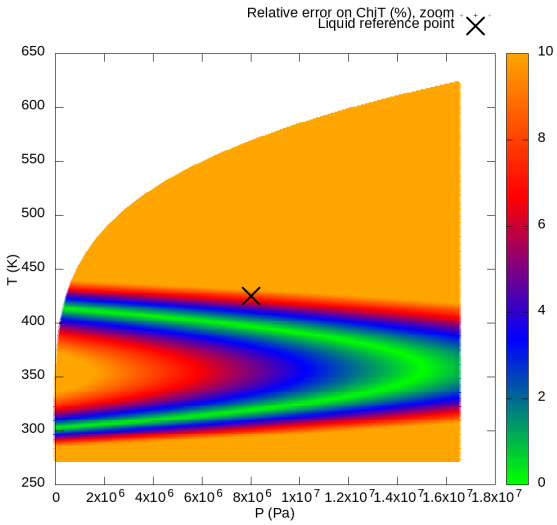

Figure 2.24 – *Relative error on χ_T, NASG.*

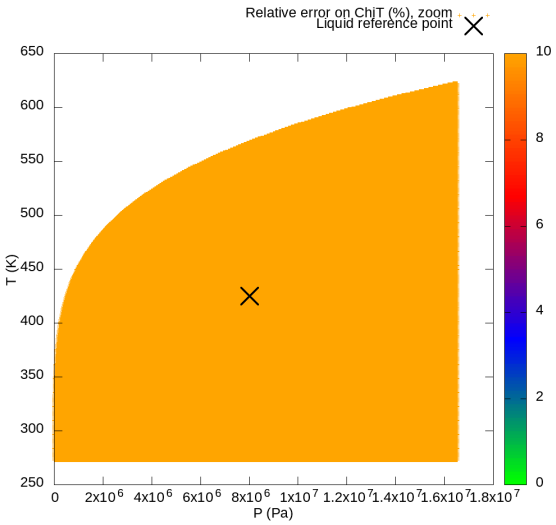

Figure 2.25 – *Relative error on χ_T, optimized NASG.*

Indicators (%)		Initial liquid NASG	Optimized liquid NASG
Mean relative errors	on μ	3.9	43
	on τ	7.2	2.9
	on s	8.0	$\simeq 800$
	on C_p	5.8	7.0
	on α_P	$\simeq 220$	$\simeq 940$
	on χ_T	23	52
Min relative errors	on μ	$\simeq 10^{-8}$	$\simeq 10^{-7}$
	on τ	0.14	$\simeq 10^{-6}$
	on s	$\simeq 10^{-7}$	$\simeq 10^{-7}$
	on C_p	$\simeq 10^{-7}$	$\simeq 10^{-6}$
	on α_P	$\simeq 10^{-4}$	$\simeq 10^{-4}$
	on χ_T	$\simeq 10^{-5}$	32
Max relative errors	on μ	$\simeq 10^{6}$	$\simeq 10^{7}$
	on τ	37	20
	on s	$\simeq 10^{6}$	$\simeq 10^{8}$
	on C_p	57	55
	on α_P	$\simeq 10^{8}$	$\simeq 10^{8}$
	on χ_T	95	98
% of domain with err $< 5\%$	on μ	96	84
	on τ	52	89
	on s	96	78
	on C_p	66	33
	on α_P	0.99	4.9
	on χ_T	28	0
	on μ, τ and C_p	48	33

Table 2.10 – *Accuracy indicators for the liquid NASG EOS, with both initial and optimized parameters.*

2.3.3.3 Liquid Chemkin EOS (CK)

In this subsection, only optimized parameters for the modified Chemkin equation (2.19) are considered; they are given in table 2.11.

Coefficients	Optimized liquid Chemkin
A (dimensionless)	3.45262684832630e1
$B\ (K^{-1})$	-2.97925617792003e-01
$C\ (K^{-2})$	1.27354545821528e-03
$D\ (K^{-3})$	-2.37411260099135e-06
$E\ (K^{-4})$	1.64275937362773e-09
$F\ (K)$	-1.91283283309239e+06/R
G (dimensionless)	-5.77209630046415e+04/R
γ (dimensionless)	2.07761293279293
$C_v\ (JK^{-1}kg^{-1})$	4.69457754849707e+02
$\Pi\ (Pa)$	1.84780882484325e8

Table 2.11 – *Optimized oefficients for Chemkin EOS* (2.19)*, for liquid.*

Chemkin EOS indicators are very similar to SG EOS, except that accuracy on C_p is far greater with Chemkin EOS (see table 2.12). Indeed, contrary to SG and NASG EOS for which C_p is constant, it depends on temperature with this EOS; a great improvement is obtained compared with SG and NASG EOS (see figure 2.29 compared with 2.13 or 2.23). In details, μ and s are accurate since $T >\simeq 350K$ (see figures 2.26 and 2.28). High accuracy on τ areas are still restricted to two limited areas (figures 2.27), slightly different from SG and NASG EOS (see figures 2.9 and 2.19). Note that α_P and χ_T are the same as SG EOS.

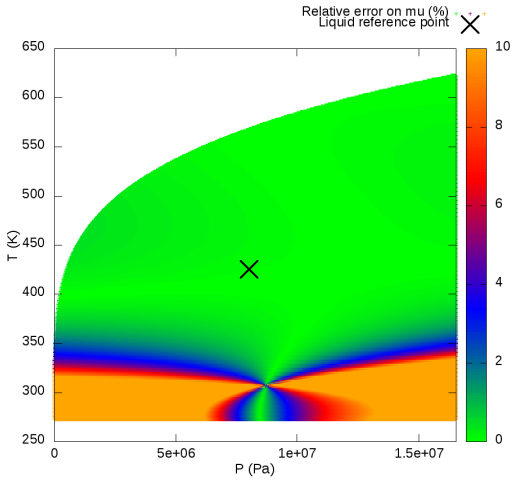

Figure 2.26 – *Relative error on μ compared with IAPWS-97, optimized liquid Chemkin EOS with error saturation at* 10%.

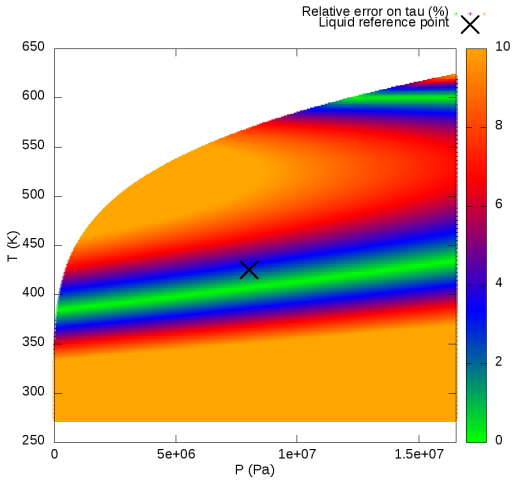

Figure 2.27 – *Relative error on τ compared with IAPWS-97, optimized liquid Chemkin EOS, with error saturation at* 10%.

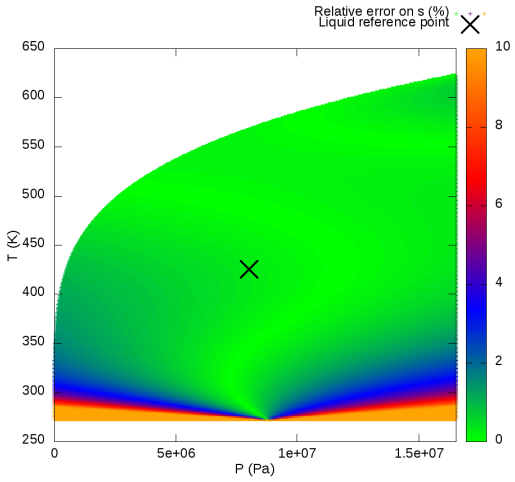

Figure 2.28 – *Relative error on s compared with IAPWS-97, optimized liquid Chemkin EOS, with error saturation at* 10%.

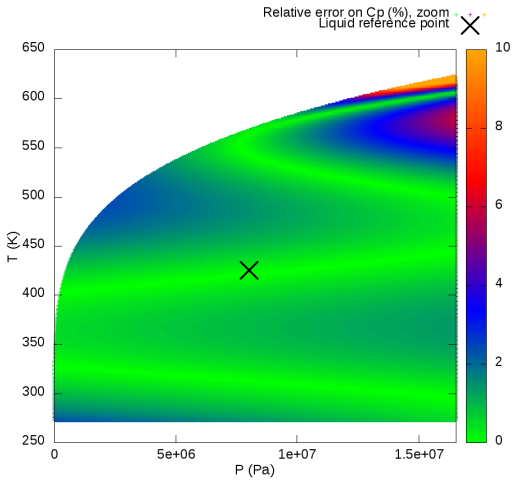

Figure 2.29 – *Relative error on C_p compared with IAPWS-97, optimized liquid Chemkin EOS, with error saturation at* 10%.

Indicators (%)		Optimized liquid CK
Mean relative errors	on μ	33
	on τ	9.5
	on s	$\simeq 130$
	on C_p	0.95
	on χ_T	95
Min relative errors	on μ	$\simeq 10^{-7}$
	on τ	$\simeq 10^{-5}$
	on s	$\simeq 10^{-7}$
	on C_p	$\simeq 10^{-7}$
	on χ_T	91
Max relative errors	on μ	$\simeq 10^{7}$
	on τ	31
	on s	$\simeq 10^{8}$
	on C_p	23
	on χ_T	100
% of domain with err $< 5\%$	on μ	83
	on τ	27
	on s	95
	on C_p	99
	on χ_T	0
	on μ, τ and C_p	27

Table 2.12 – *Accuracy indicators for the liquid Chemkin EOS, with optimized parameters.*

2.3.3.4 Liquid Noble-Able Chemkin EOS (NASG-CK)

Optimized parameters for the Noble-Able Chemkin stiffened gas equation proposed in section 2.2.5 are considered; they are given in table 2.13.

Coefficients	Optimized liquid NASG-CK
A (dimensionless)	4.69738865636393e+01
$B\ (K^{-1})$	-4.19269571479452e-01
$C\ (K^{-2})$	1.70702143968620e-03
$D\ (K^{-3})$	-3.04805662517983e-06
$E\ (K^{-4})$	2.02814588067819e-09
$F\ (K)$	-2.37769132621474e+06/R
G (dimensionless)	-5.54317321673174e+04/R
γ (dimensionless)	3.27113568773712
$C_v\ (JK^{-1}kg^{-1})$	7.24509640448929e+02
$\Pi\ (Pa)$	1.24425779880749e+09
$b\ (m^3kg^{-1})$	5.66559849022606e-04

Table 2.13 – *Optimized oefficients for Noble-Able Chemkin EOS* (2.24)*, for liquid.*

A very satisfying accuracy is obtained on μ, τ, C_p but also on s (figure 2.32), even if the optimization problem (2.48) does not take entropy into account (see table 2.14). As with the Chemkin EOS, C_p is admissible on 99% of the domain (figure 2.33); as with the optimized NASG EOS, τ is admissible on 89% of the domain (figure 2.31); but in addition, NASG-CK EOS enables to obtain a very high accuracy on μ, on about 96% of the domain (figure 2.30). Eventually, the NASG-EOS is accurate on μ, τ and C_p at the same time on about 86% of the liquid domain.
Note that α_P and χ_T are badly estimated with NASG-CK EOS.

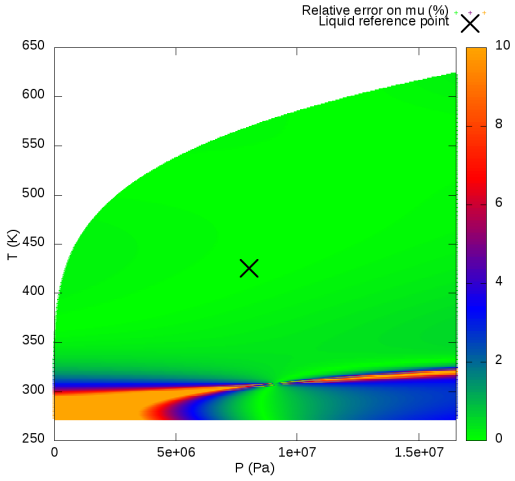

Figure 2.30 – *Relative error on μ compared with IAPWS-97, optimized liquid Noble-Able Chemkin stiffened gas EOS with error saturation at* 10%.

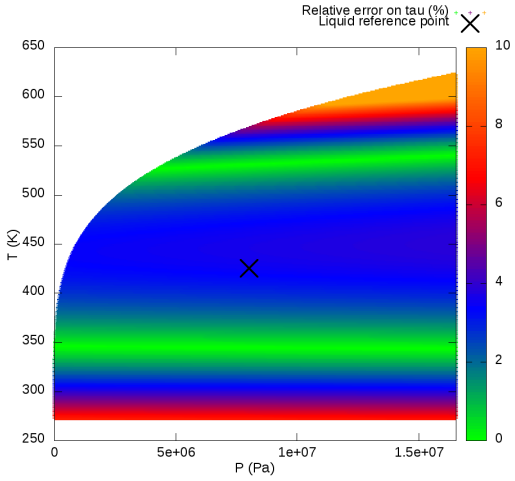

Figure 2.31 – *Relative error on τ compared with IAPWS-97, optimized liquid Noble-Able Chemkin stiffened gas EOS, with error saturation at* 10%.

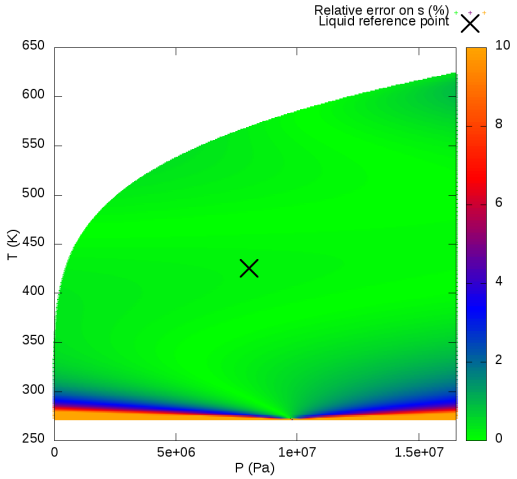

Figure 2.32 – *Relative error on s compared with IAPWS-97, optimized liquid Noble-Able Chemkin stiffened gas EOS, with error saturation at* 10%.

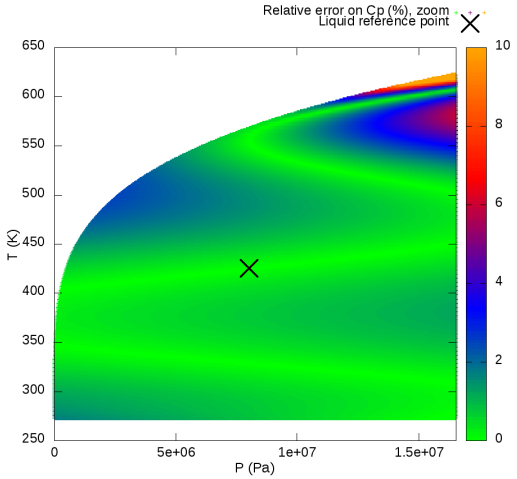

Figure 2.33 – *Relative error on C_p compared with IAPWS-97, optimized liquid Noble-Able Chemkin stiffened gas EOS, with error saturation at* 10%.

Indicators (%)		Optimized liquid NASG-CK
Mean relative errors	on μ	5.9
	on τ	2.9
	on s	75
	on C_p	0.87
	on α_P	$\simeq 100$
	on χ_T	53
Min relative errors	on μ	$\simeq 10^{-7}$
	on τ	$\simeq 10^{-6}$
	on s	$\simeq 10^{-7}$
	on C_p	$\simeq 10^{-6}$
	on α_P	$\simeq 10^{-1}$
	on χ_T	$\simeq 10^{-5}$
Max relative errors	on μ	$\simeq 10^{6}$
	on τ	20
	on s	$\simeq 10^{7}$
	on C_p	22
	on α_P	$\simeq 10^{4}$
	on χ_T	95
% of domain with err $< 5\%$	on μ	96
	on τ	89
	on s	97
	28 on C_p	99
	on α_P	$\simeq 10^{-3}$
	on χ_T	4.2
	on μ, τ and C_p	86

Table 2.14 – *Accuracy indicators for the liquid Noble-Able Chemkin stiffened gas EOS, with optimized parameters.*

2.3.3.5 Liquid Soave-Redlich-Kwong EOS (SRK)

SRK EOS is studied:

- with γ and C_v obtained with the empirical SG fitting (see 2.3.3.1) and classical coefficients given in [34]; to integrate some quantities, a reference point is needed, taken as $P_{liq}^{ref} = 80bar$, $T_{liq}^{ref} = 425K$ (see 2.2.6.2); SRK EOS with this set of parameters is called initial SRK in the following.
- with coefficients obtained thanks to the optimization procedure of section 2.3.2 (called optimized SRK in the following).

Both coefficients sets are given in table 2.15.

Coefficients	Initial liquid SRK	Optimized liquid SRK
γ (dimensionless)	2.23273707660698	1.00450055505059
C_v $(JK^{-1}kg^{-1})$	1.94360776781292e+03	4.19371448164003e+03
Ω_a (dimensionless)	0.457235529	5.56971997249541e-01
Ω_b (dimensionless)	0.0777960739	7.04917289276856e-02
m_0 $(JK^{-1}kg^{-1})$	0.3764	-3.35784103255686e-01
m_1 (m^3kg^{-1})	1.54226	4.36549985666770e+00
m_2 (m^3kg^{-1})	-0.26992	-6.59827142323528e-01
ω (m^3kg^{-1})	0.3442920843	-1.54151967373626e-03

Table 2.15 – *Coefficients for the initial and the optimized SRK EOS, for liquid, with the following reference point:* $P_{liq}^{ref} = 80bar$, $T_{liq}^{ref} = 425K$. *Initial SRK EOS coefficients are those given in [34], except for* γ *and* C_v *taken equal to those obtained with the empirical method to fit a SG (see 2.3.3.1).*

Very different behiavors are observed with SRK EOS compared with previous EOS. Accuracy for initial parameters is not satisfying for all quantities (figures 2.34, 2.36, 2.38, 2.40, 2.42).

Optimization improves accuracy, except for s, whose minimal relative error is considerably increased (see table 2.16). In details:

- accuracy on μ is correct on around half the domain, with an optimal accuracy at high temperature and pressure (figure 2.35);
- high accuracy is obtained on τ around $T \simeq 550K$ (figure 2.37);
- accuracy on C_p is very similar to SG and NASG case, with a low relative error around $T = 475K$ with a maximal error for $T >\simeq 550K$ (figure 2.41).

Then, accuracy areas are very different for C_p and the other quantities, so that the accurate domain for μ, τ and C_p is very reduced (only 2.9 % of the domain for the optimized parameters, see table 2.16).

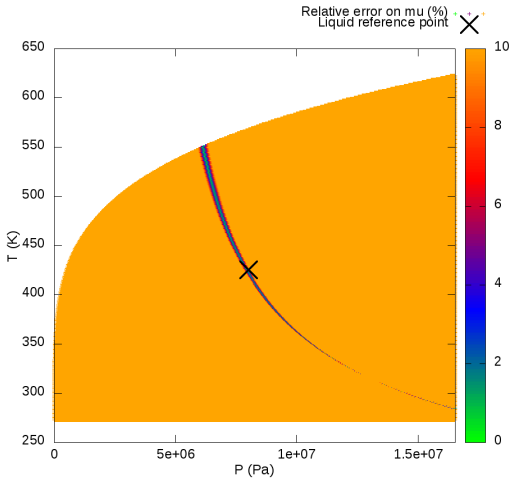

Figure 2.34 – *Relative error on μ compared with IAPWS-97, initial liquid SRK with error saturation at* 10%.

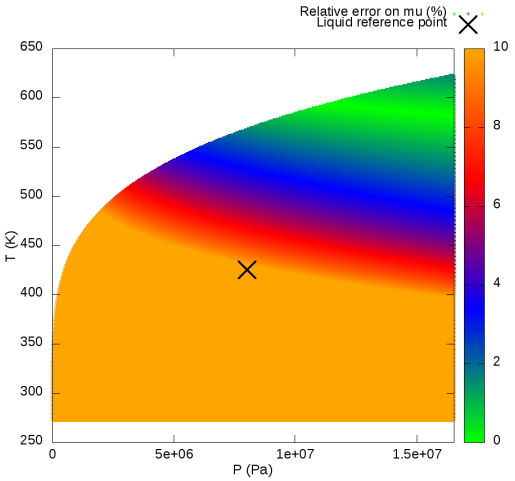

Figure 2.35 – *Relative error on μ compared with IAPWS-97, optimized liquid SRK with error saturation at* 10%.

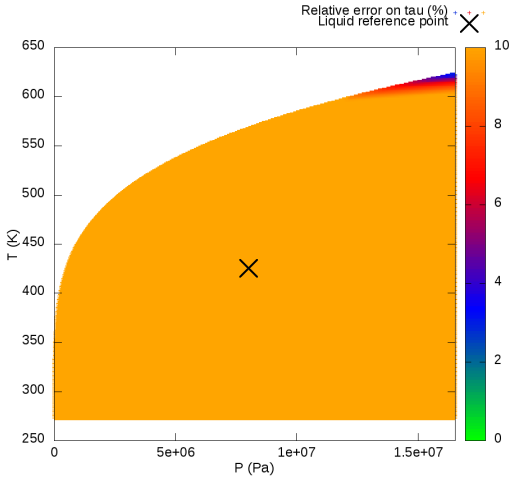

Figure 2.36 – *Relative error on τ compared with IAPWS-97, initial liquid SRK, with error saturation at* 10%.

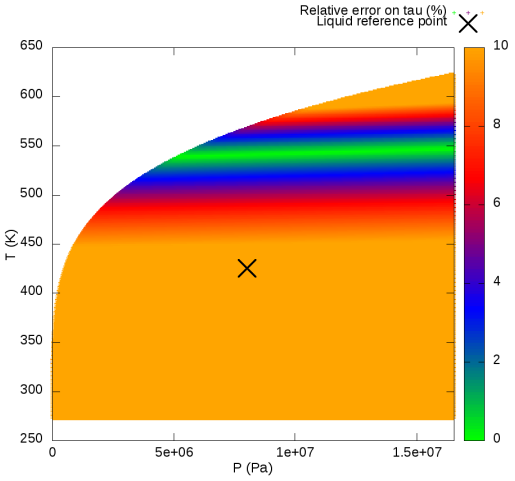

Figure 2.37 – *Relative error on τ compared with IAPWS-97, optimized liquid SRK, with error saturation at* 10%.

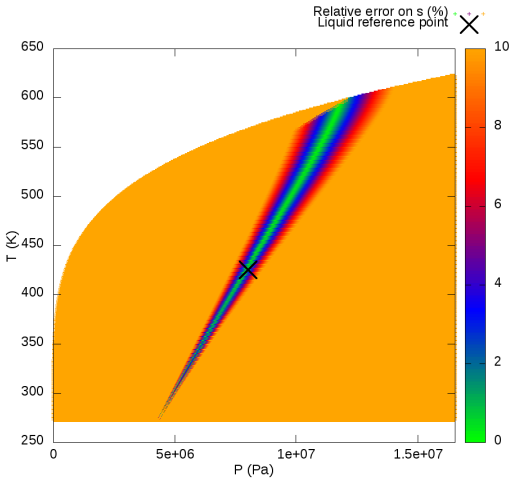

Figure 2.38 – *Relative error on s compared with IAPWS-97, initial liquid SRK, with error saturation at* 10%.

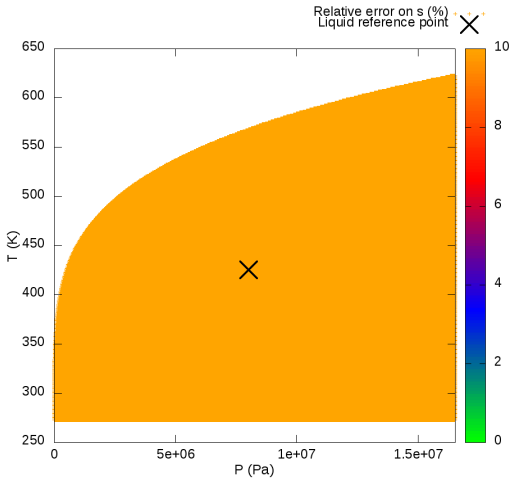

Figure 2.39 – *Relative error on s compared with IAPWS-97, optimized liquid SRK, with error saturation at* 10%.

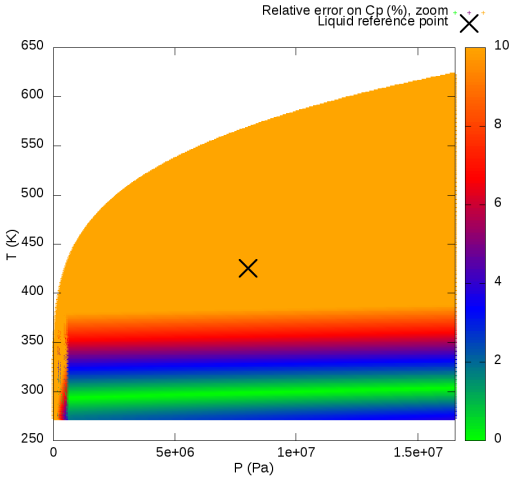

Figure 2.40 – *Relative error on C_p compared with IAPWS-97, initial liquid SRK, with error saturation at* 10%.

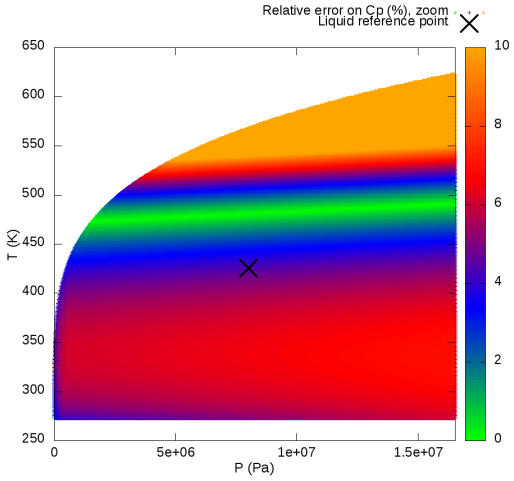

Figure 2.41 – *Relative error on C_p compared with IAPWS-97, optimized liquid SRK, with error saturation at* 10%.

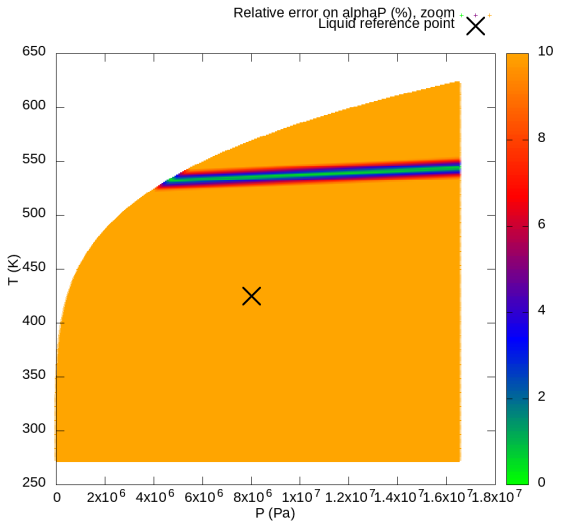

Figure 2.42 – *Relative error on α_P compared with IAPWS-97, initial liquid SRK, with error saturation at* 10%.

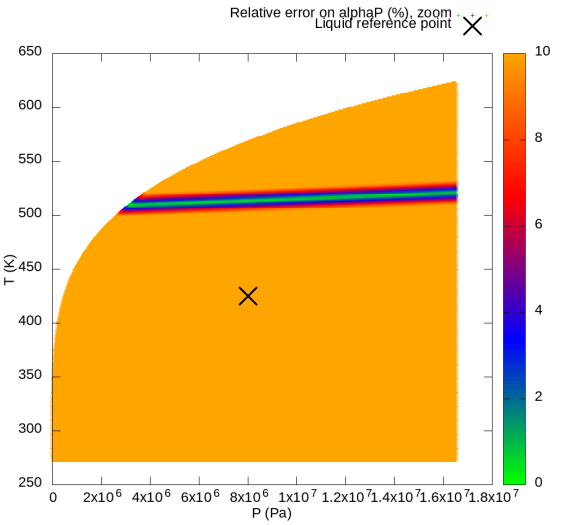

Figure 2.43 – *Relative error on α_P compared with IAPWS-97, optimized liquid SRK, with error saturation at* 10%.

Indicators (%)		SRK ini liquid	SRK opt liquid
Mean relative errors	on μ	$\simeq 10^4$	$\simeq 780$
	on τ	23	11
	on s	$\simeq 10^4$	$\simeq 10^4$
	on C_p	17	6.5
	on α_P	$\simeq 2500$	$\simeq 2300$
	on χ_T	$\simeq 10^4$	$\simeq 10^4$
Min relative errors	on μ	$\simeq 10^{-4}$	$\simeq 10^{-6}$
	on τ	2.9	$\simeq 10^{-5}$
	on s	$\simeq 10^{-5}$	16
	on C_p	$\simeq 10^{-6}$	$\simeq 10^{-5}$
	on α_P	$\simeq 10^{-5}$	$\simeq 10^{-5}$
	on χ_T	290	290
Max relative errors	on μ	$\simeq 10^9$	$\simeq 10^8$
	on τ	$\simeq 10^3$	$\simeq 860$
	on s	$\simeq 10^{10}$	$\simeq 10^{10}$
	on C_p	$\simeq 150$	$\simeq 380$
	on α_P	$\simeq 10^9$	$\simeq 10^9$
	on χ_T	$\simeq 10^7$	$\simeq 10^7$
% of domain with err $< 5\%$	on μ	0.6	26
	on τ	$\simeq 10^{-1}$	15
	on s	5	0
	on C_p	24	35
	on α_P	2.4	2.9
	on χ_T	0	0
	on μ, τ and C_p	0	2.9

Table 2.16 – *Accuracy indicators for the vapor SRK EOS, with both initial and optimized parameters.*

2.3.3.6 Conclusions for liquid

Table 2.17 sums up which phasic EOS is the most accurate to represent liquid water for each indicator of tables 2.8, 2.10, 2.12, 2.16.

Generally, among classical EOS, NASG EOS is the most accurate, except on C_p, for which Chemkin EOS is the best EOS, thanks to the dependance of C_p on temperature. The NASG-CK EOS is then the best compromise for the liquid, because it gathers the best features of NASG EOS and Chemkin EOS: the common accurate area for μ, τ and C_p represents 86% of the domain.

SRK EOS is in general less accurate, except at high temperature and high pressure.

Indicators (%)		Best EOS, liquid
Mean relative errors	on μ	NASG ini (3.9)
	on τ	NASG opt, NASG-CK (2.9)
	on s	NASG ini (8.0)
	on C_p	CK (0.95)
	on α_P	SG, CK (6.4)
	on χ_T	SRK opt (5.4)
Min relative errors	on μ	SG, NASG ini ($\simeq 10^{-8}$)
	on τ	SG, SG opt ($\simeq 10^{-7}$)
	on s	SG, NASG, CK ($\simeq 10^{-7}$)
	on C_p	NASG, CK ($\simeq 10^{-7}$)
	on α_P	SRK opt ($\simeq 10^{-6}$)
	on χ_T	SRK ($\simeq 10^{-2}$)
Max relative errors	on μ	NASG ini ($\simeq 10^{6}$)
	on τ	NASG ini (20)
	on s	NASG ini ($\simeq 10^{6}$)
	on C_p	CK (23)
	on α_P	SG, CK (32)
	on χ_T	SRK opt (13)
% of domain with err $< 5\%$	on μ	NASG ini, NASG-CK (96)
	on τ	NASG opt, NASG-CK (89)
	on s	NASG-CK (97)
	on C_p	CK, NASG-CK (99)
	on α_P	SRK opt (52)
	on χ_T	SRK (43)
	on μ, τ and C_p	NASG-CK (86)

Table 2.17 – *Best EOS for each indicator, for liquid.*

2.3.4 Vapor domain

2.3.4.1 Vapor SG

Table 2.18 give parameters of the initial SG fitted by the empirical method thanks to the reference point $P_{vap}^{ref} = 50bar$, $T_{vap}^{ref} = 575K$ (see appendix 2.A) and of the optimized SG.

Coefficients	Initial vapor SG	Optimized vapor SG
γ (dimensionless)	1.16176683761838	1.15442237458290
$C_v\ (JK^{-1}kg^{-1})$	2.70353894998533e+03	2.91668522329726e+03
$Q\ (Jkg^{-1})$	1.12547355921412e+06	1.25942536895827e+06
$\Pi\ (Pa)$	5.13028308898286e+05	-3.24993579473092e+02
$k\ (JK^{-1}kg^{-1})$	-6.94850802425439e+03	-7.77026092439033e+03

Table 2.18 – *Coefficients for the initial and optimized SG EOS for vapor. Initial SG is fitted by the empirical method with the following reference point:* $P_{vap}^{ref} = 50bar$, $T_{vap}^{ref} = 575K$.

For the initial SG, accuracy is high around the reference for μ, τ, s and C_p, but this accurate area can be wide or restricted, depending on considered quantity:

- it represents almost the whole domain for μ and s; except when $P <\simeq 10bar$ or $P >\simeq 110bar$ (figures 2.44 and 2.48).
- accurate area is focused on the vicinity of a pressure $P \simeq 50bar$ for τ and C_p, with a more restricted accurate area for C_p (figures 2.46 and 2.50).

At the end of the day, the domain of high accuracy for the main quantities of our study μ, τ and C_p is very restricted, even more than in the liquid case (6.5% of the domain in the vapor case versus 26% of the domain in the liquid case; see table 2.19 VS table 2.8).

Optimization improves accuracy on μ and τ by decreasing accuracy on C_p (figures 2.45, 2.47, and 2.51). Unfortunately, optimization improves accuracy on τ only at low pressures, which explains that we do not observe high accuracy on the three quantities μ, τ and C_p at the same time for the optimized SG (table 2.19). Accuracy on s is smaller for the optimized SG (figure 2.49).

Accuracy on α_P and χ_T is very low (figure 2.52 and table 2.19) and correct only at low pressure (figures 2.52 and 2.53).

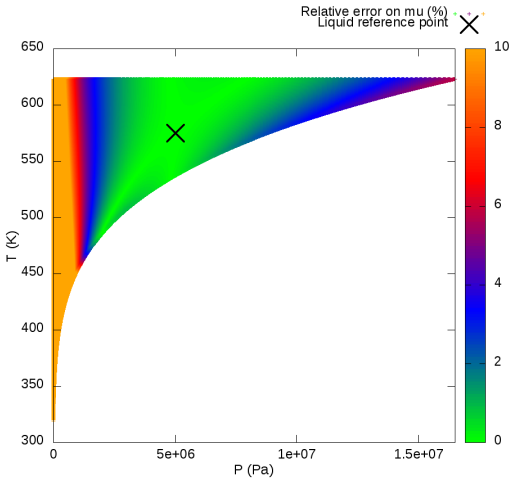

Figure 2.44 – *Relative error on μ compared with IAPWS-97, initial vapor SG, with error saturation at* 10%.

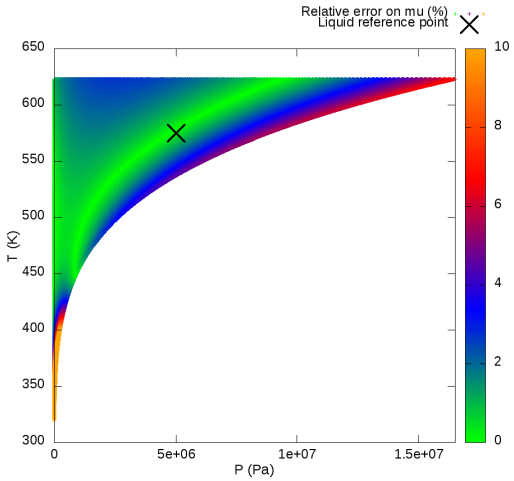

Figure 2.45 – *Relative error on μ compared with IAPWS-97, optimized vapor SG, with error saturation at* 10%.

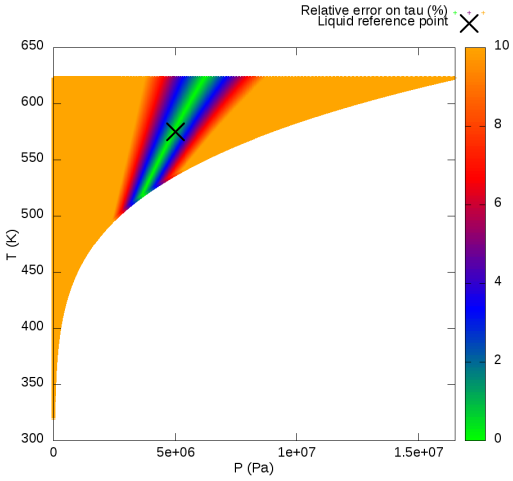

Figure 2.46 – *Relative error on τ compared with IAPWS-97, initial vapor SG, with error saturation at* 10%.

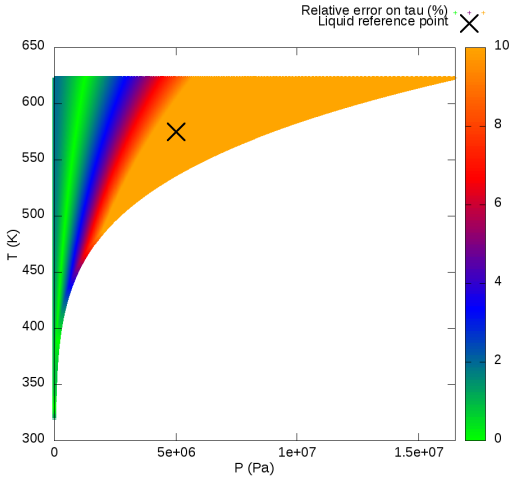

Figure 2.47 – *Relative error on τ compared with IAPWS-97, optimized vapor SG, with error saturation at* 10%.

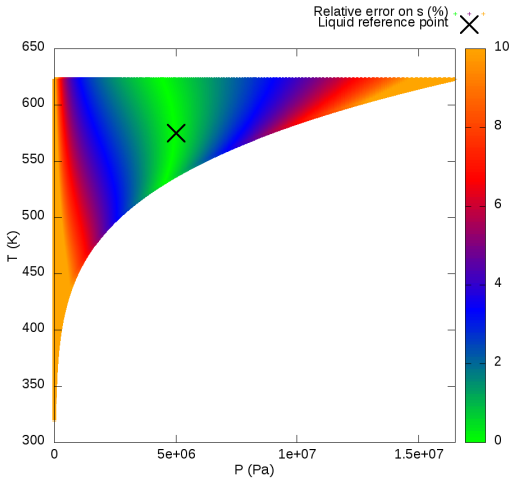

Figure 2.48 – *Relative error on s compared with IAPWS-97, initial vapor SG, with error saturation at* 10%.

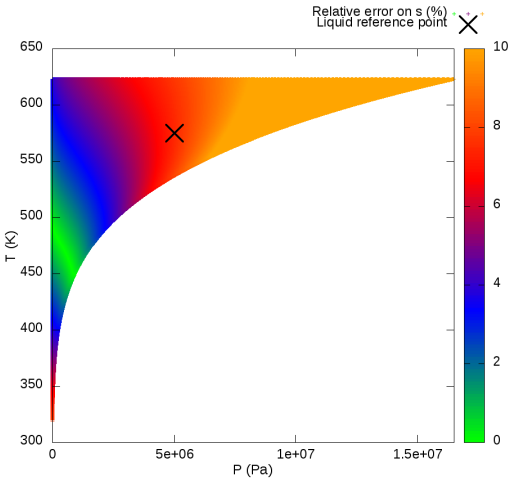

Figure 2.49 – *Relative error on s compared with IAPWS-97, optimized vapor SG, with error saturation at* 10%.

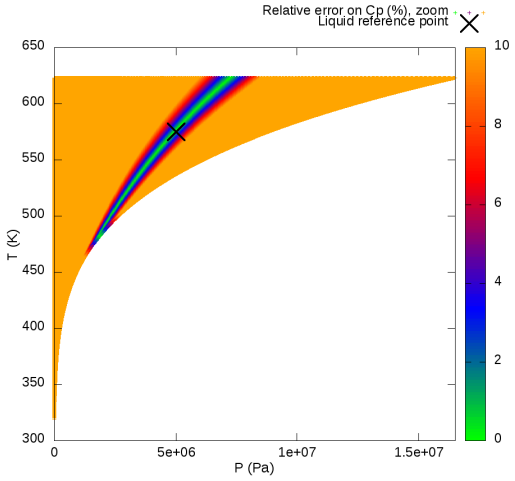

Figure 2.50 – *Relative error on C_p compared with IAPWS-97, initial vapor SG, with error saturation at* 10%.

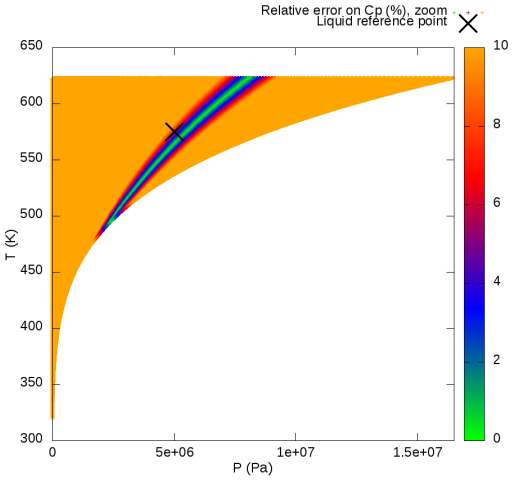

Figure 2.51 – *Relative error on C_p compared with IAPWS-97, optimized vapor SG, with error saturation at* 10%.

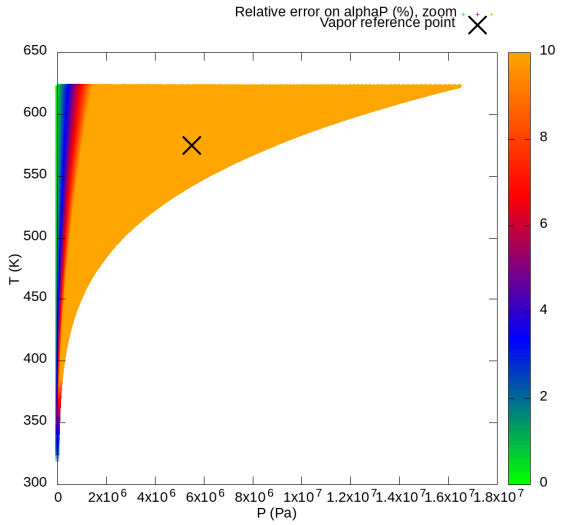

Figure 2.52 – *Relative error on α_P compared with IAPWS-97, initial and optimized vapor SG, with error saturation at* 10%.

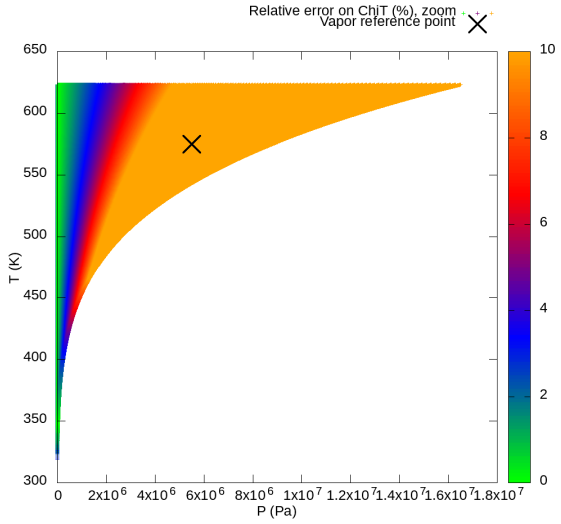

Figure 2.53 – *Relative error on χ_T compared with IAPWS-97, optimized vapor SG, with error saturation at* 10%.

Indicators (%)		Initial vapor SG	Optimized vapor SG
Mean relative errors	on μ	6.1	1.8
	on τ	24	14
	on s	4.5	6.9
	on C_p	30	34
	on α_P	38	
	on χ_T	33	16
Min relative errors	on μ	$\simeq 10^{-7}$	$\simeq 10^{-5}$
	on τ	$\simeq 10^{-6}$	$\simeq 10^{-6}$
	on s	$\simeq 10^{-7}$	$\simeq 10^{-6}$
	on C_p	$\simeq 10^{-4}$	$\simeq 10^{-4}$
	on α_P	$\simeq 10^{-1}$	$\simeq 10^{-1}$
	on χ_T	17	$\simeq 10^{-7}$
Max relative errors	on μ	$\simeq 10^{3}$	$\simeq 290$
	on τ	98	92
	on s	34	23
	on C_p	81	79
	on α_P	93	93
	on χ_T	98	72
% of domain with err $< 5\%$	on μ	76	95
	on τ	16	36
	on s	66	37
	on C_p	86	78
	on α_P	7.5	7.5
	on χ_T	0	26
	on μ, τ and C_p	6.5	0

Table 2.19 – *Accuracy indicators for the vapor SG EOS, with both initial and optimized parameters.*

2.3.4.2 Vapor NASG

Table 2.20 give parameters of the initial NASG given in [2] and of the optimized NASG.

Coefficients	Initial vapor NASG	Optimized vapor NASG
γ	1.328	1.15860489841012
$C_v\ (JK^{-1}kg^{-1})$	1.43674698795181e+03	2.90590222942452e+03
$Q\ (Jkg^{-1})$	-1.957e+06	1.17523493288959e+06
$\pi\ (Pa)$	0	1.61451609216469e2
$k\ (JK^{-1}kg^{-1})$	-5.22768268008043e+03	-7.81112365825407e+03
$b\ (m^3kg^{-1})$	0	-6.21629353832523e-03

Table 2.20 – *Coefficients for the initial and optimized NASG EOS, for vapor. Initial NASG coefficients are those given in [2] with a k deduced from the reference point data* ($P_{vap}^{ref} = 50bar$, $T_{vap}^{ref} = 575K$) *thanks to* (2.9).

Contrary to the liquid case (see section 2.3.3.2), initial NASG coefficients lead to generally unaccurate results (figures 2.54, 2.56, 2.58 and 2.60).

Optimization enables a great improvement compared with initial NASG coefficients. Compared with optimized vapor SG EOS (see section 2.3.4.1), accuracy is improved on μ, τ, s (figures 2.55, 2.57, 2.59 versus figures 2.45, 2.47, 2.49), as well as on α_P and χ_T (table 2.19 VS figures 2.63 and 2.65). For C_p, results are similar to SG case (figure 2.61). At the end of the day, the same limitation appears as in the SG case: area with a high accuracy for the three quantities μ, τ and C_p is very limited.

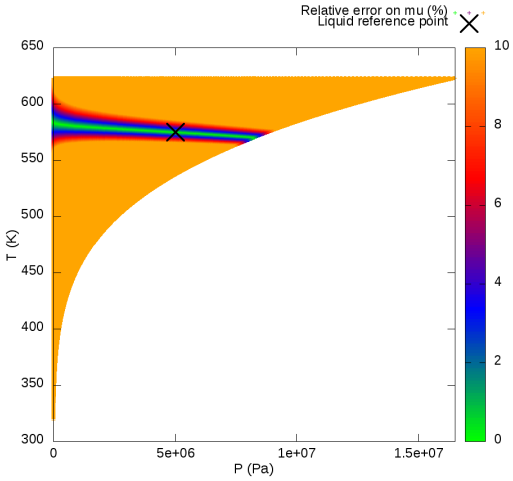

Figure 2.54 – *Relative error on μ compared with IAPWS-97, initial vapor NASG, with error saturation at* 10%.

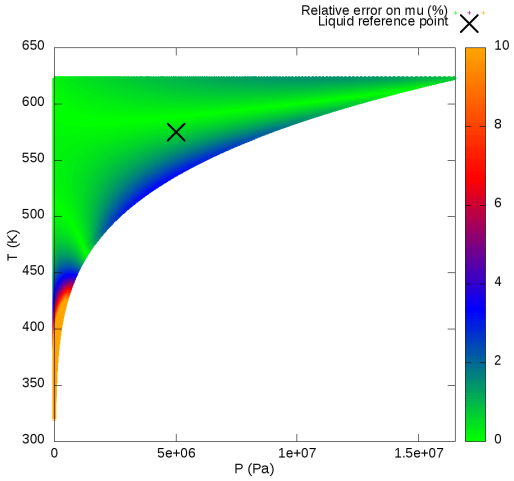

Figure 2.55 – *Relative error on μ compared with IAPWS-97, optimized vapor NASG, with error saturation at* 10%.

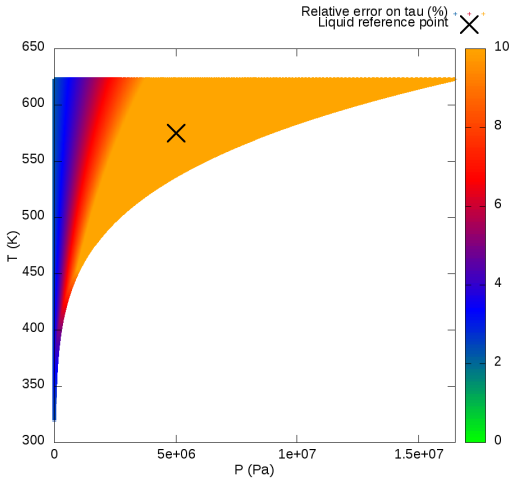

Figure 2.56 – *Relative error on τ compared with IAPWS-97, initial vapor NASG, with error saturation at* 10%.

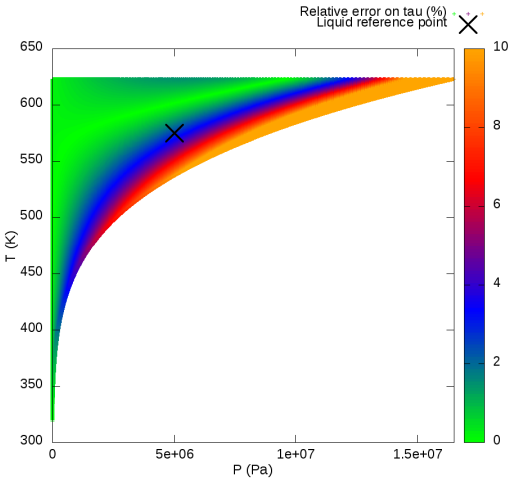

Figure 2.57 – *Relative error on τ compared with IAPWS-97, optimized vapor NASG, with error saturation at* 10%.

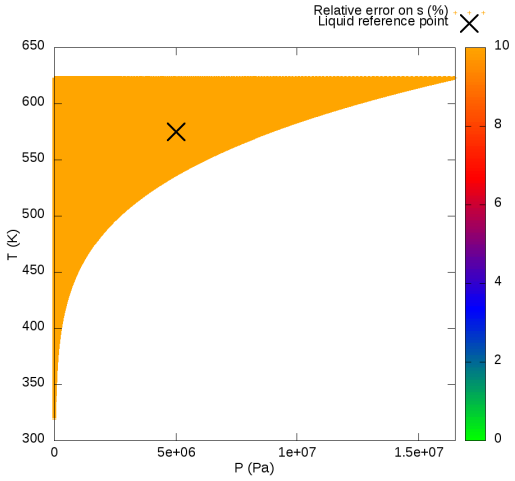

Figure 2.58 – *Relative error on s compared with IAPWS-97, initial vapor NASG, with error saturation at* 10%.

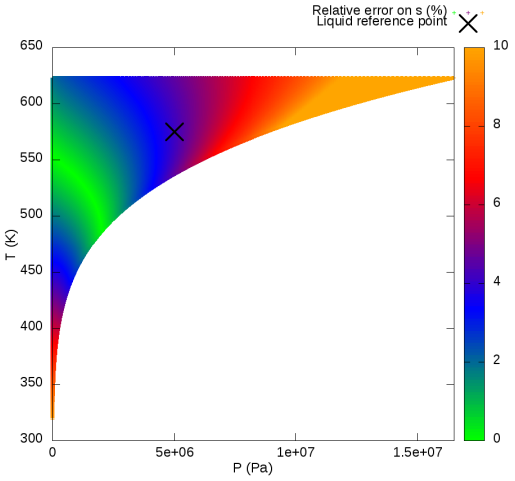

Figure 2.59 – *Relative error on s compared with IAPWS-97, optimized vapor NASG, with error saturation at* 10%.

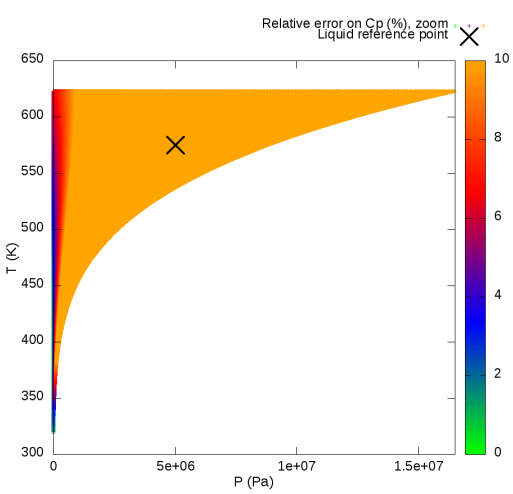

Figure 2.60 – *Relative error on C_p compared with IAPWS-97, initial vapor NASG, with error saturation at* 10%.

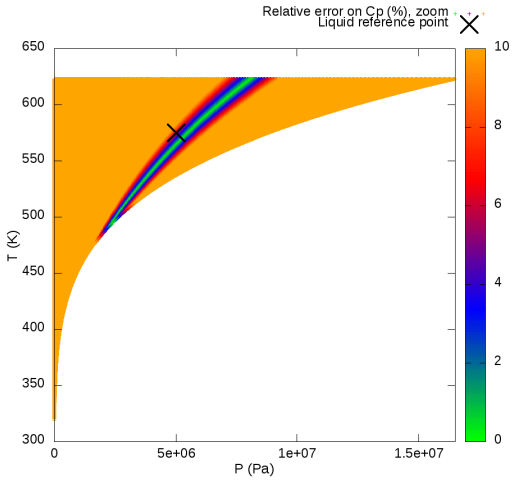

Figure 2.61 – *Relative error on C_p compared with IAPWS-97, optimized vapor NASG fitted by the empirical method, with error saturation at* 10%.

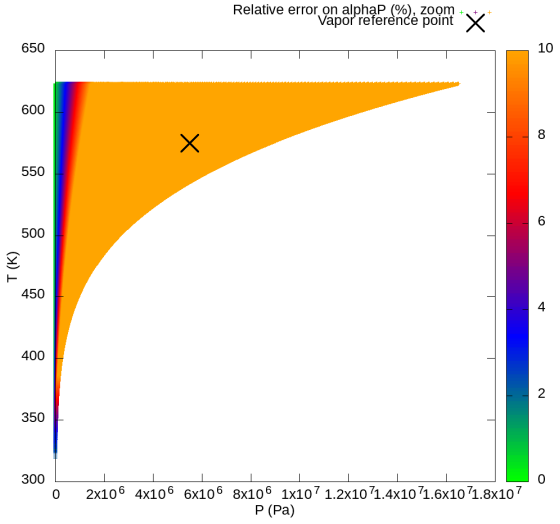

Figure 2.62 – *Relative error on α_P compared with IAPWS-97, initial vapor NASG, with error saturation at* 10%.

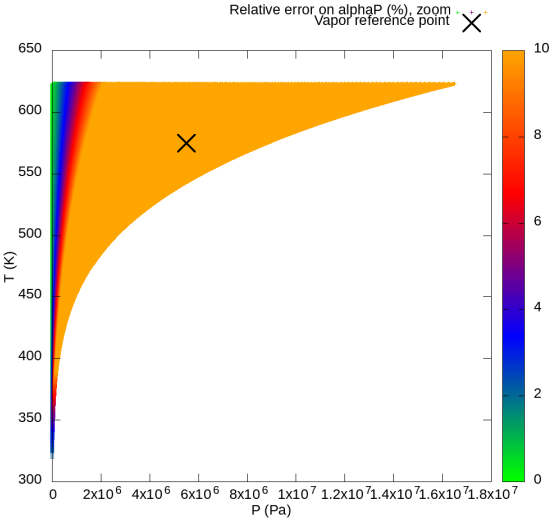

Figure 2.63 – *Relative error on α_P compared with IAPWS-97, optimized vapor NASH, with error saturation at* 10%.

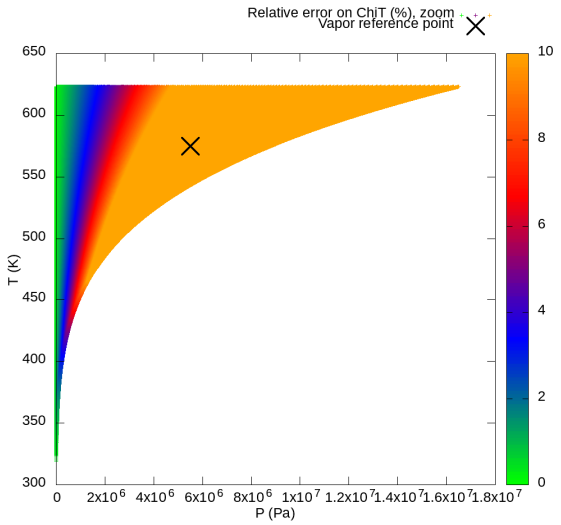

Figure 2.64 – *Relative error on χ_T compared with IAPWS-97, initial vapor NASG, with error saturation at* 10%.

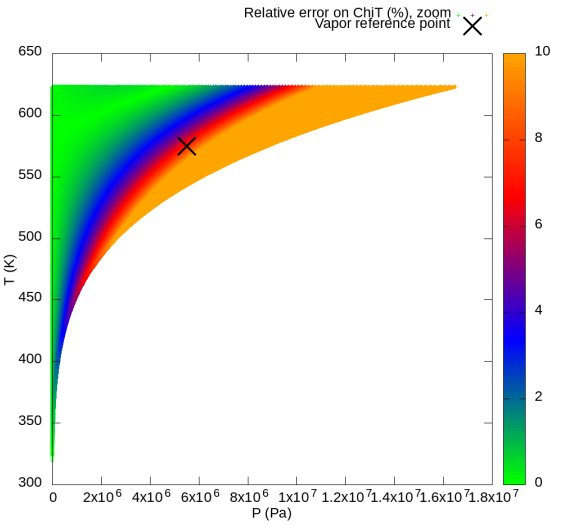

Figure 2.65 – *Relative error on χ_T compared with IAPWS-97, optimized vapor NASG, with error saturation at* 10%.

Indicators (%)		Initial vapor NASG	Optimized vapor NASG
Mean relative errors	on μ	54	1.0
	on τ	19	3.2
	on s	$\simeq 100$	4.3
	on C_p	34	34
	on α_P	32	7.7
	on χ_T	7.1	6.8
Min relative errors	on μ	$\simeq 10^{-4}$	$\simeq 10^{-6}$
	on τ	2.1	$\simeq 10^{-6}$
	on s	72	$\simeq 10^{-6}$
	on C_p	$\simeq 10^{-4}$	$\simeq 10^{-5}$
	on α_P	$\simeq 10^{-2}$	$\simeq 10^{-5}$
	on χ_T	$\simeq 10^{-6}$	$\simeq 10^{-6}$
Max relative errors	on μ	$\simeq 10^{4}$	$\simeq 500$
	on τ	$\simeq 10^{2}$	26
	on s	$\simeq 10^{2}$	19
	on C_p	88	79
	on α_P	89	69
	on χ_T	57	56
% of domain with err $< 5\%$	on μ	88	98
	on τ	16	77
	on s	0	67
	on C_p	2.7	7.6
	on α_P	9.5	40
	on χ_T	58	59
	on μ, τ and C_p	$\simeq 0$	5.6

Table 2.21 – *Accuracy indicators for the vapor NASG EOS, with both initial and optimized parameters.*

2.3.4.3 Vapor CK

Optimized parameters for the modified Chemkin equation (2.2.4) are given in table 2.22.

Coefficients	Optimized Chemkin
A (dimensionless)	-9.31481046562792
$B\ (K^{-1})$	2.73164127264464e-02
$C\ (K^{-2})$	2.09031875563400e-04
$D\ (K^{-3})$	-7.43079557985475e-07
$E\ (K^{-4})$	6.66991176623741e-10
$F\ (K)$	2.94210286709953e+06/R
G (dimensionless)	3.10175006317838e+04/R
γ (dimensionless)	1.05234866922037
$C_v\ (JK^{-1}kg^{-1})$	8.60791352097043e+03
$\Pi\ (Pa)$	-3.14865364846976e+02

Table 2.22 – *Optimized oefficients for Chemkin EOS (2.19) for vapor.*

Results (see table 2.23) are very closed to those obtained with the optimized SG EOS (section 2.3.4.1): the relative errors are small on the whole domain for μ (figure 2.66)and accuracy is limited to pressures $P <\simeq 10bar$ for τ and s (figures 2.67 and 2.68). Even if C_p depends on T, no significant improvement is observed with Chemkin EOS, contrary to the liquid case (figure 2.69 versus figure 2.29).

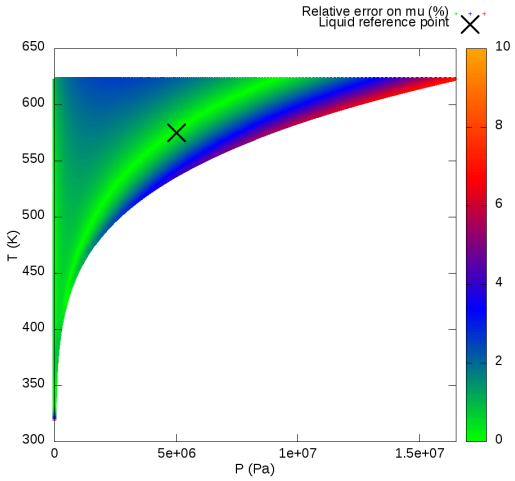

Figure 2.66 – *Relative error on μ compared with IAPWS-97, optimized vapor Chemkin EOS with error saturation at* 10%.

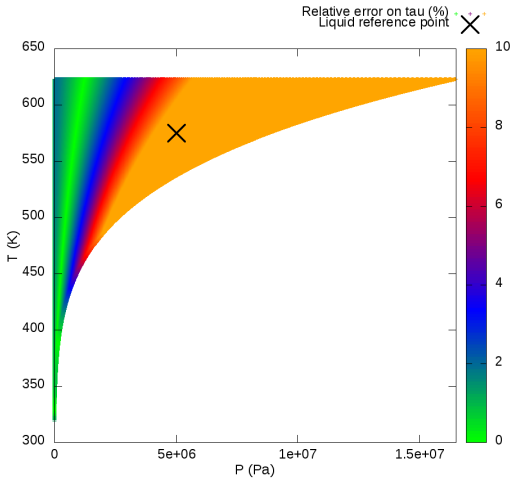

Figure 2.67 – *Relative error on τ compared with IAPWS-97, optimized vapor Chemkin EOS, with error saturation at* 10%.

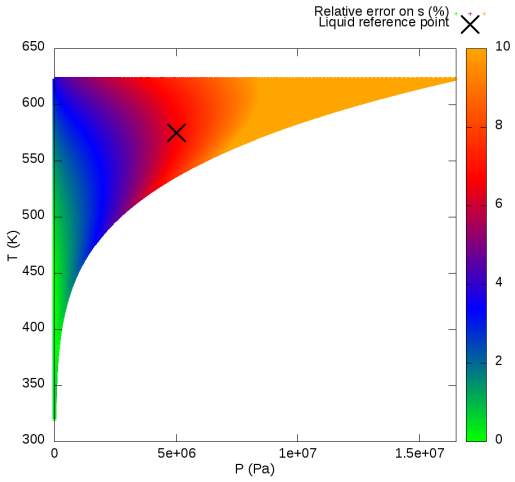

Figure 2.68 – *Relative error on s compared with IAPWS-97, optimized Chemkin EOS, with error saturation at* 10%.

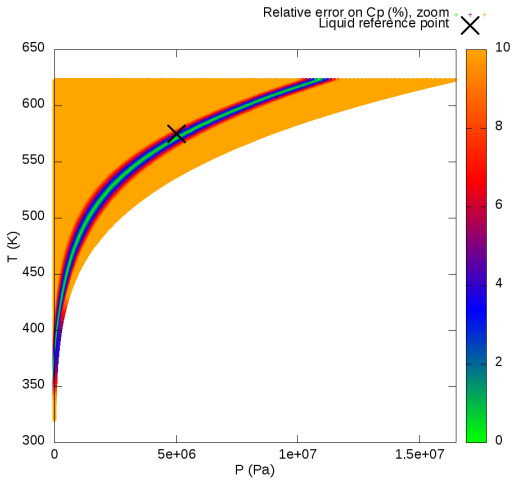

Figure 2.69 – *Relative error on C_p compared with IAPWS-97, optimized Chemkin EOS, with error saturation at* 10%.

Indicators (%)		Optimized vapor Chemkin
Mean relative errors	on μ	1.7
	on τ	14
	on s	6.4
	on C_p	31
	on χ_T	16
Min relative errors	on μ	$\simeq 10^{-6}$
	on τ	$\simeq 10^{-6}$
	on s	$\simeq 10^{-5}$
	on C_p	$\simeq 10^{-4}$
	on χ_T	$\simeq 10^{-5}$
Max relative errors	on μ	7.0
	on τ	92
	on s	23
	on C_p	$\simeq 69$
	on χ_T	72
% of domain with err $< 5\%$	on μ	96
	on τ	37
	on s	44
	on C_p	11
	on χ_T	26
	on μ, τ and C_p	3.25

Table 2.23 – *Error for the Chemkin EOS with optimized coefficients, recalled in table 2.22.*

2.3.4.4 Vapor NASG-CK

Optimized parameters for the NASG-EOS proposed in section 2.2.3 are considered; they are given in table 2.24.

Coefficients	Optimized vapor NASG-CK
A (dimensionless)	-1.02168660306695e+01
$B\ (K^{-1})$	-3.47403599702201e-03
$C\ (K^{-2})$	4.04096035980686e-04
$D\ (K^{-3})$	-1.12256098751702e-06
$E\ (K^{-4})$	9.07044783334605e-10
$F\ (K)$	3.13280017149795e+06/R
G (dimensionless)	3.49591079247605e+04/R
γ (dimensionless)	1.09330718407512
$C_v\ (JK^{-1}kg^{-1})$	4.92989464911892e+03
$\Pi\ (Pa)$	-3.94806192254752e+01
$b\ (m^3kg^{-1})$	-6.21098438524367e-03

Table 2.24 – *Optimized oefficients for Noble-Able Chemkin EOS (2.24), for vapor.*

NASG-CK EOS does not significantly improve NASG EOS results for vapor on μ (figures 2.70 VS 2.55), τ (figures 2.71 VS 2.57) or s (figures 2.72 VS 2.59). However, the common accurate area for μ, τ and C_p is improved for NASG-CK: it is about 10% of the vapor domain (table 2.25), whereas it reaches 5% for NASG and 3.25 for Chemkin. It stays limited because the restricted accurate area on C_p, very similar as the one obtained with the Chemkin EOS (figures 2.73 VS 2.61).
Like in the liquid case, α_P and χ_T are badly estimated with NASG-CK EOS (table 2.25).

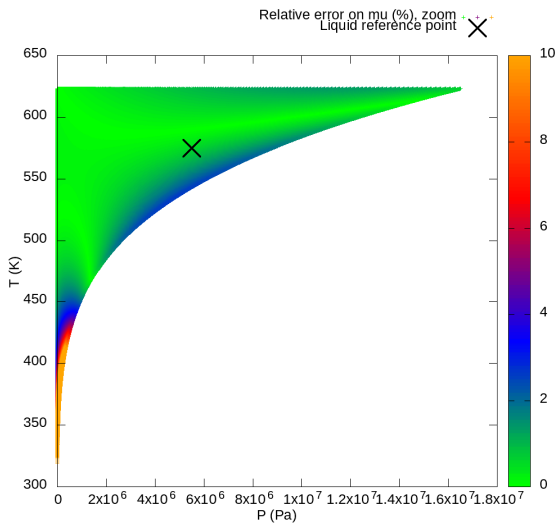

Figure 2.70 – *Relative error on μ compared with IAPWS-97, optimized vapor Noble-Able Chemkin stiffened gas EOS with error saturation at* 10%.

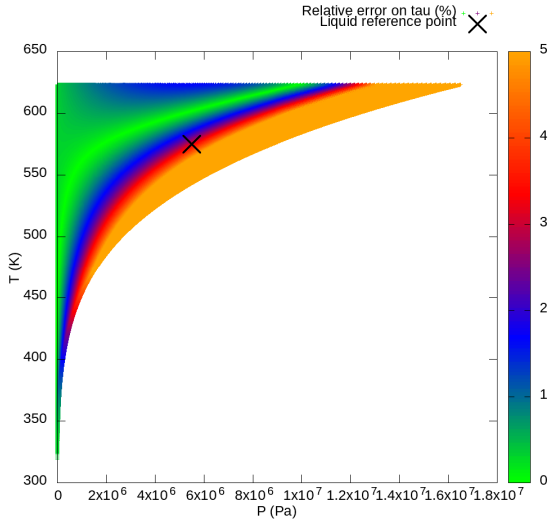

Figure 2.71 – *Relative error on τ compared with IAPWS-97, optimized vapor Noble-Able Chemkin stiffened gas EOS, with error saturation at* 10%.

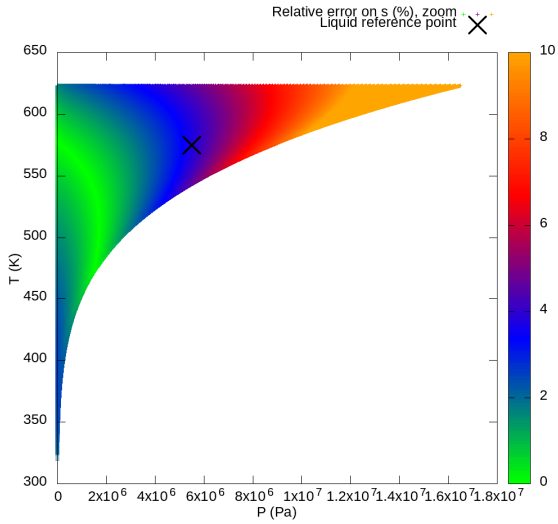

Figure 2.72 – *Relative error on s compared with IAPWS-97, optimized vapor Noble-Able Chemkin stiffened gas EOS, with error saturation at* 10%.

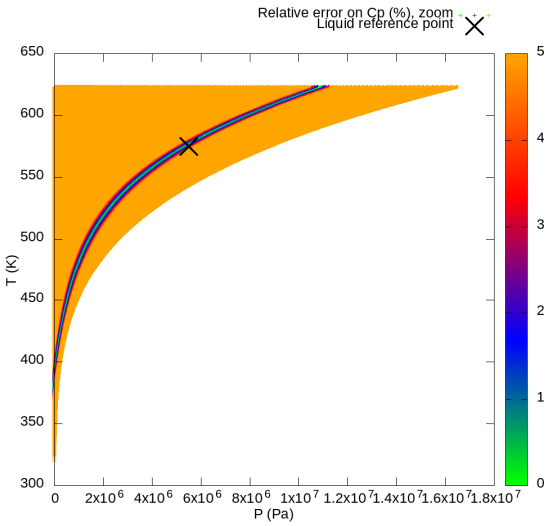

Figure 2.73 – *Relative error on C_p compared with IAPWS-97, optimized vapor Noble-Able Chemkin stiffened gas EOS, with error saturation at* 10%.

Indicators (%)		Optimized liquid NASG-CK
Mean relative errors	on μ	0.18
	on τ	0.74
	on s	0.9
	on C_p	7.3
	on α_P	24
	on χ_T	$\simeq 10^5$
Min relative errors	on μ	$\simeq 10^{-6}$
	on τ	$\simeq 10^{-6}$
	on s	$\simeq 10^{-6}$
	on C_p	$\simeq 10^{-5}$
	on α_P	93
	on χ_T	$\simeq 10^3$
Max relative errors	on μ	$\simeq 210$
	on τ	26
	on s	18
	on C_p	$\simeq 120$
	on α_P	$\simeq 100$
	on χ_T	$\simeq 10^6$
% of domain with err $< 5\%$	on μ	24
	on τ	18
	on s	17
	on C_p	2.6
	on α_P	0
	on χ_T	0
	on μ, τ and C_p	2.6

Table 2.25 – *Accuracy indicators for the vapor Noble-Able Chemkin stiffened gas EOS, with optimized parameters.*

2.3.4.5 Vapor SRK

Table 2.26 give parameters of the initial SRK EOS from [34] and of the optimized SRK EOS.

Coefficients	Initial vapor SRK	Optimized vapor SRK
γ (dimensionless)	1.15419256941954	1.15365918757890
C_v $(JK^{-1}kg^{-1})$	2.91840659838894e+03	2.97749066492949e+03
Ω_a (dimensionless)	0.457235529	4.20909756054200e-01
Ω_b (dimensionless)	0.0777960739	6.11099667214623e-02
m_0 $(JK^{-1}kg^{-1})$	0.3764	4.27963589428829e-01
m_1 (m^3kg^{-1})	1.54226	1.99955854833069e+00
m_2 (m^3kg^{-1})	-0.26992	-2.29198785005644e-01
ω (m^3kg^{-1})	0.3442920843	4.09698443741612e-01

Table 2.26 – *Coefficients for the initial and the optimized SRK EOS, for vapor, with the following reference point:* $P_{vap}^{ref} = 50bar$, $T_{vap}^{ref} = 575K$. *Initial SRK EOS coefficients are those given in [34], except for* γ *and* C_v *taken equal to those obtained with the empirical method to fit a SG (see 2.3.4.1).*

Contrary to the liquid case (see section 2.3.3.5), the initial classical SRK EOS give correct results for μ and τ: error on μ is low at high pressure and temperature (figure 2.74), and accuracy on τ is remarkable on the whole domain (figure 2.76), since relative error is less than 5% on 96% of the vapor domain (table 2.27). C_p is accurate only on a restricted area (figure 2.78), but in a similar manner to previous EOS.

Optimization only very slightly improves the accuracy since optimized parameters are very similar to initial parameters (table 2.26). Similar results to those obtained with the previous EOS are got for μ, τ and C_p, that is to say, a satisfying accuracy on the whole domain for μ and τ (figures 2.75 and 2.77), and only a quite restricted accurate area for C_p (figure 2.79). The common area of high accuracy for μ, τ and C_p is also limited ($\simeq$ 6% of the domain, see table 2.27). χ_T is better estimated (figure 2.81), whereas s is very badly represented (table 2.27).

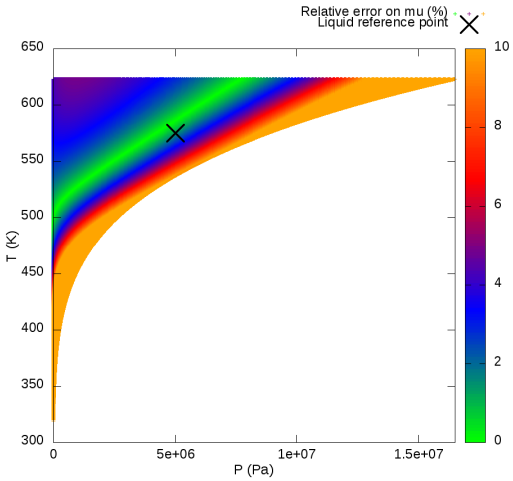

Figure 2.74 – *Relative error on μ compared with IAPWS-97, initial vapor SRK with error saturation at* 10%.

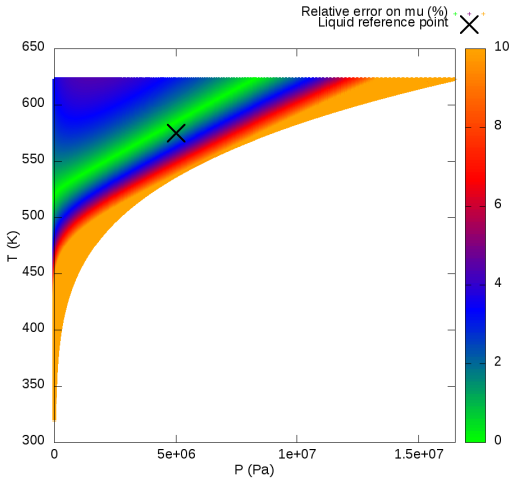

Figure 2.75 – *Relative error on μ compared with IAPWS-97, optimized vapor SRK with error saturation at* 10%.

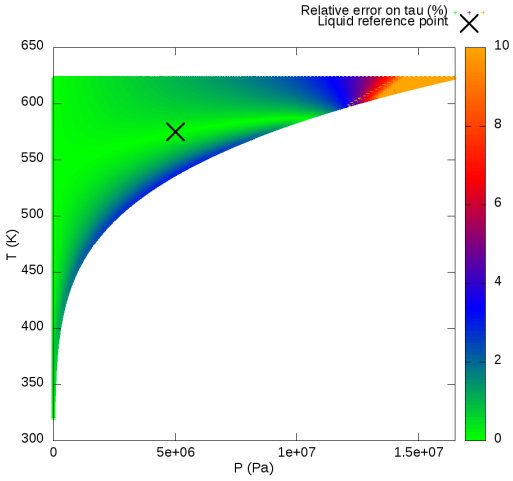

Figure 2.76 – *Relative error on τ compared with IAPWS-97, initial vapor SRK, with error saturation at* 10%.

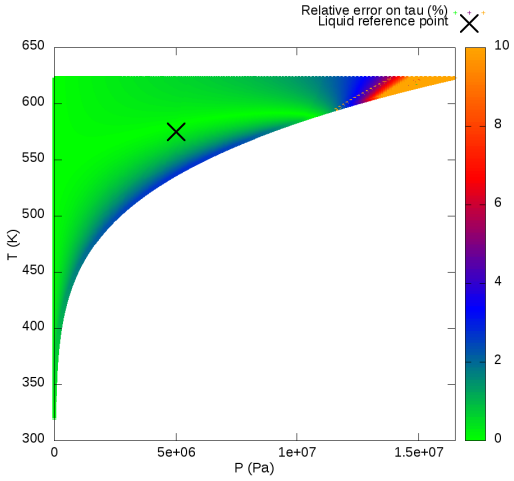

Figure 2.77 – *Relative error on τ compared with IAPWS-97, optimized vapor SRK, with error saturation at* 10%.

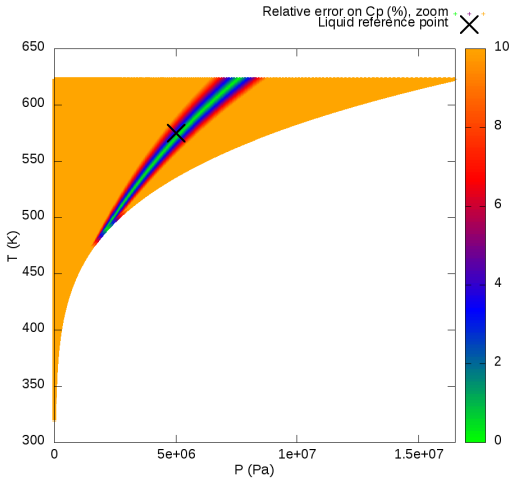

Figure 2.78 – *Relative error on C_p compared with IAPWS-97, initial vapor SRK, with error saturation at* 10%.

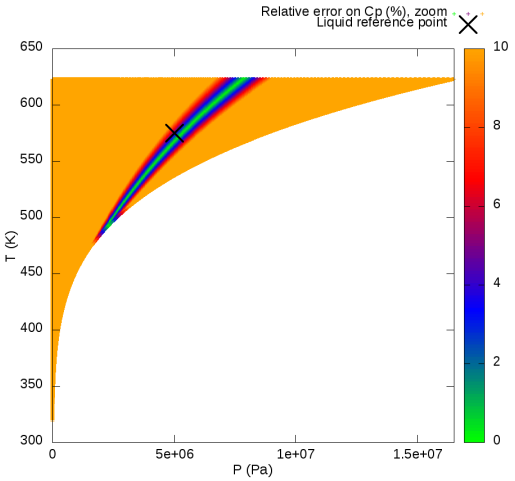

Figure 2.79 – *Relative error on C_p compared with IAPWS-97, optimized vapor SRK, with error saturation at* 10%.

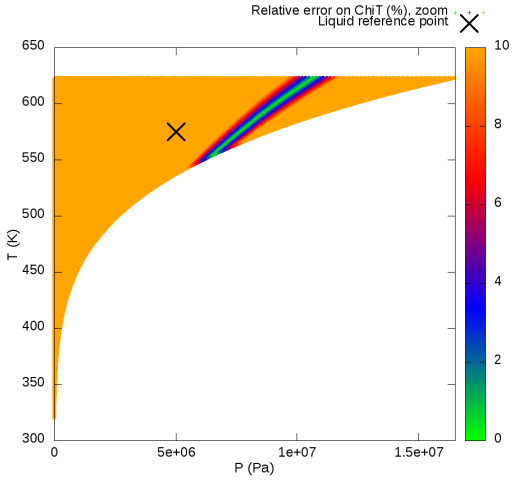

Figure 2.80 – *Relative error on χ_T compared with IAPWS-97, initial vapor SRK, with error saturation at* 10%.

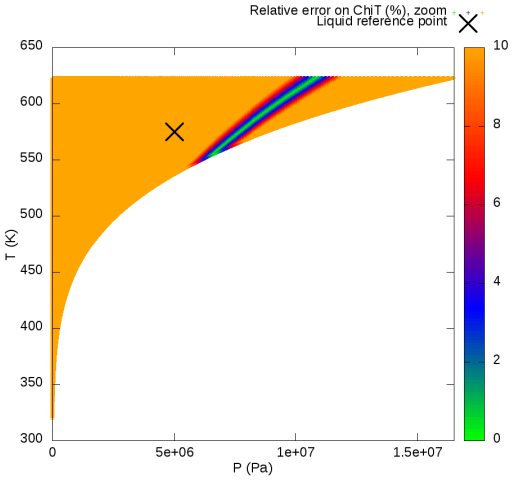

Figure 2.81 – *Relative error on χ_T compared with IAPWS-97, optimized vapor SRK, with error saturation at* 10%.

Indicators (%)		Initial vapor SRK	Optimized vapor SRK
Mean relative errors	on μ	7.0	7.4
	on τ	1.8	1.9
	on s	29	28
	on C_p	34	34
	on α_P	49	30
	on χ_T	51	51
Min relative errors	on μ	$\simeq 10^{-7}$	$\simeq 10^{-5}$
	on τ	$\simeq 10^{-7}$	$\simeq 10^{-7}$
	on s	15	2.9
	on C_p	$\simeq 10^{-4}$	$\simeq 10^{-5}$
	on α_P	15	0.52
	on χ_T	$\simeq 10^{-4}$	$\simeq 10^{-4}$
Max relative errors	on μ	$\simeq 10^{3}$	$\simeq 10^{4}$
	on τ	$\simeq 180$	$\simeq 10^{5}$
	on s	77	$\simeq 170$
	on C_p	87	$\simeq 120$
	on α_P	92	$\simeq 10^{3}$
	on χ_T	$\simeq 100$	$\simeq 10^{4}$
% of domain with err $< 5\%$	on μ	65	65
	on τ	96	97
	on s	0	0
	on C_p	7.7	7.6
	on α_P	0	0
	on χ_T	4.9	4.8
	on μ, τ and C_p	6.2	5.9

Table 2.27 – *Accuracy indicators for the vapor SRK EOS, with both initial and optimized parameters.*

2.3.4.6 Conclusions for vapor

Table 2.28 sums up which phasic EOS is the most accurate to represent vapor water for each indicator of tables 2.19, 2.21, 2.23, 2.27.

NASG EOS gives in general accurate results, but the accurate areas are different depending on the considered quantity: μ is accurate on the whole domain, but τ is accurate at $P <\simeq 25bar$ whereas C_p is accurate around $P \simeq 50bar$. Chemkin EOS gives no significant improvement compared with SG EOS, contrary to the liquid case. NASG-CK EOS improves the common accurate area for μ, τ and C_p, even if it stays limited compared with the liquid case (around 10% of the domain). At the end of the day, NASG-CK is a less interesting compromise to NASG EOS compared with the liquid case, since the accuracy gain on C_p is not really significant, whereas a variable C_p with T induces some difficulties (for instance, changing of thermodynamical plane is no more explicit).

SRK EOS is also relevant to describe vapor water, since accurate results are obtained for μ, τ and C_p for $P <\simeq 50bar$ and $T >\simeq 500K$. The accuracy is remarkable for τ, with a relative error lower than 5% on 97% of the domain. The same limitation as with SG-like EOS occurs, because the accurate area for C_p is also limited.

Indicators (%)		Best EOS, vapor
Mean relative errors	on μ	NASG-CK (0.74)
	on τ	SRK (1.8)
	on s	NASG-CK (3.6)
	on C_p	SG ini (30)
	on α_P	NASG opt (7.7)
	on χ_T	NASG opt (6.8)
Min relative errors	on μ	NASG-CK ($\simeq 10^{-8}$)
	on τ	SG & SRK ini NASG-CK ($\simeq 10^{-8}$)
	on s	SG ini ($\simeq 10^{-7}$)
	on C_p	NASG opt, SRK opt ($\simeq 10^{-5}$)
	on α_P	NASG opt ($\simeq 10^{-5}$)
	on χ_T	NASG opt ($\simeq 10^{-6}$)
Max relative errors	on μ	CK (7)
	on τ	NASG opt (26)
	on s	NASG-CK (18)
	on C_p	CK (69)
	on α_P	SG, NASG, CK (69)
	on χ_T	NASG opt (56)
% of domain with err $< 5\%$	on μ	NASG-CK (99)
	on τ	SRK opt (97)
	on s	NASG ini (96)
	on C_p	CK, NASG-CK (11)
	on α_P	NASG opt (40)
	on χ_T	NASG opt (59)
	on μ, τ and C_p	SRK opt (19)

Table 2.28 – *Best EOS for each indicator, for vapor.*

2.4 General conclusion

In order to close the model of Chapter 1, some classical EOS for water have been studied by taking IAPWS-97 as a reference. In a general way, it seems very challenging to obtain a high accuracy level on all thermodynamical quantities at the same time.

Among the tested classical EOS, the Noble-Able stiffened gas EOS appears as the best compromise between accuracy and simplicity. The NASG EOS is an admissible EOS without any condition (in the sense defined in Chapter 1), with explicit changes of thermodynamical planes. A high level of accuracy on all the main thermodynamical quantities of this study (the chemical potential μ, the specific volume τ and the heat capacity C_p) has been observed on a very large liquid domain.

We tested a modified NASG EOS, like proposed in [2], obtained by gathering the main feature of NASG EOS and Chemkin EOS: the so-called NASG-CK is accurate on μ, τ and C_p with a relative error less than 5% on more than 85% on the liquid domain. The NASG-CK EOS with the optimized parameter is admissible, with a convenient change of thermodynamical plane (even if an implicit resolution is required to change from the (τ, e)-plane to the (P, T)-plane). Surprisingly, both for NASG and NASG-CK EOS, being accurate on several thermodynamical quantities at the same point is less easy when considering the water vapor, for all the considered EOS: accurate areas are often disjointed, and C_p is badly estimated with a Chemkin-type model.

SRK EOS is a relevant alternative to NASG EOS to describe the vapor, especially to evaluate the density. However, restricting the admissible EOS to complete EOS is a practical constraint that should not be neglicted. Difficulties to build a complete EOS from an incomplete EOS have been highlighted in [10] and illustrated in this work with the SRK EOS. With more complex cubic EOS, similar problems may be encountered, in particular to control if the concavity constraints on the chemical potential are fulfilled or not.

References

[1] D. BANUTI. "Crossing the Widom-line–Supercritical pseudo-boiling". In: *The Journal of Supercritical Fluids* 98 (2015), pp. 12–16. DOI: https://doi.org/10.1016/j.supflu.2014.12.019 (cit. on pp. 70, 73, 86).

[2] P. BOIVIN, M. CANNAC, and O. LE METAYER. "A thermodynamic closure for the simulation of multiphase reactive flows". In: *International Journal of Thermal Sciences* 137 (Mar. 2019), pp. 640–649. URL: https://hal.archives-ouvertes.fr/hal-01981954 (cit. on pp. 77, 79, 92, 117, 136).

[3] F. CAUPIN. "Liquid-vapor interface, cavitation, and the phase diagram of water". In: *Physical Review E* 71.5 (2005), p. 051605. DOI: https://doi.org/10.1103/PhysRevE.71.051605 (cit. on p. 67).

[4] I. R. CONSORTIUM et al. "Fluid Property Calculator". In: *Industrial Refrigeration Consortium Website.[Online][Cited: 13 01, 20.]* (2017). URL: https://www.irc.wisc.edu/properties (cit. on p. 78).

[5] J.-P. CROISILLE. "Contribution à l'étude théorique et à l'approximation par éléments finis du système hyperbolique de la dynamique des gaz multidimensionnelle et multiespèces". PhD thesis. Paris 6, 1990 (cit. on p. 69).

[6] F. DAUDE, P. GALON, Z. GAO, and E. BLAUD. "Numerical experiments using a HLLC-type scheme with ALE formulation for compressible two-phase flows five-equation models with phase transition". In: *Computers & Fluids* 94 (May 2014), pp. 112–138. DOI: https://doi.org/10.1016/j.compfluid.2014.02.008 (cit. on pp. 67, 76, 86, 140).

[7] S. DELLACHERIE, G. FACCANONI, B. GREC, and Y. PENEL. "Accurate steam-water equation of state for two-phase flow LMNC model with phase transition". In: *Applied Mathematical Modelling* 65 (2019), pp. 207–233. DOI: 10.1016/j.apm.2018.07.028. URL: https://hal.archives-ouvertes.fr/hal-01111730 (cit. on p. 69).

[8] G. FACCANONI. "Study of a Fine Model of Liquid-Vapor Phase Change. Contribution to the Boiling Crisis Study." PhD thesis. Ecole Polytechnique X, Nov. 2008. URL: https://pastel.archives-ouvertes.fr/tel-00363460 (cit. on p. 69).

[9] G. FACCANONI, S. KOKH, and G. ALLAIRE. "Modelling and Simulation of Liquid-Vapor Phase Transition in Compressible Flows Based on Thermodynamical Equilibrium." In: *Mathematical Modelling and Numerical Analysis* 46.05 (Sept. 2012), pp. 1029–1054. URL: https://hal.archives-ouvertes.fr/hal-00976983 (cit. on p. 71).

[10] G. FACCANONI and H. MATHIS. "Admissible Equations of State for Immiscible and Miscible Mixtures". In: *ESAIM: Proceedings and Surveys* (2019). URL: https://hal.archives-ouvertes.fr/tel-00363460 (cit. on pp. 69, 72, 136).

[11] H. GHAZI. "Modelling compressible flows with phase transition and metastable states". Theses. Université de Nantes, Nov. 2018. URL: https://tel.archives-ouvertes.fr/tel-01976189 (cit. on pp. 67, 74, 81).

[12] H. GHAZI, F. JAMES, and H. MATHIS. "A nonisothermal thermodynamical model of liquid-vapor interaction with metastability". working paper or preprint. Oct. 2019. URL: https://hal.archives-ouvertes.fr/hal-02336478 (cit. on pp. 67, 74, 81).

[13] V. GIOVANGIGLI and L. MATUSZEWSKI. "Supercritical fluid thermodynamics from equations of state". In: *Physica D: Nonlinear Phenomena* 241.6 (2012), pp. 649–670. DOI: https://doi.org/10.1016/j.physd.2011.12.002 (cit. on pp. 67, 81, 82, 84).

[14] A. R. GOODWIN, J. SENGERS, and C. J. PETERS. *Applied Thermodynamics of Fluids*. The Royal Society of Chemistry, 2011, P001–509. DOI: http://dx.doi.org/10.1039/9781849730983 (cit. on pp. 67, 80).

[15] J. GROSS and G. SADOWSKI. "Perturbed-chain SAFT: An equation of state based on a perturbation theory for chain molecules". In: *Industrial & engineering chemistry research* 40.4 (2001), pp. 1244–1260. DOI: https://doi.org/10.1021/ie0003887 (cit. on p. 84).

[16] O. HURISSE. "Application of an homogeneous model to simulate the heating of two-phase flows". In: *International Journal on Finite Volumes* 11 (May 2014), http://www.latp.univ-mrs.fr/IJFV/spip.php?article52. URL: https://hal.archives-ouvertes.fr/hal-01114808 (cit. on p. 72).

[17] O. HURISSE. "Numerical simulations of steady and unsteady two-phase flows using a homogeneous model". In: *Computers and Fluids* 152 (July 2017), pp. 88–103. URL: https://hal.archives-ouvertes.fr/hal-01489039 (cit. on pp. 72, 73).

[18] A. JAMALI, A. P. VINHAL, H. BEHNEJAD, W. YAN, and G. M. KONTOGEORGIS. "Comparison of two crossover procedures for describing thermodynamic behavior of normal alkanes from singular critical to regular classical regions". In: *Fluid Phase Equilibria* 495 (2019), pp. 33–46. DOI: https://doi.org/10.1016/j.fluid.2019.04.030 (cit. on p. 74).

[19] F. JAMES and H. MATHIS. "A Relaxation model for liquid-vapor phase change with metastability". In: *Communications in Mathematical Sciences* 74.8 (2016), pp. 2179–2214. DOI: 10.4310/CMS.2016.v14.n8.a4. URL: https://hal.archives-ouvertes.fr/hal-01178947 (cit. on pp. 67, 74, 81).

[20] J. JANECEK, P. PARICAUD, M. DICKO, and C. COQUELET. "A generalized Kiselev crossover approach applied to Soave–Redlich–Kwong equation of state". In: *Fluid Phase Equilibria* 401 (2015), pp. 16–26. DOI: 10.1016/j.fluid.2015.04.024. URL: https://hal-mines-paristech.archives-ouvertes.fr/hal-01158602 (cit. on p. 74).

[21] C. JEFFERY and P. AUSTIN. "A new analytic equation of state for liquid water". In: *The Journal of chemical physics* 110.1 (1999), pp. 484–496. DOI: https://doi.org/10.1063/1.477977 (cit. on pp. 68, 80).

[22] R. J. KEE, F. M. RUPLEY, E. MEEKS, and J. A. MILLER. *CHEMKIN-III: A FORTRAN chemical kinetics package for the analysis of gas-phase chemical and plasma kinetics*. Tech. rep. Sandia National Labs., Livermore, CA (United States), 1996. URL: https://www.osti.gov/biblio/481621 (cit. on pp. 67, 77, 78).

[23] S. KISELEV. "Cubic crossover equation of state". In: *Fluid Phase Equilibria* 147.1-2 (1998), pp. 7–23. DOI: https://doi.org/10.1016/S0378-3812(98)00222-2 (cit. on p. 74).

[24] S. KISELEV, I. KOSTYUKOVA, and A. POVODYREV. "Universal crossover behavior of fluids and fluid mixtures in the critical region". In: *International Journal of Thermophysics* 12.5 (1991), pp. 877–895. DOI: https://doi.org/10.1007/BF00502413 (cit. on p. 74).

[25] G. M. KONTOGEORGIS, M. L. MICHELSEN, G. K. FOLAS, S. DERAWI, N. von SOLMS, and E. H. STENBY. "Ten years with the CPA (Cubic-Plus-Association) equation of state. Part 1. Pure compounds and self-associating systems". In: *Industrial & engineering chemistry research* 45.14 (2006), pp. 4855–4868. DOI: https://doi.org/10.1021/ie051305v (cit. on p. 84).

[26] Y. LE GUENNEC, S. LASALA, R. PRIVAT, and J.-N. JAUBERT. "A consistency test for α-functions of cubic equations of state". In: *Fluid Phase Equilibria* (Nov. 2016). DOI: 10.1016/j.fluid.2016.07.026. URL: https://hal.archives-ouvertes.fr/hal-01413873 (cit. on p. 84).

[27] O. LE MÉTAYER and R. SAUREL. "The Noble-Abel Stiffened-Gas equation of state". In: *Physics of Fluids* 28 (2016), p. 046102. DOI: 10.1063/1.4945981. URL: https://hal.archives-ouvertes.fr/hal-01305974 (cit. on pp. 67, 77).

[28] H. MATHIS. "Theoretical and numerical study of phase transition flows". PhD thesis. Université de Strasbourg, Sept. 2010. URL: https://tel.archives-ouvertes.fr/tel-00516683 (cit. on pp. 69, 72).

[29] H. MENG and V. YANG. "A unified treatment of general fluid thermodynamics and its application to a preconditioning scheme". In: *Journal of Computational Physics* 189.1 (2003), pp. 277–304. DOI: https://doi.org/10.1016/S0021-9991(03)00211-0 (cit. on p. 67).

[30] Q. NODÉ-LANGLOIS. *Loi analytique des états thermodynamiques de l'eau : formulation standard et nouvelle approche physique.* Tech. rep. EDF report, H-T63-2012-03217-FR, 2012 (cit. on pp. 68, 80).

[31] K. O'HARA. *Optimlib library*. 2018. URL: https://www.kthohr.com/optimlib.html (cit. on p. 86).

[32] A. PÉNELOUX, E. RAUZY, and R. FRÉZE. "A consistent correction for Redlich-Kwong-Soave volumes". In: *Fluid phase equilibria* 8.1 (1982), pp. 7–23. DOI: http://dx.doi.org/10.1016/0378-3812(82)80002-2 (cit. on p. 84).

[33] D.-Y. PENG and D. B. ROBINSON. "A new two-constant equation of state". In: *Industrial & Engineering Chemistry Fundamentals* 15.1 (1976), pp. 59–64. DOI: https://doi.org/10.1021/i160057a011 (cit. on p. 81).

[34] R. PRIVAT. "Développement du modèle PPR78 pour décrire, comprendre et prédire les diagrammes de phases hautes et basses pressions des systèmes binaires et des fluides pétroliers". PhD thesis. Institut National Polytechnique de Lorraine, 2008. URL: https://hal.univ-lorraine.fr/tel-01753008 (cit. on pp. 67, 80–82, 105, 130).

[35] L. QUIBEL, P. HELLUY, M. CHION, and P. RICKA. *Mélanger des gaz raides pour créer de nouvelles lois d'état*. Research Report. IRMA, Université de Strasbourg ; EDF R&D, Apr. 2019. URL: https://hal.archives-ouvertes.fr/hal-02114552 (cit. on pp. 68, 86).

[36] O. REDLICH and J. N. KWONG. "On the thermodynamics of solutions. V. An equation of state. Fugacities of gaseous solutions." In: *Chemical reviews* 44.1 (1949), pp. 233–244. DOI: https://doi.org/10.1021/cr60137a013 (cit. on p. 81).

[37] J. V. SENGERS, R. KAYSER, C. PETERS, and H. WHITE. *Equations of state for fluids and fluid mixtures*. Vol. 5. Elsevier, 2000 (cit. on p. 74).

[38] J. Y. SEYF. "Evaluation of the PR, tc-PR, CPA, PC-SAFT and IAPWS-95 models in the predicting thermodynamic properties of pure water at the supercooled, compressed liquid, saturated liquid-vapor and superheat regions". In: *Journal of Molecular Liquids* (2019), p. 111088. DOI: https://doi.org/10.1016/j.molliq.2019.111088 (cit. on p. 84).

[39] G. SOAVE. "Equilibrium constants from a modified Redlich-Kwong equation of state". In: *Chemical engineering science* 27.6 (1972), pp. 1197–1203. DOI: https://doi.org/10.1016/0009-2509(72)80096-4 (cit. on pp. 67, 81).

[40] Y. VENTIKOS and G. TZABIRAS. "A numerical method for the simulation of steady and unsteady cavitating flows". In: *Computers & Fluids* 29.1 (2000), pp. 63–88. DOI: http://dx.doi.org/10.1016/S0045-7930(98)00061-9 (cit. on p. 67).

[41] W. WAGNER and H.-J. KRETZSCHMAR. *International Steam Tables: Properties of Water and Steam Based on the Industrial Formulation IAPWS-IF97*. Springer-Verlag Berlin Heidelberg, 2008. ISBN: 9783540742340. DOI: http://dx.doi.org/10.1007/978-3-540-74234-0 (cit. on pp. 67, 75).

[42] W. WAGNER and A. PRUSS. "The IAPWS formulation 1995 for the thermodynamic properties of ordinary water substance for general and scientific use". In: *Journal of physical and chemical reference data* 31.2 (2002), pp. 387–535. DOI: https://doi.org/10.1063/1.1461829 (cit. on pp. 68, 75).

Appendices

2.A Empirical method to estimate SG coefficients

In order to estimate the coefficients for a stiffened gas EOS, an empirical method has been proposed in [6]:

1. A point (p_0, T_0) of the physical domain is chosen as reference point. It should be representative of the aimed simulation. The following thermodynamical quantities are obtained with the IAPWS-97 formulation: the specific volume $\tau_0(p_0, T_0)$, as well as the sound speed $c_0(p_0, T_0)$.

2. A temperature step ΔT is arbitrary chosen, so that : $T_1 = T_0 - \Delta T; T_2 = T_0 + \Delta T$. Two reference enthalpies are then computed with the IAPWS-97 formulation : $h_1(P_0, T_1)$ et $h_2(P_0, T_2)$. We recall that $h = e + P\tau$ and that enthalpy can be written for stiffened gas EOS: $h = C_p T + Q$.

3. Then, stiffened gas coefficients are obtained:

$$C_p = \frac{h_1 - h_2}{T_1 - T_2}; \quad Q = \frac{T_2 h_1 - T_1 h_2}{T_2 - T_1}; \quad \gamma = c_0^2/(C_p T_0) + 1$$

$$C_v = \frac{C_p}{\gamma}; \quad \Pi = (\gamma - 1) C_v T_0 \rho_0 - P_0$$

4. Finally, we chose in this work to fix s^0 so that $\mu^{SG}(P_0, T_0) = \mu^{IAPWS}(P_0, T_0)$.

2.B Maths-companies study group report (Strasbourg, November 2018): "Mixture of gases to build complex equations of state" (in French).

Rapport SEME, EDF R&D : Mélanger des gaz raides pour créer de nouvelles lois d'état

Lucie Quibel, Philippe Helluy, Marie Chion, Philippe Ricka

12-16 Novembre 2018

Abstract : EDF needs reliable numerical simulations of two-phase flow phenomena for safety issue. Some hypothetical accidental scenarios involve rapid transients with important mass transfer. A model able to account for thermodynamical disequilibria may be needed. Currently, to describe each phase, the codes use either simple analytical equations of state like the stiffened gas equation of state, realistic only around a reference point ; or look-up tables of complex equations of state, CPU-time consuming. During the "Semaine d'Etudes Maths Entreprise" (SEME), we wondered if the water steam could be approached by a stiffened gas or a mix of two stiffened gases. We first conducted an analysis of thermodynamics equations in order to formulate a state equation in the (p, T) plane, before building a parameters optimization algorithm to approximate the IAPWS-97 formulation, the reference equation of state for water built from a set of measurements.

Keywords : modeling, thermodynamics, optimization, stiffened gas.

Résumé : EDF réalise des études numériques afin de consolider la démonstration de sûreté du parc nucléaire. Afin de simuler des scénarii accidentels pouvant hypothétiquement affecter le réacteur, les codes de calculs doivent être en mesure de représenter des situations physiques complexes, fortement instationnaires avec une thermodynamique potentiellement hors-équilibre. A l'heure actuelle, les codes utilisent soit des lois d'états phasiques assez simples, de type gaz raides, réalistes uniquement près d'un point de fonctionnement ; soit des tabulations, coûteuses en temps de calcul. L'objectif de ce travail est de proposer des lois d'états réalistes pour l'eau, mais qui restent relativement simples analytiquement. Pendant la Semaine d'Etudes Maths Entreprise" (SEME), nous nous sommes intéressés à la modélisation de la vapeur d'eau. Notre idée de départ est la suivante : la vapeur d'eau peut-elle être modélisée par un mélange de deux gaz raides ? Nous avons d'abord mené une analyse des équations de la thermodynamique de façon à formuler une équation d'état dans le plan (p, T). Nous avons ensuite implémenté un algorithme pour optimiser les paramètres de ces équations afin de minimiser l'écart avec la formulation IAPWS-97, qui sert ici de loi d'état de référence pour l'eau.

Mots-clefs : modélisation, thermodynamique, optimisation, gaz raide.

Table des matières

Introduction

Afin de consolider la démonstration de sûreté des installations nucléaires, EDF réalise des simulations numériques de scénarii accidentels pouvant hypothétiquement affecter le réacteur. Un exemple classique est l'accident par perte de réfrigérant primaire, dans lequel une brèche du circuit primaire est envisagée : de l'eau à $155 bars$ et $300°C$ se retrouverait alors au contact d'air à $1 bar$. L'importante différence de pression entraînerait alors une vaporisation brutale de l'eau, ainsi que la propagation d'une onde de détente faisant rapidement chuter la pression dans le primaire. Pour connaître le plus précisément possible les niveaux de pression au cours d'un tel scénario, il est nécessaire de disposer d'un modèle compressible, capable de simuler des transitions de phase hors équilibre thermodynamique.

La R&D d'EDF développe depuis quelques années un code basé sur le modèle proposé par Helluy-Barberon [1] qui capte les comportements hors équilibre [4]. Un des axes clefs d'amélioration du modèle porte sur les lois d'états utilisées pour décrire l'eau liquide et l'eau vapeur dans le code. Pour l'instant, deux choix sont possibles :

- l'eau liquide et l'eau vapeur sont décrites par des lois d'état très simples de type "gaz raide" (Stiffened Gas) ; ces lois d'état sont analytiques, très simples à utiliser, mais ne sont précises qu'autour d'un point de référence.
- l'eau liquide et l'eau vapeur sont décrites via des lois industrielles de référence, les lois IAPWS-IF97 [7], plus réalistes mais très coûteuses en mémoire et en temps CPU.

D'un point de vue pratique, il serait souhaitable de disposer de lois d'états "intermédiaires", qui seraient à la fois plus réalistes que les lois d'état de gaz raide, mais plus simples et moins coûteuses que les lois IAPWS. Dans le cadre de la Semaine d'Etudes Maths Entreprise (SEME) qui a eu lieu à Strasbourg du 12 au 16 novembre 2018, nous nous sommes proposés de travailler sur l'idée suivante : un mélange miscible de gaz raides peut-il être considéré pour décrire l'eau de façon plus réaliste qu'un seul gaz raide ? Ce sujet a été proposé dans le cadre de la thèse de Lucie Quibel, dirigée par Philippe Helluy et encadrée par Olivier Hurisse.

1 Loi d'état d'un mélange miscible de deux gaz raides

1.1 Notion de plan thermodynamique

Une loi d'état est la donnée d'une fonction dans un plan thermodynamique. Un plan thermodynamique est constitué par deux grandeurs intensives, c'est-à-dire qui ne sont pas proportionnelles à la quantité de matière (par exemple, la température, mais aussi la masse volumique, l'énergie massique etc).

On est amenés en pratique à travailler dans plusieurs plans thermodynamiques : en effet, le plan naturel pour résoudre le système d'équations décrivant le mélange diphasique est le plan (τ, e), où τ est le volume spécifique (m^3kg^{-1}) et e est l'énergie interne spécifique (Jkg^{-1}), alors que le plan le plus intuitif pour décrire les changements d'état est le plan (p, T), avec p la pression (Pa) et T la température (K).

1.2 Equation d'état d'un gaz raide

Le gaz raide est une extension du gaz parfait, avec des paramètres supplémentaires permettant de l'adapter à un liquide. La loi d'état de gaz raide est classiquement la donnée de l'entropie dans le plan (τ, e). Celle-ci s'exprime ainsi :

$$s(\tau, e) = C\ln\left((e - Q - \pi\tau)\tau^{\gamma-1}\right) + s_0 \tag{1.1}$$

Les paramètres intervenant dans la loi d'état sont les suivants :
- C $(JK^{-1}kg^{-1})$ est la chaleur massique à volume constant,
- γ est l'exposant polytropique,
- $-\pi$ (Pa) est la pression minimale,
- Q (Jkg^{-1}) est une valeur de référence d'enthalpie,
- s_0 $(JK^{-1}kg^{-1})$ est l'entropie de référence.

Ces paramètres sont calés à l'aide de données expérimentales mesurées en un point de référence [2]. Par conséquent, l'équation est exacte au point de référence, mais sa précision diminue au fur et à mesure qu'on s'en écarte. Afin d'évaluer la qualité d'une loi d'état, il est plus simple de travailler

dans le plan (p, T) : en effet, les visualisations y sont beaucoup plus faciles et intuitives. Changer de plan thermodynamique implique de changer de fonction pour la loi d'état. L'équivalent de l'entropie s dans le plan (τ, e) est la donnée du potentiel chimique μ dans le plan (p, T).

On part de la relation de Gibbs :

$$Tds = de + pd\tau$$

d'où

$$ds = \frac{1}{T}de + \frac{p}{T}d\tau$$

et en particulier :

$$\frac{1}{T} = \left.\frac{\partial s}{\partial e}\right|_\tau \quad ; \quad \frac{p}{T} = \left.\frac{\partial s}{\partial \tau}\right|_e$$

De plus, à partir de la formule de l'entropie pour un gaz raide, on a :

$$\left.\frac{\partial s}{\partial e}\right|_\tau = \frac{C}{e - Q - \pi\tau} \; ; \; \left.\frac{\partial s}{\partial \tau}\right|_e = \frac{(\gamma-1)C}{\tau} - \frac{\pi C}{e - Q - \pi\tau}$$

d'où finalement :

$$CT = e - Q - \pi\tau \; ; \; p + \pi = (\gamma - 1)\rho CT.$$

La définition du potentiel chimique μ est la suivante :

$$\mu = e - Ts + p\tau.$$

A partir des relations précédentes, on peut finalement exprimer le potentiel chimique μ d'un gaz raide uniquement en fonction de (p, T) et des coefficients :

$$\boxed{\mu(p,T) = \gamma C T + Q - T(\gamma C \ln(T) - (\gamma - 1) C \ln(p + \pi) + K)}$$

où l'on a introduit K $(JK^{-1}kg^{-1})$ qui regroupe des termes constants.

Cette équation d'état est une équation complète : cela signifie que l'on peut retrouver toutes les grandeurs thermodynamiques à partir des dérivées partielles de μ par rapport à p et à T.

— **À partir des dérivées premières** de μ, on calcule l'entropie spécifique s $(JK^{-1}kg^{-1})$ et le volume spécifique τ (m^3kg^{-1}) :

$$\left.\frac{\partial \mu}{\partial T}\right|_P = -s \quad ; \quad \left.\frac{\partial \mu}{\partial p}\right|_T = \tau.$$

— **À partir des dérivées secondes** de μ, on calcule la capacité thermique à pression constante C_p $(JK^{-1}kg^{-1})$, le coefficient de dilatation thermique isobare α_p (K^{-1}) et le coefficient de compressibilité isotherme χ_T (Pa^{-1}) :

$$-T \left.\frac{\partial^2 \mu}{\partial T^2}\right|_P = C_p \quad ; \quad \frac{1}{\tau} \left.\frac{\partial^2 \mu}{\partial p \partial T}\right|_{T,p} = \alpha_p \quad ; \quad -\frac{1}{\tau} \left.\frac{\partial^2 \mu}{\partial p^2}\right|_T = \chi_T.$$

1.3 Mélange miscible de deux gaz raides

On considère un mélange de deux gaz miscibles. Dans un mélange miscible, on suppose que les deux gaz raides sont à l'**équilibre thermodynamique**. On peut montrer que cela se traduit par les égalités suivantes [3] :

$$\begin{cases} p = p_1 + p_2 \\ T_1 = T_2 \\ \mu_1 = \mu_2 \end{cases} \tag{1}$$

On souhaite trouver l'équation d'état du mélange à une pression de mélange p et une température de mélange T données. On peut réexprimer le système (1) ainsi : il faut trouver la pression p_1 d'équilibre entre les deux gaz, telle que :

$$f(p_1) = \mu_1(p_1, T) - \mu_2(p - p_1, T) = 0 \tag{2}$$

où :

$$f(p_1) = (\gamma_1 C_1 - \gamma_2 C_2)T + Q_1 - Q_2 - T[(\gamma_1 C_1 - \gamma_2 C_2)\ln(T) - (\gamma_1 - 1)C_1 \ln(p_1 + \pi_1) + (\gamma_2 - 1)C_2 \ln(p - p_1 + \pi_2) + K_1 - K_2]$$

Les inégalités suivantes doivent être vérifiées :

$$\begin{cases} p_1 + \pi_1 > 0 \\ p - p_1 + \pi_2 > 0 \\ -\pi_1 < p_1 < p + \pi_2 \end{cases}$$

En examinant notre fonction f, et en particulier son comportement lorsque $p_1 \to -\pi 1$ et $p_1 \to p + \pi_2$, on remarque qu'elle est monotone, change de signe, et par conséquent admet un zéro sur cet intervalle. Ainsi, l'équation 2 possède une unique solution : l'équation d'état de mélange miscible de deux gaz raides est bien définie. Finalement, l'équation d'état de mélange deux gaz raides dans le plan (p, T)

est la suivante :

$$\boxed{\mu^{MIX}(p,T) = \mu_1(p_1, T) = \mu_2(p - p_1, T)}$$

avec p_1 la solution de l'équation 2.

1.4 Vitesse du son

La vitesse du son s'exprime aussi à partir des dérivées secondes de μ. En effet par définition :

$$c^2 = \left(\frac{\partial p}{\partial \tau}\right)\Big|_s^{-1} = -\frac{\tau^2}{\left(\frac{\partial \tau}{\partial p}\right)\Big|_s}.$$

Or

$$\left(\frac{\partial \tau}{\partial p}\right)\Big|_s = \frac{\partial}{\partial p}\Big(\tau(p, T(p,s))\Big)\Big|_s = \left(\frac{\partial \tau}{\partial p}\right)\Big|_T + \left(\frac{\partial \tau}{\partial T}\right)\Big|_p \left(\frac{\partial T}{\partial p}\right)\Big|_s$$

et

$$ds = \left(\frac{\partial s}{\partial p}\right)\Big|_T dp + \left(\frac{\partial s}{\partial T}\right)\Big|_p dT$$

donne

$$\left(\frac{\partial T}{\partial p}\right)\Big|_s = -\frac{\left(\frac{\partial s}{\partial p}\right)\Big|_T}{\left(\frac{\partial s}{\partial T}\right)\Big|_P}.$$

D'où :

$$c^2 = -\tau^2 / \left(\left(\frac{\partial \tau}{\partial p}\right)\Big|_T - \left(\frac{\partial \tau}{\partial T}\right)\Big|_p \frac{\left(\frac{\partial s}{\partial p}\right)\Big|_T}{\left(\frac{\partial s}{\partial T}\right)\Big|_P} \right),$$

qui se réécrit en utilisant $\left.\frac{\partial \mu}{\partial T}\right|_P = -s$; $\left.\frac{\partial \mu}{\partial p}\right|_T = \tau$ et $-T\left.\frac{\partial^2 \mu}{\partial T^2}\right|_P = C_p$; $\frac{1}{\tau}\left.\frac{\partial^2 \mu}{\partial p \partial T}\right|_{T,p} = \alpha_p$; $-\frac{1}{\tau}\left.\frac{\partial^2 \mu}{\partial p^2}\right|_T = \chi_T$:

$$c^2 = \left(\frac{\chi_T}{\tau} - \frac{T\alpha_P^2}{C_p}\right)^{-1}. \tag{3}$$

2 Loi de référence industrielle : IAPWS-IF97

La loi IAPWS-IF97 [7] est la loi d'état industrielle de référence pour décrire l'eau. Il s'agit d'une loi analytique, obtenue à partir d'une interpolation d'un très grand nombre de données expérimentales. Dans notre travail, nous avons utilisé IAPWS pour nous constituer un set de données dans le plan (p,T) : $\mu(p,T)$, $\tau(p,T)$, $s(p,T)$, $C_p(p,T)$, $\alpha_p(p,T)$ et $\chi_T(p,T)$. Nous avons pris ces données comme des références, que notre loi d'état construite à partir de deux gaz raides doit reproduire le plus fidèlement possible.

3 Méthode d'optimisation du mélange de gaz raides

Étant donnée une carte de valeurs expérimentales μ^{IAPWS} dans le plan (p,T), notre objectif est de déterminer les valeurs des paramètres de deux gaz raides miscibles pour lesquelles la loi du mélange μ^{MIX} est en adéquation avec les données calculées avec IAPWS. Notre travail ayant une visée prédictive, nous entendons par "adéquation" la minimisation de l'erreur quadratique moyenne normalisée : $E(\gamma_1, C_1, Q_1, \pi_1, K_1, \gamma_2, C_2, Q_2, \pi_2, K_2) = E(\text{param}_1, \text{param}_2)$ avec

$$
\begin{aligned}
E(\text{param}_1, \text{param}_2) &= \frac{\|\mu^{IAPWS} - \mu^{MIX}\|_2}{\|\mu^{IAPWS}\|_2} \\
&+ \frac{\|s^{IAPWS} - s^{MIX}\|_2}{\|s^{IAPWS}\|_2} + \frac{\|\tau^{IAPWS} - \tau^{MIX}\|_2}{\|\tau^{IAPWS}\|_2} \\
&+ \frac{\|C_p^{IAPWS} - C_p^{MIX}\|_2}{\|C_p^{IAPWS}\|_2} + \frac{\|\alpha_p^{IAPWS} - \alpha_p^{MIX}\|_2}{\|\alpha_p^{IAPWS}\|_2} + \frac{\|{\chi_T}^{IAPWS} - {\chi_T}^{MIX}\|_2}{\|\chi_T^{IAPWS}\|_2}.
\end{aligned}
$$

La fonction coût comprend également les écarts de capacité thermique isobare C_p, de dilatation isobare α_P, de compressibilité isotherme χ_T, d'entropie s et de volume spécifique τ car ces grandeurs correspondent aux dérivées premières et secondes μ par rapport à p et T. En effet, caler également les dérivées est important pour que notre loi d'état puisse être utilisée en pratique : si les dérivées sont trop irréalistes, il est probable que notre loi d'état ne nous permettent pas de changer de plan thermodynamique correctement. On rappelle que :

$$\mu^{MIX}(p, T) = \mu_1(p_1, T) = \mu_2(p - p_1, T)$$

où p_1 est donné implicitement. Ainsi, p_1 est donc une fonction de l'ensemble des paramètres de chacun des gaz impliqués et des variables, c'est à dire :

$$p_1 = p_1(p, T, \gamma_1, C_1, Q_1, \pi_1, K_1, \gamma_2, C_2, Q_2, \pi_2, K_2)$$

En pratique, la valeur de p_1 pour un tel jeu de paramètres est déterminée grâce à la méthode de Newton appliquée au problème :

$$f(p_1) = \mu_1(p_1, T) - \mu_2(P - p_1, T) = 0$$

Le problème à deux gaz raides peut se formuler de la manière suivante :

$$
\left|
\begin{array}{l}
\text{trouver } \{\gamma_1, C_1, Q_1, \pi_1, K_1, \gamma_2, C_2, Q_2, \pi_2, K_2\} \\
\text{minimisant } E(\gamma_1, C_1, Q_1, \pi_1, K_1, \gamma_2, C_2, Q_2, \pi_2, K_2).
\end{array}
\right.
$$

Pour chaque jeu de paramètres $(\gamma_1, C_1, Q_1, \pi_1, K_1, \gamma_2, C_2, Q_2, \pi_2, K_2)$ on doit donc calculer les six grandeurs de mélange Φ^{MIX} à l'aide de la pression p_1 obtenue implicitement par résolution d'un algorithme de Newton.

4 Implémentation pratique

Nous avons implémenté la méthode d'optimisation des coefficients avec différents outils :

1. R : la résolution du calcul implicite de la pression p_1 par une méthode de Newton a posé problème (manque de précision).
2. Python : un algorithme a été implémenté, avec une fonction de coût tenant compte seulement de l'écart entre les potentiels chimiques μ pendant la SEME. L'algorithme converge trop lentement pour obtenir des résultats en pratique. La méthode exploitée est celle du gradient descendant, appliquée à la fonction d'erreur normalisée :

$$E(\gamma_1, C_1, Q_1, \pi_1, K_1, \gamma_2, C_2, Q_2, \pi_2, K_2) = \frac{\|\mu^{IAPWS} - \mu^{MIX}\|_2}{\|\mu^{IAPWS}\|_2}$$

Les grandes différences dans les ordres de grandeurs des différentes quantités impliquées ainsi que la sensibilité de μ aux variations de ces quantités nous ont conduites à utiliser la bibliothèque python `mpmath` permettant d'augmenter arbitrairement la précision des calculs. Des simulations ont été réalisées avec 10, 15 et 50 chiffres significatifs. Dans le premier cas,

la précision n'était pas suffisante pour que l'algorithme converge. Dans les deux autres cas, l'erreur décroît visiblement, mais à une vitesse bien trop faible pour permettre de répondre à notre question en un temps raisonnable. Toutefois, plusieurs améliorations pourraient être réalisées, qui augmenteraient sensiblement la vitesse de calcul. En particulier, certains segments de l'algorithme se prêtent bien à la parallélisation.

3. C++ : deux stratégies ont été implémentées :
   — un algorithme de gradient a été implémenté, utilisant la bibliothèque "multiprecision" de boost (MPFR) [5]
   — un algorithme en double précision appelant la bibliothèque Optimlib [6].
   En pratique, la précision arbitraire n'a finalement pas été utilisée : elle n'améliore pas les résultats obtenus en double précision, mais ralentit significativement le calcul. Parmi les algorithmes de la librairie Optimlib, les algorithmes de Nelder-Mead et de Particle Swarm Optimization sont suffisamment robustes pour permettre de diminuer significativement l'erreur. Néanmoins, nous ne sommes pas parvenus à faire diminuer l'erreur autant que souhaité. Notre critère d'arrêt est ici purement pragmatique : les paramètres d'optimisation sont les paramètres considérés comme optimisés si les algorithmes de Nelder-Mead ou de Particle Swarm Optimization n'en trouvent pas de meilleurs après 5000 itérations.

5 Résultats

Le but est de fitter un gaz raide ou un mélange de gaz raide sur des données IAPWS, sur des domaines plus ou moins étendus qui nous semblent plus ou moins simples à réprésenter par un gaz raide :

1. un domaine vapeur étendu (P variant de 40 bar à 210 bar, T variant de 700 K à 100 K) ;
2. un domaine vapeur restreint (P variant de 0.5 bar à 25 bar, T variant de 550 K à 1000K) ;
3. un domaine liquide "difficile" (P variant de 0.5 bar à 210 bar, T variant de 275 K à 350 K) ;
4. un domaine liquide "facile" (P variant de 0.8 bar à 210 bar, T variant de 350 K à 500 K) ;

Le travail n'est pas encore terminé et des résultats sont toujours en cours d'obtention. Après avoir fait quelques commentaires sur notre méthode (section 5.1), nous présentons quelques premiers résultats pour le cas 1 avec un domaine vapeur étendu (section 5.2).

5.1 Quelques commentaires sur la méthode utilisée

— Dans l'optimisation d'un seul gaz raide, nous connaissons un point de départ simple, obtenu grâce à la méthode empirique classiquement utilisée pour caler les paramètres d'un gaz raide (voir annexe). Pour le cas de mélange, le point de départ est choisi arbitrairement, ce qui demande très certainement à être amélioré.

— Le mélange miscible de deux fois le même gaz raide n'est pas le gaz raide lui-même (voir annexe). Par conséquent, même si l'intuition nous dit qu'on doit pouvoir faire mieux avec un mélange à 10 coefficients qu'avec un gaz raide à 5 paramètres, on n'est pas sûrs d'y parvenir en pratique.

— L'adimensionnement par rapport aux données calculées au point de référence, y-compris des paramètres de la loi d'état, ainsi que la normalisation des écarts par les normes de μ^{IAPWS}, s^{IAPWS}, τ^{IAPWS}, $\mathbb{C}_p^{IAPWS}$, α_p^{IAPWS} et χ_T^{IAPWS} sont deux éléments clefs pour que l'optimisation agisse bien sur l'ensemble des coefficients. Dans nos premiers essais sans adimensionnement, le rôle de γ était prépondérant et rendait négligeable l'influence des autres paramètres.

— Nous cherchons encore dans les tests en cours à déterminer l'importance relative des écarts dans la fonctionnelle E. Faut-il vraiment optimiser les écarts sur les six grandeurs μ, s, τ, C_p, α_p, χ_T ? Faut-il optimiser en priorité les grandeurs τ, C_p, α_p, χ_T ? En effet, elles nous semblent caractériser le fluide de manière plus fondamentale que μ et s, dont les valeurs

ne sont données qu'à une valeur de référence près. Faut-il pondérer les écarts avec des coefficients à déterminer ? Ce sont des pistes ouvertes que nous essayons encore d'explorer.

5.2 Cas Vapeur, 40b-210b, 700K-1000K

Le domaine d'étude est montré sur la figure 1. C'est un domaine vapeur étendu, assez régulier

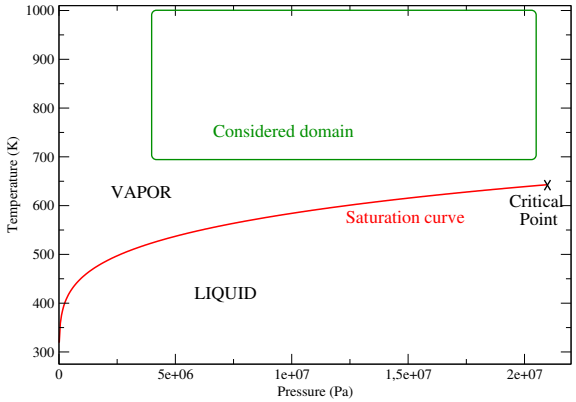

FIGURE 1: Plan pT et domaine d'étude pour le cas vapeur 40b-210b, 700K-1000K

donc classiquement plutôt bien représenté par une équation de gaz raide. La fonctionnelle utilisée dans cet exemple est la suivante :

$$
\begin{aligned}
E(\text{param}_1, \text{param}_2) = \quad &= \quad \frac{\|\mu^{IAPWS} - \mu^{MIX}\|_2}{\|\mu^{IAPWS}\|_2} \\
&+ \quad \frac{\|s^{IAPWS} - s^{MIX}\|_2}{\|s^{IAPWS}\|_2} + \frac{\|\tau^{IAPWS} - \tau^{MIX}\|_2}{\|\tau^{IAPWS}\|_2} \\
&+ \quad \frac{\|C_p^{IAPWS} - C_p^{MIX}\|_2}{\|C_p^{IAPWS}\|_2} + \frac{\|\alpha_p^{IAPWS} - \alpha_p^{MIX}\|_2}{\|\alpha_p^{IAPWS}\|_2} + \frac{\|{\chi_T}^{IAPWS} - {\chi_T}^{MIX}\|_2}{\|\chi_T^{IAPWS}\|_2}.
\end{aligned}
$$

Les tables qui suivent présentent les coefficients des gaz raides considérés :

- sur la table 1, on trouve les coefficients du gaz raide initial, calé avec la méthode empirique (voir annexe 1) et ceux du gaz raide optimisé ;
- sur la table 2, on trouve les coefficients des deux gaz raides constituant le mélange optimisé.

Coefficients	Gaz raide initial (méthode empirique)	Un seul gaz raide optimisé
γ	1.214477077	1.20145802133373e+00
$C\ (JK^{-1}kg^{-1})$	2.108076293e+03	2.13920664140770e+03
$Q\ (Jkg^{-1})$	1.369643105e+06	1.41694137339728e+06
$\pi\ (Pa)$	6.315490501e+05	-2.37137965486010e+05
$K\ (JK^{-1}kg^{-1})$	-3.14402501406409e+03	-3.57678186497858e+03

TABLE 1: Gaz raide de référence et coefficients du gaz raide optimisé

Coefficients	Gaz 1 du mélange optimisé	Gaz 2 du mélange optimisé
γ	1.20311950806197e+00	1.19466896995444e+00
C $(JK^{-1}kg^{-1})$	2.03207400575592e+03	2.32919476948296e+03
Q (Jkg^{-1})	1.38800916756918e+06	1.52312801605455e+06
π (Pa)	6.57340674871949e+06	-6.82721810684994e+06
K $(JK^{-1}kg^{-1})$	6.46385664735901e+03	6.55679096146362e+03

TABLE 2: Coefficients des deux gaz raides du mélange miscible optimisé

L'optimisation permet d'obtenir des coefficients en général proches des coefficients du gaz raide initial calé empiriquement (sauf pour le π). Le meilleur mélange est constitué de deux gaz raides assez proches l'un de l'autre (sauf les π) : pour autant, il est difficile d'en tirer une conclusion, car le mélange de deux gaz raides identiques n'a pas exactement la même équation d'état que le gaz raide initial (voir annexe 2). Les résultats sont donnés sur la table 3. L'optimisation permet de faire baisser l'erreur totale de moitié par rapport au gaz raide initial de référence : cependant, le mélange de gaz raides ne fait pas significativement mieux que le meilleur gaz raide optimisé, ce qui paraît surprenant, vu que l'on double le nombre de coefficients utilisés. L'amélioration est plus ou moins importante suivant la grandeur considérée.

- Le mélange est plus précis qu'un seul gaz raide pour μ, τ, C_p. On peut d'ailleurs noter que pour améliorer la précision sur les dérivéees, le gaz raide optimisé détériore d'un demi-ordre de grandeur la précision sur μ, alors que le mélange parvient à améliorer la précision sur μ tout en améliorant certaines dérivées.
- Le mélange est moins précis qu'un seul gaz raide pour s et χ_T, mais les écarts sont assez faibles.
- Mélange et gaz sont précis de la même manière sur α_p.

Erreurs	Gaz raide initial	Un seul gaz raide optimisé	Mélange optimisé
Erreur totale	4.78866218924500e-02	2.57292995555250e-02	2.39562743862582e-02
Erreur μ	1.64485602593960e-05	4.36455573529491e-04	1.05615437908557e-05
Erreur τ	7.54984994462873e-03	1.02017962651521e-03	8.14583537509500e-04
Erreur s	1.07952848308229e-04	9.54886315568107e-05	1.82357435983658e-04
Erreur C_p	1.92417437049477e-02	1.89677880568179e-02	1.77333060740906e-02
Erreur α_p	1.40366102175399e-03	1.40366102175399e-03	1.40366102175400e-03
Erreur χ_T	1.95669658125537e-02	3.80572664535179e-03	3.81180477312983e-03

TABLE 3: Somme des erreurs relatives en chaque point du domaine entre les données IAPWS et le gaz raide initial calé par la méthode empirique, un gaz raide optimisé et un mélange miscible de deux gaz raides optimisé. Les contributions à l'erreur totale pour chaque grandeur sont aussi présentées.

Enfin, nous présentons à titre d'illustration des cartes d'erreur relative par rapport à la référence IAPWS pour μ (figures 2, 3, 4), τ (figures 5, 6, 7) et s (figures 8, 9, 10). Ces résultats sont encourageants :

- la précision du mélange optimisé sur μ et τ est meilleure sur des domaines un peu plus étendus par rapport au gaz raide initial, sans dégradation dans les zones initialement bien estimées ;
- la dégradation de la précision pour l'entropie du mélange par rapport au gaz raide initial reste assez limitée et diffuse sur l'ensemble du domaine ;
- le meilleur gaz raide dégrade la précision μ de manière assez importante dans zone haute pression basse température du domaine. Pour ce gaz, il n'y a plus de zone à erreur quasi nulle, contrairement au gaz de départ et au mélange optimisé.

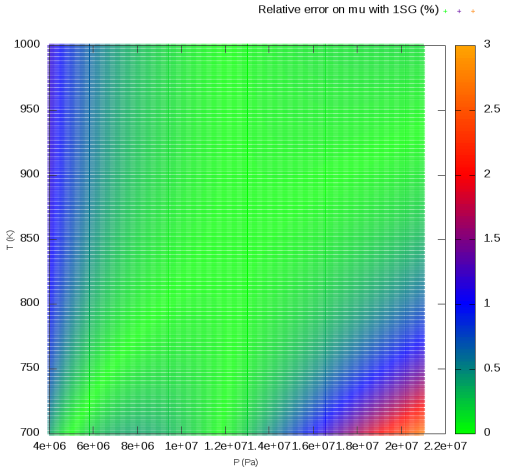

FIGURE 2: Erreur relative sur μ par rapport à IAPWS pour le gaz raide initial

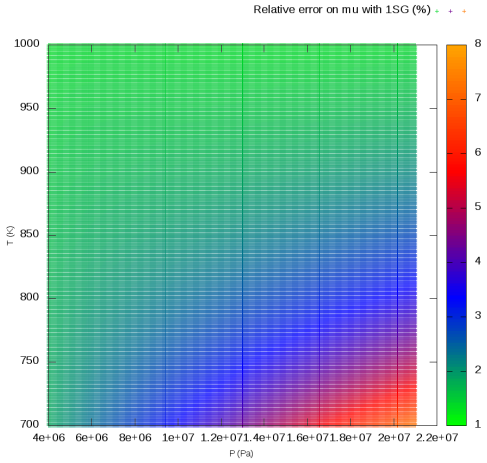

FIGURE 3: Erreur relative sur μ par rapport à IAPWS pour le gaz raide optimisé

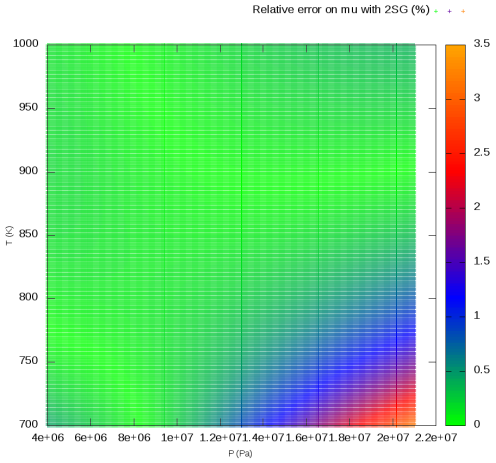

FIGURE 4: Erreur relative sur μ par rapport à IAPWS pour le mélange optimisé

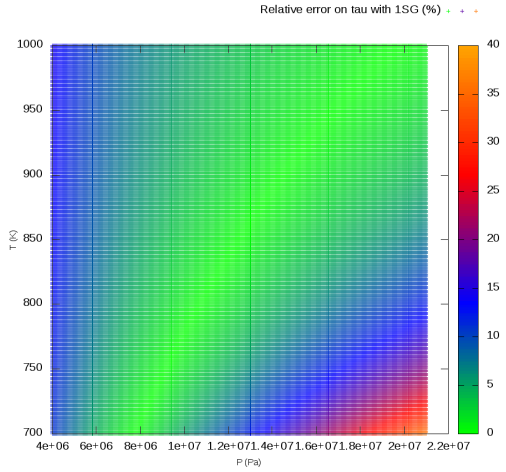

FIGURE 5: Erreur relative initiale sur τ

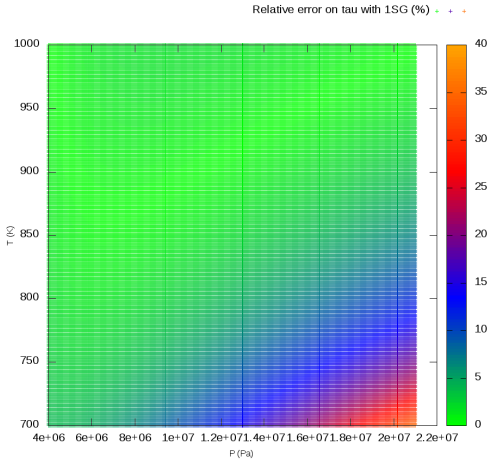

FIGURE 6: Erreur relative sur τ par rapport à IAPWS pour le gaz raide optimisé

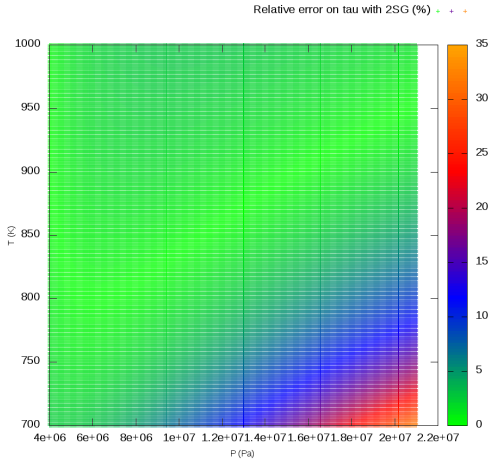

FIGURE 7: Erreur relative sur τ par rapport à IAPWS pour le mélange optimisé

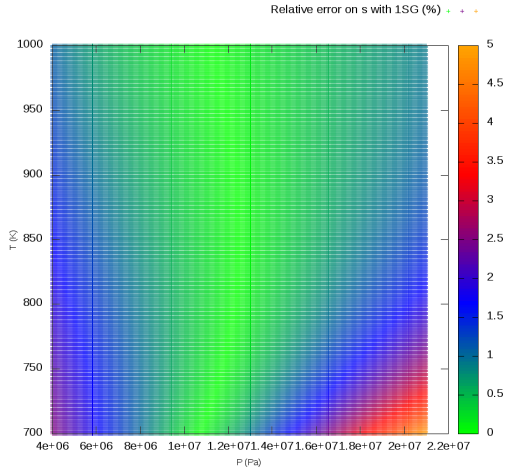

FIGURE 8: Erreur relative initiale sur s

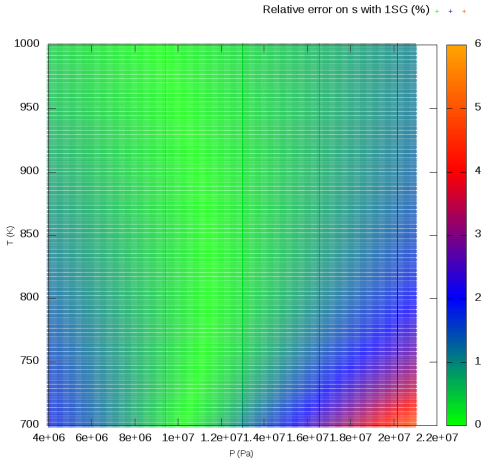

FIGURE 9: Erreur relative sur s par rapport à IAPWS pour le gaz raide optimisé

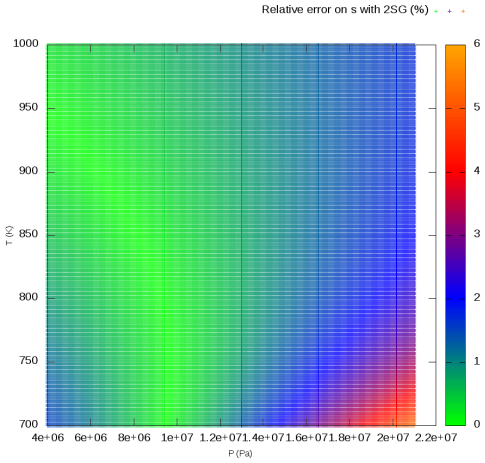

FIGURE 10: Erreur relative sur s par rapport à IAPWS pour le mélange optimisé

Conclusions

Afin de créer des lois d'état plus réalistes pour l'eau, nous avons implémenté une méthode d'optimisation de paramètres afin de fitter des gaz raides ou un mélange miscible de gaz raides à des données de référence dans le plan (p,T).

La loi d'état d'un mélange miscible de deux gaz raides n'est pas analytique dans le plan (p, T) : une inversion via un algorithme de Newton est nécessaire.

Le problème d'optimisation est difficile à résoudre en pratique : la convergence des algorithmes n'a pu être menée à bien. Différentes pistes ont été explorées pour résoudre ce problème :

— la sur-sensibilité de certains coefficients a été maîtrisée par l'admimensionnement par rapport à un point de référence central dans le domaine ;

— les inversions thermodynamiques nécessitent une bonne maîtrise de la précision : la résolution de l'algorithme de Newton pour le calcul de la loi de mélange a posé problème dans R. Néanmoins, la précision arbitraire n'a pas résolu les difficultés de convergence des algorithme d'optimisation.

Optimiser un gaz raide ou un mélange de gaz raide permet de réduire l'erreur totale sur μ, τ, s, C_p, α_p et χ_T de moitié par rapport au gaz raide de référence calé empiriquement. Le mélange de gaz raides donne de meilleurs résultats que le gaz raide optimisé, notamment sur μ. Cependant, nous nous attendions à une amélioration plus signficative par rapport à un seul gaz raide car le mélange double le nombre de paramètres de la loi d'état. Ces résultats sont tout de même encourageants et des études complémentaires sont en cours :

— D'autres domaines thermodynamiques vont être considérés, sur lesquels l'équation d'état de gaz raide est connue pour être moins précise.

— Parmi les pistes à explorer, la plus prometteuse concerne la pondération des écarts dans la fonctionnelle : faut-il optimiser sur toutes les grandeurs thermodynamiques avec des pondération différentes ? seulement sur les dérivées secondes ?

— Il est possible que la loi de gaz raide soit "trop régulière" pour être réaliste. D'autres lois d'état pourraient être mélangées pour obtenir des mélanges plus complexes.

Références

[1] T. Barberon and P. Helluy. Finite volume simulation of cavitating flows. *Computers and Fluids*, 34(7) :832–858, 2005.

[2] F. Daude, P. Galon, Z. Gao, and E. Blaud. Numerical experiments using a hllc-type scheme with ale formulation for compressible two-phase flows five-equation models with phase transition. *Computers & Fluids*, 94 :112–138, 05 2014.

[3] Gloria Faccanoni and Hélène Mathis. Admissible Equations of State for Immiscible and Miscible Mixtures. working paper or preprint, November 2018.

[4] O. Hurisse. Numerical simulations of steady and unsteady two-phase flows using a homogeneous model. *Computers and Fluids*, 2017, `https://hal.archives-ouvertes.fr/hal-01489039/file/numerical-homogeneous-two-phase-2016.pdf`.

[5] John Maddock and Christopher Kormanyos. Boost multiprecision library, 2002.

[6] Keith O'Hara. Optimlib library, 2018.

[7] W. Wagner and H.-J. Kretzschmar. *International Steam Tables : Properties of Water and Steam Based on the Industrial Formulation IAPWS-IF97*. Springer-Verlag Berlin Heidelberg, 2008.

Annexe 1 : Méthode empirique pour caler un gaz raide

La méthode de calage empirique des coefficients d'un gaz raide, définie à l'aide de [2], est la suivante :

1. On choisit un point de référence, représentatif de l'état physique dominant la simulation : (p_0, T_0). On obtient à l'aide de la loi IAPWS le volume spécifique $\tau_0(p_0, T_0)$ ainsi que la vitesse du son $c_0(p_0, T_0)$ pour cet état physique (p_0, T_0).

2. On fixe arbitrairement un ΔT tel que : $T_1 = T_0 - \Delta T; T_2 = T_0 + \Delta T$ On calcule ainsi deux enthalpies de référence à l'aide de IAPWS : $h_1(P_0, T_1)$ et $h_2(P_0, T_2)$.

3. On obtient les coefficients du gaz raide grâce aux apprixmations suivantes :

$$C_p = \frac{h_1 - h_2}{T_1 - T_2}; \quad Q = \frac{T_2 h_1 - T_1 h_2}{T_2 - T_1}; \quad \gamma = c_0^2/(C_p T_0) + 1$$

$$C_v = \frac{C_p}{\gamma}; \quad \Pi = (\gamma - 1) C_v T_0 \rho_0 - P_0$$

4. On fixe enfin e^{SG} et s^{SG} en définissant s^0 de façon à caler $\mu^{SG} = \mu^{IAPWS}(P_0, T_0)$.

Annexe 2 : Mélange miscible d'un même gaz raide

Nous considérons un gaz raide avec les coefficients $\text{param}_0 = (\gamma_0, C_0, Q_0, \Pi_0, K_0)$. On considère le mélange miscible de ce gaz avec lui-même. Dans le cas général :

$$\mu^{MIX}(p, T) = \mu_1(p_1, T) = \mu_2(p - p_1, T).$$

Dans le cas particulier que l'on considère :

$$\mu^{SAME}(p, T) = \mu_0(p_1, T) = \mu_0(p - p_1, T)$$

avec

$$\mu_0(p, T) = \gamma_0 C_0 T + Q_0 - T(\gamma_0 C_0 \ln(T) - (\gamma_0 - 1) C_0 \ln(p + \pi_0) + K_0).$$

L'équation $\mu_0(p_1, T) = \mu_0(p - p_1, T)$ nous donne :

$$\boxed{p_1 = \frac{p}{2}}.$$

Finalement :

$$\mu^{SAME}(p, T) = \mu_0(\frac{p}{2}, T).$$

Or :

$$\mu_0(\frac{p}{2}, T) = \mu_0(p, T) + T(\gamma_0 - 1) C \ln\left(1 - \frac{p}{2(p + \pi_0)}\right).$$

D'où :

$$\mu^{SAME}(p, T) = \mu_0(p, T) + T(\gamma_0 - 1) C_0 \ln\left(1 - \frac{p}{2(p + \pi_0)}\right)$$

On ne retrouve pas la même équation d'état ! Le terme supplémentaire dépend de T et de p donc va également jouer sur les dérivées de μ.

Chapter 3

A homogeneous two-phase flow model with non-condensable gas, using Noble-Able-Chemkin EOS

Introduction

In the framework of nuclear safety demonstration for pressurized water reactors, some accidental scenarii are studied (see IRSN website [33]). For instance, in case of loss of coolant accident (LOCA), pressurized water may undergo a brutal depressurization, leading to a rapid mass transfer. Such scenarii involve complex compressible two-phase flow mixtures, undergoing fast transient situations with phase transition. In addition to liquid and vapor water, other gases may be present: indeed, ambiant air may be mixed with vapor through the free surface of water, or hydrogen might appear under accidental conditions because of fuel oxydation. The proportion of non-condensable gas compared with water vapor is a parameter of importance, appearing to limit the steam condensation, as it has been beared out by experimental studies [28] as well as numerical studies [2]. Non-condensable gas is besides taken into account in the reference industrial codes classically used to simulate a vapor explosion [42, 5].

The flows of interest in this work are thus mixtures of the two following components:

- a liquid and its associated vapor (water is considered in the following), with phase transition which may occur between both phases;
- non-condensable gas, such as air.

Many models have been proposed since decades to simulate two-phase flow mixtures of liquid and vapor water. One may distinguish two main types of models:

- the so-called two-fluid model as those proposed in [3, 18, 35, 9, 17], where each phase is described by its own velocity and where the full thermodynamical disequilibrium is accounted for, in terms of pressure, temperature and chemical potential;
- the so-called homogeneous models, where all the fields have the same velocity; often, at least one additional equilibrium assumption is made (in terms of pressure, temperature...), as in [37, 1, 13, 14, 19, 12, 16]) , whereas there is no other equilibrium assumption in the model proposed in [4].

Both strategies are of interest and the choice between one or the other type of model should be made depending on the targeted applications. For instance, when dealing with accidental

scenarii such as vapor explosion, evaluating the velocity gaps between phases is very important to correctly take into account the interfacial transfers due to the dislocation of droplets, driving the heat transfer between phases (see [6, 42]). However, in terms of numerical costs, the two-velocity assumption imposes more constraints on mesh cell size, compared with an homogeneous approach, which may be restrictive for some industrial simulations.

Less references exist for two-phase flow mixtures involving an additional inert gas. Still, the same classification arises, and two-fluid-type models dealing with liquid water and miscible mixtures of steam water and gas have been proposed in [27] or [26]. Here, we chose to work on a direct extension of the homogeneous two-phase flow model proposed in [4] and studied for instance in [30, 24]. Note that a homogeneous three-phase flow model, also based on [4], has been built in [32], to deal with immiscible mixtures of three fields: we need in our present case either a model tackling both miscible and immiscible phases. The main difficulty when dealing with such homogeneous models is to build consistent thermodynamical quantities as well as a mixture equation of state complying with the second principle of thermodynamics.

Such a work has been already done in [20] for a homogeneous model with non-condensable gas. In this reference, the associated HEM model is first studied; then, two HRM models are proposed: a model without phase transition with an equilibrium in terms of chemical potential as well as a HRM model with no further equilibrium assumption than the kinematic equilibrium. The associated HEM model had been already simulated in [2], by taking advantage of some particular properties of the model equipped with stiffened gas phasic equations of state (EOS): with this particular choice for phasic EOS, the obtained mixture EOS is indeed very simple since it can be written itself as a stiffened gas EOS with coefficients depending on the non-condensable gas fraction.

In this work, we first detail in section 3.1 the modelling approach leading to the second HRM model introduced in [20]. This model copes with full disequilibrium mixtures in terms of pressure, temperature and chemical potentials: the only equilibrium assumption is the kinematic equilibrium. The main contribution of the present work is then to propose some numerical simulations based on this model, using a more realistic EOS for the liquid water : a Noble-Able Stiffened Gas (NASG) EOS (see [39], modified with the Chemkin EOS [38], as proposed in [7], called NASG-CK EOS in the sequel and described in section 3.2. Our numerical method, briefly recalled in section 3.3, relies on finite volume convective schemes and has already been implemented in similar contexts for instance in [30, 24]: we insist here above all on the thermodynamical equilibrium computation, somehow tricky due to the presence of the non-condensable gas. Note that another numerical work based on the same model has been proposed in [25] using stiffened gas EOS, but dealing with Lattice-Boltzmann method. Last, numerical results are presented: first, the code is assessed by convergence studies on several Riemann problems in section 3.4; then, some validation cases are presented in section 3.5.

3.1 Homogeneous two-phase flow model with non-condensable gas

In this section, the homogeneous model used in this work is presented. It has been built following a similar approach as the one depicted for instance in [4, 24, 32]. That is why only the main features of the model are recalled here. In particular, we insist on the miscibility assumptions as well as on the thermodynamical building, which are the less classical parts of the modelling.

For sake of readibility, a field will be designated by a subscript $k \in \mathcal{K} = \{l, v, a\}$, with l refering to liquid water, v to vapor water and a to non-condensable gas.

3.1.1 Kinematic equilibrium and general assumptions

Hypothesis 3.1
Kinematic equilibrium is assumed in the model for all fields. As a consequence, there is only one velocity U $(m.s^{-1})$ in the model, so that:

$$U = U_l = U_v = U_a. \tag{3.1}$$

□

It implies that the derivative of a given quantity Φ along a streamline does not depend on the subscript $k \in \mathcal{K}$:

$$d_k\Phi = (\partial_t\Phi + U_k\partial_x\Phi)\,dt = (\partial_t\Phi + U\partial_x\Phi)\,dt = d\Phi. \tag{3.2}$$

Note that only the kinematic equilibrium is assumed: all the other quantities (such pressures or temperatures) may be different for each field.

Moreover, the following simplifying assumptions are made:

Hypothesis 3.2
The exact geometric repartition of each field in a given amount of mixture is not known and the surface tension is neglected.

Hypothesis 3.3
Vaccuum occurence is not considered.

3.1.2 Extensive description of the considered flows

Each field $k \in \mathcal{K}$ can be described thanks to three extensive variables, like for instance in [36]: its volume $\mathcal{V}_k \geq 0$ (in m^3), its mass $\mathcal{M}_k \geq 0$ (in kg) and its internal energy $\mathcal{E}_k$ (in J). Similarly, the entire mixture can be depicted by its volume $\mathcal{V} > 0$ (in m^3), its mass $\mathcal{M} > 0$ (in kg) and its internal energy $\mathcal{E} \neq 0$ (in J). In the following, we note:

$$\Omega_k = \{W_k = (\mathcal{V}_k, \mathcal{M}_k, \mathcal{E}_k) \;/\; \mathcal{V}_k \geq 0, \mathcal{M}_k \geq 0\} \quad ; \quad \Omega = \{W = (\mathcal{V}, \mathcal{M}, \mathcal{E}) \;/\; \mathcal{V} > 0, \mathcal{M} > 0\},$$

$$\Omega_{lva} = \{W_{lva} = (W_l, W_v, W_a) \;/\; \forall k \in \mathcal{K}, W_k \in \Omega_k\}.$$

Remark 3.1 — Hypothesis 3.3 implies that there exists at least one subscript $k \in \mathcal{K}$ so that : $\Omega_k = \{W_k = (\mathcal{V}_k, \mathcal{M}_k, \mathcal{E}_k) \;/\; \mathcal{V}_k > 0, \mathcal{M}_k > 0 \text{ and } \mathcal{E}_k \neq 0\}$. □

3.1.2.1 Hybrid miscibility conditions

Hypothesis 3.4 (Miscibility constraints)
Considering a given amount of fluid characterized by $W = (\mathcal{V}, \mathcal{M}, \mathcal{E}) \in \Omega$, it can be depicted as a mixture of two **immiscible** phases:

- a liquid phase with only liquid water;
- a gaseous phase (designated by the subscript g), which is a **miscible** mixture of vapor water and non-condensable gas. □

Thanks to hypothesis 3.2, ideal miscibility and immiscibility conditions can be written, as proposed for instance in [23]. The miscibility condition for the gaseous phase leads to:

$$\begin{cases} \mathcal{V}_g = \mathcal{V}_v = \mathcal{V}_a; \\ \mathcal{M}_g = \mathcal{M}_v + \mathcal{M}_a; \\ \mathcal{E}_g = \mathcal{E}_v + \mathcal{E}_a, \end{cases} \tag{3.3}$$

whereas the immiscibility condition for the liquid-gas mixture leads to:

$$\begin{cases} \mathcal{V} = \mathcal{V}_l + \mathcal{V}_g; \\ \mathcal{M} = \mathcal{M}_l + \mathcal{M}_g; \\ \mathcal{E} = \mathcal{E}_l + \mathcal{E}_g, \end{cases} \tag{3.4}$$

Relations (3.3) and (3.4) can be rewritten with only subscripts in $\mathcal{K}$ as:

$$\begin{cases} \mathcal{V} = \mathcal{V}_l + \mathcal{V}_v = \mathcal{V}_l + \mathcal{V}_a; \\ \mathcal{M} = \mathcal{M}_l + \mathcal{M}_v + \mathcal{M}_a; \\ \mathcal{E} = \mathcal{E}_l + \mathcal{E}_v + \mathcal{E}_a. \end{cases} \tag{3.5}$$

Then, considering $W = (\mathcal{V}, \mathcal{M}, \mathcal{E}) \in \Omega$, we note $\Omega_{lva}(W)$ the subset of all the mixtures characterized by W verifying the miscibility conditions (3.5), i.e.:

$$\Omega_{lva}(W) = \{W_{lva} \in \Omega_{lva} \,/\, \mathcal{V} = \mathcal{V}_l + \mathcal{V}_v = \mathcal{V}_l + \mathcal{V}_a,\ \mathcal{M} = \mathcal{M}_l + \mathcal{M}_v + \mathcal{M}_a,\ \mathcal{E} = \mathcal{E}_l + \mathcal{E}_v + \mathcal{E}_a.\}.$$

Moreover, since a is a non-condensable gas, the following hypothesis holds:

Hypothesis 3.5
A mass of non-condensable gas $\mathcal{M}_a$ is only convected within the flow. Then, when considering a fixed mass of mixture $\mathcal{M} = \mathcal{M}_l + \mathcal{M}_v + \mathcal{M}_a$ (i.e. a closed system), the mass of non-condensable gas $\mathcal{M}_a$ inside $\mathcal{M}$ remains constant within time:

$$d\mathcal{M} = 0 \quad \Longrightarrow \quad d\mathcal{M}_a = 0 \ \ \& \ \ d\mathcal{M}_l = -d\mathcal{M}_v.$$

□

Remark 3.2 — Note that conditions (3.4) are exactly those considered when building the model [4] from extensive variables in [24], except that the gaseous phase is now a miscible mixture of vapor and non-condensable gas, instead of pure vapor. □

Last, we introduce the phasic fractions, which will be very useful in the following. For any $k \in \mathcal{K}$, we note α_k the volume fraction of the field k within the flow, y_k the mass fraction and z_k the energy fraction, defined as follows:

$$\alpha_k = \frac{\mathcal{V}_k}{\mathcal{V}} \quad ; \quad y_k = \frac{\mathcal{M}_k}{\mathcal{M}} \quad ; \quad z_k = \frac{\mathcal{E}_k}{\mathcal{E}}. \tag{3.6}$$

Relation (3.5) can be rewritten as:

$$\left\{ \begin{array}{rcll} 1 & = & \alpha_l + \alpha_v & \text{and} \quad \alpha_v = \alpha_a; \\ 1 & = & y_l + y_v + y_a; & \\ 1 & = & z_l + z_v + z_a. & \end{array} \right. \tag{3.7}$$

Thanks to the miscibility constraints (3.7), only one volume fraction, two mass fractions and two energy fractions are required to completely describe the system. In the following, we arbitrarily choose α_v, y_v, y_a, z_v and z_a. The liquid fractions are then deduced from the gaseous fractions and from (3.7).

Hypothesis 3.6 (Monophasic cases or cases with one missing field)
One phase or one field may be absent:

- if vapor water v (respectively non-condensable gas a) is absent, then $\mathcal{M}_v = 0$, $\mathcal{V}_v = 0$ and $\mathcal{E}_v = 0$ (resp. $\mathcal{M}_a = 0$, $\mathcal{V}_a = 0$ and $\mathcal{E}_a = 0$), so that conditions (3.5) and (3.7) become:

$$\forall k \in \{v, a\} \quad \left\{ \begin{array}{l} \mathcal{V} = \mathcal{V}_l + \mathcal{V}_k; \\ \mathcal{M} = \mathcal{M}_l + \mathcal{M}_k; \\ \mathcal{E} = \mathcal{E}_l + \mathcal{E}_k; \end{array} \right. \quad \text{and} \quad \left\{ \begin{array}{rcl} 1 & = & \alpha_l + \alpha_k; \\ 1 & = & y_l + y_k; \\ 1 & = & z_l + z_k. \end{array} \right. \tag{3.8}$$

- if liquid water is absent, then $\mathcal{M}_l = 0$, $\mathcal{V}_l = 0$ and $\mathcal{E}_l \neq 0$, so that conditions (3.5) and (3.7) become:

$$\left\{ \begin{array}{l} \mathcal{V} = \mathcal{V}_v = \mathcal{V}_a; \\ \mathcal{M} = \mathcal{M}_v + \mathcal{M}_a; \\ \mathcal{E} = \mathcal{E}_v + \mathcal{E}_a; \end{array} \right. \quad \text{and} \quad \left\{ \begin{array}{rcl} 1 & = & \alpha_v = \alpha_a; \\ 1 & = & y_v + y_a; \\ 1 & = & z_v + z_a. \end{array} \right. \tag{3.9}$$

- pure monophasic cases l, v or a are also possible. □

The states with only l and a or the states with only v and a lead to degenerate equilibrium hypotheses that will be described in property 3.4.

3.1.2.2 Chosen approach in order to derive the equations

The same approach as [32, 24] (among other references) is used to derive the model equations. A given amount of fluid characterized by the mixture quantities $W = (\mathcal{V}, \mathcal{M}, \mathcal{E}) \in \Omega$ is considered. By adopting a Lagrangian point of view, the modelling is proceeded in two steps:

1. first, the fluid element is considered as fixed, closed and isolated from the rest of the flow: its evolution should comply with the second principle of thermodynamics;

2. then, the interaction with the surrounding fluid is considered: the fluid element should evolve within time in accordance with Newton laws and the first principle of thermodynamics.

The second step is exactly the same as the one used for instance in [32, 24]: the approach leads to depict the mixture by Euler-type equations for the mixture quantities, i.e. density, momentum and total energy. The reader can refer to the previous references or to [4, 15, 34, 21, 41, 36, 30, 32] to have more details. We only highlight that hypothesis 3.1 and operator (3.2) are the key ingredients to derive the equations.

The first step allows to properly define the mixture thermodynamical quantities such as pressure and to build equations and source terms enabling to return towards the thermodynamical equilibrium within time. The thermodynamical behavior of the considered mixtures of l, v and a with hybrid miscibility constraints has already been studied in [20]. In the rest of the section, we will derive a similar approach, adapted to our model framework.

3.1.2.3 Equation of state (EOS) for each field

In order to close the system, a complete equation of state (EOS) is required for each field $k \in \mathcal{K}$. As in [30, 32, 24], a natural way to define such an EOS is to consider an extensive entropy $W_k \in \Omega_k \mapsto S_k(W_k)$ (in $J.K^{-1}$) as thermodynamical potential for each field $k \in \mathcal{K}$, with $W_k = (\mathcal{V}_k, \mathcal{M}_k, \mathcal{E}_k)$.

In order to ensure the hyperbolicity of the final model, some properties are required for each k-field EOS $W_k \in \Omega_k \mapsto S_k(W_k)$ (see section 3.1.4).

Property 3.1 (Required properties for a k-field EOS $W_k \in \Omega_k \mapsto S_k(W_k)$)
A k-field EOS $W_k \in \Omega_k \mapsto S_k(W_k)$ is an admissible EOS ensuring the hyperbolicity of the final model (see [32, 24] and section 3.1.4) if the following properties hold:

$$\begin{array}{ll} (I) & W_k \in \Omega_k \mapsto S_k(W_k) \text{ is } \mathcal{C}^2. \\ (II) & W_k \in \Omega_k \mapsto S_k(W_k) \text{ is concave.} \\ (III) & \forall a \in \mathbb{R}^+, \forall W_k \in \Omega_k,\ S_k(aW_k) = aS_k(W_k). \\ (IV) & \forall W_k \in \Omega_k,\ \left.\dfrac{\partial S_k}{\partial \mathcal{E}_k}\right|_{\mathcal{V}_k,\mathcal{E}_k} > 0. \end{array}$$

□

In agreement with the Classical Irreversible Thermodynamics (CIT) theory, the classical Gibbs relation holds for each field $k \in \mathcal{K}$:

$$T_k d_k \mathcal{S}_k = d_k \mathcal{E}_k + P_k d_k \mathcal{V}_k - \mu_k d_k \mathcal{M}_k, \tag{3.10}$$

which can be rewritten thanks to (3.2) as:

$$T_k d\mathcal{S}_k = d\mathcal{E}_k + P_k d\mathcal{V}_k - \mu_k d\mathcal{M}_k. \tag{3.11}$$

Since $S_k(\mathcal{V}_k, \mathcal{M}_k, \mathcal{E}_k)$ is a complete EOS for field k, all the thermodynamical quantitites can be computed thanks to the derivatives of S_k:

Definition 3.1 (Thermodynamical quantities for a k-field)
Considering a field $k \in \mathcal{K}$, its pressure P_k (in Pa), its temperature T_k (in K) and its Gibbs free enthalpy μ_k (in $J.kg^{-1}$) can be derived in accordance with the chosen complete EOS $W_k \in \Omega_k \mapsto S_k(W_k)$, thanks to the Gibbs relation (3.11):

$$\frac{P_k}{T_k} = \left.\frac{\partial S_k}{\partial \mathcal{V}_k}\right|_{\mathcal{M}_k,\mathcal{E}_k}, \tag{3.12}$$

$$\frac{1}{T_k} = \left.\frac{\partial S_k}{\partial \mathcal{E}_k}\right|_{\mathcal{V}_k,\mathcal{M}_k} > 0, \tag{3.13}$$

$$\frac{\mu_k}{T_k} = -\left.\frac{\partial S_k}{\partial \mathcal{M}_k}\right|_{\mathcal{V}_k,\mathcal{E}_k}. \tag{3.14}$$

□

3.1.2.4 Defining the thermodynamical quantities for the mixture

Definition 3.2 (Mixture entropy S)
Recalling that $W_k = (\mathcal{V}_k, \mathcal{M}_k, \mathcal{E}_k) \in \Omega_k$, we consider $W_{lva} = (W_l, W_v, W_a)$ and $W = (\mathcal{V}, \mathcal{M}, \mathcal{E}) \in \Omega$ so that $W_{lva} \in \Omega_{lva}(W)$. As in [20], we define the entropy of the mixture S as:

$$W \in \Omega \mapsto S(W) = S_l(W_l) + S_v(W_v) + S_a(W_a). \tag{3.15}$$

□

Note that the previous definition of the mixture entropy (3.15) is in accordance with the ideal miscibility conditions (3.5) that we have previously assumed. However, it should be modified if surface tension (or other effects, see [17]) had to be accounted for.

From (3.15) and (3.11) and using operator (3.2), a Gibbs relation for the mixture entropy S can be derived after simple computations using the relation $d\Phi_k = \Phi d\left(\frac{\Phi_k}{\Phi}\right) + \frac{\Phi_k}{\Phi} d\Phi$ and the definition of the fractions (3.6).

Definition 3.3 (Mixture quantities)
A mixture pressure P (Pa), a mixture temperature T (in K) and a mixture Gibbs enthalpy μ (in $J.kg^{-1}$) can be exhibited by identifying them in the following mixture Gibbs relation:

$$\begin{aligned} dS &= \frac{1}{T}\left(Pd\mathcal{V} - \mu d\mathcal{M} + d\mathcal{E}\right) \\ &+ \mathcal{V}\sum_{k\in\mathcal{K}} \frac{P_k}{T_k} d\alpha_k \\ &- \mathcal{M}\sum_{k\in\mathcal{K}} \frac{\mu_k}{T_k} dy_k \\ &+ \mathcal{E}\sum_{k\in\mathcal{K}} \frac{1}{T_k} dz_k. \end{aligned} \tag{3.16}$$

They read:

$$\frac{P}{T} = \sum_{k\in\mathcal{K}} \alpha_k \frac{P_k}{T_k}, \tag{3.17}$$

$$\frac{\mu}{T} = \sum_{k\in\mathcal{K}} y_k \frac{\mu_k}{T_k}, \tag{3.18}$$

$$\frac{1}{T} = \sum_{k\in\mathcal{K}} z_k \frac{1}{T_k}. \tag{3.19}$$

□

We interpret Gibbs relation (3.16) as follows:

- the first part $\frac{1}{T}\left(Pd\mathcal{V} - \mu d\mathcal{M} + d\mathcal{E}\right)$ gathers terms due to the mixture itself; they vanish when the flow element is considered as fixed, closed and isolated from the rest of the flows, at it will be studied in section 3.1.2.5.
- the second part $\mathcal{V}\sum_{k\in\mathcal{K}} \frac{P_k}{T_k} d\alpha_k - \mathcal{M}\sum_{k\in\mathcal{K}} \frac{\mu_k}{T_k} dy_k + \mathcal{E}\sum_{k\in\mathcal{K}} \frac{1}{T_k} dz_k$ gather exchange terms between the three fields.

3.1.2.5 Second principle of thermodynamics and thermodynamical equilibrium

In this section we consider a closed system isolated from the rest of the flow : a fixed amount of mixture characterized by $W = (\mathcal{V}, \mathcal{M}, \mathcal{E}) \in \Omega$. It implies now:

$$d\mathcal{V} = 0 \quad ; \quad d\mathcal{M} = 0 \quad ; \quad d\mathcal{E} = 0.$$

More precisely, we consider all the physical states $W_{lva} = (W_l, W_v, W_a) \in \Omega_{lva}(W)$.

Recalling the hypothesis 3.5 due to the non-condensable gas, we have $d\mathcal{M}_a = 0$ and $d\mathcal{M}_l = -d\mathcal{M}_v$, i.e.:

$$dy_a = 0 \quad \text{and} \quad dy_l = -dy_v.$$

Moreover, thanks to the miscibility conditions (3.5), Gibbs relation can be rewritten as a function of α_v, y_v, y_a, z_v and z_a, since:

$$\alpha_l = 1 - \alpha_v \quad \text{and} \quad \alpha_v = \alpha_a \quad ; \quad y_l = 1 - y_v - y_a \quad ; \quad z_l = 1 - z_v - z_a.$$

Then, for the considered isolated system, Gibbs relation (3.16) can thus be simplified as follows:

$$\begin{aligned} dS \;=\; & \mathcal{V}\left(\left(\frac{P_v}{T_v} + \frac{P_a}{T_a}\right) - \frac{P_l}{T_l}\right) d\alpha_v \\ + \; & \mathcal{M}\left(\frac{\mu_l}{T_l} - \frac{\mu_v}{T_v}\right) dy_v \\ + \; & \mathcal{E}\left(\frac{1}{T_v} - \frac{1}{T_l}\right) dz_v + \mathcal{E}\left(\frac{1}{T_a} - \frac{1}{T_l}\right) dz_a, \end{aligned} \tag{3.20}$$

which allows to identify the mixture pressure P and the mixture temperature T:

$$P(Y,\tau,e) = \frac{(1-\alpha_v)\frac{P_l}{T_l} + \alpha_v\left(\frac{P_v}{T_v} + \frac{P_a}{T_a}\right)}{\frac{1-z_v-z_a}{T_l} + \frac{z_v}{T_v} + \frac{z_a}{T_a}} \quad ; \quad \frac{1}{T}(Y,\tau,e) = \frac{1-z_v-z_a}{T_l} + \frac{z_v}{T_v} + \frac{z_a}{T_a}. \tag{3.21}$$

In order to comply with the second principle of thermodynamics, we have to postulate some form for $d\alpha_k$, dy_k and dz_k, ensuring that the mixture entropy will increase for the considered isolated system, i.e. so that $dS \geq 0$, with dS defined through the Gibbs relation (3.20).

Hypothesis 3.7
As initially proposed in [4], we assume the following time evolution for the fractions:

$$\begin{cases} \forall k \in \mathcal{K},\ d\alpha_k = \dfrac{\bar{\alpha_k} - \alpha_k}{\lambda} \\ \forall k \in \{l, v\},\ dy_k = \dfrac{\bar{y_k} - y_k}{\lambda} \quad \text{and} \quad dy_a = 0, \\ \forall k \in \mathcal{K},\ dz_k = \dfrac{\bar{z_k} - z_k}{\lambda}, \end{cases} \tag{3.22}$$

□

where $\lambda > 0$ and for all $k \in \mathcal{K}$, $\bar{\alpha_k} = \dfrac{\bar{V_k}}{V}$, $\bar{y_k} = \dfrac{\bar{M_k}}{M}$ and $\bar{z_k} = \dfrac{\bar{E_k}}{E}$, with $\bar{W}_{lva} = (\bar{W}_l, \bar{W}_v, \bar{W}_a) \in \Omega_{lva}(W)$ the state that the system will asymptotically reach within time. Note that λ may be defined as a function of time, of space, of W... The only constraint on λ is its positivity:

$$\lambda > 0.$$

Property 3.2 (Concavity of the mixture extensive entropy)
S is strictly concave on $\Omega_{lva}(W)$. More details are given in appendix 3.A.

Property 3.3
If $\bar{W}_{lva}$ is defined as the maximum of the mixture entropy S (which exists and is unique thanks to the strict concavity of S), then the second principle is ensured. If the equilibrium state $\bar{W}_{lva}$ is not reached on a border of $\Omega_{lva}(W)$ (that is to say, if $\bar{W}_{lva}$ is a two-phase mixture with all the three fields l, v and a), $\bar{W}_{lva}$ can be characterized by the first order conditions for the existence of extremums, that give here:

$$\begin{cases} T_l(\bar{\mathcal{V}}_l, \bar{\mathcal{M}}_l, \bar{\mathcal{E}}_l) = T_v(\bar{\mathcal{V}}_v, \bar{\mathcal{M}}_v, \bar{\mathcal{E}}_v) = T_a(\bar{\mathcal{V}}_a, \bar{\mathcal{M}}_a, \bar{\mathcal{E}}_a) \\ P_l(\bar{\mathcal{V}}_l, \bar{\mathcal{M}}_l, \bar{\mathcal{E}}_l) = P_v(\bar{\mathcal{V}}_v, \bar{\mathcal{M}}_v, \bar{\mathcal{E}}_v) + P_a(\bar{\mathcal{V}}_a, \bar{\mathcal{M}}_a, \bar{\mathcal{E}}_a) \\ \mu_l(\bar{\mathcal{V}}_l, \bar{\mathcal{M}}_l, \bar{\mathcal{E}}_l) = \mu_v(\bar{\mathcal{V}}_v, \bar{\mathcal{M}}_v, \bar{\mathcal{E}}_v). \end{cases} \tag{3.23}$$

□

The second equilibrium coincides with the Dalton law.

Property 3.4 (Equilibrium states with one or two missing fields)
The thermodynamical equilibrium may be reached on a border of $\Omega_{lva}(W)$ and then, conditions (3.23) are no more relevant. Depending on the present components, the following conditions should be used to determine the thermodynamical equilibrium:

- with a two-phase mixture of liquid and steam water: the same conditions as for instance [30, 24] hold:
$$\begin{cases} T_l(\bar{\mathcal{V}}_l, \bar{\mathcal{M}}_l, \bar{\mathcal{E}}_l) = T_v(\bar{\mathcal{V}}_v, \bar{\mathcal{M}}_v, \bar{\mathcal{E}}_v) \\ P_l(\bar{\mathcal{V}}_l, \bar{\mathcal{M}}_l, \bar{\mathcal{E}}_l) = P_v(\bar{\mathcal{V}}_v, \bar{\mathcal{M}}_v, \bar{\mathcal{E}}_v) \\ \mu_l(\bar{\mathcal{V}}_l, \bar{\mathcal{M}}_l, \bar{\mathcal{E}}_l) = \mu_v(\bar{\mathcal{V}}_v, \bar{\mathcal{M}}_v, \bar{\mathcal{E}}_v). \end{cases} \tag{3.24}$$
- with a non-miscible two-phase mixture of liquid water and non-condensable gas (l and a), the following conditions hold, since no phase transition occurs:
$$\begin{cases} T_l(\bar{\mathcal{V}}_l, \bar{\mathcal{M}}_l, \bar{\mathcal{E}}_l) = T_a(\bar{\mathcal{V}}_a, \bar{\mathcal{M}}_a, \bar{\mathcal{E}}_a) \\ P_l(\bar{\mathcal{V}}_l, \bar{\mathcal{M}}_l, \bar{\mathcal{E}}_l) = P_a(\bar{\mathcal{V}}_a, \bar{\mathcal{M}}_a, \bar{\mathcal{E}}_a). \end{cases} \tag{3.25}$$
- with a miscible monophasic gaseous mixture vapor water and non-condensable gas (v and a), only one condition remains:
$$T_v(\bar{\mathcal{V}}_v, \bar{\mathcal{M}}_v, \bar{\mathcal{E}}_v) = T_a(\bar{\mathcal{V}}_a, \bar{\mathcal{M}}_a, \bar{\mathcal{E}}_a). \tag{3.26}$$

□

3.1.3 Final system of equations

3.1.3.1 Intensive quantities

We introduce some notations for the intensive quantities:

- $\rho = \frac{\mathcal{M}}{\mathcal{V}}$ stands for the density (in $kg.m^{-3}$);
- $\tau = \frac{1}{\rho} = \frac{\mathcal{V}}{\mathcal{M}}$ for the specific volume;
- $e = \frac{\mathcal{E}}{\mathcal{M}}$ stands for the specific internal energy (in $J.kg^{-1}$), $E = e + \frac{1}{2}|U|^2$ for the total specific energy;
- $s = \frac{\mathcal{S}}{\mathcal{M}}$ stands for the specific entropy (in $J.K^{-1}.kg^{-1}$).

A quantity Φ without a subscript designates a mixture quantity, whereas a quantity Φ_k refers to field $k \in \mathcal{K}$.

3.1.3.2 Final system of partial differential equations (PDE)

Finally, the model can be written with the intensive variables, by applying Newton laws and first principle of thermodynamics (see [24]) and by using the source terms (3.22) exhibited in the previous section:

$$\left\{\begin{array}{l}
\dfrac{\partial}{\partial t}(\rho\alpha_v)+\dfrac{\partial}{\partial x}(\rho U\alpha_v)=\rho\dfrac{(\bar{\alpha_v}-\alpha_v)}{\lambda},\\
\dfrac{\partial}{\partial t}(\rho y_v)+\dfrac{\partial}{\partial x}(\rho U y_v)=\rho\dfrac{(\bar{y_v}-y_v)}{\lambda},\\
\dfrac{\partial}{\partial t}(\rho y_a)+\dfrac{\partial}{\partial x}(\rho U y_a)=0,\\
\dfrac{\partial}{\partial t}(\rho z_v)+\dfrac{\partial}{\partial x}(\rho U z_v)=\rho\dfrac{(\bar{z_v}-z_v)}{\lambda},\\
\dfrac{\partial}{\partial t}(\rho z_a)+\dfrac{\partial}{\partial x}(\rho U z_a)=\rho\dfrac{(\bar{z_a}-z_a)}{\lambda},\\
\dfrac{\partial}{\partial t}(\rho)+\dfrac{\partial}{\partial x}(\rho U)=0,\\
\dfrac{\partial}{\partial t}(\rho U)+\dfrac{\partial}{\partial x}(\rho U^2+P)=0,\\
\dfrac{\partial}{\partial t}(\rho E)+\dfrac{\partial}{\partial x}(U(\rho E+P))=0.
\end{array}\right. \tag{3.27}$$

We note $Y=(\alpha_v,y_v,y_a,z_v,z_a)$ and we recall the constraints that give α_l, y_l and z_l from Y:

$$\left\{\begin{array}{lcll}
1 & = & \alpha_l+\alpha_v & \& \quad \alpha_v=\alpha_a;\\
1 & = & y_l+y_v+y_a;\\
1 & = & z_l+z_v+z_a.
\end{array}\right.$$

Some useful relations between mixture and phasic quantities can be written:

$$\forall k\in\mathcal{K},\quad \tau_k=\frac{\alpha_k}{y_k}\tau \quad ; \quad e_k=\frac{z_k}{y_k}e. \tag{3.28}$$

In order to close system (3.27), the user must specify one equation of state for each field k (see section 3.2) and a time-scale $\lambda>0$ describing the return to the thermodynamical equilibrium. For the latter, few references exist in the litterature to estimate λ based on physical considerations. For instance, in [24], a proposition has been made, by considering time scales from nucleation theory. In the present work, only instantaneous or quasi-instantaneous return towards equilibrium will be considered, by taking $\lambda\simeq 0$.

The definitions of the thermodynamical quantities introduced in the previous section are rewritten with intensive variables. First, Gibbs relation for a field $k\in\mathcal{K}$ reads:

$$T_k ds_k = de_k + P_k d\tau_k, \tag{3.29}$$

where

$$\frac{1}{T_k}=\left.\frac{\partial s_k}{\partial e_k}\right|_{\tau_k} \quad ; \quad \frac{P_k}{T_k}=\left.\frac{\partial s_k}{\partial \tau_k}\right|_{e_k}. \tag{3.30}$$

Moreover, we recall the definition of the chemical potential μ_k:

$$\mu_k = e_k - T_k s_k + P_k\tau_k. \tag{3.31}$$

The mixture entropy definition (3.15) becomes:

$$s(Y,\tau,e)=(1-y_v-y_a)s_l(\tau_l,e_l)+y_v s_v(\tau_v,e_v)+y_a s_a(\tau_a,e_a), \tag{3.32}$$

so that the mixture Gibbs relation (3.16) gives, since $d\mathcal{M} = 0$:

$$\begin{aligned} ds &= \frac{1}{T}\left(Pd\tau + de\right) + \tau\left(\left(\frac{P_v}{T_v} + \frac{P_a}{T_a}\right) - \frac{P_l}{T_l}\right) d\alpha_v \\ &+ \left(\frac{\mu_l}{T_l} - \frac{\mu_v}{T_v}\right) dy_v \\ &+ e\left(\frac{1}{T_v} - \frac{1}{T_l}\right) dz_v + e\left(\frac{1}{T_a} - \frac{1}{T_l}\right) dz_a, \end{aligned} \tag{3.33}$$

where:

$$P(Y,\tau,e) = \frac{(1-\alpha_v)\frac{P_l}{T_l} + \alpha_v\left(\frac{P_v}{T_v} + \frac{P_a}{T_a}\right)}{\frac{1-z_v-z_a}{T_l} + \frac{z_v}{T_v} + \frac{z_a}{T_a}} \quad ; \quad \frac{1}{T}(Y,\tau,e) = \frac{1-z_v-z_a}{T_l} + \frac{z_v}{T_v} + \frac{z_a}{T_a}. \tag{3.34}$$

Some concavity properties can be exhibited for the entropies: s is strictly concave relatively to Y for a given (τ, e) and s is strictly concave relatively to (τ, e) for a given Y (see appendix 3.A). Last, we recall the definition of the mixture sound speed c $(m.s^{-1})$:

$$\begin{aligned} c^2 &= -\tau^2 \left.\frac{\partial P}{\partial \tau}\right|_{s,Y} = -\tau^2 \left.\frac{\partial P}{\partial \tau}\right|_{e,Y} + \tau^2 P \left.\frac{\partial P}{\partial e}\right|_{\tau,Y} \\ &= -\tau^2 T\left(\left.\frac{\partial^2 s}{\partial \tau^2}\right|_{e,Y} + P^2 \left.\frac{\partial^2 s}{\partial e^2}\right|_{\tau,Y} - 2P \left.\frac{\partial^2 s}{\partial \tau \partial e}\right|_{Y}\right), \end{aligned} \tag{3.35}$$

which can be rewritten thanks to the partial derivatives of the phasic intensive entropies s_k, since:

$$\left.\frac{\partial^2 s}{\partial \tau^2}\right|_{e,Y} = \sum_{k\in\mathcal{K}} \frac{\alpha_k^2}{y_k}\frac{\partial^2 s_k}{\partial \tau_k^2} \quad ; \quad \left.\frac{\partial^2 s}{\partial e^2}\right|_{\tau,Y} = \sum_{k\in\mathcal{K}} \frac{z_k^2}{y_k}\frac{\partial^2 s_k}{\partial e_k^2} \quad ; \quad \left.\frac{\partial^2 s}{\partial \tau \partial e}\right|_{Y} = \sum_{k\in\mathcal{K}} \frac{\alpha_k z_k}{y_k}\frac{\partial^2 s_k}{\partial \tau_k \partial e_k}.$$

3.1.4 Main properties of the model

The present model possesses interesting mathetical properties. They are only summarized here but the reader can refer to [4, 15, 34, 21, 41, 36, 30, 32] for more details about models with a similar convective structure and to [20] for details about a homogeneous model with the same thermodynamical building.

Property 3.5 (Structure of waves)
Since the system (3.27) is an Euler-type system, the eigenstructure of the model is composed of:

- two genuinely non-linear waves associated with the eigenvalues $U \pm c$, where c is the mixture sound speed $(m.s^{-1})$, defined by:

$$c^2 = -\tau^2 \left.\left(\frac{\partial p}{\partial \tau}\right)\right|_s = -\frac{\tau^2}{\left.\left(\frac{\partial \tau}{\partial p}\right)\right|_s}; \tag{3.36}$$

- one linearly degenerate wave associated with the eigenvalue U. □

Property 3.6 (Hyperbolicity)
The two following conditions ensure the hyperbolicity of the model:

(I) : the specific phasic entropies $(\tau_k, e_k) \mapsto s_k(\tau_k, e_k)$ are concave;

(II) : the mixture temperature T is non-negative.

The proof is straightforward recalling equation (3.35): the hyperbolicity holds since the eigenvalues are real, which is obviously the case if $c^2 \geq 0$, what is ensured since previous conditions are verified.

Property 3.7 (Jump conditions)
Shocks are defined in a unique manner through the Rankine-Hugoniot relations. This property is due to the strict concavity of s with respect to (τ, e) when fractions are fixed. □

Property 3.8 (Maximum principle on fractions)
Assuming that initial and boundary conditions on fractions are so that $Y \in [0,1]^5$, then the fractions remain in $[0,1]^5$. This property can be proved thanks to the classical lemma proved in [40].

3.2 Equations of state (EOS)

The model presented in section 3.1 requires some thermodynamical closures i.e. one complete phasic EOS for each field l, v and a, verifying the conditions (I)-(IV) from property 3.1, rewritten as follows with intensive variables:

Property 3.9 (Required properties for a k-field EOS $(\tau_k, e_k) \mapsto s_k(\tau_k, e_k)$)
A k-field EOS $(\tau_k, e_k) \mapsto s_k(\tau_k, e_k)$ is an admissible EOS ensuring the hyperbolicity of the final model (see [32, 24] and appendix 3.A) if the following properties hold:

$$\begin{array}{ll} (I) & (\tau_k, e_k) \mapsto s_k(\tau_k, e_k) \text{ is } \mathcal{C}^2. \\ (II) & (\tau_k, e_k) \mapsto s_k(\tau_k, e_k) \text{ is concave.} \\ (III) & \forall (\tau_k, e_k),\ \left.\dfrac{\partial s_k}{\partial e_k}\right|_{\tau_k} > 0. \end{array}$$

□

The phasic EOS used in this work are presented here.

We recall that a thermodynamical plane is made up of two intensive physical quantities ϕ_1 and ϕ_2, varying in a domain $\text{dom}(\phi_1, \phi_2)$. An EOS is a function describing a thermodynamical potential Ψ in a thermodynamical plane (ϕ_1, ϕ_2) and an EOS $(\phi_1, \phi_2) \mapsto \Psi(\phi_1, \phi_2)$ is a complete EOS when all the thermodynamical quantities can be defined from the successive derivatives of Ψ with respect to ϕ_1 and ϕ_2. A very comprehensive list of possible thermodynamical potentials can be found in appendix A of [15] and Chapter 2 of [13]. In practice, the model of section 3.1 requires at least **one thermodynamical potential** (described in its natural thermodynamical plane in table 3.1) and a **compatible change of variables towards another thermodynamical plane**, as it will be explained in more details in section 3.3. In this work, we need indeed to use the following two thermodynamical planes:

- **the specific entropy s in (τ, e)-plane**: indeed, most classical numerical methods (see section 3.3.1) require the mixture pressure P, computed with (3.34) using the phasic pressures and temperatures, themselves obtained from τ_k and e_k (easily deduced from the convected variables ρ, ρE, $\rho\alpha_k$, ρy_k, ρz_k). Furthermore, this choice allows to handle shock waves with quite simple numerical schemes;
- **the Gibbs potential $\mu = e - Ts + P\tau$ in (P, T)-plane**, since the thermodynamical equilibrium is computed in (P, T)-plane with an algorithm adapted from [14] (see section 3.3.3).

Some quantities can also be computed with the second derivative of a thermodynamical potential, for instance, the heat capacity at constant pressure C_p:

$$C_p = -T \left.\frac{\partial^2 \mu}{\partial T^2}\right|_P . \tag{3.37}$$

Notice that, thanks to assumption (III) of property 3.9, there is a bijective change of variables to switch from $s(\tau, e)$ towards $e(\tau, s)$ [10, 41].

The stiffened gas (SG) EOS is often used, as in [29, 30], because of its simplicity and its analytical form enabling to easily change of thermodynamical plane. In the following, SG EOS will be used for vapor water v and non-condensable gas a (see section 3.2.1).

Potential	Entry plane	"Gibbs relation"	Conjugate variables
μ	(P,T)	$d\mu = -sdT + \tau dP$	$\tau = \left.\frac{\partial \mu}{\partial P}\right\|_T ; s = -\left.\frac{\partial \mu}{\partial T}\right\|_P$
s	(τ,e)	$ds = \frac{P}{T}d\tau + \frac{1}{T}de$	$\frac{P}{T} = \left.\frac{\partial s}{\partial \tau}\right\|_e ; \frac{1}{T} = \left.\frac{\partial s}{\partial e}\right\|_\tau$
e	(τ,s)	$de = Tds - Pd\tau$	$P = -\left.\frac{\partial e}{\partial \tau}\right\|_s ; T = \left.\frac{\partial e}{\partial s}\right\|_\tau$

Table 3.1 – *Potentials defining a complete EOS in a given thermodynamical plane.*

In [24], a more realistic EOS has been tested: it consists in a look-up table based on IAPWS-97 formulation [45], one industrial reference EOS dedicated to water. Here, we aim to propose a compromise between the simplicity of a SG and the numerical costs and difficulties of a IAPWS look-up table (see [24]), by choosing a semi-analytical EOS for the liquid l: a Noble-Able stiffened gas EOS [39, 7] modified with the Chemkin EOS [38], called NASG-CK EOS in the following (see section 3.2.2).

3.2.1 Stiffened gas EOS for the gaseous fields v and a

We recall the stiffened gas EOS in (τ,e)-plane:

$$\forall k \in \{v,a\}, s_k(\tau_k,e_k) = C_{v,k}\ln\left((e_k - Q_k - \pi_k\tau_k)\tau_k^{\gamma_k-1}\right) + s_{0k}. \tag{3.38}$$

The stiffened gas parameters are the following, for $k \in \{v,a\}$:

- $C_{v,k}$ $(J.K^{-1}.kg^{-1})$ is the calorific capacity at constant volume,
- γ_k is the adiabatic index, a non-dimensional coefficient greater than 1,
- $-\Pi_k$ (Pa) is the minimal admissible pressure (which can be negative),
- Q_k $(J.kg^{-1})$ is a reference enthalpy,
- s_{0k} $(J.K^{-1}.kg^{-1})$ is a reference entropy.

The coefficients, given in appendix 3.B, are evaluated with the method proposed in [11].

The EOS can be easily inverted in (P,T)-plane using the definition $\mu = e - Ts + P\tau$:

$$\forall k \in \{v,a\}, \mu_k(P_k,T_k) = \gamma_k C_{v,k}T_k + Q_k - T_k(\gamma_k C_{v,k}\ln(T_k) - (\gamma_k-1)C_{v,k}\ln(P_k+\Pi_k) + k_k), \tag{3.39}$$

with a constant k_k (in $J.K^{-1}.kg^{-1}$), defined in accordance with (3.38) and (3.41):

$$k_k = C_{v,k}\ln(C_{v,k}) + C_{v,k}(\gamma_k-1)\ln(C_{v,k}(\gamma_k-1)) + s_{0k}. \tag{3.40}$$

Other quantities can be deduced using table 3.1:

$$\begin{aligned}
\forall k \in \{v,a\}, \tau_k(P_k,T_k) &= \frac{C_{v,k}(\gamma_k-1)T_k}{P_k+\Pi_k} \\
s_k(P_k,T_k) &= \gamma_k C_{v,k}\ln(T_k) - (\gamma_k-1)C_{v,k}\ln(P_k+\Pi_k) + k_k; \\
e_k(P_k,T_k) &= C_{v,k}T_k + Q_k + C_{v,k}(\gamma_k-1)T_k\frac{\Pi_k}{P_k+\Pi_k}; \\
C_{p_k}(P_k,T_k) &= \gamma_k C_{v,k}.
\end{aligned} \tag{3.41}$$

It can be easily checked that property 3.9 is verified for a SG EOS.

3.2.2 Noble-Able-Chemkin stiffened gas EOS for the liquid l

In [7], the authors proved that Noble-Able Stiffened gas (NASG) EOS can be extended to cope with a variable heat capacity at constant pressure C_p (in $J.K^{-1}.kg^{-1}$) depending on the temperature: in particular, they recommend to define C_p with the NASA polynomials, used in the Chemkin EOS [38].

3.2.2.1 Definition in (P,T)-plane

Thus, we propose the following EOS, by gathering the main features of NASG EOS and Chemkin EOS i.e. the introduction of a specific volume b_l ($m^3.kg^{-1}$) and a variable C_{p_l} defined as a polynomial of T_l:

$$\begin{aligned}
&\mu_l(P_l,T_l) = \mu_l^0(T_l) + b_l P_l + \mathcal{C}_l(T)\ln(P_l+\Pi_l), \\
\text{with:}\quad &\mu_l^0(T_l) = RT_l\left(A_l(1-\ln(T_l)) - \frac{B_l}{2}T_l - \frac{C_l}{6}T_l^2 - \frac{D_l}{12}T_l^3 - \frac{E_l}{20}T_l^4 + \frac{F_l}{T_l} - G_l\right), \\
&\mathcal{C}_l(T_l) = C_{v,l}(\gamma_l-1)T_l, \\
&R = \frac{r}{M} \text{ the perfect gas constant, with } r = 8.31446261815324\ J.kg^{-1}.mol^{-1} \text{ and } M = 18.01528\ g.mo
\end{aligned} \tag{3.42}$$

Other quantities can be deduced from (3.43) using table 3.1:

$$\begin{aligned}
\tau_l(P_l,T_l) &= b_l + \frac{C_{v,l}(\gamma_l-1)T_l}{P_l+\Pi_l}; \\
s_l(P_l,T_l) &= R\left(A_l\ln(T_l) + B_lT_l + \frac{C_l}{2}T_l^2 + \frac{D_l}{3}T_l^3 + \frac{E}{4}T_l^4 + G_l\right) - C_{v,l}(\gamma-1)\ln(P_l+\Pi_l); \\
C_{p_l}(T_l) &= R(A_l + B_lT_l + C_lT_l^2 + D_lT_l^3 + E_lT_l^4).
\end{aligned} \tag{3.43}$$

3.2.2.2 Definition in (τ,e)-plane

Inverting the NASG-CK EOS from the (P_l,T_l)-plane towards the (τ_l,e_l)-plane requires an implicit resolution. Supposing that τ_l and e_l are known as functions of (P_l,T_l), we aim to get $s_l(\tau_l,e_l)$:

1. first, P_l can be written as a function of τ_l and T_l:

$$P_l = \frac{C_{v,l}(\gamma_l-1)T_l}{\tau_l-b_l} - \Pi_l = P_l(\tau_l,T_l); \tag{3.44}$$

2. then, e_l can be rewritten as a function of τ_l and T_l only:

$$e_l = RT_l(A_l + \frac{B_l}{2}T_l + \frac{C_l}{3}T_l^2 + \frac{D_l}{4}T_l^3 + \frac{E_l}{5}T_l^4 + \frac{F_l}{T_l}) - C_{v,l}(\gamma_l - 1)T_l + \Pi_l(\tau_l - b_l) = e_l(\tau_l, T_l); \tag{3.45}$$

3. last, T_l can be deduced from τ_l and e_l by implicitely solving the previous equation (for instance with a secant method algorithm).

At the end of day, we speak about "semi-analytical" EOS for NASG-CK because, up to an implicit resolution of $e_l = (\tau_l, T_l)$ to find T_l, the complete EOS in (τ_l, e_l)-plane $s_l(\tau(P_l, T_l), e_l(\tau_l, T_l))$ can be obtained from $\mu_l(P_l, T_l)$.

3.2.2.3 Admissibility condition of NASG-CK EOS

Property 3.10
The Noble-Able Chemkin EOS (3.43) is an admissible EOS ensuring property 3.9 since:

$$C_{p_l}(T_l) - C_{v,l}(\gamma_l - 1) \geq 0 \tag{3.46}$$

□

It has been numerically checked that (3.46) holds for the coefficients used in this work (given in appendix 3.B).

Proof:
Here we focus on the concavity of $(\tau_l, e_l) \mapsto s_l(\tau_l, e_l)$ because all the other requirements from property 3.9 can be easily proved. Recalling from table 3.1:

$$\left.\frac{ds_l}{d\tau_l}\right|_{e_l} = \frac{P_l}{T_l} \quad ; \quad \left.\frac{ds_l}{de_l}\right|_{\tau_l} = \frac{1}{T_l},$$

one needs now to evaluate the second derivatives of $(\tau_l, e_l) \mapsto s_l(\tau_l, e_l)$. Using (3.45), we can deduce an implicit relation $T_l = T_l(\tau_l, e_l)$ and we get:

$$de_l = (C_{p_l}(T_l) - C_{v,l}(\gamma_l - 1))dT_l + \Pi_l d\tau_l, \tag{3.47}$$

so that:

$$\left.\frac{\partial T_l}{\partial \tau_l}\right|_{e_l} = -\Pi_l(C_{p_l}(T_l) - C_{v,l}(\gamma_l - 1))^{-1}, \tag{3.48}$$

and

$$\left.\frac{\partial T_l}{\partial e_l}\right|_{\tau_l} = (C_{p_l}(T_l) - C_{v,l}(\gamma_l - 1))^{-1}. \tag{3.49}$$

Moreover, using (3.44), we get also:

$$P_l = \frac{C_{v,l}(\gamma_l - 1)T_l(\tau_l, e_l)}{\tau_l - b_l} - \Pi_l, \tag{3.50}$$

so that:

$$\left.\frac{\partial P_l}{\partial \tau_l}\right|_{e_l} = -\frac{C_{v,l}(\gamma_l - 1)T_l}{(\tau_l - b_l)^2} + \frac{C_{v,l}(\gamma_l - 1)}{(\tau_l - b_l)} \left.\frac{\partial T_l}{\partial \tau_l}\right|_{e_l}. \tag{3.51}$$

It reads then:

$$\frac{\partial^2 s_l}{\partial \tau_l \partial e_l} = \frac{\partial}{\partial \tau_l}\left(\frac{1}{T_l}\right)\Big|_{e_l} = -\frac{1}{T_l^2}\left.\frac{\partial T_l}{\partial \tau_l}\right|_{e_l} = \frac{\Pi_l}{T_l^2}(C_{p_l}(T_l) - C_{v,l}(\gamma_l - 1))^{-1}; \tag{3.52}$$

$$\left.\frac{\partial^2 s_l}{\partial e_l^2}\right|_{\tau_l} = \frac{\partial}{\partial e_l}\left(\frac{1}{T_l}\right)\Big|_{\tau_l} = -\frac{1}{T_l^2}\left.\frac{\partial T_l}{\partial e_l}\right|_{\tau_l} = -\frac{1}{T_l^2}(C_{p_l}(T_l) - C_{v,l}(\gamma_l - 1))^{-1} = -\frac{1}{\Pi_l}\frac{\partial^2 s_l}{\partial \tau_l \partial e_l}; \tag{3.53}$$

$$\begin{aligned}
\left.\frac{\partial^2 s_l}{\partial \tau_l^2}\right|_{e_l} &= \frac{\partial}{\partial \tau_l}\left(\frac{P_l}{T_l}\right)\Big|_{\tau_l} = \frac{1}{T_l}\left.\frac{\partial P_l}{\partial \tau_l}\right|_{e_l} - \frac{P_l}{T_l^2}\left.\frac{\partial T_l}{\partial \tau_l}\right|_{e_l} \\
&= \left.\frac{\partial T_l}{\partial \tau_l}\right|_{e_l}\left(\frac{C_{v,l}(\gamma_l - 1)}{T_l(\tau_l - b_l)} - (\frac{C_{v,l}(\gamma_l - 1)}{T_l(\tau_l - b_l)} - \frac{\Pi_l}{T_l^2})\right) - \frac{C_{v,l}(\gamma_l - 1)}{(\tau_l - b_l)^2} \\
&= -\frac{\Pi_l^2}{T_l^2}(C_{p_l}(T_l) - C_{v,l}(\gamma_l - 1))^{-1} - \frac{C_{v,l}(\gamma_l - 1)}{(\tau_l - b_l)^2} \\
&= -\Pi_l \frac{\partial^2 s_l}{\partial \tau_l \partial e_l} - \frac{C_{v,l}(\gamma_l - 1)}{(\tau_l - b_l)^2}.
\end{aligned} \tag{3.54}$$

Since $C_{p_l}(T_l) - C_{v,l}(\gamma_l - 1) \geq 0$, we get:

$$\begin{aligned}
&\left.\frac{\partial^2 s_l}{\partial \tau_l^2}\right|_{e_l} \leq 0 \quad ; \quad \left.\frac{\partial^2 s_l}{\partial e_l^2}\right|_{\tau_l} \leq 0 \quad ; \quad \frac{\partial^2 s_l}{\partial \tau_l \partial e_l} \geq 0 \\
&\left.\frac{\partial^2 s_l}{\partial \tau_l^2}\right|_{e_l}\left.\frac{\partial^2 s_l}{\partial e_l^2}\right|_{\tau_l} - \left(\frac{\partial^2 s_l}{\partial \tau_l \partial e_l}\right)^2 = \left(\frac{\partial^2 s_l}{\partial \tau_l \partial e_l}\right)^2 (1-1) + \frac{\partial^2 s_l}{\partial \tau_l \partial e_l}\frac{C_{v,l}(\gamma_l - 1)}{(\tau_l - b_l)^2 \Pi_l} \\
&= \frac{\partial^2 s_l}{\partial \tau_l \partial e_l}\frac{C_{v,l}(\gamma_l - 1)}{(\tau_l - b_l)^2 \Pi_l} \geq 0,
\end{aligned} \tag{3.55}$$

which prove that $(\tau_l, e_l) \mapsto s_l(\tau_l, e_l)$ is indeed concave as required by property 3.9.

3.2.2.4 Accuracy of NASG-CK EOS

Most EOS coefficients (A_l, B_l, C_l, D_l, E_l, γ_l, $C_{v,l}$, Π_l and b_l) have been evaluated by fitting the specific volume τ_l and the heat capacity C_{p_l} to data obtained with IAPWS EOS (see chapter 2). The remaining coefficients F_l and G_l have been defined by fitting T_{sat} (computed by imposing $\mu_l(P, T_{sat}(P)) = \mu_v(P, T_{sat}(P))$) with the saturation temperature computed with IAPWS (see figure 3.1).

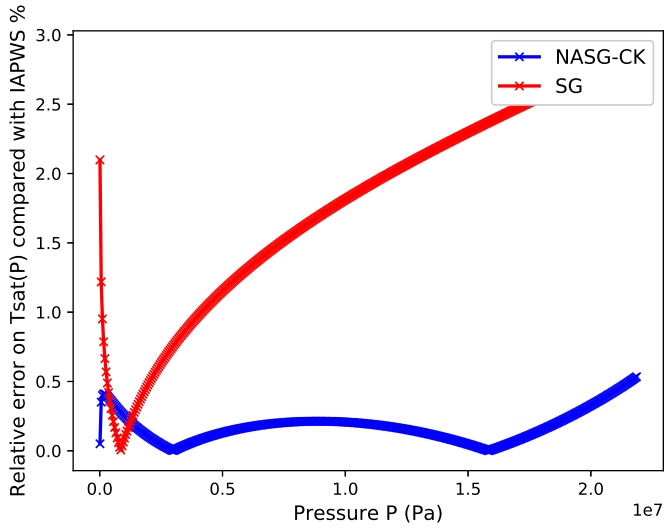

Figure 3.1 – *Relative error on $T_{sat}(P)$ obtained by balancing $\mu_l(P,T)$ and $\mu_v(P,T)$ compared with IAPWS, when considering NASG-CK or SG EOS for liquid.*

We compared NASG-CK EOS with coefficients from appendix 3.B with a SG EOS fitted with the emperical method from [11] on a large liquid domain, following the same guidelines as those proposed in chapter 2. Recalling the definition of the relative error err_ϕ for a quantity ϕ:

$$err_\phi = \left| \frac{\phi^{EOS} - \phi^{IAPWS}}{\phi^{IAPWS}} \right|,$$

we chose the following (subjective) indicators, gathering in table 3.2:

- the mean, minimal and maximal relative error for each quantity;
- the percentage of the physical domain where the relative error is smaller than 5% for each quantity;
- the percentage of the physical domain where the relative error is smaller than 5% for the three quantities τ and C_p at the same time;

Error maps for τ_l (figures 3.2 and 3.3) and C_{p_l} (figures 3.4 and 3.5) are also given, showing the relative error at each point (P_l, T_l), with an error limited by a ceiling of 5%.

All the previous indicators show that NASG-CK EOS is far more accurate than a SG EOS on a large liquid domain.

Indicators (%)		NASG CK EOS	SG EOS
Mean relative errors	on τ	2.9	7.2
	on C_p	0.87	5.8
Min relative errors	on τ	$\simeq 10^{-6}$	0.14
	on C_p	$\simeq 10^{-6}$	$\simeq 10^{-7}$
Max relative errors	on τ	20	38
	on C_p	21	56
% of domain with err $< 5\%$	on τ	89	52
	on C_p	99	66
	on τ and C_p	89	52

Table 3.2 – *Comparison of accuracy indicators for NASGCK EOS and SG on a large liquid domain, relatively to IAPWS*

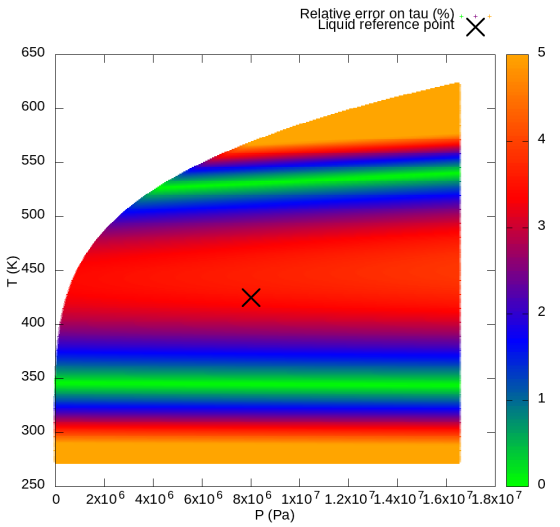

Figure 3.2 – *Relative error on τ compared with IAPWS-97 for NASGCK EOS, with error saturation at* 5%.

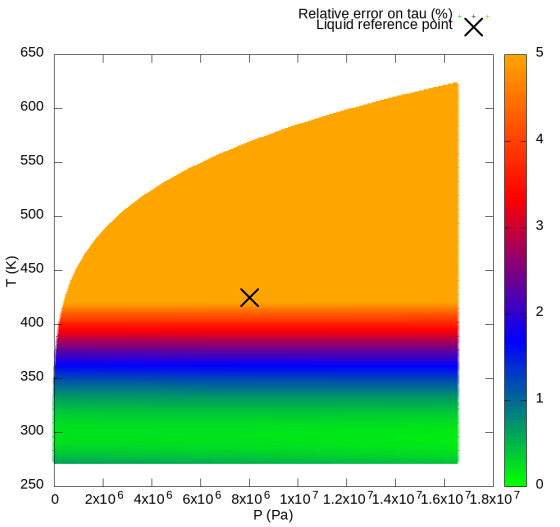

Figure 3.3 – *Relative error on τ compared with IAPWS-97 for SG EOS, with error saturation at* 5%.

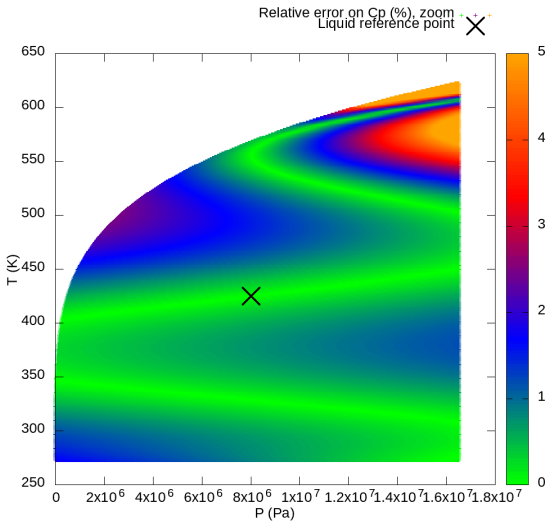

Figure 3.4 – *Relative error on C_p compared with IAPWS-97 for NASGCK EOS, with error saturation at* 5%.

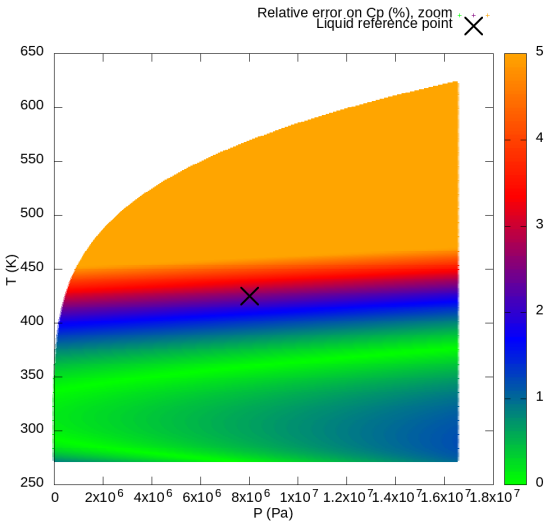

Figure 3.5 – *Relative error on C_p compared with IAPWS-97 for SG EOS, with error saturation at* 5%.

3.3 Numerical implementation

The numerical implementation is carried out following the same numerical strategy as in [30, 24]. We will only recall here the main features of the method and we refer to the previous references for more details. The numerical method is based on a fractional step method [46] using a Lie-Trotter splitting (with a unique sub-iteration). More precisely, system of equations (3.27) can be rewritten as:

$$\frac{\partial W}{\partial t} = -\frac{\partial \mathcal{F}(W)}{\partial x} + \mathcal{G}(W), \quad W(t=0) = W^0, \tag{3.56}$$

where $\mathcal{F}$ correspond to the convective flux and $\mathcal{G}$ to the source terms. A straightforward Lie-Trotter splitting is chosen, consisting in solving at time $t = t^n$ the following two sub-systems during a time step Δt^n:

$$(i) \quad \frac{\partial W_a}{\partial t} = -\frac{\partial \mathcal{F}(W)}{\partial x}, \quad W_a(t^n) = W^n, \tag{3.57}$$

which gives $W_a(t^n + \Delta t^n)$:

$$(ii) \quad \frac{\partial W_b}{\partial t} = -\frac{\partial \mathcal{G}(W)}{\partial x}, \quad W_b(t = t^n) = W_a(t^n + \Delta t^n). \tag{3.58}$$

which gives $W(t^{n+1}) = W_b(t^n + \Delta t^n)$. Since this splitting is first order with respect to time, each sub-system is solved using first order schemes.

3.3.1 Numerical schemes to solve the convective sub-system (3.57)

First sub-system (3.57) takes into account the convective part: it is solved with first-order explicit and conservative finite volumes schemes. Their general form for a one-dimensional framework with cells Ω_i is:

$$|\Omega_i|(W_i^{n+1} - W_i^n) = -\Delta t^n((F(W_i^n, W_{i+1}^n) - F(W_{i-1}^n, W_i^n)), \tag{3.59}$$

where W_i^n denotes the space-average value of W on the cell Ω_i at time t^n. Note that other methods may be used, as in [25] where a similar model has been implemented using a Lattice-Boltzmann method. In this work, two different schemes are used: Rusanov scheme [44] and a relaxation scheme proposed in [8] and described in details in [24]. We recall very briefly their main features and we refer to previous references for more details.

For the Rusanov scheme, the numerical flux is:

$$F(W_l, W_r) = \frac{1}{2}(\mathcal{F}(W_l) + \mathcal{F}(W_r)) - \frac{\max(\Lambda_r, \Lambda_l)}{2}(W_r - W_l), \tag{3.60}$$

where Λ_r (resp. Λ_l) is the spectral radius of the convection matrix $\nabla_W \mathcal{F}$ at $W = W_r$ (resp. $W = W_l$). The time step Δt^n at iteration n should satisfy the CFL constraint:

$$\frac{\Delta t^n}{\Delta x} \max(\Lambda_r, \Lambda_l) < \frac{1}{2}. \tag{3.61}$$

As far as the relaxation scheme is concerned, an enlarged hyperbolic system is introduced, associated with a strong relaxation term, so that the relaxation procedure enables to

formally recover the initial system of equations. The enlarged system to solve is then the following:

$$\begin{cases} \partial_t(\rho Y) + \partial_x(\rho Y U) = 0; \\ \partial_t \rho + \partial_x(\rho U) = 0; \\ \partial_t(\rho U) + \partial_x(\rho U^2 + \Pi) = 0; \\ \partial_t(\rho \Sigma) + \partial_x(\rho U \Sigma + U\Pi) = 0; \\ \partial_t(\rho \mathcal{T}) + \partial_x(\rho \mathcal{T} U) = \dfrac{1}{\epsilon}\rho(\tau - \mathcal{T}); \end{cases} \tag{3.62}$$

where the relaxation source terms for $\mathcal{T}$ are characterized by the parameter $\epsilon \geq 0$. Some additional variables have been introduced to build system (3.62): one additional scalar unknown $\mathcal{T}$ with the initial condition:

$$\forall x,\ \mathcal{T}(0,x) = \tau(0,x);$$

a new pressure Π:

$$\Pi = P(Y, \mathcal{T}, e) + a^2(\mathcal{T} - \tau); \tag{3.63}$$

and a relaxation specific total energy Σ:

$$\Sigma = \frac{u^2}{2} + e + \frac{\Pi^2 - P^2(Y, \mathcal{T}, e)}{2a^2}, \tag{3.64}$$

as well as a positive parameter a is a positive parameter, which sould satisfy the following sub-characteristic condition:

$$a > \max\left(\frac{c_l(Y_l, \tau_l, e_l)}{\tau_l}, \frac{c_r(Y_r, \tau_r, e_r)}{\tau_r}\right). \tag{3.65}$$

The numerical flux is the following:

$$F(W_l, W_r) = \left(\frac{YU}{\tau}, \frac{U}{\tau}, \frac{U^2}{\tau} + \Pi, \frac{U\Sigma}{\tau} + U\Pi\right),$$

where Y, τ, U, Σ are the components of $\mathcal{Z}\left(x/t = 0, Z_l, Z_r\right)$, the self-similar solution $\mathcal{Z}\left(x/t, Z_l, Z_r\right)$ of the Riemann problem at the interface separating cells l and r, so that Π=$\Pi(Y, \tau, \Sigma)$.

3.3.2 Applying the source terms through sub-system (3.58)

The return towards thermodynamical equilibrium is accounted for with the second subsystem (3.58):

$$\begin{cases} \dfrac{\partial}{\partial t}(Y) = \dfrac{\bar{Y}(\tau, e) - Y}{\lambda(t)}; \\ \dfrac{\partial}{\partial t}(\rho) = 0; \\ \dfrac{\partial}{\partial t}(\rho U) = 0; \\ \dfrac{\partial}{\partial t}(\rho E) = 0. \end{cases} \tag{3.66}$$

In this second subsystem (3.66), τ and e are constant. We make furthermore the approximation: $\lambda(t) = \lambda(0)$, so that the fractions can be computed as the exact solutions of the approximated sub-system:

$$\frac{\partial Y}{\partial t} = \frac{\bar{Y}(\tau(0), e(0)) - Y}{\lambda(0)}. \tag{3.67}$$

For an initial condition given by the value at time t^n, the final approximation at time $t^{n+1} = t^n + \Delta t^n$ then reads:

$$\left\{ \begin{array}{l} Y(t^{n+1}) = Y(t^n)\, e^{\frac{-\Delta t^n}{\lambda(t^n)}} + \bar{Y}(t^n) \left(1 - e^{\frac{-\Delta t^n}{\lambda(t^n)}}\right); \\ \rho(t^{n+1}) = \rho(t^n); \\ U(t^{n+1}) = U(t^n); \\ e(t^{n+1}) = e(t^n). \end{array} \right. \tag{3.68}$$

Remark 3.3 — For a sake of simplicity, both sub-systems (3.57) and (3.58) are solved using only one time-step. Since the explicit numerical scheme of the convective sub-system imposes a stability constraint on this time-step, this second step is achieved using an implicit scheme. □

The major difficulty in this step is in fact to compute the thermodynamical equilibrium $\bar{Y}$: the algorithm, based on [14], is briefly explained in the next section 3.3.3 and fully described in appendix 3.D.

Remark 3.4 (Alternative splitting for source terms) — Instead of applying all the source terms during the same step, one might consider another Lie splitting in three steps:

1. a convection step, the same as (3.57);
2. a first step, in which T_v and T_a are balanced;
3. a second step, in which the gaseous mixture $v + a$ is balanced with the liquid l. □

3.3.3 Principles enabling to compute the thermodynamical equilibrium

After the convection step, (y_a, τ, e) are known and we need now to find the equilibrium fractions $\bar{Y}(y_a, \tau, e) = (\bar{\alpha}_v, \bar{y}_v, \bar{z}_v, y_a)$ enabling to maximize the mixture entropy s (3.32). The main procedure is the following:

ALGORITHM 3.1 (Type of equilibrium) — Arguments: (y_a, τ, e).

- **If $y_a = 0$**: the equilibrium is a monophasic state with only field a, so that:

$$\bar{\alpha}_v = 0 \quad ; \quad \bar{y}_v = 0 \quad ; \quad \bar{z}_v = 0 \quad ; \quad \bar{z}_a = 1.$$

- **Else if $y_a = 0$**: we try to compute an equilibrium state with the two fields l and v using ALGORITHM 3.2 (LV), computing a potential equilibrium $\bar{Y}^{lv}(y_a, \tau, e) = (\tilde{\alpha}_v^{lv}, \tilde{y}_v^{lv}, \tilde{z}_v^{lv}, \tilde{z}_a^{lv})$.
  - **If $\tilde{Y}^{lv}$ is admissible** (i.e. if all the fractions are in $]0, 1[$):

$$\bar{Y}^{lv} = \tilde{Y}.$$

  - **Else**: the equilibrium state is a monophasic state with only l or only v. More precisely, the equilibrium state is the monophasic state maximizing the entropy:

* **If** $s_l(\tau, e) > s_v(\tau, e)$: the equilibrium is a pure liquid water state, so that:

$$\bar{\alpha}_v = 0 \quad ; \quad \bar{y}_v = 0 \quad ; \quad \bar{z}_v = 0 \quad ; \quad \bar{z}_a = 0.$$

* **Else**: the equilibrium is a pure vapor water state, so that:

$$\bar{\alpha}_v = 1 \quad ; \quad \bar{y}_v = 1 \quad ; \quad \bar{z}_v = 1 \quad ; \quad \bar{z}_a = 0.$$

- **Else**: we try to compute an equilibrium state $\bar{Y}^{lva}(y_a, \tau, e)$ with the three fields l, v and a, determined using ALGORITHM 3.3 (LVA):

$$\bar{Y}^{lva} = \tilde{Y}.$$

  – **If** $\bar{Y}^{lva}$ **is admissible** (i.e. if all the fractions are in $]0, 1[$):

$$\bar{Y}^{lva} = \tilde{Y}.$$

  – **Else**: the equilibrium state is a mixture of l and a, or a mixture of v and a. Both possible states $\bar{Y}^{la}(y_a, \tau, e)$ and $\bar{Y}^{va}(y_a, \tau, e)$ are computed using ALGORITHM 3.4 (LA) and ALGORITHM 3.5 (VA), thanks to conditions from property 3.4. The physical state is obtained by comparing both mixture entropies $s_{ka} = (1 - y_a)s_k(\tilde{\tau}_k, \tilde{e}_k) + y_a s_a(\tilde{\tau}_a, \tilde{e}_a)$, $k = l, v$:

    * **If** $s_{la}(y_a, \tau, e) > s_{va}(y_a, \tau, e)$: the equilibrium is a two-phase mixture of liquid water and non-condensable gas, so that

$$\bar{Y}^{la} = \tilde{Y}.$$

    * **Else**: the equilibrium is a miscible gaseous mixture of vapor water and non-condensable gas, so that:

$$\bar{Y}^{va} = \tilde{Y}.$$

The previous procedure calls algorithms to compute the thermodynamical equilibrium, depending on the fields which are actually present in the mixture. These algorithms are described in details in appendix 3.D. The LV-equilibrium (ALGORITHM 3.2) and the LVA-equilibrium (ALGORITHM 3.3) algorithms are based on the algorithm initially proposed in [14]. The key idea is to change of thermodynamical plane. Indeed, if we consider the LVA-case, the equilibrium is characterized by the four following equations in the (τ, e)-plane:

$$\begin{array}{rcl} P_l(\tau_l, e_l) & = & P_v(\tau_v, e_v) + P_a(\tau_a, e_a); \\ T_l(\tau_l, e_l) & = & T_v(\tau_v, e_v); \\ T_v(\tau_v, e_v) & = & T_a(\tau_a, e_a); \\ \mu_l(P_l(\tau_l, e_l), T_l(\tau_l, e_l)) & = & \mu_v(P_v(\tau_v, e_v), T_v(\tau_v, e_v)); \end{array} \tag{3.69}$$

since the previous system can be rewritten using relations $\tau_k = \dfrac{\alpha_k}{y_k}\tau$ and $e_k = \dfrac{z_k}{y_k}e$ for $k = l, v, a$: the four remaining unknowns are thus the equilibrium fractions, noted $\bar{\alpha}_v$, $\bar{y}_v$, $\bar{z}_v$ and $\bar{z}_a$. Instead of looking for these fractions $\bar{\alpha}_v$, $\bar{y}_v$, $\bar{z}_v$ and $\bar{z}_a$ satisfying (3.69), the tip is to rather consider the following unknowns $\bar{P}_v$, $\bar{P}_a$, $\bar{T}$ and $\bar{y}_v$. Miscibility constraints (3.7) enable to get

a system equivalent to system (3.69) in pressure-temperature plane:

$$\begin{array}{rcl} \bar{y}_v \times \tau_v(\bar{P}_v, \bar{T}) & = & y_a \times \tau_a(\bar{P}_a, \bar{T}); \\ \tau & = & (1-\bar{y}_v) \times \tau_l(\bar{P}_v + \bar{P}_a, \bar{T}) + \bar{y}_v \times \tau_v(\bar{P}_v, \bar{T}); \\ e & = & (1-\bar{y}_v) \times e_l(\bar{P}_v + \bar{P}_a, \bar{T}) + \bar{y}_v \times e_v(\bar{P}_v, \bar{T}) + y_a \times e_a(\bar{P}_a, \bar{T}); \\ \mu_l(\bar{P}_v + \bar{P}_a, \bar{T}) & = & \mu_v(\bar{P}_v, \bar{T}). \end{array} \tag{3.70}$$

With the particular choice for phasic EOS considered in section 3.2, system (3.70) can be rewritten as a system of two coupled equations of only two variables ($\bar{P}_v$ and $\bar{P}_a$), solved in ALGORITHM 3.3 with a Broyden algorithm, as described in appendix 3.D.

Remark 3.5 (Analytical phasic EOS for vapor and non-condensable gas) — Without specifying any phasic EOS, the only obvious simplification of system (3.70) is to replace $\bar{y}_v$ by its expression as a function of $\bar{P}_v$, $\bar{P}_a$ and $\bar{T}$ obtained from the first equation of (3.70):

$$\bar{y}_v = y_a \frac{\tau_a(\bar{P}_a, \bar{T})}{\tau_v(\bar{P}_v, \bar{T})}.$$

It remains a system of three coupled equations of three unknowns $\bar{P}_v$, $\bar{P}_a$ and $\bar{T}$. Our particular choice of stiffened gas EOS for the vapor and the non-condensable gas enables us to get an explicit formula for $\bar{T}$ as a function of $\bar{P}_v$ and $\bar{P}_a$.

However, we tried to replace the SG phasic EOS for vapor by a Noble-Able equation [39]: in that case, equations of system (3.69) are much more coupled because of the specific volume b_v, so that we did not succeed in getting a simpler form as a three coupled equations of three unknowns for system (3.69). We decided then to limit ourselves to a SG EOS for vapor, in order to simplify the numerical implementation.

Remark 3.6 (Threshold for fractions) — In practice, a threshold $\epsilon_{frac} = 10^{-12}$ is defined in the code for the fractions: a fraction $1 \geq \varphi > 1 - \epsilon_{frac}$ will be taken equal to 1 and a fraction $0 \leq \varphi < \epsilon_{frac}$ will be taken equal to 0. □

3.4 Verification test cases

In order to verify the implementation of the numerical methods as well as the thermodynamical equilibrium computation, convergence studies are performed on Riemann problems for which a unique analytical solution can be exhibited.

As in [24, 29], particular Riemann problems with only a contact wave and a shock wave are built. More precisely, we consider a one-dimensional domain $x \in [0\ m, 1\ m]$, discretized using uniform meshes, with an initial discontinuity at $x_d = 0.5\ m$. The exact solution (see figure 3.6) consists in the left and right initial states, respectively W^L and W^R, separated by a uniform intermediate state W^*. The nature of waves is the following:

- the wave travelling at $U - C$ is a ghost wave;
- the wave travelling at U, separating left state W^L and intermediate state W^*, is a contact-wave;
- the wave travelling at $U + C$, separating intermediate state W^* and right state W^R, is a shock-wave.

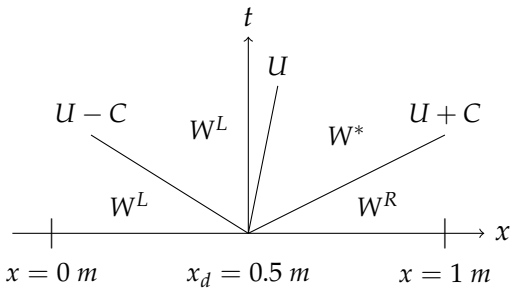

Figure 3.6 – Riemann problem with one intermediate state; U-C: ghost wave; U: contact wave; U+C: shock wave

Like in [24], two types of Riemann problems are considered:

- "out-of-equilibrium" Riemann problems, with $\lambda \to \infty$: only the convective part of model 3.1 is tested;
- "at-equilibrium" Riemann problem, with $\lambda \to 0$: first, the convective terms are taken into account and the thermodynamical equilibrium is then enforced through the source terms.

Computing the analytical solutions is classical but somehow tricky because of the non-condensable gas: the method is presented in the next section. Then, convergence results for out-of-equilibrium Riemann problems (section 3.4.2) and for at-equilibrium Riemann problems (section 3.4.3) are presented. The initial data for each test case are reported in appendix 3.C. Convergence studies are performed by computing the relative L^1-error, defined as follows: for an approximated solution Ψ^{approx} and an exact solution Ψ^{exact}, since the mesh size is uniform, the relative L^1-error is computed at time t^n on the whole mesh as:

$$\frac{\sum_i |\Psi_i^{approx,n} - \Psi^{exact}(x_i, t^n)|}{\sum_i |\Psi^{exact}(x_i, t^n)|},$$

where x_i is the barycenter of the cell i. Obviously, when $\sum_i |\Psi^{exact}(x_i, t^n)| = 0$ (i.e. $\Psi^{exact} = 0$), this relative error is meaningless and we then consider the mere L^1-error:

$$\sum_i |\Psi_i^{approx,n} - \Psi^{exact}(x_i, t^n)|.$$

3.4.1 General method to build analytical solutions

The main approach is the same as the one used in [22, 30, 24]. First a left state W^L is chosen; then the intermediate state W^* is computed across the contact wave from W^L; last, the right state W^R is obtained from W^* through the shock wave. We recall the Rankine-Hugoniot jump relations:

$$\begin{cases} J[Y] = 0 \\ [J] = 0 \\ J^2[\tau] + [P] = 0 \\ J\left([e] + [\tau]\dfrac{P^L + P^R}{2}\right) = 0 \end{cases} \tag{3.71}$$

where $J = \rho(U - \sigma)$ with σ the speed of the discontinuity and where $[\Phi] = \Phi^R - \Phi^L$ denotes the difference of the value of the quantity Φ on the right of the discontinuity Φ^R and on the left of the discontinuity Φ^L. For a contact-wave, $\sigma = U$ whereas for a $U + c$-shock-wave, $\sigma = U + c$.

For a **out-of-equilibrium Riemann problem**, P is the mixture pressure from (3.34), so that $P = P(Y, \tau, e)$, directly evaluated with the variables Y, τ, e computed through the convection step (3.57).

For an **at-equilibrium Riemann problem**, P is always computed with (3.34), but no more with the convected fractions Y: this time, $P = P(\bar{Y}, \tau, e) = \bar{P}$, with $\bar{Y} = \bar{Y}(Y, \tau, e)$ the equilibrium fractions computed with algorithms from appendix 3.D. We highlight that, for Riemann problems at equilibrium, **only the mass fraction y_a is convected** and still complies with $J[y_a] = 0$: the other equilibrium fractions $\bar{\alpha}_v$, $\bar{y}_v$, $\bar{z}_v$ and $\bar{z}_a$ do not verify the jump relations anymore.

The detailled algorithms enabling to build such Riemann problems are given in appendix 3.E.

3.4.2 Out-of-equilibrium test cases

Two out-of-equilibrium Riemann problems are considered:

- a first Riemann problem with relatively low pressures, around 1 bar (see initial data in appendix 3.C.1);
- a second Riemann problem with relatively high pressures, between 150 bar and 200 bar (see initial data in appendix 3.C.2).

In both cases, the expected convergence rate of $\frac{1}{2}$, due to the presence of the contact wave, is observed on the convergence curves (see figures 3.7 and 3.8). Note that the errors are higher for the second case at high pressures.

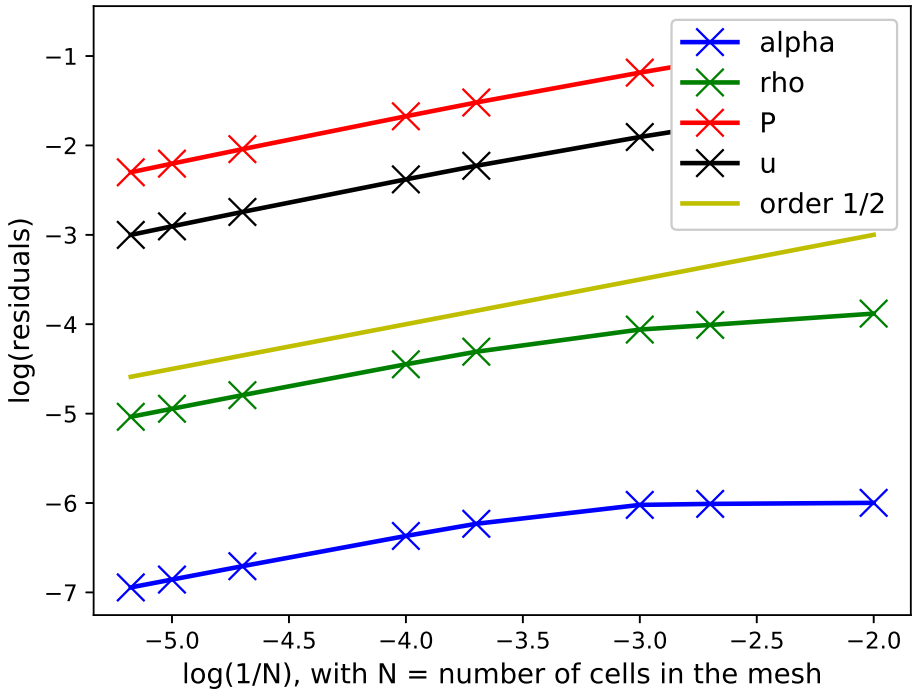

Figure 3.7 – *Convergence curve for Riemann problem 1 (out-of-equilibrium, low pressures) : meshes from 100 to 150 000 cells*

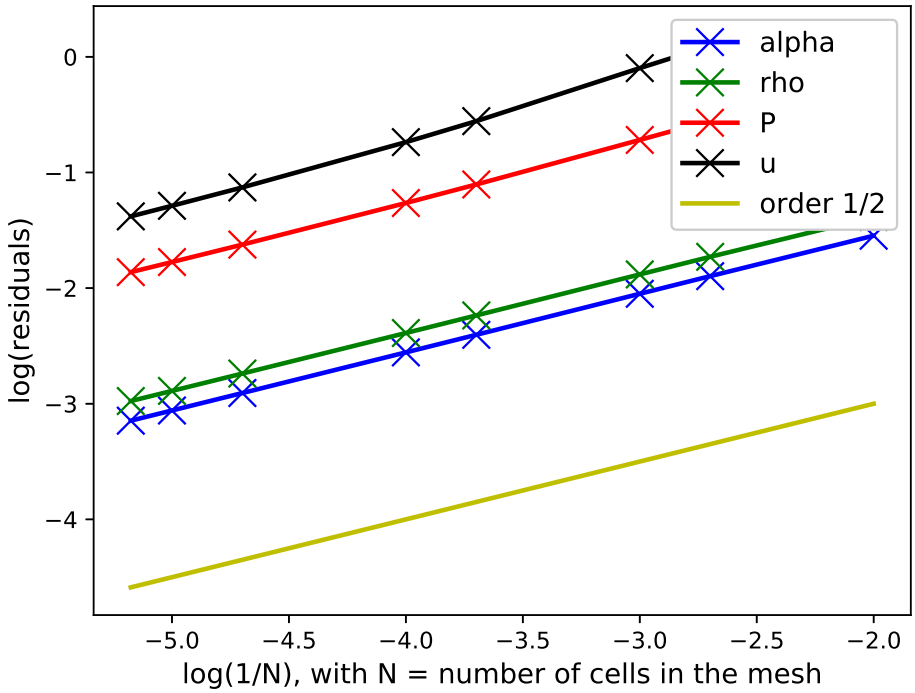

Figure 3.8 – *Convergence curve for Riemann problem 2 (out-of-equilibrium, high pressures) : meshes from 100 to 150 000 cells*

3.4.3 At-equilibrium test cases

Two at-equilibrium Riemann problems are considered:

- a first Riemann problem, with an initial pressure gap around 10 bar (see initial data in appendix 3.C.3);
- a more brutal Riemann problem, with an initial pressure gap around 150 bar, in order to prepare the validation case SUPERCANON of section 3.5 (see initial data in appendix 3.C.4).

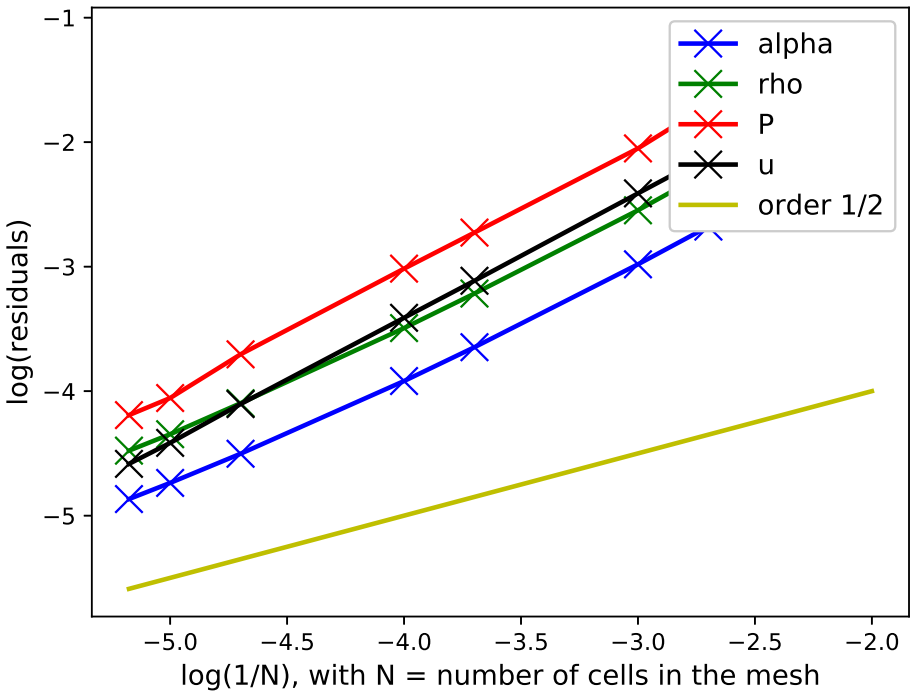

Figure 3.9 – *Convergence curve for Riemann problem 3 (at-equilibrium, with a* $\simeq$ *10 bar pressure gap) : meshes from 100 to 150 000 cells*

In both cases, the asymptotical convergence rate is between $\frac{1}{2}$ and 1, as expected (see figures 3.9 and 3.10). A higher initial pressure gap seems to induce a slightly higher error on the pressure, but not really on the other quantities.

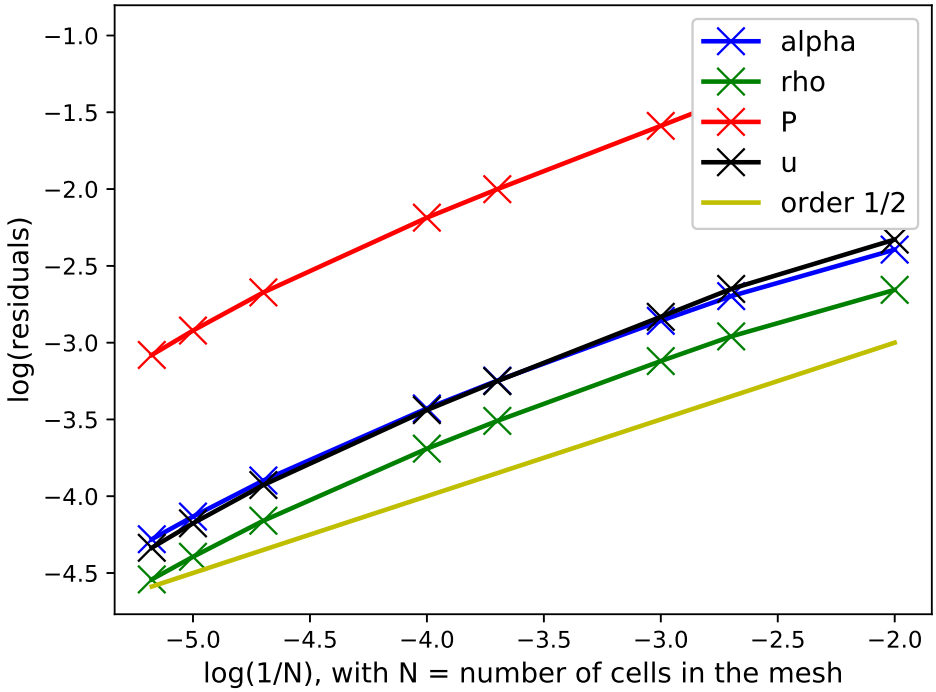

Figure 3.10 – *Convergence curve for Riemann problem 4 (at-equilibrium, with a* $\simeq$ 150 *bar pressure gap) : meshes from 100 to 150 000 cells*

3.5 Validation test case: SUPERCANON simulations

A validation test case is now considered, based on the SUPERCANON experiment [43], aiming to reproduce a simplified loss of coolant accident (LOCA) scenario. The experimental set-up is described on figure 3.11. A tube is filled with pressurized liquid water at 150 bar and 300°C (in order to be representative of the primary circuit of a pressurized water reactor). At the beginning of the experiment, the cap is removed, so that the liquid water is now at the contact of the ambiant air at 1 bar and 20°C.

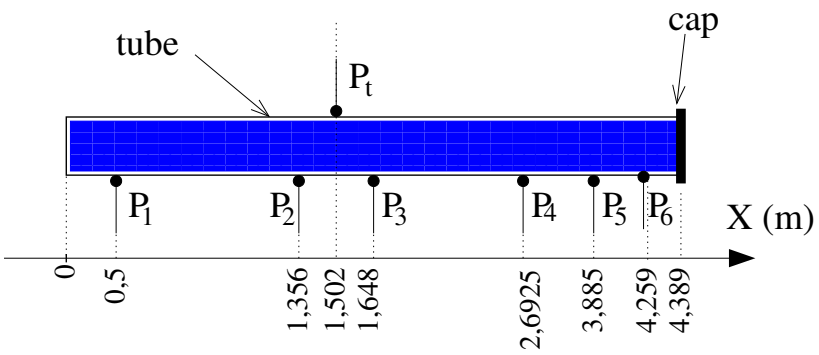

Figure 3.11 – *SUPERCANON experimental set-up [43]*

A rough description of the main phenomena occuring during a SUPERCANON run is the following: the initial pressure gap creates a fast depressurization wave, which travels in the tube to the left. The pressure drop reaches then a pressure around the saturation pressure, leading to the vaporisation of a small amount of liquid. The vapor fraction then increases slowly and the pressure remains almost constant until the arrival of the vaporisation front. This vaporisation front, which travels from the opening of the tube to the end of the tube, produces smoother changes of the pressure. It is responsible for the last pressure drop. Figure 3.12 shows the pressure within time, measured at point P1 (see figure 3.11): because of the importance of the initial pressure gap (around 150 bar), the observed pressure plateau does not match with the expected saturation pressure. It appears that the flow remains out of the thermodynamical equilibrium for a moment within a run, in particular close to the wall when the depressurization wave reaches the bottom of the tube. Previous numerical works [30, 31] based on a similar homogeneous model as the one studied here [4] highlight that taking into account the out-of-equilibrium effects is essential to obtain qualitatively correct results.

In the following, SUPERCANON simulations are performed on a mesh containing 500 cells, on a domain of 10 meters, including the tube in its left part. The present work aims to better assess the importance of several parameters:

- the chosen phasic EOS for the liquid water, by comparing NASG-CK EOS with a classical stiffened gas EOS;
- the initial air mass fraction dissolved in liquid water. Liquid water has been degased in SUPERCANON experiment, but the residual air fraction, even if it is very small, may have a strong influence on the simulations, as it has been highlighted in similar simulations [2];
- the relaxation time parameter λ, defined in hypothesis 3.7. Some toy laws have been used in [30, 31], leading to a great agreement with the experimental results. These laws are here compared with a simplified model based on the nucleation theory, proposed in [24].

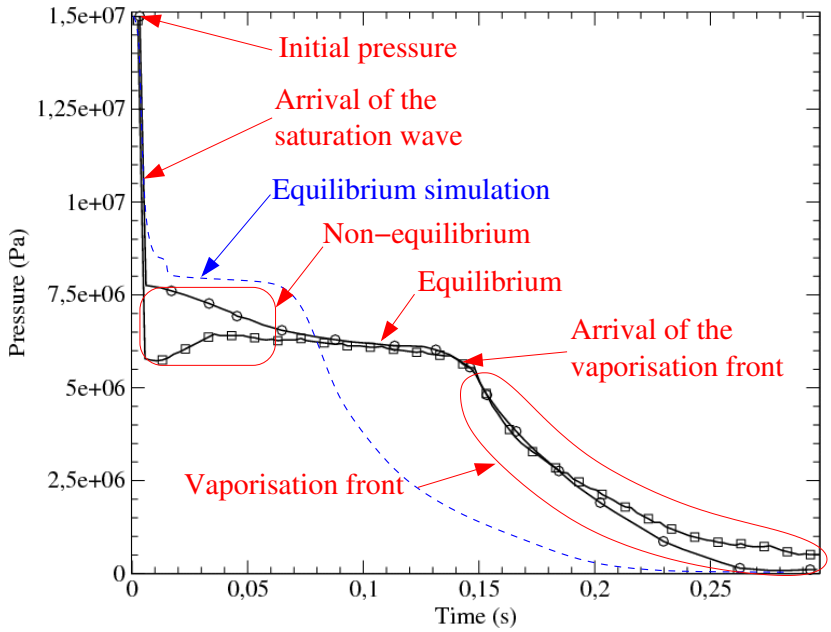

Figure 3.12 – *SUPERCANON experimental set-up [43]*

3.5.1 At-equilibrium simulations

Simulations are performed by taking $\lambda = 0$ and by chosing several y_a. First results can be seen on figure 3.13. When the air mass fraction is very small (cases $y_a = 10^{-6}$, $y_a = 10^{-8}$, $y_a = 0$), the pressure suddently decreases and is then almost constant for a while. The pressure plateau on point P1 is overestimated, as expected because of the thermodynamical equilibrium assumption (see figure 3.13a). The more air there is, the smoother is the pressure drop. When the air mass fraction is quite important (cases $y_a = 10^{-2}$, $y_a = 10^{-3}$), the pressure drop is even delayed and becomes so smooth that the plateau is no more observed. For cases $y_a = 10^{-6}$, $y_a = 10^{-8}$, $y_a = 0$, the slightly different initial air mass fraction leads to slight differences in the very first miliseconds of the experiment (see figure 3.13b). Figures 3.14 and 3.15 show snapshots of the pressure within X (m) at four time steps. The air induces indeed a small pressure overshoot following the depressurization wave in these cases.

3.5.2 Out-of-equilibrium simulations

First results have been obtained by using a toy law for λ, improved from [30] and also used in [31]. The law is the following:

$$\lambda = t_{toy} = \lambda_0 \, f(\alpha_v) \, e^{-\left(\frac{|\alpha_v - \bar{\alpha}_v|}{\delta\alpha}\right)^2}, \tag{3.72}$$

where the function $\alpha \in [0,1] \mapsto f(\alpha)$ corresponds to 3 constant values with cosine connections to get a smooth function, as defined on figure 3.16. The law used to compute the results presented below has the following parameters : $\lambda_0 = 10^{-2}$ s et $\delta\alpha = 5.75\,10^{-4}$, $a = 1$, $b = 0.05$, $c = 0$, $\alpha_1 = 0$, $\alpha_2 = 0.15$, $\alpha_3 = 0.25$, $\alpha_4 = 0.65$.

Figure 3.17 shows some first results obtained without air in the initial liquid water. Further comparisons have to be done, with several initial air fractions y_a in the liquid water.

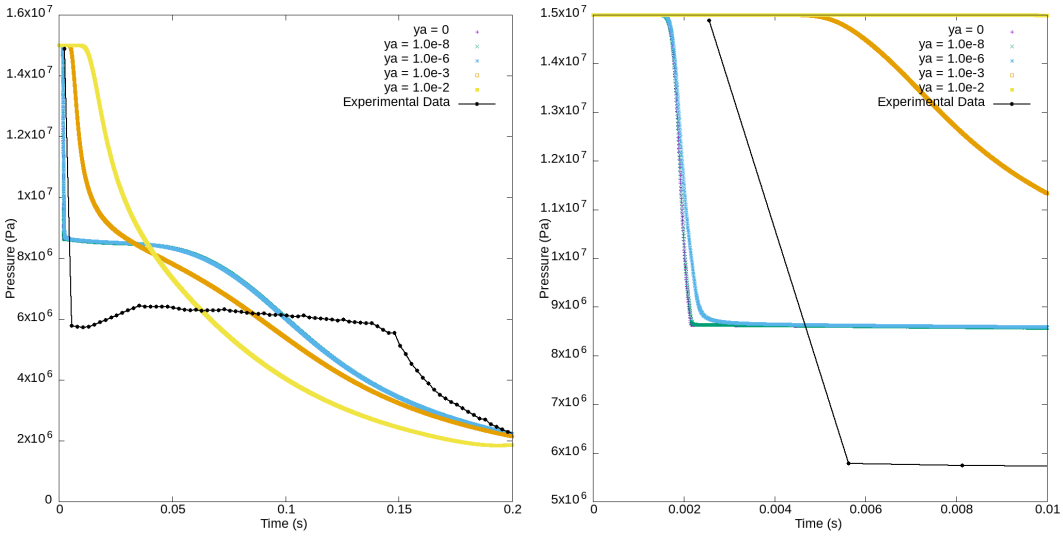

(a) *Comparison between simulations and experimental data.*

(b) *Zoom on the first miliseconds: differences arise, depending on y_a.*

Figure 3.13 – *Pressure (Pa) within time (s) at point P1 (see figure 3.11): at-equilibrium simulation ($\lambda = 0$), using NASG-CK EOS for the liquid with several initial air fractions y_a.*

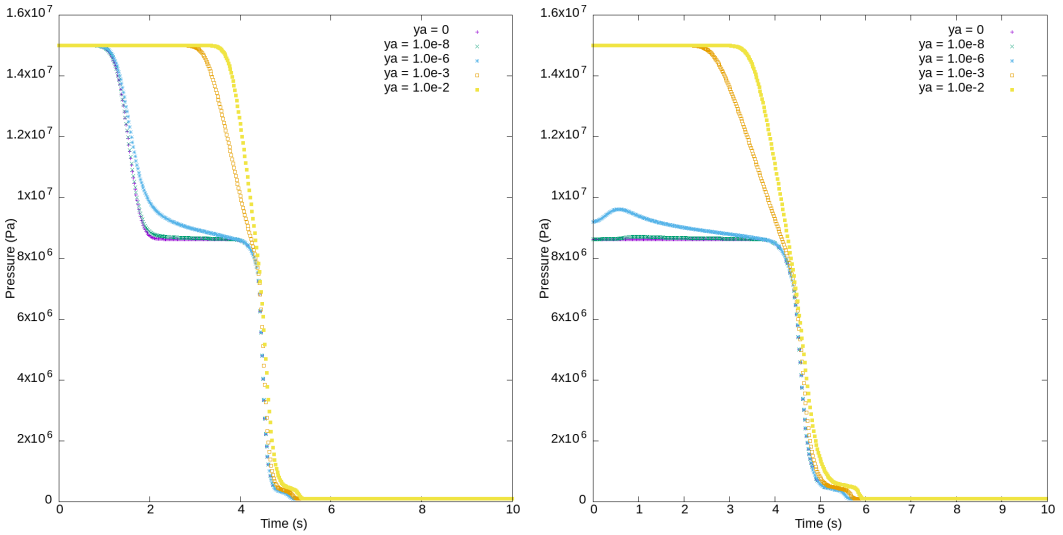

(a) *Snapshot at $t = 1.5\ 10^{-3}s$*

(b) *Snapshot at $t = 2.2\ 10^{-3}s$*

Figure 3.14 – *Pressure (Pa) within X (m) at several time steps: at-equilibrium simulation ($\lambda = 0$), using NASG-CK EOS for the liquid with several initial air fractions y_a.*

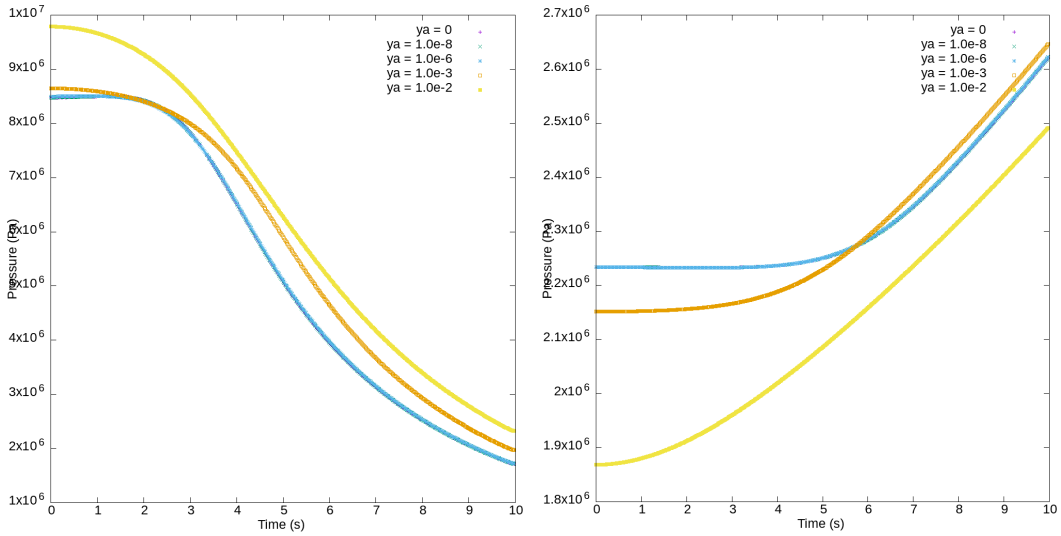

(a) *Snapshot at* $t = 3.0\ 10^{-2}s$ (b) *Snapshot at* $t = 2.0\ 10^{-1}s$

Figure 3.15 – *Pressure (Pa) within X (m) at several time steps: at-equilibrium simulation* ($\lambda = 0$)*, using NASG-CK EOS for the liquid with several initial air fractions* y_a.

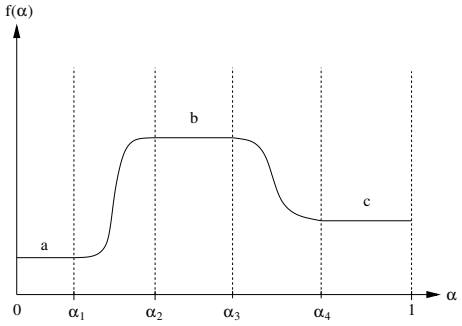

Figure 3.16 – *Definition of the function* $\alpha \in [0,1] \mapsto f(\alpha)$ *used for the definition of* λ.

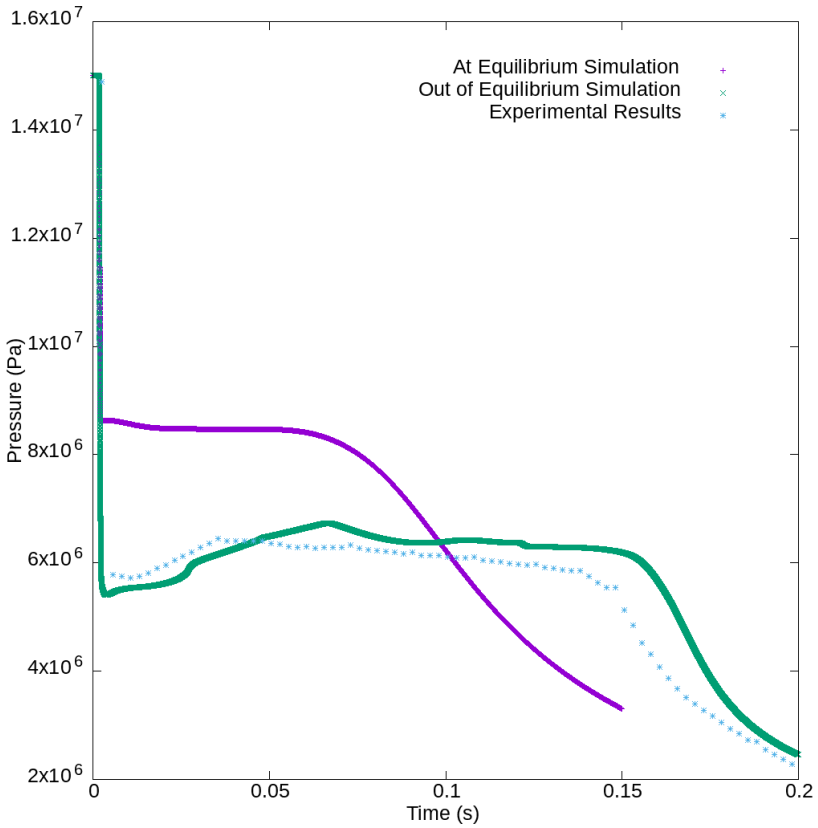

Figure 3.17 – *Pressure (Pa) within time (s) at point P1 (see figure 3.11): at-equilibrium simulation ($\lambda = 0$) and out-of-equilibrium simulation ($\lambda = t_{toy}$, see (3.72)), using NASG-CK EOS for the liquid.*

Conclusion

The homogeneous model based on [4] and already studied in [20] has been implemented by using a quite realistic phasic equation of state for the liquid water: an extension of the Noble-Able stiffened gas [39], modified with the Chemkin EOS [38], as proposed in [7]. The main difficulty arises with the computation of the thermodynamical equilibrium: that is why the algorithms have been carefully detailled in this work. The model has been first verified on Riemann problems. Last, simulations based on the SUPERCANON experiment [43] have been presented.

References

[1] G. ALLAIRE, S. CLERC, and S. KOKH. "A five-equation model for the numerical simulation of interfaces in two-phase flows". In: *Comptes Rendus de l'Académie des Sciences - Series I - Mathematics* 331.12 (2000), pp. 1017–1022. URL: http://www.sciencedirect.com/science/article/pii/S0764444200017535 (cit. on p. 157).

[2] M. BACHMANN, S. MÜLLER, P. HELLUY, and H. MATHIS. "A Simple Model for Cavitation with Non-condensable Gases". In: *Hyperbolic Problems: Theory, Numerics and Applications*. Vol. 18. World Scientific, 2012, pp. 289–296. DOI: 10.1142/9789814417099_0024. URL: https://hal.archives-ouvertes.fr/hal-01420483 (cit. on pp. 157, 158, 186).

[3] M. BAER and J. NUNZIATO. "A two-phase mixture theory for the deflagration-to-detonation transition (DDT) in reactive granular materials". In: *Journal of Multiphase Flows* 12 (1986), pp. 861–889. DOI: https://doi.org/10.1016/0301-9322(86)90033-9 (cit. on p. 157).

[4] T. BARBERON and P. HELLUY. "Finite volume simulation of cavitating flows". In: *Computers and Fluids* 34.7 (2005), pp. 832–858. URL: https://hal.archives-ouvertes.fr/hal-00139597 (cit. on pp. 157–160, 162, 164, 167, 186, 191).

[5] F. BARRE and M. BERNARD. "The CATHARE code strategy and assessment". In: *Nuclear engineering and design* 124.3 (1990), pp. 257–284. DOI: https://doi.org/10.1016/0029-5493(90)90296-A (cit. on p. 157).

[6] G. BERTHOUD. "Vapor explosions". In: *Annual Review of Fluid Mechanics* 32.1 (2000), pp. 573–611. DOI: https://doi.org/10.1146/annurev.fluid.32.1.573 (cit. on p. 158).

[7] P. BOIVIN, M. CANNAC, and O. LE METAYER. "A thermodynamic closure for the simulation of multiphase reactive flows". In: *International Journal of Thermal Sciences* 137 (Mar. 2019), pp. 640–649. URL: https://hal.archives-ouvertes.fr/hal-01981954 (cit. on pp. 158, 170, 171, 191).

[8] C. CHALONS and J.-F. COULOMBEL. "Relaxation approximation of the Euler equations". In: *Journal of Mathematical Analysis and Applications* 348.2 (2008), pp. 872–893. ISSN: 0022-247X. URL: https://hal.archives-ouvertes.fr/hal-01838843 (cit. on p. 176).

[9] F. COQUEL, T. GALLOUËT, J.-M. HÉRARD, and N. SEGUIN. "Closure laws for a two-fluid two-pressure model". In: *Comptes Rendus Mathématique* 334.10 (2002), pp. 927–932. URL: https://hal.archives-ouvertes.fr/hal-01484345 (cit. on p. 157).

[10] J.-P. CROISILLE. "Contribution à l'étude théorique et à l'approximation par éléments finis du système hyperbolique de la dynamique des gaz multidimensionnelle et multiespèces". PhD thesis. Paris 6, 1990 (cit. on p. 169).

[11] F. DAUDE, P. GALON, Z. GAO, and E. BLAUD. "Numerical experiments using a HLLC-type scheme with ALE formulation for compressible two-phase flows five-equation models with phase transition". In: *Computers & Fluids* 94 (May 2014), pp. 112–138. DOI: https://doi.org/10.1016/j.compfluid.2014.02.008 (cit. on pp. 170, 174).

[12] P. DOWNAR-ZAPOLSKI, Z. BILICKI, L. BOLLE, and J. FRANCO. "The non-equilibrium relaxation model for one-dimensional flashing liquid flow". In: *International Journal of Multiphase Flow* 22.3 (1996), pp. 473–483. DOI: https://doi.org/10.1016/0301-9322(95)00078-X (cit. on p. 157).

[13] G. FACCANONI. "Study of a Fine Model of Liquid-Vapor Phase Change. Contribution to the Boiling Crisis Study." PhD thesis. Ecole Polytechnique X, Nov. 2008. URL: https://pastel.archives-ouvertes.fr/tel-00363460 (cit. on pp. 157, 169).

[14] G. FACCANONI, S. KOKH, and G. ALLAIRE. "Modelling and Simulation of Liquid-Vapor Phase Transition in Compressible Flows Based on Thermodynamical Equilibrium." In: *Mathematical Modelling and Numerical Analysis* 46.05 (Sept. 2012), pp. 1029–1054. URL: https://hal.archives-ouvertes.fr/hal-00976983 (cit. on pp. 157, 169, 178, 179, 200).

[15] G. FACCANONI and H. MATHIS. "Admissible Equations of State for Immiscible and Miscible Mixtures". In: *ESAIM: Proceedings and Surveys* (2019). URL: https://hal.archives-ouvertes.fr/tel-00363460 (cit. on pp. 162, 167, 169, 195).

[16] E. FAUCHER, J.-M. HÉRARD, M. BARRET, and C. TOULEMONDE. "Computation of flashing flows in variable cross-section ducts". In: *International Journal of Computational Fluid Dynamics* 13.3 (2000), pp. 365–391. URL: https://hal.archives-ouvertes.fr/hal-01580046 (cit. on p. 157).

[17] S. GAVRILYUK and R. SAUREL. "Mathematical and Numerical Modeling of Two-phase Compressible Flows with Micro-inertia". In: *J. Comput. Phys.* 175.1 (Jan. 2002), pp. 326–360. ISSN: 0021-9991. DOI: http://dx.doi.org/10.1006/jcph.2001.6951 (cit. on pp. 157, 163).

[18] J. GLIMM, D. SALTZ, and D. SHARP. "Two-pressure two-phase flow". In: *Advances In Nonlinear Partial Differential Equations And Related Areas: A Volume in Honor of Professor Xiaqi Ding*. World Scientific, 1998, pp. 124–148. DOI: https://doi.org/10.1142/9789812815811_0008 (cit. on p. 157).

[19] H. GUILLARD and A. MURRONE. *A five equation reduced Model for compressible two phase flow problems*. Tech. rep. RR-4778. INRIA, Mar. 2003. URL: https://hal.inria.fr/inria-00071808 (cit. on p. 157).

[20] H. MATHIS. "A thermodynamically consistent model of a liquid-vapor fluid with a gas". In: *ESAIM: Mathematical Modelling and Numerical Analysis* 53.1 (2019), pp. 63–84. DOI: https://doi.org/10.1051/m2an/2018044 (cit. on pp. 158, 162, 163, 167, 191).

[21] P. HELLUY. "Simulation numérique des écoulements multiphasiques: de la théorie aux applications". Habilitation à diriger des recherches. Université du Sud Toulon Var, 2005. URL: https://tel.archives-ouvertes.fr/tel-00657839 (cit. on pp. 162, 167).

[22] P. HELLUY, O. HURISSE, and E. LE COUPANEC. "Verification of a two-phase flow code based on an homogeneous model". In: *International Journal on Finite Volumes* 13 (Nov. 2016). URL: https://hal.archives-ouvertes.fr/hal-01396200 (cit. on p. 182).

[23] P. HELLUY and N. SEGUIN. "Relaxation models of phase transition flows". In: *ESAIM: Mathematical Modelling and Numerical Analysis* 40.2 (2006), pp. 331–352. URL: https://hal.archives-ouvertes.fr/hal-00139607 (cit. on p. 160).

[24] P. HELLUY, O. HURISSE, and L. QUIBEL. "Assessment of numerical schemes for complex two-phase flows with real equations of state". In: *Computers and Fluids* 196.104347 (Jan. 2020). URL: https://hal.archives-ouvertes.fr/hal-02315038 (cit. on pp. 158–162, 165, 166, 169, 170, 176, 181, 182, 186).

[25] P. HELLUY, O. HURISSE, and L. QUIBEL. "Simulation of a liquid-vapour compressible flow by a Lattice Boltzmann Method". working paper or preprint. Jan. 2020. URL: https://hal.archives-ouvertes.fr/hal-02451368 (cit. on pp. 158, 176).

[26] J.-M. HÉRARD, O. HURISSE, and L. QUIBEL. "Simulations of liquid-vapor water flows with incondensable gases on the basis of a two-fluid model". 2020 (cit. on p. 158).

[27] J.-M. HÉRARD and H. MATHIS. "A three-phase flow model with two miscible phases". In: *ESAIM: Mathematical Modelling and Numerical Analysis* 53, 1373-1389 (Apr. 2019). URL: https://hal.archives-ouvertes.fr/hal-01976938 (cit. on p. 158).

[28] J. HUANG, J. ZHANG, and L. WANG. "Review of vapor condensation heat and mass transfer in the presence of non-condensable gas". In: *Applied thermal engineering* 89 (2015), pp. 469–484. DOI: https://doi.org/10.1016/j.applthermaleng.2015.06.040 (cit. on p. 157).

[29] O. HURISSE. "Application of an homogeneous model to simulate the heating of two-phase flows". In: *International Journal on Finite Volumes* 11 (May 2014), http://www.latp.univ–mrs.fr/IJFV/spip.php?article52. URL: https://hal.archives-ouvertes.fr/hal-01114808 (cit. on pp. 169, 181).

[30] O. HURISSE. "Numerical simulations of steady and unsteady two-phase flows using a homogeneous model". In: *Computers and Fluids* 152 (July 2017), pp. 88–103. URL: https://hal.archives-ouvertes.fr/hal-01489039 (cit. on pp. 158, 162, 165, 167, 169, 176, 182, 186, 187).

[31] O. HURISSE and L. QUIBEL. "Simulations of a simplified LOCA scenario with a non-equilibrium homogeneous model". 2020. URL: https://hal.archives-ouvertes.fr/hal-02901408 (cit. on pp. 186, 187).

[32] O. HURISSE and L. QUIBEL. "A homogeneous model for compressible three-phase flows involving heat and mass transfer." In: *ESAIM: Proceedings and Surveys* 66 (2019), pp. 84–108. URL: https://hal.archives-ouvertes.fr/hal-01976903 (cit. on pp. 158, 159, 161, 162, 167, 169, 195).

[33] IRSN. *Accidents graves pouvant affecter un réacteur à eau pressurisée*. 2011. URL: https://www.irsn.fr/fr/connaissances/installations_nucleaires/les-accidents-nucleaires/ (visited on 09/30/2019) (cit. on p. 157).

[34] S. JAOUEN. "Etude mathématique et numérique de stabilité pour des modeles hydrodynamiques avec transition de phase". PhD thesis. Paris 6, 2001 (cit. on pp. 162, 167).

[35] H. JIN, J. GLIMM, and D. SHARP. "Compressible two-pressure two-phase flow models". In: *Physics letters A* 353.6 (2006), pp. 469–474. DOI: https://doi.org/10.1016/j.physleta.2005.11.087 (cit. on p. 157).

[36] J. JUNG. "Numerical simulations of two-fluid flow on multicores accelerator". PhD thesis. Université de Strasbourg, Oct. 2013. URL: https://tel.archives-ouvertes.fr/tel-00876159 (cit. on pp. 159, 162, 167, 195).

[37] A. K. KAPILA, R. MENIKOFF, J. B. BDZIL, S. F. SON, and D. S. STEWART. "Two-phase modeling of deflagration-to-detonation transition in granular materials: Reduced equations". In: *Physics of Fluids* 13.10 (2001), pp. 3002–3024. DOI: https://doi.org/10.1063/1.1398042 (cit. on p. 157).

[38] R. J. KEE, F. M. RUPLEY, E. MEEKS, and J. A. MILLER. *CHEMKIN-III: A FORTRAN chemical kinetics package for the analysis of gas-phase chemical and plasma kinetics*. Tech. rep. Sandia National Labs., Livermore, CA (United States), 1996. URL: https://www.osti.gov/biblio/481621 (cit. on pp. 158, 170, 171, 191).

[39] O. LE MÉTAYER and R. SAUREL. "The Noble-Abel Stiffened-Gas equation of state". In: *Physics of Fluids* 28 (2016), p. 046102. DOI: 10.1063/1.4945981. URL: https://hal.archives-ouvertes.fr/hal-01305974 (cit. on pp. 158, 170, 180, 191).

[40] R. LEWANDOWSKI and B. MOHAMMADI. "Existence and positivity results for the φ-θ and a modified k- ε two-equation turbulence models". In: *Mathematical Models and Methods in Applied Sciences* 3.02 (1993), pp. 195–215. DOI: https://doi.org/10.1142/S0218202593000114 (cit. on p. 168).

[41] H. MATHIS. "Theoretical and numerical study of phase transition flows". PhD thesis. Université de Strasbourg, Sept. 2010. URL: https://tel.archives-ouvertes.fr/tel-00516683 (cit. on pp. 162, 167, 169, 195).

[42] R. MEIGNEN, B. RAVERDY, S. PICCHI, and J. LAMOME. "The challenge of modeling fuel–coolant interaction: Part II–Steam explosion". In: *Nuclear Engineering and Design* 280 (2014), pp. 528–541. DOI: http://dx.doi.org/10.1016/j.nucengdes.2014.08.028 (cit. on pp. 157, 158).

[43] B. RIEGEL. "Contribution à l'étude de la décompression d'une capacité en régime diphasique". PhD thesis. 1978 (cit. on pp. 186, 187, 191).

[44] V. V. RUSANOV. "The calculation of the interaction of non-stationary shock waves with barriers". In: *Zhurnal Vychislitel'noi Matematiki i Matematicheskoi Fiziki* 1.2 (1961), pp. 267–279. DOI: https://doi.org/10.1016/0041-5553(62)90062-9 (cit. on p. 176).

[45] W. WAGNER and H.-J. KRETZSCHMAR. *International Steam Tables: Properties of Water and Steam Based on the Industrial Formulation IAPWS-IF97*. Springer-Verlag Berlin Heidelberg, 2008. ISBN: 9783540742340. DOI: http://dx.doi.org/10.1007/978-3-540-74234-0 (cit. on p. 170).

[46] N. YANENKO. *Méthode à pas fractionnaires: résolutions de problèmes polydimensionnels de physique mathématique*. Collection Intersciences. A. Colin, 1968. URL: https://books.google.fr/books?id=JBIyvgAACAAJ (cit. on p. 176).

Appendices

3.A Concavity of the intensive entropies

Here, we recall the consequences of property 3.1 in terms of concavity, without detailling the proofs. Indeed, they can be very easily. We refer to [32] for detailled proofs, adapted from [15, 41, 36], in a very similar case: indeed, in [32], the model deals with a three-phase flow model describing three immiscible components, which leads to the same definition as (3.15) for the mixture entropy.

Property 3.11 (Concavity of the extensive mixture entropy)
$W \in \Omega \mapsto S(W)$ is concave. Moreover, if we consider the manifold $\tilde{\Omega} = \{W \in \Omega / \mathcal{M} > 0 \text{ is fixed}\}$, then $W \in \tilde{\Omega} \mapsto S(W)$ is strictly concave. □

Property 3.12 (Concavity of the intensive phasic entropy)
$W_k \in \Omega_k \mapsto s_k(\tau_k, e_k)$ is concave. □

Property 3.13 (Concavity of the intensive mixture entropy)
We recall the notation $Y = (\alpha_v, y_v, y_a, z_v, z_a)$.

(I) : For a given (τ, e), $Y \in [0,1]^5 \mapsto s(Y, \tau, e)$ is strictly concave. This property implies that s admits a unique maximum reached on a fraction set $\bar{Y}$, which is defined as the thermodynamical equilibrium.

(II) : For a given $Y \in [0,1]^5$, $(\tau, e) \mapsto s(Y, \tau, e)$ is strictly concave. This property allows to define the shock wave in a unique manner. □

3.B Coefficients for NASG-CK EOS and SG EOS

Coefficients	Liquid NASG-CK
A_l (dimensionless)	4.69738865636393e+01
B_l (K^{-1})	-4.19269571479452e-01
C_l (K^{-2})	1.70702143968620e-03
D_l (K^{-3})	-3.04805662517983e-06
E_l (K^{-4})	2.02814588067819e-09
F_l (K)	-2.519604765e+06/R
G_l (dimensionless)	-5.573536947e+04/R
γ_l (dimensionless)	3.27113568773712
$C_{v,l}$ $(JK^{-1}kg^{-1})$	7.24509640448929e+02
Π_l (Pa)	1.24425779880749e+09
b_l (m^3kg^{-1})	5.66559849022606e-04

Table 3.B.1 – *Coefficients for Noble-Able Chemkin EOS* (3.43)*, for liquid.*

Coefficients	Liquid SG
γ (dimensionless)	1.39864082368510
C_v $(JK^{-1}kg^{-1})$	3.19641035947920e+03
Q (Jkg^{-1})	-1.24606074764184e+06
Π (Pa)	4.79690712132593e+08
k $(JK^{-1}kg^{-1})$	3.07594603384284e+02

Table 3.B.2 – *Coefficients for stiffened gas EOS, for liquid, obtained from the optimization process in Chapter 2*

where $k = C_v \ln(C_v) + C_v(\gamma - 1)\ln(C_v(\gamma - 1)) + s_0$.

Coefficients	Vapor SG
γ (dimensionless)	1.15442237458290
C_v $(JK^{-1}kg^{-1})$	2.91668522329726e+03
Q (Jkg^{-1})	1.25942536895827e+06
Π (Pa)	-3.24993579473092e+02
k $(JK^{-1}kg^{-1})$	-7.77026092439033e+03

Table 3.B.3 – *Coefficients for stiffened gas EOS, for vapor, obtained from the optimization process in Chapter 2*

where $k = C_v \ln(C_v) + C_v(\gamma - 1)\ln(C_v(\gamma - 1)) + s_0$.

Coefficients	Air SG
γ (dimensionless)	1.4
C_v $(JK^{-1}kg^{-1})$	719.0
Q (Jkg^{-1})	0
Π (Pa)	0
k $(JK^{-1}kg^{-1})$	0

Table 3.B.4 – *Coefficients for stiffened gas EOS, for air, considered as a perfect gas*

3.C Initial data for Riemann problems test cases

3.C.1 Out-of-equilibrium Riemann problems

Data	Left state	Intermediate state	Right state
α	9.83232179608806 10^{-1}	9.87041861906529 10^{-1}	9.87041861906529 10^{-1}
y	3.17380286565343 10^{-2}	4.03113857253491 10^{-2}	4.03113857253491 10^{-2}
z	4.91959192421520 10^{-1}	5.44567894139035 10^{-1}	5.44567894139035 10^{-1}
y_a	5.0 10^{-2}	6.18446225562366 10^{-2}	6.18446225562366 10^{-2}
z_a	8.83504641470457 10^{-2}	9.77984087865951 10^{-2}	9.77984087865951 10^{-2}
τ (m^3/kg)	5.4427805669757310^{-2}	6.886350393192439 10^{-2}	6.89635039319242 10^{-2}
u (m/s)	1.0	1.0	-2.15013291878029
P (Pa)	1.86680031787657 10^5	1.86680031787657 10^5	8.74466577184921 10^4

Table 3.C.1 – Out-of-equilibrium test case 1 (low pressures). $\sigma = 2170.29190638504$ m/s

Data	Left state	Intermediate state	Right state
α	0	9.19694593615943 10^{-1}	9.19694593615943 10^{-1}
y	0	2.85573530078594 10^{-1}	2.85573530078594 10^{-1}
z	0	6.30189314804280 10^{-1}	6.30189314804280 10^{-1}
y_a	0	2.98982265612722 10^{-1}	2.98982265612722 10^{-1}
z_a	0	1.14386879858482 10^{-1}	1.14386879858482 10^{-1}
τ (m^3/kg)	1.31548928051287 10^{-3}	6.08942521668654 10^{-3}	5.98942521668655 10^{-3}
u (m/s)	100.0	100.0	122.564444506511
P (Pa)	1.49999999999962 10^7	1.49999999999962 10^7	2.00915415588632 10^7

Table 3.C.2 – Out-of-equilibrium test case 2 (high pressures) : $\sigma = 1474.04497378469$ m/s

3.C.2 At-equilibrium Riemann problems

Data	Left state	Intermediate state	Right state
α	2.83455356934630 10^{-1}	6.11774284813328 10^{-1}	3.99122663398670 10^{-1}
y	4.25625125846829 10^{-3}	8.70625146760066 10^{-3}	1.0 10^{-2}
z	1.51011070725486 10^{-2}	2.91840921657732 10^{-2}	3.35291837019411 10^{-2}
y_a	2.0 10^{-2}	3.0 10^{-2}	3.0 10^{-2}
z_a	9.24831478659724 10^{-3}	1.32498062560992 10^{-2}	1.32417151719985 10^{-2}
τ (m^3/kg)	1.6382140748807462 10^{-3}	1.9485538689275692 10^{-3}	2.080256962546277 10^{-3}
u (m/s)	1.0	1.0	-9.71690290715716
P (Pa)	8.00000000000805 10^{6}	7.99999999999713 10^{6}	7.12794753132892 10^{6}

Table 3.C.3 – At-equilibrium test case 3 (smooth case) : $\sigma = 159.557115470034$ m/s

Data	Left state	Intermediate state	Right state
α	4.55806467748821 10^{-1}	6.35814523035530 10^{-1}	9.88240646295054 10^{-1}
y	2.79348914129385 10^{-2}	5.74662402110775 10^{-2}	1.0 10^{-1}
z	7.30830106253936 10^{-2}	1.44714572786685 10^{-1}	4.11152591599341 10^{-1}
y_a	5.0 10^{-2}	9.0 10^{-2}	9.0 10^{-2}
z_a	1.81366554653765 10^{-2}	3.15417178714970 10^{-2}	4.39343919538099 10^{-2}
τ (m^3/kg)	2.18882462814298 10^{-3}	3.0386914611470485 10^{-3}	7.55537631384807 10^{-2}
u (m/s)	1.0	1.0	-1028.59799314035
P (Pa)	1.49999999999975 10^{7}	1.50000000000035 10^{7}	3.21668487111682 10^{5}

Table 3.C.4 – At-equilibrium test case 4 (high pressure gap) : $\sigma = 44.1445568183537$ m/s

3.D Algorithms to compute the thermodynamical equilibrium

Here, we present the four auxiliary algorithms, called in the main algorithm 3.1. They are built among the same principles in [14], enabling to compute the thermodynamical equilibrium, depending on the fields which are actually present in the mixture, as explained in properties 3.3 and 3.4. Note that ALGORITHM 3.2 is independent from the choice of phasic EOS, whereas the other algorithms **take advantage of the particular form of the stiffened gas EOS used for the vapor and the non-condensable gas** (see remark 3.5).

ALGORITHM 3.2 (Equilibrium with two fields l and v) — Arguments: (τ, e).
Liquid-vapor equilibrium satisfies:

$$\begin{array}{rcccl} P_l(\tau_l, e_l) & = & P_v(\tau_v, e_v) & = & \bar{P}; \\ T_l(\tau_l, e_l) & = & T_v(\tau_v, e_v) & = & \bar{T}; \\ \mu_l(P_l, T_l) & = & \mu_v(P_v, T_v), & & \end{array} \tag{3.73}$$

with $\tau_k = \frac{\alpha_k}{y_k}\tau$ and $e_k = \frac{z_k}{y_k}e$ for $k = l, v$.

Instead of looking for fractions $\bar{\alpha}_v$, $\bar{y}_v$ and $\bar{z}_v$ satisfying (3.73), the unknowns $\bar{P}$, $\bar{T}$ and $\bar{y}_v$ are considered. Last equation from (3.73):

$$\mu_l(\bar{P}, \bar{T}) = \mu_v(\bar{P}, \bar{T}), \tag{3.74}$$

enables to define the saturation temperature $\bar{T} = T_{sat}(\bar{P})$. For each tested $\bar{P}$, the saturation temperature $\bar{T}$ is then obtained by using a secant method algorithme solving (3.74).

Our entry arguments (τ, e) give us two more equations due to the miscibility constraints (3.8), both depending on $\bar{y}_v$, which are:

$$\begin{array}{rcl} \tau & = & (1-\bar{y}_v) \times \tau_l(\bar{P}, T_{sat}(\bar{P})) + \bar{y}_v \times \tau_v(\bar{P}, T_{sat}(\bar{P})), \\ e & = & (1-\bar{y}_v) \times e_l(\bar{P}, T_{sat}(\bar{P})) + \bar{y}_v \times e_v(\bar{P}, T_{sat}(\bar{P})). \end{array} \tag{3.75}$$

First equation of (3.75) leads to an explicit formula for $\bar{y_v}$, as a function of $\bar{P}$:

$$\bar{y_v} = \bar{y}_v(\bar{P}) = \frac{\tau - \tau_l(\bar{P}, T_{sat}(\bar{P}))}{\tau_v(\bar{P}, T_{sat}(\bar{P})) - \tau_l(\bar{P}, T_{sat}(\bar{P}))}. \tag{3.76}$$

The resolution is finally achieved with a secant method algorithm by looking for $\bar{P}$ verifying:

$$e = (1-\bar{y}_v(\bar{P})) \times e_l(\bar{P}, T_{sat}(\bar{P})) + \bar{y}_v(\bar{P}) \times e_v(\bar{P}, T_{sat}(\bar{P})), \tag{3.77}$$

using the previous definition (3.76) for $\bar{y}_v(\bar{P})$.

ALGORITHM 3.3 (Equilibrium with three fields *l*, *v* and *a*) — Arguments: (y_a, τ, e). Thermodynamical equilibrium (3.23) is characterized in (τ, e)-plane, as depicted in property 3.3, by:

$$\begin{array}{rcccl} P_l(\tau_l, e_l) & = & P_v(\tau_v, e_v) + P_a(\tau_a, e_a) & = & \bar{P}; \\ T_l(\tau_l, e_l) & = & T_v(\tau_v, e_v) & = & \bar{T}; \\ T_v(\tau_v, e_v) & = & T_a(\tau_a, e_a) & = & \bar{T}; \\ \mu_l(P_l(\tau_l, e_l), T_l(\tau_l, e_l)) & = & \mu_v(P_v(\tau_v, e_v), T_v(\tau_v, e_v)); & & \end{array} \tag{3.78}$$

As already explained in section 3.3.3, instead of looking for $\bar{\alpha}_v$, $\bar{y}_v$, $\bar{z}_v$ and $\bar{z}_a$ satisfying (3.78), the following unknows are considered in pressure-temperature plane: $\bar{P}_v$, $\bar{P}_a$, $\bar{T}$ and $\bar{y}_v$. Miscibility constraints (3.7) enable to get a system equivalent to system (3.78) in pressure-temperature plane:

$$\begin{array}{rcl} \bar{y}_v \times \tau_v(\bar{P}_v, \bar{T}) & = & y_a \times \tau_a(\bar{P}_a, \bar{T}); \\ \tau & = & (1 - \bar{y}_v) \times \tau_l(\bar{P}_v + \bar{P}_a, \bar{T}) + \bar{y}_v \times \tau_v(\bar{P}_v, \bar{T}); \\ e & = & (1 - \bar{y}_v) \times e_l(\bar{P}_v + \bar{P}_a, \bar{T}) + \bar{y}_v \times e_v(\bar{P}_v, \bar{T}) + y_a \times e_a(\bar{P}_a, \bar{T}); \\ \mu_l(\bar{P}_v + \bar{P}_a, \bar{T}) & = & \mu_v(\bar{P}_v, \bar{T}). \end{array} \tag{3.79}$$

The previous system is solved as follows, in three steps:

1. Thanks to the particular form of the stiffened gas EOS, the first equation of (3.79) gives an explicit definition of $\bar{y}_v$ as a function of $\bar{P}_v$ and $\bar{P}_a$:

$$\bar{y}_v = y_a = \frac{C_{v,a}(\gamma_a - 1)}{C_{v,v}(\gamma_v - 1)} \frac{(\bar{P}_v + \Pi_v)}{(\bar{P}_a + \Pi_a)}) = \bar{y}_v(\bar{P}_v, \bar{P}_a). \tag{3.80}$$

2. **The stiffened gas formula is used** to compute $\bar{T}$. Indeed, its particular form enables to decouple $\bar{T}$ and $\bar{y}_v$ in the second equation of (3.79) :

$$\begin{array}{rcl} \bar{T} & = & (\tau - (1 - y_a - \bar{y}_v) b_l) \left((1 - y_a - \bar{y}_v) C_{v,l}(\gamma_l - 1) + y_a C_{v,a}(\gamma_a - 1) \right)^{-1} \\ & = & \bar{T}(\bar{P}_v, \bar{P}_a). \end{array} \tag{3.81}$$

3. We still need to solve the following system relatively to $(\bar{P}_v, \bar{P}_a)$, for instance with a Broyden algorithm:

$$\left\{ \begin{array}{ll} (f_1): & \mu_l(\bar{P}_v + \bar{P}_a, \bar{T}) = \mu_v(\bar{P}_v, \bar{T}) \\ (f_2): & e = (1 - \bar{y}_v - y_a) \times e_l(\bar{P}_v + \bar{P}_a, \bar{T}) + \bar{y}_v \times e_v(\bar{P}_v, \bar{T}) + y_a \times e_a(\bar{P}_a, \bar{T}) \\ \text{with:} & \bar{y}_v = \bar{y}_v(\bar{P}_v, \bar{P}_a) \text{ from (3.80)} \quad \text{and} \quad \bar{T} = \bar{T}(\bar{P}_v, \bar{P}_a) \text{ from (3.81)}. \end{array} \right.$$

A difficulty arising with Broyden algorithm is to propose a relevant starting point. Several choices are tested in the code:

- correlations obtained with R from large data sets;
- pressures obtained after solving a dichotomy on either (f_1) or (f_2), by fixing either P_v or P_a;
- pressure P_v obtained with the same τ and e but $y_a = 0$.

However, Broyden algorithm may still fail. A double dichotomy on P_v, and then P_a has also been implemented, but it has also a lack of robustness since we have difficulties to define some bounds for P_v and P_a.

ALGORITHM 3.4 (Equilibrium with two fields l and a) — Arguments: (τ, e).
In this case:

$$y_v = 0 \quad ; \quad y_l = 1 - y_a.$$

Conditions from property 3.4 are recalled, with $\tau_k = \frac{\alpha_k}{y_k}\tau$ and $e_k = \frac{z_k}{y_k}e$ for $k = l, a$:

$$\begin{array}{rcccl} P_l(\tau_l, e_l) & = & P_a(\tau_a, e_a) & = & \bar{P}; \\ T_l(\tau_v, e_v) & = & T_a(\tau_a, e_a) & = & \bar{T}; \end{array} \tag{3.82}$$

Due to our entry arguments (τ, e), unknowns $\bar{P}$, $\bar{T}$ are once more relevant, and miscibility constraints (3.8) lead to:

$$\begin{array}{rcl} \tau & = & (1 - y_a) \times \tau_l(\bar{P}, \bar{T}) + y_a \times \tau_a(\bar{P}, \bar{T}), \\ e & = & (1 - y_a) \times e_l(\bar{P}, \bar{T}) + y_a \times e_a(\bar{P}, \bar{T}). \end{array} \tag{3.83}$$

Due to the particular form of the stiffened gas EOS, the first equation of (3.83) leads to an explicit definition of $\bar{T}$ as a function of $\bar{P}$:

$$\bar{T} = (\tau - (1 - y_a)b_l)\left(\frac{y_a C_{v,a}(\gamma_a - 1)}{\bar{P} + \Pi_a} + \frac{(1 - y_a)C_{v,l}(\gamma_l - 1)}{\bar{P} + \Pi_l}\right)^{-1} = \bar{T}(\bar{P}), \tag{3.84}$$

so that there is only one implicit equation in $\bar{P}$ left:

$$\begin{array}{ll} (f): & e = (1 - y_a) \times e_l(\bar{P}, \bar{T}(\bar{P})) + y_a \times e_a(\bar{P}, \bar{T}(\bar{P})), \\ \text{with:} & \bar{T} = \bar{T}(\bar{P}) \text{ from (3.84)}. \end{array} \tag{3.85}$$

The resolution is finally achieved by looking for $\bar{P}$ verifying equation (3.85) with a secant method algorithm.

ALGORITHM 3.5 (Equilibrium with two fields v and a) — Arguments: (τ, e).
In this case:

$$y_l = 0 \quad ; \quad y_v = 1 - y_a.$$

Only one condition is obtained from property 3.4:

$$\bar{T} = T_v(\tau_v, e_v) = T_a(\tau_a, e_a). \tag{3.86}$$

In pressure-temperature plane, the miscibility constraints from hypothesis 3.6 lead to the following condition;:

$$\tau = y_a \tau_a(\bar{P}_a, \bar{T}) = (1 - y_a)\tau_v(\bar{P}_v, \bar{T}),$$

which implies (**because we use stiffened gas EOS**):

$$\bar{T} = \frac{(e - (y_a Q_a + (1 - y_a)Q_v)}{y_a C_{v,a} + (1 - y_a)C_{v,v}} + (\Pi_a + \Pi_v)\tau.$$

Finally, $\bar{P}_a$ and $\bar{P}_v$ can be explicitly deduced thanks to **the stiffened gas phasic EOS**:

$$\bar{P}_k = \frac{y_k C_{v,k}(\gamma_k - 1)\bar{T}}{\tau} - \Pi_k, \quad k = v, a.$$

3.E Analytical solutions for the model

For a sake of readibility, let us highlight that all the variables are initialized since y_a and phasic pressures and temperatures are given through the following function $\text{INIT}(y_a, P_l, P_v, P_a, T_l, T_v, T_a)$:

ALGORITHM 3.6 (Initialization) — $\text{INIT}(y_a, P_l, P_v, P_a, T_l, T_v, T_a) \rightarrow (\alpha, y_v, z_v, z_a, \tau, e, P, T)$:

1. Using the phasic EOS:
   - $\tau_l = b_l + \dfrac{C_{v,l}(\gamma_l - 1)T_l}{P_l + \Pi_l}$ and $\tau_k = \dfrac{C_{v,k}(\gamma_k - 1)T_l}{P_k + \Pi_k}$ for $k = v, a$.
   - $e_l = RT_l(A_l + \frac{B_l}{2}T_l + \frac{C_l}{3}T_l^2 + \frac{D_l}{4}T_l^3 + \frac{E_l}{5}T_l^4 + \frac{F_l}{T_l}) - P_l(\tau_l - b_l)$ and $e_k = C_{v,k}T_k + Q_k + (\tau_k - b_k)\Pi_k$ for $k = v, a$.
2. Using miscibility constraints (3.7):
   - $y_v = y_a\dfrac{\tau_a}{\tau_v}$ so that $y_l = 1 - y_a - y_v$;
   - $\tau = y_l\tau_l + y_a\tau_a$;
   - $e = y_le_l + y_ve_v + y_ae_a$.
3. Using the definition of phasic fractions:
   - $\alpha = \alpha_v = \alpha_a = y_v\dfrac{\tau_v}{\tau}$;
   - $z_k = y_k\dfrac{e_k}{e}$ for $k = v, a$.
4. Using the definition of mixture pressure and temperature (3.34):

$$P = \frac{(1-\alpha_v)\frac{P_l}{T_l} + \alpha_v(\frac{P_v}{T_v} + \frac{P_a}{T_a})}{\frac{1-z_v-z_a}{T_l} + \frac{z_v}{T_v} + \frac{z_a}{T_a}} \quad ; \quad \frac{1}{T} = \frac{1-z_v-z_a}{T_l} + \frac{z_v}{T_v} + \frac{z_a}{T_a}.$$

Our methods to build analytical Riemann problems are now presented in the two following algorithms.

ALGORITHM 3.7 (Building of an out-of-equilibrium Riemann problem) — Approach:

1. We define the left state W^L:
   - by choosing U^L, P_k^L and T_k^L for $k \in \mathcal{K}$;
   - by deducing the other quantities α_v^L, y_v^L, z_v^L, z_a^L, e^L, τ^L, P^L and T^L from $\text{INIT}(y_a^L, P_l^L, P_v^L, P_a^L, T_l^L, T_v^L, T_a^L)$.
2. Then, we define the intermediate state W^*:

- by imposing $U^* = U^L$ (due to (3.71) through a contact);
- by choosing P_k^* and T_k^* for $k \in \mathcal{K}$;
- by finding thanks to dichotomy algorithm y_a^* so that

$$P^*(y_a^*) = P^L \text{ (due to (3.71) through a contact).}$$

  Indeed, for each tested $\tilde{y}_a^*$, we use $\text{INIT}(\tilde{y}_a^*, P_l^*, P_v^*, P_a^*, T_l^*, T_v^*, T_a^*)$, so that we get a value for $\tilde{P}^* = \tilde{P}^*(\tilde{y}_a^*)$.
- once y_a^* is found, the other quantities are computed with $\text{INIT}(y_a^*, P_l^*, P_v^*, P_a^*, T_l^*, T_v^*, T_a^*)$.

3. Last, we define the right state W^R:
   - by imposing $\alpha_v^R = \alpha_v^*$, $y_v^R = y_v^*$, $y_a^R = y_a^*$, $z_v^R = z_v^*$ and $z_a^R = z_a^*$ (due to (3.71) through a shock);
   - by arbitrarely imposing τ^R;
   - by looking for e^R verifying the last Rankine-Hugoniot equation through a shock:

$$e^R - e^* + (\tau^R - \tau^*)\frac{P^R(e^R, ...) + P^*}{2} = 0$$

     where, using (3.34),

$$P^R = P^R(e^R, \tau^R, \alpha_v^R, y_v^R, y_a^R, z_v^R, z_a^R);$$

   - and last by deducing with (3.71) $J^2 = \dfrac{-P^R + P^*}{\tau^R - \tau*}$, and then $U^R = U^* - \dfrac{P^R - P*}{J}$ and $\sigma = U^R - J\tau^R$.

ALGORITHM 3.8 (Building of an at-equilibrium Riemann problem) — Approach:

1. We define the left state W^L:
   - by choosing U^L;
   - by choosing P_k^L and T_k^L to comply with thermodynamical equilbrium, so that:

$$P_l^L = P_v^L + P_a^L \quad \text{and} \quad T_k^L = T_{sat}(P_v^L, P_a^L)\ \forall k \in \mathcal{K};$$

   - by deducing the other quantities α_v^L, y_v^L, z_v^L, z_a^L, e^L, τ^L, P^L and T^L from $\text{INIT}(y_a^L, P_l^L, P_v^L, P_a^L, T_l^L, T_v^L, T_a^L)$.
2. Then, we define the intermediate state W^*:
   - by imposing $U^* = U^L$ (due to (3.71) through a contact);

- by choosing P_k^* and T_k^* to comply with thermodynamical equilibrium) i.e. by choosing
$$P_l^* = P_l^L \quad \text{and} \quad P_k^* \neq P_k^L,$$
so that:
$$P_v^L + P_a^L = P_v^* + P_a^* \quad \text{and} \quad T_k^L = T_{sat}(P_v^*, P_a^*) \quad \forall k \in \mathcal{K};$$
- and then, by deducing the other quantities α_v^*, y_v^*, z_v^*, z_a^*, e^*, τ^*, P^* and T^* from $\text{INIT}(y_a^*, P_l^*, P_v^*, P_a^*, T_l^*, T_v^*, T_a^*)$.

3. Last, we define the right state W^R:
   - by imposing $y_a^R = y_a^*$ (due to (3.71) through a shock);
   - by arbitrarely defining $y_v^R \neq y_v^*$;
   - by looking for P_v^R verifying the last Rankine-Hugoniot equation through a shock:
$$e^R(P_v^R, ...) - e^* + (\tau^R(P_v^R, ...) - \tau^*)\frac{P_v^R + P_a^R(P_v^R, ...) + P^*}{2} = 0;$$
   We detail the terms from the previous equation:
   - as y_v^R and y_a^R are given, P_a^R is imposed by P_v^R through the constraints $y_a\tau_a = y_v\tau_v$ for SG EOS, so that:
$$P_a^R = \frac{y_a^R}{y_v^R}\frac{C_{v,a}(\gamma_a - 1)}{C_{v,v}(\gamma_v - 1)}(P_v^R + \Pi_v) - \Pi_a = P_a^R(P_v^R);$$
   - once P_v^R and P_a^R are known, T^R is defined as
$$T^R = T_{sat}(P_v^R, P_a^R),$$
     by equalizing the chemical potentials via a dichotomy algorithm:
$$\mu_l(P_v^R + P_a^R(P_v^R), T^R) = \mu_v(P_v^R, T^R).$$
   - e^R and τ^R can be evaluated with P_v^R, P_a^R and T^R thanks to phasic EOS (cf ALGORITHM 3.6):
$$e^R = \sum_{k\in\mathcal{K}} y_k^R e_k(P_k^R, T^R(P_v^R));$$
$$\tau_R = (1 - y_a^R - y_v^R)\tau_l(P_v^R + P_a^R(P_v^R), T^R(P_v^R)) + y_v^R\tau_v(P_v^R, T^R(P_v^R).$$
- Last by deducing with (3.71) $J^2 = \dfrac{-P^R + P^*}{\tau^R - \tau*}$, and then $U^R = U^* - \dfrac{P^R - P*}{J}$ and $\sigma = U^R - J\tau^R$.

Chapter 4

A four-field three-phase flow model with both miscible and immiscible components.

The main content of this chapter has been published under the reference:

J.-M. Hérard , O. Hurisse and L. Quibel, A four-field three-phase flow model with both miscible and immiscible components, *ESAIM:Mathematical Modelling and Numerical Analysis*, 2020.

Abstract

A three-phase flow model with hybrid miscibility constraints is proposed: three immiscible phases are considered (liquid water, liquid metal and gas) but the gaseous phase is composed with two miscible components (steam water and non-condensable gas). The modelling approach is based on the building of an entropy inequality for the system of partial differential equations: once an interfacial velocity is given by the user, the model is uniquely defined, up to some relaxation time scales, and source terms complying with the second principle of thermodynamics can then be provided. The convective part of the system is hyperbolic when fulfilling a non-resonance condition and classical properties are studied (Riemann invariants, symmetrization). A key property is that the system possesses uniquely defined jump conditions. Last, preservation of thermodynamically admissible states and pressure relaxation are investigated.

Introduction

In the framework of nuclear safety demonstration for pressurized water reactors, some accidental scenarii are studied (see IRSN website [45]). They involve compressible flows undergoing fast transient situations with mass transfer. Steam explosion (see [8]) falls into this category and its accurate simulation is still a challenging problem [10]. It might occur when very hot liquid metal particles interact with quiet liquid water. Liquid water heated by metal suddendly changes into steam and a steam layer appears around metal particles. Heat transfer is thus inhibited until this layer becomes unstable. A steam explosion may then arise, leading to pressure waves likely to damage the surronding structures.

In addition to metal, liquid and steam water, other gases may be present: indeed, ambiant air may be mixed with vapor when metal comes into the free surface of water, or hydrogen might appear under accidental conditions because of fuel oxydation. Then, the proportion of non-condensable gas compared with water vapor in the gaseous layer around metal particles has a strong influence on the probability of observing a steam explosion or not [2], since non-condensable gas limits steam condensation [41]. Numerical studies also bear out the effect of the inert gas quantity on condensation, like in [4]. Non-condensable gas is besides taken into account in the reference industrial codes classically used to simulate a vapor explosion [52, 7].

Our aim in this work is to propose a meaningful model with suitable mathematical properties for the previous applications, describing a flow with four components: liquid and steam water, liquid metal particles and non-condensable gas. Moreover, our model needs to cope with mass transfer between liquid and steam water, and to correctly manage shock waves. We insist on the fact that only a modelling work will be presented here: perspectives and references concerning the numerical simulation will be discussed in conclusion.

A wide range of two-phase flow models has been proposed since decades. Fewer references are available about three-phase flow models, see [34, 35, 53, 27, 43, 10, 55, 39, 29]. Among all these models, two classes can be distinguished: models based on the multifluid approach [5, 48, 13, 23, 34, 35, 53, 10, 55, 39, 29], where each component has its own velocity field, and models based on the homogeneous approach [6, 3, 19, 33, 47, 31, 42, 27, 43, 32], where the kinematic equilibrium is assumed between all constituents.

The choice between one approach or the other is a matter of interest and can be discussed regarding characteristic time scales for the considered system. Indeed, the targeted applications are rapid transients where the phases are almost always out of equilibrium, so that the system dynamics is driven by return towards equilibrium and convective effects. The mechanical, kinematic or thermal transfers between phases occur at different characteristic time scales, so that lots of classical modelling approaches may suppose some instantaneous partial equilibria, in terms of pressure, velocity or temperature: such partial relaxations enable to build a hierarchy of models as depicted in [20]. By noting τ_p the pressure relaxation time scale, τ_u the velocity relaxation time scale and τ_T the temperature relaxation time scale, the following ordering[1] is often assumed, based on estimations obtained for instance in [48]:

$$0 < \tau_p, \tau_u << \tau_T.$$

τ_p and τ_u can be differently ordered depending on the considered model, as recalled in the introduction of [51]. Note that evaluating each phasic velocity is sometimes unavoidable, like for the vapor explosion (see [8, 52]) where the velocity gaps are required to estimate

[1] This hierarchy is not absolute and may depend on the considered physical situation as explained in [25].

interfacial transfers through the interfacial area. To numerically take into account the kinematic disequibrium, a time step Δt smaller than τ_u is required. A homogeneous model does not impose this constraint on Δt and is thus far cheaper on industrial meshes; but thanks to the computing cost drop, the multifluid approach is today more and more affordable and thus requires a relevant modelling.

Both approaches have their own strengths and their own difficulties. The homogeneous models have a simpler convective structure than the multifluid models (for instance, compare [43] with [35], two models describing the same mixture with three immiscible phases). Nevertheless, a mixture equation of state should be carefully built in the homogeneous models (see [27, 43]), whereas the thermodynamical behavior is decoupled phase by phase in the multifluid models. Numerically, building the mixture equation of state in a homogeneous model can be somehow tricky when considering realistic equations of state, so that very robust numerical schemes are required as highlighted in [32]. Moreover, for some applications like for the vapor explosion (see [8, 52]), evaluating each phasic velocity is sometimes unavoidable, because the velocity gaps are required to estimate interfacial transfers through the interfacial area. The velocity gaps are indeed the key ingredient enabling to model the dislocation effects of the liquid metal droplets, that induce a high heat transfer between metal and water which may lead to an explosion.

The present model is derived from the multifluid approach. It belongs to a family of models developped since 2000 [13, 21, 35, 36, 34, 38, 39], built among a similar strategy, by imposing the following minimal requirements:

- to be hyperbolic;
- to possess a physically relevant entropy inequality;
- to possess uniquely defined jump conditions.

Moreover, the preservation of the thermodynamical admissible domain should be ensured and the symmetrizability is also expected (see [17, 55, 39]). Thanks to the previous properties, problems with an analytical solution, which may involve shock waves, can be built, and one may thus request that two different numerical schemes should converge towards a unique solution when refining the mesh. This is also a key feature to verify numerical codes intented for safety study purposes. The initial model [13, 21] is a two-phase flow model with two immiscible phases, similar to the original Baer-Nunziato model [5]. Both barotropic model and model with energy have been studied. The counterpart of this model has been proposed in [35], with three immiscible phases; its barotropic version [34] has been implemented in [10], and the full model with energy equation in [9]. A hybrid two-phase flow model with three components has been last developed in [39]: steam water and non-condensable gas are miscible whereas liquid and gaseous phase are immiscible.

The present model aims to simultaneously tackle all the features of these previous models: three immiscible phases are present (liquid water, liquid metal and gas) like in [35] and the gaseous phase is composed with two miscible components (steam water and non-condensable gas) like in [39].

The model is based on a system of conservation laws with additional non-conservative terms involving an interfacial velocity $\mathbf{v}_I$. Our modelling effort focuses on the correct definition of the non-conservative terms: we only focus on models admitting a relevant entropy inequality and uniquely defined jump conditions that degenerate towards the classical Euler framework when considering single-phase flows.

Section 4.1 is devoted to the building of an entropy inequality. From the partial differential equations, a natural mixture entropy is derived: once $\mathbf{v}_I$ is given by the user, the model

is uniquely defined, up to some relaxation time scales. Several submodels can be studied by chosing a particular form for $\mathbf{v}_I$. Following a classical approach, admissible source terms complying with entropy growth within time can be found.

Section 4.2 focuses on the properties of the convective part of such models. For any $\mathbf{v}_I$, hyperbolicity is ensured, unless resonance occurs. Then, two submodels are considered for which unique jump conditions can be easily exhibited: when $\mathbf{v}_I$ is equal to $\mathbf{u}_s$, one of the phasic velocities, or when $\mathbf{v}_I$ is defined as $\mathbf{u}_m$, the average of the phasic velocities. Hence, we retrieve the "classical" two-phase flow results (see [13]). For both cases, the convective structure is precisely described in terms of waves and Riemann invariants. It is also shown that the quasi-linear system admits a symmetric form, ensuring that the Cauchy problem based on this model has a unique local-in-time smooth solution [49] (while excluding the resonance).

Last, in section 4.3, the case $\mathbf{v}_I = \mathbf{u}_s$ is more deeply studied, by giving some useful properties that might help to prepare a future numerical implementation of the model. We shall see that the thermodynamically admissible domain is preserved for simple equations of state. The natural pressure equilibria, satisfying the Dalton's law, are not violated, and the relaxation system ensures that initial pressure gaps will relax towards zero, so that pressure equilibria will be recovered, provided that some meaningful restrictions on initial pressure differences hold.

4.1 A four-field three-phase flow model

The considered flows are composed of four fields, representing the following components: liquid metal, liquid water, vapor and gas. For sake of readibility, we define: $\mathcal{K} = \{s, l, v, g\}$, and each field will be identified in the following by a subscript $k \in \mathcal{K}$: subscript s refers to liquid metal; subscript l refers to liquid; subscript v refers to vapor and subscript g refers to gas.
First, a system of conservation laws describing the four fields is written, based on Euler equations with additionnal terms modelling the interfacial exchanges. A natural entropy equality is associated to this system.
Several submodels can then be studied, depending on the miscibility constraints. In our application, vapor and gas are miscible whereas liquid metal, liquid water and gaseous mixture are immiscible.
Closure laws for non conservative terms satisfying minimal entropy dissipation are proposed. Last, particular forms are proposed for the source terms: as the model should comply with entropy growth for weak solutions, some constraints can be exhibited.

4.1.1 General framework

4.1.1.1 Set of variables and notations

Let us consider a field k, $k \in \mathcal{K}$. The following set of variables Y_k is considered:

$$\mathbf{Y}_k = (\alpha_k, m_k, m_k \mathbf{u}_k, \alpha_k E_k)^t, \tag{4.1}$$

where α_k is the statistical fraction, m_k is the partial mass (in $kg.m^{-3}$), $\mathbf{u}_k \in \mathbb{R}^3$ is the velocity (in $m.s^{-1}$) and E_k is the total energy (in $J.m^{-3}$), i.e. the sum of kinetic energy and internal energy.

Let us then precise some notations: P_k stands for pressure (in Pa); T_k for temperature (in K); we note also $a_k = T_k^{-1}$; ϵ_k for internal energy (in $J.kg^{-1}.m^{-3}$); s_k for entropy (in $J.K^{-1}.kg^{-1}.m^{-3}$) and c_k for sound velocity (in $m.s^{-1}$). Density ρ_k (in $kg.m^{-3}$) is defined by $m_k = \alpha_k \rho_k$.

Remark 4.1 — Note that for all $k \in \mathcal{K}$, $\alpha_k \in]0, 1[$: monophasic cases or cases with one or more missing phases are excluded. □

4.1.1.2 Equation of state

Thermodynamically, a field k is described with the following equation of state for internal energy: $\epsilon_k(P_k, \rho_k)$. This choice is relevant regarding our previous choice for $\mathbf{Y}_k$ (4.1): with another thermodynamical entry-plane, other more natural definitions of $\mathbf{Y}_k$ would have been preferred. E_k can now be explicitely written:

$$E_k = \rho_k \epsilon_k(P_k, \rho_k) + \frac{1}{2} \rho_k \mathbf{u}_k^2. \tag{4.2}$$

The equation of state defines a physically admissible domain, i.e. a set $\mathbb{E}_k = \{(P_k, \rho_k) \in \mathbb{R} \times \mathbb{R}^{+*} / \epsilon_k(P_k, \rho_k) \geq 0\}$. For all $(P_k, \rho_k) \in \mathbb{E}_k$, c_k, s_k and T_k are then defined thanks to ϵ_k with the following positivity constraints :

$$\rho_k c_k^2 = \left(\frac{\partial \epsilon_k}{\partial P_k}\bigg|_{\rho_k} \right)^{-1} \left(\frac{P_k}{\rho_k} - \rho_k \left. \frac{\partial \epsilon_k}{\partial \rho_k} \right|_{P_k} \right) > 0, \tag{4.3}$$

$$s_k(P_k,\rho_k) \text{ so that } c_k^2 \left.\frac{\partial s_k}{\partial P_k}\right|_{\rho_k} + \left.\frac{\partial s_k}{\partial \rho_k}\right|_{P_k} = 0, \tag{4.4}$$

and

$$T_k = \left.\frac{\partial \epsilon_k}{\partial P_k}\right|_{\rho_k} \times \left(\left.\frac{\partial s_k}{\partial P_k}\right|_{\rho_k}\right)^{-1} > 0. \tag{4.5}$$

A requirement for the model is to preserve within time the admissible domain $\mathbb{E}_k$ and the positivity constraints (4.3) and (4.5): this property will be studied in section 4.3.1.

4.1.1.3 Set of partial differential equations

In order to build the complete set of partial differential equations for the whole closed system, balance equations for each variable of $\mathbf{Y}_k$, $k \in \mathcal{K}$, are written. It leads to the following system of equations for the state variable $\tilde{\mathbf{Y}} = \bigcup_{k\in\mathcal{K}} \mathbf{Y}_k$:

$$\left\{\begin{array}{rcl} \partial_t \alpha_k + \mathbf{v}_I(\tilde{\mathbf{Y}}).\nabla\alpha_k &=& \Phi_k(\tilde{\mathbf{Y}}) \\ \partial_t m_k + \nabla.(m_k\mathbf{u}_k) &=& \Gamma_k(\tilde{\mathbf{Y}}) \\ \partial_t(m_k\mathbf{u}_k) + \nabla.(m_k\mathbf{u}_k\otimes\mathbf{u}_k) + \nabla(\alpha_k P_k) + \sum\limits_{k'\neq k} \Pi_{kk'}(\tilde{\mathbf{Y}})\nabla\alpha_{k'} &=& \mathbf{S}_{\mathbf{Q}k}(\tilde{\mathbf{Y}}) \\ \partial_t(\alpha_k E_k) + \nabla.(\alpha_k\mathbf{u}_k(E_k+P_k)) - \sum\limits_{k'\neq k} \Pi_{kk'}(\tilde{\mathbf{Y}})\partial_t\alpha_{k'} &=& S_{Ek}(\tilde{\mathbf{Y}}) \end{array}\right. \tag{4.6}$$

Exchanges between the four fields inside the closed system are accounted for by non conservative terms as well as source terms $\Phi_k(\tilde{\mathbf{Y}})$, $\Gamma_k(\tilde{\mathbf{Y}})$, $\mathbf{S}_{\mathbf{Q}k}(\tilde{\mathbf{Y}})$ and $S_{Ek}(\tilde{\mathbf{Y}})$. Non conservative terms involve an interfacial velocity $\mathbf{v}_I(\tilde{\mathbf{Y}})$ and interfacial pressures $\left(\Pi_{kk'}(\tilde{\mathbf{Y}})\right)_{(k,k')\in\mathcal{K}^2,k\neq k'}$.

Remark 4.2 — For sake of simplicity, we consider that source terms as well as interfacial closures depend only on $\tilde{\mathbf{Y}}$. More complex models could assume for instance a dependance on both $\tilde{\mathbf{Y}}$ and gradients of the components of $\tilde{\mathbf{Y}}$ (see [56, 1, 36] and remarks 4.4 in section 4.1.3.1 and 4.7 in section 4.2.1.2). □

As we consider a closed system, without external contributions, we assume that mass, momentum and energy exchanges between fields should balance when the mean flow is considered. It implies the following constraints on the closure terms:

$$\sum_{k\in\mathcal{K}} \Gamma_k(\tilde{\mathbf{Y}}) = 0 \quad ; \quad \sum_{k\in\mathcal{K}} \mathbf{S}_{\mathbf{Q}k}(\tilde{\mathbf{Y}}) = 0 \quad ; \quad \sum_{k\in\mathcal{K}} S_{Ek}(\tilde{\mathbf{Y}}) = 0. \tag{4.7}$$

and:

$$\sum_{k\in\mathcal{K}}\sum_{k'\neq k} \Pi_{kk'}(\tilde{\mathbf{Y}})\partial_\xi\alpha_{k'} = 0, \quad \xi \in \{t,x,y,z\}. \tag{4.8}$$

At this step, nothing more can be said about Φ_k. In the next subsection 4.1.2, vacuum occurence will be excluded and additionnal assumptions about miscibility will be made.

4.1.1.4 Mixture entropy

The mixture entropy η is defined as:

$$\eta(\tilde{\mathbf{Y}}) = \sum_{k\in\mathcal{K}} m_k s_k. \tag{4.9}$$

This choice is very classical. It can be proven (see appendix 4.A) that smooth solutions of (4.6) verify the following entropy equality:

$$\partial_t \eta(\tilde{\mathbf{Y}}) + \nabla.\mathbf{f}_\eta(\tilde{\mathbf{Y}}) + \mathcal{A}_\eta(\tilde{\mathbf{Y}}, (\nabla\alpha_k)_{k\in\mathcal{K}}) = RHS_\eta(\tilde{\mathbf{Y}}), \tag{4.10}$$

where the entropy flux reads:

$$\mathbf{f}_\eta(\tilde{\mathbf{Y}}) = \sum_{k\in\mathcal{K}} m_k s_k \mathbf{u}_k, \tag{4.11}$$

and

$$\mathcal{A}_\eta(\tilde{\mathbf{Y}}, (\nabla\alpha_k)_{k\in\mathcal{K}}) = \sum_{k\in\mathcal{K}} T_k^{-1}(\mathbf{v}_I - \mathbf{u}_k).\left(\sum_{k'\neq k} \Pi_{kk'}(\tilde{\mathbf{Y}})\nabla\alpha_{k'} + P_k\nabla\alpha_k\right), \tag{4.12}$$

and

$$\begin{aligned} RHS_\eta(\tilde{\mathbf{Y}}) \;=& \sum_{k\in\mathcal{K}} T_k^{-1}\left\{ S_{Ek} + \sum_{k'\neq k} \Pi_{kk'}(\tilde{\mathbf{Y}})\Phi_{k'}(\tilde{\mathbf{Y}}) - \Gamma_k(\tilde{\mathbf{Y}})\epsilon_k \right. \\ & \left. -\mathbf{u}_k.(\mathbf{S}_{\mathbf{Q}k} - \tfrac{\Gamma_k(\tilde{\mathbf{Y}})}{2}\mathbf{u}_k) + \rho_k\frac{\partial\epsilon_k}{\partial\rho_k}\left(\rho_k\Phi_k(\tilde{\mathbf{Y}}) - \Gamma_k(\tilde{\mathbf{Y}})\right)\right\} \\ & + \sum_{k\in\mathcal{K}}\left\{ s_k\Gamma_k(\tilde{\mathbf{Y}}) + \rho_k\frac{\partial s_k}{\partial\rho_k}(\Gamma_k(\tilde{\mathbf{Y}}) - \rho_k\Phi_k(\tilde{\mathbf{Y}}))\right\}. \end{aligned} \tag{4.13}$$

A model with minimal entropy dissipation is defined as a model based on system (4.6) fulfilling:

$$\mathcal{A}_\eta(\tilde{\mathbf{Y}}, (\nabla\alpha_k)_{k\in\mathcal{K}}) = 0. \tag{4.14}$$

Only such models will be considered in the following.

4.1.2 Miscibility constraints

In [35], a model with three immiscible phases has been studied. Here, we consider hybrid miscibility conditions, as represented in the figure 4.1:

- vapor and gas are miscible and form a gaseous phase;
- gaseous phase, liquid water and liquid metal are immiscible.

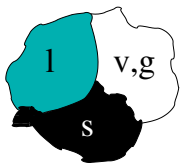

Figure 4.1 – Scheme of the miscibility constraints for the considered three-phase flow system.

It implies the following constraints:

$$\alpha_v = \alpha_g \quad ; \quad \alpha_s + \alpha_l + \alpha_v = 1. \tag{4.15}$$

Only two void fractions are independent; we keep α_s and α_l. The state variable can be reduced:

$$\mathbf{Y} = \left((\alpha_s, \alpha_l) \bigcup \left(\bigcup_{k\in\mathcal{K}} (m_k, m_k\mathbf{u}_k, \alpha_k E_k)\right)\right)^t \in \mathbb{R}^{22}. \tag{4.16}$$

We need to impose (otherwise constraints (4.15) would be violated):

$$\Phi_v(\mathbf{Y}) = \Phi_g(\mathbf{Y}) \quad ; \quad \Phi_s(\mathbf{Y}) + \Phi_l(\mathbf{Y}) + \Phi_v(\mathbf{Y}) = 0. \tag{4.17}$$

Thus, taking into account constraints (4.15) in (4.6), the system of partial differential equations for $\mathbf{Y}$ reads:

$$\left\{\begin{array}{rcl} \partial_t \alpha_s + \mathbf{v}_I(\mathbf{Y}).\nabla\alpha_s &=& \Phi_s(\mathbf{Y}) \\ \partial_t \alpha_l + \mathbf{v}_I(\mathbf{Y}).\nabla\alpha_l &=& \Phi_l(\mathbf{Y}) \\ \partial_t m_k + \nabla.(m_k\mathbf{u}_k) &=& \Gamma_k(\mathbf{Y}) \\ \partial_t(m_k\mathbf{u}_k) + \nabla.(m_k\mathbf{u}_k\otimes\mathbf{u}_k) + \nabla(\alpha_k P_k) + K_{ks}(\mathbf{Y})\nabla\alpha_s + K_{kl}(\mathbf{Y})\nabla\alpha_l &=& \mathbf{S}_{\mathbf{Q}_k}(\mathbf{Y}) \\ \partial_t(\alpha_k E_k) + \nabla.(\alpha_k\mathbf{u}_k(E_k+P_k)) - K_{ks}(\mathbf{Y})\partial_t\alpha_s - K_{kl}(\mathbf{Y})\partial_t\alpha_l &=& S_{Ek}(\mathbf{Y}) \end{array}\right. \tag{4.18}$$

where

$$\begin{array}{rclcrcl} K_{ls} &=& \Pi_{ls} - \Pi_{lv} - \Pi_{lg} & ; & K_{ll} &=& -\Pi_{lv} - \Pi_{lg} \quad ; \\ K_{vs} &=& -\Pi_{vg} + \Pi_{vs} & ; & K_{vl} &=& \Pi_{vl} - \Pi_{vg} \quad ; \\ K_{gs} &=& -\Pi_{gv} + \Pi_{gs} & ; & K_{gl} &=& \Pi_{gl} - \Pi_{gv} \quad ; \\ K_{ss} &=& -\Pi_{sv} - \Pi_{sg} & ; & K_{sl} &=& \Pi_{sl} - \Pi_{sv} - \Pi_{sg} \quad . \end{array} \tag{4.19}$$

4.1.3 Entropy inequality constraints

Using entropy equality (4.10), closures are proposed in this section:

- given $v_I(\mathbf{Y})$, a unique set $(K_{kk'}(\mathbf{Y}))_{k\in\mathcal{K},k'\in\{s,l\}}$ complying with (4.8) is determined by looking for solutions with minimal entropy dissipation (4.14).
- source terms fulfilling the constraints (4.7) and (4.17) need to comply with entropy growth for smooth solutions.

4.1.3.1 Closures for interfacial terms fulfilling the minimal entropy dissipation

Interfacial velocity is assumed to have the following form:

$$\boxed{\mathbf{v}_I(\mathbf{Y}) = \sum_{k\in\mathcal{K}} \beta_k \mathbf{u}_k,} \tag{4.20}$$

where, because of Galilean invariance principle:

$$\sum_{k\in\mathcal{K}} \beta_k = 1. \tag{4.21}$$

Since, intuitively, we expect that v_I is some kind of average of the velocity fields, an additionnal (but not mandatory) constraint is imposed:

$$\forall k \in \mathcal{K},\ \beta_k \geq 0. \tag{4.22}$$

Remark 4.3 — The exact form for $(\beta_k)_{k\in\mathcal{K}}$ is a key point in the modelling procedure and will be detailed later on, in section 4.2.1.2. □

PROPOSITION 4.1 (SOLUTION WITH MINIMAL ENTROPY DISSIPATION)
For the interfacial velocity defined by (4.20), there exists a unique set of $(K_{kk'}(\mathbf{Y}))_{k\in\mathcal{K},k'\in\{s,l\}}$ *fulfilling (4.8) and complying with minimal entropy dissipation (4.14). The solution reads:*

$$\begin{array}{rclcrcl}
K_{ls} &=& \mathfrak{T}\beta_l T_l(P_s-(P_v+P_g)) &;& K_{ll} &=& -P_l+\mathfrak{T}\beta_l T_l(P_l-(P_v+P_g));\\
K_{vs} &=& P_v+\mathfrak{T}\beta_v T_v(P_s-(P_v+P_g)) &;& K_{vl} &=& P_v+\mathfrak{T}\beta_v T_v(P_l-(P_v+P_g));\\
K_{gs} &=& P_g+\mathfrak{T}\beta_g T_g(P_s-(P_v+P_g)) &;& K_{gl} &=& P_g+\mathfrak{T}\beta_g T_g(P_l-(P_v+P_g));\\
K_{ss} &=& -P_s+\mathfrak{T}\beta_s T_s(P_s-(P_v+P_g)) &;& K_{sl} &=& \mathfrak{T}\beta_s T_s(P_l-(P_v+P_g))
\end{array}$$

$$\text{where } \mathfrak{T}=\left(\sum_{k\in\mathcal{K}}\beta_k T_k\right)^{-1}. \tag{4.23}$$

The proof as well as the final system satisfied by $(K_{kk'}(\mathbf{Y}))_{k\in\mathcal{K},k'\in\{s,l\}}$ are given in appendix 4.B.

Remark 4.4 — We could consider more complex closures for $K_{kk'}$. For instance, we could replace formely the current $\Pi^0_{kk'}(\mathbf{Y})$ given by (4.19) and (4.23) by:

$$\Pi_{kk'}(\mathbf{Y},\nabla\alpha_l,\nabla\alpha_s)=\Pi^0_{kk'}(\mathbf{Y})+\Pi_{kk'}{}^{1,l}(\mathbf{Y})\times\nabla\alpha_l+\Pi_{kk'}{}^{1,s}(\mathbf{Y})\times\nabla\alpha_s,$$

as proposed for instance in [56, 36]. In that case, we would have an additional dissipative contribution in the entropy inequality, as soon as the additional quadratic form has the appropriate sign. However, it would introduce additional terms for which we do not have (a priori) relevant closures to propose, see [36].

□

4.1.3.2 Admissible source terms

Particular forms are assumed for the source terms.

The mass transfer term $\Gamma_k(\mathbf{Y})$ is defined as a sum of dyadic contributions:

$$\Gamma_k=\sum_{k'\neq k}\Gamma_{kk'}. \tag{4.24}$$

Note that the gas g is non-condensable, so that:

$$\Gamma_g=0 \quad\text{and}\quad \forall k\in\mathcal{K},\ \Gamma_{gk}=\Gamma_{kg}=0.$$

The momentum contribution is decomposed into a drag term and a mass transfer term:

$$\mathbf{S}_{\mathbf{Q}k}=\sum_{k'\neq k}\mathbf{D}_{kk'}+\sum_{k'\neq k}\Gamma_{kk'}\mathbf{v}_{\mathbf{kk'}}. \tag{4.25}$$

Last, pure thermal transfer, drag effets and mass transfer are taken into account in the total energy source term:

$$S_{Ek}=\sum_{k'\neq k}\Psi_{kk'}+\sum_{k'\neq k}\mathbf{v}_{\mathbf{kk'}}\mathbf{D}_{kk'}+\sum_{k'\neq k}\Gamma_{kk'}H_{kk'}. \tag{4.26}$$

For sake of readibility, the dependance on $\mathbf{Y}$ has been omitted for the previous introduced terms $\Gamma_{kk'}$, $\mathbf{D}_{kk'}$, $\psi_{kk'}$, $\mathbf{v}_{\mathbf{kk'}}$ and $H_{kk'}$. A consequence of (4.7) is that the following dyadic transfers cancel each other:

$$\Gamma_{kk'}+\Gamma_{k'k}=0 \quad;\quad \mathbf{D}_{kk'}+\mathbf{D}_{k'k}=0 \quad;\quad \Psi_{kk'}+\Psi_{k'k}=0. \tag{4.27}$$

Indeed, for instance, $\Gamma_{kk'}$ represents the mass transfer from phase k towards phase k': this mass transfer is exactly equal to the mass transfer obtained by phase k' from phase k (which can be seen as the opposite of the mass transfer taken from phase k' and given to phase k). Now, considering the second term in S_{E_K}:

$$\sum_{k' \neq k} \mathbf{v_{kk'}} \mathbf{D}_{kk'} = \sum_{k'>k} (\mathbf{v_{kk'}} \mathbf{D}_{kk'} + \mathbf{v_{k'k}} \mathbf{D}_{k'k}) = \sum_{k'>k} (\mathbf{v_{kk'}} - \mathbf{v_{k'k}}) \mathbf{D}_{kk'} = 0,$$

The previous term is indeed equal to zero because each dyadic bound is independent. This leads to $\mathbf{v_{kk'}} - \mathbf{v_{k'k}} = 0$. Similar equations can be written for the third term in S_{E_K}, so that we finally get:

$$\mathbf{v_{kk'}} = \mathbf{v_{k'k}} \quad ; \quad H_{kk'} = H_{k'k}. \tag{4.28}$$

The source terms have to comply with the entropy growth within time for weak solutions:

$$\partial_t \eta(\mathbf{Y}) + \nabla . \mathbf{f}_\eta(\mathbf{Y}) + \mathcal{A}_\eta(\mathbf{Y}, \nabla \alpha_k) \geq 0. \tag{4.29}$$

It implies some constraints on the right-hand-side term $RHS_\eta(\mathbf{Y})$ of entropy equality (4.10). $RHS_\eta(\mathbf{Y})$ (4.13) can be rewritten by isolating each independent effect in four different contributions:

$$RHS_\eta = RHS_\eta^\Phi + RHS_\eta^\Psi + RHS_\eta^D + RHS_\eta^\Gamma. \tag{4.30}$$

In order to satisfy the second principle, each contribution needs to be positive on its own.

- *Contribution RHS_η^Φ:*

$$\begin{aligned} RHS_\eta^\Phi &= \sum_k \left(-\rho_k^2 \frac{\partial s_k}{\partial \rho_k} \Phi_k + a_k \sum_{k'} \Pi_{kk'} \Phi_{k'} + \rho_k^2 \frac{\partial \epsilon_k}{\partial \rho_k} \Phi_k \right) \\ &= \sum_k a_k \left(\sum_{k'} \Pi_{kk'} \Phi_{k'} + P_k \Phi_k \right), \end{aligned} \tag{4.31}$$

where $a_k = T_k^{-1}$. Using miscibility constraints (4.17), we get:

$$\begin{array}{rcccccl} RHS_\eta^\Phi &=& \Phi_l \{ & a_l(P_l + K_{ll}) & + & a_v(-P_v + K_{vl}) & \\ &+& & a_g(-P_g + K_{gl}) & + & a_s K_{sl} & \} \\ &+& \Phi_s \{ & a_l K_{ls} & + & a_v(-P_v + K_{vs}) & \\ &+& & a_g(-P_g + K_{gs}) & + & a_s(P_s + K_{ss}) & \}. \end{array} \tag{4.32}$$

It becomes by injecting the general solution for the $(K_{kk'})_{k,k' \in \mathcal{K}}$:

$$\begin{aligned} &RHS_\eta^\Phi = \\ &\mathfrak{D} \left(\prod_k a_k \right) \left\{ \Phi_l (P_l - (P_v + P_g)) + \Phi_s (P_s - (P_v + P_g)) \right\}. \end{aligned} \tag{4.33}$$

Recalling that $\mathfrak{D} = (a_l a_v a_g \beta_s + a_l a_v a_s \beta_g + a_l a_g a_s \beta_v + a_v a_g a_s \beta_l)^{-1}$ and $a_k = T_k^{-1} > 0$, the final entropy constraint on the Φ_k prefactors reads :

$$\Phi_l (P_l - (P_v + P_g)) + \Phi_s (P_s - (P_v + P_g)) \geq 0. \tag{4.34}$$

Finally, an admissible model for Φ_l and Φ_s is the following :

$$\begin{pmatrix} \Phi_l \\ \Phi_s \end{pmatrix} = \mathcal{D} \begin{pmatrix} P_l - (P_v + P_g) \\ P_s - (P_v + P_g) \end{pmatrix}, \tag{4.35}$$

where $\mathcal{D}$ is a symmetric positive semi-definite matrix:

$$\mathcal{D} = \begin{pmatrix} d_{11} & d_{12} \\ d_{12} & d_{22} \end{pmatrix}, \quad d_{11} > 0,\ d_{22} > 0,\ d_{12} = \sqrt{d_{11} d_{22}} \sin(\theta), \theta \in \mathbb{R}.$$

- *Contribution RHS_η^Ψ:*

  Since:
  $$RHS_\eta^\Psi = \sum_k a_k \Big(\sum_{k' \neq k} \Psi_{kk'} \Big), \tag{4.36}$$
  a simple constraint on $(\Psi_{kk'})_{k,k' \in \mathcal{K}}$ is obtained:
  $$\forall (k,k') \in \mathcal{K}^2, k \neq k', (a_k - a_{k'}) \Psi_{kk'} \geq 0. \tag{4.37}$$

- *Contribution RHS_η^D:*

  It reads:
  $$RHS_\eta^D = \sum_k a_k \sum_{k' \neq k} (\mathbf{v_{kk'}} \mathbf{D_{kk'}} - \mathbf{u_k} \sum_{k' \neq k} \mathbf{D_{kk'}}). \tag{4.38}$$
  We assume the following particular form for $\mathbf{v_{kk'}}$ to comply with the Galilean invariance principle:
  $$\begin{array}{l} \mathbf{v_{kk'}} = \beta_{kk'} \mathbf{u_k} + (1 - \beta_{kk'}) \mathbf{u_{k'}}, \\ \text{with } \beta_{kk'} \in [0,1] \text{ and } \beta_{kk'} + \beta_{k'k} = 1, \end{array} \tag{4.39}$$
  with $\beta_{kk'} + \beta_{k'k} = 1$ because, due to equation (4.27), $v_{kk'} = v_{k'k}$. Then, we get the following constraint on $(\mathbf{D_{kk'}})_{k,k' \in \mathcal{K}}$:
  $$\begin{array}{l} \forall (k,k') \in \mathcal{K}^2, k \neq k', \\ [a_k(1 - \beta_{kk'}) + a_{k'}(1 - \beta_{k'k})](\mathbf{u_{k'}} - \mathbf{u_k}) \mathbf{D_{kk'}} \geq 0. \end{array} \tag{4.40}$$

- *Contribution RHS_η^Γ:*

  The chemical potential μ_k $(J.kg^{-1})$ is defined by: $\mu_k = \epsilon_k - T_k s_k + \frac{p_k}{\rho_k}$. RHS_η^Γ can be written as:
  $$\begin{array}{rcl} RHS_\eta^\Gamma & = & -\sum_k \sum_{k' \neq k} a_k \mu_k \Gamma_{kk'} \\ & + & \sum_k a_k \sum_{k' \neq k} (H_{kk'} + \frac{u_k^2}{2} - \mathbf{u_k} \mathbf{v_{kk'}}) \Gamma_{kk'}. \end{array} \tag{4.41}$$
  Previous expression (4.41) suggests a simple choice for $H_{kk'}$ and $\mathbf{v_{kk'}}$ (in accordance with (4.39)):
  $$H_{kk'} = \frac{\mathbf{u_k} \mathbf{u_{k'}}}{2} \quad ; \quad \mathbf{v_{kk'}} = \frac{1}{2}(\mathbf{u_k} + \mathbf{u_{k'}}). \tag{4.42}$$
  With this assumption, a simple constraint on $\Gamma_{kk'}$ can be written:
  $$\forall (k,k') \in \mathcal{K}^2, k \neq k', (a_k \mu_k - a_{k'} \mu_{k'}) \Gamma_{kk'} \geq 0. \tag{4.43}$$

Source terms complying with the second principle of thermodynamics can now be explicitely introduced, like for instance in [51]. They involve relaxation time scales, that need to be defined by the user; some propositions can be found for instance see [46] for τ_u and also [18, 32] for τ_Γ and τ_T, and more recently [22, 40, 11] for τ_p relaxation time scales (considering different averaging processes).

4.2 Properties of the convective part of the model

Some interesting properties of the model built in section 4.1 are now highlighted. For sake of simplicity, only the 1D-case will be considered in the sequel. It is not restrictive since the system (4.18) is invariant by rotation: thanks to a projection on the normal direction, a one-dimensional system can always be written, while neglecting variations in the transversal directions.

4.2.1 Structure of the convective system

The following state vector is considered :

$$\mathbf{W} = (\alpha_l, \alpha_s, \rho_l, u_l, P_l, \rho_v, u_v, P_v, \rho_g, u_g, P_g, \rho_s, u_s, P_s)^t. \tag{4.44}$$

The homogeneous system of equations associated with (4.18) can be rewritten for smooth solutions in the quasi-linear form :

$$\partial_t \mathbf{W} + \mathbf{B}(\mathbf{W})\partial_x \mathbf{W} = 0 \tag{4.45}$$

with $\mathbf{B}$ a block matrix:

$$\mathbf{B} = \begin{pmatrix} \mathcal{C}_{\mathcal{I}} & \mathbf{0}_{3\times2} & \mathbf{0}_{3\times2} & \mathbf{0}_{3\times2} & \mathbf{0}_{3\times2} \\ \mathcal{C}_{\mathbf{l}} & \mathcal{B}_{\mathbf{l}} & \mathbf{0}_{3\times3} & \mathbf{0}_{3\times3} & \mathbf{0}_{3\times3} \\ \mathcal{C}_{\mathbf{v}} & \mathbf{0}_{3\times3} & \mathcal{B}_{\mathbf{v}} & \mathbf{0}_{3\times3} & \mathbf{0}_{3\times3} \\ \mathcal{C}_{\mathbf{g}} & \mathbf{0}_{3\times3} & \mathbf{0}_{3\times3} & \mathcal{B}_{\mathbf{g}} & \mathbf{0}_{3\times3} \\ \mathcal{C}_{\mathbf{s}} & \mathbf{0}_{3\times3} & \mathbf{0}_{3\times3} & \mathbf{0}_{3\times3} & \mathcal{B}_{\mathbf{s}} \end{pmatrix} \tag{4.46}$$

where, with the notation $\mathfrak{c}_k = \dfrac{(v_I - u_k)}{m_k} \left.\dfrac{\partial \epsilon_k}{\partial P_k}\right|_{\rho_k}^{-1}$ and $\partial_{\rho_k}\epsilon_k = \left.\dfrac{\partial \epsilon_k}{\partial \rho_k}\right|_{P_k}$:

$$\mathcal{C}_{\mathcal{I}} = \begin{pmatrix} v_I & 0 \\ 0 & v_I \end{pmatrix} \quad ; \quad \mathcal{C}_{\mathbf{l}} = \begin{pmatrix} -\frac{\rho_l}{\alpha_l}(v_I - u_l) & 0 \\ \frac{P_l + K_{ll}}{m_l} & \frac{K_{ls}}{m_l} \\ \mathfrak{c}_l(\rho_l^2 \partial_{\rho_l}\epsilon_l + K_{ll}) & \mathfrak{c}_l K_{ls} \end{pmatrix}; \tag{4.47}$$

$$\mathcal{C}_{\mathbf{s}} = \begin{pmatrix} 0 & -\frac{\rho_s}{\alpha_s}(v_I - u_s) \\ \frac{K_{sl}}{m_s} & \frac{P_s + K_{ss}}{m_s} \\ \mathfrak{c}_s K_{sl} & \mathfrak{c}_s(\rho_s^2 \partial_{\rho_s}\epsilon_s + K_{ss}) \end{pmatrix}; \tag{4.48}$$

$$\forall k \in \{v, g\}, \mathcal{C}_{\mathbf{k}} = \begin{pmatrix} \frac{\rho_k}{\alpha_k}(v_I - u_k) & \frac{\rho_k}{\alpha_k}(v_I - u_k) \\ \frac{-P_k + K_{kl}}{m_k} & \frac{-P_k + K_{ks}}{m_k} \\ \mathfrak{c}_k(-\rho_k^2 \partial_{\rho_k}\epsilon_k + K_{kl}) & \mathfrak{c}_k(-\rho_k^2 \partial_{\rho_k}\epsilon_k + K_{ks}) \end{pmatrix}; \tag{4.49}$$

$$\forall k \in \mathcal{K}, \mathcal{B}_{\mathbf{k}} = \begin{pmatrix} u_k & \rho_k & 0 \\ 0 & u_k & \tau_k \\ 0 & \rho_k c_k^2 & u_k \end{pmatrix}. \tag{4.50}$$

For the closure (4.20) $v_I = \sum_{k\in\mathcal{K}} \beta_k u_k$, matrices $C_k, k \in \mathcal{K}$ can be rewritten **taking into account** (4.23) and introducing the following notations:

$$\Delta u_k = v_I - u_k \; \forall k \in \mathcal{K}; \tag{4.51}$$

$$\Delta P_k = P_k - (P_v + P_g),\ k \in \{l, s\}; \tag{4.52}$$

$$\mathcal{C}_{\mathbf{l}} = \begin{pmatrix} -\frac{\rho_l}{\alpha_l}\Delta u_l & 0 \\ \frac{\mathfrak{T}\beta_l T_l}{m_l}\Delta P_l & \frac{\mathfrak{T}\beta_l T_l}{m_l}\Delta P_s \\ \frac{\Delta u_l}{m_l}\left[(\partial_{P_l}\epsilon_l)^{-1}\mathfrak{T}\beta_l T_l \Delta P_l - \rho_l^2 c_l{}^2\right] & \frac{\Delta u_l}{m_l}\left[(\partial_{P_l}\epsilon_l)^{-1}\mathfrak{T}\beta_l T_l \Delta P_s\right] \end{pmatrix}; \tag{4.53}$$

$$\mathcal{C}_{\mathbf{s}} = \begin{pmatrix} 0 & -\frac{\rho_s}{\alpha_s}\Delta u_s \\ \frac{\mathfrak{T}\beta_s T_s}{m_s}\Delta P_l & \frac{\mathfrak{T}\beta_s T_s}{m_s}\Delta P_s \\ \frac{\Delta u_s}{m_s}\left[(\partial_{P_s}\epsilon_s)^{-1}\mathfrak{T}\beta_s T_s \Delta P_l\right] & \frac{\Delta u_s}{m_s}\left[(\partial_{P_s}\epsilon_s)^{-1}\mathfrak{T}\beta_s T_s \Delta P_s - \rho_s^2 {c_s}^2\right] \end{pmatrix}; \tag{4.54}$$

$$\forall k \in \{v,g\}, \mathcal{C}_{\mathbf{k}} = \begin{pmatrix} \frac{\rho_k}{\alpha_k}\Delta u_k & \frac{\rho_k}{\alpha_k}\Delta u_k \\ \frac{\mathfrak{T}\beta_k T_k}{m_k}\Delta P_l & \frac{\mathfrak{T}\beta_k T_k}{m_k}\Delta P_s \\ \frac{\Delta u_k}{m_k}\left[(\partial_{P_k}\epsilon_k)^{-1}\mathfrak{T}\beta_k T_k \Delta P_l + \rho_k^2 {c_k}^2\right] & \frac{\Delta u_k}{m_k}\left[(\partial_{P_k}\epsilon_k)^{-1}\mathfrak{T}\beta_k T_k \Delta P_s + \rho_k^2 {c_k}^2\right] \end{pmatrix}. \tag{4.55}$$

4.2.1.1 Hyperbolicity

PROPOSITION 4.2 (HYPERBOLICITY)
*The system (4.45) is **hyperbolic** with the following eigenvalues:*

$$\begin{array}{cccc} \lambda_{1,2} = v_I; & & & \\ \lambda_3 = u_l\,; & \lambda_4 = u_v\,; & \lambda_5 = u_g\,; & \lambda_6 = u_s\,; \\ \lambda_7 = u_l + c_l\,; & \lambda_8 = u_v + c_v\,; & \lambda_9 = u_g + c_g\,; & \lambda_{10} = u_s + c_s; \\ \lambda_{11} = u_l - c_l\,; & \lambda_{12} = u_v - c_v\,; & \lambda_{13} = u_g - c_g\,; & \lambda_{14} = u_s - c_s. \end{array} \tag{4.56}$$

Associated right eigenvectors span the whole space $\mathbb{R}^{14}$, except if resonance occurs, that is to say:

$$\begin{array}{c} \Delta u_l^2 - c_l^2 = (v_I - u_l)^2 - c_l^2 = 0 \;\; or \;\; \Delta u_v^2 - c_v^2 = (v_I - u_v)^2 - c_v^2 = 0 \;\; or \\ \Delta u_g^2 - c_g^2 = (v_I - u_g)^2 - c_g^2 = 0 \;\; or \;\; \Delta u_s^2 - c_s^2 = (v_I - u_s)^2 - c_s^2 = 0. \end{array} \tag{4.57}$$

The proof consists in exhibiting the eigenvectors. They are given in appendix 4.C.

4.2.1.2 Structure of waves

The definition of a Riemann invariant is recalled: considering an eigenvalue λ admitting n eigenvectors $(\mathbf{r}_k)_k$, a Riemann invariant I_λ associated to λ is a scalar quantity verifying:

$$\forall k \in [|1,n|], \nabla_{\mathbf{W}} I_\lambda(\mathbf{W}).\mathbf{r}_k(\mathbf{W}) = 0.$$

A very important requirement for our model is to correctly manage the non-conservative terms thanks to uniquely defined jump relations. Indeed, it guarantees that two different consistent and stable numerical schemes will converge towards the same solution by refining the mesh. However, this property will not hold if 1,2-fields associated with v_I are genuinely non linear. To avoid this problem, $(\beta_k)_{k\in\mathcal{K}}$ can be chosen so that 1,2-fields associated with v_I are linearly degenerate (see [13] for two-phase flow models).
Only two particular choices for $(\beta_k)_{k\in\mathcal{K}}$ will be considered:

- $\beta_s = 1$ and $\beta_l = \beta_v = \beta_g = 0$ so that:

$$v_I = u_s; \tag{4.58}$$

- $\beta_k = \frac{m_k}{M}\ \forall k \in \mathcal{K}$ with $M = \sum_{k\in\mathcal{K}} m_k$, so that

$$v_I = u_m = \sum_{k\in\mathcal{K}} \frac{m_k}{M} u_k. \tag{4.59}$$

Remark 4.5 — These choices for v_I are not the only ones: for example, for the two-phase flow case, a wider family of suitable models (e.g. that ensure linear degeneracy) has been exhibited in [15] (see also [26]). □

Remark 4.6 — The property of linear degeneracy for the coupling wave is fully **independent** from the chosen closures for the $(\Pi_{kk'})_{k,k'\in\mathcal{K}}$. With the latter choices for v_I, even if the mixture entropy is defined in a different way than (4.9) (which also implies a different expression for $\Pi_{kk'}$), the property of linear degeneracy for the coupling wave still holds, as well as the hyperbolicity for the convective system (see appendix 4.C). □

We emphasize that, in the sequel, the set of $(\Pi_{kk'})$ **complies with** (4.23). The following three propositions can then be straightforwardly proved after rather long but simple computations.

PROPOSITION 4.3 (NATURE OF THE COUPLING WAVE)
If $v_I = u_s$ or if $v_I = u_m$, fields associated with $\lambda_1 = \lambda_2 = v_I$ are linearly degenerate.

- *If $v_I = u_m$: u_m is an eigenvalue of multiplicity 2; there are 12 Riemann invariants:*

$$\begin{aligned}
&I^1_{v_I=u_m}(\mathbf{W}) = u_m\ ;\\
&I^2_{v_I=u_m}(\mathbf{W}) = s_s - s_l\ ;\ I^3_{v_I=u_m}(\mathbf{W}) = s_s - s_v\ ;\ I^4_{v_I=u_m}(\mathbf{W}) = s_s - s_g\ ;\\
&I^5_{v_I=u_m}(\mathbf{W}) = m_l(u_m - u_l)\ ;\ I^6_{v_I=u_m}(\mathbf{W}) = m_v(u_m - u_v)\ ;\\
&I^7_{v_I=u_m}(\mathbf{W}) = m_g(u_m - u_g)\ ;\\
&I^8_{v_I=u_m}(\mathbf{W}) = \epsilon_l + \tfrac{P_l}{\rho_l} + \tfrac{1}{2}(u_m - u_l)^2\ ;\\
&I^9_{v_I=u_m}(\mathbf{W}) = \epsilon_v + \tfrac{P_v}{\rho_v} + \tfrac{1}{2}(u_m - u_v)^2\ ;\\
&I^{10}_{v_I=u_m}(\mathbf{W}) = \epsilon_g + \tfrac{P_g}{\rho_g} + \tfrac{1}{2}(u_m - u_g)^2\ ;\\
&I^{11}_{v_I=u_m}(\mathbf{W}) = \epsilon_s + \tfrac{P_s}{\rho_s} + \tfrac{1}{2}(u_m - u_s)^2\ ;\\
&I^{12}_{v_I=u_m}(\mathbf{W}) = \sum_{k\in\mathcal{K}} \left\{\alpha_k P_k + m_k(u_m - u_k)^2\right\},
\end{aligned} \tag{4.60}$$

  verifying for all $k \in [|1, 12|]$:

$$\nabla_{\mathbf{W}} I^k_{v_I=u_m}.\mathbf{r}_1(\mathbf{W}) = \nabla_{\mathbf{W}} I^k_{v_I=u_m}.\mathbf{r}_2(\mathbf{W}) = 0.$$

- *If $v_I = u_s$: $u_s = \lambda_1 = \lambda_2 = \lambda_6$ is an eigenvalue of multiplicity 3; there are then 11 Riemann invariants:*

$$\begin{aligned}
&I^1_{v_I=u_s}(\mathbf{W}) = u_s\ ;\\
&I^2_{v_I=u_s}(\mathbf{W}) = s_l\ ;\ I^3_{v_I=u_s}(\mathbf{W}) = s_v\ ;\ I^4_{v_I=u_s}(\mathbf{W}) = s_g\ ;\\
&I^5_{v_I=u_s}(\mathbf{W}) = m_l(u_s - u_l)\ ;\ I^6_{v_I=u_s}(\mathbf{W}) = m_v(u_s - u_v)\ ;\\
&I^7_{v_I=u_s}(\mathbf{W}) = m_g(u_s - u_g)\ ;\\
&I^8_{v_I=u_s}(\mathbf{W}) = \epsilon_l + \tfrac{P_l}{\rho_l} + \tfrac{1}{2}(u_s - u_l)^2\ ;\\
&I^9_{v_I=u_s}(\mathbf{W}) = \epsilon_v + \tfrac{P_v}{\rho_v} + \tfrac{1}{2}(u_s - u_v)^2\ ;\\
&I^{10}_{v_I=u_s}(\mathbf{W}) = \epsilon_g + \tfrac{P_g}{\rho_g} + \tfrac{1}{2}(u_s - u_g)^2\ ;\\
&I^{11}_{v_I=u_s}(\mathbf{W}) = \sum_{k\in\mathcal{K}} \left\{\alpha_k P_k + m_k(u_s - u_k)^2\right\},
\end{aligned} \tag{4.61}$$

  verifying for all $k \in [|1, 11|]$:

$$\nabla_{\mathbf{W}} I^k_{v_I=u_s}.\mathbf{r}_1(\mathbf{W}) = \nabla_{\mathbf{W}} I^k_{v_I=u_s}.\mathbf{r}_2(\mathbf{W}) = \nabla_{\mathbf{W}} I^k_{v_I=u_s}.\mathbf{r}_6(\mathbf{W}) = 0.$$

PROPOSITION 4.4 ($u_j \pm c_j$-WAVES)
Fields associated with eigenvalues $\lambda_7 = u_l + c_l$, $\lambda_8 = u_v + c_v$, $\lambda_9 = u_g + c_g$ and $\lambda_{10} = u_s + c_s$ as well as fields associated with $\lambda_{11} = u_l - c_l$, $\lambda_{12} = u_v - c_v$, $\lambda_{13} = u_g - c_g$ and $\lambda_{14} = u_s - c_s$ are genuinely non linear and admit 13 Riemann invariants (by noting $k \in [|1, 13|]$):

$$\nabla_{\mathbf{W}} I^k_{u_l+c_l}.\mathbf{r}_7(\mathbf{W}) = \nabla_{\mathbf{W}} I^k_{u_v+c_v}.\mathbf{r}_8(\mathbf{W}) = \nabla_{\mathbf{W}} I^k_{u_g+c_g}.\mathbf{r}_9(\mathbf{W}) = \nabla_{\mathbf{W}} I^k_{u_s+c_s}.\mathbf{r}_{10}(\mathbf{W}) = 0$$

and

$$\nabla_{\mathbf{W}} I^k_{u_l-c_l}.\mathbf{r}_{11}(\mathbf{W}) = \nabla_{\mathbf{W}} I^k_{u_v-c_v}.\mathbf{r}_{12}(\mathbf{W}) = \nabla_{\mathbf{W}} I^k_{u_g-c_g}.\mathbf{r}_{13}(\mathbf{W}) = \nabla_{\mathbf{W}} I^k_{u_s-c_s}.\mathbf{r}_{14}(\mathbf{W}) = 0.$$

They read, for $j \in \mathcal{K}$:

$$\forall k \in \mathcal{K} \setminus \{j\} : \quad \begin{array}{l} I^1_{u_j \pm c_j}(\mathbf{W}) = s_j \; ; \; I^2_{u_j \pm c_j}(\mathbf{W}) = \; u_j \mp \int_0^{\rho_j} \frac{c_j(r, s_j)}{r} dr \; ; \\ I^3_{u_j \pm c_j}(\mathbf{W}) = \alpha_l \; ; \; I^4_{u_j \pm c_j}(\mathbf{W}) = \alpha_s \; ; \\ I^{5,6,7}_{u_j \pm c_j}(\mathbf{W}) = \rho_k \; ; \; I^{8,9,10}_{u_j \pm c_j}(\mathbf{W}) = u_k \; ; \\ I^{11,12,13}_{u_j \pm c_j}(\mathbf{W}) = P_k. \end{array} \tag{4.62}$$

PROPOSITION 4.5 (u_j-WAVES)
If $v_I = u_m$(resp. if $v_I = u_s$): fields associated with eigenvalues $\lambda_3 = u_l$, $\lambda_4 = u_v$, $\lambda_5 = u_g$, $\lambda_6 = u_s$ (resp. $\lambda_3 = u_l$, $\lambda_4 = u_v$, $\lambda_5 = u_g$) are linearly degenerated. They admit 13 Riemann invariants I_{u_j}, $j \in \mathcal{K}$ (resp. $j \in \mathcal{K} \setminus \{s\}$):

$$\begin{array}{ll} \forall k \in \mathcal{K} \setminus \{j\} : & I^1_{u_j}(\mathbf{W}) = u_j \; ; \; I^2_{u_j}(\mathbf{W}) = P_j \; ; \; I^3_{u_j}(\mathbf{W}) = \alpha_l \; ; \; I^4_{u_j}(\mathbf{W}) = \alpha_s \; ; \\ (\text{resp. } \forall k \in \mathcal{K} \setminus \{s, j\} :) & I^{5,6,7}_{u_j}(\mathbf{W}) = \rho_k \; ; \; I^{8,9,10}_{u_j}(\mathbf{W}) = u_k \; ; \\ & I^{11,12,13}_{u_j}(\mathbf{W}) = P_k. \end{array} \tag{4.63}$$

Remark 4.7 — Other choices for $v_I(\mathbf{W}, \nabla\alpha_l, \nabla\alpha_s)$ have been proposed for instance in [56]. They read:

$$v_I(\mathbf{W}, \nabla\alpha_l, \nabla\alpha_s) = v_I^0(\mathbf{W}) + {a_I}^{1,l}(\mathbf{W}) \times \nabla\alpha_l + {a_I}^{1,s}(\mathbf{W}) \times \nabla\alpha_s.$$

for which we may choose for instance the velocity v_I^0 from equation (20). Structure of the governing equations for α_l and α_s will be modified and of course, proposition 1 should be modified. One should be careful that the choice of $v_I^0(\mathbf{W})$ should lead to uniquely defined jump conditions.

4.2.1.3 Jump conditions field by field

An isolated discontinuity travelling at speed σ separating two states L (left) and R (right) is considered. The operator $[.]$ refers to the jump of a quantity accross the σ-discontinuity, so that $[g] = g_R - g_L$.

PROPOSITION 4.6 (JUMP CONDITIONS)
Accross an isolated discontinuity travelling at speed σ, the following jump conditions hold for each genuinely nonlinear p-field, $p \in [|7, 14|]$:

$$\begin{array}{l} [\alpha_k] = 0; \\ [\rho_k(u_k - \sigma)] = 0; \\ [\rho_k u_k(u_k - \sigma) + P_k] = 0; \\ [E_k(u_k - \sigma) + P_k u_k] = 0; \\ [\rho_{k'}] = 0 \; ; \; [u_{k'}] = 0 \; ; \; [p_{k'}] = 0 \quad \forall k' \in \mathcal{K} \setminus \{k\}. \end{array} \tag{4.64}$$

Note that the p-Riemann invariants and the jump conditions coincide for the linearly degenerate p-fields, $p \in [|1, 6|]$. Except for the coupling wave associated with $\lambda_{1,2} = v_I$, the jump conditions are those of a single-phase Euler system.

Since the mixture entropy η is defined by $\eta = \sum_{i \in \mathcal{K}} m_i s_i$ and recalling the general jump condition for η:

$$(I) : -\sigma[\eta] + [f_\eta] > 0,$$

the mixture entropy η will also be modified through a $\sigma = u_k \pm c_k$ shock-wave because of the contribution of the phase k. Indeed, since for any quantity $\varphi_{k'}$, $[\varphi_{k'}] = 0 \; \forall k' \neq k$, (I) reads through a $\sigma = u_k \pm c_k$ shock-wave:

$$(I) : -\sigma[m_k s_k] + [m_k s_k u_k] > 0.$$

As s_k increases through a $u_k \pm c_k$ shock-wave, η will also increase.

4.2.1.4 Connecting solutions through the coupling wave

Analytical solutions are very useful to build some verification test cases for the model. Let us consider a one-dimensional Riemann problem for system (4.45): the solution is a self similar function composed of intermediate states separated by the p-waves ($p \in [|1, 14|]$) of the system. If it is a very tricky task to solve such Riemann problems in a general way (hence giving arbitrary left and right initial states), an easier way of building analytical solutions however exists from a given left state by prescribing the wave structure of the system (from left to right). Indeed, since the sequencing and the nature of waves is known, each intermediate state can be built step by step. More precisely, for a given left state in $\mathbb{R}^{14}$ just before any single p-wave, $p \in [|3, 14|]$, we can straightforwardly deduce from Riemann invariants (or jump conditions) the right state, while enforcing one scalar quantity on the right side.

As far as the coupling 1,2-wave is concerned, for a given left state $\mathbf{W}^L$ in $\mathbb{R}^{14}$ and for a given $(\alpha_s^R > 0, \alpha_l^R > 0, \rho_s^R > 0)$ with $1 > \alpha_s^R + \alpha_l^R$, the approach is the following **in the case** $v_I = u_s$.

Step 1: Compute $(X_l, X_v, X_g) = (\rho_l^R, \rho_v^R, \rho_g^R)$.

Indeed, by introducing the enthalpy $h_k(\rho_k, s_k) = \epsilon(\rho_k, s_k) + \frac{P_k(\rho_k, s_k)}{\rho_k}$:

$$\begin{array}{rll} I^8_{u_s}(\mathbf{W}) & = I^8_{u_s}(\mathbf{W}^L) & = h_l(\rho_l^L, s_l^L) + \frac{1}{2}(u_s^L - u_l^L)^2 \\ & = I^8_{u_s}(\mathbf{W}^R) & = h_l(\rho_l^R, s_l^R) + \frac{1}{2}(u_s^R - u_l^R)^2. \end{array}$$

Since:

$$s_l^L = s_l^R = I^2_{u_s}(\mathbf{W}^L) \quad ; \quad u_l^R(\mathbf{W}^L, X_l) = u_s^L - \frac{I^5_{u_s}(\mathbf{W}^L)}{\alpha_l^R X_l},$$

an equation enabling to get X_l as a function of $\mathbf{W}_L$ and α_l^R is obtained:

$$I^8_{u_s}(\mathbf{W}^L) = h_l(X_l, I^2_{u_s}(\mathbf{W}^L)) + \frac{1}{2}\left(\frac{I^5_{u_s}(\mathbf{W}^L)}{\alpha_l^R X_l}\right)^2.$$

Similarly, we get X_v and X_g, by solving:

$$I^9_{u_s}(\mathbf{W}^L) = h_v(X_v, I^3_{u_s}(\mathbf{W}^L)) + \frac{1}{2}\left(\frac{I^6_{u_s}(\mathbf{W}^L)}{(1-\alpha_l^R - \alpha_s^R)X_v}\right)^2$$

and

$$I^{10}_{u_s}(\mathbf{W}^L) = h_g(X_g, I^4_{u_s}(\mathbf{W}^L)) + \frac{1}{2}\left(\frac{I^7_{u_s}(\mathbf{W}^L)}{(1-\alpha_l^R - \alpha_s^R)X_g}\right)^2.$$

Step 2: Once $(X_l, X_v, X_g) = (\rho_l^R, \rho_v^R, \rho_g^R)$ are known, we deduce (P_l^R, P_v^R, P_g^R) such that:

$$I^2_{u_s}(\mathbf{W}^L) = s_l(P_l^R, X_l)\ ;\ I^3_{u_s}(\mathbf{W}^L) = s_v(P_v^R, X_v)\ ;\ I^4_{u_s}(\mathbf{W}^L) = s_g(P_g^R, X_g)$$

and also (u_l^R, u_v^R, u_g^R) using:

$$u_l^R(\mathbf{W}^L, X_l) = u_s^L - \frac{I^5_{u_s}(\mathbf{W}^L)}{\alpha_l^R X_l},$$

$$u_v^R(\mathbf{W}^L, X_v) = u_s^L - \frac{I^6_{u_s}(\mathbf{W}^L)}{(1-\alpha_l^R - \alpha_s^R)X_v},$$

$$u_g^R(\mathbf{W}^L, X_g) = u_s^L - \frac{I^7_{u_s}(\mathbf{W}^L)}{(1-\alpha_l^R - \alpha_s^R)X_g}.$$

Step 3: The remaining unknown P_s^R comes from:

$$I^{11}_{u_s}(\mathbf{W}^L) - \sum_{k\in\mathcal{K}\setminus\{s\}} (\alpha_k P_k + m_k(u_s - u_k)^2)^R = \alpha_s^R P_s^R.$$

Step 4: One should carefully check whether the right state is admissible or not.

Remark 4.8 — In the case $v_I = u_m$, the connection through the coupling wave $\lambda_{1,2}$ is far more complex because Riemann invariants $I^2_{u_m}(\mathbf{W}) = s_s - s_l$, $I^3_{u_m}(\mathbf{W}) = s_s - s_v$ and $I^4_{u_m}(\mathbf{W}) = s_s - s_g$ couple all the phases. □

4.2.2 Symmetrization

Even if our model can not be written in a conservative form, some theoretical results hold when symmetrizability is proved : indeed, Kato's theorem [49] on quasi-linear symmetric systems induces that, far from resonance, there exists a unique local-in-time smooth solution to the Cauchy problem.

PROPOSITION 4.7 (SYMMETRIZATION)
We restrict to smooth solutions of (4.45). *Then, system* (4.45) *is symmetrizable: there exists* g *a* $\mathcal{C}^1$*-diffeomorphism from* $\mathbb{R}^{14}$ *to* $\mathbb{R}^{14}$, $g : \mathbf{W} \mapsto \tilde{\mathbf{W}}$ *with:*

$$\partial_t \tilde{\mathbf{W}} + \mathbf{C}(\tilde{\mathbf{W}})\partial_x \tilde{\mathbf{W}} = 0,$$

so that there exists $\mathbf{S}(\tilde{\mathbf{W}})$ *a symmetric positive definite matrix satisfying:*

$$\mathbf{S}(\tilde{\mathbf{W}})\partial_t \tilde{\mathbf{W}} + \tilde{\mathbf{C}}(\tilde{\mathbf{W}})\partial_x \tilde{\mathbf{W}} = 0 \; ; \; \tilde{\mathbf{C}}(\tilde{\mathbf{W}}) = \mathbf{S}(\tilde{\mathbf{W}})\mathbf{C}(\tilde{\mathbf{W}}) \text{ and } \tilde{\mathbf{C}} = \tilde{\mathbf{C}}^t.$$

A general proof by construction, similar to [55, 39] and based on cumbersome computations, is given in appendix 4.D. Here, we propose a simpler proof, motivated by [24], but only valid in the one-dimensional case.
Resonance excluded, system (4.45) is hyperbolic, and thus, diagonalizable. By noting $\mathbf{L}$ the matrix concatening the left eigenvectors, there exists $\mathbf{D}$ a diagonal matrix so that $\mathbf{B} = \mathbf{L}^{-1}\mathbf{D}\mathbf{L}$ and $\partial_t \mathbf{W} + \mathbf{L}^{-1}\mathbf{D}\mathbf{L}\partial_x \mathbf{W} = 0$. Then, the symmetric positive definite matrix $\mathbf{S} = \mathbf{L}^t\mathbf{L}$ suits: $\mathbf{S}\mathbf{B} = \mathbf{L}^t\mathbf{D}\mathbf{L}$ is indeed symmetric and $\mathbf{S}\partial_t \mathbf{W} + \mathbf{S}\mathbf{B}\partial_x \mathbf{W} = 0$.
Note that in general this proof can not be extended in the multidimensional case, because, if $\partial_t \mathbf{W} + \mathbf{B}_x\partial_x \mathbf{W} + \mathbf{B}_y\partial_y \mathbf{W} = 0$, the left eigenvectors of $\mathbf{B}_x$ and $\mathbf{B}_y$ are usually different for real systems coming from fluid mechanics.

4.3 A few remarks about the model

In this section, **only the case $\boxed{v_I = u_s}$ is considered.**

Model (4.45) reads then, when restricting to regular solutions:

$$\left\{\begin{array}{lrcl}
 & \partial_t\alpha_l + u_s\partial_x\alpha_l = \Phi_l & = & \Phi_l \\
 & \partial_t\alpha_s + u_s\partial_x\alpha_s = \Phi_s & = & \Phi_s \\
 & \partial_t\rho_l + u_l\partial_x\rho_l + \rho_l\partial_x u_l - \dfrac{\rho_l(u_s-u_l)}{\alpha_l}\partial_x\alpha_l & = & S_{\rho_l} \\
 & \partial_t\rho_s + u_s\partial_x\rho_s + \rho_s\partial_x u_s & = & S_{\rho_s} \\
(k = v, g) & \partial_t\rho_k + u_k\partial_x\rho_k + \rho_k\partial_x u_k + \dfrac{\rho_k(u_s-u_k)}{\alpha_k}(\partial_x\alpha_l + \partial_x\alpha_s) & = & S_{\rho_k} \\
(k \in \mathcal{K}\setminus\{s\}) & \partial_t u_k + u_k\partial_x u_k + \tau_k\partial_x P_k & = & S_{u_k} \\
 & \partial_t u_s + u_s\partial_x u_s + \tau_s\partial_x P_s + \dfrac{1}{m_s}\left(\Delta P_l\partial_x\alpha_l + \Delta P_s\partial_x\alpha_s\right) & = & S_{u_s} \\
 & \partial_t P_l + u_l\partial_x P_l + \rho_l c_l^2\partial_x u_l - \dfrac{\rho_l c_l^2(u_s-u_l)}{\alpha_l}\partial_x\alpha_l & = & S_{P_l} \\
 & \partial_t P_s + u_s\partial_x P_s + \rho_s c_s^2\partial_x u_s & = & S_{P_s} \\
(k = v, g) & \partial_t P_k + u_k\partial_x P_k + \rho_k c_k^2\partial_x u_k + \dfrac{\rho_k c_k^2(u_s-u_k)}{\alpha_k}(\partial_x\alpha_l + \partial_x\alpha_s) & = & S_{P_k}
\end{array}\right. \tag{4.65}$$

Subsection 4.1.3.2 highlighted that the source terms should satisfy constraints depending on relative phasic gaps, i.e.:

$$\underline{\Delta u} = \begin{pmatrix} \Delta u_l = u_s - u_l \\ \Delta u_v = u_s - u_v \\ \Delta u_g = u_s - u_g \end{pmatrix} \text{ (see (4.51))};$$

$$\underline{\Delta P} = \begin{pmatrix} \Delta P_l = P_l - (P_v + P_g) \\ \Delta P_s = P_s - (P_v + P_g) \end{pmatrix} \text{ (see (4.52))};$$

$$\underline{\Delta a} = \begin{pmatrix} a_s - a_l \\ a_s - a_v \\ a_s - a_g \end{pmatrix} \quad ; \quad \underline{\Delta a\mu} = \begin{pmatrix} a_s\mu_s - a_l\mu_l \\ a_s\mu_s - a_v\mu_v \\ a_s\mu_s - a_g\mu_g \end{pmatrix}.$$

These dependances are the following:

$$\begin{pmatrix} \Phi_l \\ \Phi_s \end{pmatrix} = \mathcal{D}\underline{\Delta P}, \text{ with } \mathcal{D} \text{ symmetric positive definite matrix (see (4.35))};$$
$$S_{\rho_k} = S_{\rho_k}(\underline{\Delta P}, \underline{\Delta a\mu}); \quad S_{u_k} = S_{u_k}(\underline{\Delta P}, \underline{\Delta u}, \underline{\Delta a\mu});$$
$$S_{P_k} = S_{P_k}(\underline{\Delta P}, \underline{\Delta u}, \underline{\Delta a}, \underline{\Delta a\mu}) \quad \forall k \in \mathcal{K}.$$

We recall that the previous terms are deduced from the closures satisfying constraints (4.35), (4.37), (4.39), (4.40), (4.43) written in section 4.1.3.2.

4.3.1 Preservation of the thermodynamically admissible domain

Let us recall the definition of the thermodynamically admissible domain:

$$\mathbb{E}_k \ = \ \{(P_k, \rho_k) \in \mathbb{R}\times\mathbb{R}^{+*} \ / \ \epsilon_k(P_k, \rho_k) \geq 0\}.$$

We wish to check whether $\mathbb{E}_k$, $k \in \mathcal{K}$, is preserved by the convective part of our model (without source terms) for a given equation of state. We consider for instance the stiffened gas equation of state for each phase $k \in \mathcal{K}$:

$$P_k + \gamma_k\Pi_k = (\gamma_k - 1)\rho_k\epsilon_k, \quad \gamma_k > 1, \quad \Pi_k \geq 0. \tag{4.66}$$

For this equation of state (4.66), $\mathbb{E}_k$ reads:

$$\mathbb{E}_k = \{(P_k, \rho_k) \in \mathbb{R} \times \mathbb{R}^{+*} / P_k > -\Pi_k\}.$$

Let us define $\mathcal{P}_k = m_k \epsilon_k - \Pi_k \alpha_k$. Note that $\mathcal{P}_k \geq 0$ is equivalent to $(P_k, \rho_k) \in \mathbb{E}_k$. Thus, we aim to study the sign of $\mathcal{P}_k$ for each phase $k \in \mathcal{K}$ by writting an equation on $\mathcal{P}_k$ from ϵ_k (see (4.84) in appendix 4.A) with $v_I = u_s$.
For $k \in \mathcal{K}$:

$$\partial_t \mathcal{P}_k + u_k \partial_x \mathcal{P}_k + \mathcal{P}_k \left(\gamma_k \partial_x u_k + (\gamma_k - 1)(u_k - u_s)\partial_x(\ln(\alpha_k)\right) = 0. \tag{4.67}$$

Equation (4.67) can be rewritten as:

$$\forall k \in \mathcal{K}, \quad \partial_t \mathcal{P}_k + u_k \partial \mathcal{P}_k + \gamma_k \mathcal{P}_k \partial_x v_k = 0,$$

by defining:

$$\partial_x v_k = \partial_x u_k + \frac{(\gamma_k - 1)}{\gamma_k}(u_k - u_s)\partial_x(\ln(\alpha_k)).$$

Using a classical lemma proved in [50], the following proposition holds:

PROPOSITION 4.8 (PRESERVATION OF $\mathbb{E}_k$ FOR A SMOOTH SOLUTION)
Considering $T > 0$ and a 1-D spatial domain $\Omega \subset \mathbb{R}$, under the following assumptions:

- $u_k \in \mathcal{L}^\infty([0,T] \times \Omega)$,
- $\partial_x u_k + (\gamma_k - 1)(u_k - u_s)\partial_x(\ln(\alpha_k)) \in \mathcal{L}^\infty([0,T] \times \Omega)$ *for* $k \in \mathcal{K}$,

since initial conditions ensure an admissible thermodynamical state for all phases, i.e.:

- $\mathcal{P}_k(t = 0, x) \geq 0 \; \forall k \in \mathcal{K}$;
- $\mathcal{P}_k(t > 0, x \in \Gamma_k^-(t)) \geq 0 \; \forall k \in \mathcal{K}$,
  with $\Gamma_k^-(t) = \{x \in \partial\Omega / \; (\mathbf{u}_k.\mathbf{n})(t,x) < 0\}$,

then, Ω_k is preserved within time for all phases ***for a regular solution****, i.e.:*

$$\mathcal{P}_k(0 \leq t \leq T, x) \geq 0 \quad \forall k \in \mathcal{K}.$$

Remark 4.9 — Recalling that $v_I = u_s$, for solutions with discontinuities, it can be proved, following an approach very similar to [35], that the solution of a one-dimensional Riemann problem with stiffened gas equation of state for all phases will remain physically relevant, since the connection of states through the waves of the system ensures that $0 \leq \alpha_k$, $0 \leq m_k$ and $0 \leq \mathcal{P}_k$. □

4.3.2 Preservation of pressure equilibria

An important requirement for the model is the preservation of pressure equilibria. Then, when taking the following uniform state as initial conditions in (4.65) without mass source terms:

$$\begin{cases} u_k = 0 \quad \forall k \in \mathcal{K}; \\ P_l = P_s = P_0; \\ P_v = \tilde{P}_0 \quad ; \quad P_g = P_0 - \tilde{P}_0; \\ T_k = T_0 \quad \forall k \in \mathcal{K}, \end{cases} \tag{4.68}$$

since $\partial_x u_k = \partial_x P_k = 0$ and $u_k = 0$ for all $k \in \mathcal{K}$, pressure equilibria are indeed maintained within time, regardless of $\partial_x \alpha_l$ and $\partial_x \alpha_s$ at time $t = 0$.

4.3.3 Effects of the pressure relaxation

Without mass, momentum and energy transfer and without convection terms (i.e. "$\partial_x = 0$"), the system should naturally relax towards pressure equilibria $P_l = P_v + P_g = P_s$.

Still assuming now that $v_I = u_s$, and recalling the admissible form for Φ_l and Φ_s (4.35), model (4.18) without convection and without mass, momentum and energy source terms reads:

$$\left\{\begin{array}{rcl} \partial_t \begin{pmatrix} \alpha_l \\ \alpha_s \end{pmatrix} & = & \mathcal{D} \begin{pmatrix} \Delta P_l \\ \Delta P_s \end{pmatrix} \\ \partial_t(m_k) & = & 0 \\ \partial_t(m_k u_k) & = & 0 \\ \partial_t(\alpha_l E_l) + P_l \partial_t \alpha_l & = & 0 \\ (k = v, g) \quad \partial_t(\alpha_k E_k) - P_k(\partial_t \alpha_s + \partial_t \alpha_l) & = & 0 \\ \partial_t(\alpha_s E_s) - \Delta P_l \partial_t \alpha_l + (P_v + P_g)\partial_t \alpha_s & = & 0, \end{array}\right. \tag{4.69}$$

where $\mathcal{D}$ is a symmetric positive definite matrix. From equations on $\alpha_k E_k$, equations on phasic pressures can be written (see appendix 4.A), by noting $A_k = \dfrac{\rho_k c_k^2}{\alpha_k}$:

$$\left\{\begin{array}{l} \partial_t P_k + A_k \partial_t \alpha_k = 0 \quad (k = l, v, g), \\ \partial_t P_s - (\alpha_s \rho_s \partial_{P_s} \epsilon_s)^{-1} \Delta P_l \partial_t \alpha_l + \left\{ A_s - (\alpha_s \rho_s \partial_{P_s} \epsilon_s)^{-1} \Delta P_s \right\} \partial_t \alpha_s = 0. \end{array}\right. \tag{4.70}$$

Then, equations on $\Delta P_l = P_l - (P_v + P_g)$ and $\Delta P_s = P_s - (P_v + P_g)$, expressing the deviation from pressure equilibria, are obtained:

$$\partial_t \begin{pmatrix} \Delta P_l \\ \Delta P_s \end{pmatrix} + \mathcal{A}\mathcal{D} \begin{pmatrix} \Delta P_l \\ \Delta P_s \end{pmatrix} = \mathbf{0}, \tag{4.71}$$

with:

$$\mathcal{A}(\Delta P_l, \Delta P_s) = \begin{pmatrix} A_{lvg} & A_{vg} \\ A_{vg} - B_s \Delta P_l & A_{vgs} - B_s \Delta P_s \end{pmatrix}, \tag{4.72}$$

where $A_{vg} = A_v + A_g$, $A_{lvg} = A_l + A_{vg}$, $A_{vgs} = A_{vg} + A_s$ and $B_s = (m_s \partial_{P_s} \epsilon_s)^{-1}$. ΔP_l and ΔP_s are coupled, so that we are not able to analytically solve the previous system. An approximated resolution is proposed, by considering a frozen convection matrix $\mathcal{A}^*\mathcal{D}^*$, obtained by freezing ΔP_l and ΔP_s. It leads to the following simplified system:

$$\partial_t \begin{pmatrix} \Delta P_l \\ \Delta P_s \end{pmatrix} + \mathcal{A}^*\mathcal{D}^* \begin{pmatrix} \Delta P_l \\ \Delta P_s \end{pmatrix} = \mathbf{0}, \tag{4.73}$$

with $\mathcal{A}^*$ the following matrix, independent from ΔP_l and ΔP_s at time t:

$$\mathcal{A}^* = \begin{pmatrix} A^*_{lvg} & A^*_{vg} \\ A^*_{vg} - B^*_s \Delta P^*_l & A^*_{vgs} - B^*_s \Delta P^*_s \end{pmatrix} \tag{4.74}$$

and

$$\mathcal{D}^* = \begin{pmatrix} d^*_{11} & d^*_{12} \\ d^*_{12} & d^*_{22} \end{pmatrix}, \quad d^*_{11} > 0,\ d^*_{22} > 0,\ d^*_{12} = \sqrt{d^*_{11} d^*_{22}}\sin(\theta), \theta \in \mathbb{R}. \tag{4.75}$$

Then, studying the spectrum of $\mathcal{A}^*\mathcal{D}^*$ gives pressure relaxation conditions. From now, $.^*$ on the matrix coefficients will be omitted in the computations for a sake of readibility and the two eigenvalues of $\mathcal{A}^*\mathcal{D}^*$ are noted $\lambda_\pm$.

We assume from now that the equation of state for phase "s" is such that: $\partial_{P_s} \epsilon_s > 0$. One can now exhibit conditions ensuring relaxation, depending on the type of eigenvalues:

- if $\lambda_\pm \in \mathbb{R}$, there are two conditions:

$$\lambda_+ + \lambda_- = \mathrm{tr}(\mathcal{A}^*\mathcal{D}^*) > 0 \tag{4.76}$$

and

$$\lambda_+\lambda_- = \det(\mathcal{A}^*\mathcal{D}^*) \geq 0. \tag{4.77}$$

- otherwise, only condition (4.74) is required; condition (4.75) is automatically fulfilled since $\lambda_+\lambda_- = |\lambda_\pm|^2 = \det(\mathcal{A}^*\mathcal{D}^*)$; moreover, condition (4.74) is sufficient in order to ensure the return towards pressure equilibria; however, oscillations may occur in some areas of the domain since $\mathrm{Im}(\lambda_\pm) \neq 0$.

Since $\det(\mathcal{D}) > 0$, (4.75) requires that $\det(\mathcal{A}^*) \geq 0$. Hence, the following two quantities must be positive:

$$\begin{aligned} \mathrm{tr}(\mathcal{A}^*\mathcal{D}) &= d_{11}A_{lvg} + 2d_{12}A_{vg} + d_{22}A_{vgs} \\ &\quad - B_s\left\{ d_{12}\Delta P_l^* + d_{22}\Delta P_s^* \right\} \\ &= \underbrace{d_{11}A_l + d_{22}A_s + A_{vg}(d_{11} + d_{22} + 2d_{12})}_{>0} \\ &\quad - B_s\left\{ d_{12}\Delta P_l^* + d_{22}\Delta P_s^* \right\}, \end{aligned} \tag{4.74}$$

$$\begin{aligned} \det(\mathcal{A}^*) &= A_{lvg}A_{vgs} - A_{vg}^2 \\ &\quad + B_s\left\{ A_{vg}\Delta P_l^* - A_{lvg}\Delta P_s^* \right\} \\ &= A_lA_s + A_{ls}A_{vg} \\ &\quad + B_s\left\{ A_{vg}\Delta P_l^* - A_{lvg}\Delta P_s^* \right\}. \end{aligned} \tag{4.75}$$

Now, we introduce $|\Delta P| = \max(|\Delta P_l|, |\Delta P_s|)$ and only the worst case will be considered for each condition to obtain a sufficient constraint on $|\Delta P|$:

- for (4.74), the worst case occurs when $d_{12}\Delta P_l > 0$ and $\Delta P_s > 0$ and we get:

$$|\Delta P| < \frac{d_{11}A_l + d_{22}A_s + A_{vg}(d_{11} + d_{22} + 2d_{12})}{B_s(|d_{12}| + d_{22})} = \underbrace{\mathcal{S}_1}_{>0}. \tag{4.76}$$

- for (4.75), the worst case occurs when $\Delta P_l < 0$ and $\Delta P_s > 0$ and we get:

$$|\Delta P| < \frac{A_lA_s + A_{ls}A_{vg}}{B_s(A_{vg} + A_{lvg})} = \underbrace{\mathcal{S}_2}_{>0}; \tag{4.77}$$

The previous observations are summarized in the following proposition:

PROPOSITION 4.9 (THRESHOLD EFFECT FOR PRESSURE RELAXATION)
Since the equation of state of phase "s" is such $\partial_{P_s}\epsilon_s > 0$, the relaxation system relaxes towards equilibrium when initial pressure gaps are small enough. A threshold effect is thus observed: pressure relaxation is ensured as soon as $|\Delta P| = \max(|\Delta P_l|, |\Delta P_s|)$ is bounded as follows, depending on the type of $\lambda_\pm$, the eigenvalues of the system (4.73):

- $|\Delta P| < \min(\mathcal{S}_1, \mathcal{S}_2)$ *if* $\lambda_\pm \in \mathbb{R}$;
- $|\Delta P| < \mathcal{S}_1$ *otherwise.*

Remark 4.10 — Orders of magnitude for $\mathcal{S}_1$ and $\mathcal{S}_2$ are now evaluated for data close to primary nuclear reactor conditions by considering stiffened gas equations of state for all components. This coarse assumption is still reasonable for liquid water and liquid metal at high pressures. Moreover, we assume that $d_{12} = 0$. In this case, (4.76) becomes:

$$|\Delta P| < \frac{d_{11}A_l + d_{22}A_s + A_{vg}(d_{11} + d_{22})}{B_s d_{22}} = \mathcal{S}_1.$$

In particular, since A_l, A_{vg} and d_{kk} are all positive:

$$\mathcal{S}_1 \geq A_s B_s^{-1}.$$

Furthermore:

$$\mathcal{S}_2 \geq \frac{A_s A_{lvg}}{2B_s A_{lvg}} = \frac{1}{2} A_s B_s^{-1}.$$

For a stiffened gas, $B_s^{-1} = \dfrac{\alpha_s}{\gamma_s - 1}$ i.e. $A_s B_s^{-1} = \dfrac{\rho_s c_s^2}{\gamma_s - 1}$. Uranium dioxyd is taken as metal field s so that $\rho_s \simeq 10900\ kg.m^{-3}$ and $c_s \simeq 1800\ m.s^{-1}$. Moreover, $\gamma_s - 1 \simeq 1$. Finally:

$$\min(\mathcal{S}_1, \mathcal{S}_2) \geq \frac{1}{2} A_s B_s^{-1} \simeq 10^5\ bar.$$

It means that the maximal phasic pressure gap $|\Delta P|$ needs to be smaller than a huge value of pressure. Then, both constraints (4.76) and (4.77) are thus not limiting for our targeted applications. □

Remark 4.11 — Let us recall that the present model belongs to a model family. A pressure relaxation process has already been exhibited for models with two or three fields. We sum up in table 4.1 remarkable behaviors that have been observed in previous works.

Nb phases	Fields	Model type	Threshold effect ?	Oscillations ?	Ref
2	liquid $\oplus$ vapor	Barotropic	No	No	[12], see (4.78) in item (i)
2	liquid $\oplus$ vapor	With Energy	Yes	No	[9] (appendix A2)
2	liquid $\oplus$ (vapor+gas)	With Energy	Yes	No	[39], see (4.79) in item (ii)
3	liquid $\oplus$ vapor $\oplus$ metal	Barotropic	No	**May exist (stable)**	[10]
3	liquid $\oplus$ vapor $\oplus$ metal	With Energy	Yes	**May exist (stable)**	[9]
3	liquid $\oplus$ (vapor+gas) $\oplus$ metal	With Energy	Yes	**May exist (stable)**	(4.73)

Table 4.1 – Classical behaviors concerning the pressure relaxation for models with two or three phases. $\phi_1 \oplus \phi_2$ means that ϕ_1 and ϕ_2 are two immiscible fields whereas $\phi_1 + \phi_2$ means that ϕ_1 and ϕ_2 are miscible. A threshold effect appears in some cases: pressure relaxation is ensured only if the initial pressure gap(s) is (are) small enough. Pressure relaxation can be uniform towards 0, or some oscillations may occur in some area of the domain. For each model, a bibliographic reference [.] describing the considered model is given. When the pressure relaxation is not explained in [.], the suitable equation is recalled in the present document (the corresponding equation number is given in (.)).

For barotropic models (without energy equation), pressure relaxation is ensured unconditionaly, whereas for models with an energy equation, a threshold effect appears, i.e. relaxation occurs only if the initial pressure gap(s) is (are) small enough. Pressure relaxation is uniform only in the two-phase flow case. When three phases coexist, oscillations may occur in the relaxation process.

We briefly comment table 4.1 as follows. We insist on the difference between fields and phases: a phase is a field or the mixture of two (or more) miscible fields.

(i) We recall the relaxation pressure equation for a barotropic model with two immiscible phases (l and v), which can be very easily obtained from the model described for instance in [12]. By noting $\Delta P = P_l - P_v$ and still neglecting spatial derivatives, we get:

$$\partial_t \Delta P + \left(\sum_{k=l,v} \frac{\rho_k c_k^2}{\alpha_k} \right) \tilde{d} \Delta P = 0, \quad \tilde{d} > 0. \tag{4.78}$$

As $\sum_{k=l,v} \frac{\rho_k c_k^2}{\alpha_k} > 0$, ΔP unconditionally and uniformly relaxes.

(ii) Then, the model proposed in [39] is also a two phase flow model, with three fields (l, v, g), whose two are miscible gases (v and g). There is only one "efficient" pressure gap $\Delta P_l = P_l - (P_v + P_g)$. The obtained pressure relaxation equation is then very similar to (4.78), except that an additional term appears since the model is no more barotropic:

$$\partial_t \Delta P_l + \left(\sum_{k=l,v,g} \frac{\rho_k c_k^2}{\alpha_k} + (m_l \partial_{P_l} \epsilon_l)^{-1} \Delta P_l \right) \hat{d} \Delta P_l = 0, \quad \hat{d} > 0. \tag{4.79}$$

Pressure relaxation process occurs when the following constraint is satisfied:

$$|\Delta P_l^{t=0}| < m_l \partial_{P_l} \epsilon_l \sum_{k=l,v,g} \frac{\rho_l c_k^2}{\alpha_k}. \tag{4.80}$$

Once the previous constraint fulfilled, for this hybrid model, pressure uniformly relaxes without oscillations, unlike for the four-field model studied in this work with three "real" phases (4.73). □

Conclusion

A three-phase flow model with four components has been proposed and studied, with both immiscible phases (liquid water, liquid metal and gaseous phase) and miscible phases (steam and non-condensable gas). The whole modelling approach has been presented, by specifying step by step the consequences of each additional assumption. On the one hand, the choice of a mixture entropy enforces unique closures for the non-conservative terms of the equations: the model is then uniquely defined, up to some relaxation time scales to be prescribed by the user. On the other hand, particular choices for the interfacial velocity v_I lead to a linearly degenerate coupling wave and thus uniquely defined jump conditions, independently from the chosen closure for $(\Pi_{kk'})_{k,k'\in\mathcal{K}}$ (i.e. the LD-property holds even with another definition of the entropy as (4.9)).

A particular admissible submodel has been deeply studied: the case $v_I = u_s$. The model is hyperbolic, complies with the second principle of thermodynamics and admits uniquely defined jump conditions, which enables to build analytical solutions.

Despite the hybrid miscibility conditions, no major mathematical difficulty appears, comparing with the immiscible three-phase flow model [35]. Still, note that the Dalton's law holds here: the relevant pressure gaps to consider for our present model are $P_l - (P_v + P_g)$ and $P_s - (P_v + P_g)$. However, the direct generalization to models with more than three phases and hybrid miscibility constraints is not obvious; whereas properties like the convexity of the entropy or the existence of a symmetric form for the convective system, have been proved in [55] for multiphasic barotropic models containing N immiscible pure phases, with N arbitrarily large.

The next step will obviously concern the numerical approximation of the present model.

Restricting to the approximation of the convective part, rough schemes, for instance those currently implemented in [10, 9] in order to obtain approximate solutions of immiscible three-phase flow models [34, 35], are not accurate enough : they require too fine meshes that are hardly affordable for industrial multi-dimensional applications. Thus they should be clearly improved using more accurate schemes. Actually, while restricting to two-phase flow models, we recall that the numerical scheme, initially developped in [21, 37] for the two-phase flow case with immiscible components, has been indeed much improved, both in terms of accuracy and stability, using the relaxation scheme [16, 14]; a detailed comparison of the latter with other schemes, namely the approximate Godunov solver [57], and the HLLC scheme [58], confirmed its advantages and strong potentialities. Moreover, a recent accurate and efficient relaxation scheme has been proposed in [54] for the barotropic immiscible three-phase flow model [34], which is precisely an extension of the one developped in [16, 14] for two-phase flows with immiscible components. This new relaxation scheme relies on the properties of the coupling wave: such a method should certainly be suitable for our model too, thanks to the properties listed in section 3.

Relaxation procedures to tackle the source terms require additional efforts. The strategy developed in [10, 9] still relies on the use of the fractional step method (used in [37]), and treats separately convective terms and source terms. The latter contain the velocity pressure relaxation step which is rather tricky (see also [28] for similar issues). Moreover, these techniques might certainly be improved, while getting rid of the fractional step strategy, and introducing a more coupled numerical approach, as suggested by [44]. Obviously, a lot of work has still to be done on these aspects.

In order to avoid introducing a fourth field with its own velocity for the non-condensable gas as done in the present work, another idea might be to consider a three-phase flow model with three immiscible phases like in [35], and to replace the vapor water by a miscible mix-

ture of vapor water and non-condensable gas with a unique velocity and a unique mixture equation of state. The main difficulty is then to build this mixture equation of state for the miscible gaseous phase, complying with the second principle and enabling to manage the phase transition for water.
Modelling the phase transition as a chemical reaction like in [30] would perhaps enable to treat the gaseous phase. However, it would require a entire new work, to completely study the compatibility of such thermodynamical hypotheses with the current formalism (in particular, the fact that we have an energy equation for each phase contrary to [30]) and its consequences in terms of hyperbolicity.
The mixture equation of state for the gaseous phase could also be built with the same guidelines as those used for instance in [6, 42]. A first step would be to develop a bifluid two-phase flow model based on [13], with such an EOS for the miscible mixture of non-condensable gas and vapor water. If this "hybrid" two-phase flow model (with both miscible and immiscible phases) had all the required properties, it would certainly be interesting to consider the extension of this approach to a three-phase flow hybrid model (with both miscible and immiscible components).

Acknowledgements

The authors thank the reviewers for their very careful reading. The last author receives financial support by ANRT through an EDF/CIFRE grant number 2017/0476. Neuronal facilities were provided by EDF.

References

[1] R. ABGRALL and R. SAUREL. "Discrete Equations for Physical and Numerical Compressible Multiphase Mixtures". In: *J. Comput. Phys.* 186.2 (Apr. 2003), pp. 361–396. ISSN: 0021-9991. DOI: https://doi.org/10.1016/S0021-9991(03)00011-1 (cit. on p. 212).

[2] R. AKIYOSHI, S. NISHIO, and I. TANASAWA. "A study on the effect of non-condensible gas in the vapor film on vapor explosion". In: *International journal of heat and mass transfer* 33.4 (1990), pp. 603–609. DOI: https://doi.org/10.1016/0017-9310(90)90159-R (cit. on p. 208).

[3] G. ALLAIRE, S. CLERC, and S. KOKH. "A five-equation model for the numerical simulation of interfaces in two-phase flows". In: *Comptes Rendus de l'Académie des Sciences - Series I - Mathematics* 331.12 (2000), pp. 1017–1022. URL: http://www.sciencedirect.com/science/article/pii/S0764444200017535 (cit. on p. 208).

[4] M. BACHMANN, S. MÜLLER, P. HELLUY, and H. MATHIS. "A Simple Model for Cavitation with Non-condensable Gases". In: *Hyperbolic Problems: Theory, Numerics and Applications*. Vol. 18. World Scientific, 2012, pp. 289–296. DOI: 10.1142/9789814417099_0024. URL: https://hal.archives-ouvertes.fr/hal-01420483 (cit. on p. 208).

[5] M. BAER and J. NUNZIATO. "A two-phase mixture theory for the deflagration-to-detonation transition (DDT) in reactive granular materials". In: *Journal of Multiphase Flows* 12 (1986), pp. 861–889. DOI: https://doi.org/10.1016/0301-9322(86)90033-9 (cit. on pp. 208, 209).

[6] T. BARBERON and P. HELLUY. "Finite volume simulation of cavitating flows". In: *Computers and Fluids* 34.7 (2005), pp. 832–858. URL: https://hal.archives-ouvertes.fr/hal-00139597 (cit. on pp. 208, 233).

[7] F. BARRE and M. BERNARD. "The CATHARE code strategy and assessment". In: *Nuclear engineering and design* 124.3 (1990), pp. 257–284. DOI: https://doi.org/10.1016/0029-5493(90)90296-A (cit. on p. 208).

[8] G. BERTHOUD. "Vapor explosions". In: *Annual Review of Fluid Mechanics* 32.1 (2000), pp. 573–611. DOI: https://doi.org/10.1146/annurev.fluid.32.1.573 (cit. on pp. 208, 209).

[9] H. BOUKILI and J.-M. HÉRARD. "Simulation and preliminary validation of a three-phase flow model with energy". working paper or preprint. Jan. 2020. URL: https://hal.archives-ouvertes.fr/hal-02426425 (cit. on pp. 209, 230, 232).

[10] H. BOUKILI and J.-M. HÉRARD. "Relaxation and simulation of a barotropic three-phase flow model". In: *ESAIM: Mathematical Modelling and Numerical Analysis* 53 (2019), pp. 1031–1059. DOI: 10.1051/m2an/2019001. URL: https://hal.archives-ouvertes.fr/hal-01745161 (cit. on pp. 208, 209, 230, 232).

[11] M. CHUBERRE and N. SEGUIN. *Étude asymptotique pour des écoulements compressibles diphasiques*. Tech. rep. Université Rennes 1, IRMAR, 2019. URL: http://perso.eleves.ens-rennes.fr/people/Meriadec.Chuberre/Memoire_M2.pdf (cit. on p. 217).

[12] F. COQUEL, J.-M. HÉRARD, and K. SALEH. "A splitting method for the isentropic Baer-Nunziato two-phase flow model." In: *ESAIM: Proceedings* 38 (2012), pp. 241–256. URL: https://hal.archives-ouvertes.fr/hal-01265218 (cit. on p. 230).

[13] F. COQUEL, T. GALLOUËT, J.-M. HÉRARD, and N. SEGUIN. "Closure laws for a two-fluid two-pressure model". In: *Comptes Rendus Mathématique* 334.10 (2002), pp. 927–932. URL: https://hal.archives-ouvertes.fr/hal-01484345 (cit. on pp. 208–210, 219, 233).

[14] F. COQUEL, J.-M. HÉRARD, and K. SALEH. "A positive and entropy-satisfying finite volume scheme for the Baer–Nunziato model". In: *Journal of Computational Physics* 330 (2017), pp. 401–435. URL: https://hal.archives-ouvertes.fr/hal-01261458 (cit. on p. 232).

[15] F. COQUEL, J.-M. HÉRARD, K. SALEH, and N. SEGUIN. "A class of two-fluid two-phase flow models". In: *42nd AIAA Fluid Dynamics Conference and Exhibit*. New Orleans, United States: AIAA, June 2012. DOI: 10.2514/6.2012-3356. URL: https://hal.archives-ouvertes.fr/hal-01582645 (cit. on p. 220).

[16] F. COQUEL, J.-M. HÉRARD, K. SALEH, and N. SEGUIN. "A Robust Entropy-Satisfying Finite Volume Scheme for the Isentropic Baer-Nunziato Model". In: *ESAIM: Mathematical Modelling and Numerical Analysis* 48.1 (2014), pp. 165–206. URL: https://hal.archives-ouvertes.fr/hal-00795568 (cit. on p. 232).

[17] F. COQUEL, J.-M. HÉRARD, K. SALEH, and N. SEGUIN. "Two properties of two-velocity two-pressure models for two-phase flows". In: *Communications in Mathematical Sciences* 12.3 (2014). URL: https://hal.archives-ouvertes.fr/hal-00788902 (cit. on p. 209).

[18] P. DOWNAR-ZAPOLSKI, Z. BILICKI, L. BOLLE, and J. FRANCO. "The non-equilibrium relaxation model for one-dimensional flashing liquid flow". In: *International Journal of Multiphase Flow* 22.3 (1996), pp. 473–483. DOI: https://doi.org/10.1016/0301-9322(95)00078-X (cit. on p. 217).

[19] G. FACCANONI, S. KOKH, and G. ALLAIRE. "Modelling and Simulation of Liquid-Vapor Phase Transition in Compressible Flows Based on Thermodynamical Equilibrium." In: *Mathematical Modelling and Numerical Analysis* 46.05 (Sept. 2012), pp. 1029–1054. URL: https://hal.archives-ouvertes.fr/hal-00976983 (cit. on p. 208).

[20] T. FLÅTTEN and H. LUND. "Relaxation two-phase flow models and the subcharacteristic condition". In: *Mathematical Models and Methods in Applied Sciences* 21.12 (2011), pp. 2379–2407. DOI: https://doi.org/10.1142/S0218202511005775 (cit. on p. 208).

[21] T. GALLOUËT, J.-M. HÉRARD, and N. SEGUIN. "Numerical modeling of two-phase flows using the two-fluid two-pressure approach". In: *Mathematical Models and Methods in Applied Sciences* volume 14, numéro 5 (2004), pp. 663–700. URL: https://hal.archives-ouvertes.fr/hal-00003327 (cit. on pp. 209, 232).

[22] S. GAVRILYUK. "The structure of pressure relaxation terms: the one-velocity case". In: *EDF internal report, H-I83-2014-0276-EN* (2014) (cit. on p. 217).

[23] S. GAVRILYUK and R. SAUREL. "Mathematical and Numerical Modeling of Two-phase Compressible Flows with Micro-inertia". In: *J. Comput. Phys.* 175.1 (Jan. 2002), pp. 326–360. ISSN: 0021-9991. DOI: http://dx.doi.org/10.1006/jcph.2001.6951 (cit. on p. 208).

[24] S. GAVRILYUK, N. MAKARENKO, and S. SUKHININ. *Waves in continuous media*. Springer, 2017 (cit. on p. 224).

[25] S. GAVRILYUK and R. SAUREL. "Rankine–Hugoniot relations for shocks in heterogeneous mixtures". In: *Journal of Fluid Mechanics* 575 (2007), pp. 495–507. DOI: https://doi.org/10.1017/S002211200600449 (cit. on p. 208).

[26] V. GUILLEMAUD. "Modelling and numerical simulation of two-phase flows using the two-fluid two-pressure approach". PhD thesis. (in French), Université de Provence - Aix-Marseille I, Mar. 2007. URL: https://tel.archives-ouvertes.fr/tel-00169178 (cit. on p. 220).

[27] H. MATHIS. "A thermodynamically consistent model of a liquid-vapor fluid with a gas". In: *ESAIM: Mathematical Modelling and Numerical Analysis* 53.1 (2019), pp. 63–84. DOI: https://doi.org/10.1051/m2an/2018044 (cit. on pp. 208, 209).

[28] E. HAN, M. HANTKE, and S. MÜLLER. "Efficient and robust relaxation procedures for multi-component mixtures including phase transition". In: *J. Comput. Physics* 338 (2017), pp. 217–239. DOI: https://doi.org/10.1016/J.JCP.2017.02.066 (cit. on p. 232).

[29] M. HANTKE and S. MÜLLER. "Closure conditions for a one temperature non-equilibrium multi-component model of baer-nunziato type". In: *ESAIM: Proceedings and Surveys* 66 (2019), pp. 42–60. DOI: https://doi.org/10.1051/proc/201966003 (cit. on p. 208).

[30] M. HANTKE and S. MÜLLER. "Analysis and simulation of a new multi-component two-phase flow model with phase transitions and chemical reactions". In: *Quarterly Applied Mathematics* 76 (2018), pp. 253–287. DOI: https://doi.org/10.1090/qam/1498 (cit. on p. 233).

[31] P. HELLUY and N. SEGUIN. "Relaxation models of phase transition flows". In: *ESAIM: Mathematical Modelling and Numerical Analysis* 40.2 (2006), pp. 331–352. URL: https://hal.archives-ouvertes.fr/hal-00139607 (cit. on p. 208).

[32] P. HELLUY, O. HURISSE, and L. QUIBEL. "Assessment of numerical schemes for complex two-phase flows with real equations of state". In: *Computers and Fluids* 196.104347 (Jan. 2020). URL: https://hal.archives-ouvertes.fr/hal-02315038 (cit. on pp. 208, 209, 217).

[33] P. HELLUY and H. MATHIS. "Pressure laws and fast Legendre transform". In: *Mathematical Models and Methods in Applied Sciences* 21.4 (June 2010), pp. 745–775. DOI: 10.1142/S0218202511005209. URL: https://hal.archives-ouvertes.fr/hal-00424061 (cit. on p. 208).

[34] J.-M. HÉRARD. "A class of compressible multiphase flow models". In: *Comptes Rendus Mathématique* 354.9 (2016), pp. 954–959. URL: https://hal.archives-ouvertes.fr/hal-01348880 (cit. on pp. 208, 209, 232).

[35] J.-M. HÉRARD. "A three-phase flow model". In: *Mathematical and Computer Modelling* 45 (2007), pp. 732–755. DOI: 10.1016/j.mcm.2006.07.018. URL: https://hal.archives-ouvertes.fr/hal-01265367 (cit. on pp. 208, 209, 213, 226, 232).

[36] J.-M. HÉRARD. "An hyperbolic two-fluid model in a porous medium". In: *Comptes Rendus Mécanique* 336 (2008), pp. 650–655. DOI: 10.1016/j.crme.2008.06.005. URL: https://hal.archives-ouvertes.fr/hal-01265406 (cit. on pp. 209, 212, 215).

[37] J.-M. HÉRARD and O. HURISSE. "A fractional step method to compute a class of compressible gas–liquid flows". In: *Computers and Fluids* 55 (2012), pp. 57–69. DOI: 10.1016/j.compfluid.2011.11.001. URL: https://hal.archives-ouvertes.fr/hal-01265315 (cit. on p. 232).

[38] J.-M. HÉRARD and H. LOCHON. "A simple turbulent two-fluid model". In: *Comptes Rendus Mécanique* 344.11-12 (2016), pp. 776–783. DOI: 10.1016/j.crme.2016.10.010. URL: https://hal.archives-ouvertes.fr/hal-01339435 (cit. on p. 209).

[39] J.-M. HÉRARD and H. MATHIS. "A three-phase flow model with two miscible phases". In: *ESAIM: Mathematical Modelling and Numerical Analysis* 53, 1373-1389 (Apr. 2019). URL: https://hal.archives-ouvertes.fr/hal-01976938 (cit. on pp. 208, 209, 224, 230, 243).

[40] M. HILLAIRET. "On Baer-Nunziato Multiphase Flow Models". In: *ESAIM: Proceedings and Surveys* 66 (2019), pp. 61–83. URL: https://www.esaim-proc.org/articles/proc/pdf/2019/02/proc196604.pdf (cit. on p. 217).

[41] J. HUANG, J. ZHANG, and L. WANG. "Review of vapor condensation heat and mass transfer in the presence of non-condensable gas". In: *Applied thermal engineering* 89 (2015), pp. 469–484. DOI: https://doi.org/10.1016/j.applthermaleng.2015.06.040 (cit. on p. 208).

[42] O. HURISSE. "Numerical simulations of steady and unsteady two-phase flows using a homogeneous model". In: *Computers and Fluids* 152 (July 2017), pp. 88–103. URL: https://hal.archives-ouvertes.fr/hal-01489039 (cit. on pp. 208, 233).

[43] O. HURISSE and L. QUIBEL. "A homogeneous model for compressible three-phase flows involving heat and mass transfer." In: *ESAIM: Proceedings and Surveys* 66 (2019), pp. 84–108. URL: https://hal.archives-ouvertes.fr/hal-01976903 (cit. on pp. 208, 209).

[44] D. IAMPIETRO. "Contribution to the simulation of low-velocity compressible two-phase flows with high pressure jumps using homogeneous and two-fluid approaches". Ph.D. thesis. Aix-Marseille Université, Nov. 2018. URL: https://tel.archives-ouvertes.fr/tel-01919156 (cit. on p. 232).

[45] IRSN. *Accidents graves pouvant affecter un réacteur à eau pressurisée*. 2011. URL: https://www.irsn.fr/fr/connaissances/installations_nucleaires/les-accidents-nucleaires/ (visited on 09/30/2019) (cit. on p. 208).

[46] M. ISHII. *Thermo-Fluid Dynamics theory of two-phase flow*. Eyrolles, 1975 (cit. on p. 217).

[47] J. JUNG. "Numerical simulations of two-fluid flow on multicores accelerator". PhD thesis. Université de Strasbourg, Oct. 2013. URL: https://tel.archives-ouvertes.fr/tel-00876159 (cit. on p. 208).

[48] A. K. KAPILA, R. MENIKOFF, J. B. BDZIL, S. F. SON, and D. S. STEWART. "Two-phase modeling of deflagration-to-detonation transition in granular materials: Reduced equations". In: *Physics of Fluids* 13.10 (2001), pp. 3002–3024. DOI: https://doi.org/10.1063/1.1398042 (cit. on p. 208).

[49] T. KATO. "The Cauchy problem for quasi-linear symmetric hyperbolic systems". In: *Archive for Rational Mechanics and Analysis* 58.3 (1975), pp. 181–205. DOI: https://doi.org/10.1007/BF00280740 (cit. on pp. 210, 224).

[50] R. LEWANDOWSKI and B. MOHAMMADI. "Existence and positivity results for the φ-θ and a modified k- ε two-equation turbulence models". In: *Mathematical Models and Methods in Applied Sciences* 3.02 (1993), pp. 195–215. DOI: https://doi.org/10.1142/S0218202593000114 (cit. on p. 226).

[51] H. LOCHON. "Modélisation et simulation d'écoulements transitoires eau-vapeur en approche bifluide". PhD thesis. Aix Marseille Université, 2016. URL: https://tel.archives-ouvertes.fr/tel-01379453/document (cit. on pp. 208, 217).

[52] R. MEIGNEN, B. RAVERDY, S. PICCHI, and J. LAMOME. "The challenge of modeling fuel–coolant interaction: Part II–Steam explosion". In: *Nuclear Engineering and Design* 280 (2014), pp. 528–541. DOI: http://dx.doi.org/10.1016/j.nucengdes.2014.08.028 (cit. on pp. 208, 209).

[53] S. MÜLLER, M. HANTKE, and P. RICHTER. "Closure conditions for non-equilibrium multi-component models". In: *Continuum Mechanics and Thermodynamics* 28.4 (2016), pp. 1157–1189. DOI: https://doi.org/10.1007/s00161-015-0468-8 (cit. on p. 208).

[54] K. SALEH. "A relaxation scheme for a hyperbolic multiphase flow model. Part I: barotropic eos". In: *ESAIM: Mathematical Modelling and Numerical Analysis* 53, 1763-1795 (Apr. 2019). URL: https://hal.archives-ouvertes.fr/hal-01737681 (cit. on p. 232).

[55] K. SALEH and N. SEGUIN. "Some mathematical properties of a barotropic multiphase flow model". working paper or preprint. Dec. 2019. URL: https://hal.archives-ouvertes.fr/hal-01921027 (cit. on pp. 208, 209, 224, 232, 243).

[56] R. SAUREL, S. GAVRILYUK, and F. RENAUD. "A multiphase model with internal degrees of freedom: application to shock–bubble interaction". In: *Journal of Fluid Mechanics* 495 (2003), pp. 283–321. DOI: https://doi.org/10.1017/S002211200300630X (cit. on pp. 212, 215, 221).

[57] D. W. SCHWENDEMAN, C. W. WAHLE, and A. K. KAPILA. "The Riemann problem and a high-resolution Godunov method for a model of compressible two-phase flow". In: *Journal of Computational Physics* 212.2 (2006), pp. 490–526. DOI: https://doi.org/10.1016/j.jcp.2005.07.012 (cit. on p. 232).

[58] S. TOKAREVA and E. F. TORO. "HLLC-type Riemann solver for the Baer–Nunziato equations of compressible two-phase flow". In: *Journal of Computational Physics* 229.10 (2010), pp. 3573–3604. DOI: https://doi.org/10.1007/978-3-642-17884-9_10 (cit. on p. 232).

Appendices

4.A Entropy equality

A smooth solution is considered. From (4.18), additional phasic equations can be written for density, velocity:

$$\partial_t \rho_k + \mathbf{u}_k.\nabla\rho_k + \rho_k \nabla.\mathbf{u}_k + \frac{\rho_k}{\alpha_k}(\mathbf{u}_k - \mathbf{v_I}).\nabla\alpha_k = \frac{\Gamma_k - \rho_k \Phi_k}{\alpha_k}; \tag{4.81}$$

$$\begin{aligned} &\partial_t \mathbf{u_k} + \mathbf{u}_k.\nabla\mathbf{u}_k + \tau_k \nabla P_k \\ &+\frac{1}{m_k}(P_k\nabla\alpha_k + \sum_{k'\neq k}\Pi_{kk'}\nabla\alpha_{k'}) = \frac{\mathbf{S_{Qk}} - \mathbf{u}_k\Gamma_k}{m_k}. \end{aligned} \tag{4.82}$$

The governing equation for the kinetic energy can then be deduced:

$$\begin{aligned} \partial_t\left(\frac{m_k\mathbf{u}_k^2}{2}\right) + \nabla.\left(\frac{m_k\mathbf{u}_k^2}{2}\mathbf{u}_k\right) + \alpha_k\mathbf{u}_k.\nabla P_k + P_k\mathbf{u}_k.\nabla\alpha_k \\ + \sum_{k'\neq k}\Pi_{kk'}\mathbf{u}_k.\nabla\alpha_{k'} = \mathbf{u}_k.(\mathbf{S_{Qk}} - \frac{\Gamma_k\mathbf{u}_k}{2}). \end{aligned} \tag{4.83}$$

Recalling the definition of the total energy E_k (4.2), the equation on internal energy can be written by substracting the total energy equation and the previous kinetic energy equation :

$$\begin{aligned} &\partial_t\epsilon_k + \mathbf{u}_k.\nabla\epsilon_k + \frac{P_k}{\rho_k}\nabla.\mathbf{u}_k + \frac{(\mathbf{v}_I - \mathbf{u}_k)}{m_k}\sum_{k'\neq k}\Pi_{kk'}\nabla\alpha_{k'} \\ &= \frac{1}{m_k}\underbrace{(S_{E_k} + \sum_{k'\neq k}\Pi_{kk'}\Phi_{k'} - \mathbf{u}_k.(\mathbf{S_{Qk}} - \frac{\Gamma_k\mathbf{u_k}}{2})}_{S_{\epsilon_k}} - \epsilon_k\Gamma_k). \end{aligned} \tag{4.84}$$

The internal energy is the equation of state, given in the (P_k, ρ_k)-plane. Dependance on P can then be explicitely written from the previous equation, since $\epsilon_k(P_k, \rho_k)$:

$$\begin{aligned} &\partial_t P_k + \mathbf{u}_k.\nabla P_k + \rho_k c_k^2 \nabla.\mathbf{u}_k \\ &+ \left.\frac{\partial\epsilon_k}{\partial P_k}\right|_{\rho_k}^{-1}\frac{(\mathbf{v}_I - \mathbf{u}_k)}{m_k}\left(\sum_{k'\neq k}\Pi_{kk'}\nabla\alpha_{k'} + \rho_k^2\left.\frac{\partial\epsilon_k}{\partial\rho_k}\right|_{P_k}\nabla\alpha_k\right) \\ &= \frac{1}{m_k}\left.\frac{\partial\epsilon_k}{\partial P_k}\right|_{\rho_k}^{-1}\left(S_{\epsilon_k} - \epsilon_k\Gamma_k + \rho_k\left.\frac{\partial\epsilon_k}{\partial\rho_k}\right|_{P_k}(\rho_k\Phi_k - \Gamma_k)\right) = S_{P_k}. \end{aligned} \tag{4.85}$$

The entropy definition $s_k(\rho_k, P_k)$ (4.4) can now be used to deduce the phasic specific entropy equation:

$$\begin{aligned} &\partial_t s_k + \mathbf{u}_k.\nabla s_k + a_k\frac{(\mathbf{v_I} - \mathbf{u}_k)}{m_k}\left(\sum_{k'\neq k}\Pi_{kk'}\nabla\alpha_{k'} + P_k\nabla\alpha_k\right) \\ &= \left.\frac{\partial s}{\partial P_k}\right|_{\rho_k} S_{P_k} + \left.\frac{\partial s_k}{\partial\rho_k}\right|_{P_k}\frac{\Gamma_k - \rho_k\Phi_k}{\alpha_k}. \end{aligned} \tag{4.86}$$

The definition of mixture entropy (4.9) gives the mixture entropy governing equation.

4.B Unicity of $(K_{kk'})_{k,k'\in\mathcal{K}}$ for a given v_I

Minimal entropy dissipation (4.12) reads:

$$\begin{aligned} &\mathcal{A}_\eta(\mathbf{Y},(\nabla\alpha_k)_{k\in\mathcal{K}})=0\\ \text{i.e. }&\sum_{k\in\mathcal{K}} T_k^{-1}(\mathbf{v}_I-\mathbf{u}_k).\left(\sum_{k'\neq k}\Pi_{kk'}(\mathbf{Y})\nabla\alpha_{k'}+P_k\nabla\alpha_k\right)=0. \end{aligned} \tag{4.87}$$

There are three independent relative velocities, for instance:

$$\mathbf{u}_s-\mathbf{u}_l \quad ; \quad \mathbf{u}_s-\mathbf{u}_v \quad ; \quad \mathbf{u}_s-\mathbf{u}_g.$$

Because of miscibility constraints (4.15), there are only two independent gradients, for instance:

$$\nabla\alpha_l;\nabla\alpha_s,$$

and it reads:

$$\nabla\alpha_v=-\nabla\alpha_l-\nabla\alpha_s=\nabla\alpha_g.$$

Finally, $\mathcal{A}_\eta(\mathbf{Y},\nabla\alpha_k)=0$ reads:

$$\begin{array}{rcl} \mathcal{A}_\eta^{ll}(\mathbf{u}_s-\mathbf{u}_l).\nabla\alpha_l & + & \mathcal{A}_\eta^{ls}(\mathbf{u}_s-\mathbf{u}_l).\nabla\alpha_s\\ + \quad \mathcal{A}_\eta^{vl}(\mathbf{u}_s-\mathbf{u}_v).\nabla\alpha_l & + & \mathcal{A}_\eta^{vs}(\mathbf{u}_s-\mathbf{u}_v).\nabla\alpha_s\\ + \quad \mathcal{A}_\eta^{gl}(\mathbf{u}_s-\mathbf{u}_g).\nabla\alpha_l & + & \mathcal{A}_\eta^{gs}(\mathbf{u}_s-\mathbf{u}_g).\nabla\alpha_s=0, \end{array} \tag{4.88}$$

which implies in fact six constraints:

$$\mathcal{A}_\eta^{ll}=0;\quad \mathcal{A}_\eta^{ls}=0;\quad \mathcal{A}_\eta^{vl}=0;\quad \mathcal{A}_\eta^{vs}=0;\quad \mathcal{A}_\eta^{gl}=0;\quad \mathcal{A}_\eta^{gs}=0, \tag{4.89}$$

where, for $k\in\{l,s\}$:

$$\begin{array}{l} \mathcal{A}_\eta^{lk}=(1-\beta_l)a_lK_{lk}-\beta_la_vK_{vk}-\beta_la_gK_{gk}-\beta_la_sK_{sk}-\mathfrak{S}_2^k,\\ \mathcal{A}_\eta^{vk}=-\beta_va_lK_{lk}+(1-\beta_v)a_vK_{vk}-\beta_va_gK_{gk}-\beta_va_sK_{sk}-\mathfrak{S}_3^k,\\ \mathcal{A}_\eta^{gk}=-\beta_ga_lK_{lk}-\beta_ga_vK_{vk}+(1-\beta_g)a_gK_{gk}-\beta_ga_sK_{sk}-\mathfrak{S}_4^k, \end{array} \tag{4.90}$$

where:

$$\mathfrak{S}^l=\begin{pmatrix}0\\ \mathfrak{S}_2^l\\ \mathfrak{S}_3^l\\ \mathfrak{S}_4^l\end{pmatrix}=\begin{pmatrix}0\\ -a_lP_l(1-\beta_l)-a_vP_v\beta_l-a_gP_g\beta_l\\ a_lP_l\beta_v+a_vP_v(1-\beta_v)-a_gP_g\beta_v\\ a_lP_l\beta_g-a_vP_v\beta_g+a_gP_g(1-\beta_g)\end{pmatrix};$$

$$\mathfrak{S}^s=\begin{pmatrix}0\\ \mathfrak{S}_2^s\\ \mathfrak{S}_3^s\\ \mathfrak{S}_4^s\end{pmatrix}=\begin{pmatrix}0\\ -a_vP_v\beta_l-a_gP_g\beta_l+a_sP_s\beta_l\\ a_vP_v(1-\beta_v)-a_gP_g\beta_v+a_sP_s\beta_v\\ -a_vP_v\beta_g+a_gP_g(1-\beta_g)+a_sP_s\beta_g\end{pmatrix}.$$

Moreover, the balance momentum constraint (4.8) gives two additional equations:

$$K_{ll}+K_{vl}+K_{gl}+K_{sl}=0 \quad ; \quad K_{ls}+K_{vs}+K_{gs}+K_{ss}=0. \tag{4.91}$$

Finally, for given β_k, $(K_{kk'})_{k,k'\in\mathcal{K}}$ are solutions of the following system:

$$\begin{pmatrix}\mathfrak{M} & \mathbf{0}_{4\times4}\\ \mathbf{0}_{4\times4} & \mathfrak{M}\end{pmatrix}\mathfrak{K}=\begin{pmatrix}\mathfrak{S}^l\\ \mathfrak{S}^s\end{pmatrix}, \tag{4.92}$$

with:

$$\mathfrak{M} = \begin{pmatrix} 1 & 1 & 1 & 1 \\ (1-\beta_l)a_l & -\beta_l a_v & -\beta_l a_g & -\beta_l a_s \\ -\beta_v a_l & (1-\beta_v)a_v & -\beta_v a_g & -\beta_v a_s \\ -\beta_g a_l & -\beta_g a_v & (1-\beta_g)a_g & -\beta_g a_s \end{pmatrix},$$

$$\mathfrak{K} = (K_{ll}, K_{vl}, K_{gl}, K_{sl}, K_{ls}, K_{vs}, K_{gs}, K_{ss})^t.$$

As:

$$\det \begin{pmatrix} \mathfrak{M} & \mathbf{0_{4\times 4}} \\ \mathbf{0_{4\times 4}} & \mathfrak{M} \end{pmatrix} = (a_l a_v a_s \beta_g + a_l a_g a_s \beta_v + a_v a_g a_s \beta_l + a_l a_v a_g \beta_s)^2 \neq 0, \tag{4.93}$$

the system (4.92) is inversible. The final solution is given by (4.19).

4.C Eigenvectors of the system (4.45)

It must be reminded that α_l and α_s can not be equal to 0 or 1. Eigenvectors can be exhibited independently from the chosen mixture entropy (i.e. **without expliciting** $(\Pi_{kk'})_{k,k' \in \mathcal{K}}$). Recalling:

$$\Delta u_k = v_I - u_k \; \forall k \in \mathcal{K};$$

we use the following notations in the sequel, with $i \in \{l,s\}, j \in \{v,g\}, k \in \{l,s\}$:

$$x^k_{\rho_i} = \frac{1}{\alpha_i((\Delta u_i)^2 - c_i^2)} \left[-\rho_i (\Delta u_i)^2 + (P_i + K_{ik})\{1 + (\partial_{P_i}\epsilon_i)^{-1}\tau_i\} \right];$$

$$x^k_{u_i} = \frac{\Delta u_i}{\alpha_i((\Delta u_i)^2 - c_i^2)} \left[-{c_i}^2 + \tau_i (P_i + K_{ik})\{1 + (\partial_{P_i}\epsilon_i)^{-1}\tau_i\} \right];$$

$$x^k_{P_i} = \frac{1}{\alpha_i((\Delta u_i)^2 - c_i^2)} \left[-\rho_i (\Delta u_i)^2 {c_i}^2 + (P_i + K_{ik})\{c_i^2 + (\Delta u_i)^2 (\partial_{P_i}\epsilon_i)^{-1}\tau_i\} \right];$$

$$z^k_{\rho_i} = \frac{1}{\alpha_i((\Delta u_i)^2 - c_i^2)} \left[K_{ik}\{1 + (\partial_{P_i}\epsilon_i)^{-1}\tau_i\} \right];$$

$$z^k_{u_i} = \frac{\Delta u_i}{\alpha_i((\Delta u_i)^2 - c_i^2)} \left[\tau_i K_{ik}\{1 + (\partial_{P_i}\epsilon_i)^{-1}\tau_i\} \right];$$

$$z^k_{P_i} = \frac{1}{\alpha_i((\Delta u_i)^2 - c_i^2)} \left[K_{ik}\{c_i^2 + (\Delta u_i)^2 (\partial_{P_i}\epsilon_i)^{-1}\tau_i\} \right].$$

$$y^k_{\rho_j} = \frac{1}{\alpha_j((\Delta u_j)^2 - c_j^2)} \left[\rho_j (\Delta u_j)^2 + (K_{jk} - P_j)\{1 + (\partial_{P_j}\epsilon_j)^{-1}\tau_j\} \right];$$

$$y^k_{u_j} = \frac{\Delta u_j}{\alpha_j((\Delta u_j)^2 - c_j^2)} \left[{c_j}^2 + \tau_j (K_{jk} - P_j)\{1 + (\partial_{P_j}\epsilon_j)^{-1}\tau_j\} \right];$$

$$y^k_{P_j} = \frac{1}{\alpha_j((\Delta u_j)^2 - c_j^2)} \left[\rho_j (\Delta u_j)^2 {c_j}^2 + (K_{jk} - P_j)\{c_j^2 + (\Delta u_j)^2 (\partial_{P_j}\epsilon_j)^{-1}\tau_j\} \right];$$

Eigenvectors $\mathbf{r_k}$ for the homogeneous system (4.45) are given below, with the same order as in (4.56) (resonance is excluded).

$$\begin{aligned} \mathbf{r_1} = \; (1,0, \; & x^l_{\rho_l}, x^l_{u_l}, x^l_{P_l}, \\ & y^l_{\rho_v}, y^l_{u_v}, y^l_{P_v}, \\ & y^l_{\rho_g}, y^l_{u_g}, y^l_{P_g}, \\ & z^l_{\rho_s}, z^l_{u_s}, z^l_{P_s}); \end{aligned}$$

$$\begin{aligned} \mathbf{r_2} = \; (0,1, \; & z^s_{\rho_l}, z^s_{u_l}, z^s_{P_l}, \\ & y^s_{\rho_v}, y^s_{u_v}, y^s_{P_v}, \\ & y^s_{\rho_g}, y^s_{u_g}, y^s_{P_g}, \\ & x^s_{\rho_s}, x^s_{u_s}, x^s_{P_s}); \end{aligned}$$

$$\mathbf{r_3} = (0,0,1,0,0,0,0,0,0,0,0,0,0,0)^t \; ; \; \mathbf{r_4} = (0,0,0,0,0,1,0,0,0,0,0,0,0,0)^t;$$

$$\mathbf{r_5} = (0,0,0,0,0,0,0,0,1,0,0,0,0,0)^t \; ; \; \mathbf{r_6} = (0,0,0,0,0,0,0,0,0,0,0,0,1,0,0)^t;$$

$$\mathbf{r_7} = (0,0,\frac{\rho_l}{c_l},1,\rho_l c_l,0,0,0,0,0,0,0,0,0)^t \; ; \; \mathbf{r_8} = (0,0,0,0,0,\frac{\rho_v}{c_v},1,\rho_v c_v,0,0,0,0,0,0)^t;$$

$$\mathbf{r_9} = (0,0,0,0,0,0,0,0,\frac{\rho_g}{c_g},1,\rho_g c_g,0,0,0)^t \; ; \; \mathbf{r_{10}} = (0,0,0,0,0,0,0,0,0,0,0,\frac{\rho_s}{c_s},1,\rho_s c_s)^t;$$

$$\mathbf{r_{11}} = (0, 0, -\frac{\rho_l}{c_l}, 1, -\rho_l c_l, 0, 0, 0, 0, 0, 0, 0, 0, 0)^t \; ; \; \mathbf{r_{12}} = (0, 0, 0, 0, 0, -\frac{\rho_v}{c_v}, 1, -\rho_v c_v, 0, 0, 0, 0, 0, 0)^t;$$

$$\mathbf{r_{13}} = (0, 0, 0, 0, 0, 0, 0, 0, -\frac{\rho_g}{c_g}, 1, -\rho_g c_g, 0, 0, 0)^t \; ; \; \mathbf{r_{14}} = (0, 0, 0, 0, 0, 0, 0, 0, 0, 0, 0, -\frac{\rho_s}{c_s}, 1, -\rho_s c_s)^t.$$

4.D Symmetrization

The proof for the symmetrization of system (4.45) is given in the multidimensional case. It is a direct extension of the proofs presented in [55] or [39].
The case $\boxed{v_I = u_m}$ is treated, but the case $v_I = u_s$ would have been very similar.
A different state vector as (4.44) is considered :

$$\tilde{\mathbf{W}} = (\alpha_l, \alpha_s, s_l, u_l, P_l, s_v, u_v, P_v, s_g, u_g, P_g, s_s, u_s, P_s)^t. \tag{4.94}$$

The associated convective matrix $\tilde{\mathbf{B}}(\tilde{\mathbf{W}})$ keeps the same structure as (4.46); only the block matrices $\mathcal{B}_\mathbf{k}, k \in \mathcal{K}$ should be slightly modified and replaced by $\tilde{\mathcal{B}_\mathbf{k}}$:

$$\forall k \in \mathcal{K}, \tilde{\mathcal{B}_\mathbf{k}} = \begin{pmatrix} u_k & 0 & 0 \\ 0 & u_k & \tau_k \\ 0 & \rho_k c_k^2 & u_k \end{pmatrix}. \tag{4.95}$$

We aim to build a suitable matrix $\mathbf{S}$ enabling to symmetrize the system. We assume a particular block symmetric structure for $\mathbf{S}$:

$$\mathbf{S} = \begin{pmatrix} a_0^2 \mathbf{Id}_{2\times 2} & \mathcal{M_l}^t & \mathcal{M_v}^t & \mathcal{M_g}^t & \mathcal{M_s}^t \\ \mathcal{M_l} & \mathcal{D_l} & \mathbf{0}_{3\times 3} & \mathbf{0}_{3\times 3} & \mathbf{0}_{3\times 3} \\ \mathcal{M_v} & \mathbf{0}_{3\times 3} & \mathcal{D_v} & \mathbf{0}_{3\times 3} & \mathbf{0}_{3\times 3} \\ \mathcal{M_g} & \mathbf{0}_{3\times 3} & \mathbf{0}_{3\times 3} & \mathcal{D_g} & \mathbf{0}_{3\times 3} \\ \mathcal{M_s} & \mathbf{0}_{3\times 3} & \mathbf{0}_{3\times 3} & \mathbf{0}_{3\times 3} & \mathcal{D_s} \end{pmatrix}; \forall k \in \mathcal{K}, \mathcal{D_k} = \begin{pmatrix} 1 & 0 & 0 \\ 0 & \rho_k^2 c_k^2 & 0 \\ 0 & 0 & 1 \end{pmatrix}, \tag{4.96}$$

with $a_0 \in \mathbb{R}$ and $\mathcal{M_k} \in \mathbb{R}^{3\times 2}, k \in \mathcal{K}$, satisfying some constraints to determine.

- *Step 1 of the proof:* $\mathbf{S}\tilde{\mathbf{B}}$ *is symmetric*:

  Imposing $\mathbf{S}\tilde{\mathbf{B}} = \tilde{\mathbf{B}}^t\mathbf{S}$ induces some conditions:

  1. $\mathcal{D_k}\tilde{\mathcal{B}_\mathbf{k}} = \tilde{\mathcal{B}_\mathbf{k}}^t\mathcal{D_k}$ for any $k \in \mathcal{K}$, which can be easily checked;
  2. $\tilde{\mathcal{B}_\mathbf{k}}^t\mathcal{M_k} = v_I\mathcal{M_k} + \mathcal{D_k}\mathcal{C_k}$:
     excluding resonance conditions (i.e. if $|u_k - u_m| \neq c_k$) and since $u_m \neq u_k$, $(\tilde{\mathcal{B}_\mathbf{k}}^t - v_I\mathbf{Id}_{3\times 3})$ is inversible, a suitable definition for $\mathcal{M_k}$ is obtained:

     $$\mathcal{M}_k = (\mathcal{B_k}^t - v_I\mathbf{Id}_{3\times 3})^{-1}\mathcal{D_k}\mathcal{C_k}; \tag{4.97}$$

  3. $a_0^2 v_I \mathbf{Id}_{2\times 2} + \sum_{k\in\mathcal{K}} \mathcal{M_k}^t\mathcal{C_k} = a_0^2 v_I \mathbf{Id}_{2\times 2} + \sum_{k\in\mathcal{K}} \mathcal{C_k}^t\mathcal{M_k}$:
     one can check that for any $k \in \mathcal{K}$, $\mathcal{M_k}^t\mathcal{C_k} = \mathcal{C_k}^t\mathcal{M_k}$, thanks to the previous definition for $\mathcal{M_k}$ and the property $\mathcal{D_k}\tilde{\mathcal{B}_\mathbf{k}}^n = (\tilde{\mathcal{B}_\mathbf{k}}^n)^t\mathcal{D_k}$, $n \in \mathbb{N}$.

- *Step 2 of the proof:* $\mathbf{S}$ *is semi-definite positive*:

  Using the block structure, $\mathbf{S}$ can be rewritten as follows:

  $$\mathbf{S} = \begin{pmatrix} a_0^2\mathbf{Id}_{2\times 2} & \mathcal{M}^t \\ \mathcal{M} & \mathcal{D} \end{pmatrix}; \quad \mathcal{M} \in \mathbb{R}^{12\times 2}; \quad \mathcal{D} \in \mathbb{R}^{12\times 12}.$$

  Consider the quadratic form Ψ associated to $\mathbf{S}$: $\Psi : \underline{X} = (x, y) \in \mathbb{R}^{2\times 12} \mapsto \underline{X}^t\mathbf{S}\underline{X} = a_0^2||x||^2 + 2x^t\mathcal{M}^t y + y^t\mathcal{D}^t y$. We will impose conditions so that $\Psi(x, y) > 0 \; \forall (x, y) \neq (0, 0)$.

If $x = 0$ and $y \neq 0$ or $x \neq 0$ and $y = 0$, $\varphi(x,y) > 0$. We assume from now $x \neq 0$ and $y \neq 0$. Moreover, we introduce $v = \frac{y}{||x||}$, $z = \frac{x}{||x||}$ and $\mathcal{D}^{\frac{1}{2}}$ the square root matrix of $\mathcal{D}$ (since $\mathcal{D}$ is diagonal with strictly positive eigenvalues):

$$\begin{aligned}\Psi(x,y) &= ||x||^2 \left(a_0^2 + 2(\mathcal{D}^{-\frac{1}{2}}\mathcal{M}z)^t\mathcal{D}^{\frac{1}{2}}v + (\mathcal{D}^{\frac{1}{2}}v)^t(\mathcal{D}^{\frac{1}{2}}v)\right) \\ &= ||x||^2 \left(||\mathcal{D}^{\frac{1}{2}}v + (z^t\mathcal{M}^t\mathcal{D}^{-\frac{1}{2}})^t||^2 + a_0^2 - ||\mathcal{D}^{-\frac{1}{2}}\mathcal{M}z||^2\right).\end{aligned}$$

The following constraint on a_0 is obtained:

$$\forall z, a_0^2 - ||z^t\mathcal{M}^t\mathcal{D}^{-\frac{1}{2}}||^2 > 0, \tag{4.98}$$

which leads to the following sufficient condition, where $\rho(.)$ denotes the spectral radius of a matrix:

$$a_0 \geq \rho(\mathcal{M}^t\mathcal{D}^{-\frac{1}{2}}). \tag{4.99}$$

Finally, by multiplying on the left system (4.45) by $\mathbf{S}$ defined in (4.96) and fulfilling both (4.97) and (4.99), we get as expected a symmetric system.

Chapter 5

Numerical error analysis for boundary conditions of the Euler system

The main content of this chapter has been published as proceedings of the conference Finite Volume for Complex Applications IX (June 15-19, 2020, Bergen, Norway) under the reference:

C. Colas, M. Ferrand, J.-M. Hérard, O. Hurisse, E. Le Coupanec, and L. Quibel, A Numerical Convergence Study of some Open Boundary Conditions for Euler Equations.

The proceedings are reproduced in part 5.1. An additional study, in which open boundary conditions are tested with relaxation schemes, is then presented in part 5.2.

5.1 FVCA proceedings : Open boundary conditions with a VFRoe-ncv scheme

Abstract

We discuss herein the suitability of some open boundary conditions. Considering the Euler system of gas dynamics, we compare approximate solutions of one-dimensional Riemann problems in a bounded sub-domain with the restriction in this sub-domain of the exact solution in the infinite domain. Assuming that no information is known from outside of the domain, some basic open boundary condition specifications are given, and a measure of the L^1-norm of the error inside the computational domain enables to show consistency errors in situations involving outgoing shock waves, depending on the chosen boundary condition formulation. This investigation has been performed with Finite Volume methods, using approximate Riemann solvers in order to compute numerical fluxes for inner interfaces and boundary interfaces.

Introduction

Concerning computational fluid dynamics, industrial simulations are frequently performed with a partial or total unknown fluid state outside of the computational domain. How are boundary conditions dealt with when no information is known outside? Here the one-dimensional Euler equations governing inviscid compressible fluid flows are considered. The unknowns ρ, u, P respectively denote the density, the velocity and the pressure of the fluid, while the momentum is $Q = \rho u$. The total energy E is such that $E = \rho\left(\frac{u^2}{2} + \varepsilon\right)$. The internal energy $\varepsilon(P,\rho)$ is prescribed by the EOS (Equation Of State). In the sequel, we denote by $\boldsymbol{W} = (\rho, Q, E)^t$ the conservative variable, $\boldsymbol{Y} = (s, u, P)^t$ the non-conservative variable, with s the entropy, and $\boldsymbol{F}(\boldsymbol{W}) = (Q, Qu + P, (E+P)\,u)^t$ the flux function, so that the set of governing equations reads:

$$\partial_t \boldsymbol{W} + \partial_x \boldsymbol{F}(\boldsymbol{W}) = 0. \tag{5.1}$$

The speed of sound, denoted by c, is such that $c^2 = \left(\frac{P}{\rho^2} - \frac{\partial e(P,\rho)}{\partial \rho}\right) / \left(\frac{\partial e(P,\rho)}{\partial P}\right)$.

There exists a huge literature on open boundary problems [17, 10, 14, 18]. Among these, one pioneering work on boundary conditions for bounded domain may be found in [1]. Actually, the present work addresses the issue of open numerical boundary conditions to get waves outside of the computational domain and can be connected to the work of [11]. The solution of Euler system (5.1) is sought in $\mathbb{R} \times (0,T)$, with time $T \in \mathbb{R}_+^*$, without boundary conditions, see [21]. This solution, expected to be known and unique, is denoted by $\boldsymbol{W}_{\Omega_\infty}^{exact}(\underline{x},t)$ for $(\underline{x},t) \in \mathbb{R} \times (0,T)$.

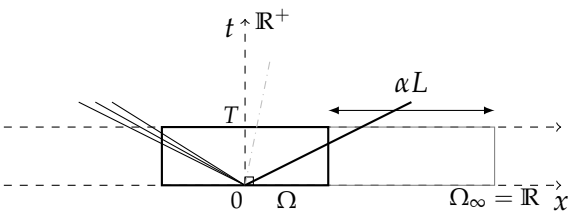

Figure 5.1 – *Bounded computational domain $\Omega \subsetneq \Omega_\infty$, with Ω_∞ a spatial infinite domain.*

In contrast, the numerical approximations, denoted by $\boldsymbol{W}_{\Omega}^{\Delta\underline{x},\Delta t}(\underline{x},t)$ for $(\underline{x},t) \in \Omega \times (0,T)$, are performed in a bounded computational sub-domain $\Omega \subsetneq \Omega_\infty$ (see Figure 5.1) with prescribed open inlet/outlet boundary conditions on $\partial\Omega$.

For this purpose, artificial boundaries are introduced on $\partial\Omega$. Then, numerical boundary conditions, depending on the time and space steps, must be prescribed on $\partial\Omega$. When $(\Delta\underline{x},\Delta t) \to (0,0)$, we assume that some (unique) converged approximation, denoted by $\boldsymbol{W}_{\Omega}^{0,0}(\underline{x},t)$ for $(\underline{x},t) \in \Omega \times (0,T)$, is obtained. Eventually, we wonder whether $\boldsymbol{W}_{\Omega}^{0,0}(\underline{x},t)$ for $(\underline{x},t) \in \Omega \times (0,T)$, coincides with the restriction of the exact solution to Ω, $\boldsymbol{W}_{\Omega_\infty}^{exact}(\underline{x},t)$ for $(\underline{x},t) \in \Omega \times (0,T)$, or not. In the latter case, the converged approximation $\boldsymbol{W}_{\Omega}^{0,0}$ will be said to be **non-consistent**.

For the Euler system (5.1), a measure of a subsonic state in the last inner cell N (eigenvalues $\lambda_1(\mathbf{W}_N^n) < 0$ and $\lambda_{2,3}(\mathbf{W}_N^n) > 0$) at a right outlet will require one scalar external information, whereas in the supersonic case ($\lambda_{1,2,3}(\mathbf{W}_N^n) > 0$), the upwind state will be privileged. Actually, we recall that in the subsonic case, the approach of [8, 9] may provide some way to cope with the lack of information.

A first drawback of the latter approach is that the sign of eigenvalues may easily change: signs of eigenvalues $\lambda_k(\mathbf{W}_N^n)$ are not necessarily representative of what happens really at the right boundary when computing true waves associated with the 1D Riemann problem with the initial condition: $\boldsymbol{W}_L = \mathbf{W}_N^n$ and $\boldsymbol{W}_R = \mathbf{W}_{ext}^n$ (unless when $\mathbf{W}_{ext}^n = \mathbf{W}_N^n$). A very instructive example is given in [11] Sect. 3.2, while restricting on a scalar problem (Burgers equation). A second question is: assuming that nothing is known about the exterior state $\mathbf{W}_{ext}^n$, how does the solution, inside the computational sub-domain, depend on the choice of $\mathbf{W}_{ext}^n$?

Herein, the aim consists in testing suitable numerical boundary conditions in the sense that they converge towards the – not necessarily regular – exact solution.

5.1.1 Finite volume method

We briefly recall the basis of the explicit finite volume scheme VFRoe-ncv, an approximate Godunov scheme using non conservative variables [12, 13]. For the sake of simplicity, regular meshes of the one-dimensional computational domain are considered of size $\Delta x = x_{i+1/2} - x_{i-1/2}$, $i \in \{1,...,N\}$, and $\Delta t^n = t^{n+1} - t^n$ is the time step, $n \in \mathbb{N}$. The time step is given by some CFL condition in order to gain stability. Let $\mathbf{W}_i^n$ be an approximation of the mean value $\dfrac{1}{\Delta x}\displaystyle\int_{x_{i-1/2}}^{x_{i+1/2}} \boldsymbol{W}(x,t^n)dx$. Time-space integration of system (5.1) over $[x_{i-1/2},x_{i+1/2}] \times \left[t^n,t^{n+1}\right]$ provides the standard following scheme:

$$\Delta x(\mathbf{W}_i^{n+1} - \mathbf{W}_i^n) + \Delta t^n \left(\mathbf{g}_{i+\frac{1}{2}}^n - \mathbf{g}_{i-\frac{1}{2}}^n\right) = 0\,, \tag{5.2}$$

where $\mathbf{g}_{i+1/2}^n$ is the numerical flux through the interface $\{x_{i+1/2}\} \times \left[t^n,t^{n+1}\right]$. For so-called spatially first-order scheme, $\mathbf{g}_{i+1/2}^n = \mathbf{g}(\mathbf{W}_i^n,\mathbf{W}_{i+1}^n)$. The numerical flux $\mathbf{g}_{i+1/2}^n$ is obtained by solving the linearized Riemann problem:

$$\left\{\begin{array}{l} \partial_t \boldsymbol{Y} + \boldsymbol{B}(\widetilde{\boldsymbol{Y}})\partial_x \boldsymbol{Y} = 0\,, \\ \boldsymbol{Y}(x,t^n) = \left\{\begin{array}{ll} \mathbf{Y}_i^n & \text{if } x < x_{i+\frac{1}{2}}\,, \\ \mathbf{Y}_{i+1}^n & \text{if } x > x_{i+\frac{1}{2}}\,, \end{array}\right. \end{array}\right. \tag{5.3}$$

where $\widetilde{\boldsymbol{Y}} = (\mathbf{Y}_i^n + \mathbf{Y}_{i+1}^n)/2$ and $\boldsymbol{B}(\boldsymbol{Y})$ stands for the following matrix:

$$\boldsymbol{B}(\boldsymbol{Y}) = (\partial_{\boldsymbol{Y}}\boldsymbol{W})^{-1}\,\partial_{\boldsymbol{W}}\boldsymbol{F}(\boldsymbol{W})\partial_{\boldsymbol{Y}}\boldsymbol{W}\,.$$

Once the exact solution $\boldsymbol{Y}^\star\left(\frac{x-x_{i+1/2}}{t};\mathbf{Y}_i^n,\mathbf{Y}_{i+1}^n\right)$ of problem (5.3) is computed, the numerical flux is defined as:

$$\mathbf{g}_{i+\frac{1}{2}}^n = \mathbf{g}(\mathbf{W}_i^n,\mathbf{W}_{i+1}^n) = \boldsymbol{F}(\boldsymbol{W}(\boldsymbol{Y}^\star(0;\mathbf{Y}_i^n,\mathbf{Y}_{i+1}^n))\,. \tag{5.4}$$

This numerical flux will be used for both inner interfaces and boundary interfaces.

5.1.2 Numerical boundary conditions for outgoing waves

We propose numerical artificial boundary conditions when no information is given on the open boundary of the computational sub-domain. One possible approach is to determine an artificial state $\mathbf{W}_{ext}^n$ in the virtual cell, symmetric of the boundary cell $\mathbf{W}_i^n$, outside of the sub-domain. The numerical boundary flux is then obtained by $\mathbf{g}_{1/2}^n = \mathbf{g}(\mathbf{W}_{ext,1}^n,\mathbf{W}_1^n)$ and $\mathbf{g}_{N+1/2}^n = \mathbf{g}(\mathbf{W}_N^n,\mathbf{W}_{ext,N}^n)$. In the following, we assume that the exterior state is connected to the interior state either by a rarefaction wave or a shock wave.

5.1.2.1 Outgoing rarefaction wave

5.1.2.1.1 Formulation assuming the invariance of the interior state BC_0

The first boundary condition, widely used in industrial simulations, simply consists in taking the interior state $\mathbf{W}_i^n$ of the boundary cell at each time step t^n

$$\mathbf{W}_{ext}^n = \mathbf{W}_N^n\,. \tag{5.5}$$

The numerical boundary flux thus reads $\mathbf{g}_{N+1/2}^n = \mathbf{g}(\mathbf{W}_N^n,\mathbf{W}_N^n) = \boldsymbol{F}(\mathbf{W}_N^n)$. This technique does not need any knowledge about the wave structure.

5.1.2.1.2 Formulation using the wave structure and an extrapolation of the interior state BC_r

The second boundary condition is built by using the two associated Riemann invariants of the regular wave and a third additional scalar relation. Note that, for an ideal gas, the exact velocity profile is linear w.r.t. x at time t^n. Thus, for an ideal gas EOS such that $\rho\varepsilon = P/(\gamma-1)$, with $\gamma > 1$, we get:

$$\rho_{ext}^n = \rho_N^n\left(1-\frac{\gamma-1}{2}\frac{u_{N-1}^n-u_N^n}{c_N^n}\right)^{\frac{2}{\gamma-1}}\,,\; P_{ext}^n = P_N^n\left(1-\frac{\gamma-1}{2}\frac{u_{N-1}^n-u_N^n}{c_N^n}\right)^{\frac{2\gamma}{\gamma-1}}$$

and $u_{ext}^n = 2u_N^n - u_{N-1}^n$. The numerical boundary flux is computed by $\mathbf{g}_{N+1/2}^n = \mathbf{g}(\mathbf{W}_N^n,\mathbf{W}_{ext}^n)$. This technique connects the interior state with the exterior virtual state by using the rarefaction wave structure.

5.1.2.2 Outgoing shock wave

5.1.2.2.1 Formulation assuming the invariance of the interior state BC_0

Same as for rarefaction wave, see case *a*. (5.5).

5.1.2.2.2 Formulation using the far-field state BC_s

The boundary interior cell N is connected with the right initial state W_R^0 by a virtual exterior cell of physical size αL, with L the domain length and $\alpha \in \mathbb{R}_+^*$ a parameter, see Figure 5.1. Inspired by [7], this exterior state $\mathbf{W}_{ext}^n$ is updated with the numerical flux and the known state W_R^0 such that:

$$\alpha L \left(\mathbf{W}_{ext}^n - \mathbf{W}_{ext}^{n-1} \right) + \Delta t^{n-1} \left(\mathbf{g}(\mathbf{W}_{ext}^{n-1}, W_R^0) - \mathbf{g}(\mathbf{W}_N^{n-1}, \mathbf{W}_{ext}^{n-1}) \right) = 0 \,. \tag{5.6}$$

This technique gives the following asymptotic update of the exterior state $\mathbf{W}_{ext}^n$ when $\alpha \to +\infty$ for a finite time step Δt^{n-1}: $\lim_{\alpha \to +\infty} \mathbf{W}_{ext}^n = \mathbf{W}_{ext}^{n-1}$. The exterior state is steady and therefore equal to its initial state $\mathbf{W}_{ext}^0$, which is the right state W_R^0. The numerical boundary flux thus yields: $\mathbf{g}_{N+1/2}^n = \mathbf{g}(\mathbf{W}_N^n, W_R^0)$. This asymptotic boundary condition amounts to impose, in the virtual exterior cell, the right state W_R^0 known from the initial condition of the Cauchy problem.

5.1.3 Numerical results

We discuss below some results of this preliminary study. Other results with distinct EOS are available in [5]. Two subsonic test cases, corresponding to 1D Riemann problems with a diatomic ideal gas EOS ($\gamma = \frac{7}{5}$), are performed with CFL$= 0.5$. The first one is a pure left outgoing 1-rarefaction wave with the initial condition:

$$\begin{cases} (\rho_L, u_L, P_L) = \left(1\,\mathrm{kg/m^3}, 0\,\mathrm{m/s}, 10^5\,\mathrm{Pa}\right), \\ (\rho_R, u_R, P_R) = \left(0.5\,\mathrm{kg/m^3}, 242.2\,\mathrm{m/s}, 3.789 \times 10^4\,\mathrm{Pa}\right). \end{cases}$$

The second one is a pure right outgoing 3-shock wave with the initial condition:

$$\begin{cases} (\rho_L, u_L, P_L) = \left(1\,\mathrm{kg/m^3}, 418.3\,\mathrm{m/s}, 2.75 \times 10^5\,\mathrm{Pa}\right), \\ (\rho_R, u_R, P_R) = \left(0.5\,\mathrm{kg/m^3}, 0\,\mathrm{m/s}, 10^5\,\mathrm{Pa}\right). \end{cases}$$

The numerical convergence of the scheme, when waves are gone out of the bounded computational domain $\Omega = (-200\,\mathrm{m}, 200\,\mathrm{m})$, is measured with the L^1-norm of the error.

For smooth waves, the boundary conditions BC_0 and BC_r enable to guarantee consistency when waves are going out ($t_0 < t < t_1$) or are gone out ($t > t_1$) of Ω. The numerical errors and the rates of convergence are collected in Table 5.1 and Fig. 5.2 for an outgoing rarefaction wave, and in Table 5.2 and Fig. 5.3 when the whole rarefaction wave has left the computational domain. As expected for an ideal gas EOS [13], the numerical rates of convergence for variables (u, P) are approximately 0.85 – close to 1 – when $t < t_1$ (see Table 5.1), and thus similar to those arising for $t < t_0$, see [13, 12]. Table 5.2 shows greater orders of convergence which may be due to the fact that the exact solution becomes fully constant for $t > t_1$. The BC_r condition gives very similar errors and does not provide more accurate approximations.

In contrast, the BC_0 condition does not ensure the consistency of the scheme for an outgoing shock wave (at $t > t_0$, shock is outside of Ω), see Figure 5.4: clearly, approximate solutions converge towards another solution when $(\Delta x, \Delta t) \to (0, 0)$.

The BC_s boundary condition, for a finite value of the parameter $\alpha > 0$, is still not consistent, see Figure 5.5. At the limit $\alpha \to +\infty$, the asymptotic condition BC_s allows to retrieve the consistency of the approximate solution with the exact solution.

Further works aim at considering another boundary condition for outgoing shock waves based on an imposed scalar value outside and the Rankine-Hugoniot relations. The issue of the supersonic shock wave case and of the dependence on the scheme [19] are being examined. To our knowledge, this measured loss of consistency has not been pointed out before.

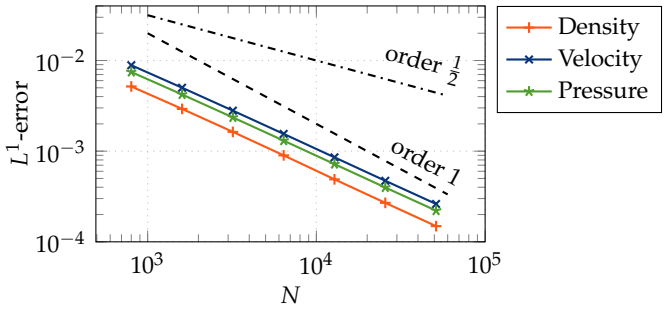

Figure 5.2 – BC_0: *L^1 convergence curves for the rarefaction wave at $t_0 < t < t_1$.*

Table 5.1 – BC_0: *L^1 convergence orders for the rarefaction wave at $t_0 < t < t_1$.*

Δx (m)	N	ρ L^1-error	ρ cnv. order	u L^1-error	u cnv. order	P L^1-error	P cnv. order
5e-1	800	5.172e-3		8.868e-3		2.371e-3	
2.5e-1	1600	2.925e-3	0.8221	5.009e-3	0.8241	1.335e-3	0.8243
1.25e-1	3200	1.631e-3	0.8426	2.798e-3	0.8403	7.478e-4	0.8402
6.25e-2	6400	8.984e-4	0.8605	1.550e-3	0.8518	4.194e-4	0.8516
3.125e-2	12800	4.891e-4	0.8774	8.548e-4	0.8587	2.379e-4	0.8582
1.5625e-2	25600	2.691e-4	0.8621	4.714e-4	0.8588	1.386e-4	0.8579
7.8125e-3	51200	1.489e-4	0.8533	2.617e-4	0.8491	8.461e-5	0.8474

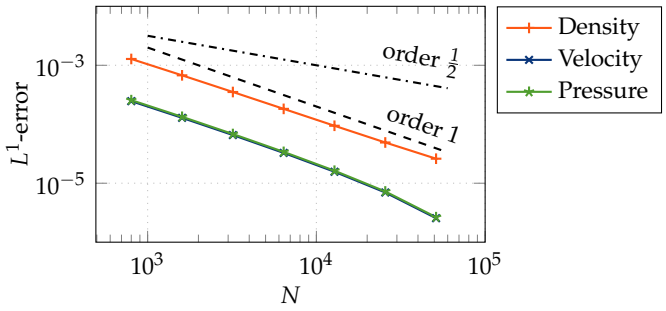

Figure 5.3 – BC_0: *L^1 convergence curves for the rarefaction wave at $t > t_1$.*

Table 5.2 – BC_0: *L^1 convergence orders for the rarefaction wave at $t > t_1$.*

Δx (m)	N	ρ L^1-error	ρ cnv. order	u L^1-error	u cnv. order	P L^1-error	P cnv. order
5e-1	800	1.279e-3		2.462e-4		2.562e-4	
2.5e-1	1600	6.755e-4	0.9211	1.284e-4	0.9384	1.337e-4	0.9383
1.25e-1	3200	3.522e-4	0.9395	6.557e-5	0.9700	6.826e-5	0.9700
6.25e-2	6400	1.823e-4	0.9502	3.265e-5	1.0061	3.399e-5	1.0061
3.125e-2	12800	9.423e-5	0.9521	1.565e-5	1.0608	1.629e-5	1.0609
1.5625e-2	25600	4.904e-5	0.9420	6.962e-6	1.1687	7.247e-6	1.1687
7.8125e-3	51200	2.604e-5	0.9134	2.551e-6	1.4486	2.655e-6	1.4486

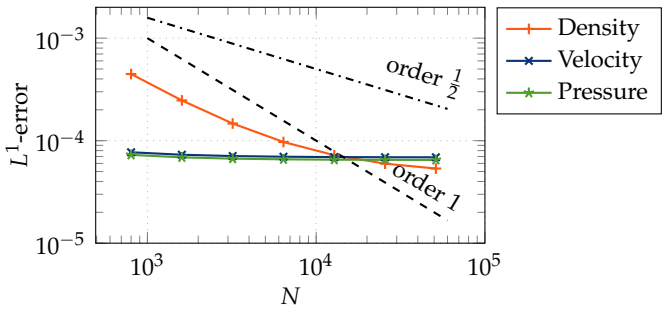

Figure 5.4 – BC_0: *L^1 convergence curves for the shock wave at $t > t_0$.*

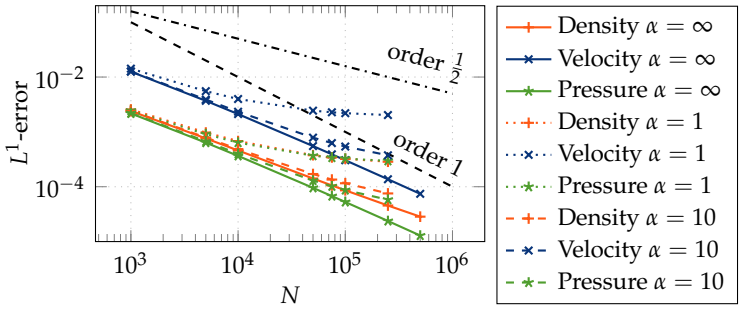

Figure 5.5 – BC_s: *L^1 convergence curves for the shock tube at $t > t_0$.*

Acknowledgement

The first author received a financial support by ANRT through an EDF-CIFRE contract 2016/0728. The last author also receives a financial support by ANRT through an EDF-CIFRE contract 2017/0476. All computational facilities were provided by EDF R&D.

5.2 Further study on open boundary conditions with relaxation schemes

5.2.1 Some relaxation schemes

The general framework is still numerical first-order explicit and conservative finite volumes schemes, with the same general form as (5.2):

$$\Delta x(\mathbf{W}_i^{n+1} - \mathbf{W}_i^n) + \Delta t^n \left(\mathbf{g}_{i+\frac{1}{2}}^n - \mathbf{g}_{i-\frac{1}{2}}^n\right) = 0.$$

For this new study, schemes involving a relaxation parameter will be compared with VFRoe-ncv scheme used in the previous part:

- a relaxation scheme proposed by C. Chalons and J.-F. Coulombel (called "relaxCC" in the following) [4];
- a VFRoe-ncv scheme with energy relaxation [13], as proposed by F. Coquel and B. Perthame (called "relaxCP" in the following) [6];
- Rusanov scheme [20].

5.2.1.1 Relaxation scheme (relaxCC)

The scheme was initially proposed in [4] and is based on the work of [16, 22, 6, 2]. The main idea is to compute the numerical flux on the basis of an enlarged hyperbolic system associated with a strong relaxation term. This enlarged system is chosen so that all its characteristic fields are linearly degenerate. The relaxation term, accounted for in the enlarged system by a source term, then allows to recover formally the initial system of equations.

One additional scalar unknown $\mathcal{T}$ is introduced with the initial condition, so that $\mathcal{T}$ will relax towards τ, the specific volume ($m^3.kg^{-1}$):

$$\forall x,\ \mathcal{T}(0,x) = \tau(0,x).$$

A new pressure Π is also defined, which can be seen as a linearization of the pressure P with respect to the variable τ around $\mathcal{T}$:

$$\Pi = P(\mathcal{T}, e) + a^2(\mathcal{T} - \tau), \tag{5.7}$$

where a is a positive constant. At last, a relaxation specific total energy Σ is introduced in order to be consistent with the pressure Π:

$$\Sigma = \frac{u^2}{2} + e + \frac{\Pi^2 - P^2(\mathcal{T}, e)}{2a^2}. \tag{5.8}$$

We set $\boldsymbol{Z}$ the enlarged variable: $\boldsymbol{Z} = (\tau, u, \Sigma, \mathcal{T})$. The enlarged system to solve is then the following:

$$\begin{cases} \partial_t \rho + \partial_x(\rho u) = 0 \\ \partial_t(\rho u) + \partial_x(\rho u^2 + \Pi) = 0 \\ \partial_t(\rho\Sigma) + \partial_x(\rho u\Sigma + u\Pi) = 0 \\ \partial_t(\rho\mathcal{T}) + \partial_x(\rho\mathcal{T}u) = \dfrac{1}{\epsilon}\rho(\tau - \mathcal{T}), \end{cases} \tag{5.9}$$

where the relaxation source terms for $\mathcal{T}$ is characterized by the parameter $\epsilon \geq 0$. All the characteristic fields of the convective part of system (5.9) are linearly degenerate and associated with the wave velocities:

$$\lambda_1 = u_l - a\tau_l, \quad \lambda_2 = u^*, \quad \lambda_3 = u_r + a\tau_r, \tag{5.10}$$

with:

$$u^* = \frac{1}{2}(u_l + u_r) + \frac{1}{2a}(\Pi_l - \Pi_r). \tag{5.11}$$

The parameter a, that appears in the definitions of Π and σ (resp. (5.7) and (5.8)), should satisfy a stability condition which is related to the so-called sub-characteristic condition (see [2]) for the enlarged system (5.9):

$$a > \max\left(\frac{c_l(\tau_l, e_l)}{\tau_l}, \frac{c_r(\tau_r, e_r)}{\tau_r}\right), \tag{5.12}$$

where $c(\tau, e)$ denotes the sound speed associated with the pressure law P, which reads for the perfect gas:

$$c(\tau, e) = -\tau^2 \left.\frac{\partial P}{\partial \tau}\right|_s = \sqrt{\gamma \tau P}.$$

Moreover, a is chosen so that the eigenvalues fulfill the relation:

$$\lambda_1 < \lambda_2 < \lambda_3, \tag{5.13}$$

where λ_k is detailed in (5.10).

Remark 5.1 — In practice, a is chosen locally and defined as follows, thanks to a constant a', fixed for a given simulation:

$$a = a' \times \max\left(\frac{c_l(\tau_l, e_l)}{\tau_l}, \frac{c_r(\tau_r, e_r)}{\tau_r}\right), \quad a' \in [1, +\infty[. \tag{5.14}$$

□

The default entry for a' is $a' = 1.01$.

Thanks to relations (5.13), the self-similar solution $\boldsymbol{Z}(x/t, \boldsymbol{Z}_l, \boldsymbol{Z}_r)$ of the Riemann problem at the interface separating two cells (l and r) for the convective part of system (5.9) can be written:

$$\mathcal{Z}\left(\frac{x}{t}, \boldsymbol{Z}_l, \boldsymbol{Z}_r\right) = \begin{cases} \boldsymbol{Z}_l, & \text{if } x/t < \lambda_1 \\ \boldsymbol{Z}_l^*, & \text{if } \lambda_1 < x/t < \lambda_2 \\ \boldsymbol{Z}_r^*, & \text{if } \lambda_2 < x/t < \lambda_3 \\ \boldsymbol{Z}_r, & \text{if } \lambda_3 < x/t \end{cases} \tag{5.15}$$

with

$$\tau_l^* = \tau_l + \frac{1}{a}(u^* - u_l) \quad ; \quad \tau_r^* = \tau_r - \frac{1}{a}(u^* - u_r)\,; \tag{5.16}$$

$$\Sigma_l^* = \Sigma_l + \frac{1}{a}(\Pi_l u_l - \Pi^* u^*) \quad ; \quad \Sigma_r^* = \Sigma_r - \frac{1}{a}(\Pi_r u_r - \Pi^* u^*)\,; \tag{5.17}$$

$$\mathcal{T}_l^* = \mathcal{T}_l \quad ; \quad \mathcal{T}_r^* = \mathcal{T}_r; \tag{5.18}$$

$$u_l^* = u_r^* = u^* \quad ; \quad \Pi_l^* = \Pi_r^* = \Pi^*; \tag{5.19}$$

where we have set:

$$\Pi^* = \frac{1}{2}(\Pi_l + \Pi_r) + \frac{a}{2}(u_l - u_r)$$

and where u^* is given in (5.11). From a numerical point of view, we have chosen an instantaneous relaxation: $\epsilon \to 0$. As a consequence, we have $\mathcal{T} \to \tau$, $\Pi \to P$ and $\Sigma \to E$, so that the two-point numerical flux corresponding to the relaxation scheme [4] is solely based on the value $\mathcal{Z}(x/t = 0, \boldsymbol{Z}_l, \boldsymbol{Z}_r)$ of the solution $\mathcal{Z}$ at the interface between the two-cells l and r. It reads:

$$\mathbf{g}_{i+\frac{1}{2}}^n = \mathbf{g}(\mathbf{W}_i^n, \mathbf{W}_{i+1}^n) = \left(\frac{u}{\tau}, \frac{u^2}{\tau} + \Pi, \frac{u\Sigma}{\tau} + u\Pi\right), \tag{5.20}$$

where τ, u, and Σ are the components of $\mathcal{Z}(x/t = 0, \boldsymbol{Z}_l, \boldsymbol{Z}_r)$ and where Π also arises from the solution $\mathcal{Z}(x/t = 0, \boldsymbol{Z}_l, \boldsymbol{Z}_r)$.

5.2.1.2 VFRoe-ncv scheme with energy relaxation (relaxCP)

The method, proposed in [6] and [13], is based on VFRoe-ncv flux used with a modified energy. As in [13], a parameter Γ is introduced, such as the following subcharacteristic condition is satisfied:

$$\Gamma > \max(\Gamma_1, \Gamma_2), \tag{5.21}$$

with:

$$\Gamma_1 = \max_{(\Omega_i)_{i\in[|0,N-1|]}} (1 + \tau \left.\frac{\partial P}{\partial e}\right|_\tau) \quad ; \quad \Gamma_2 = \max_{(\Omega_i)_{i\in[|0,N-1|]}} (-\frac{\tau}{P} \left.\frac{\partial P}{\partial \tau}\right|_e + \tau \left.\frac{\partial P}{\partial e}\right|_\tau). \tag{5.22}$$

Remark 5.2 — Γ is defined uniquely on the whole mesh and recomputed at each time step, thanks to a constant a', fixed for a given simulation:

$$\Gamma = a' \times \max(\Gamma_1, \Gamma_2), \quad a' \in [1, +\infty[. \tag{5.23}$$

□

The default entry for a' is $a' = 1.1$.

A modified energy $\hat{e}$ is introduced:

$$\hat{e} = e - \tau \frac{P}{\Gamma - 1}. \tag{5.24}$$

A modified linearized Riemann problem, similar to (5.3), can be written by considering this modified energy (5.24). Once the exact solution is computed, the numerical flux is the same as for the VFRoe-ncv scheme (5.4).

Remark 5.3 — Contrary to classical VFRoe-ncv scheme, relaxCP does not need an entropy correction [15].

5.2.1.3 Rusanov scheme

For the Rusanov scheme [20], the numerical flux is:

$$\mathbf{g}^n_{i+\frac{1}{2}} = \mathbf{g}(\mathbf{W}^n_i, \mathbf{W}^n_{i+1}) = \frac{1}{2}(\boldsymbol{F}(\mathbf{W}^n_i) + \boldsymbol{F}(\mathbf{W}^n_{i+1})) - \frac{\max(\Lambda^n_{i+1}, \Lambda^n_i)}{2} \left(\boldsymbol{W}^n_{i+1} - \boldsymbol{W}^n_i\right), \tag{5.25}$$

where Λ^n_{i+1} (resp. Λ^n_i) is the spectral radius of the convection matrix $\nabla_{\boldsymbol{W}}\boldsymbol{\mathcal{F}}$ at $\boldsymbol{W} = \boldsymbol{W}^n_{i+1}$ (resp. $\boldsymbol{W} = \boldsymbol{W}^n_i$). The time step Δt^n at iteration n should satisfy the CFL constraint:

$$\frac{\Delta t^n}{\Delta x} \max(\Lambda^n_{i+1}, \Lambda^n_i) < \frac{1}{2}. \tag{5.26}$$

In order to exhibit some similar behaviors to the relaxation schemes, the Rusanov flux (5.25) has been rewritten as:

$$\mathbf{g}^n_{i+\frac{1}{2}} = \frac{1}{2}(\boldsymbol{F}(\mathbf{W}^n_i) + \boldsymbol{F}(\mathbf{W}^n_{i+1})) - a' \times \frac{\max(\Lambda^n_{i+1}, \Lambda^n_i)}{2} \left(\boldsymbol{W}^n_{i+1} - \boldsymbol{W}^n_i\right), \quad a' \in [1, +\infty[. \tag{5.27}$$

5.2.2 Riemann problem with waves leaving the domain

A one-dimensional Riemann problem is now studied with measure of the discrete L^1 error. Depending on the abscissa of the initial discontinuity, a 1-rarefaction wave (case 1, Figure 5.7) or a 3-shock wave (case 2, Figure 5.8) has left the domain at the end of the simulation, whereas the other waves are still inside.

5.2.2.1 Presentation of the test case

5.2.2.1.1 Initial data

Steam water is considered. The initial data, written on the table 5.3, are chosen so that $u - c$-wave is a 1-depressurization wave, u-wave is a 2-contact wave and $u + c$-wave is a 3-shock wave, as depicted on Figure 5.6.

Data	Left State	Right State
τ (m^3/kg)	$1.216179963554413\ 10^{-2}$	$2.432359927108826\ 10^{-2}$
u (m/s)	0	0
P (bar)	100	50
T (K)	320	320

Table 5.3 – *Initial data for the studied Riemann problem*

Perfect gas equation of state is chosen, with the following parameters :

$$\left[\begin{array}{c} C_{V,v} = 4.477815802223535\ 10^3\ JK^{-1}kg^{-1}, \\ \gamma_v = 1.084875362318841, \\ s_v^0 = -3.928832266299204\ 10^4\ JK^{-1}kg^{-1}. \end{array}\right.$$

Final time for the simulation is fixed to $t_{\text{end}} = 10^{-3}s$. Three cases are studied, by changing x_{ini} the abscisse of the initial discontinuity between left state and right state :

- reference case, $x_{\text{ini}} = 0.5m$: all the waves are still inside the domain at the end of the simulation (cf Figure 5.6);
- case 1, $x_{\text{ini}} = 0.1m$: 1-rarefaction wave travels to the left and is out of the domain at the end of the simulation; the other waves are still inside the domain (cf Figure 5.7);
- case 2, $x_{\text{ini}} = 0.8m$: 3-shock wave travels to the right and is out of the domain at the end of the simulation; the other waves are still inside the domain (cf Figure 5.8).

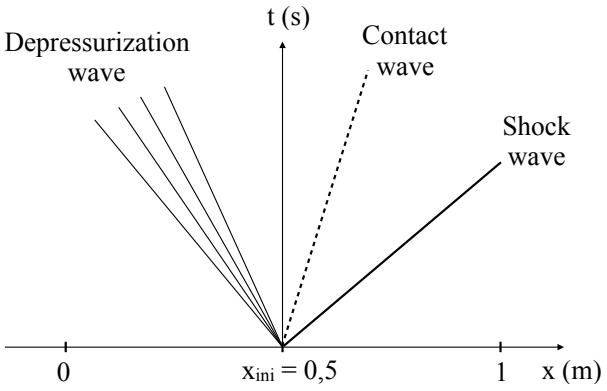

Figure 5.6 – *Reference Riemann problem without out-going waves (infinite domain).*

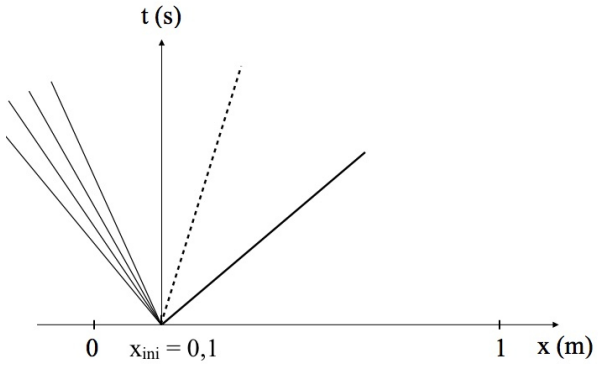

Figure 5.7 – *Case 1: Riemann problem with a left-going 1-rarefaction wave: the depressurisation wave is outside the domain when $t = t_{end}$ whereas contact wave and shock wave are still inside the domain.*

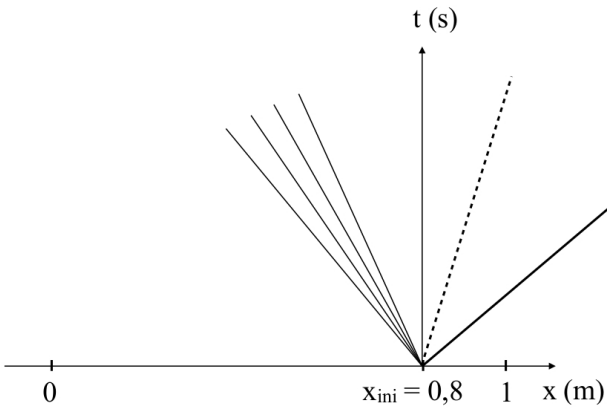

Figure 5.8 – *Case 2: Riemann problem with a right-going 3-shock wave: the shock wave is outside the domain when $t = t_{end}$ whereas contact wave and depressurisation wave are still inside the domain.*

5.2.2.1.2 Reference problem without out-going waves

Figure 5.9 shows convergence curves on pressure P (Pa), velocity u $(m.s^{-1})$ and density ρ $(kg.m^{-3})$, obtained for the reference problem without out-going waves. The approximations have been computed with the four considered schemes, by considering BC_0 as boundary conditions on both exterior borders of the domain. Because of the contact wave, the expected convergence rate is $\frac{1}{2}$, whereas the expected convergence rate for an isolated shock wave would have been 1 [13]. The observed asymptotic convergence rate is obviously between $\frac{1}{2}$ and 1 for all quantities and for all schemes: the numerical approximation converges towards the right solution.

The numerical solution as well as the theorical solution at the final time are given in Figure 5.11. The fan of the rarefaction wave goes from $X \simeq 0.15m$ to $X \simeq 0.25m$. The contact wave is visible on the density curve at $X \simeq 0.6m$. The shock wave is around the abscisse $X \simeq 0.92m$. Moreover, it has been checked that the numerical approximations remain also consistent when using different boundary conditions than BC_0: for instance, Figure 5.10 shows convergence curves similar to Figure 5.9 by using BC_r for the left boundary of the domain and BC_s for the right boundary of the domain.

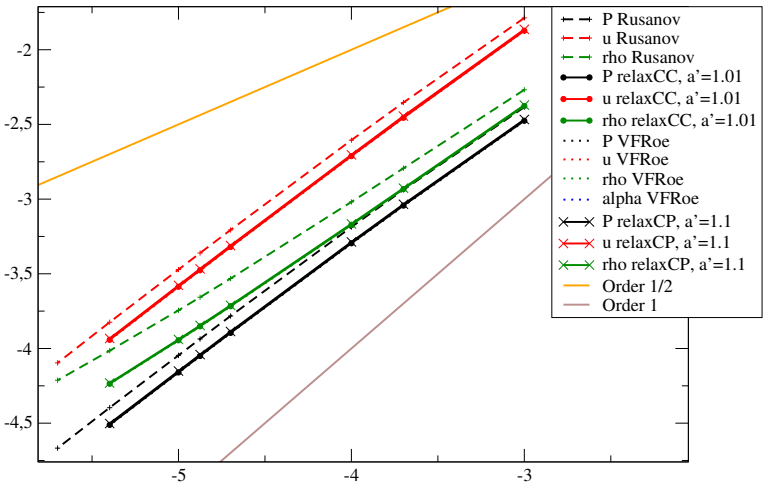

Figure 5.9 – *Convergence curve for the reference case (without out-going waves) with BC_0 for all the studied schemes. Error ($\log_{10}$) as a function of mesh size ($\log_{10}$), with a cell number from 1000 until 500 000 or 1 000 000.*

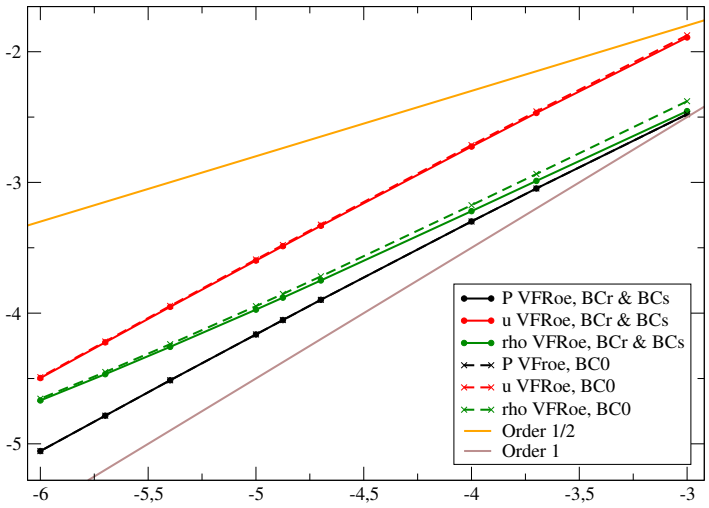

Figure 5.10 – *Convergence curve for the reference case (without out-going waves) with VFRoe-ncv scheme and when using BC_0 or when using BC_r and BC_s. Error ($\log_{10}$) as a function of mesh size ($\log_{10}$), with a cell number from 1000 until 250 000 or 1 000 000.*

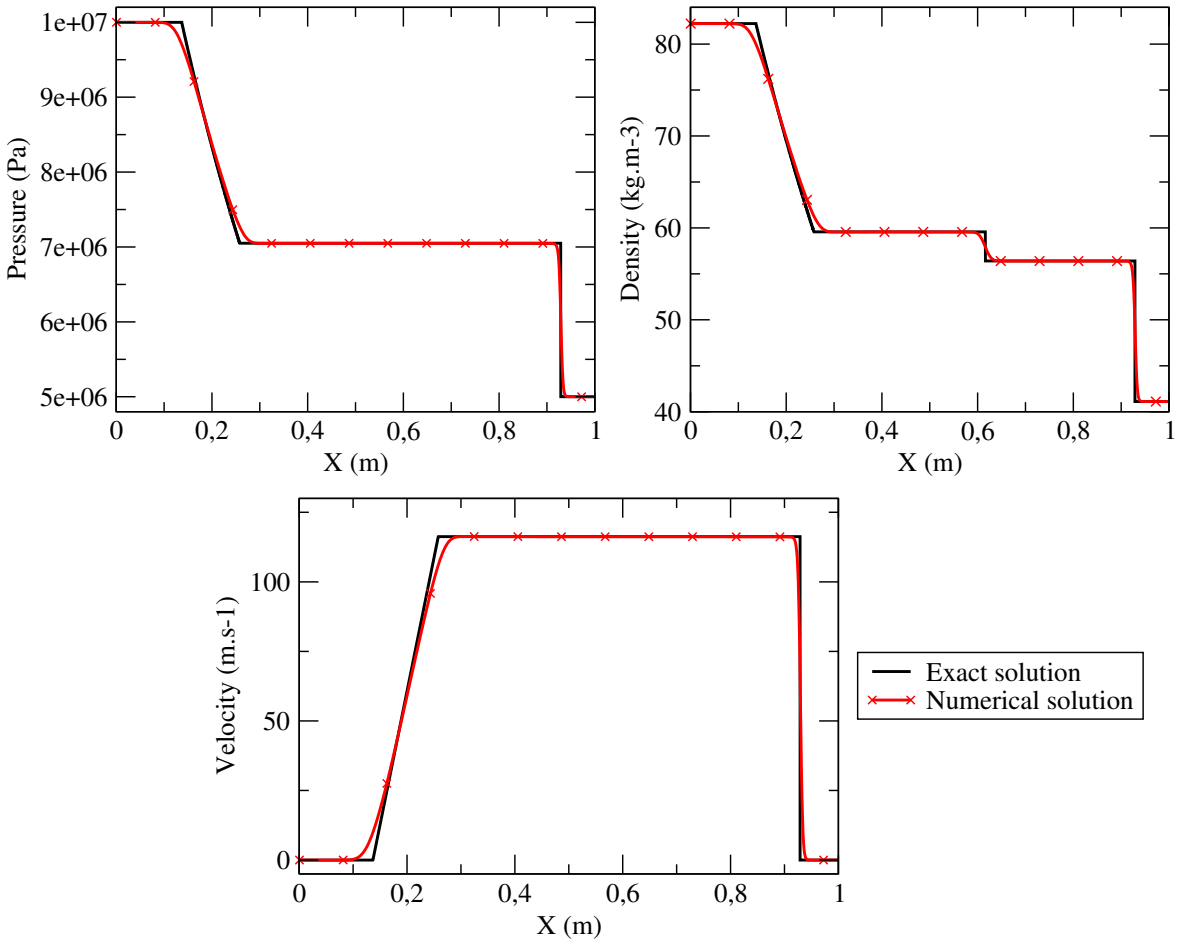

Figure 5.11 – *Reference case with VFRoe-ncv scheme and BC_0. Pressure (Pa), density ($kg.m^{-3}$) and velocity ($m.s^{-1}$) as a function of X (m) at the final time $t_{end} = 10^{-3}s$. The exact solution (plain black line) and the numerical solution obtained with VFRoe-ncv scheme (red line with crosses) on a mesh with 1000 cells are compared.*

From now, each scheme is studied on its own on case 1 (Figure 5.7) and on case 2 (Figure 5.8). Depending on the scheme, several boundary conditions described in section 5.1.2 are tested. The table 5.4 sums up all the tests presented in the next subsections.

	1-rarefaction wave out (case 1)		**3-shock wave out** (case 2)	
Scheme	§	**Tested BC**	§	**Tested BC**
VFRoe-ncv	5.2.2.2	BC_0	5.2.2.2	BC_0; BC_s
relaxCC	5.2.2.3.1	BC_0	5.2.2.3.2	BC_0; BC_s
relaxCP	5.2.2.4.1	BC_0	5.2.2.4.2	BC_0; BC_s
Rusanov	5.2.2.5.1	BC_0	5.2.2.5.2	BC_0; BC_s

Table 5.4 – *Summary of the tested boundary conditions for each scheme.*

5.2.2.2 Synthesis for VFRoe-ncv in (τ, u, P)

VFRoe-ncv has been once more tested, this time in variable (τ, u, P) (contrary to part 5.1, where variable $Y = (s, u, P)$ was used). We recover exactly the same results as in part 5.1, as summarized in table 5.5.

	1-rarefaction wave out		**3-shock wave out**	
Scheme	**BC ?**	**Consistent ?**	**BC ?**	**Consistent ?**
VFRoe-ncv	BC_0	**Yes**	BC_0	**No**
			BC_s	**Yes**

Table 5.5 – *Consistency of the numerical solution with out-going waves obtained with VFRoe-ncv scheme in (τ, u, P) for tested boundary conditions.*

Remark 5.4 — VFRoe-ncv scheme in variable (τ, u, P) with perfect gas equation of state has remarkable theoretical properties [3]: among them, jump relations of VFRoe-ncv scheme in variable (τ, u, P) and exact Rankine-Hugoniot relations for the physical system are equivalent. Nevertheless, BC_s works also with VFRoe-ncv scheme in variable (s, u, P), for which such property does not hold. Thus, particular properties of VFRoe-ncv scheme in (τ, u, P) are not sufficient to explain the consistency obtained with BC_s.

5.2.2.3 Out-going waves with relaxation scheme relaxCC

When implementing relaxCC scheme, a parameter a must be chosen by the user satisfying the subcharacteristic condition (5.12):

$$a > \max\left(\frac{c_l(\tau_l, , e_l)}{\tau_l}, \frac{c_r(\tau_r, , e_r)}{\tau_r}\right).$$

a is defined in practise using a constant a' (5.14), fixed for a given simulation:

$$a = a' \times \max\left(\frac{c_l}{\tau_l}, \frac{c_r}{\tau_r}\right), \quad a' \in [1, +\infty[.$$

5.2.2.3.1 1-rarefaction wave out: consistency of BC_0 depending on a

Relaxation scheme relaxCC is tested on case 1 with condition BC_0 from 5.1.2.1.1. As shown on convergence curves (Figure 5.12), consistency depends on the chosen a': for $a' > 1$, an error plate is observed from quite coarse meshes (from 5000 cells), whereas when $a' = 1$, error curves are linear with a slope between $\frac{1}{2}$ and 1 as expected. Indeed, for $a' > 1$, a spurious intermediate state for P, u and ρ appears, because of a spurious rarefaction wave with a fan centered at $X \simeq 0.3m$ (see Figure 5.13), probably due to a spurious contact wave occuring around $X \simeq 0.35m$.

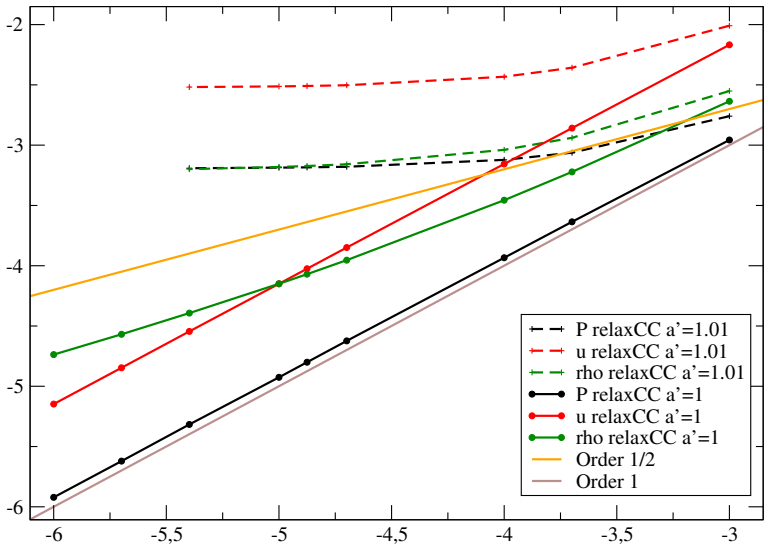

Figure 5.12 – *Case 1 with relaxCC scheme and BC_0. Convergence curve with a 1-rarefaction wave going-out, with relaxCC tested with two different a' : error ($\log_{10}$) as a function of mesh size ($\log_{10}$), with a cell number from 1000 until 1 000 000 or 250 000.*

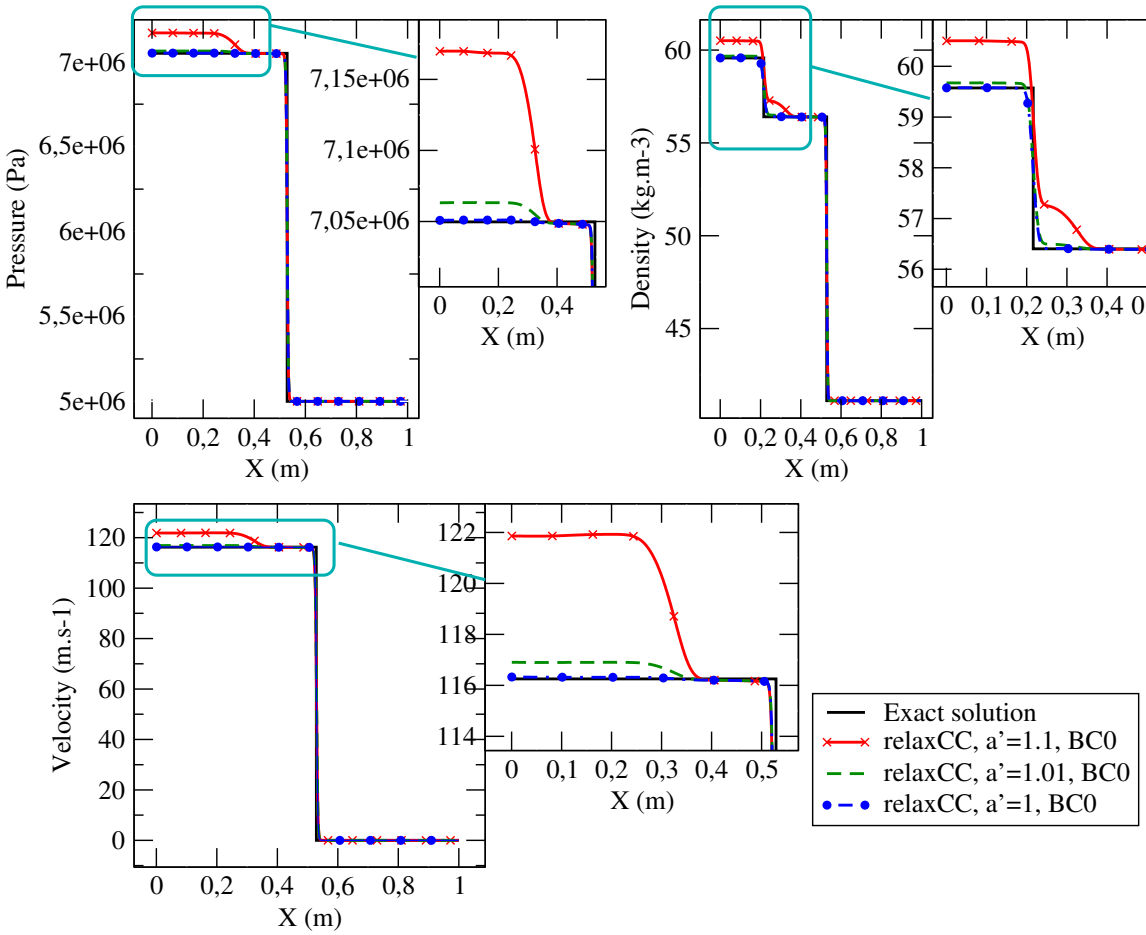

Figure 5.13 – *Case 1 with relaxCC scheme and BC_0. Pressure (Pa), density ($kg.m^{-3}$) and velocity ($m.s^{-1}$) as a function of X (m) at the final time $t_{end} = 10^{-3}s$. The little windows show zoom on the area close to the outflow. The exact solution is compared with numerical solutions obtained with relaxCC tested with several a' on a mesh containing 1000 cells.*

5.2.2.3.2 3-shock wave out: inconsistency of all the tested boundary conditions

a) With boundary condition BC_0 (5.1.2.1.1):

Relaxation scheme relaxCC is tested with varying $a' \geq 1$ and BC_0 on case 2. As observed on numerical solution (Figure 5.15), a spurious rarefaction wave occurs in $X \simeq 0.875m$. The closer a' is to 1, the smaller is the gap with the correct solution, but even $a' = 1$ gives an inconsistent solution at convergence (Figure 5.14).

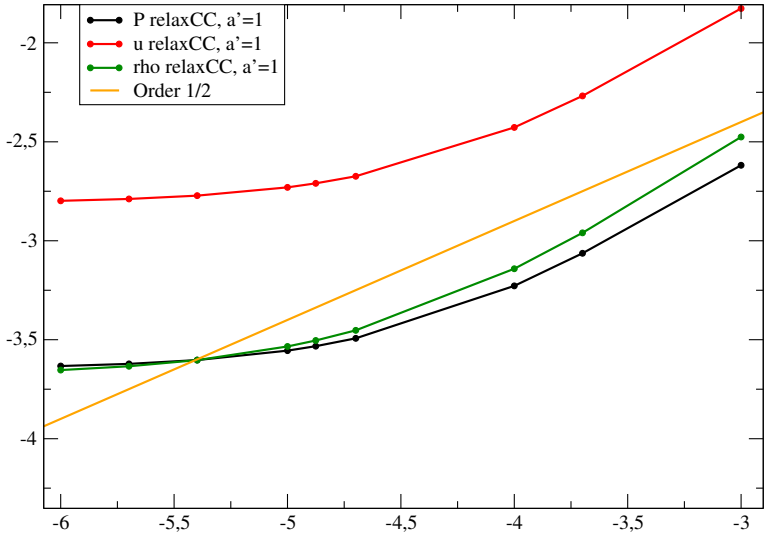

Figure 5.14 – *Case 2 with relaxCC scheme and BC_0. Convergence curve with a 3-shock wave going-out, with relaxCC and $a' = 1$: error ($\log_{10}$) as a function of mesh size ($\log_{10}$), with a cell number from 1000 until 1 000 000 or 250 000.*

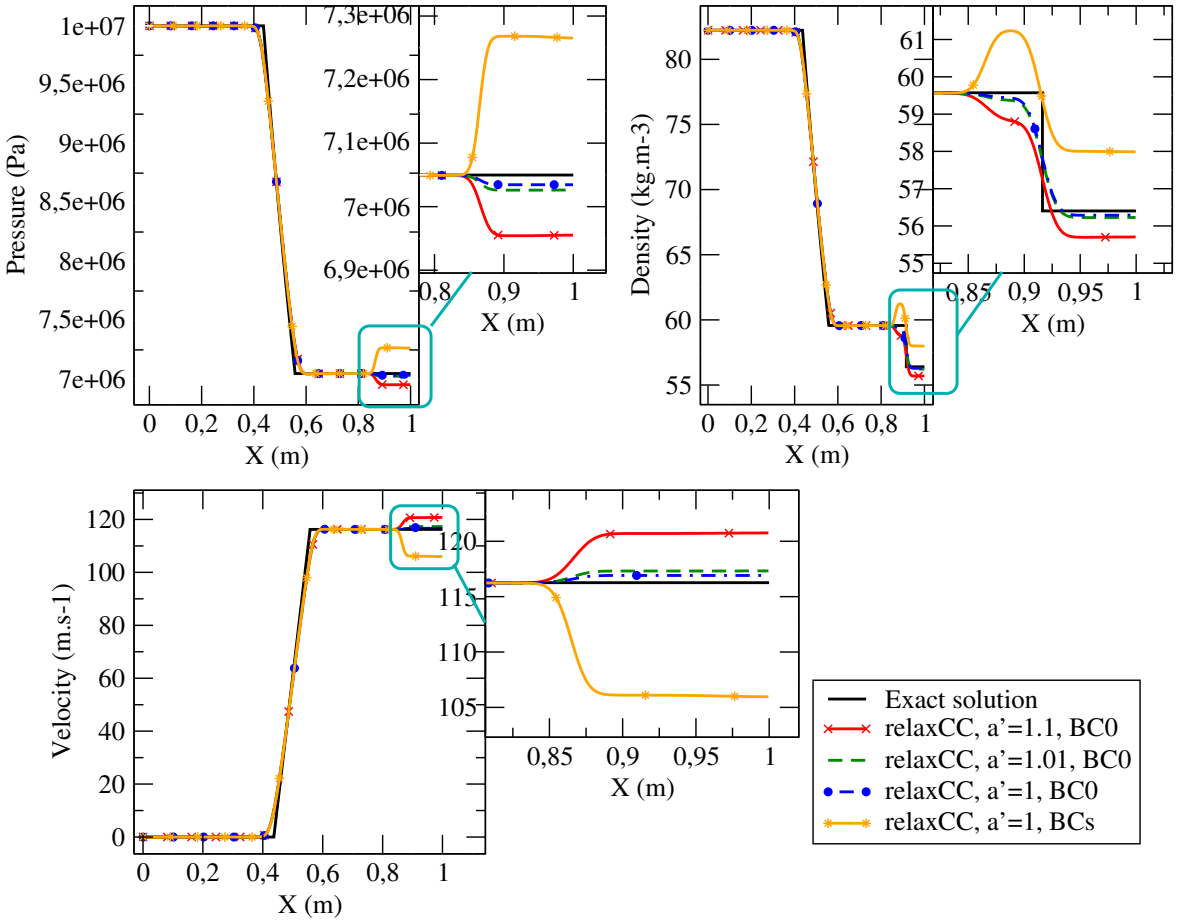

Figure 5.15 – *Case 2 with relaxCC scheme and BC_0 or BC_s. Pressure (Pa), density ($kg.m^{-3}$) and velocity ($m.s^{-1}$) as a function of X (m) at the final time $t_{end} = 10^{-3}s$. The little windows show zoom on the area close to the outflow. The exact solution is compared with numerical solutions obtained with relaxCC tested with several a' on a mesh containing 1000 cells.*

b) With boundary condition BC_s (5.6):

Relaxation scheme relaxCC coupled with BC_s leads to an inconsistent solution for all $a' \geq 1$. An obvious spurious intermediate state can be seen in the numerical solution on Figure 5.15 for $a' = 1$.

5.2.2.3.3 Synthesis for relaxCC

Results are summarized in table 5.6.

	1-rarefaction wave out			3-shock wave out		
Scheme	**BC ?**	**a′?**	**Consistent ?**	**BC ?**	**a′?**	**Consistent ?**
relaxCC	BC_0	$a' > 1$	**No**	BC_0	$a' = 1$	**No**
		$a' = 1$	**Yes**			
				BC_s	$a' = 1$	**No**

Table 5.6 – *Consistency of the numerical solution with out-going waves obtained with relaxCC scheme for tested boundary conditions.*

With relaxCC scheme, the consistency of the numerical solution depends on a, the relax-

ation parameter of the subcharacteristic condition (5.12). Defining $a = a' \times \max\left(\frac{c_l}{\tau_l}, \frac{c_r}{\tau_r}\right), a' \in [1, +\infty[$, the following choice seems mandatory to recover a consistent solution when the rarefaction wave has left the domain: $a' = 1$ i.e.

$$\boxed{a = \max\left(\frac{c_l}{\tau_l}, \frac{c_r}{\tau_r}\right).} \tag{5.28}$$

However, even with (5.28), the numerical solution obtained with relaxCC and BC_0 is inconsistent when the shock wave is out.

Moreover, BC_s does not enable to get a consistent solution when the shock wave is gone. Then, boundary condition BC_s, consistent with VFRoe-ncv scheme for an out-going 3-shock, is not compatible with any numerical scheme.

In order to better understand the influence of a, Figure 5.16 shows how a' modifies the solution for the reference case without out-going waves: for a high $a' = 10$, relaxCC is far more diffusive than for a' around 1. Nevertheless, the link between a' and the numerical diffusion of the scheme is not sufficient to explain the influence of a' on consistency when waves travel outside the domain. Indeed, on Figure 5.16, curves obtained by relaxCC with $a' = 1$, relaxCC with $a' = 1.1$ and or VFRoe-ncv are very hard to distinguish: thus, the numerical diffusion is not significantly different on this case for relaxCC with $a' \simeq 1$ and for VFRoe-ncv, whereas consistency is very sensitive to a' for the out-going 1-rarefaction wave, and whereas condition BC_s works for VFRoe-ncv and not for relaxCC.

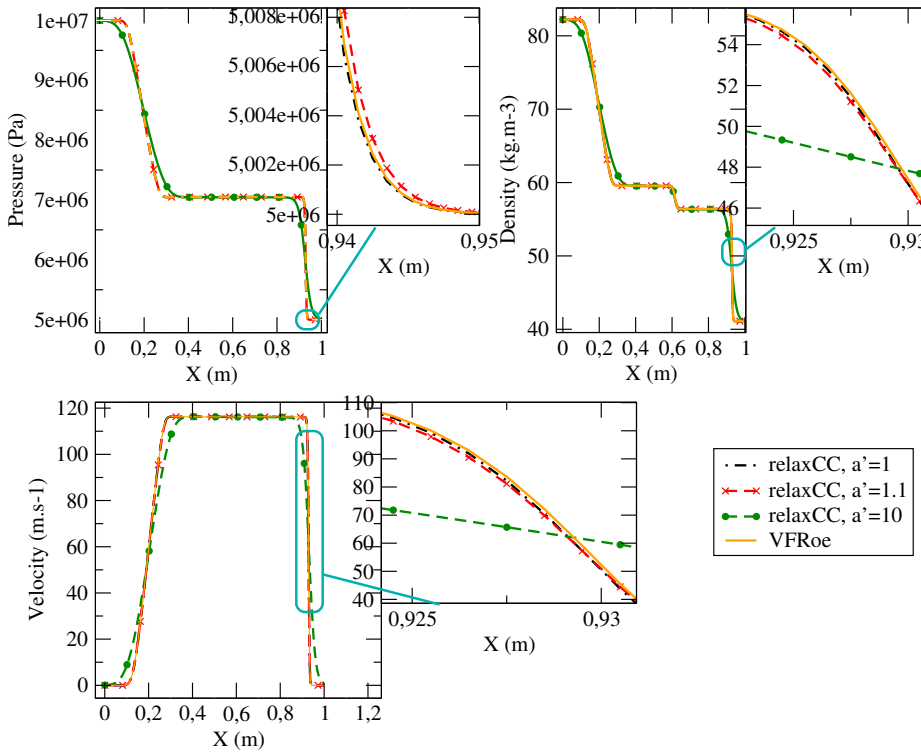

Figure 5.16 – *Reference case (without out-going waves) with relaxCC for $a' = 1$, $a' = 1.1$, $a' = 10$ and VFRoe-ncv. Pressure (Pa), density ($kg.m^{-3}$) and velocity ($m.s^{-1}$) as a function of X (m) at the final time $t_{end} = 10^{-3}s$ on a mesh containing 1000 cells. The little windows show zooms on the shock wave.*

5.2.2.4 Out-going waves with relaxation scheme relaxCP

For relaxCP scheme, a parameter Γ is needed fulfilling the subcharacteristic constraint (5.21):

$$\Gamma > \max(\Gamma_1, \Gamma_2).$$

In practise, Γ is defined with (5.23) thanks to a constant a', fixed for a given simulation:

$$\Gamma = a' \times \max(\Gamma_1, \Gamma_2), \quad a' \in [1, +\infty[.$$

5.2.2.4.1 1-rarefaction wave out: a similar behavior to relaxCC

When considering case 1 with the rarefaction wave out and relaxCP using a boundary condition BC_0, a similar behavior to relaxCC is observed: the obtained solution is consistent only when $a' = 1$ (Figure 5.17), i.e. when:

$$\Gamma = \max(\Gamma_1, \Gamma_2). \tag{5.29}$$

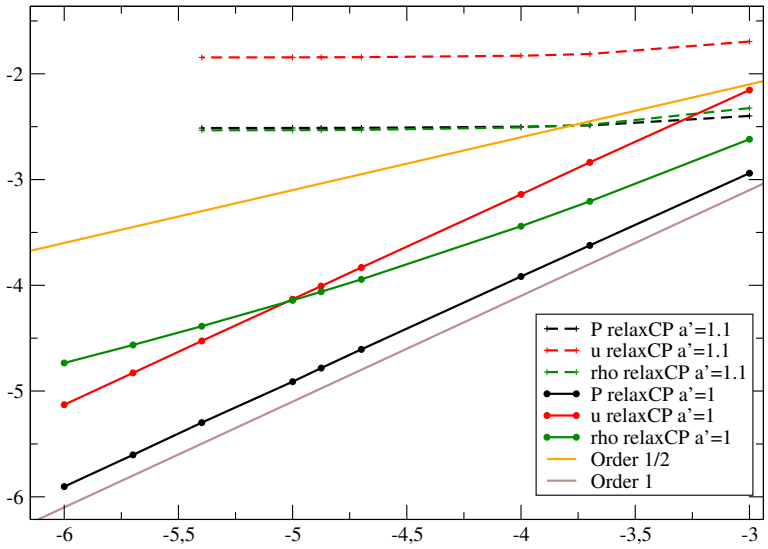

Figure 5.17 – *Case 1 with relaxCP scheme and BC_0. Convergence curve with a 1-rarefaction wave going-out, with relaxCP tested with two different a' : error ($\log_{10}$) as a function of mesh size ($\log_{10}$), with a cell number from 1000 until 1 000 000.*

5.2.2.4.2 3-shock wave out: a similar behavior to VFRoe-ncv

Relaxation scheme relaxCP is tested here only with (5.29): $\Gamma = \max(\Gamma_1, \Gamma_2)$.

a) With boundary condition BC_0 (5.1.2.1.1):

Like VFRoe-ncv and relaxCC, relaxCP associated with BC_0 leads to an inconsistent solution.

b) With boundary condition BC_s (5.6):

Convergence towards the right solution occurs for relaxCP associated with BC_s (Figure 5.18), probably because the scheme is based on VFRoe-ncv flux.

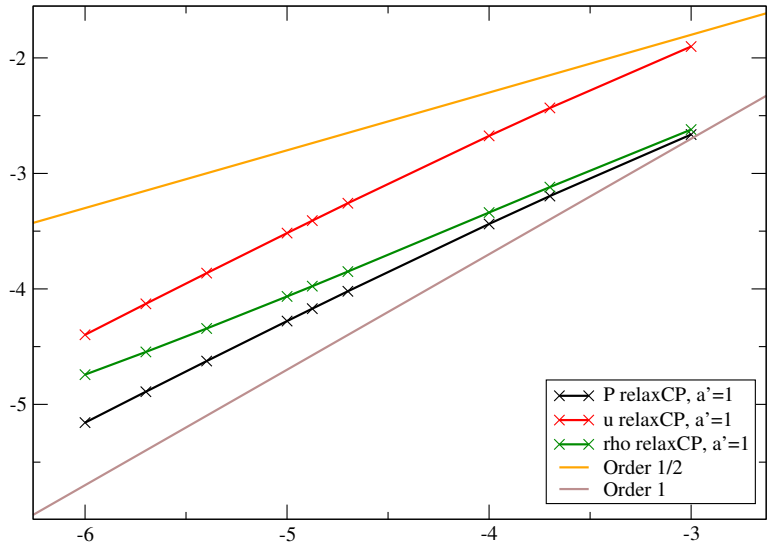

Figure 5.18 – *Case 2 with relaxCP scheme and BC_0. Convergence curve with a 3-shock wave going-out, with relaxCC and $a' = 1$: error ($\log_{10}$) as a function of mesh size ($\log_{10}$), with a cell number from 1000 until 500 000.*

5.2.2.4.3 Synthesis for relaxCP

Results are summarized in table 5.7.

	1-rarefaction wave out			3-shock wave out		
Scheme	**BC ?**	**a′?**	**Consistent ?**	**BC ?**	**a′?**	**Consistent ?**
relaxCP	BC_0	$a' > 1$	**No**	BC_0	$a' = 1$	**No**
		$a' = 1$	**Yes**			
				BC_s	$a' = 1$	**Yes**

Table 5.7 – *Consistency of the numerical solution with out-going waves obtained with relaxCP scheme for tested boundary conditions.*

A similar behavior has been highlighted for both relaxation schemes relaxCC and relaxCP: the consistency of the numerical solution when the rarefaction wave travels out of the domain depends on the relaxation parameter (a for relaxCC and Γ for relaxCP). In both cases, the relaxation parameter should be chosen equal to the limit value fulfilling the relaxation constraint ((5.28) corresponding to the subcharacteristic conditions (5.12) for relaxCC and (5.29) corresponding to (5.21) for relaxCP).

However, as far as the case 2 is concerned, i.e. when the shock wave is out, relaxCP with $a' = 1$ behaves like VFRoe-ncv: BC_0 gives an inconsistent solution while BC_s gives a consistent solution.

5.2.2.5 Out-going waves with Rusanov scheme

We recall that the Rusanov flux (5.25) has been rewritten as:

$$\mathbf{g}_{i+\frac{1}{2}}^n = \frac{1}{2}(\boldsymbol{F}(\mathbf{W}_i^n) + \boldsymbol{F}(\mathbf{W}_{i+1}^n)) - a' \times \frac{\max(\Lambda_{i+1}^n, \Lambda_i^n)}{2}\left(\boldsymbol{W}_{i+1}^n - \boldsymbol{W}_i^n\right), \quad a' \in [1, +\infty[.$$

In the following, the classical Rusanov flux (with $a' = 1$) is used in section 5.2.2.5.1 whereas different values for a' are tested in 5.2.2.5.2.

5.2.2.5.1 1-rarefaction wave: consistency of BC_0

For case 1, BC_0 is also consistent when used with Rusanov scheme (Figure 5.19).

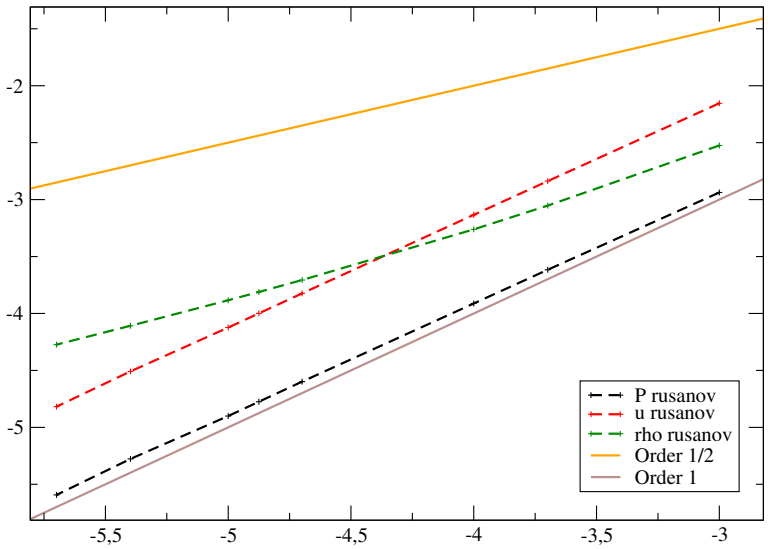

Figure 5.19 – *Case 1 with Rusanov scheme and BC_0. Convergence curve with a 1-rarefaction wave going-out: error ($\log_{10}$) as a function of mesh size ($\log_{10}$), with a cell number from 1000 until 1 000 000.*

5.2.2.5.2 3-shock wave: inconsistency and relaxCC-like behavior

a) With boundary condition BC_0 (5.1.2.1.1):

For case 2, BC_0 is also inconsistent when used with Rusanov scheme. On Figure 5.20, several a' have been tested. Results suggest a relaxCC-like behavior: there probably exists a a' between 1 and 1.5 enabling the convergence towards the right solution, like $a' = 1$ for relaxCC. Nevertheless, no theoretical hint enables to guess the suitable a'.

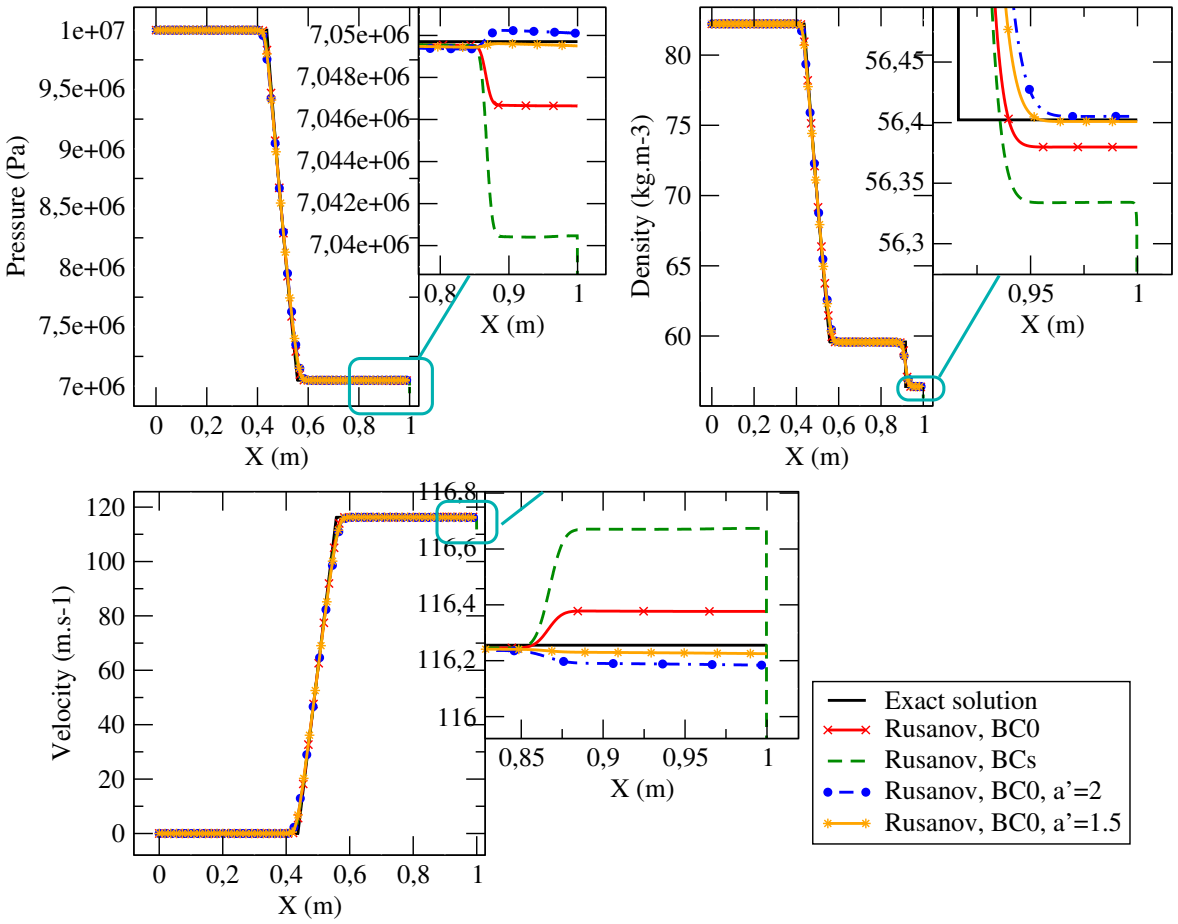

Figure 5.20 – *Case 2 with Rusanov scheme and BC_0 or BC_s. Pressure (Pa), density ($kg.m^{-3}$) and velocity ($m.s^{-1}$) as a function of X (m) at the final time $t_{end} = 10^{-3}s$. The little windows show zoom on the area close to the outflow. The exact solution is compared with numerical solutions obtained with Rusanov scheme on a mesh containing 5000 cells. Rusanov scheme is associated with BC_0 or BC_s. A similar behavior to relaxCC scheme is highlighted by testing several coefficients a'.*

b) With boundary condition BC_s (5.6):

For case 2, like with relaxCC, BC_s is inconsistent with Rusanov scheme (Figure 5.20).

5.2.2.5.3 Synthesis for Rusanov

Results are summarized in table 5.8.

	1-rarefaction wave out		**3-shock wave out**	
Scheme	**BC ?**	**Consistent ?**	**BC ?**	**Consistent ?**
Rusanov	BC_0	**Yes**	BC_0	**No**
			BC_s	**No**

Table 5.8 – *Consistency of the numerical solution with out-going waves obtained with Rusanov scheme for tested boundary conditions.*

Conclusions

This chapter aimed to propose boundary conditions for Euler system simulated in finite volume framework with explicit first-order numerical schemes, compatible with waves travelling out from the computation domain. Some formulations of boundary conditions have been presented in section 5.1.2. They have been tested in section 5.1.3 and in section 5.2.2 on a Riemann problems, with a 1-rarefaction outgoing wave or a 3-shock outgoing wave. Main results are recalled on table 5.9.

	1-rarefaction wave out		**3-shock wave out**	
Scheme	**BC ?**	**Consistent ?**	**BC ?**	**Consistent ?**
VFRoe-ncv	BC_0	**Yes**	BC_0	**No**
			BC_s	**Yes**
relaxCC ($a' = 1$)	BC_0	**Yes**	BC_0	**No**
			BC_s	**No**
relaxCP ($a' = 1$)	BC_0	**Yes**	BC_0	**No**
			BC_s	**Yes**
Rusanov	BC_0	**Yes**	BC_0	**No**
			BC_s	**No**

Table 5.9 – *Synthesis of the most important consistency results depending on the out-going wave, the chosen numerical scheme and the tested boundary condition.*

When a 1-rarefaction wave is out, standard boundary condition BC_0 enables to get a consistent solution for all the tested numerical schemes. Nevertheless, the relaxation schemes (the one proposed by C. Chalons and J.-F. Coulombel in [4], called relaxCC in this chapter, and VFRoe-ncv with energy relaxation [13] proposed by F. Coquel and B. Perthame in [6], called relaxCP) require a particular choice of relaxation parameter. Indeed, the relaxation parameter needs to be **exactly equal to the lower boundary prescribed by the subcharacteristic condition** ((5.28) given by (5.12) for relaxCC and (5.29) by (5.21) for relaxCP) to obtain a consistent solution.

When a 3-shock has left the domain, for all the tested numerical schemes, standard boundary condition BC_0 leads to an inconsistent solution. Modified boundary conditions have been proposed in section 5.1.2.

One proposed approach consists in adding a virtual domain with a fixed size αL at end of the computation domain of size L, with $\alpha >> 1$. The asymptotic version of this formulation with an infinite virtual domain, called BC_s, enables to recover the consistency of the numerical solution when using a VFRoe-ncv scheme: it works in the same way with VFRoe-ncv in variable (τ, u, P), VFRoe-ncv in variable (s, u, P) or with VFRoe-ncv with energy relaxation "relaxCP". Unfortunately, BC_s does not work with relaxation scheme relaxCC or with Rusanov scheme. For now, we are not able to explain this result.

Finally, standard boundary condition BC_0 seems sufficient while regular structures leave the computational domain, like a rarefaction wave. However, if a shock wave may leave the computational domain, consistency is not ensured by using BC_0 since it may lead to an inconsistent solution. Further study in part 5.2 highlighted that, for now, we are not able to

exhibit a consistent open boundary condition compatible with any numerical scheme.

References

[1] C. BARDOS, A.-Y. LEROUX, and J.-C. NÉDÉLEC. "First order quasilinear equations with boundary conditions". In: *Communications in Partial Differential Equations* 4.9 (1979), pp. 1017–1034. DOI: https://doi.org/10.1080/03605307908820117 (cit. on p. 246).

[2] F. BOUCHUT. *Nonlinear stability of finite Volume Methods for hyperbolic conservation laws And Well-Balanced schemes for sources*. Springer Science & Business Media, 2004 (cit. on pp. 253, 254).

[3] T. BUFFARD, T. GALLOUËT, and J.-M. HÉRARD. "A sequel to a rough Godunov scheme: application to real gases". In: *Computers and Fluids* 29.7 (2000), pp. 813–847. URL: https://hal.archives-ouvertes.fr/hal-01579990 (cit. on p. 260).

[4] C. CHALONS and J.-F. COULOMBEL. "Relaxation approximation of the Euler equations". In: *Journal of Mathematical Analysis and Applications* 348.2 (2008), pp. 872–893. ISSN: 0022-247X. URL: https://hal.archives-ouvertes.fr/hal-01838843 (cit. on pp. 253, 254, 271).

[5] C. COLAS. "Time-implicit integral formulation for fluid flow modelling in congested media". PhD Thesis. Aix-Marseille Université, Nov. 2019. URL: https://tel.archives-ouvertes.fr/tel-02382958 (cit. on p. 249).

[6] F. COQUEL and B. PERTHAME. "Relaxation of energy and approximate Riemann solvers for general pressure laws in fluid dynamics". In: *SIAM Journal on Numerical Analysis* 35.6 (1998), pp. 2223–2249. DOI: https://doi.org/10.1137/S0036142997318528 (cit. on pp. 253, 255, 271).

[7] M. DEININGER, U. IBEN, and C.-D. MUNZ. "Coupling of three- and one-dimensional hydraulic flow simulations". In: *Computers & Fluids* 190 (2019), pp. 128–138. ISSN: 0045-7930. URL: http://www.sciencedirect.com/science/article/pii/S0045793019301823 (cit. on p. 249).

[8] F. DUBOIS. "Boundary conditions and the Osher scheme for the Euler equations of gas dynamics." In: *Internal Report CMAP 170, Ecole Polytechnique, Palaiseau, France* (1987) (cit. on p. 247).

[9] F. DUBOIS and P. LE FLOCH. "Boundary conditions for nonlinear hyperbolic systems of conservation laws". In: *J. Diff Equations* 71.1 (1988), pp. 93–122. DOI: https://doi.org/10.1016/0022-0396(88)90040-X (cit. on p. 247).

[10] B. ENGQUIST and A. MAJDA. "Absorbing boundary conditions for the numerical simulation of waves". English (US). In: *Mathematics of Computation* 31.139 (1977), pp. 629–651. ISSN: 0025-5718 (cit. on p. 246).

[11] T. GALLOUËT. "Boundary conditions for hyperbolic equations or systems". In: *Numerical Mathematics and Advanced Applications*. Ed. by M. FEISTAUER, V. DOLEJŠÍ, P. KNOBLOCH, and K. NAJZAR. Berlin, Heidelberg: Springer Berlin Heidelberg, 2004, pp. 39–55. ISBN: 978-3-642-18775-9. DOI: https://doi.org/10.1007/978-3-642-18775-9_3 (cit. on pp. 246, 247).

[12] T. GALLOUËT, J.-M. HÉRARD, and N. SEGUIN. "On the use of symmetrizing variables for vacuum". In: *Calcolo* 40.3 (2003), pp. 163–194. URL: https://hal.archives-ouvertes.fr/hal-00003439 (cit. on pp. 247, 249).

[13] T. GALLOUËT, J.-M. HÉRARD, and N. SEGUIN. "Some recent Finite Volume schemes to compute Euler equations using real gas EOS". In: *International Journal for Numerical Methods in Fluids* 39 (2002), pp. 1073–1138. URL: https://hal.archives-ouvertes.fr/hal-01290885 (cit. on pp. 247, 249, 253, 255, 257, 271).

[14] G. W. HEDSTROM. "Nonreflecting boundary conditions for nonlinear hyperbolic systems". In: *Journal of Computational Physics* 30 (1979), pp. 222–237 (cit. on p. 246).

[15] O. HURISSE. "Application of an homogeneous model to simulate the heating of two-phase flows". In: *International Journal on Finite Volumes* 11 (May 2014), http://www.latp.univ–mrs.fr/IJFV/spip.php?article52. URL: https://hal.archives-ouvertes.fr/hal-01114808 (cit. on p. 255).

[16] S. JIN and Z. XIN. "The relaxation schemes for systems of conservation laws in arbitrary space dimensions". In: *Communications on pure and applied mathematics* 48.3 (1995), pp. 235–276. DOI: https://doi.org/10.1002/cpa.3160480303 (cit. on p. 253).

[17] I. ORLANSKI. "A simple boundary condition for unbounded hyperbolic flows". In: *Journal of Computational Physics* 21.3 (1976), pp. 251–269 (cit. on p. 246).

[18] T. J. POINSOT and S. K. LELE. "Boundary conditions for direct simulations of compressible viscous flows". In: *Journal of Computational Physics* 101.1 (1992), pp. 104–129. DOI: 10.1016/0021-9991(92)90046-2 (cit. on p. 246).

[19] L. QUIBEL. "Simulation d'écoulements diphasiques eau-vapeur avec un modèle homogène". PhD Thesis in preparation. Université de Strasbourg. URL: http://www.theses.fr/s188859 (cit. on p. 250).

[20] V. V. RUSANOV. "The calculation of the interaction of non-stationary shock waves with barriers". In: *Zhurnal Vychislitel'noi Matematiki i Matematicheskoi Fiziki* 1.2 (1961), pp. 267–279. DOI: https://doi.org/10.1016/0041-5553(62)90062-9 (cit. on pp. 253, 255).

[21] J. SMOLLER. *Shock Waves and Reaction-Diffusion Equations*. Vol. 258. A Series of Comprehensive Studies in Mathematics. New York: Springer-Verlag, 1994. ISBN: 0-387-94529-6 (cit. on p. 246).

[22] I. SULICIU. "On the thermodynamics of fluids with relaxation and phase transitions. Fluids with relaxation". In: *Internat. J. Engrg. Sci* 36 (1998), pp. 921–947 (cit. on p. 253).

Conclusions et perspectives

Les travaux développés dans cette thèse visent à modéliser des écoulements multiphasiques susceptibles d'apparaître au cours de scénarios accidentels pouvant hypothétiquement affecter un réacteur à eau pressurisée (REP). Il s'agit d'écoulements subissant des transitoires rapides, avec des changements de phase et dans lesquels des ondes de pression sont générées. Leur modélisation nécessite des modèles multiphasiques capables de gérer les transitions de phase de l'eau de façon réaliste. Plus précisément, dans cette thèse, différents écoulements multiphasiques ont été étudiés, comprenant les composants suivants :

- uniquement de l'eau, sous forme liquide ou sous forme vapeur, comme dans le chapitre 1 ;
- de l'eau ainsi que du gaz incondensable, comme dans le chapitre 3 ;
- de l'eau, du gaz incondensable ainsi que du métal liquide, représentatif du corium qui pourrait se former lors de conditions accidentelles, comme dans le chapitre 4.

Afin d'être en mesure de vérifier les outils numériques développés, en cohérence avec les exigences des autorités de sûreté nucléaire (ASN), les modèles considérés dans ce travail respectent tous un cahier des charges minimal de propriétés mathématiques :

- ils sont **hyperboliques**, afin d'assurer la stabilité en temps fini des solutions numériques ;
- ils admettent une **inégalité d'entropie**, qui permet de sélectionner la solution physique du système, satisfaisant le second principe de la thermodynamique ;
- les **relations de saut** du système sont définies de façon unique, ce qui permet de bien définir les chocs.

Les contributions de cette thèse sont liées à différentes étapes du processus de modélisation.

Travaux théoriques de modélisation

Au chapitre 4, un nouveau modèle multifluide respectant le cahier des charges précédent a été proposé et étudié. Ce travail est purement théorique et la prochaine étape est évidemment l'implémentation numérique du modèle. Un modèle similaire, triphasique à trois champs immiscibles, proposé dans [9], a été simulé dans [5, 4]. Néanmoins, ces travaux simulent la partie convective du système à l'aide du schéma de Rusanov : l'enjeu est maintenant de développer des schémas numériques plus précis, en s'appuyant par exemple sur le schéma développé dans [7] pour le modèle bifluide [6]. Des propriétés intéressantes, notamment en termes de relaxation de pression, ont été mises en évidence dans le chapitre

4 : elles constituent des prérequis théoriques qui nous laissent penser qu'une extension du schéma numérique [7] pourrait effectivement être construite, moyennant une quantité de travail importante.

Fermetures thermodynamiques des modèles

Une grande partie de ce travail de thèse est dédié à l'étude des fermetures thermodynamiques de modèles multiphasiques. Ainsi, des lois d'état classiques ont été passées en revue au chapitre 2. Leurs propriétés mathématiques ont été étudiées, afin de s'assurer de leur compatibilité avec nos modèles d'intérêt. De plus, leur précision a été évaluée au regard d'une loi de référence pour l'eau, la formulation IAPWS [13]. La loi d'état de Noble-Able stiffened gas (NASG) [11] ainsi que son extension avec une capacité calorifique à pression constante fonction de la température (NASG-CK) [3] semblent constituer des compromis intéressants en termes de complexité et de précision.

Des travaux complémentaires méritent d'être menés, notamment sur des cas de validation, afin de mieux cerner les écarts de précision des différentes lois d'état. En particulier, il serait intéressant de comparer les lois NASG et NASG-CK à des lois tabulées (construites en respectant la relation de Gibbs, comme expliqué au chapitre 1), que ce soient des tables reposant sur la formulation IAPWS comme au chapitre 1, ou bien que ce soient des tables utilisant d'autres lois de référence, comme par exemple les tables NBS-NRC [8], réputées pour être plus précises que IAPWS pour les hautes pressions et autour du point critique.

De plus, il a été mis en évidence dans [10] que certaines situations de transitoires rapides (comme dans l'expérience SUPERCANON [12]) induisent des écoulements qui persistent quelques instants en dehors de l'équilibre thermodynamique (de façon observable). Afin de prendre en compte ces effets, les modèles étudiés permettent de considérer une pression et une température phasiques propres à chaque champ et le retour à l'équilibre thermodynamique est assuré par des termes sources de relaxation. Ces termes sources font intervenir des échelles de temps, qu'on peut choisir strictement positives, de façon à retarder le retour à l'équilibre. Néanmoins, peu de références sont disponibles dans la littérature pour définir de telles échelles de temps. C'est pourquoi un modèle simplifié a été proposé dans le chapitre 1, fondé sur la théorie classique de la nucléation :

$$t_{nuc} = \left(\frac{a_0}{\Delta P}\right)^3 \exp\left(\frac{\varphi E_a}{k_B T}\right);$$

il s'agit d'une échelle de temps définie sur le modèle d'une loi d'Arrhénius, avec une énergie d'activation E_a modulée par un paramètre $\varphi \in [0,1]$ lié à la quantité d'impuretés présentes dans le liquide. Plus les impuretés sont nombreuses, plus la vaporisation est facilitée. De premiers résultats qualitatifs intéressants ont été obtenus. Cependant, le modèle nécessite encore des améliorations, notamment pour la définition du préfacteur a_0.

Vérification et validation de modèles fermés à l'aide d'équations d'état réalistes

Enfin, un important travail de vérification des modèles a été mené à bien dans cette thèse.

Ainsi, dans le chapitre 1, le modèle diphasique homogène proposé dans [2] a été fermé à l'aide d'une tabulation de la formulation IAPWS [13]. Construire la tabulation en veillant à maintenir la relation de Gibbs permet donc de ne pas introduire d'inconsistance dans le modèle (au seuil de convergence des algorithmes de Newton près, permettant de changer

de plan thermodynamique), si bien qu'on est en mesure d'exhiber des solutions analytiques pour le modèle et de réaliser des études de convergence en maillage satisfaisantes.

Dans le chapitre 3, le modèle homogène avec prise en compte des gaz incondensables a lui aussi été vérifié. Dans ce chapitre, la difficulté principale est issue du calcul de l'équilibre thermodynamique, et plus précisément, de la gestion des équilibres où l'un des champs au moins est absent. Le seuil de fraction sous lequel un champ est considéré comme manquant est un paramètre assez délicat à manipuler en pratique.

De plus, le calcul de l'équilibre thermodynamique à trois champs se complexifie rapidement dès que l'on choisit des lois d'état plus complexes que des lois de gaz raides. En effet, dans le cas où des lois de gaz raides sont choisies pour tous les champs, la loi de mélange obtenue est elle-même similaire à une loi de gaz raide, avec des paramètres fonctions des fractions massiques [1]. Ce n'est plus le cas dans le chapitre 3 : lorsque le liquide est décrit avec la loi NASG-CK et que la vapeur et l'air sont décrits à l'aide de gaz raides, le calcul de l'équilibre exige la résolution d'un système de deux équations non-linéaires à deux inconnues, parfois piégeuse à mettre en oeuvre numériquement. En prenant des lois d'état un peu plus complexes pour la vapeur et l'air (par exemple, des lois NASG), le système à résoudre devient même un système de trois équations couplées non-linéaires à trois inconnues. Dès lors, le gain en termes de complexité à utiliser des lois semi-analytiques par rapport à une tabulation IAPWS devient plus hypothétique, et il serait intéressant d'effectuer davantage de comparaisons, en termes de temps de calcul et de gain de précision. On peut supposer que l'intérêt principal des lois semi-analytiques de type NASG-CK reste leur robustesse dans des cas très brutaux, comme dans le cas de validation SUPERCANON.

Enfin, des cas de vérification monophasiques ont également été mis en place au chapitre 5, afin d'évaluer différentes conditions limites dans des configurations avec des ondes de détente et des ondes de choc sortant du domaine de calcul au cours la simulation. Une inconsistance a été mise en évidence pour certaines conditions limites, suivant les schémas de convection utilisés. En particulier, lorsqu'une onde de choc sort du domaine de calcul, nous n'avons pas réussi à proposer une formulation de conditions limites qui conduise à une solution numérique consistante pour tout schéma numérique. Des études théoriques complémentaires doivent probablement être menées pour être en mesure d'expliquer ce constat.

Références

[1] M. BACHMANN, S. MÜLLER, P. HELLUY et H. MATHIS. "A Simple Model for Cavitation with Non-condensable Gases". In : *Hyperbolic Problems: Theory, Numerics and Applications*. T. 18. World Scientific, 2012, p. 289-296. DOI : 10.1142/9789814417099_0024. URL : https://hal.archives-ouvertes.fr/hal-01420483 (cf. p. 277).

[2] T. BARBERON et P. HELLUY. "Finite volume simulation of cavitating flows". In : *Computers and Fluids* 34.7 (2005), p. 832-858. URL : https://hal.archives-ouvertes.fr/hal-00139597 (cf. p. 276).

[3] P. BOIVIN, M. CANNAC et O. LE METAYER. "A thermodynamic closure for the simulation of multiphase reactive flows". In : *International Journal of Thermal Sciences* 137 (mar. 2019), p. 640-649. URL : https://hal.archives-ouvertes.fr/hal-01981954 (cf. p. 276).

[4] H. BOUKILI et J.-M. HÉRARD. "Simulation and preliminary validation of a three-phase flow model with energy". working paper or preprint. Jan. 2020. URL : https://hal.archives-ouvertes.fr/hal-02426425 (cf. p. 275).

[5] H. BOUKILI et J.-M. HÉRARD. "Relaxation and simulation of a barotropic three-phase flow model". In : *ESAIM: Mathematical Modelling and Numerical Analysis* 53 (2019), p. 1031-1059. DOI : 10.1051/m2an/2019001. URL : https://hal.archives-ouvertes.fr/hal-01745161 (cf. p. 275).

[6] F. COQUEL, T. GALLOUËT, J.-M. HÉRARD et N. SEGUIN. "Closure laws for a two-fluid two-pressure model". In : *Comptes Rendus Mathématique* 334.10 (2002), p. 927-932. URL : https://hal.archives-ouvertes.fr/hal-01484345 (cf. p. 275).

[7] F. COQUEL, J.-M. HÉRARD, K. SALEH et N. SEGUIN. "A Robust Entropy-Satisfying Finite Volume Scheme for the Isentropic Baer-Nunziato Model". In : *ESAIM: Mathematical Modelling and Numerical Analysis* 48.1 (2014), p. 165-206. URL : https://hal.archives-ouvertes.fr/hal-00795568 (cf. p. 275, 276).

[8] L. HAAR. *NBS/NRC steam tables*. CRC Press, 1984 (cf. p. 276).

[9] J.-M. HÉRARD. "A class of compressible multiphase flow models". In : *Comptes Rendus Mathématique* 354.9 (2016), p. 954-959. URL : https://hal.archives-ouvertes.fr/hal-01348880 (cf. p. 275).

[10] O. HURISSE. "Numerical simulations of steady and unsteady two-phase flows using a homogeneous model". In : *Computers and Fluids* 152 (juil. 2017), p. 88-103. URL : https://hal.archives-ouvertes.fr/hal-01489039 (cf. p. 276).

[11] O. LE MÉTAYER et R. SAUREL. "The Noble-Abel Stiffened-Gas equation of state". In : *Physics of Fluids* 28 (2016), p. 046102. DOI : 10.1063/1.4945981. URL : https://hal.archives-ouvertes.fr/hal-01305974 (cf. p. 276).

[12] B. RIEGEL. "Contribution à l'étude de la décompression d'une capacité en régime diphasique". Thèse de doct. 1978 (cf. p. 276).

[13] W. WAGNER et H.-J. KRETZSCHMAR. *International Steam Tables: Properties of Water and Steam Based on the Industrial Formulation IAPWS-IF97*. Springer-Verlag Berlin Heidelberg, 2008. ISBN : 9783540742340. DOI : http://dx.doi.org/10.1007/978-3-540-74234-0 (cf. p. 276).

Annexes

A A homogeneous model for compressible three-phase flows involving heat and mass transfer

ESAIM: PROCEEDINGS AND SURVEYS, September 2019, Vol. 66, p. 84-108
Philippe Helluy, Jean-Marc Hérard and Nicolas Seguin Editors

A HOMOGENEOUS MODEL FOR COMPRESSIBLE THREE-PHASE FLOWS INVOLVING HEAT AND MASS TRANSFER.

Olivier Hurisse[1] and Lucie Quibel[2]

Abstract. A homogeneous model is proposed in order to deal with the simulation of fast transient three-phase flows involving heat and mass transfer. The model accounts for the full thermodynamical disequilibrium between the three phases in terms of pressure, temperature and Gibbs enthalpy. The heat and mass transfer between the phases is modeled in agreement with the second law of thermodynamics, which ensures a stable return to the thermodynamical equilibrium. The set of partial differential equations associated with this model is based on the Euler set of equations supplemented by a complex pressure law, and by six scalar-equations that allow to account for the thermodynamical disequilibrium. It therefore inherits a simple wave structure and possesses important mathematical properties such as: hyperbolicity, unique shock definition through Rankine-Hugoniot relations, positivity of the mixture fractions. Hence the computation of approximated solutions is possible using classical algorithms, which is illustrated by an example of simulation of a steam-explosion.

Keywords Homogeneous model, three-phase flows, heat transfer, mass transfer, steam explosion.

Introduction

The steam explosion phenomenon occurs in industrial plants when some heated materials (solid or molten solid) come into contact with cold water [4]. The brutal heat transfer from the heated material to the liquid leads to a sudden and brutal production of steam. This steam expands quickly and strong shock waves are produced in the liquid phase, which propagate inside the devices and may damage some of them. When the steam bubble expands in an open domain, for example in a pool with a free surface, some hot materials (solid, steam and/or liquid) are expelled at high velocity. Such a phenomenon occurs in the steel industry (foundry), causing casualties and damages. In the framework of the safety demonstration for the nuclear power plants, some specific scenarii involving steam explosion are studied. This is for instance the case for the Fuel Coolant Interactions (FCI) which occur in the Reactivity Initiated Accident (RIA) [25] or when the corium comes into

[1] EDF Research and Development, Fluid Mechanics, Energy and Environment Department, 6 quai Watier, 78400 Chatou, France,
IMSIA, UMR 9219, ENSTA ParisTech-EDF-CNRS-CEA, Université Paris-Saclay, 828 Boulevard des Maréchaux, 91762 Palaiseau Cedex, France.
e-mail: olivier.hurisse@edf.fr

[2] EDF Research and Development, Fluid Mechanics, Energy and Environment Department, 6 quai Watier, 78400 Chatou, France,
IRMA, UMR CNRS 7501, 7 rue Descartes, 6 quai Watier, 67000 Strasbourg, France,
e-mail: lucie.quibel@edf.fr

Article published online by EDP Sciences and available at https://www.esaim-proc.org or https://doi.org/10.1051/proc/201966005

contact with some water collected in the basemat (in the reactor pit) under the vessel.

The aim of the studies based on these scenarii is to evaluate the mechanical load on the structures of the devices of the plant. This obviously requires to get an accurate prediction of the pressure waves released by the sudden vaporization of the water, and it clearly advocates for the modelisation of the compressibility of both the liquid phase and the vapor phase. In the three-phase flow model proposed in this paper, we assume that the solid (or molten solid) phase is also compressible. This allows to keep a uniform and consistent thermodynamical treatment of the three phases. The stiffness of the thermodynamical behaviour of the solid phase, which has a very low compressibility, may be accounted for by choosing an appropriate Equation Of State. Moreover, in such fast transient flows corresponding to small characteristic time scales, the assumption of the thermodynamical equilibrium between the phases might be a limitation. In [8, 23, 29, 30], some comparisons between numerical simulations and experiments of fast depressurization of water highlight the importance of the thermodynamical disequilibrium. Therefore, it seems important for the proposed model to allow to account for the complete thermodynamical disequilibrium (i.e. with respect to pressure, temperature and Gibbs enthalpy), while also permitting to easily relax towards the thermodynamical equilibrium when necessary.

There exist few three-phase flow models that fulfill these requirements. The standard multifluid approach, derived from the standard two-fluid approach [24], assumes that the pressures of the three phases are always equal. The resulting system of equations may be associated with ill-posed initial-value problems. This is an important drawback, in particular when dealing with fast transient situations. This mathematical issue of the system of equations has its origin in the instantaneous pressure equilibrium [14, 17, 21], and to tackle that point a three-phase flow model involving pressure disequilibrium has been proposed in [19, 20, 33]. The latter is a three-phase flow model that can be seen as an extension of the two-phase model proposed in [2, 27]. In these models, each phase is described by its own velocity field, and by its own pressure and temperature. Hence they account for the full dynamical and thermodynamical disequilibrium between the three phases. Unfortunately, the convective part of the system of equations as a very complex wave structure. In particular, two successive waves can be very close. An accurate numerical simulation of such a situation would thus require very small mesh sizes/time steps in order to permit to distinguish these two neighboring waves on the approximated solutions. Moreover, for these models, each phasic quantity (velocity, specific volume, total energy) is described by its own partial derivative equation. As a consequence, the system of partial derivative equations degenerates in the case of vanishing phases. These situations may therefore be tricky to handle with these multifluid models, at least with a method which remains consistent with the set of equations. In this paper, we intend to propose a model with a more simple wave structure, and that would be able to handle easily vanishing-phase cases which often occur in the simulation of industrial scenarii. Hence we make here the assumption that the three phases have the same velocity. Therefore, the model described in the sections below belongs to the family of the so-called homogeneous models. If this assumption of dynamical equilibrium leads to a more simple description of three-phase flows, the range of applications of the homogeneous model is restricted with respect to multifluid models. In particular, for some situations a homogeneous model might be less relevant for slow transcients: for instance the simulation of the sedimentation due to gravity.

The model proposed in this paper is a straightforward extension of the two-phase flow model proposed in [3, 12, 18, 26, 31]. In [22, 23] the latter has been tested for fast transient steam-liquid water flows and the results show a quite satisfactory agreement with experimental measurements, even for flows involving a strong thermodynamical disequilibrium. We thus propose the extension of this two-phase flow model in order to deal with fast-transient three-phase flows with high thermodynamical disequilibrium. This model draws its strength from the assumption of full thermodynamical disequilibrium (each phase possesses its own internal temperature and its own internal pressure) and from the second law of thermodynamics [7] on which the thermodynamical behaviour of the flow is based. The building of the model relies on two steps: the modeling of the setting of the three phases at a “microscopic scale” and a “macroscopic” modeling of the behaviour of a volume of the

three-phase mixture within the whole flow. On the one hand, the second law of thermodynamics allows to define: the thermodynamical properties of the mixture (the mean pressure and the mean temperature) and the time-evolution of the setting of the three phases within a volume of mixture. Thanks to the dissipation property associated with the second law of thermodynamics, this evolution represents a stable return to the thermodynamical equilibrium when considering a closed volume of mixture. On the other hand, the time-evolution of a mixture-volume is classically described through the first law of thermodynamics and Newton's law. We then end up with a system of equations which is based on the Euler set of equations associated with a complex pressure law and supplemented by six equations that account for the thermodynamical disequilibrium between the phases.

In Section 1 the model is built on the basis of [26, 31]. The closures that are then obtained ensure some good mathematical and physical properties for the system of equations: hyperbolicity of the convective part of the system, uniqueness of the definition of the shocks, entropy dissipation, stable return to thermodynamical equilibrium. These properties are gathered in Section 2. They are a serious advantage when the goal of the model is to be used to perform numerical simulations including shock patterns. The model proposed in Section 1 remains a quite general three-phase flow model, and in Section 3 we introduce some specific features that are mandatory for the steam-explosion modeling. We then specify the fact that mass transfer only occurs between the liquid water and its vapour phase, and we introduce the heating of a solid phase through a source term. At last, in Section 4, we present the numerical simulation of the heating of a solid phase mixed with liquid which leads to steam generation and strong pressure waves. In this simulation, the water phases are described using the IAPWS 97 thermodynamical laws [36].

1. Modeling three-phase flows with a homogeneous model

In this section, we build a homogeneous model which describes a mixture of three-phase. The assumptions are introduced throughout the section. In order to write the model we proceed in two steps by adopting a Lagrangian point of view. We first propose to model the thermodynamic behaviour of a volume of the mixture using the second law of thermodynamic. This first step of the modeling process follows the process proposed in [26, 31] for two-phase flows. Then the first law of thermodynamics and Newton's law are applied to describe the evolution of this volume within the whole flow.

1.1. Some definitions and assumptions

Let us consider a volume $\mathcal{V}$ (in m^3) of the three-phase mixture which is associated with a mass $\mathcal{M}$ (in kg) and an internal extensive energy $\mathcal{E}$ (in J). Each phase $i = \{1, 2, 3\}$ occupies a volume $\mathcal{V}_i$, has a mass $\mathcal{M}_i$ and an internal energy $\mathcal{E}_i$. We assume the following properties for the mixture.

- (H_{1a}) The geometric repartition of the phases inside the volume $\mathcal{V}$ is not taken into account.
- (H_{1b}) The surface tension is neglected.
- (H_2) The three phases are **not miscible**.
- (H_3) Vacuum occurrence is not considered here.

With these assumptions, the volume $\mathcal{V}$, the mass $\mathcal{M}$ and the internal energy $\mathcal{E}$ can be written:

$$\left\{ \begin{array}{l} \mathcal{V} = \mathcal{V}_1 + \mathcal{V}_2 + \mathcal{V}_3, \\ \mathcal{M} = \mathcal{M}_1 + \mathcal{M}_2 + \mathcal{M}_3, \\ \mathcal{E} = \mathcal{E}_1 + \mathcal{E}_2 + \mathcal{E}_3. \end{array} \right. \tag{1}$$

It allows to treat naturally the cases where only one or two of the three phases are present. The hypothesis (H_2) and (H_3) are mandatory to write the first equation of (1) on the volumes. In [18, 32], the miscible case has been investigated and it leads to a different system (1). Assumption (H_3) implies that we consider that $\mathcal{V}$, $\mathcal{M}$ and $\mathcal{E}$ are non-negative: $(\mathcal{V}, \mathcal{M}, \mathcal{E}) \in (\mathbb{R}_+^*)^3$.

1.2. **The second law of thermodynamics**

In this section we use the second law of the thermodynamics to define the time evolution of the quantities $(\mathcal{V}_i, \mathcal{M}_i, \mathcal{E}_i)$ for an isolated mixture, that is for a fixed $(\mathcal{V}, \mathcal{M}, \mathcal{E})$. We assume that the extensive phasic entropies η_i (in J/K) are defined such that the following properties hold:

(H_4) $(\mathcal{V}_i, \mathcal{M}_i, \mathcal{E}_i) \mapsto \eta_i(\mathcal{V}_i, \mathcal{M}_i, \mathcal{E}_i)$ is C^2 on $(\mathbb{R}_+)^3$;
(H_5) $(\mathcal{V}_i, \mathcal{M}_i, \mathcal{E}_i) \mapsto \eta_i(\mathcal{V}_i, \mathcal{M}_i, \mathcal{E}_i)$ is concave;
(H_6) $\forall a \in \mathbb{R}_+^*,\ \forall (\mathcal{V}_i, \mathcal{M}_i, \mathcal{E}_i) \in (\mathbb{R}_+)^3,\ \eta_i(a\mathcal{V}_i, a\mathcal{M}_i, a\mathcal{E}_i) = a\eta_i(\mathcal{V}_i, \mathcal{M}_i, \mathcal{E}_i)$;
(H_7) $\forall (\mathcal{V}_i, \mathcal{M}_i, \mathcal{E}_i),\ \dfrac{\partial \eta_i}{\partial \mathcal{E}_i}_{|\mathcal{V}_i, \mathcal{M}_i} > 0.$

Remark 1. *When $\mathcal{M}_i \neq 0$ (i.e. when phase i exists), assumption (H_6) allows to define a specific entropy (in $J/K/kg$) from the extensive entropy η_i by setting $a = 1/\mathcal{M}_i$. The specific entropy s_i, thus, only depends on $\mathcal{V}_i/\mathcal{M}_i$ and $\mathcal{E}_i/\mathcal{M}_i$:*

$$s_i\left(\frac{\mathcal{V}_i}{\mathcal{M}_i}, \frac{\mathcal{E}_i}{\mathcal{M}_i}\right) = \eta_i\left(\frac{\mathcal{V}_i}{\mathcal{M}_i}, 1, \frac{\mathcal{E}_i}{\mathcal{M}_i}\right) = \frac{\eta_i(\mathcal{V}_i, \mathcal{M}_i, \mathcal{E}_i)}{\mathcal{M}_i},$$

where the second equality assumes an abuse of notation with respect to the dimension of the entropy.
Hence, η_i is a complete Equation Of State (EOS), from which we define the pressure P_i, the temperature T_i and the Gibbs enthalpy μ_i (or Gibbs free enthalpy, in J/kg):

$$\frac{1}{T_i} = \frac{\partial \eta_i}{\partial \mathcal{E}_i}_{|\mathcal{V}_i, \mathcal{M}_i}, \tag{2}$$

$$\frac{P_i}{T_i} = \frac{\partial \eta_i}{\partial \mathcal{V}_i}_{|\mathcal{M}_i, \mathcal{E}_i}, \tag{3}$$

and

$$\frac{\mu_i}{T_i} = -\frac{\partial \eta_i}{\partial \mathcal{M}_i}_{|\mathcal{V}_i, \mathcal{E}_i}. \tag{4}$$

It should be noticed that the assumption (H_7) is equivalent to ensure that the temperature T_i are non-negative. Moreover, these definitions imply the classical Gibbs relation used in the Classical Irreversible Thermodynamics (CIT) theory:

$$T_i d\eta_i = d\mathcal{E}_i + P_i d\mathcal{V}_i - \mu_i d\mathcal{M}_i. \tag{5}$$

Remark 2. *Recalling assumption (H_6), we have:*

$$\forall a \in \mathbb{R}_+^*,\ \forall (\mathcal{V}_i, \mathcal{M}_i, \mathcal{E}_i),\ \eta_i(a\mathcal{V}_i, a\mathcal{M}_i, a\mathcal{E}_i) = a\eta_i(\mathcal{V}_i, \mathcal{M}_i, \mathcal{E}_i).$$

Hence, by deriving this relation with respect to a and by applying $a = 1$, we get:

$$\forall (\mathcal{V}_i, \mathcal{M}_i, \mathcal{E}_i),\ \eta_i(\mathcal{V}_i, \mathcal{M}_i, \mathcal{E}_i) = \frac{\partial \eta_i}{\partial \mathcal{V}_i}_{|\mathcal{M}_i, \mathcal{E}_i} \mathcal{V}_i + \frac{\partial \eta_i}{\partial \mathcal{M}_i}_{|\mathcal{V}_i, \mathcal{E}_i} \mathcal{M}_i, + \frac{\partial \eta_i}{\partial \mathcal{E}_i}_{|\mathcal{V}_i, \mathcal{M}_i} \mathcal{E}_i,$$

and therefore using the definitions (2), (3) and (4) we obtain the relation

$$\mathcal{M}_i \mu_i = \mathcal{E}_i + P_i \mathcal{V}_i - T_i \eta_i. \tag{6}$$

The thermodynamic behaviour of the phase i is defined by the entropy η_i and the Gibbs relations (5) and (6). We now assume that the extensive entropy of the mixture η is the sum of the extensive entropy of each phase:

(H_8) the extensive mixture-entropy is

$$W \mapsto \eta(W) = \sum_i \eta_i(\mathcal{V}_i, \mathcal{M}_i, \mathcal{E}_i), \tag{7}$$

where for the sake of simplicity, we set $W = (\mathcal{V}_1, \mathcal{M}_1, \mathcal{E}_1, \mathcal{V}_2, \mathcal{M}_2, \mathcal{E}_2, \mathcal{V}_3, \mathcal{M}_3, \mathcal{E}_3)$. Thanks to the assumptions $(H_4) - (H_6)$ on the phasic entropies, the mixture entropy η satisfies the properties:

- $W \to \eta(W)$ is C^2 on $(\mathbb{R}_+)^9$;
- $W \to \eta(W)$ is concave;
- $\forall a \in \mathbb{R}_+^*,\ \forall W \in (\mathbb{R}_+)^9,\ \eta(aW) = a\eta(W)$.

The details of the proof of these properties can be found in Appendix 5.1. By deriving the mixture entropy defined by (7) and by using the phasic Gibbs relations (5) we find:

$$d\eta = \sum_i \left(\frac{1}{T_i} d\mathcal{E}_i + \frac{P_i}{T_i} d\mathcal{V}_i - \frac{\mu_i}{T_i} d\mathcal{M}_i \right). \tag{8}$$

This relation can be rewritten in terms of the mixture quantities $(\mathcal{V}, \mathcal{M}, \mathcal{E})$ by using the chain-rule $d\phi_i = \phi\ d(\phi_i/\phi) + \phi_i/\phi\ d\phi$. This yields:

$$\begin{aligned} d\eta = \quad & \textstyle\sum_i \left(\frac{\mathcal{E}_i}{\mathcal{E}} \frac{1}{T_i} \right) d\mathcal{E} + \sum_i \left(\frac{\mathcal{V}_i}{\mathcal{V}} \frac{P_i}{T_i} \right) d\mathcal{V} - \sum_i \left(\frac{\mathcal{M}_i}{\mathcal{M}} \frac{\mu_i}{T_i} \right) d\mathcal{M} \\ & + \textstyle\sum_i \left(\mathcal{E} \frac{1}{T_i} d\left(\frac{\mathcal{E}_i}{\mathcal{E}} \right) + \mathcal{V} \frac{P_i}{T_i} d\left(\frac{\mathcal{V}_i}{\mathcal{V}} \right) - \mathcal{M} \frac{\mu_i}{T_i} d\left(\frac{\mathcal{M}_i}{\mathcal{M}} \right) \right). \end{aligned} \tag{9}$$

Relation (9) is the Gibbs relation for the mixture, from which the mixture temperature T, the mixture pressure P and the mixture Gibbs enthalpy μ can be defined. Indeed we have:

$$\frac{1}{T} = \frac{\partial \eta}{\partial \mathcal{E}}_{|\mathcal{V}, \mathcal{M}, \frac{\mathcal{V}_i}{\mathcal{V}}, \frac{\mathcal{M}_i}{\mathcal{M}}, \frac{\mathcal{E}_i}{\mathcal{E}}} = \sum_i \left(\frac{\mathcal{E}_i}{\mathcal{E}} \frac{1}{T_i} \right), \tag{10}$$

$$\frac{P}{T} = \frac{\partial \eta}{\partial \mathcal{V}}_{|\mathcal{M}, \mathcal{E}, \frac{\mathcal{V}_i}{\mathcal{V}}, \frac{\mathcal{M}_i}{\mathcal{M}}, \frac{\mathcal{E}_i}{\mathcal{E}}} = \sum_i \left(\frac{\mathcal{V}_i}{\mathcal{V}} \frac{P_i}{T_i} \right), \tag{11}$$

and

$$\frac{\mu}{T} = -\frac{\partial \eta}{\partial \mathcal{M}}_{|\mathcal{V}, \mathcal{E}, \frac{\mathcal{V}_i}{\mathcal{V}}, \frac{\mathcal{M}_i}{\mathcal{M}}, \frac{\mathcal{E}_i}{\mathcal{E}}} = \sum_i \left(\frac{\mathcal{M}_i}{\mathcal{M}} \frac{\mu_i}{T_i} \right). \tag{12}$$

Hence, thanks to assumption (H_7), we get that:

$$\forall W \in (\mathbb{R}_+)^9,\ \frac{\partial \eta}{\partial \mathcal{E}}_{|\mathcal{V}, \mathcal{M}, \frac{\mathcal{V}_i}{\mathcal{V}}, \frac{\mathcal{M}_i}{\mathcal{M}}, \frac{\mathcal{E}_i}{\mathcal{E}}} > 0, \tag{13}$$

which also means that the mixture temperature T is non-negative.

Until now, we have considered the extensive mixture entropy η, which is defined on $(\mathbb{R}_+)^9$. We propose now to introduce the intensive entropy. For this purpose, let us define $\mathcal{H}(\mathcal{M})$, the subset of $(\mathbb{R}_+)^9$ such that:

$$\mathcal{H}(\mathcal{M}) = \left\{ W \in (\mathbb{R}_+)^9; \sum_i \mathcal{M}_i = \mathcal{M} \right\},$$

and $\tilde{\eta}$, the restriction of η to $\mathcal{H}(\mathcal{M})$:

$$\forall \tilde{W} \in \mathcal{H}(\mathcal{M}),\ \tilde{\eta}(\tilde{W}) = \eta(\tilde{W}).$$

It can be proved that $\tilde{\eta}$ is strictly concave on $\mathcal{H}(\mathcal{M})$. The detail of the proof is given in Appendix 5.2.

Some thermodynamical properties of the mixture have been examined above. As in [3] we choose to assume that the time-evolutions of the quantities $(\mathcal{V}_i, \mathcal{M}_i, \mathcal{E}_i)$ for a fixed $(\mathcal{V}, \mathcal{M}, \mathcal{E})$ (i.e. for an isolated system) are of the form:

$$(H_9) \quad \left\{ \begin{array}{l} d\left(\frac{\mathcal{V}_i}{\mathcal{V}}\right) = \frac{\overline{\mathcal{V}}_i - \mathcal{V}_i}{\lambda\, \mathcal{V}} dt; \\ d\left(\frac{\mathcal{M}_i}{\mathcal{M}}\right) = \frac{\overline{\mathcal{M}}_i - \mathcal{M}_i}{\lambda\, \mathcal{M}} dt; \\ d\left(\frac{\mathcal{E}_i}{\mathcal{E}}\right) = \frac{\overline{\mathcal{E}}_i - \mathcal{E}_i}{\lambda\, \mathcal{E}} dt; \end{array} \right. \tag{14}$$

where the quantities $(\overline{\mathcal{V}}_i, \overline{\mathcal{M}}_i, \overline{\mathcal{E}}_i)$ and the time-scale $\lambda > 0$ have to be defined. The second law of thermodynamics applied to our system states that: when it is isolated, the mixture entropy must increase. In other words, when $d\mathcal{V} = d\mathcal{M} = d\mathcal{E} = 0$, the models chosen for $d\mathcal{V}_i$, $d\mathcal{M}_i$ and $d\mathcal{E}_i$ must lead to an increase of the mixture entropy $\tilde{\eta}$. The quantities $(\overline{\mathcal{V}}_i, \overline{\mathcal{M}}_i, \overline{\mathcal{E}}_i)$ and the time-scale λ are chosen to comply with the second law of thermodynamics. Since $\tilde{\eta}$ is strictly concave, the plane which is tangent to $\tilde{\eta}$ at any point $\tilde{W}$ of $\mathcal{H}(\mathcal{M})$ is above $\tilde{\eta}$. This can be written:

$$\forall \tilde{W}_0 \in \mathcal{H}(\mathcal{M}),\ \tilde{\eta}(\tilde{W}_0) \leq \eta(\tilde{W}) + \nabla_{\tilde{W}}(\eta)(\tilde{W}).(\tilde{W}_0 - \tilde{W}). \tag{15}$$

By deriving $\tilde{\eta}$ with $d\mathcal{V} = d\mathcal{M} = d\mathcal{E} = 0$ we get:

$$d\tilde{\eta} = (\nabla_W(\eta)\, dW) = \nabla_W(\eta) \left(\frac{\overline{W} - W}{\lambda}\right)\ dt, \tag{16}$$

where $\overline{W} = (\overline{\mathcal{V}}_1, \overline{\mathcal{M}}_1, \overline{\mathcal{E}}_1, \overline{\mathcal{V}}_2, \overline{\mathcal{M}}_2, \overline{\mathcal{E}}_2, \overline{\mathcal{V}}_3, \overline{\mathcal{M}}_3, \overline{\mathcal{E}}_3)$. Then, thanks to the inequality (15), we have:

$$d\tilde{\eta} \geq \frac{1}{\lambda}(\tilde{\eta}(\overline{W}) - \tilde{\eta}(W))\ dt. \tag{17}$$

Finally, one possible choice for $\overline{W}$ is to choose the point that realizes the maximum of the entropy $\tilde{\eta}$ for a fixed $(\mathcal{V}, \mathcal{M}, \mathcal{E})$:

$$\tilde{\eta}(\overline{W}) = \max_{\mathcal{D}(\mathcal{V},\mathcal{M},\mathcal{E})} (\tilde{\eta}(W)), \tag{18}$$

where $\mathcal{D}(\mathcal{V}, \mathcal{M}, \mathcal{E}) = \{W;\ W \in \mathcal{H}(\mathcal{M}), \sum_i \mathcal{V}_i = \mathcal{V}, \sum_i \mathcal{E}_i = \mathcal{E}\}$. Since $\tilde{\eta}$ is strictly concave on $\mathcal{H}(\mathcal{M})$, this point exists and is unique in $\mathcal{H}(\mathcal{M})$. This ensures that $\tilde{\eta}(\overline{W}) > \tilde{\eta}(W)$ and therefore that the mixture entropy increases. The Gibbs relation (9) reads on $\mathcal{D}(\mathcal{V}, \mathcal{M}, \mathcal{E})$:

$$\begin{array}{rl} d\tilde{\eta} = & \mathcal{V}\left(\frac{P_1}{T_1} - \frac{P_3}{T_3}\right) d\left(\frac{\mathcal{V}_1}{\mathcal{V}}\right) + \mathcal{V}\left(\frac{P_2}{T_2} - \frac{P_3}{T_3}\right) d\left(\frac{\mathcal{V}_2}{\mathcal{V}}\right) \\ & + \mathcal{M}\left(\frac{\mu_3}{T_3} - \frac{\mu_1}{T_1}\right) d\left(\frac{\mathcal{M}_1}{\mathcal{M}}\right) + \mathcal{M}\left(\frac{\mu_3}{T_3} - \frac{\mu_2}{T_2}\right) d\left(\frac{\mathcal{M}_2}{\mathcal{M}}\right) \\ & + \mathcal{E}\left(\frac{1}{T_1} - \frac{1}{T_3}\right) d\left(\frac{\mathcal{E}_1}{\mathcal{E}}\right) + \mathcal{E}\left(\frac{1}{T_2} - \frac{1}{T_3}\right) d\left(\frac{\mathcal{E}_2}{\mathcal{E}}\right). \end{array} \tag{19}$$

When the maximum $\overline{W}$ is reached in the interior of the domain $\mathcal{D}(\mathcal{V}, \mathcal{M}, \mathcal{E})$, i.e. when the three phases coexist, the derivative of the entropy with respect to $\mathcal{V}_i$, $\mathcal{M}_i$ and $\mathcal{E}_i$ vanish and by the Gibbs relation (19) we get that the pressure, the temperature and Gibbs enthalpy of all the phases are equal:

$$\begin{array}{l} P_1(\overline{\mathcal{V}_1}, \overline{\mathcal{M}_1}, \overline{\mathcal{E}_1}) = P_2(\overline{\mathcal{V}_2}, \overline{\mathcal{M}_2}, \overline{\mathcal{E}_2}) = P_3(\overline{\mathcal{V}_3}, \overline{\mathcal{M}_3}, \overline{\mathcal{E}_3}), \\ T_1(\overline{\mathcal{V}_1}, \overline{\mathcal{M}_1}, \overline{\mathcal{E}_1}) = T_2(\overline{\mathcal{V}_2}, \overline{\mathcal{M}_2}, \overline{\mathcal{E}_2}) = T_3(\overline{\mathcal{V}_3}, \overline{\mathcal{M}_3}, \overline{\mathcal{E}_3}), \\ \mu_1(\overline{\mathcal{V}_1}, \overline{\mathcal{M}_1}, \overline{\mathcal{E}_1}) = \mu_2(\overline{\mathcal{V}_2}, \overline{\mathcal{M}_2}, \overline{\mathcal{E}_2}) = \mu_3(\overline{\mathcal{V}_3}, \overline{\mathcal{M}_3}, \overline{\mathcal{E}_3}). \end{array} \tag{20}$$

When the maximum $\overline{W}$ is not reached in the interior of $\mathcal{D}(\mathcal{V}, \mathcal{M}, \mathcal{E})$, the three phases do not coexist. The maximum is then reached on a bounadry of the domain and at least one phase is not present. In such a

case, the equilibrium state may be composed of two phases, say phases i and $j \neq i$, such that their pressures, temperatures and chemical potentials are equal:

$$\begin{array}{l} P_i(\overline{\mathcal{V}_i}, \overline{\mathcal{M}_i}, \overline{\mathcal{E}_i}) = P_j(\overline{\mathcal{V}_j}, \overline{\mathcal{M}_j}, \overline{\mathcal{E}_j}), \\ T_i(\overline{\mathcal{V}_i}, \overline{\mathcal{M}_i}, \overline{\mathcal{E}_i}) = T_j(\overline{\mathcal{V}_j}, \overline{\mathcal{M}_j}, \overline{\mathcal{E}_j}), \\ \mu_i(\overline{\mathcal{V}_i}, \overline{\mathcal{M}_i}, \overline{\mathcal{E}_i}) = \mu_j(\overline{\mathcal{V}_j}, \overline{\mathcal{M}_j}, \overline{\mathcal{E}_j}), \end{array} \tag{21}$$

with $\overline{\mathcal{V}_k} = 0$, $\overline{\mathcal{M}_k} = 0$, $\overline{\mathcal{E}_k} = 0$ for $k \notin \{i, j\}$. If there does not exist a couple of phases ensuring (21) and if (20) has no solution, then the equilibrium state corresponds to a single-phase state containing the phase i that possesses the maximum entropy $\eta_i(\mathcal{V}, \mathcal{M}, \mathcal{E})$.

1.3. The first law of thermodynamics and Newton's law

Section 1.2 describes a model for the evolution of the proportion of each phase in the element of fluid $(\mathcal{V}, \mathcal{M}, \mathcal{E})$ when it is isolated from the rest of the flow. We now propose to model the behavior of the flow of the element of fluid $(\mathcal{V}, \mathcal{M}, \mathcal{E})$ along a streamline. We adopt here a classical point of view for fluid dynamics and other approaches are possible has the use of variational principle, see among others [10, 15]. We assume that:

- (H_{10}) all the phases present in the element $(\mathcal{V}, \mathcal{M}, \mathcal{E})$ are convected with the same velocity U;
- (H_{11}) the mass $\mathcal{M}$ is conserved;
- (H_{12}) the variation of the volume $\mathcal{V}$ is due to the divergence of the velocity field U;
- (H_{13}) the variation of the velocity U follows Newton's law;
- (H_{14}) the first law of thermodynamics applies to the energy $\mathcal{E}$.

Assumption (H_{10}) is in fact mandatory and implicitly admitted in Section 1.2 to write the Gibbs relation for the mixture entropy. Assumption (H_{11}) allows to define some specific quantities in Section 2. It leads to the equation:

$$d\mathcal{M} = 0. \tag{22}$$

Assumption (H_{12}) is classical and reads:

$$d\mathcal{V} = \mathcal{V}\nabla_x \cdot (U)\, dt. \tag{23}$$

For the sake of simplicity, we only consider here the force due to the pressure gradient. The momentum equation arises from (H_{13}) and can be written:

$$d(\mathcal{M}U) = -\mathcal{V}\nabla_x (P)\, dt, \tag{24}$$

where the pressure P is the same that the one defined in (11). At last, the first law of thermodynamics (H_{14}) states that the variation of the energy $\mathcal{E}$ is due to the work of the external forces and to the heat Qdt (in J) supplied to the system by its surroundings. Since we only consider here the forces due to the pressure, the variation of the energy is:

$$d\mathcal{E} = -Pd\mathcal{V} + Qdt. \tag{25}$$

1.4. The set of PDE in intensive form

The equations (14), (22), (23), (24) and (25) define the evolution of the quantities $\mathcal{V}_1$, $\mathcal{M}_1$, $\mathcal{E}_1$, $\mathcal{V}_2$, $\mathcal{M}_2$, $\mathcal{E}_2$, $\mathcal{V}_3$, $\mathcal{M}_3$, $\mathcal{E}_3$ and U. The mass conservation (22) allows us to write the model using specific quantities (per unit of mass). Therefore we define the specific volume of the mixture $\tau = \mathcal{V}/\mathcal{M}$ (in m^3/kg), the specific energy of the mixture $e = \mathcal{E}/\mathcal{M}$ (in J/kg). The specific entropy S (in $J/K/kg$) is defined as the entropy per unit of mass:

$$\forall \tilde{W} \in \mathcal{H}(\mathcal{M}),\ S(\tilde{W}) = \frac{\tilde{\eta}(\tilde{W})}{\mathcal{M}}. \tag{26}$$

Thanks to the properties of the entropy $\tilde{\eta}$ and the entropies η_i, we have $\forall \tilde{W} \in \mathcal{H}(\mathcal{M})$:

$$S(\tilde{W}) = \frac{\tilde{\eta}(\tilde{W})}{\mathcal{M}} = \tilde{\eta}(\tilde{W}/\mathcal{M}) = \sum_i \eta_i \left(\frac{\mathcal{V}_i}{\mathcal{M}}, \frac{\mathcal{M}_i}{\mathcal{M}}, \frac{\mathcal{E}_i}{\mathcal{M}} \right) = \sum_i \eta_i \left(\alpha_i \frac{\mathcal{V}}{\mathcal{M}}, y_i, z_i \frac{\mathcal{E}}{\mathcal{M}} \right),$$

which for $y_i \neq 0$ and by using the notation of Remark 1 gives:

$$\forall \tilde{W} \in \mathcal{H}(\mathcal{M}),\ S(\tilde{W}) = \sum_i y_i\ s_i \left(\frac{\alpha_i}{y_i}\tau, \frac{z_i}{y_i} e \right).$$

The volume fraction $\alpha_i = \frac{\mathcal{V}_i}{\mathcal{V}}$ of phase i, the mass fraction $y_i = \frac{\mathcal{M}_i}{\mathcal{M}}$ of phase i and the energy fraction $z_i = \frac{\mathcal{E}_i}{\mathcal{E}}$ of phase i play an important role in the model since they describe how the phases are mixed to compose $(\mathcal{V}, \mathcal{M}, \mathcal{E})$. Note that, since $(\mathcal{V}_i, \mathcal{M}_i, \mathcal{E}_i)$ belongs to $(\mathbb{R}_+)^3$ and $(\mathcal{V}, \mathcal{M}, \mathcal{E})$ belongs to $(\mathbb{R}_+^*)^3$, each fraction belong to $[0, 1]$. In the following, they will be respectively denoted by α_i, y_i and z_i. The set of equations (1) implies that we have:

$$\sum_i \alpha_i = \sum_i y_i = \sum_i z_i = 1, \tag{27}$$

and

$$\sum_i d\alpha_i = \sum_i dy_i = \sum_i dz_i = 0. \tag{28}$$

The Gibbs relation for the specific entropy S can be deduced from the Gibbs relation (9), and it is:

$$\begin{array}{rl} dS = & \frac{1}{T} de + \frac{P}{T} d\tau \\ & + \tau \left(\frac{P_1}{T_1} - \frac{P_3}{T_3} \right) d\alpha_1 + \tau \left(\frac{P_2}{T_2} - \frac{P_3}{T_3} \right) d\alpha_2 \\ & + \left(\frac{\mu_3}{T_3} - \frac{\mu_1}{T_1} \right) dy_1 + \left(\frac{\mu_3}{T_3} - \frac{\mu_2}{T_2} \right) dy_2 \\ & + e \left(\frac{1}{T_1} - \frac{1}{T_3} \right) dz_1 + e \left(\frac{1}{T_2} - \frac{1}{T_3} \right) dz_2, \end{array} \tag{29}$$

with the mixture temperature and the mixture pressure:

$$\frac{1}{T} = \sum_i \left(z_i \frac{1}{T_i} \right) \qquad \text{and} \qquad \frac{P}{T} = \sum_i \left(\alpha_i \frac{P_i}{T_i} \right). \tag{30}$$

The equations (14) on $(\mathcal{V}_i, \mathcal{M}_i, \mathcal{E}_i)$ can also be re-written using the fractions:

$$\left\{ \begin{array}{l} d\alpha_i = \frac{\overline{\alpha}_i - \alpha_i}{\lambda} dt; \\ dy_i = \frac{\overline{y}_i - y_i}{\lambda} dt; \\ dz_i = \frac{\overline{z}_i - z_i}{\lambda} dt; \end{array} \right. \tag{31}$$

where the equilibrium fractions are $\overline{\alpha}_i = \overline{\mathcal{V}}_i/\mathcal{V}$, $\overline{y}_i = \overline{\mathcal{M}}_i/\mathcal{M}$ and $\overline{z}_i = \overline{\mathcal{E}}_i/\mathcal{E}$. At last, the equations of the previous subsection (23), (24) and (25) read using the specific quantities:

$$\left\{ \begin{array}{l} d\tau = \tau \nabla_x \cdot (U)\, dt; \\ dU = -\tau \nabla_x (P)\, dt; \\ de = -P d\tau + \tilde{Q} dt; \end{array} \right. \tag{32}$$

where $\tilde{Q}dt = Q/\mathcal{M}dt$ is the specific heat (in J/kg) supplied to the system. In the following, we set $\tilde{Q} = 0$ and a specific emphasis on the heating source term is proposed in Section 3. The derivative $d\phi$ of a variable ϕ

corresponds here to the derivative along a streamline of the flow, which can also be written:

$$d\phi = \frac{\partial}{\partial t}(\phi) + U\nabla_x \cdot (\phi),$$

hence, the set of equations (27), (31) and (32) can be written in conservative form:

$$\begin{cases} \frac{\partial}{\partial t}(\rho Y) + \nabla_x \cdot (\rho U Y) = \rho \Gamma_Y, \\ \frac{\partial}{\partial t}(\rho) + \nabla_x \cdot (\rho U) = 0, \\ \frac{\partial}{\partial t}(\rho U) + \nabla_x \cdot (\rho U \otimes U) + \nabla_x (P) = 0, \\ \frac{\partial}{\partial t}(\rho E) + \nabla_x \cdot (U(\rho E + P)) = 0, \end{cases} \tag{33}$$

where $\rho = 1/\tau$ is the mixture density, and $E = e + |U|^2/2$ is the specific total energy of the mixture. The fraction vector Y gathers the fractions of phase 1 and 2: $Y = (\alpha_1, y_1, z_1, \alpha_2, y_2, z_2)$. The fractions of the third phase are deduced from Y through the relations (27). The source-term vector Γ_Y is then:

$$\Gamma_Y = \frac{\overline{Y} - Y}{\lambda}, \quad \text{where} \quad \overline{Y} = (\overline{\alpha_1}, \overline{y_1}, \overline{z_1}, \overline{\alpha_2}, \overline{y_2}, \overline{z_2}). \tag{34}$$

The temperature law and the pressure law for the mixture are given by definitions (10) and (11). By using the specific quantities they read:

$$\frac{1}{T(Y,\tau,e)} = \sum_i \frac{z_i}{T_i\left(\frac{\alpha_i}{y_i}\tau, \frac{z_i}{y_i}e\right)} \qquad \text{and} \qquad \frac{P(Y,\tau,e)}{T(Y,\tau,e)} = \sum_i \alpha_i \frac{P_i\left(\frac{\alpha_i}{y_i}\tau, \frac{z_i}{y_i}e\right)}{T_i\left(\frac{\alpha_i}{y_i}\tau, \frac{z_i}{y_i}e\right)}. \tag{35}$$

2. Properties of the whole model

In this section, we present the main mathematical properties of the model. We focus here on the properties that are mandatory for a model to be used in a numerical simulation process [16].

Without any loss of generality, and since the system is invariant under frame rotation, we consider here for the sake of simplicity system (33) for a one-dimensional space variable x, that is:

$$\begin{cases} \frac{\partial}{\partial t}(\rho Y) + \frac{\partial}{\partial x}(\rho U Y) = \rho \Gamma_Y, \\ \frac{\partial}{\partial t}(\rho) + \frac{\partial}{\partial x}(\rho U) = 0, \\ \frac{\partial}{\partial t}(\rho U) + \frac{\partial}{\partial x}\left(\rho U^2 + P\right) = 0, \\ \frac{\partial}{\partial t}(\rho E) + \frac{\partial}{\partial x}(U(\rho E + P)) = 0, \end{cases} \tag{36}$$

with $Y = (\alpha_1, y_1, z_1, \alpha_2, y_2, z_2)$ and $E = e + U^2/2$. The closure relation for the pressure is given by relations (10) and (11):

$$P = \frac{\sum_i \left(\alpha_i \frac{P_i\left(\frac{z_i}{y_i} e, \frac{\alpha_i}{y_i}\tau\right)}{T_i\left(\frac{z_i}{y_i} e, \frac{\alpha_i}{y_i}\tau\right)} \right)}{\sum_i \left(\frac{z_i}{T_i\left(\frac{z_i}{y_i} e, \frac{\alpha_i}{y_i}\tau\right)} \right)} \qquad \text{and} \qquad \frac{1}{T} = \sum_i \left(\frac{z_i}{T_i\left(\frac{z_i}{y_i} e, \frac{\alpha_i}{y_i}\tau\right)} \right), \tag{37}$$

where $\alpha_3 = 1 - (\alpha_1 + \alpha_2)$, $y_3 = 1 - (y_1 + y_2)$ and $z_3 = 1 - (z_1 + z_2)$. The phasic pressure and temperature laws P_i and T_i must be specified by the user.

The sound speed c of system (36) is defined as:

$$c^2 = -\tau^2 \frac{\partial}{\partial \tau}(P)_{|e,Y} + \tau^2 P \frac{\partial}{\partial e}(P)_{|\tau,Y}\,. \tag{38}$$

Using formulas (37) for the mixture pressure P and the mixture temperature T, it can be written:

$$-\frac{c^2}{T\tau^2} = \sum_i \frac{1}{y_i} (-\alpha_i, P z_i)\ (d^2 s_i) \begin{pmatrix} -\alpha_i \\ P z_i \end{pmatrix}, \tag{39}$$

where $d^2 s_i$ stands for the Hessian matrix of the phasic entropies $(\tau_i, e_i) \mapsto s_i(\tau_i, e_i)$:

$$d^2 s_i = \begin{pmatrix} \dfrac{\partial^2 (s_i)}{\partial \tau_i \partial \tau_i} & \dfrac{\partial^2 (s_i)}{\partial \tau_i \partial e_i} \\ \dfrac{\partial^2 (s_i)}{\partial \tau_i \partial e_i} & \dfrac{\partial^2 (s_i)}{\partial e_i \partial e_i} \end{pmatrix}. \tag{40}$$

We recall that the phasic sound speeds are defined as:

$$-\frac{c_i^2}{T_i \tau_i^2} = (-1, P_i)\ d^2 s_i \begin{pmatrix} -1 \\ P_i \end{pmatrix}. \tag{41}$$

It must be emphasized that this mixture celerity c is, thus, not a barycenter of the phasic celerities c_i. We already know from (13) that the mixture temperature T is non-negative. Hence, if the specific phasic-entropies $(\tau_i, e_i) \mapsto s_i(\tau_i, e_i)$ are strictly concave, the square of the mixture sound-speed c^2 is non-negative. Assumption (H_5) on the concavity of the phasic entropies η_i, implies that the specific entropies s_i (see Appendix 5.3) are also concave and thus that $c^2 \geq 0$. In order to enforce the strict hyperbolicity of the model, the user has to specify strictly concave EOS $(\tau_i, e_i) \mapsto s_i(\tau_i, e_i)$ for each phase.

The convective part of system (36) is based on the Euler set of equations associated with a complex mixture EOS. Hence, it inherits from the eigenstructure of the Euler system and is composed of three waves: a contact discontinuity associated with the velocity U, and two genuinely non-linear waves $U \pm c$. Provided that $c > 0$, the fractions Y are constant across the shock waves since they are associated with the contact discontinuity U. It can be proved (see Appendix 5.3) that the specific entropy $(\tau, e) \mapsto S(Y, \tau, e)$ is strictly concave, which ensures that the shock waves associated with the genuinely non-linear waves $U \pm c$ are uniquely defined through the Rankine-Hugoniot relations.

Concerning the equilibrium fraction $\overline{Y}$, it has been shown in Appendix 5.3 that the specific entropy $S(Y, \tau, e)$ is strictly concave with respect to Y on $[0, 1]^3$. Therefore, there exists a unique equilibrium fraction $\overline{Y}(\tau, e)$

corresponding to the maximum of S at a given (τ, e). We now recall the following classical lemma.

Lemma. *Let Ω be a subset of $\mathbb{R}$. Let Ψ, a, Π and U be some sufficiently regular applications, with the following properties:*

- $\Psi : (\Omega \times [0,T] \to \mathbb{R}, (x,t) \mapsto \Psi(x,t))$;
- $a : (\Omega \times [0,T] \to \mathbb{R}, (x,t) \mapsto a(x,t))$, $a \in L^\infty(\Omega \times [0,T])$;
- $\Pi : (\Omega \times [0,T] \to \mathbb{R}, (x,t) \mapsto \Pi(x,t))$, $\Pi \geq 0$;
- $U : (\Omega \times [0,T] \to \mathbb{R}, (x,t) \mapsto U(x,t))$,
  $U \in L^\infty(\Omega \times [0,T])$ *and* $\dfrac{\partial}{\partial x}(U) \in L^\infty(\Omega \times [0,T])$;

and such that:

$$\frac{\partial}{\partial t}(\Psi(x,t)) + U\frac{\partial}{\partial x}(\Psi(x,t)) = a(x,t)\Psi(x,t) + \Pi(x,t). \tag{42}$$

Suppose that for all $x_b \in \partial\Omega$, the boundary of Ω, $\Psi(x_b,t) \geq 0$ if $(U \cdot n)(x_b,t) \leq 0$, where n is the outward normal of Ω. With all these assumptions, if $\Psi(x, t=0) \geq 0$ then for all $0 \leq t \leq T$, $\Psi(x,t) \geq 0$.

This lemma can be used to prove the following property.

Property. *For regular solutions, and under the assumptions of the Lemma, the fraction α_i, y_i and z_i remain in $[0,1]$.*

In order to prove the property above, we proceed for the volume fractions α_i, and the same demonstration holds for y_i and z_i. Since $\sum_i \alpha_i = \sum_i \overline{\alpha}_i = 1$, we have from (36):

$$\frac{\partial}{\partial t}(\alpha_i(x,t)) + U\frac{\partial}{\partial x}(\alpha_i(x,t)) = a_i(x,t)\alpha_i(x,t) + \Pi_i(x,t),$$

with $a_i = -1/\lambda$ and $\Pi_i = \overline{\alpha}_i/\lambda$. The equilibrium volume fraction $\overline{\alpha}_i$ belongs to $[0,1]$ and the time scale λ must be chosen non-negative, so that we obviously have $\Pi_i \geq 0$. The lemma can be straightforward applied for $\Psi = \alpha_i$ which remains positive under the assumptions of the lemma. This proof can obviously be extended to the fractions y_i and z_i which, thus, also remain positive.

3. The specific case of the steam explosion

The model proposed in the sections above deals with general three-phase flows. It can for example be used to perform simulations involving the same material in liquid, vapor and solid state (for the simulation of the sudden depressurization of CO_2 pipes for instance). Relations (20) then define the triple point when the three phases coexist in a stable manner. When only two phases coexist in a stable manner, say phase 1 and phase 2, system (20) reduces to:

$$\begin{aligned} P_1(\overline{\mathcal{V}_1}, \overline{\mathcal{M}_1}, \overline{\mathcal{E}_1}) &= P_2(\overline{\mathcal{V}_2}, \overline{\mathcal{M}_2}, \overline{\mathcal{E}_2}), \\ T_1(\overline{\mathcal{V}_1}, \overline{\mathcal{M}_1}, \overline{\mathcal{E}_1}) &= T_2(\overline{\mathcal{V}_2}, \overline{\mathcal{M}_2}, \overline{\mathcal{E}_2}), \\ \mu_1(\overline{\mathcal{V}_1}, \overline{\mathcal{M}_1}, \overline{\mathcal{E}_1}) &= \mu_2(\overline{\mathcal{V}_2}, \overline{\mathcal{M}_2}, \overline{\mathcal{E}_2}), \end{aligned} \tag{43}$$

which defines the saturation curve between phase 1 and phase 2 (of course the saturation curves between phase 1 and phase 3, and between phase 2 and phase 3 are defined by permuting the indices in (43)). In this section we propose further assumptions that allow to deal with the steam explosion [4]. We are interested here in situations where one of the three phases represents a material, and the two others represent the same fluid in the liquid state and in the vapour state. In the following, phase 1 stands for the liquid phase, phase 2 for the vapour phase and phase 3 for the inert phase.

Since the phase 3 is inert, its partial mass $\mathcal{M}_3/\mathcal{M}$ will remain constant:

$$d\left(\frac{\mathcal{M}_3}{\mathcal{M}}\right) = 0.$$

Moreover, due to the mass transfer between the liquid phase and the vapour phase, each variation of the liquid mass is balanced by the variation of the vapour phase, and conversely, which can be written:

$$d\left(\frac{\mathcal{M}_1}{\mathcal{M}}\right) + d\left(\frac{\mathcal{M}_2}{\mathcal{M}}\right) = 0.$$

These two additional rules modify the entropy equation (19) into the following equation:

$$\begin{aligned} d\tilde{\eta} = \quad & \mathcal{V}\left(\tfrac{P_1}{T_1} - \tfrac{P_3}{T_3}\right) d\left(\tfrac{\mathcal{V}_1}{\mathcal{V}}\right) + \mathcal{V}\left(\tfrac{P_2}{T_2} - \tfrac{P_3}{T_3}\right) d\left(\tfrac{\mathcal{V}_2}{\mathcal{V}}\right) \\ & + \mathcal{M}\left(\tfrac{\mu_2}{T_2} - \tfrac{\mu_1}{T_1}\right) d\left(\tfrac{\mathcal{M}_1}{\mathcal{M}}\right) \\ & + \mathcal{E}\left(\tfrac{1}{T_1} - \tfrac{1}{T_3}\right) d\left(\tfrac{\mathcal{E}_1}{\mathcal{E}}\right) + \mathcal{E}\left(\tfrac{1}{T_2} - \tfrac{1}{T_3}\right) d\left(\tfrac{\mathcal{E}_2}{\mathcal{E}}\right). \end{aligned} \tag{44}$$

Hence the Gibbs enthalpy of the inert phase μ_3 does not play any role in the entropy dissipation. Nevertheless, its pressure and its temperature are still part of the relaxation process, since the equilibrium state is now defined as:

$$\begin{aligned} & P_1(\overline{\mathcal{V}_1}, \overline{\mathcal{M}_1}, \overline{\mathcal{E}_1}) = P_2(\overline{\mathcal{V}_2}, \overline{\mathcal{M}_2}, \overline{\mathcal{E}_2}) = P_3(\overline{\mathcal{V}_3}, \overline{\mathcal{M}_3}, \overline{\mathcal{E}_3}), \\ & T_1(\overline{\mathcal{V}_1}, \overline{\mathcal{M}_1}, \overline{\mathcal{E}_1}) = T_2(\overline{\mathcal{V}_2}, \overline{\mathcal{M}_2}, \overline{\mathcal{E}_2}) = T_3(\overline{\mathcal{V}_3}, \overline{\mathcal{M}_3}, \overline{\mathcal{E}_3}), \\ & \mu_1(\overline{\mathcal{V}_1}, \overline{\mathcal{M}_1}, \overline{\mathcal{E}_1}) = \mu_2(\overline{\mathcal{V}_2}, \overline{\mathcal{M}_2}, \overline{\mathcal{E}_2}), \end{aligned} \tag{45}$$

where $\overline{\mathcal{M}_3} = \mathcal{M}_3$ is constant along the streamlines. Therefore, the system of equations (36) and the closure laws (37) are not modified. Nevertheless, the equilibrium fractions must be computed using the intensive form of the relations (45), that is:

$$\begin{aligned} & P_1\left(\tfrac{\overline{z_1}}{\overline{y_1}}e, \tfrac{\overline{\alpha_1}}{\overline{y_1}}\tau\right) = P_2\left(\tfrac{\overline{z_2}}{\overline{y_2}}e, \tfrac{\overline{\alpha_2}}{\overline{y_2}}\tau\right) = P_3\left(\tfrac{\overline{z_3}}{\overline{y_3}}e, \tfrac{\overline{\alpha_3}}{\overline{y_3}}\tau\right), \\ & T_1\left(\tfrac{\overline{z_1}}{\overline{y_1}}e, \tfrac{\overline{\alpha_1}}{\overline{y_1}}\tau\right) = T_2\left(\tfrac{\overline{z_2}}{\overline{y_2}}e, \tfrac{\overline{\alpha_2}}{\overline{y_2}}\tau\right) = T_3\left(\tfrac{\overline{z_3}}{\overline{y_3}}e, \tfrac{\overline{\alpha_3}}{\overline{y_3}}\tau\right), \\ & \mu_1\left(\tfrac{\overline{z_1}}{\overline{y_1}}e, \tfrac{\overline{\alpha_1}}{\overline{y_1}}\tau\right) = \mu_2\left(\tfrac{\overline{z_2}}{\overline{y_2}}e, \tfrac{\overline{\alpha_2}}{\overline{y_2}}\tau\right), \end{aligned} \tag{46}$$

where $\overline{y_3}(x,t) = y_3(x,t)$ for every point (x,t).

In order to deal with steam explosions, another mandatory ingredient for the model is to cope with external heating source terms. In particular, some complex chemical reactions occurring in the bulk of the inert phase may lead to an increase of its internal energy. For the sake of simplicity, these terms have been omitted in the previous sections and they are introduced here. In the following, we focus on the time variation of the mixture, and without loss of generality, we set $U = 0$. Let us assume that the heating of the mixture is such that:

$$\begin{aligned} & \text{(i)} \quad \text{the specific volume of each phase is constant,} \quad d(\tau_i) = 0; \\ & \text{(ii)} \quad \text{the partial mass of each phase is constant,} \quad d(\alpha_i\rho_i) = 0; \\ & \text{(iii)} \quad \text{the internal energy of each phase is such that,} \quad d(\alpha_i\rho_i e_i) = \alpha_i\rho_i q_i dt; \end{aligned} \tag{47}$$

where $q_i dt$ is the specific heat received by phase i. Thanks to the assumptions (i) and (ii), the specific volume of the mixture is constant $d(\tau) = 0$, and the volume and the mass fractions of the three phases are constant: $d(\alpha_i) = 0$ and $d(y_i) = 0$. We also get from (iii) that the variation of the specific energy of the mixture $\rho e = (\sum_i \alpha_i\rho_i e_i)$ is:

$$d(\rho e) = \sum_i \alpha_i\rho_i q_i dt = \rho\tilde{Q}dt,$$

where $\tilde{Q}$ has been introduced in Section 1.4. Then the time evolution of the energy fraction $z_i = (\alpha_i \rho_i e_i)/(\rho e)$ is:

$$\rho e \; d(z_i) = \alpha_i \rho_i q_i dt - z_i \rho \tilde{Q} dt = \rho(y_i q_i - z_i \tilde{Q}) dt.$$

Hence, when the phases are heated by an external source q_i, system of equations (36) becomes:

$$\left\{ \begin{array}{l} \dfrac{\partial}{\partial t}(\rho \alpha_i) + \dfrac{\partial}{\partial x}(\rho U \alpha_i) = \rho \Gamma_{\alpha_i}, \quad i = 1,2,3, \\ \dfrac{\partial}{\partial t}(\rho y_i) + \dfrac{\partial}{\partial x}(\rho U y_i) = \rho \Gamma_{y_i}, \quad i = 1,2,3, \\ \dfrac{\partial}{\partial t}(\rho z_i) + \dfrac{\partial}{\partial x}(\rho U z_i) = \rho \Gamma_{z_i} + \rho \dfrac{y_i q_i - z_i \tilde{Q}}{e}, \quad i = 1,2,3, \\ \dfrac{\partial}{\partial t}(\rho) + \dfrac{\partial}{\partial x}(\rho U) = 0, \\ \dfrac{\partial}{\partial t}(\rho U) + \dfrac{\partial}{\partial x}\left(\rho U^2 + P\right) = 0, \\ \dfrac{\partial}{\partial t}(\rho E) + \dfrac{\partial}{\partial x}(U(\rho E + P)) = \rho \tilde{Q}, \end{array} \right. \tag{48}$$

with $\tilde{Q} = \sum_i y_i q_i$, and $\sum_i \alpha_i = \sum_i y_i = \sum_i z_i = 1$. The source terms Γ_{α_i}, Γ_{y_i} and Γ_{z_i} are the source terms associated with the thermodynamical relaxation Γ_Y defined in (34). In our particular case, we recall that $\Gamma_{y_3} = 0$ since the phase 3 is inert.

Remark 3. *The positivity results of Section 2 for z_i still hold provided that q_i/e_i and $\tilde{Q}/e$ remain bounded. Indeed, the equation for z_i of system (48) can also be written:*

$$\frac{\partial}{\partial t}(z_i(x,t)) + U \frac{\partial}{\partial x}(z_i(x,t)) = a_i(x,t) z_i(x,t) + \Pi_i(x,t),$$

with $a_i = -1/\lambda + (q_i/e_i - \tilde{Q}/e)$ and $\Pi_i = \overline{z}_i/\lambda$. The lemma of Section 2 can then still be applied here.

Accounting for the phasic heating source terms represents an important feature of the model. The latter possesses three energy equations through: the energy fraction equations and the mixture energy equation, and this allows the user to specify how the energies of the three different phases vary according to external sources. This is typically not the case for the classical homogeneous model [9], which is widely used for industrial simulations.

4. An example of numerical simulation: steam explosion during a Reactivity Induced Accident

As an illustration of the capability of the model (48), we propose in this section a simple heating test case which may be seen as a simplified situation of RIA. A sketch of the test case has been plotted in Figure 1. We consider that some fuel particles are released from the fuel rod which has a radius $R_1 = 5\ 10^{-3}\ m$. Within the ring delimited by R_1 and $R_2 = 6\ 10^{-3}\ m$, the liquid water contains fuel particles with a volume fraction $\alpha_f = 0.01$, thus the liquid volume-fraction is $\alpha_l = 0.99$ and the steam volume-fraction $\alpha_v = 0$. The computational domain is the ring $[R_1, R_3 = 2\ 10^{-2}\ m]$. At the beginning of the simulation, $t = 0$, we assume that there is no vapor in the domain, and that the liquid and the fuel particles are at the same pressure $P = 155.0\ bars$ and at the same temperature $T = 613\ K$. We recall that the saturation temperature for the water at 155.0 *bars* is equal to 618 K. We also assume that the initial velocity is equal to zero.

A constant heating source term q_f is then applied at $t = 0$ to the fuel-particle phase according to system (48). This source term arises from the chemical reactions that occur in the fuel particles. It has been arbitrarily chosen equal to $q_f = 2\ 10^{10}\ W/kg$. It should be mentioned that in a more realistic RIA situation, the heating source term q_f is negligible with respect to the heat transfer due to the initial temperature disequilibrium between the liquid water and the fuel particles. Nevertheless, accounting for such disequilibrium requires a realistic time scale λ. This is the case when considering pressure disequilibrium for steam-liquid configurations as reported in [23], and this is also the case for temperature disequilibrium in the case of three-phase flows. For the sake of simplicity, we consider here an instantaneous relaxation time scale $\lambda = 0$ which unfortunately does not allow for strong initial temperature-disequilibrium.

The EOS for the liquid water and for the steam are based on the IAPWS 97 formulation [36], whereas the fuel particles are modeled using a Stiffened Gas EOS [28]. The specific entropy of the fuel-particle phase then reads:

$$s_f(\tau_f, e_f) = C_{V,f} \ln\left((e_f - Q_f - \tau_f \Pi_f)\tau_f^{\gamma_f}\right) + s_{0,f},$$

where $C_{V,f}$, Q_f, Π_f, γ_f, and $s_{0,f}$ are parameters. The corresponding pressure and temperature laws are:

$$P_f = (\gamma_f - 1)\frac{e_f - Q_f}{\tau_f} - \gamma_f \Pi_f, \quad \text{and} \quad T_f = \frac{e_f - Q_f - \tau_f \Pi_f}{C_{V,f}}.$$

Since there is no mass transfer involving the phase f, the parameter $s_{0,f}$ is useless and it has thus been set here to zero: $s_{0,f} = 0$. The other coefficients have been estimated using the data for uranium dioxide [1] at a temperature of 623 K. The specific enthalpy of the uranium dioxide, $h_f = e_f + P_f \tau_f$, is given as its difference to the reference specific enthalpy at $T = 298\ K$. Unfortunately, it seems that no information can be found on the latter. Hence we have arbitrarily chosen the value $h_0 = 5.0\ 10^4\ J/kg$. The other data, collected in [1], are:

$$\rho_f(623\ K) = 10850\ kg/m^3, \quad C_{P,f}(623\ K) = 294\ J/kg/K.$$

No information is available for the sound speed c_f and we, therefore, impose a value of $c_f = 6000\ m/s$ which is an order of magnitude of the sound speed for steel. The EOS parameters are then computed using the relations:

$$\begin{array}{rcl}
h_f = Q_f + C_{P,f}T = h_0 + C_{P,f}(T - 623) & \Longrightarrow & Q_f = h_0 - C_{P,f} \times 623 \\
c_f^2 = (\gamma_f - 1)C_{P,f}T & \Longrightarrow & \gamma_f = 1 + \frac{c_f^2}{C_{P,f}T} \\
C_{P,f} = \gamma_f C_{V,f} & \Longrightarrow & C_{V,f} = \frac{C_{P,f}}{\gamma_f} \\
\rho_f = \frac{P + \Pi_f}{(\gamma_f - 1)C_{V,f}T} & \Longrightarrow & \Pi_f = (\gamma_f - 1)\rho_f C_{V,f} T - P
\end{array}$$

where the pressure is $P = 155.0\ 10^5\ Pa$.

By the way of a comparison, we also perform a simulation without fuel particle (i.e. $\alpha_f = y_f = z_f = 0$). The heating source term q'_f is then applied to the vapour and to the liquid: $q_l = q_v = q'_f$ in the fixed domain $[R_1, R_2]$. According to (48), the specific heat received by the mixture is then $(y_l q_l + y_v q_v)dt = q'_f\ dt$. In the simulation with fuel particles, the mass of fuel is conserved and the total heat received by the mixture is linearly increasing with time. On the other hand, in the simulation without fuel particle, the heat is received by a fixed volume that contains a non-constant mass of mixture. Roughly speaking, the mass of fluid in the domain $[R_1, R_2]$ decreases when the time increases because the temperature increases due to the heating of the fluid. It is thus not easy to predict the total amount of heat received by the mixture for the simulation without fuel particle. For the comparison, we impose *equivalent initial heating source terms*. For the simulation involving fuel particles, it is equal to:

$$\alpha_f \rho_f\ q_f\ V \sim 0.01 \times 10850\ q_f\ V,$$

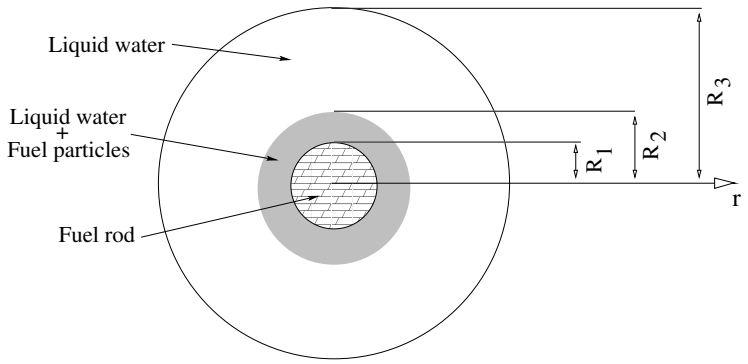

FIGURE 1. Geometrical sketch of the test case of Section 4: a cylindrical fuel rod (radius R_1) releases some hot fuel particles in the neighboring liquid (radius R_2). The computational domain corresponds to the fluid domain $r \in [R_1, R_3]$.

and for the simulation without fuel particle:

$$\alpha_l \rho_l \; q'_f \; V \sim 1.0 \times 680 \; q'_f \; V,$$

where V is the volume between R_1 and R_2. If we impose the two quantities to be equal, this yields $q'_f \sim 680/108.50 \; q_f$. We insist that the total amounts of heat injected in the domains during the whole simulations are different. Since for the simulation without fuel particle, the specific heat is injected in a fixed domain with a diminishing amount of mass (due to the increase of the temperature, the density decreases), the total amount of heat injected is indeed lower than for the simulation with the fuel particles.

The numerical scheme used to obtain the approximated solutions of system (48) is classical. Since the test case considered here is symmetric with respect to the axis $r = 0$, system (48) is written in axi-symmetric formulation. The overall scheme is based on a fractional step approach [37] in which the convective part and the source terms are treated successively. For the convective part, the numerical scheme is a finite volume scheme [11] where the numerical fluxes are approximated by a Rusanov scheme [34]. The relaxation source terms are then solved following the scheme described in [23]. The main difficulty concerning these source terms is to compute the equilibrium fractions. This computation follows the idea of [13, 23] when the equilibrium is a liquid-steam-fuel equilibrium or a liquid-steam equilibrium. When the equilibrium involves the solid phase and only one phase among the water phases, the pressure-temperature equilibrium is solved using a classical Broyden method with Sherman-Morrison update of the inverse of the Jacobian [5, 6, 35]. Accounting for the heating source term is the last step of the algorithm; its is discretized using a semi-implicit Euler scheme that preserves the positivity of the energy fractions. In the latter the heating source terms q_i are explicited and the system of ordinary differential equations associated to the heating source term is then solved analytically. In our simulation, the source terms q_i are constant so that the scheme corresponds to an exact integration of the heating source terms for each time-step.

The overall scheme described above is then used to perform the two simulations for a mesh with 4000 cells and with a uniform radial mesh-size. In Figure 2 the values across the time are plotted at $r = (R_1 - R_2)/2$, whereas different pressure and volume-fraction profiles along the radius r are plotted at five different instants in Figure 3. The Figure 4 shows the trajectory in time of each simulation in the pressure-temperature plane. The results obtained for the two configurations exhibit significant differences. First of all, since the time-scale λ has been chosen equal to zero, the thermodynamical equilibrium is achieved instantaneously. Hence, when the mixture fractions are in $]0, 1[$ the two phases have the same pressure and temperature which are on the saturation curve.

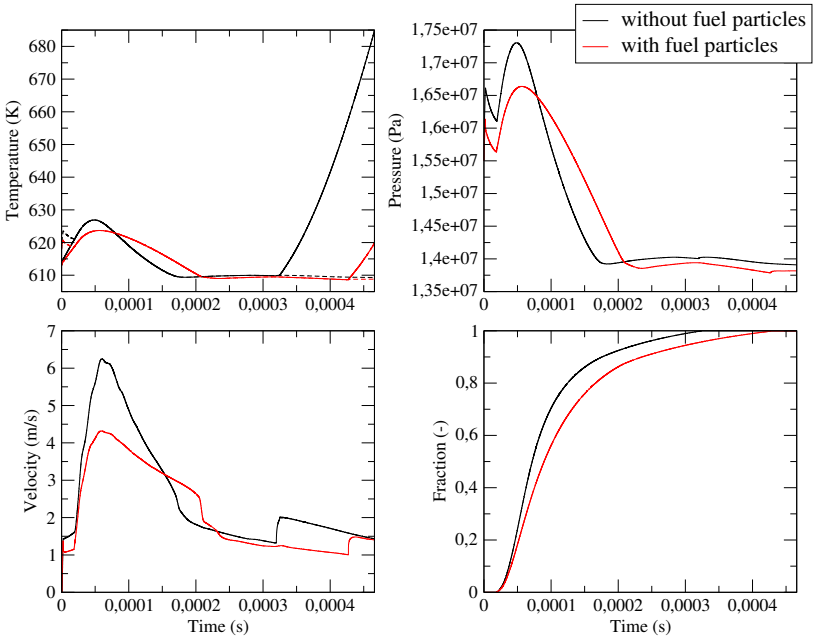

FIGURE 2. Temperature (temperature : plain line, saturation temperature : dashed line), pressure, velocity and volume fraction with respect to the time at the radius $r = (R_1 + R_2)/2$ (i.e. the center of the initial heating zone). The black curves represent the simulation without fuel particle, and the red curves represent the results for the simulation with fuel particles.

This can be verified with the trajectories of Figure 4 and with the temperature/volume fraction curves of Figure 2. When considering the time evolution of the results in the heating zone (see Figures 2 and 4), the simulation can be split into three periods which are:

- the heating of the liquid, which corresponds to the beginning of the simulation, until the steam volume-fraction becomes positive;
- the vaporization of the liquid, which corresponds to the time interval for which the volume-fraction is in $]0, 1[$;
- and the heating of the steam, which corresponds to the end of the simulation, when the steam volume-fraction is equal to 1.

In the heating zone, the maximum of the pressure magnitude arises during the second period. It can be observed that the simulation with fuel particles reaches a lower pressure which then decreases slower in time. The pressure wave that is then generated through the domain (see Figure 3) has a lower magnitude. It can also be seen from Figure 2 that in the heating zone the apparition of steam arises at almost the same time (at time $1.86\ 10^{-5}\ s$ with fuel particles and $1.94\ 10^{-5}\ s$ without fuel particle), whereas the complete vaporization of the liquid is achieved earlier without fuel particle (at time $4.227\ 10^{-4}\ s$ with fuel particles and $3.25\ 10^{-4}\ s$ without fuel particle). Once the heating zone only contains steam, the temperature rapidly increases. Hence, despite the lower amount of energy received by the fluid in the simulation without fuel particle, the associated results seem to correspond to a slightly more important level of severity of the steam explosion.

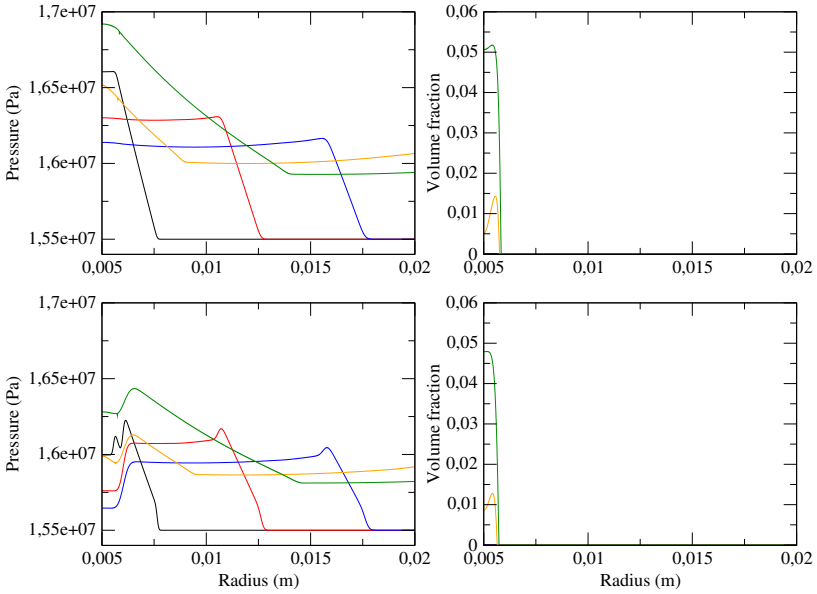

FIGURE 3. Pressure (left) en volume fraction (right) along the radius r at different times: black at $t = 2.44\ 10^{-6}\ s$, red at $t = 9.74\ 10^{-6}\ s$, blue at $t = 1.17\ 10^{-5}\ s$, orange at $t = 2.44\ 10^{-5}\ s$, and at green $t = 3.17\ 10^{-5}\ s$. The two upper plots correspond to the simulation without fuel particle and the two lower plots to the simulation with fuel particles. The steam appears in the domain at around $t = 1.9\ 10^{-5}\ s$.

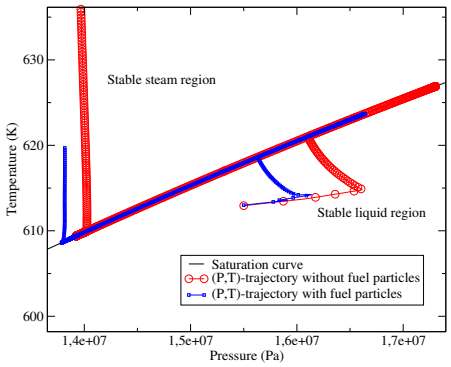

FIGURE 4. Trajectories in the pressure-temperature plane along the simulation time at the radius $r = (R_1 + R_2)/2$ (i.e. the center of the initial heating zone). The simulation without fuel particle is plotted using red circles, and the simulation with fuel particles is plotted using blue squares. The black plain line represents the saturation curve.

CONCLUSION

The homogeneous three-phase flow model proposed here relies on Newton's law, the first and second laws of thermodynamics. It accounts for the compressibility of the three phases and for the heat and the mass transfer between the phases through the thermodynamical disequilibrium between the phases (in terms of pressure, temperature and Gibbs enthalpy). Since no equilibrium assumption is done, the model should not be restricted

to the representation of thermodynamical phenomenon at "large time-scale" and fine physical aspects of the thermodynamics might be caught. This feature seems mandatory when dealing with fast transient flows induced by the flashing of some liquid. From a mathematical point of view, the resulting model possesses very interesting properties, which allows to build efficient numerical schemes. In Section 4, an example of the simulations of the flashing of liquid water undergoing a violent heating has therefore been proposed to illustrate the capability of the model to be used in an industrial configuration. Even if the relaxation time-scale used in these simulations has been set to zero, the homogeneous model proposed in this paper allows to perform transient simulations involving strong pressure waves. Actually, some realistic models for the relaxation time-scale should be proposed on the basis of physical considerations in order to improve the simulations of Section 4.

5. Appendices

5.1. Properties of the extensive mixture-entropy

In this section, we give the proofs that the intensive mixture-entropy (7) is such that:

(i) $W \to \eta(W)$ is C^2 on $(\mathbb{R}_+)^9$;
(ii) $W \to \eta(W)$ is concave;
(iii) $\forall a \in \mathbb{R}_+^*,\ \forall W \in (\mathbb{R}_+)^9,\ \eta(aW) = a\eta(W)$;

where we set $W_i = (\mathcal{V}_i, \mathcal{M}_i, \mathcal{E}_i)$ and, with a small abuse of notation,

$$W = (W_1, W_2, W_3) = (\mathcal{V}_1, \mathcal{M}_1, \mathcal{E}_1, \mathcal{V}_2, \mathcal{M}_2, \mathcal{E}_2, \mathcal{V}_3, \mathcal{M}_3, \mathcal{E}_3).$$

The mixture entropy then reads: $\eta(W) = \sum_i \eta_i(W_i)$.

Proof of property (i). The use of assumption (H_4) gives a straightforward proof of property (i).

Proof of property (ii). Thanks to assumption (H_5), we know that $W_i \mapsto \eta_i(W_i)$ is concave. So that we have:

$$\forall (\tilde{W}_i, \bar{W}_i) \in (\mathbb{R}_+)^3 \times (\mathbb{R}_+)^3,\ \forall a \in [0,1],\ \eta_i(a\tilde{W}_i + (1-a)\bar{W}_i) \geq a\eta_i(\tilde{W}_i) + (1-a)\eta_i(\bar{W}_i).$$

Let us choose $(\tilde{W}, \bar{W}) \in (\mathbb{R}_+)^9 \times (\mathbb{R}_+)^9$ and $a \in [0,1]$. We have:

$$\begin{aligned} \eta(a\tilde{W} + (1-a)\bar{W}) = &\ \textstyle\sum_i \eta_i(a\tilde{W}_i + (1-a)\bar{W}_i) \\ &\geq \textstyle\sum_i a\eta_i(\tilde{W}_i) + (1-a)\eta_i(\bar{W}_i) \quad = a\eta(\tilde{W}) + (1-a)\eta(\bar{W}), \end{aligned}$$

which proves that $W \to \eta(W)$ is concave on $(\mathbb{R}_+)^9$.

Proof of property (iii). We use here assumption (H_6) which states that:

$$\forall a \in \mathbb{R}_+^*,\ \forall W_i \in (\mathbb{R}_+)^3,\ \eta_i(aW_i) = a\eta_i(W_i).$$

Let us choose $W \in (\mathbb{R}_+)^9$ and $a > 0$. Then we have:

$$\eta(aW) = \sum_i \eta_i(aW_i) = a \sum_i \eta_i(W_i) = a\eta(W).$$

5.2. Concavity of the mixture entropy $\tilde{\eta}$

The entropy $\tilde{\eta}$ is the restriction of η on $\mathcal{H}(\mathcal{M}) \subset (\mathbb{R}_+)^9$:

$$\mathcal{H}(\mathcal{M}) = \left\{ W \in (\mathbb{R}_+)^9; \sum_i \mathcal{M}_i = \mathcal{M} \right\}.$$

We then have:

$$\forall \tilde{W} \in \mathcal{H}(\mathcal{M}),\ \tilde{\eta}(\tilde{W}) = \eta(\tilde{W}).$$

Obviously, since η fulfills properties (i)-(iii) recalled in Appendix 5.1, the entropy $\tilde{\eta}$ satisfies:

(i) $W \to \tilde{\eta}(W)$ is C^2 on $\mathcal{H}(\mathcal{M})$;
(ii) $W \to \tilde{\eta}(W)$ is concave;
(iii) $\forall a \in \mathbb{R}_+^*,\ \forall W \in \mathcal{H}(\mathcal{M}),\ \tilde{\eta}(aW) = a\tilde{\eta}(W)$;

The demonstration given here can be found in a more general form in [26]. The sketch of the proof is the following. We first exhibit the degeneracy manifold of the Hessian of the entropy η. Then we prove that its intersection with $\mathcal{H}(\mathcal{M})$ contains a single point. As a consequence, the degeneracy manifold of the Hessian of $\tilde{\eta}$ also resumes to a single point, which proves that it is strictly concave.

Let us choose $a > 0$ and $X \in (\mathbb{R}_+)^9$. We then set $Y = aX$. By deriving $\eta(Y)$ with respect to X, we get:

$$\nabla_X \left(\eta(Y)\right) = \nabla_Y \left(\eta(Y)\right) \cdot \nabla_X \left(Y\right) = a \nabla_Y \left(\eta(Y)\right).$$

Since we have $\eta(Y) = \eta(aX) = a\eta(X)$, and since $a \neq 0$, we have:

$$\nabla_Y \left(\eta(Y)\right) = \nabla_X \left(\eta(X)\right).$$

If we derive the relation above with respect to a, we find that:

$$0 = \frac{\partial}{\partial a} \left(\nabla_X \left(\eta(X)\right)\right) = \frac{\partial}{\partial a} \left(\nabla_Y \left(\eta(Y)\right)\right) = \nabla_Y^2 \left(\eta(Y)\right) \cdot \frac{\partial}{\partial a} \left(Y\right) = \nabla_Y^2 \left(\eta(Y)\right) \cdot X,$$

and, thus:

$$\nabla_Y^2 \left(\eta(Y)\right) \cdot X = 0,$$

which for $a = 1$ leads to:

$$\nabla_Y^2 \left(\eta(Y)\right) \cdot Y = 0.$$

The degeneracy manifold of the Hessian of the entropy η at a point W is thus the set $\mathcal{D}_\eta(W) = \{bW, b \in \mathbb{R}\}$. This implies that the entropy η can not be strictly concave.

For any point W in $\mathcal{H}(\mathcal{M})$, we have $\sum_i \mathcal{M}_i = \mathcal{M}$. Hence, for all $b > 0$, bW is such that $\sum_i b\mathcal{M}_i = b\mathcal{M}$, and bW is not in $\mathcal{H}(\mathcal{M})$ except if $b = 1$. So that we have:

$$\forall W \in \mathcal{H}(\mathcal{M}),\ \mathcal{H}(\mathcal{M}) \cap \mathcal{D}_\eta(W) = \{W\}.$$

This proves that the kernel of the Hessian $\tilde{\eta}$, the restriction of η to $\mathcal{H}(\mathcal{M})$, is restricted to a single point. As a consequence, $\tilde{\eta}$ is strictly concave on $\mathcal{H}(\mathcal{M})$.

5.3. **Concavity of the intensive entropies**

We first demonstrate that the phasic intensive entropy s_i, introduced in Section 1.2:

$$\mathcal{M}_i \ s_i \left(\frac{\mathcal{V}_i}{\mathcal{M}_i}, \frac{\mathcal{E}_i}{\mathcal{M}_i}\right) = \eta_i(\mathcal{V}_i, \mathcal{M}_i, \mathcal{E}_i),$$

is concave with respect to $(\mathcal{V}_i/\mathcal{M}_i, \mathcal{E}_i/\mathcal{M}_i)$. We choose two sets of variables $(\mathcal{V}_i^*, \mathcal{M}_i^*, \mathcal{E}_i^*)$ and $(\mathcal{V}_i^\#, \mathcal{M}_i^\#, \mathcal{E}_i^\#)$ in $(\mathbb{R}_+)^3$ such that $\mathcal{M}_i^\# = \mathcal{M}_i^* = \mathcal{M}_i$. We then have for any $a \in [0, 1]$:

$$\begin{aligned} a\mathcal{M}_i^* s_i \left(\tfrac{\mathcal{V}_i^*}{\mathcal{M}_i^*}, \tfrac{\mathcal{E}_i^*}{\mathcal{M}_i^*}\right) + (1-a)\mathcal{M}_i^\# s_i \left(\tfrac{\mathcal{V}_i^\#}{\mathcal{M}_i^\#}, \tfrac{\mathcal{E}_i^\#}{\mathcal{M}_i^\#}\right) = \\ a\eta_i(\mathcal{V}_i^*, \mathcal{M}_i^*, \mathcal{E}_i^*) + (1-a)\eta_i(\mathcal{V}_i^\#, \mathcal{M}_i^\#, \mathcal{E}_i^\#). \end{aligned}$$

Thanks to the concavity of $(\mathcal{V}_i, \mathcal{M}_i, \mathcal{E}_i) \mapsto \eta_i(\mathcal{V}_i, \mathcal{M}_i, \mathcal{E}_i)$ (assumption (H_5)), we get that:

$$\begin{aligned} a\mathcal{M}_i^* s_i \left(\tfrac{\mathcal{V}_i^*}{\mathcal{M}_i^*}, \tfrac{\mathcal{E}_i^*}{\mathcal{M}_i^*}\right) + (1-a)\mathcal{M}_i^\# s_i \left(\tfrac{\mathcal{V}_i^\#}{\mathcal{M}_i^\#}, \tfrac{\mathcal{E}_i^\#}{\mathcal{M}_i^\#}\right) \leq \\ \eta_i(a\mathcal{V}_i^* + (1-a)\mathcal{V}_i^\#, a\mathcal{M}_i^* + (1-a)\mathcal{M}_i^\#, a\mathcal{E}_i^* + (1-a)\mathcal{E}_i^\#). \end{aligned}$$

Hence, following the definition of the entropy s_i, we have:

$$a\mathcal{M}_i^* s_i\left(\frac{\mathcal{V}_i^*}{\mathcal{M}_i^*},\frac{\mathcal{E}_i^*}{\mathcal{M}_i^*}\right)+(1-a)\mathcal{M}_i^{\#} s_i\left(\frac{\mathcal{V}_i^{\#}}{\mathcal{M}_i^{\#}},\frac{\mathcal{E}_i^{\#}}{\mathcal{M}_i^{\#}}\right)\leq (a\mathcal{M}_i^*+(1-a)\mathcal{M}_i^{\#})s_i\left(\frac{a\mathcal{V}_i^*+(1-a)\mathcal{V}_i^{\#}}{(a\mathcal{M}_i^*+(1-a)\mathcal{M}_i^{\#})},\frac{a\mathcal{E}_i^*+(1-a)\mathcal{E}_i^{\#}}{(a\mathcal{M}_i^*+(1-a)\mathcal{M}_i^{\#})}\right).$$

The assumption that $\mathcal{M}_i^{\#}=\mathcal{M}_i^*=\mathcal{M}_i$ allows to obtain:

$$as_i\left(\frac{\mathcal{V}_i^*}{\mathcal{M}_i^*},\frac{\mathcal{E}_i^*}{\mathcal{M}_i^*}\right)+(1-a)s_i\left(\frac{\mathcal{V}_i^{\#}}{\mathcal{M}_i^{\#}},\frac{\mathcal{E}_i^{\#}}{\mathcal{M}_i^{\#}}\right)\quad\leq\quad s_i\left(\frac{a\mathcal{V}_i^*+(1-a)\mathcal{V}_i^{\#}}{\mathcal{M}_i},\frac{a\mathcal{E}_i^*+(1-a)\mathcal{E}_i^{\#}}{\mathcal{M}_i}\right).$$

and we obviously have:

$$\begin{aligned}s_i\left(\frac{a\mathcal{V}_i^*+(1-a)\mathcal{V}_i^{\#}}{\mathcal{M}_i},\frac{a\mathcal{E}_i^*+(1-a)\mathcal{E}_i^{\#}}{\mathcal{M}_i}\right)&=s_i\left(a\frac{\mathcal{V}_i^*}{\mathcal{M}_i}+(1-a)\frac{\mathcal{V}_i^{\#}}{\mathcal{M}_i},a\frac{\mathcal{E}_i^*}{\mathcal{M}_i}+(1-a)\frac{\mathcal{E}_i^{\#}}{\mathcal{M}_i}\right)\\&=s_i\left(a\frac{\mathcal{V}_i^*}{\mathcal{M}_i^*}+(1-a)\frac{\mathcal{V}_i^{\#}}{\mathcal{M}_i^{\#}},a\frac{\mathcal{E}_i^*}{\mathcal{M}_i^*}+(1-a)\frac{\mathcal{E}_i^{\#}}{\mathcal{M}_i^{\#}}\right),\end{aligned}$$

so that we finally get

$$as_i\left(\frac{\mathcal{V}_i^*}{\mathcal{M}_i^*},\frac{\mathcal{E}_i^*}{\mathcal{M}_i^*}\right)+(1-a)s_i\left(\frac{\mathcal{V}_i^{\#}}{\mathcal{M}_i^{\#}},\frac{\mathcal{E}_i^{\#}}{\mathcal{M}_i^{\#}}\right)\leq s_i\left(a\frac{\mathcal{V}_i^*}{\mathcal{M}_i^*}+(1-a)\frac{\mathcal{V}_i^{\#}}{\mathcal{M}_i^{\#}},a\frac{\mathcal{E}_i^*}{\mathcal{M}_i^*}+(1-a)\frac{\mathcal{E}_i^{\#}}{\mathcal{M}_i^{\#}}\right).$$

As a consequence, the intensive phasic entropy

$$(\mathcal{V}_i/\mathcal{M}_i,\mathcal{E}_i/\mathcal{M}_i)\mapsto s_i(\mathcal{V}_i/\mathcal{M}_i,\mathcal{E}_i/\mathcal{M}_i)$$

is concave with respect to $(\mathcal{V}_i/\mathcal{M}_i,\mathcal{E}_i/\mathcal{M}_i)$.

We consider now the intensive mixture entropy S (26) defined on $\mathcal{H}(\mathcal{M})$ by:

$$\mathcal{M}\ S(Y,\tau,e)=\tilde{\eta}(W).$$

We set

$$\tau=\frac{\mathcal{V}}{\mathcal{M}},\ e=\frac{\mathcal{E}}{\mathcal{M}},\ Y=(\alpha_1,y_1,z_1,\alpha_2,y_2,z_2,\alpha_3,y_3,z_3),\ \alpha_i=\frac{\mathcal{V}_i}{\mathcal{V}},\ y_i=\frac{\mathcal{M}_i}{\mathcal{M}},\ z_i=\frac{\mathcal{E}_i}{\mathcal{E}}.$$

We choose two points:

$$W^*=(\mathcal{V}_1^*,\mathcal{M}_1^*,\mathcal{E}_1^*,\mathcal{V}_2^*,\mathcal{M}_2^*,\mathcal{E}_2^*,\mathcal{V}_3^*,\mathcal{M}_3^*,\mathcal{E}_3^*),$$

and

$$W^{\#}=(\mathcal{V}_1^{\#},\mathcal{M}_1^{\#},\mathcal{E}_1^{\#},\mathcal{V}_2^{\#},\mathcal{M}_2^{\#},\mathcal{E}_2^{\#},\mathcal{V}_3^{\#},\mathcal{M}_3^{\#},\mathcal{E}_3^{\#}),$$

such that $\sum_i\mathcal{M}_i^*=\mathcal{M}^*=\mathcal{M}$ and $\sum_i\mathcal{M}_i^{\#}=\mathcal{M}^{\#}=\mathcal{M}=\mathcal{M}'$. We then have $(W^*,W^{\#})\in\mathcal{H}(\mathcal{M})\times\mathcal{H}(\mathcal{M})$. For any $a\in[0,1]$, thanks to the strict concavity of $\tilde{\eta}$ on $\mathcal{H}(\mathcal{M})$, we have:

$$\begin{aligned}a\mathcal{M}^*S\left(Y^*,\tau^*,e^*\right)+(1-a)\mathcal{M}^{\#}S\left(Y^{\#},\tau^{\#},e^{\#}\right)&=a\tilde{\eta}\left(W^*\right)+(1-a)\tilde{\eta}\left(W^{\#}\right)\\&<\tilde{\eta}\left(aW^*+(1-a)W^{\#}\right)\end{aligned}\tag{49}$$

where

$$\begin{aligned}&\tau^*=\frac{\mathcal{V}^*}{\mathcal{M}^*},\ e^*=\frac{\mathcal{E}^*}{\mathcal{M}^*},\\&Y^*=(\alpha_1^*,y_1^*,z_1^*,\alpha_2^*,y_2^*,z_2^*,\alpha_3^*,y_3^*,z_3^*),\ \alpha_i^*=\frac{\mathcal{V}_i^*}{\mathcal{V}^*},\ y_i^*=\frac{\mathcal{M}_i^*}{\mathcal{M}^*},\ z_i^*=\frac{\mathcal{E}_i^*}{\mathcal{E}^*},\\&\tau^{\#}=\frac{\mathcal{V}^{\#}}{\mathcal{M}^{\#}},\ e^{\#}=\frac{\mathcal{E}^{\#}}{\mathcal{M}^{\#}},\\&Y^{\#}=(\alpha_1^{\#},y_1^{\#},z_1^{\#},\alpha_2^{\#},y_2^{\#},z_2^{\#},\alpha_3^{\#},y_3^{\#},z_3^{\#}),\ \alpha_i^{\#}=\frac{\mathcal{V}_i^{\#}}{\mathcal{V}^{\#}},\ y_i^{\#}=\frac{\mathcal{M}_i^{\#}}{\mathcal{M}^{\#}},\ z_i^{\#}=\frac{\mathcal{E}_i^{\#}}{\mathcal{E}^{\#}}.\end{aligned}$$

The definition of the entropy S leads to:

$$\tilde{\eta}\left(aW^* + (1-a)W^{\#}\right) \quad = \quad \mathcal{M}' S\left(Y', \tau', e'\right), \tag{50}$$

with the following definitions:

$$\mathcal{M}' = a\mathcal{M}^* + (1-a)\mathcal{M}^{\#} = \mathcal{M}, \quad \tau' = \frac{a\mathcal{V}^* + (1-a)\mathcal{V}^{\#}}{a\mathcal{M}^* + (1-a)\mathcal{M}^{\#}}, \quad e' = \frac{a\mathcal{E}^* + (1-a)\mathcal{E}^{\#}}{a\mathcal{M}^* + (1-a)\mathcal{M}^{\#}},$$
$$\alpha_i' = \frac{a\mathcal{V}_i^* + (1-a)\mathcal{V}_i^{\#}}{a\mathcal{V}^* + (1-a)\mathcal{V}^{\#}}, \quad y_i' = \frac{a\mathcal{M}_i^* + (1-a)\mathcal{M}_i^{\#}}{a\mathcal{M}^* + (1-a)\mathcal{M}^{\#}}, \quad z_i' = \frac{a\mathcal{E}_i^* + (1-a)\mathcal{E}_i^{\#}}{a\mathcal{E}^* + (1-a)\mathcal{E}^{\#}}.$$

Hence, by combining equations (49) and (50), and by using the fact that $\mathcal{M}^* = \mathcal{M}^{\#} = \mathcal{M}$, we finally get:

$$aS\left(Y^*, \tau^*, e^*\right) + (1-a)S\left(Y^{\#}, \tau^{\#}, e^{\#}\right) < S\left(Y', \tau', e'\right). \tag{51}$$

Since we have $\mathcal{M}^* = \mathcal{M}^{\#}$, the specific volumes τ', the specific energy e' and the mass fraction y_i' can be written:

$$\tau' = a\tau^* + (1-a)\tau^{\#}, \quad e' = ae^* + (1-a)e^{\#} \quad \text{and} \quad y_i' = ay_i^* + (1-a)y_i^{\#}.$$

The volume fraction α_i' and the energy fraction z_i' are not specific quantities and they can thus not be written using the same weights a. We get for the volume fraction:

$$\alpha_i' = \frac{a\mathcal{V}^*}{a\mathcal{V}^* + (1-a)\mathcal{V}^{\#}}\alpha_i^* + \frac{(1-a)\mathcal{V}^{\#}}{a\mathcal{V}^* + (1-a)\mathcal{V}^{\#}}\alpha_i^{\#},$$

and for the energy fraction

$$z_i' = \frac{a\mathcal{E}^*}{a\mathcal{E}^* + (1-a)\mathcal{E}^{\#}}z_i^* + \frac{(1-a)\mathcal{E}^{\#}}{a\mathcal{E}^* + (1-a)\mathcal{E}^{\#}}z_i^{\#}.$$

We can now obtain easily two results of concavity for the specific mixture-entropy S.

First, if we assume that $\mathcal{V}^* = \mathcal{V}^{\#} = \mathcal{V}$ and $\mathcal{E}^* = \mathcal{E}^{\#} = \mathcal{E}$, the volume fraction and the energy fraction are $\alpha_i' = a\alpha_i^* + (1-a)\alpha_i^{\#}$ and $z_i' = az_i^* + (1-a)z_i^{\#}$. Moreover, the specific volume of the mixture is $\tau = \tau' = \tau^* = \tau^{\#}$ and the specific energy of the mixture is $e = e' = e^* = e^{\#}$. Therefore, relation (51) becomes:

$$aS\left(Y^*, \tau^*, e^*\right) + (1-a)S\left(Y^{\#}, \tau^{\#}, e^{\#}\right) < S\left(a(Y^*, \tau^*, e^*) + (1-a)(Y^{\#}, \tau^{\#}, e^{\#})\right),$$

which proves that, for a given mixture specific volume τ and a given specific energy e, the specific mixture entropy S is strictly concave:

$$\forall(\tau, e) \in (\mathbb{R}_+^*)^2, \quad Y \mapsto S(Y, \tau, e) \quad \text{is strictly concave.}$$

This result is important because it ensures that for a closed system (i.e. $de = d\tau = 0$) the equilibrium fraction $\overline{Y}$ defining the thermodynamical equilibrium is uniquely defined.

If we now assume that $\alpha_i^* = \alpha_i^{\#}$ and $z_i^* = z_i^{\#}$, we get that $\alpha' = \alpha_i^* = \alpha_i^{\#}$ and $z' = z_i^* = z_i^{\#}$. Relation (51) then becomes:

$$aS\left(Y^*, \tau^*, e^*\right) + (1-a)S\left(Y^{\#}, \tau^{\#}, e^{\#}\right) < S\left(a(Y^*, \tau^*, e^*) + (1-a)(Y^{\#}, \tau^{\#}, e^{\#})\right),$$

which proves that for a given fraction Y, the specific mixture entropy S is strictly concave:

$$\forall Y \in [0,1]^3, \quad (\tau, e) \mapsto S(Y, \tau, e) \quad \text{is strictly concave.}$$

This property allows to define in a unique manner the shock waves for system (36). Indeed, when considering a Riemann problem for the convective part of system (36), it can be noticed that the fractions Y only vary through the contact wave U. Hence the fractions Y are constant across a shock wave. The property above then ensures that the specific entropy S is strictly concave through the shock waves.

References

[1] Thermophysical properties of materials for nuclear engineering: A tutorial and collection of data. Technical report, International Atomic Energy Agency, IAEA-THPH, 2008.

[2] M.R. Baer and J.W. Nunziato. A two-phase mixture theory for the deflagration-to-detonation transition (ddt) in reactive granular materials. *International journal of multiphase flow*, 12(6):861–889, 1986.

[3] T. Barberon and P. Helluy. Finite volume simulation of cavitating flows. *Computers & fluids*, 34(7):832–858, 2005.

[4] G. Berthoud. Vapor explosions. *Annual Review of Fluid Mechanics*, 32(1):573–611, 2000.

[5] C.G. Broyden. A class of methods for solving nonlinear simultaneous equations. *Mathematics of computation*, 19(92):577–593, 1965.

[6] C.G. Broyden. On the discovery of the "good broyden" method. *Mathematical programming*, 87(2):209–213, 2000.

[7] H. B. Callen. *Thermodynamics and an Introduction to Thermostatistics*. Willey, 1985.

[8] F. Crouzet, F. Daude, P. Galon, J.-M. Hérard, O. Hurisse, and Y. Liu. Validation of a two-fluid model on unsteady liquid–vapor water flows. *Computers & Fluids*, 119:131–142, 2015.

[9] P. Downar-Zapolski, Z. Bilicki, L. Bolle, and J. Franco. The non-equilibrium relaxation model for one-dimensional flashing liquid flow. *International journal of multiphase flow*, 22(3):473–483, 1996.

[10] F. Drui, A. Larat, S. Kokh, and M. Massot. A hierarchy of simple hyperbolic two-fluid models for bubbly flows. *arXiv preprint arXiv:1607.08233*, 2016.

[11] R. Eymard, T. Gallouët, and R. Herbin. Finite volume methods. *Handbook of numerical analysis*, 7:713–1018, 2000.

[12] G. Faccanoni. *Study of a Fine Model of Liquid-Vapor Phase Change. Contribution to the Boiling Crisis Study.* Phd thesis, Ecole Polytechnique X (France) - Università di Trento (Italie), November 2008, https://pastel.archives-ouvertes.fr/tel-00363460.

[13] G. Faccanoni, S. Kokh, and G. Allaire. Modelling and simulation of liquid-vapor phase transition in compressible flows based on thermodynamical equilibrium. *ESAIM: Mathematical Modelling and Numerical Analysis*, 46(5):1029–1054, 2012.

[14] T. Gallouët, P. Helluy, J.-M. Hérard, and J. Nussbaum. Hyperbolic relaxation models for granular flows. *ESAIM: Mathematical Modelling and Numerical Analysis*, 44(2):371–400, 2010.

[15] S. Gavrilyuk and R. Saurel. Mathematical and numerical modeling of two-phase compressible flows with micro-inertia. *Journal of Computational Physics*, 175(1):326–360, 2002.

[16] E. Godlewski and P.-A. Raviart. *Numerical approximation of hyperbolic systems of conservation laws*, volume 118. Springer Science & Business Media, 2013.

[17] V. Guillemaud. *Modelling and numerical simulation of two-phase flows using the two-fluid two-pressure approach.* Phd thesis, Université de Provence - Aix-Marseille I, March 2007, https://tel.archives-ouvertes.fr/tel-00169178.

[18] P. Helluy and N. Seguin. Relaxation models of phase transition flows. *ESAIM: Mathematical Modelling and Numerical Analysis*, 40(2):331–352, 2006.

[19] J.-M. Hérard. An hyperbolic three-phase flow model. *Comptes rendus hebdomadaires des séances de l'Académie des sciences*, 2006.

[20] J.-M. Hérard. A three-phase flow model. *Mathematical and Computer Modelling*, 45:732–755, 2007.

[21] J.-M. Hérard and O. Hurisse. A simple method to compute standard two-fluid models. *International Journal of Computational Fluid Dynamics*, 19(7):475–482, 2005.

[22] O. Hurisse. Application of an homogeneous model to simulate the heating of two-phase flows. *International Journal on Finite Volumes*, 11:1–37, May 2014, https://hal.archives-ouvertes.fr/hal-01114808.

[23] O. Hurisse. Numerical simulations of steady and unsteady two-phase flows using a homogeneous model. *Computers and Fluids*, 152:88–103, July 2017.

[24] M. Ishii. *Thermofluid dynamic theory of two-phase flow*. Collection de la Direction des Etudes et Recherches d'Electricité de France, Collection Eyrolles, 1975.

[25] L. Jernkvist and A. Massih. Nuclear fuel behaviour under reactivity-initiated accident (ria) condition: State-of-the-art report. Technical report, Nuclear Energy Agency, Organisation for Economic Co-operation and Development, NEA/CSNI/R(2010)1, 2010.

[26] J. Jung. *Numerical simulations of two-fluid flow on multicores accelerator*. Phd thesis, Université de Strasbourg, October 2013, https://tel.archives-ouvertes.fr/tel-00876159.

[27] A.K. Kapila, S.F. Son, J.B. Bdzil, R. Menikoff, and D.S. Stewart. Two-phase modeling of ddt: Structure of the velocity-relaxation zone. *Physics of Fluids*, 9(12):3885–3897, 1997.

[28] O. Le Métayer, J. Massoni, and R. Saurel. Elaborating equations of state of a liquid and its vapor for two-phase flow models. *International Journal of Thermal Sciences*, 43(3):265–276, 2004.

[29] H. Lochon. *Modelling and simulation of steam-water transients using the two-fluid approach.* Phd thesis, Aix Marseille Université, October 2016, https://tel.archives-ouvertes.fr/tel-01379453.

[30] H. Lochon, F. Daude, P. Galon, and J.-M. Hérard. Comparison of two-fluid models on steam-water transients. *ESAIM: Mathematical Modelling and Numerical Analysis*, 50(6):1631–1657, 2016.

[31] H. Mathis. *Theoretical and numerical study of flows with phase transition*. Phd thesis, Université de Strasbourg, September 2010, https://tel.archives-ouvertes.fr/tel-00516683.

[32] H. Mathis. A thermodynamically consistent model of a liquid-vapor fluid with a gas. Working paper or preprint, October 2017, https://hal.archives-ouvertes.fr/hal-01615591.
[33] S. Müller, M. Hantke, and P. Richter. Closure conditions for non-equilibrium multi-component models. *Continuum Mechanics and Thermodynamics*, 28(4):1157–1189, 2016.
[34] V.V. Rusanov. Calculations of interaction of non-steady shock waves with obstacles. *J. Comp. Math. Phys.*, 1:267–279, 1961.
[35] J. Sherman and W.J. Morrison. Adjustment of an inverse matrix corresponding to a change in one element of a given matrix. *The Annals of Mathematical Statistics*, 21(1):124–127, 1950.
[36] W. Wagner and H.-J. Kretzschmar. IAPWS industrial formulation 1997 for the thermodynamic properties of water and steam. *International Steam Tables: Properties of Water and Steam Based on the Industrial Formulation IAPWS-IF97*, pages 7–150, 2008.
[37] N.N. Yanenko. *Méthode à pas fractionnaires. Résolutions de problèmes polydimensionnels de physique mathématique*. Armand Colin, 1968.

B Simulation of a liquid-vapour compressible flow by a Lattice Boltzmann Method

Simulation of a liquid-vapour compressible flow by a Lattice Boltzmann Method

Philippe Helluy, Olivier Hurisse and Lucie Quibel

Abstract This work is devoted to the numerical resolution of a compressible three-phase flow with phase transition by a Lattice-Boltzmann Method (LBM). The flow presents complex features and large variations of physical quantities. The LBM is a robust numerical method that is entropy stable and that can be extended to second order accuracy without additional numerical cost. We present preliminary numerical results, which confirm its competitiveness compared to other Finite Volume methods.

Key words: Lattice Boltzmann Method, compressible flow, phase transition.
MSC (2010)**:** 35Q79, 76M12, 76M28

1 Introduction

In this work, we are interested in the numerical resolution of a hyperbolic system arising in thermohydraulics. The objective is to compute a three-phase flow made of liquid water, vapour and an inert gas (such as air, for instance). Because of the envisaged range of pressure and temperature, there can be phase transition between the liquid and its vapour.

The Equation Of State (EOS) is complex and presents large variations of the thermodynamical parameters. It can be obtained from physical experiments and tabula-

Philippe Helluy
IRMA UMR 7501, Inria Tonus
Université de Strasbourg, France
e-mail: philippe.helluy@unistra.fr

Olivier Hurisse, Lucie Quibel
EDF R&D, 6 quai Watier, 78400 Chatou, France.
e-mail: olivier.hurisse@edf.fr, lucie.quibel@edf.fr

tions. It generally leads to very costly numerical methods, where most of the time is spent in the evaluation of the EOS. In addition, if because of the approximation the EOS does not satisfy some convexity properties, the resulting system of conservation laws may not be hyperbolic and thus unstable. Here we use a simplified pressure law obtained from an entropy optimization procedure. The pressure law was first described in [1]. By construction, it ensures a convex hyperbolic domain and thus stability of some classical Finite Volume (FV) schemes such as Godunov-type schemes [7] or the Bouchut kinetic scheme [2].

The standard FV method is only first order. Its accuracy can be improved by slope reconstruction/limitation techniques. But this induces a cost and a more difficult parallelization because the computation stencil is enlarged.

In this work, we replace the FV scheme by a Lattice Boltzmann Method (LBM). The LBM is based on an abstract kinetic representation of the hyperbolic system. Then the scheme is a succession of free transport steps solved by an exact characteristic shift and relaxation operations that are local to the cell. This makes the LBM very efficient and easy to parallelize. In addition, by simply changing the relaxation parameter, it is possible to adjust the numerical viscosity of the LBM and to achieve second order with no additional cost.

We apply the whole approach for computing a vapour explosion test case.

2 Kinetic approximation of conservation laws

2.1 Vectorial kinetic approximation with over-relaxation

In this work, we are interested in the numerical resolution of a hyperbolic system arising in thermohydraulics. The vector of unknown is denoted $\mathbf{u}(x,t) \in \mathbb{R}^m$. The system has the general form

$$\partial_t \mathbf{u} + \partial_x \mathbf{f}(\mathbf{u}) = 0. \tag{1}$$

The flux $\mathbf{f}$ is a smooth function $\mathbb{R}^m \mapsto \mathbb{R}^m$ satisfying the hyperbolicity property: its jacobian matrix $\mathbf{f}'(\mathbf{u})$ is diagonalizable with real eigenvalues for all $\mathbf{u}$ in the hyperbolicity domain $\mathscr{C}$, which is assumed to be convex. The relaxation approach, introduced by Jin and Xin [9], consists in replacing (1) by an extended system of the form

$$\partial_t \mathbf{u} + \partial_x \mathbf{z} = 0, \tag{2}$$

$$\partial_t \mathbf{z} + \lambda^2 \partial_x \mathbf{u} = \mu. \tag{3}$$

The speed λ is a positive constant. The new vector $\mathbf{z}$ is called the approximated flux. The source term μ is designed in such a way that $\mathbf{z} \simeq \mathbf{f}(\mathbf{u})$. We introduce a time step $\Delta t > 0$ and the Dirac comb:

$$\Psi(t) = \sum_{i\in\mathbb{Z}} \delta(t - i\Delta t).$$

The source term μ is then defined by

$$\mu(x,t) = \Omega\Psi(t)\left(\mathbf{f}(\mathbf{u}(x,t)) - \mathbf{z}(x,t^-)\right), \quad \mathbf{I} \le \Omega \le 2\mathbf{I}.$$

In the more general case, Ω is a matrix called the relaxation matrix. Inequalities on matrices have to be understood, as usual, in the sense of the associated quadratic forms. From the distribution theory, we see that at time $t = i\Delta t$, $\mathbf{z}$ is discontinuous: $\mathbf{z}(x,t^+) \neq \mathbf{z}(x,t^-)$, and

$$\mathbf{z}(x,t^+) = \Omega\mathbf{f}(\mathbf{u}(x,t)) + (\mathbf{I} - \Omega)\mathbf{z}(x,t^-).$$

If the relaxation matrix $\Omega = \mathbf{I}$, we recover in this way the classical first order splitting Jin-Xin algorithm, where $\mathbf{z} = \mathbf{f}(\mathbf{u})$ at the end of each time step. The **over-relaxation** corresponds to $\Omega = 2\mathbf{I}$. It can be proved that the resulting scheme is a second order $O(\Delta t^2)$ approximation of (1). See [3, 5], for instance, and included references.

We can diagonalize the linear hyperbolic operator arising from the left-hand side of (2)-(3). In this way, we obtain a kinetic interpretation of the Jin-Xin approximation. For this, we consider the change of variables

$$\mathbf{k}^+ = \frac{\mathbf{u}}{2} + \frac{\mathbf{z}}{2\lambda}, \quad \mathbf{k}^- = \frac{\mathbf{u}}{2} - \frac{\mathbf{z}}{2\lambda}.$$

$$\mathbf{u} = \mathbf{k}^+ + \mathbf{k}^-, \quad \mathbf{z} = \lambda\mathbf{k}^+ - \lambda\mathbf{k}^-.$$

Then we get

$$\partial_t\mathbf{k}^+ + \lambda\partial_x\mathbf{k}^+ = \mathbf{r}^+, \quad \partial_t\mathbf{k}^- - \lambda\partial_x\mathbf{k}^- = \mathbf{r}^-, \tag{4}$$

where

$$\mathbf{r}^\pm(x,t) = \Omega\Psi(t)\left(\mathbf{k}^{eq,\pm}(\mathbf{u}(x,t^-)) - \mathbf{k}^\pm(x,t^-)\right),$$

and the "Maxwellian" states $\mathbf{k}^{eq,\pm}$ are given by

$$\mathbf{k}^{eq,\pm}(\mathbf{u}) = \frac{\mathbf{u}}{2} \pm \frac{\mathbf{f}(\mathbf{u})}{2\lambda}.$$

In other words, from these calculations, we see that most of the time, the kinetic variables $\mathbf{k}^+$ and $\mathbf{k}^-$ satisfy free transport equations at velocity $\pm\lambda$, with relaxation to equilibrium at each time step.

2.2 Equivalent equation

The equivalent equation allows to better understand the effect of the relaxation matrix Ω. Let us introduce the "flux error" $\mathbf{y} := \mathbf{z} - \mathbf{f}(\mathbf{u})$. The following result holds:

Theorem 1 *If the relaxation matrix satisfies* $\mathbf{I} < \Omega < 2\mathbf{I}$ *and if* $\mathbf{y} = 0$ *at the initial time, then, up to second order terms in* $O(\Delta t^2)$, $\mathbf{u}$ *is a solution of the following system of conservation laws*

$$\partial_t \mathbf{u} + \partial_x \mathbf{f}(\mathbf{u}) = \Delta t \partial_x \left((\Omega^{-1} - \frac{1}{2}\mathbf{I})(\lambda^2 \mathbf{I} - \mathbf{f}'(\mathbf{u})^2)\partial_x \mathbf{u} \right) + O(\Delta t^2).$$

Remark 1 The proof is based on standard Taylor expansions. For a rigorous formulation and proof, we refer to [4]. The approach is classical in the analysis of the Lattice Boltzmann Method (LBM). See also for instance [6, 10, 5].

Remark 2 The above analysis allows to recover formally the so-called sub-characteristic condition. Assuming that $\mathbf{I} < \Omega < 2\mathbf{I}$, the second order ("viscous") terms have the good sign, which ensures stability of the model, if the following matrix is positive:

$$\mathbf{V}(\mathbf{u}) = \lambda^2 \mathbf{I} - \mathbf{f}'(\mathbf{u})^2 > 0. \tag{5}$$

3 Numerical methods

Our objective is to design a specific Lattice Boltzmann Method (LBM) for approximating three-phase flow. For comparison, we need a classical finite volume method, which we describe now.

3.1 Finite volume method

The finite volume scheme (FV scheme in the sequel) is constructed for approximating the solutions of (1). We denote by Δx the space step and by Δt the time step. We assume that the space step and the time step are related by a Courant-Friedrichs-Lewy (CFL) relation $\Delta t = \beta \frac{\Delta x}{\lambda}$, where $\beta > 0$ is the CFL number. We use the same velocity λ in the FV and LBM methods for defining the CFL number. Because of the sub-characteristic condition (5), λ is larger than the wave speeds of (1). We thus expect that the FV scheme will be stable at least for $\beta < 1$.

We look for an approximation

$$\mathbf{u}_i^n \simeq \frac{1}{\Delta x} \int_{x_{i-1/2}}^{x_{i+1/2}} \mathbf{u}(x, t_n) dx \simeq \mathbf{u}(x_i, t_n), \quad x_i = i\Delta x, \quad t_n = n\Delta t.$$

We consider the FV scheme

$$\frac{\mathbf{u}_i^{n+1} - \mathbf{u}_i^n}{\Delta t} + \frac{\mathbf{f}(\mathbf{u}_i^n, \mathbf{u}_{i+1}^n) - \mathbf{f}(\mathbf{u}_{i-1}^n, \mathbf{u}_i^n)}{\Delta x} = 0.$$

The numerical flux $\mathbf{f}(\cdot,\cdot)$ is the Rusanov flux given by

$$\mathbf{f}(\mathbf{u},\mathbf{v}) = \frac{\mathbf{f}(\mathbf{u})+\mathbf{f}(\mathbf{v})}{2} - \frac{\max(\rho(\mathbf{f}'(\mathbf{u})),\rho(\mathbf{f}'(\mathbf{v})))}{2}(\mathbf{v}-\mathbf{u}),$$

where $\rho(\mathbf{M})$ is the spectral radius of matrix $\mathbf{M}$.

3.2 Lattice Boltzmann Method (LBM)

In the LBM scheme, we assume that the CFL number $\beta = 1$. This allows to solve the free transport steps exactly. More precisely, if we also denote by $\mathbf{u}_i^n$, $\mathbf{z}_i^n$, $\mathbf{k}_i^{\pm,n}$ the approximation of $\mathbf{u}$, $\mathbf{z}$ and $\mathbf{k}^{\pm}$ at points x_i and time t_n, the transport step is given by simple shift operations, which solve the free transport equations (4) exactly

$$\mathbf{k}_i^{-,n+1-} = \mathbf{k}_{i+1}^{-,n}, \quad \mathbf{k}_i^{+,n+1-} = \mathbf{k}_{i-1}^{+,n}.$$

Then, one takes

$$\mathbf{u}_i^{n+1} = \mathbf{k}_i^{-,n+1-} + \mathbf{k}_i^{+,n+1-}, \quad \mathbf{z}_i^{n+1-} = -\lambda\mathbf{k}_i^{-,n+1-} + \lambda\mathbf{k}_i^{+,n+1-}.$$

The relaxation step is then

$$\mathbf{z}_i^{n+1} = \mathbf{z}_i^{n+1-} + \Omega(\mathbf{u}_i^{n+1})\left(\mathbf{f}(\mathbf{u}_i^{n+1}) - \mathbf{z}_i^{n+1-}\right).$$

4 Application to a three-phase flows

We wish to apply the above theory to a compressible three-phase flow model (two gases and a liquid). Because of strong variations in pressure and temperature, the liquid will undergo phase transition, which requires a proper mathematical model. The unknowns are the density ρ, the velocity u, the pressure p, the internal energy e and the mass fraction of the inert gas

$$\varphi = \varphi_3.$$

The total energy E is the sum of the internal energy and the kinetic energy:

$$E = \rho e + \frac{1}{2}\rho u^2.$$

The pressure Equation Of State (EOS) is of the form

$$p = p(\rho, e, \varphi).$$

The three-phase flow model is a system of conservation laws of the form (1) with

$$\mathbf{u} = (\rho, \rho u, \rho E, \rho \varphi)^\mathsf{T}, \quad \mathbf{f}(\mathbf{u}) = (\rho u, \rho u^2 + p, (\rho E + p)u, \rho u \varphi)^\mathsf{T}.$$

Now we sketch the practical construction of the three-phase pressure law. This construction has to be done with care in order to ensure that the hyperbolicity domain $\mathscr{C}$ is convex. The general principles are mainly given in [8, 1]. We recall them now.

4.1 Entropy optimization

The mass fractions of the phases are noted φ_i, the volume fractions, α_i and the energy fractions, ζ_i. The phase specific volumes τ_i and energies e_i are related to the mixture specific volume τ and energy e by

$$\tau_i = \frac{\alpha_i}{\varphi_i}\tau, \quad e_i = \frac{\zeta_i}{\varphi_i}e. \tag{6}$$

The mass fraction φ_3 of the inert gas is supposed to be fixed and given. We thus introduce the vector of the unknown fractions $Y = (\varphi_1, \varphi_2, \alpha_1, \alpha_2, \alpha_3, \zeta_1, \zeta_2, \zeta_3)$. The unknown fractions satisfy the following constraints

$$Y \in Q := [0,1]^8 \cap \{\alpha_1 = \alpha_3, \alpha_1 + \alpha_2 = 1, \varphi_1 + \varphi_2 + \varphi_3 = 1, \zeta_1 + \zeta_2 + \zeta_3 = 1\}. \tag{7}$$

These constraints are justified by the fact that the two gases are perfectly miscible (Dalton's law) and that the liquid and the gases are non-miscible. The mixture entropy is then given by a convex optimization problem:

$$s(\tau, e, \varphi_3) = \max_{Y \in Q} \sum_{i=1}^{3} \varphi_i s_i(\frac{\alpha_i}{\varphi_i}\tau, \frac{\zeta_i}{\varphi_i}e), \tag{8}$$

where s_i is the entropy function of phase (i).

Once the optimization problem is solved, the temperature T and the pressure p of the mixture are then given by

$$T = 1/\frac{\partial s}{\partial e} \quad p = T\frac{\partial s}{\partial \tau}.$$

The major advantage of the above construction is that it ensures that the hyperbolicity domain is convex. We now give more details on the computations (initially presented in [1].)

We thus consider a mixture of three phases (1), (2) and (3) representing the vapour, the liquid and the non-condensable gas (air), respectively. The liquid is not miscible with the two others, while the vapour and the gas are miscible. We only admit phase transition between vapour (1) and liquid (2). Each phase obeys a stiffened gas

Equation Of State (EOS), where the entropy function s_i is defined by

$$s_i(\tau_i, e_i) = C_i \ln((e_i - Q_i - \pi_i\tau_i)\tau_i^{\gamma_i - 1}) + s_i^0 \quad i = 1,2,3. \tag{9}$$

In this formula, C_i is the specific heat at constant volume, Q_i is the heat of formation, π_i is the reference pressure and s_i^0 the reference entropy. The specific energy is noted e_i and the specific volume τ_i is the inverse of the density $1/\rho_i$.

Let us recall some basic computations related to the stiffened gas EOS. The temperature T_i and the pressure p_i are given by

$$\frac{1}{T_i} = \frac{\partial s_i}{\partial e_i}, \quad \frac{p_i}{T_i} = \frac{\partial s_i}{\partial \tau_i}.$$

With (9) this implies the following relations

$$C_i T_i = e_i - Q_i - \pi_i \tau_i, \tag{10}$$

$$p_i + \pi_i = (\gamma_i - 1)\rho_i C_i T_i. \tag{11}$$

The chemical potential $\mu_i = e_i + p_i\tau_i - T_i s_i$ is given by

$$\mu_i = Q_i + \gamma_i C_i T_i - T_i \left(C_i \ln(C_i T_i \tau_i^{\gamma_i - 1}) + s_0^i \right).$$

It is interesting to also write it in the (p,T) variables. This is obtained by noting that

$$\tau_i = \frac{(\gamma_i - 1)C_i T_i}{p_i + \pi_i},$$

then (dropping the indices for better readability)

$$\mu = Q + \gamma CT - CT\left(\gamma \ln(CT) - (\gamma - 1)\ln(p + \pi) + (\gamma - 1)\ln(\gamma - 1) + s^0/C\right).$$

Introducing

$$K = (\gamma - 1)\ln(\gamma - 1) + s^0/C, \quad K' = CK + \gamma C \ln C,$$

we get

$$\mu = Q + \gamma CT - CT\left(\gamma \ln(CT) - (\gamma - 1)\ln(p + \pi) + K\right),$$

or

$$\mu = Q + \gamma CT - CT\left(\gamma \ln(T) - (\gamma - 1)\ln(p + \pi)\right) - K'T.$$

The last expression allows to fit the values of $K_1' - K_2'$ by taking values of (p,T) on the saturation curve, where $\mu_1(p,T) = \mu_2(p,T)$. Once one gets K' (up to a constant), we deduce K and then s^0

$$s^0 = CK - C(\gamma - 1)\ln(\gamma - 1).$$

In practice, the reference entropy s^0 for the inert gas (3) does not need to be evaluated, because there will be no mass transfer with this gas.

In the same spirit, we observe that the Euler equations are still valid if we replace ε by $\varepsilon - \varphi_3 Q_3$. This means that in practice, we can take $Q_3 = 0$. Realistic parameters, adjusted with physical experiments are given in Table 1.

We now consider a mixture of the three phases. We denote by V_i the volume, M_i the mass and E_i the energy of each phase (i). We wish to compute the pressure law for a mixture of volume V, mass M and energy E. In other words, we want to compute the pressure from the knowledge of $\tau = V/M$, $e = E/M$ and the mass fraction $\varphi_3 = M_3/M$ of the non-condensable gas, i.e.,

$$p = p(\tau, e, \varphi_3).$$

We introduce the volume fraction $\alpha_i = V_i/V$, the mass fraction $\varphi_i = M_i/M$ and the energy fraction $\zeta_i = E_i/E$ of phase (i).

With the help of the fractions, we can express the partial intensive quantities from the global ones

$$\tau_i = \frac{\alpha_i}{\varphi_i}\tau, \quad e_i = \frac{\zeta_i}{\varphi_i}e. \tag{12}$$

We also have, of course, because $\rho = 1/\tau$

$$\rho_i = \frac{\varphi_i}{\alpha_i}\rho. \tag{13}$$

Because phases (1) and (3) are miscible and phase (3) is non-miscible with the other phases, the volumes are subject to the constraints

$$V_1 = V_3, \quad V_1 + V_2 = V. \tag{14}$$

The conservation of mass and energy reads

$$M = M_1 + M_2 + M_3, \quad E = E_1 + E_2 + E_3.$$

From these constraints, we deduce

$$\alpha_1 = \alpha_3, \qquad \alpha_1 + \alpha_2 = 1, \tag{15}$$

$$\varphi_1 + \varphi_2 + \varphi_3 = 1, \quad \zeta_1 + \zeta_2 + \zeta_3 = 1. \tag{16}$$

In this way, we justify the form of the constraint set Q already introduced in (7). The optimization problem (8) can thus also be written

$$s(\tau, e, \varphi_3) = \max_{0 \le \varphi_1, \alpha_1, \zeta_1, \zeta_2 \le 1} s_{\text{mix}}(\tau, e, \varphi_3; \varphi_1, \alpha_1, \zeta_1, \zeta_2), \tag{17}$$

with

$$\zeta_3 = 1 - \zeta_2 - \zeta_1, \quad \varphi_2 = 1 - \varphi_1 - \varphi_3, \quad \alpha_3 = \alpha_1, \quad \alpha_2 = 1 - \alpha_1,$$

and

$$s_{\text{mix}}(\tau, e, \varphi_3; \varphi_1, \alpha_1, \zeta_1, \zeta_2) = \sum_{i=1}^{3} \varphi_i s_i(\frac{\alpha_i}{\varphi_i}\tau, \frac{\zeta_i}{\varphi_i}e).$$

At this point, the entropy would depend on τ, e, φ_3 but also on $\alpha_1, \varphi_1, \zeta_1, \zeta_2$. We have to eliminate the four supplementary fractions by successive optimization with respect to (ζ_1, ζ_2), α_1 and then φ_1. This correspond to three steps, which consist in considering the temperature, the pressure and the chemical equilibrium.

4.2 Temperature equilibrium.

The first step is to optimize the mixture entropy (8) with respect to ζ_1 and ζ_2. We compute the derivative of s_{mix} with respect to ζ_1 and ζ_2 and obtain

$$\frac{\partial}{\partial \zeta_1} s_{\text{mix}} = \frac{1}{T_1} - \frac{1}{T_3}, \quad \frac{\partial}{\partial \zeta_2} s_{\text{mix}} = \frac{1}{T_2} - \frac{1}{T_3}.$$

We assume that the optimum is reached for $T = T_1 = T_2 = T_3$. We can then eliminate the energy fractions (ζ_1, ζ_2). Using relations (10) and (12), we obtain

$$\sum_{i=1}^{3} \varphi_i C_i T = e - \sum_{i=1}^{3} \varphi_i Q_i - \sum_{i=1}^{3} \alpha_i \pi_i \tau.$$

We then define the following mixture parameters:

$$\begin{array}{ll} C = \sum_{i=1}^{3} \varphi_i C_i, & Q = \sum_{i=1}^{3} \varphi_i Q_i, \\ \pi = \sum_{i=1}^{3} \alpha_i \pi_i, & \gamma = \frac{\sum_{i=1}^{3} \varphi_i \gamma_i C_i}{\sum_{i=1}^{3} \varphi_i C_i}, \end{array} \tag{18}$$

in such a way that

$$CT = e - Q - \pi\tau.$$

Analogously, we define the mean pressure by

$$p = \sum_{i=1}^{3} \alpha_i p_i = \alpha_1(p_1 + p_3) + (1 - \alpha_1)p_2.$$

Thus

$$p + \pi = \sum_{i=1}^{3} \alpha_i(\gamma_i - 1)\rho_i C_i T.$$

with (13) we get

$$p + \pi = (\gamma - 1)\rho C T. \tag{19}$$

We conclude that assuming the temperature equilibrium leads again to a stiffened gas EOS for the mean pressure

$$p = (\gamma - 1)\rho(e - Q) - \gamma\pi,$$

where the mixture parameters are defined by (18). In this way, the mixture parameters do not depend on the energy fractions. Let us also remark that we could, but we do not have to, compute the energy fractions. Maybe it would be interesting to anyway compute them, at least for verifying that they are between 0 and 1 and that the phase temperatures T_i are indeed > 0...

4.3 Pressure equilibrium.

The derivative of s_{mix} with respect to the gas volume fraction α_1 is given by

$$\frac{\partial}{\partial \alpha_1} s_{\text{mix}} = \frac{p_1}{T_1} + \frac{p_3}{T_3} - \frac{p_2}{T_2}$$

Assuming temperature equilibrium, we have thus

$$\frac{\partial}{\partial \alpha_1} s_{\text{mix}} = \frac{p_1 + p_3 - p_2}{T}.$$

If the entropy optimum is reached for $0 < \alpha_1 < 1$, we recover the physical fact that the pressure mixture p has to satisfy

$$p = p_1 + p_3 = p_2.$$

In other words, the gas pressure $\tilde{p}$ is given by the Dalton law $\tilde{p} = p_1 + p_3$. And the non-miscibility of the gases with the liquid implies that the liquid pressure p_2 is equal to the gas pressure $\tilde{p}$.

Using relation (19), we get

$$\left((\gamma_1 - 1) \frac{\varphi_1}{\alpha_1} \frac{C_1}{C} + (\gamma_3 - 1) \frac{\varphi_3}{\alpha_1} \frac{C_3}{C} \right) \rho CT - \pi_1 - \pi_3 = (\gamma_2 - 1) \frac{1 - \varphi_1 - \varphi_3}{1 - \alpha_1} \frac{C_2}{C} \rho CT \; - \; \pi_2, \tag{20}$$

where

$$CT = e - Q - (\alpha_1(\pi_1 + \pi_3 - \pi_2) + \pi_2)\tau. \tag{21}$$

If we multiply (20) by $\alpha_1(1 - \alpha_1)$, we obtain a second order equation in α_1.The difficulty is that this equation does not always admit one single root in $(0,1)$ denoted by $\alpha_1(\varphi_1)$. Another difficulty is that the temperature has to be > 0.

From now on, in order to get simpler calculations, we assume that the two gases are perfect gases, which leads to

$$\pi_1 = \pi_3 = 0.$$

We also assume that for the liquid,

$$\pi_2 \neq 0.$$

From the temperature expression (21), imposing $T \geq 0$, we then obtain the following constraint on α_2:

$$\alpha_2 \leq \frac{\rho(e-Q)}{\pi_2}.$$

Therefore,

$$\alpha_1 \in [1-\delta, 1], \quad \delta = \min(1, \max(0, \frac{\rho(e-Q)}{\pi_2}).$$

In this expression, it is important to remember that Q depends on φ_1 from (18).

Actually, mathematically, it could happen that the optimum is attained at a boundary of the interval $[1-\delta, 1]$. This can be decided by considering the sign of $\frac{\partial}{\partial \alpha_1} s_{\text{mix}}$ at $\alpha_1 = 1-\delta$ or $\alpha_1 = 1$. If the temperature is positive, $\frac{\partial}{\partial \alpha_1} s_{\text{mix}}$ has the same sign as $p_1 + p_3 - p_2$.

We thus consider the pressure difference

$$\Delta p(\alpha_1) = p_1 + p_3 - p_2,$$

and the algorithm for finding the maximum with respect to α_1 is the following:

- if $\Delta p(1-\delta) < 0$ then the liquid is more stable than the vapor and $\alpha_1(\varphi_1) = 1-\delta$.
- else if $\Delta p(1) > 0$ then the gases are more stable than the liquid and $\alpha_1(\varphi_1) = 1$.
- else, it is possible to equilibrate the pressures and one computes $\alpha_1(\varphi_1)$ such that $\Delta p(\alpha_1) = 0$. The equation can be solved by a dichotomy algorithm or directly by solving a second order equation.

4.4 Chemical equilibrium.

Finally, we proceed to the optimization with respect to φ_1. Assuming temperature equilibrium, the partial derivative of the entropy is now given by

$$\frac{\partial}{\partial \varphi_1} s_{\text{mix}} = -\frac{\mu_1 - \mu_2}{T}.$$

The first step is to express the chemical potential as a function of τ, e and φ_1. For this, we write

$$\mu_i = Q_i + \frac{C_i}{C}(e - Q - \pi\tau) \times \left(\gamma_i - \frac{s_i^0}{C_i} - \ln\left(\frac{C_i}{C}(e-Q-\pi\tau)\left(\frac{\alpha_i}{\varphi_i}\tau\right)^{\gamma_i - 1}\right)\right),$$

where the mixture parameters C, Q, π are given by (18). Now we need to determine φ_1 in order to compute the pressure law. Going back to the constrained optimization problem, we apply the same procedure as for the pressure equilibrium.

We first compute the maximal mass fraction $\varphi_1 \in [0, 1-\varphi_3]$ such that $CT = e - Q(\varphi_1) - \pi(\alpha_1(\varphi_1)) \geq 0$. Let us denote by $\varphi_{1,\max}$ this fraction.

- if $\mu_1(\varphi_{1,\max}) < \mu_2(\varphi_{1,\max})$, the mass fraction of the vapor $\varphi_1 = \varphi_{1,\max}$ corresponds to a stable case. If $\varphi_{1,\max} = 1-\varphi_3$ then $\varphi_2 = 0$, i.e., the mixture contains no liquid but vapor only;
- else if $\mu_1(0) > \mu_2(0)$, the mass fraction of the vapor $\varphi_3 = 0$ corresponds to a stable case, thus $\varphi_2 = 1-\varphi_3$, i.e., the mixture contains no vapor but liquid only;
- else the mixture is necessarily at saturation and we have to compute the mass fraction φ_1 such that $\mu_1(\varphi_1) = \mu_2(\varphi_1)$. This gives a mass fraction such that $0 < \varphi_1 < \varphi_{1,\max}$, i.e., the mixture is at saturation and contains vapor and liquid and $\varphi_2 = 1-\varphi_1-\varphi_3$. The equation is solved by a dichotomy algorithm.

Once the mass fraction φ_1 is computed, it is possible to compute all the other quantities and thus the mixture pressure $p = p(\tau, e, \varphi_3)$ according to (19).

4.5 Numerical application

For practical applications, one needs first to adjust the physical constants appearing in the expression of the entropy. As we have shown in another chapter of this thesis, the stiffened gas law is too simple to give a very accurate description of the liquid-vapor mixture. Anyway, it is possible to represent at least qualitatively the main features of the pressure law.

An example of possible parameters are given in Table 1. Those parameters have been adjusted in order to respect the speeds of sounds in the different phases and to fit the saturation curve in a given region.. Once these parameters are been fixed, then it is possible to apply the algorithms given in Section 4 for computing the pressure law. However, in practical applications, we have observed that it is not so easy to compute the entropy-optimal point. Indeed it is difficult to ensure that the fractions remain in the interval $[0, 1]$ because of rounding errors, and non-physical values may arise.

In order to put in evidence the practical difficulty, we introduce a numerical example. We consider the following density and energy of the mixture

$$\rho = 817.12 \text{ kg/m}^3, \quad e = 4.1848 \times 10^5 \text{J/kg}.$$

We also fix the mass fraction of the inert gas to

$$\varphi_3 = 10^{-6}.$$

We then plot the vapor volume fraction $\alpha_1(\varphi_1)$ that realizes the maximum of the entropy with respect to α_1. In this case, $\delta = 1$ (see Section 4.3). We then obtain the plot of Figure 1.

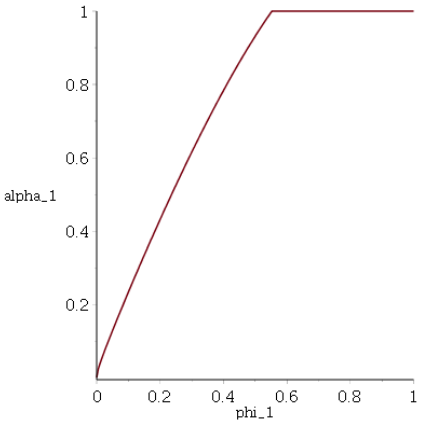

Fig. 1 Vapor equilibrium volume fraction as a function of the mass fraction.

As is physically intuitive, $\alpha_1$is an increasing function of φ_1 and $\alpha_1(0) = 0$, $\alpha_1(1) = 1$. We also put in evidence a threshold value φ^* of φ_1 such that $\alpha_1(\varphi_1) = 1$ if $\varphi_1 \geq \varphi^*$. This corresponds to a saturation of the constraint $\alpha_1 \leq 1$ in the optimization problem. When $\varphi_1 \geq \varphi^*$, it is no more possible to ensure that $p_1 + p_3 = p_2$.

We assume now that the entropy is optimized with respect to α_1, i.e. that $\alpha_1 = \alpha_1(\varphi_1)$. On Figure 2, we then plot the difference of chemical potentials $\mu_1(\varphi_1) - \mu_2(\varphi_1)$.

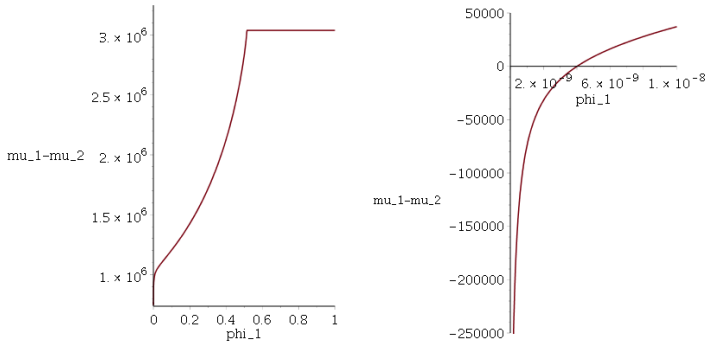

Fig. 2 Chemical potential difference as a function of the vapor mass fraction. General view (left). Zoom around $\varphi_1 = 0$ (right). The zoomed picture shows that in the equilibrium mixture there will be a little amount of vapor.

We also observe on this picture a constraint saturation effect. At a first glance, it seems that this difference is always positive and thus that the optimum corresponds to $\varphi_1 = 0$. However, when one zooms around $\varphi_1 = 0$ it is clear that there must be a little amount of vapor in the mixture. It sounds physically. Indeed, in reality if we consider some liquid water left in a room filled with air at a given temperature T, then the water will be changed into vapor until the partial pressure of a vapor reaches the saturation pressure $p_{\text{sat}}(T)$. This phenomenon is related to the relative humidity of air. It is interesting that the stiffened gas modeling allows to recover this behavior.

5 Vapour explosion test

We consider a test case relevant for thermohydraulics. This is quite a realistic modelling of a sudden depressurization of a heated liquid in a pipe. The left (L) part of the pipe is filled with pressurized heated water. The right (R) part of the pipe is filled with air at ambient temperature and pressure. The numerical parameters are summed up in Table 1.

param.	vapour (1)	liquid (2)	gas (3)
γ_i	1.3	3	1.4
π_i (Pa)	0	8533×10^5	0
C_i (J.kg^{-1}.K^{-1})	1615.38	1400	719.28
Q_i (J.kg^{-1})	1.892×10^6	-1.1148×10^6	0
s_i^0	583.46	16658.99	263.62

	liquid (L)	air (R)
ρ	554.09	1.186245
e	1161999.729	210749.040
φ	10^{-6}	$1 - 10^{-6}$

Table 1 Left: physical parameters for the three phases. Right:initial data for the vapor explosion test case.

At time $t = 0$, the liquid-air separation is removed. We plot several physical quantities at time $t = 1.2$ms. We expect a complex wave structure. From left to right: a rarefaction wave running into the liquid, a slower vaporization wave running into the liquid, a contact wave, and finally a shock wave running into the air. Let us remark the presence of a non-standard split wave made of two simple waves. This is a typical feature of Riemann problems with non-convex equations of state arising from phase transition problematics.

The LBM is tested with a kinetic velocity $\lambda = 2500$ m/s, an over-relaxation parameter $\Omega = \mathbf{I}$ (first order) and $\Omega = 1.9\mathbf{I}$ (improved precision). The second order LBM scheme with $\Omega = 2\mathbf{I}$ is unstable here, which is not surprising because there is a shock wave to capture.

The results of the LBM scheme with $\Omega = \mathbf{I}$ are plotted on Figure 3.

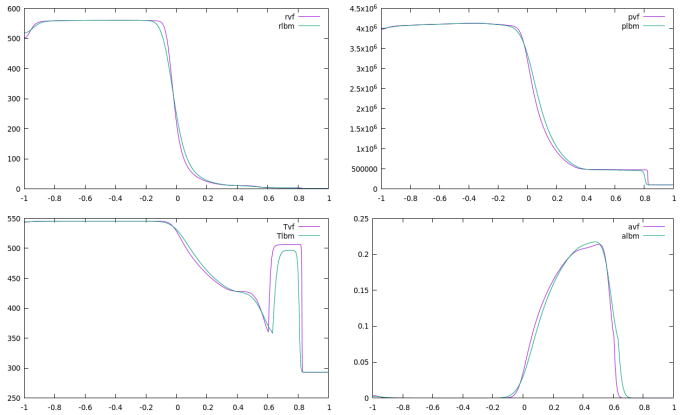

Fig. 3 Numerical solution of the Riemann problem described in Table 1. Top left: density, top right: pressure, bottom left: temperature, bottom right: vapour mass fraction. Comparison between the Finite Volume and Lattice Boltzmann Method with $\Omega = \mathbf{I}$ on a mesh with 2000 cells.

We observe that the results of the LBM and FV scheme are similar. It also appears that with $\Omega = \mathbf{I}$ the LBM scheme is more diffusive than the FV scheme. This could be expected because in this case, the LBM scheme is nothing else than a Rusanov scheme with a fixed numerical viscosity proportional to λ. In the Rusanov scheme, the numerical viscosity is adjusted in a slightly more clever way.

On Figure 4, we compare the numerical solutions obtained by the FV scheme and the LBM scheme with $\Omega = 1.9\mathbf{I}$.

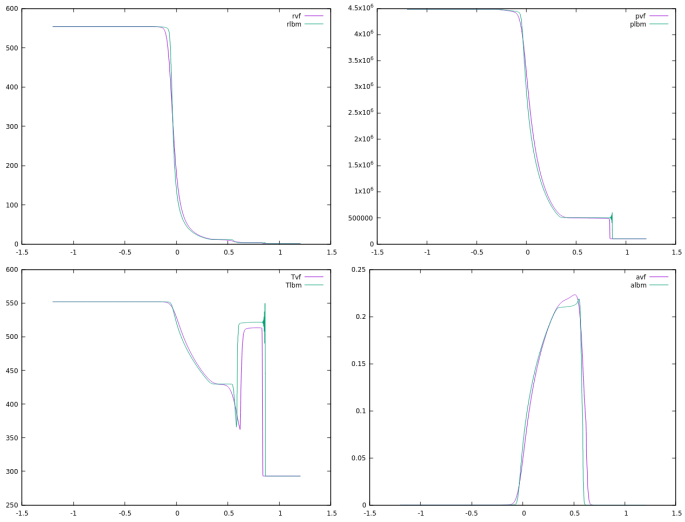

Fig. 4 Numerical solution of the Riemann problem described in Table 1. Top left: density, top right: pressure, bottom left: temperature, bottom right: vapour mass fraction. Comparison between the Finite Volume and Lattice Boltzmann Method with $\Omega = 1.9\mathbf{I}$ on a mesh with 2000 cells.

We observe a better precision of the improved LBM scheme with $\Omega = 1.9\mathbf{I}$: the simple waves are better resolved. We observe small oscillations in the discontinuities. It is not surprising because $\Omega = 1.9\mathbf{I}$ corresponds almost to a second order scheme without limiters. We are currently working on a better strategy for adapting locally the value of Ω for suppressing oscillations.

Finally, we compare the performance of the FV scheme and the LBM scheme. The main computation loop of our code is parallelized with simple OpenMP directives. The program is executed on a 2×8 cores Intel Xeon computer. The frequency of the CPU is of 1.70GHz. We compare the CPU time of the FV and LBM implementation for several mesh sizes.

number of cells	500	1000	2000
FV	6 s	19 s	72 s
LBM	1 s	4 s	14 s

Table 2 CPU time comparison between the FV and LBM implementations.

We observe that the LBM approach is more than 4 times faster than the FV approach. The reasons are that the stability time step of the Rusanov scheme is approximately twice smaller than the LBM time step and that the FV numerical flux requires two evaluations of the physical flux instead of one for the LBM method.

An interesting feature of the LBM approach is also that the CPU time does not depend on the value of Ω. A second order MUSCL extension of the Rusanov scheme

would imply approximately a doubled CPU time, because of the slope reconstructions algorithm.

6 Conclusion

We have constructed a numerical scheme based on the LBM. This scheme is faster and more precise than a classical FV method. It has been successfully validated on a complex three-phase flow with phase transition. It is possible to adjust its precision and stability thanks to the over-relaxation parameter Ω, with no additional computational cost. In future works we will study strategies for completely avoiding numerical oscillations in shock waves. This can certainly be achieved because the LBM scheme with $\Omega = \mathbf{I}$ is free of oscillations and entropy-dissipative.

References

1. Mathieu Bachmann, Siegfried Müller, Philippe Helluy, and Hélène Mathis. A simple model for cavitation with non-condensable gases. In *Hyperbolic Problems: Theory, Numerics and Applications (In 2 Volumes)*, pages 289–296. World Scientific, 2012.
2. François Bouchut. Construction of BGK models with a family of kinetic entropies for a given system of conservation laws. *Journal of Statistical Physics*, 95(1-2):113–170, 1999.
3. David Coulette, Emmanuel Franck, Philippe Helluy, Michel Mehrenberger, and Laurent Navoret. High-order implicit palindromic discontinuous galerkin method for kinetic-relaxation approximation. *Computers & Fluids*, 190:485 – 502, 2019.
4. Clémentine Courtès, David Coulette, Emmanuel Franck, and Laurent Navoret. Vectorial kinetic relaxation model with central velocity. application to implicit relaxations schemes. 2018.
5. Florence Drui, Emmanuel Franck, Philippe Helluy, and Laurent Navoret. An analysis of over-relaxation in a kinetic approximation of systems of conservation laws. *Comptes Rendus Mécanique*, 347(3):259–269, 2019.
6. François Dubois. Equivalent partial differential equations of a lattice boltzmann scheme. *Computers & Mathematics with Applications*, 55(7):1441–1449, 2008.
7. Amiram Harten, Peter D Lax, and Bram van Leer. On upstream differencing and godunov-type schemes for hyperbolic conservation laws. *SIAM review*, 25(1):35–61, 1983.
8. Philippe Helluy and Hélène Mathis. Pressure laws and fast legendre transform. *Mathematical Models and Methods in Applied Sciences*, 21(04):745–775, 2011.
9. Shi Jin and Zhouping Xin. The relaxation schemes for systems of conservation laws in arbitrary space dimensions. *Communications on Pure and Applied Mathematics*, 48(3):235–276, 1995.
10. Hiroshi Otomo, Bruce M Boghosian, and François Dubois. Two complementary lattice-boltzmann-based analyses for nonlinear systems. *Physica A: Statistical Mechanics and its Applications*, 486:1000–1011, 2017.

Cette thèse porte sur la modélisation et la simulation d'écoulements multiphasiques qui pourraient apparaître lors de scénarios accidentels pouvant hypothétiquement affecter un réacteur à eau pressurisée. Un modèle homogène diphasique a d'abord été fermé à l'aide une loi tabulée construite à partir de la formulation IAPWS-IF97. Puisque la table a été construite de façon à respecter la relation de Gibbs, la vérification du modèle via des études de convergence en maillage a pu être menée à bien. Sur les cas de validation, une bonne prise en compte des effets hors-équilibre, via la définition d'échelle de temps de retour vers l'équilibre thermodynamique, semble déterminante pour obtenir des résultats réalistes. La quantité de gaz incondensables a de plus une grande influence sur les résultats. Une revue bibliographique de lois d'état classiques a enfin mis en évidence que les lois d'état semi-analytiques de type Noble-Able Stiffened Gas apparaissent comme un bon compromis en termes de précision et d'efficacité. Une autre partie de ces travaux concerne la proposition d'un nouveau modèle triphasique multi-vitesse, destiné à modéliser les phénomènes de type explosion vapeur. Enfin, un travail transversal à la thèse a porté sur la vérification de conditions limites pour le système d'Euler monophasique.

This PhD work deals with the modelling and the simulation of multphasic flows, which may appear during hypothetical accidental scenarios, which might affect the primary circuit of a pressurized water reactor. A homogeneous two-phase flow model has been closed with a look-up table based on the IAPWS-IF97 formulation. As the look-up table fulfills the Gibbs relation, verification of the model has been achieved thanks to convergence studies. On validation test cases, out-of-equilibrium effects have to be taken into account to get realistic results, through the definition of a time scale for the return towards thermodynamical equilibrium. The proportion of non-condensable gas in the mixture has a strong influence on results. Classical equations of state (EOS) have morevover been studied. Noble-Stiffened gas EOS appears as a good compromise in terms of accuracy and efficiency. Another part of this work consists in the proposition of a new three-phase flow multifluid model with four fields to model the explosion vapor phenomenon. Last, some classical numerical boundary conditions for the monophasic Euler system have been verified.

INSTITUT DE RECHERCHE MATHÉMATIQUE AVANCÉE
UMR 7501
Université de Strasbourg
CNRS
IRMA, UMR 7501
7 rue René Descartes
F-67000 STRASBOURG

Tél. 03 68 85 01 29

irma.math.unistra.fr
irma@math.unistra.fr

IRMA 2020/006
http://tel.archives-ouvertes.fr/tel-02941486